

**Synthesis, Properties, and Evaluation of Mn(I)
Tetracarbonyl Complexes Designed for Therapeutic
Release of Carbon Monoxide**

Benjamin James Aucott

PhD

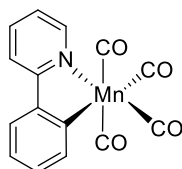
University of York

Chemistry

September 2018

Abstract

This Thesis comprises an investigation of $[\text{Mn}(\text{ppy})(\text{CO})_4]$ ($\text{ppy} = 2\text{-phenylpyridyl}$), **88**, and related Mn(I) tetracarbonyl complexes, for application as carbon monoxide-releasing molecules (CORMs). The photochemical behaviour of $[\text{Mn}(\text{ppy})(\text{CO})_4]$ was studied using ultrafast time-resolved infrared spectroscopy (TRIR) to probe light-triggered CO-release (Chapter 2). Compared to the isoelectronic complex $[\text{Cr}(\text{bpy})(\text{CO})_4]$, a striking difference in the balance between CO-release and unreactive excited state formation is observed, providing insight into why photo-CO release is inefficient in some compounds. Novel intermediates in light-triggered CO dissociation were detected on the picosecond timescale including C-H σ -complexes. Over longer (minute) timescales, complementary *in situ* infrared experiments suggested possible production of multinuclear Mn-hydroxy clusters in wet organic solvents. Thus, new evidence for the light-triggered CO-release mechanism is provided.



88

Three novel ferrocene-containing $[\text{Mn}(\text{ppy})(\text{CO})_4]$ -derived CORMs, a family of compounds incorporating two organometallic therapeutic moieties within the same molecule, are described (Chapter 3). Although these CORMs are all redox-active and were all capable of photo-induced CO-release it was not possible to achieve redox-triggered CO-release. To further probe the possibility of redox-triggered CO-release, tetracarbonyl Mn compounds incorporating a cyclometalated azo ligand, a metal-free redox-active moiety, also shown to increase the CO-release wavelength of tricarbonyl Mn(I) complexes, were synthesised (Chapter 4). Although CO-release at a higher wavelength of light can be attributed to the azo, redox-release is not possible and TRIR shows that unreactive excited states dominate over CO photodissociation. Thus, this work demonstrates the need to consider both efficiency and wavelength in designing triggered-CO release and emphasises the value of the mechanistic work described.

Finally, fluorescent labelling of a $[\text{Mn}(\text{ppy})(\text{CO})_4]$ derivative is reported (Chapter 5). Confocal microscopy of mammalian and bacterial samples proves that viable cells of both types will uptake such CORMs and the methodology for assaying the antibiotic activity of photoCORMs is significantly improved to minimise age effects of the bacteria.

List of Contents

Abstract.....	2
List of Contents.....	3
List of Figures.....	8
List of Schemes.....	29
List of Tables.....	34
Additional Materials.....	36
Acknowledgements.....	37
Author's Declaration.....	38
1 Introduction.....	39
1.1 Carbon Monoxide in Biology.....	39
1.1.1 Toxicity.....	39
1.1.2 Endogenous CO Production.....	40
1.1.3 Physiological and Therapeutic Effects of CO.....	43
1.1.3.1 Relationship of CO with Soluble Guanylyl Cyclase.....	43
1.1.3.2 Relationship of CO with Reactive Oxygen Species.....	44
1.1.3.3 Effect of CO on Inducible NO Synthase.....	46
1.1.3.4 Effect of CO on Ion Channels.....	46
1.1.3.5 Role of CO in Mitrogen-Activated Protein Kinase Pathways.....	46
1.1.3.6 Applications of CO in Cancer.....	48
1.1.3.7 Antimicrobial Properties of CO.....	48
1.1.4 Summary.....	49
1.2 Delivery Methods for CO.....	49
1.2.1 Inhalation of CO Gas.....	49
1.2.2 Metal-Based CORMs.....	50
1.2.2.1 Carbon Monoxide as a Ligand.....	50
1.2.2.2 'Thermal' CORMs.....	52
1.2.2.3 Enzyme-Triggered CORMs.....	62
1.2.2.4 Metal Carbonyl PhotoCORMs.....	64
1.2.2.5 Development of CORM Co-Ligands.....	68
1.2.3 Metal-Free CORMs.....	73
1.3 Understanding and Designing CORMs.....	76
1.3.1 Effects of Metal Fragments – CORMs as Antimicrobials.....	76
1.3.2 Methods of CO Detection.....	81
1.3.2.1 Myoglobin Assay.....	81

1.3.2.2	Electrochemical CO Detection.....	84
1.3.2.3	Turn-on Fluorescent Probes	84
1.3.2.4	Headspace Analysis	85
1.3.3	Mechanistic Tools to Study CORMs	86
1.3.3.1	Infrared Spectroscopy	86
1.3.3.2	Magnetic Resonance	87
1.3.3.3	UV-Visible Spectroscopy	88
1.3.3.4	Mass Spectrometry.....	89
1.3.3.5	Quantum Yield.....	89
1.3.3.6	Luminescence.....	90
1.4	PhotoCORMs Based on [Mn(ppy)(CO) ₄].....	92
1.5	Aims and Objectives	95
2	Ultrafast Time-Resolved Infrared Spectroscopy of [Mn(ppy)(CO) ₄]	97
2.1	Background	97
2.1.1	Ultrafast TRIR Studies of PhotoCORMs.....	97
2.1.2	Photochemistry of [Cr(bpy)(CO) ₄]	101
2.1.3	Time-Resolved Multiple Probe Spectroscopy (TR ^{MPS}).....	104
2.2	Spectroscopic Characterisation of [Mn(ppy)(CO) ₄]	105
2.2.1	Ground State Infrared Spectrum of [Mn(ppy)(CO) ₄] (88).....	105
2.2.2	Electronic transitions of [Mn(ppy)(CO) ₄].....	109
2.3	Ultrafast TRIR Spectroscopy of [Mn(ppy)(CO) ₄]	112
2.3.1	Acetonitrile	112
2.3.2	Alkane Solvents	119
2.3.3	Dichloromethane.....	125
2.3.4	Toluene	127
2.3.5	Ethers	129
2.3.5.1	Tetrahydrofuran	129
2.3.5.2	1,4-Dioxane.....	138
2.3.5.3	<i>n</i> -Bu ₂ O	139
2.3.6	Dimethyl sulfoxide.....	142
2.4	DFT Calculations	147
2.5	Discussion.....	152
2.5.1	Triplet Excited State.....	152
2.5.2	Binding Mode and Reactivity of Solvent Complexes.....	155
2.5.3	PhotoCORM Design	160
2.5.4	Implications of TRIR Results for Catalysis	160

2.6	Conclusions.....	162
3	Synthesis and Evaluation of CO-Release from a Series of Ferrocenyl CORMs	164
3.1	Background.....	164
3.2	Synthesis of Ferrocenyl CORMs	170
3.2.1	Synthesis of Compound 132	170
3.2.2	Synthesis of 133.....	177
3.2.3	Synthesis of 134.....	183
3.3	Electrochemistry of Complexes 132-134.....	185
3.3.1	Infrared Spectroelectrochemistry.....	189
3.4	Photochemistry and CO Release.....	192
3.4.1	Monitoring Photolysis By UV-Visible Spectroscopy.....	192
3.4.2	In situ Infrared Spectroscopic Studies of CORM Degradation.....	194
3.4.3	CO Release to Myoglobin.....	198
3.4.4	TRIR Studies.....	210
3.5	Solubilisation of 132 by Oxidation	215
3.6	Conclusions.....	217
4	Characterisation of Cyclometalated Azo Mn(I) CORMs.....	218
4.1	Background.....	218
4.1.1	Using Azo Ligands to Make Visible Light-Activated PhotoCORMs.....	218
4.1.2	Redox Properties of Azo Compounds.....	224
4.2	Synthesis of Azo Dye Complexes.....	225
4.3	Photochemical CO release	234
4.3.1	Calculated and Experimental UV-Visible Absorption Spectra.....	234
4.3.2	Photochemical CO Release to Myoglobin	236
4.3.3	Ultrafast Time-Resolved Infrared Spectroscopy of 172 and 173.....	241
4.3.3.1	Complex 172.....	242
4.3.3.2	Complex 173.....	248
4.3.3.3	Discussion of Ultrafast Results	252
4.4	Investigation of the Redox Properties of Complex 172	254
4.4.1	Infrared Spectroelectrochemistry	255
4.4.2	UV-Visible Spectroelectrochemistry	261
4.5	Conclusions.....	262
5	Synthesis, Imaging, and Antimicrobial Testing of a Coumarin-Tagged CORM.....	265
5.1	Background.....	265
5.2	Synthesis of a Functionalisable Azide-Containing CORM Building Block.....	267
5.3	Synthesis of a Coumarin-Tagged CORM	272

5.3.1	Confocal Microscopy with Human 293T Embryonic Kidney Cells	277
5.3.2	Confocal Microscopy with <i>E. coli</i>	280
5.4	Toxicity Studies With Mn(I) PhotoCORMs	283
5.5	Conclusions.....	289
6	Conclusions and Future Work.....	290
6.1	Photochemical CO-release from [Mn(ppy)(CO) ₄] and related complexes	290
6.1.1	TRIR Studies for PhotoCORM Design.....	290
6.1.2	Isomerisation of ether and DMSO solvent C-H σ -complexes	292
6.2	Redox-Tagged CORMs.....	292
6.3	Antimicrobial and Imaging Studies	295
7	Experimental	298
7.1	TR ^{MPS}	298
7.1.1	Calibration of Spectra	299
7.2	Myoglobin CO-Release Assay.....	299
7.3	Electrochemistry	302
7.3.1	Spectroelectrochemistry.....	304
7.4	<i>E. coli</i> Growth Curves.....	304
7.4.1	Media and Agar Plates	304
7.4.2	<i>E. coli</i> Growth Curve Experiments	305
7.5	Confocal Microscopy	306
7.6	Single Crystal X-Ray Diffraction	306
7.7	Reagents, Conditions and Solvents.....	306
7.8	Nuclear Magnetic Resonance Spectroscopy	306
7.9	Infrared Spectroscopy	307
7.10	Mass Spectrometry.....	307
7.11	Elemental Analysis	307
7.12	UV-Visible Spectroscopy	307
7.13	Melting Point Determination	308
7.14	Chromatography	308
7.15	Synthesis	308
7.15.1	General Synthetic Procedures	308
7.15.2	Compound Synthesis and Characterisation.....	309
Appendix 1:	Published Paper.....	341
Appendix 2:	X-Ray Diffraction Data.....	352
Compound 132:	352

Compound 133.....	354
Compound 148.....	356
Compound 170.....	358
Compound 173.....	360
Compound 188.....	362
Compound 189.....	364
Compound 197.....	366
Appendix 3: UV-Visible Spectroscopic Data	368
Appendix 4: TRIR Spectroscopic Data.....	374
Appendix 5: Growth Curves	377
Appendix 6: NMR Spectra.....	379
Appendix 7: Mass Spectrum of [132] ⁺	413
Abbreviations.....	414
References.....	418

List of Figures

Figure 1: X-ray crystal structure of HO-1 with its haem substrate bound. Image produced from Protein Data Bank entry 1N45 ³⁸ using PyMOL. ³⁹	42
Figure 2: Structure of compounds YC-1 and BAY 41-2272.	44
Figure 3: Mechanistic hypothesis for the CO-induced generation of ROS in the mitochondria by inhibition of cytochrome c oxidase. Adapted from C. S. F. Queiroga, A. S. Almeida and H. L. A. Vieira, <i>Biochem. Res. Int.</i> , 2012, Article ID 749845, 9 pages under a Creative Commons Attribution Licence. ¹⁷	45
Figure 4: Common binding modes of CO to transition metals	51
Figure 5: The MO diagram for CO.	51
Figure 6: Interactions of CO MOs with transition metal orbitals.	52
Figure 7: A timeline of some of the published developments in the field of thermal CORMs discussed in this Section, from the first CORMs paper in 2002 to the more recent shift to more sophisticated design strategies and CO release triggers. ⁸⁶⁻⁹⁶	53
Figure 8: Structure of CORM-3, complex 5.	55
Figure 9: Crystal structure of the complex formed by CORM-3 and a histidine residue in hen egg white lysozyme. Reproduced with permission from T. Santos-Silva, A. Mukhopadhyay, J. D. Seixas, G. J. L. Bernardes, C. C. Romão and M. J. Romão, <i>J. Am. Chem. Soc.</i> , 2011, 133, 1192–5.	57
Figure 10: Thermal CORMs synthesized and tested by Doctorovich and co-workers. ⁹²	58
Figure 11: Relationship of DFT-calculated Ir-CO bond strength (in kcal/mol) and the observed rate constant for CO loss (plotted on a logarithmic scale in units of s ⁻¹). The red line was added to show the qualitative trend. Reprinted with permission from D. E. Bikiel, E. G. Solveyra, F. Di Salvo, H. M. S. Milagre, M. N. Eberlin, R. S. Corrêa, J. Ellena, D. A. Estrin and F. Doctorovich, <i>Inorg. Chem.</i> , 2011, 50, 2334–2345. Copyright 2011 American Chemical Society.	59
Figure 12: A selection of thermal metal-based CORMs. B ₁₂ refers to the cyanocobalamin cofactor.	60
Figure 13: Thermal CORM 23 triggered by magnetic heating of maghemite nanoparticles.	62
Figure 14: Esterase-triggered ET-CORMs.	63
Figure 15: Recent photoCORMs. ¹²⁸⁻¹³³	66
Figure 16: Photosensitiser complex 41.	67

Figure 17: Coordination and drug spheres of a metal-based CORM as coined by Romão <i>et al.</i>	69
Figure 18: Conjugate of a Mn photoCORM with vitamin B ₁₂ , where the Co represents the cyanocobalamin.	71
Figure 19 A: Effect of CO gas (15 min/hour) on survival of <i>E. coli</i> and <i>S. aureus</i> under microaerobic conditions. B: Plated serial dilutions of cultures after 4h of exposure to CO (+) or N ₂ (-). Reproduced with permission from L. S. Nobre, J. D. Seixas, C. C. Romao and L. M. Saraiva, <i>Antimicrob. Agents Chemother.</i> , 2007, 51, 4303–4307. Copyright American Society for Microbiology 2007.	77
Figure 20 A: Effect of CORM-2 on survival rates of <i>E. coli</i> and <i>S. aureus</i> . B: Plated serial dilutions of cultures after four hours of exposure to CO (+) or N ₂ (-) in the presence or absence of Hb. Reproduced with permission from L. S. Nobre, J. D. Seixas, C. C. Romao and L. M. Saraiva, <i>Antimicrob. Agents Chemother.</i> , 2007, 51, 4303–4307. Copyright American Society for Microbiology 2007.	77
Figure 21: Addition of amino acids (arrows indicate the time of addition) protects <i>E. coli</i> from the cytotoxic effects of CORM-3. Black circles show no addition, white circles 60 μM CORM only and red triangles 60 μM CORM-3 and 120 μM of the amino acid. Adapted with permission from H. M. Southam, T. W. Smith, R. L. Lyon, C. Liao, C. R. Trevitt, L. A. Middlemiss, F. L. Cox, J. A. Chapman, S. F. El-Khamisy, M. Hippler, M. P. Williamson, P. J. F. Henderson and R. K. Poole, <i>Redox Biol.</i> , 2018, 18, 114–123.	79
Figure 22: Antimicrobial effect of TryptoCORM, complex 37, on <i>E. coli</i> . Reproduced with permission from J. S. Ward, J. M. Lynam, J. Moir and I. J. S. Fairlamb, <i>Chem. Eur. J.</i> , 2014, 20, 15061–15068. ¹³⁰	80
Figure 23: Spectral changes upon the binding of CO to deoxy-Mb, forming Mb-CO. The ligand L represents a histidine residue to which the haem cofactor is bound.	82
Figure 24: Confocal fluorescence microscopy images during CO release from photoCORM 77 inside cells. Left 465-496 nm emission from photoCORM 77. Right: The same sample after 405 nm photolysis showing emission above 660 nm. Adapted with permission from A. E. Pierri, A. Pallaoro, G. Wu and P. C. Ford, <i>J. Am. Chem. Soc.</i> , 2012, 134, 18197–18200. Copyright, American Chemical Society, 2012.	91
Figure 25: Schematic of key excited states in the photochemistry of [Cr(bpy)(CO) ₄], updated from the summary by Vlček and co-workers ²⁰⁰ to reflect sequential population of the ³ MLCT states. ¹⁷⁵	103
Figure 26: Infrared spectrum of [Mn(ppy)(CO) ₄] in MeCN, recorded at 2 cm ⁻¹ resolution. Assignments based on vibrational analyses of analogous <i>cis</i> -[ML ₂ (CO) ₄] complexes. ²¹¹	106

Figure 27: Symmetry elements (excluding the identity) of the C_{2v} point group superimposed on complex $[Mn(ppy)(CO)_4]$. The C_s point group features only the identity and $\sigma(yz)$ symmetry elements. This molecule may be considered to have C_s or <i>pseudo-C_{2v}</i> symmetry.	107
Figure 28: Visualisation of the vibrational modes for $[Mn(ppy)(CO)_4]$. Normal modes of the same symmetry may also participate in mixing.	108
Figure 29: UV-visible spectra of $[Mn(ppy)(CO)_4]$ in acetonitrile at low concentrations to show the intense $\pi-\pi^*$ ppy transitions. Left: Spectra at the concentrations shown. Right: Beer-Lambert plot with linear fit giving $\epsilon(230\text{ nm}) = (2.56 \pm 0.08) \times 10^4\text{ dm}^3\text{ mol}^{-1}\text{ cm}^{-1}$	109
Figure 30: UV-visible spectra of $[Mn(ppy)(CO)_4]$ in acetonitrile at higher concentrations to show the low-energy band. Left: Spectra at the concentrations shown. Right: Beer-Lambert plot with linear fit giving $\epsilon(355\text{ nm}) = (3.05 \pm 0.11) \times 10^3\text{ dm}^3\text{ mol}^{-1}\text{ cm}^{-1}$	109
Figure 31: DFT-optimised structure and calculated molecular orbitals for $[Mn(ppy)(CO)_4]$ (carbon grey, hydrogen white, manganese pink, nitrogen blue, oxygen red). Isosurfaces shown at $0.5\text{ e}\text{ \AA}^{-3}$	111
Figure 32: TRIR spectra of $[Mn(ppy)(CO)_4]$ in MeCN at selected pump-probe delays with a pump wavelength of 355 nm. The asterisks and insets show the triplet excited state. A spectrum of the ground state of $[Mn(ppy)(CO)_4]$ in MeCN is provided for reference, scaled by a factor of 100.	113
Figure 33: The change in absorbance of the excited state at 2019 cm^{-1} from 1 to 50 ps. The dashed line represents a single exponential fit with a lifetime of $4.1 \pm 0.2\text{ ps}$	116
Figure 34: TRIR spectra showing the photolysis of $[Mn(ppy)(CO)_4]$ at a pump wavelength of 400 nm. The asterisks show the positions of the triplet excited state bands.	118
Figure 35: Continuous irradiation of an acetonitrile solution of $[Mn(ppy)(CO)_4]$, monitored by in situ infrared spectroscopy at a resolution of 4 cm^{-1} , with spectra collected after the irradiation times indicated. The solution was irradiated by a 400 nm LED drawing 6.0 W power. The difference spectra shown are relative to a reference spectrum recorded immediately before irradiation began.	119
Figure 36: TRIR spectra of $[Mn(ppy)(CO)_4]$ in <i>n</i> -heptane at selected pump-probe delays up to 100 ps, using a pump wavelength of 355 nm. The asterisks show the triplet excited state. An infrared spectrum of the ground state of $[Mn(ppy)(CO)_4]$, recorded on an FTIR spectrometer, is included at 1 % scale for reference.	120
Figure 37: TRIR spectra of $[Mn(ppy)(CO)_4]$ in <i>n</i> -heptane at selected pump-probe delays of 100 ps and longer, using a pump wavelength of 355 nm. The asterisks show the triplet excited state.	121

Figure 38: TRIR spectra of [Mn(ppy)(CO) ₄] in <i>n</i> -heptane under an N ₂ atmosphere at the pump-probe delays shown, using a pump wavelength of 355 nm. Conversion of 113 _{hep} into 113 _{OH2} is observed going from bottom to top. Experiment performed by Anders Hammarbäck.....	122
Figure 39: Continuous irradiation of an <i>n</i> -hexane solution of [Mn(ppy)(CO) ₄], monitored by <i>in situ</i> infrared spectroscopy at a resolution of 4 cm ⁻¹ , with spectra collected after the irradiation times shown on the graph. The solution was irradiated by a 400 nm LED drawing 6.0 W power. The difference spectra shown are relative to a reference spectrum recorded immediately before irradiation began.	124
Figure 40: TRIR spectra of [Mn(ppy)(CO) ₄] in CH ₂ Cl ₂ at selected pump-probe delays up to 1 ns. A pump wavelength of 355 nm was used. The asterisks show the triplet excited state.	126
Figure 41: TRIR spectra of [Mn(ppy)(CO) ₄] in CH ₂ Cl ₂ at selected pump-probe delays of 1 ns and longer. A pump wavelength of 355 nm was used. The asterisks show the triplet excited state.	127
Figure 42: TRIR spectra of [Mn(ppy)(CO) ₄] in toluene at selected pump-probe delays up to 1 ns. A pump wavelength of 355 nm was used. The asterisks show the triplet excited state.	128
Figure 43: TRIR spectra of [Mn(ppy)(CO) ₄] in toluene at selected pump-probe delays of 1 ns and longer. A pump wavelength of 355 nm was used. The asterisks show the triplet excited state.	129
Figure 44: TRIR spectra of [Mn(ppy)(CO) ₄] in THF under air at selected pump-probe delays. A pump wavelength of 355 nm was used. The asterisks show the triplet excited state. The arrows indicate the direction of change in absorbance of the bands over time.....	130
Figure 45: Kinetics of the isomerisation of 113 _{THF(σ)} to 113 _{THF(O)} in THF under air. The bands at 1912 cm ⁻¹ for complex 113 _{THF(σ)} (black squares) and 1999 cm ⁻¹ for complex 113 _{THF(O)} (red circles) were monitored over time. The dashed lines represent single exponential fits to the data giving mean lifetimes of (15.1 ± 2.2) ps for 113 _{THF(σ)} and (18.9 ± 1.6) ps for 113 _{THF(O)} . The open symbols represent the delays from 1-4 ps which were excluded from the single exponential fits due to the effect of initial vibrational cooling and solvation.	132
Figure 46: TRIR spectra of [Mn(ppy)(CO) ₄] in dry THF under N ₂ at selected pump-probe delays. A pump wavelength of 355 nm was used. The asterisks show the triplet excited state. The arrows indicate the direction of change in absorbance of the bands over time.	133
Figure 47: Kinetics of the isomerisation of 113 _{THF(σ)} to 113 _{THF(O)} in dry THF under N ₂ from 5 to 99 ps. The bands at 1912 cm ⁻¹ for complex 113 _{THF(σ)} (black squares) and 1999 cm ⁻¹ for complex 113 _{THF(O)} (red circles) were monitored over time. The dashed lines represent single exponential	

fits to the data giving mean lifetimes of (17.6 ± 1.3) ps for $113_{\text{THF}(\sigma)}$ and (18.7 ± 0.8) ps for $113_{\text{THF}(\text{O})}$	134
Figure 48: TRIR spectra of $[\text{Mn}(\text{ppy})(\text{CO})_4]$ in THF- <i>d</i> 8 at selected pump-probe delays. A pump wavelength of 355 nm was used. The asterisks show the triplet excited state. The arrows indicate the direction of change in absorbance of the bands over time. The high-wavenumber bleach at 2073 cm^{-1} was not observable due to absorbance by the solvent.....	135
Figure 49: Kinetics of the isomerisation of $113_{\text{THF}(\sigma)}$ to $113_{\text{THF}(\text{O})}$ in THF- <i>d</i> 8 from 5 to 99 ps. The bands at 1911 cm^{-1} for complex $113_{\text{THF}(\sigma)}$ (black squares) and 1999 cm^{-1} for complex $113_{\text{THF}(\text{O})}$ (red circles) were monitored over time. The dashed lines represent single exponential fits to the data giving mean lifetimes of (17.7 ± 3.7) ps for $113_{\text{THF}(\sigma)}$ and (17.0 ± 1.8) ps for $113_{\text{THF}(\text{O})}$	135
Figure 50: TRIR spectra of $[\text{Mn}(\text{ppy})(\text{CO})_4]$ in THF under a CO atmosphere at long pump-probe delays. A pump wavelength of 355 nm was used. The asterisks show the triplet excited state. The arrows indicate the direction of change in absorbance of the bands over time.	137
Figure 51: TRIR spectra of $[\text{Mn}(\text{ppy})(\text{CO})_4]$ in 1,4-dioxane at selected pump-probe delays. A pump wavelength of 355 nm was used. The asterisks show the triplet excited state. The arrows indicate the direction of change in absorbance of the bands over time.....	138
Figure 52: Kinetics of the isomerisation of $113_{\text{diox}(\sigma)}$ to $113_{\text{diox}(\text{O})}$ in 1,4-dioxane from 5 to 74 ps. The bands at 1919 cm^{-1} for complex $113_{\text{diox}(\sigma)}$ (black squares) and 1999 cm^{-1} for complex $113_{\text{diox}(\text{O})}$ (red circles) were monitored over time. The dashed lines represent single exponential fits to the data giving mean lifetimes of (10.8 ± 1.2) ps for $113_{\text{diox}(\sigma)}$ and (12.8 ± 0.8) ps for $113_{\text{diox}(\text{O})}$	139
Figure 53: TRIR spectra of $[\text{Mn}(\text{ppy})(\text{CO})_4]$ in <i>n</i> -Bu ₂ O at selected pump-probe delays. A pump wavelength of 355 nm was used. The asterisks show the triplet excited state. The arrows indicate the direction of change in absorbance of the bands over time.....	140
Figure 54: Kinetics of the isomerisation of $113_{\text{nbu}2\sigma(\sigma)}$ to $113_{\text{nbu}2\sigma(\text{O})}$ in <i>n</i> -Bu ₂ O from 5 to 1000 ps. The bands at 1918 cm^{-1} for complex $113_{\text{nbu}2\sigma(\sigma)}$ (black squares) and 2004 cm^{-1} for complex $113_{\text{nbu}2\sigma(\text{O})}$ (red circles) were monitored over time. The dashed lines represent single exponential fits to the data giving mean lifetimes of (103 ± 26) ps for $113_{\text{nbu}2\sigma(\sigma)}$ and (88 ± 29) ps for $113_{\text{nbu}2\sigma(\text{O})}$	140
Figure 55: TRIR spectra of $[\text{Mn}(\text{ppy})(\text{CO})_4]$ in DMSO at selected pump-probe delays. A pump wavelength of 355 nm was used. The asterisks show the triplet excited state. The arrows indicate the direction of change in absorbance of the bands over time. Experiment conducted by Anders Hammarbäck.	142

Figure 56: Kinetic plots to study the isomerisation of $113_{\text{DMSO}(\text{G})}$ to $113_{\text{DMSO}(\text{S})}$ and $113_{\text{DMSO}(\text{O})}$ in DMSO from 5 to 100 ps. The bands at 1907 cm^{-1} for complex $113_{\text{DMSO}(\text{G})}$ (blue triangles), 1994 cm^{-1} for complex $113_{\text{DMSO}(\text{O})}$ (red circles), and 2007 cm^{-1} (black squares) for $113_{\text{DMSO}(\text{S})}$ were monitored over time. The fit for $113_{\text{DMSO}(\text{S})}$ was started at 20 ps due to overlap with a decaying band of vibrationally hot $113_{\text{DMSO}(\text{G})}$ at early times. The dashed lines represent single exponential fits to the data giving mean lifetimes of (11.5 ± 1.5) ps for $113_{\text{DMSO}(\text{G})}$, (19.6 ± 1.5) ps for $113_{\text{DMSO}(\text{O})}$ and (23.0 ± 7.9) ps for $113_{\text{DMSO}(\text{G})}$	145
Figure 57: Continuous irradiation of a DMSO solution of $[\text{Mn}(\text{ppy})(\text{CO})_4]$, monitored by in situ infrared spectroscopy at a resolution of 4 cm^{-1} , with spectra collected after the irradiation times shown on the graph. The solution was irradiated by a 365 nm LED drawing 6.0 W power. The difference spectra shown are relative to a reference spectrum recorded immediately before irradiation began.	146
Figure 58: Structure of $113_{\text{DMSO}(\text{O})}$, $113_{\text{DMSO}(\text{S})}$ and $[\text{TS}_{\text{DMSO}}]$ showing Mn-O and Mn-S bond lengths. Atom colours: carbon grey, hydrogen white, manganese pink, nitrogen blue and oxygen red. Energies are Gibbs energies at 298 K at the D3-PBE0/def2-TZVPP//BP86/SVP(P) level with COSMO solvent correction in DMSO.	159
Figure 59: Structures of Chloroquine and Ferroquine.	168
Figure 60: The replacement of a phenyl group in the active anti-cancer compound tamoxifen with a ferrocenyl group gives ferrocifen, the parent compound of a family of anti-cancer drug candidates.....	169
Figure 61: Three ferrocenyl CORM targets for synthesis and characterization.	169
Figure 62: Infrared spectrum of complex 132 recorded in CH_2Cl_2 solution.....	174
Figure 63: A 700 MHz ^1H NMR spectrum of complex 132 in CDCl_3 at 298 K. Expansions of the spectrum are shown in the insets.....	175
Figure 64: An X-ray crystal structure of compound 132 with hydrogen atoms omitted for clarity. Atoms are displayed as thermal ellipsoids at 50% probability. Selected bond lengths (\AA): C(1)-Mn(1) = 2.056(5), C(12)-Mn(1) = 1.836(6), C(13)-Mn(1) = 1.805(6), C(14)-Mn(1) = 1.853(5), C(15)-Mn(1) = 1.867(5), N(1)-Mn(1) = 2.059(4). Selected bond angles ($^\circ$): C(1)-Mn(1)-N(1) = 80.04(18), C(12)-Mn(1)-C(1) = 174.9(2), C(14)-Mn(1)-(C15) = 168.8(2), C(13)-Mn(1)-N(1) = 172.65(19), C(13)- Mn(1)-C(12) = 92.3(2), C(15)-Mn(1)-(C1) = 84.1(2)	177
Figure 65: Stack of 700 MHz NMR of complex 133 (top) and protonated ligand 148 (bottom) recorded in CDCl_3 at 298 K.	181
Figure 66: X-ray crystal structure of protonated ligand 148 with hydrogen atoms omitted for clarity. Atoms are displayed as thermal ellipsoids at 50% probability. Selected bond lengths (\AA):	

C(9)-C(12) = 1.485(5), C(5)-C(6) = 1.472(5), C(16)-N(1) = 1.366(5), C(7)-C(8) = 1.383(5), C(3)-C(4) = 1.421(5), C(1)-Fe(1) = 2.037(4) Selected bond angles (°): C(6)-C(5)-C(1) = 124.0(3), N(1)-C(12)-C(9) = 116.8(3) Selected torsion angles (°): C(8)-C(9)-C(12)-N(1) = 21.6(5), C(1)-C(5)-C(6)-C(7) = 8.9(6).....182

Figure 67: An X-ray crystal structure of compound 133 with hydrogen atoms omitted for clarity. Atoms are displayed as thermal ellipsoids at 50% probability. Selected bond lengths (Å): C(11)-Mn(1) = 2.0538(13), C(22)-Mn(1) = 1.8622(15), C(23)-Mn(1) = 1.8344(14), C(24)-Mn(1) = 1.8048(14), C(25)-Mn(1) = 1.8541(15), N(1)-Mn(1) = 2.0694(12) Selected bond angles (°): C(11)-Mn(1)-N(1) = 79.83(5), C(24)-Mn(1)-N(1) = 172.14(5), C(23)-Mn(1)-C(11) = 176.65(6), C(25)-Mn(1)-C(22) = 167.63(6), C(23)-Mn(1)-N(1) = 97.07(6), C(24)-Mn(1)-C(23) = 90.79(6). Selected torsion angles (°): N(1)-C(5)-C(6)-C(11) = 0.49(17), C(10)-C(9)-C(12)-C(13) = 20.3(2).....182

Figure 68: Stack of 700 MHz NMR spectra of complex 134 (top) and protonated ligand 149 (bottom) in CD₂Cl₂ at 298 K.....184

Figure 69: Cyclic voltammogram of complex 132. Scan rate: 100 mV s⁻¹, solvent: CH₂Cl₂, electrolyte: 1 M tetra *n*-butylammonium hexafluorophosphate, analyte concentration: 5 mM. 186

Figure 70: Cyclic voltammogram of a CH₂Cl₂ solution of 5 mM of both compound 132 and ferrocene. The electrolyte concentration was 1 M tetra *n*-butylammonium hexafluorophosphate and the scan rate was 100 mV s⁻¹.187

Figure 71: Infrared spectroelectrochemistry of complexes 132-134 (panels A–C, respectively). Initial spectra before the potential steps are shown at the Open Circuit Potential (OCP). Experiments were performed in CH₂Cl₂ at a concentration of 5.0 mM in the presence of 1.0 M tetra *n*-butylammonium hexafluorophosphate as the electrolyte. All spectra are subject to a single point baseline correction at 2050 cm⁻¹. (D) Selected spectra from the oxidation step of panel C showing the isosbestic points upon oxidation.....190

Figure 72: UV-visible monitoring of the degradation of compound 132 in CH₂Cl₂ when irradiated with 400 nm light at a power of 2.4 W, beginning at 23 min. The final three spectra were the result of 20 W irradiation. The concentration of 132 was 33 μM. Arrows show the changes in the bands over time.193

Figure 73: Comparison of 2.4 and 6.0 W irradiation of a solution of 33 μM compound 132 at 400 nm. Error bars are shown on the 2.4 W run. Three repeats were performed – the median data set was plotted with error bars corresponding to one standard deviation.....194

Figure 74: Selected *in situ* infrared spectra of a 12 mM DMSO solution of complex 132 showing the changes upon LED irradiation (6.0 W, 365 nm). The results are presented as

difference spectra with reference to a spectrum recorded immediately before irradiation began. The resolution used was 2 cm ⁻¹ . The times given are the time since the irradiation began.	196
Figure 75: Peak heights of selected wavenumbers over the course of the irradiation experiment with 12 mM complex 132 in DMSO.	196
Figure 76: Selected <i>in situ</i> infrared spectra of a 20 mM DMSO solution of complex 133 showing the changes upon LED irradiation (6.0 W, 365 nm). The results are presented as difference spectra with reference to a spectrum recorded immediately before irradiation began. The resolution used was 2 cm ⁻¹ . The times given are the time since the irradiation began.	197
Figure 77: Peak heights of selected wavenumbers over the course of the irradiation experiment of 20 mM 133 in DMSO.	198
Figure 78: UV-visible spectra of standard samples of deoxy-Mb and Mb-CO.	199
Figure 79: UV-visible standard spectrum of deoxy-Mb (black) compared to the spectrum at the start of Mb assay when complex 133 has been added to give a 40 μM solution containing 0.5% DMSO (red).	199
Figure 80: Standards and experimental spectra corrected based on the isosbestic point at 510 nm.	200
Figure 81: A spectrum due to CORM absorbance and scattering from precipitation, generated from the four isosbestic points of deoxy-Mb and Mb-CO.	201
Figure 82: Experimental spectra after the isosbestic point correction for a Mb assay featuring irradiation of 40 μM complex 133. Spectra recorded every 10 minutes.	202
Figure 83: The error from the four-point correction of each experimental spectrum assessed by the difference between the corrected experimental spectrum and spectra of the appropriate concentration generated from the deoxy-Mb and Mb-CO standards.	203
Figure 84: The release of CO to deoxy-Mb by a 40 μM solution of complex 133. The experiment was run in the dark until irradiation with a 400 nm LED at a power of 5.0 W began where indicated. Irradiation was performed in cycles of 2 minutes on, 3 minutes off.	204
Figure 85. The release of CO to deoxy-Mb by a 10 μM solution of complex 134. The experiment was run in the dark until irradiation with a 400 nm LED at a power of 5.0 W began where indicated. Irradiation was performed in cycles of 2 minutes on, 3 minutes off. Experiment performed in collaboration with Samuel Andrew.	205
Figure 86: Effect of successive additions of the proton source [HNMe ₂ Ph]BF ₄ to a 20 mM solution of 134 in CH ₂ Cl ₂ as monitored by <i>in situ</i> infrared spectroscopy of the carbonyl bands. Experiment performed in collaboration with Samuel Andrew.	206

Figure 87: Effect of successive additions of the proton source [HNMe2Ph]BF ₄ to a 20 mM solution of 134 in CH ₂ Cl ₂ as monitored by <i>in situ</i> infrared spectroscopy of the carbonyl bands. The changes to selected bands are shown. Experiment performed in collaboration with Samuel Andrew.....	207
Figure 88: Frontier molecular orbitals of complex 134 as calculated by DFT (PBE0/DGTZVP/DEF2TV level of theory).	209
Figure 89; Precipitation of complex 132 when a 40 uM solution in phosphate buffer 0.5% DMSO was made. Irradiation at 400 nm and a power of 5 W in cycles of 2 minutes on, 3 minutes off from 30 min did not lead to CO release.....	210
Figure 90: A TR ^M PS experiment with ferrocenyl CORM 133 in THF. A pump wavelength of 355 nm was used.....	211
Figure 91: Kinetic plots from 5 to 100 ps to monitor the isomerisation of 150 _{THF(G)} to 150 _{THF(O)} using the 150 _{THF(G)} band at 1913 cm ⁻¹ and the 150 _{THF(O)} band at 1998 cm ⁻¹ . The dotted lines represent single exponential fits with lifetimes of (21.0 ± 1.1) ps and (25.1 ± 2.6) ps for the growth of the 1998 cm ⁻¹ band and loss of the 1913 cm ⁻¹ band respectively.	212
Figure 92: A TR ^M PS experiment with ferrocenyl CORM 132 in <i>n</i> -heptane showing short pump-probe delays. The asterisks denote the excited state bands. A pump wavelength of 355 nm was used.	213
Figure 93: A TR ^M PS experiment with ferrocenyl CORM 132 in <i>n</i> -heptane showing long pump-probe delays. A pump wavelength of 355 nm was used.	214
Figure 94: Water-compatible anions used with the ferricenium cation in anti-cancer studies. .	215
Figure 95: Pyridyl and amine Mn(I) tricarbonyl complexes studied by Mascharak and co-workers. ²⁹⁸	219
Figure 97: Energy differences between the metal-based occupied orbitals and the LUMO involved in the MLCT transition of Mn(I) tricarbonyls with different N-donor and bromide/MeCN co-ligands. Image adapted with permission from <i>Acc. Chem. Res.</i> , 2014, 47, 2603–2611. ¹²⁷ Copyright 2014 American Chemical Society.....	220
Figure 98: Mn(I) tricarbonyl complex featuring an azo group as one of the N-donors, developed by Mascharak and co-workers. Image adapted with permission from <i>Acc. Chem. Res.</i> , 2014, 47, 2603–2611. ¹²⁷ Copyright 2014 American Chemical Society.....	222
Figure 99: General structure of complexes synthesised by Zobi and co-workers. ³⁰¹	222
Figure 100: Visible light azo dye photoCORM 161 synthesised and tested by Fairlamb and co-workers. The graph is from the PhD thesis of Jonathan Ward and shows the decomposition of	

161 upon irradiation with 2.4 W power LED light, as assessed by UV-visible spectroscopy. ¹³⁷	223
Figure 101: Normalised infrared spectra of complexes 172 (black) and 173 (red) in CH ₂ Cl ₂ solution recorded at 2 cm ⁻¹ resolution.....	228
Figure 102: 400 MHz NMR spectra of compounds 169, 172 and 173 in CDCl ₃ at 298 K.....	230
Figure 103 An X-ray crystal structure of compound 170 with hydrogen atoms omitted for clarity. Atoms are displayed as thermal ellipsoids at 50% probability. Selected bond lengths (Å): N(1)-N(2) = 1.278(2), C(9)-Mn(1) = 2.0346(19), C(15)-Mn(1) = 1.869(2), C(16)-Mn(1) = 1.815(2), C(17)-Mn(1) = 1.858(2), C(18)-Mn(1) = 1.846(2), N(1)-Mn(1) = 2.0505(16) Selected bond angles (°): C(9)-Mn(1)-N(1) = 77.92(7), C(16)-Mn(1)-N(1) = 168.53(8), C(18)-Mn(1)-C(9) = 176.45(8), C(17)-Mn(1)-C(15) = 173.45(8), C(18)-Mn(1)-N(1) = 98.56(7), C(16)-Mn(1)-C(18) = 92.82(8).	231
Figure 104: An X-ray crystal structure of compound 173 with hydrogen atoms omitted for clarity. Atoms are displayed as thermal ellipsoids at 50% probability. Selected bond lengths (Å): N(1)-N(2) = 1.299(3), C(1)-Mn(1) = 2.018(2), C(10)-Mn(1) = 1.877(3), C(11)-Mn(1) = 1.861(3), C(12)-Mn(1) = 1.801(3), C(13)-Mn(1) = 1.849(3), N(1)-Mn(1) = 2.083 (2) Selected bond angles (°): C(1)-Mn(1)-N(1) = 77.74(9), C(12)-Mn(1)-N(1) = 167.63(10), C(13)-Mn(1)-C(1) = 177.44(11), C(10)-Mn(1)-C(11) = 173.17(11), C(13)-Mn(1)-N(1) = 104.11(10), C(13)-Mn(1)-C(12) = 88.19(12).....	231
Figure 105: A 400 MHz spectrum of the crude material after cyclometalation of azobenzene 176 with [MeMn(CO) ₅] recorded at 298 K in CDCl ₃	233
Figure 106: UV-visible spectra in CH ₂ Cl ₂ of azo compound 169, and cyclometalated complexes 172 and 173. The dashed lines represent the LED wavelengths used for irradiation of the complexes to probe CO dissociation.....	235
Figure 107: The CO release profiles of 172 in the dark and upon LED irradiation. A concentration of 10 μM 172 was used for all assays, with 50-60 μM myoglobin. Irradiation was performed at a power of 6.0 W in cycles of 3 minutes off, 2 minutes on from 30 minutes onwards.....	236
Figure 108: Exhaustive CO release from 10 μM 172 using 365 nm LED irradiation. Irradiation was performed at a power of 6.0 W in cycles of 3 minutes off, 2 minutes off from 30 minutes onwards.....	240
Figure 109: The CO release behavior of 10 μM 173 in the dark and upon LED irradiation. Irradiation at 525 and 400 nm was performed at a power of 6.0 W in cycles of 3 minutes off, 2 minutes off from 30 minutes onwards.	241

Figure 110: TRIR spectra of complex 172 in THF under air at picosecond pump-probe delays. A pump wavelength of 355 nm was used. The arrows indicate the direction of change in absorbance of the bands over time. A scaled spectrum of the ground state of complex 172 in THF is shown for reference.	242
Figure 111: TRIR spectra of complex 172 in THF under air at picosecond pump-probe delays comparing the delays at 2 and 100 ps – the data are from the same experiment as that in Figure 108. A scaled spectrum of the ground state of complex 172 in THF is shown for reference. ...	243
Figure 112: Kinetic profiles of selected TRIR bands for 172 on the picosecond timescale. The dashed lines are single exponential fits.....	244
Figure 113: TRIR spectra of complex 172 in THF under air at nanosecond pump-probe delays. A pump wavelength of 355 nm was used. The arrows indicate the direction of change in absorbance of the bands over time. A scaled spectrum of the ground state of complex 172 in THF is shown for reference.	245
Figure 114: Kinetic profiles of selected TRIR bands for 172 on the nanosecond timescale. The dashed lines are single exponential fits.....	246
Figure 115: TRIR spectrum of 172 in THF under air at a pump-probe delay of 1 μ s. A pump wavelength of 355 nm was used. A scaled spectrum of the ground state of complex 172 in THF is shown for reference.	247
Figure 116: TRIR spectra of 173 in THF under air at picosecond pump-probe delays. A pump wavelength of 355 nm was used. The arrows indicate the changes of the photoproduct bands over time. A scaled spectrum of the ground state of complex 173 in THF is shown for reference.	249
Figure 117: TRIR spectra of 173 in THF under air comparing 2 and 100 ps pump-probe delays for clarity. The arrows indicate the changes of the photoproduct bands over time. The graph shows the same data as Figure 114.	249
Figure 118: TRIR spectra of 173 in THF under air at nanosecond pump-probe delays. A pump wavelength of 355 nm was used. The arrows indicate the changes of the photoproduct and bleach bands over time. A scaled spectrum of the ground state of complex 173 in THF is shown for reference.....	250
Figure 119: TRIR spectrum of 173 in THF under air at a pump-probe delay of 1 μ s. A pump wavelength of 355 nm was used. A scaled spectrum of the ground state of complex 173 in THF is shown for reference.....	251
Figure 120: Jablonski diagram summarising the behavior of azo complexes 172 and 173.....	253

Figure 121: Cyclic voltammogram of a 1.0 mM solution of complex 172 in CH₂Cl₂ under Ar. The electrolyte was 100 mM tetrabutylammonium hexafluorophosphate. A scan rate of 100 mV s⁻¹ was used.254

Figure 122: Infrared spectroelectrochemistry experiment with complex 172 in CH₂Cl₂ at a concentration of 5.0 mM in the presence of 1.0 M tetra n-butylammonium hexafluorophosphate. Panel A: Complex 172 at the open circuit potential of +446 mV vs the Pt pseudo-reference electrode, followed by a potential step to -1 V. Panel B: Further spectra after longer times at -1 V. Panel C: Initial spectra after the potential step to +1 V. Panel D: Further spectra after longer times at +1 V.256

Figure 123: UV-visible spectroelectrochemistry experiment with complex 172 in CH₂Cl₂ at a concentration of 100 μM in the presence of 500 mM tetra n-butylammonium hexafluorophosphate. Panel A: Complex 172 at the open circuit potential of +0.01 V vs Ag/AgCl, followed by a potential step to -1 V vs Ag/AgCl. Panel B: Further spectra after longer times at -1 V vs Ag/AgCl. Panel C: Time evolution of the bands observed in panels A and B. Panel D: Spectra after a potential of +1 V vs Ag/AgCl was applied.261

Figure 124: Growth curves for *E. coli* showing the effect of complex 95 both in the dark (orange circles) and in the presence of irradiation (green triangles). Control experiments with no CORM in the dark (blue diamonds) and with irradiation (red squares) are also overlaid. Where irradiation took place, a 400 nm LED drawing 2.4 W power was used for 3 minutes off, 2 minutes on between 1-3 hours. This data is taken from the PhD thesis of Jonathan Ward.¹³⁷ ..266

Figure 125: Growth curves for *E. coli* showing the effect of pre-irradiated complex 95. The blue triangles represent no addition of CORM or irradiation, the red squares show the effect of adding CORM 95 after pre-irradiation. Error bars represent the standard deviation from three measurements. This data is taken from the PhD thesis of Jonathan Ward.¹³⁷267

Figure 126: An X-ray crystal structure of compound 188 with hydrogen atoms omitted for clarity. Atoms are displayed as thermal ellipsoids at 50 % probability. Selected bond lengths (Å): C(11)-Mn(1) = 2.054(3), C(13)-Mn(1) = 1.841(3), C(14)-Mn(1) = 1.796(3), C(15)-Mn(1) = 1.857(3), C(16)-Mn(1) = 1.842(3), N(1)-Mn(1) = 2.073(2). Selected bond angles (°): C(11)-Mn(1)-N(1) = 79.53(11), C(16)-Mn(1)-C(11) = 172.33(12), C(13)-Mn(1)-(C15) = 166.55(12), C(14)-Mn(1)-N(1) = 172.93(12), C(14)- Mn(1)-C(16) = 93.50(13), C(15)-Mn(1)-(C11) = 81.79(12).270

Figure 127: An X-ray crystal structure of compound 189 with hydrogen atoms omitted for clarity. Atoms are displayed as thermal ellipsoids at 50 % probability. Selected bond lengths (Å): C(11)-Mn(1) = 2.0574(14), C(21)-Mn(1) = 1.8595(14), C(22)-Mn(1) = 1.8025(15), C(23)-Mn(1) = 1.8303(15), C(24)-Mn(1) = 1.8476(14), N(1)-Mn(1) = 2.0661(11). Selected bond

angles (°): C(11)-Mn(1)-N(1) = 79.64(5), C(23)-Mn(1)-C(11) = 173.00(6), C(24)-Mn(1)-(C21) = 168.48(6), C(22)-Mn(1)-N(1) = 173.35(6), C(22)-Mn(1)-C(23) = 92.02(6), C(21)-Mn(1)-(C11) = 80.95(5).271

Figure 128: An X-ray crystal structure of compound 197 with hydrogen atoms omitted for clarity. Atoms are displayed as thermal ellipsoids at 50 % probability. Selected bond lengths (Å): C(11)-Mn(1) = 2.048(2), C(28)-Mn(1) = 1.853(3), C(29)-Mn(1) = 1.864(3), C(30)-Mn(1) = 1.8310(3), C(31)-Mn(1) = 1.8451(3), N(1)-Mn(1) = 2.065(2). Selected bond angles (°): C(11)-Mn(1)-N(1) = 79.45(9), C(31)-Mn(1)-C(11) = 174.82(10), C(28)-Mn(1)-(C29) = 168.69(12), C(30)-Mn(1)-N(1) = 171.61(10), C(30)-Mn(1)-C(31) = 90.66(12), C(28)-Mn(1)-(C11) = 81.32(10).274

Figure 129: UV-Visible spectrum of 197 in CH₂Cl₂ at a concentration of 26.2 μM.274

Figure 130: Myoglobin CO release assay with 10 μM compound 197 and *ca.* 47 μM myoglobin. Irradiation with a 400 nm LED at a power of 4.8 W began at 18.3 min and was provided in cycles of 3 minutes off, 2 minutes on.277

Figure 131: T293 cells after incubation with 50 nM 197 for 30 min. Left: Fluorescence response of 197 - emission collected between 410 nm to 597 nm. Centre: Image recorded of the cells in the same region, using white light. Right: Overlay of the emission and white light images. Each image is 425 x 425 μm.277

Figure 132: CORM-free control experiment using T293 cells. Each image is 425 x 425 μm. Left: Fluorescence response from the cells and solution - emission collected between 410 nm to 597 nm. Centre: Image recorded of the cells in the same region, using white light. Right: Overlay of the emission and white light images. Each image is 425 x 425 μm.278

Figure 133: Addition of PI (2 μL of 400 μg / mL stain added to a 350 μL well) as a live/dead stain. Top left: CORM 197 fluorescence (50 nM, excitation 405 nm, emission 410-597 nm). Top right: white light image of the cells. Bottom left: PI fluorescence (excitation 561 nm, emission 569-740 nm). Bottom right: Overlay of all three images. Each image is 425 x 425 μm.279

Figure 134: Z-stack images using the same conditions as Figure 129.280

Figure 135: Autofluorescence control images after a CORM-free PBS/DMSO solution was added to the culture and incubated for 30 min. Left: 405 nm excitation with 410-627 nm emission. Right: Image recorded with white light. Image sizes are 135 x 135 μm.281

Figure 136: Addition of 10 μM CORM 197 to an *E. coli* culture. Top left: Coumarin fluorescence (excitation 405 nm, emission 410-556 nm). Top right: PI fluorescence (excitation

561 nm, emission 566-719 nm). Bottom left: White light. Bottom right: Overlay of all three images. Image sizes are 135 x 135 μm	282
Figure 137: Growth curves with <i>E. coli</i> BL21 under the conditions shown. Each point is the mean of three separate repeats from different cultures, and the error bars show standard deviation. Irradiation with a 2.4 W power 400 nm LED took place between 1 and 3 hours and comprised cycles of 3 minutes off, 2 minutes on.....	284
Figure 138: Growth curves with <i>E. coli</i> BL21 under the conditions shown. All cultures containing DMSO were 1% DMSO by volume. The TryptoCORM concentration used was 25 μM . Irradiation with a 2.4 W power 400 nm LED took place between 1 and 3 hours and comprised cycles of 3 minutes off, 2 minutes on.....	285
Figure 139: Growth curves with <i>E. coli</i> BL21 under the conditions shown. All cultures containing DMSO were 1% DMSO by volume. The TryptoCORM concentration used was 100 μM . Irradiation with a 2.4 W power 400 nm LED took place between 0 and 2 hours and comprised cycles of 3 minutes off, 2 minutes on.....	286
Figure 140: Growth curves with <i>E. coli</i> BL21 under the conditions shown. All cultures containing DMSO were 1% DMSO by volume. The concentrations of 197 and 199 used were 100 μM . Irradiation with a 2.4 W power 400 nm LED took place between 0 and 2 hours and comprised cycles of 3 minutes off, 2 minutes on.....	287
Figure 141: Growth curves with <i>E. coli</i> BL21 under the conditions shown. All cultures containing DMSO were 1% DMSO by volume. The concentration of 95 used was 100 μM . Irradiation with a 2.4 W power 400 nm LED took place between 0 and 2 hours and comprised cycles of 3 minutes off, 2 minutes on.	288
Figure 142: Key photoCORMs studied and compared in this Thesis.....	291
Figure 143: Alkyne 46 developed by Jonathan Ward and used in this Thesis, and complementary novel azide 188, developed in this Thesis.....	292
Figure 144: Novel redox-active CORMs tested for redox-triggered CO-release in this Thesis.	293
Figure 145: Structure of complex 209.	295
Figure 146: Irradiation control unit developed at the University of York. On the left side is a dimmer switch and power readout to control the power drawn by the LED. On the right side is a programmable timer function that allows repeated on/off cycles.	301
Figure 147 Left: LED embedded in a cuvette lid to irradiate samples inside a UV-visible spectrometer during myoglobin CO release assays. Right – The LED lid attaches to a PMMA	

cuvette and plus into the back of the irradiation control unit, which is in turn powered by the mains.....301

Figure 148: An X-ray crystal structure of compound 132 with hydrogen atoms omitted for clarity. Atoms are displayed as thermal ellipsoids at 50% probability. Selected bond lengths (Å): C(1)-Mn(1) = 2.056(5), C(12)-Mn(1) = 1.836(6), C(13)-Mn(1) = 1.805(6), C(14)-Mn(1) = 1.853(5), C(15)-Mn(1) = 1.867(5), N(1)-Mn(1) = 2.059(4). Selected bond angles (°): C(1)-Mn(1)-N(1) = 80.04(18), C(12)-Mn(1)-C(1) = 174.9(2), C(14)-Mn(1)-(C15) = 168.8(2), C(13)-Mn(1)-N(1) = 172.65(19), C(13)-Mn(1)-C(12) = 92.3(2), C(15)-Mn(1)-(C1) = 84.1(2).....352

Figure 149: An X-ray crystal structure of compound 133 with hydrogen atoms omitted for clarity. Atoms are displayed as thermal ellipsoids at 50% probability. Selected bond lengths (Å): C(11)-Mn(1) = 2.0538(13), C(22)-Mn(1) = 1.8622(15), C(23)-Mn(1) = 1.8344(14), C(24)-Mn(1) = 1.8048(14), C(25)-Mn(1) = 1.8541(15), N(1)-Mn(1) = 2.0694(12) Selected bond angles (°): C(11)-Mn(1)-N(1) = 79.83(5), C(24)-Mn(1)-N(1) = 172.14(5), C(23)-Mn(1)-C(11) = 176.65(6), C(25)-Mn(1)-C(22) = 167.63(6), C(23)-Mn(1)-N(1) = 97.07(6), C(24)-Mn(1)-C(23) = 90.79(6). Selected torsion angles (°): N(1)-C(5)-C(6)-C(11) = 0.49(17), C(10)-C(9)-C(12)-C(13) = 20.3(2).354

Figure 150: X-ray crystal structure of protonated ligand 148 with hydrogen atoms omitted for clarity. Atoms are displayed as thermal ellipsoids at 50% probability. Selected bond lengths (Å): C(9)-C(12) = 1.485(5), C(5)-C(6) = 1.472(5), C(16)-N(1) = 1.366(5), C(7)-C(8) = 1.383(5), C(3)-C(4) = 1.421(5), C(1)-Fe(1) = 2.037(4) Selected bond angles (°): C(6)-C(5)-C(1) = 124.0(3), N(1)-C(12)-C(9) = 116.8(3) Selected torsion angles (°): C(8)-C(9)-C(12)-N(1) = 21.6(5), C(1)-C(5)-C(6)-C(7) = 8.9(6).....356

Figure 151: An X-ray crystal structure of compound 170 with hydrogen atoms omitted for clarity. Atoms are displayed as thermal ellipsoids at 50% probability. Selected bond lengths (Å): N(1)-N(2) = 1.278(2), C(9)-Mn(1) = 2.0346(19), C(15)-Mn(1) = 1.869(2), C(16)-Mn(1) = 1.815(2), C(17)-Mn(1) = 1.858(2), C(18)-Mn(1) = 1.846(2), N(1)-Mn(1) = 2.0505(16) Selected bond angles (°): C(9)-Mn(1)-N(1) = 77.92(7), C(16)-Mn(1)-N(1) = 168.53(8), C(18)-Mn(1)-C(9) = 176.45(8), C(17)-Mn(1)-C(15) = 173.45(8), C(18)-Mn(1)-N(1) = 98.56(7), C(16)-Mn(1)-C(18) = 92.82(8).358

Figure 152: An X-ray crystal structure of compound 173 with hydrogen atoms omitted for clarity. Atoms are displayed as thermal ellipsoids at 50% probability. Selected bond lengths (Å): N(1)-N(2) = 1.299(3), C(1)-Mn(1) = 2.018(2), C(10)-Mn(1) = 1.877(3), C(11)-Mn(1) = 1.861(3), C(12)-Mn(1) = 1.801(3), C(13)-Mn(1) = 1.849(3), N(1)-Mn(1) = 2.083 (2) Selected bond angles (°): C(1)-Mn(1)-N(1) = 77.74(9), C(12)-Mn(1)-N(1) = 167.63(10), C(13)-Mn(1)-C(1) = 177.44(11), C(10)-Mn(1)-C(11) = 173.17(11), C(13)-Mn(1)-N(1) = 104.11(10), C(13)-Mn(1)-C(12) = 88.19(12).....360

Figure 153: An X-ray crystal structure of compound 188 with hydrogen atoms omitted for clarity. Atoms are displayed as thermal ellipsoids at 50 % probability. Selected bond lengths (Å): C(11)-Mn(1) = 2.054(3), C(13)-Mn(1) = 1.841(3), C(14)-Mn(1) = 1.796(3), C(15)-Mn(1) = 1.857(3), C(16)-Mn(1) = 1.842(3), N(1)-Mn(1) = 2.073(2). Selected bond angles (°): C(11)-Mn(1)-N(1) = 79.53(11), C(16)-Mn(1)-C(11) = 172.33(12), C(13)-Mn(1)-(C15) = 166.55(12), C(14)-Mn(1)-N(1) = 172.93(12), C(14)-Mn(1)-C(16) = 93.50(13), C(15)-Mn(1)-(C11) = 81.79(12).362

Figure 154: An X-ray crystal structure of compound 189 with hydrogen atoms omitted for clarity. Atoms are displayed as thermal ellipsoids at 50 % probability. Selected bond lengths (Å): C(11)-Mn(1) = 2.0574(14), C(21)-Mn(1) = 1.8595(14), C(22)-Mn(1) = 1.8025(15), C(23)-Mn(1) = 1.8303(15), C(24)-Mn(1) = 1.8476(14), N(1)-Mn(1) = 2.0661(11). Selected bond angles (°): C(11)-Mn(1)-N(1) = 79.64(5), C(23)-Mn(1)-C(11) = 173.00(6), C(24)-Mn(1)-(C21) = 168.48(6), C(22)-Mn(1)-N(1) = 173.35(6), C(22)-Mn(1)-C(23) = 92.02(6), C(21)-Mn(1)-(C11) = 80.95(5).364

Figure 155: An X-ray crystal structure of compound 197 with hydrogen atoms omitted for clarity. Atoms are displayed as thermal ellipsoids at 50 % probability. Selected bond lengths (Å): C(11)-Mn(1) = 2.048(2), C(28)-Mn(1) = 1.853(3), C(29)-Mn(1) = 1.864(3), C(30)-Mn(1) = 1.8310(3), C(31)-Mn(1) = 1.8451(3), N(1)-Mn(1) = 2.065(2). Selected bond angles (°): C(11)-Mn(1)-N(1) = 79.45(9), C(31)-Mn(1)-C(11) = 174.82(10), C(28)-Mn(1)-(C29) = 168.69(12), C(30)-Mn(1)-N(1) = 171.61(10), C(30)-Mn(1)-C(31) = 90.66(12), C(28)-Mn(1)-(C11) = 81.32(10).366

Figure 156 Left: Spectra of 132 in CH₂Cl₂ at the concentrations shown. Right: Beer-Lambert plot for 132 in CH₂Cl₂ at 270 nm. The dashed line is a linear fit giving ϵ (270 nm) = $(2.84 \pm 0.5) \times 10^4 \text{ dm}^3 \text{ mol}^{-1} \text{ cm}^{-1}$368

Figure 157 Left: Spectra of 133 in CH₂Cl₂ at the concentrations shown. Right: Beer-Lambert plot for 133 in CH₂Cl₂ at 460 nm. The dashed line is a linear fit giving ϵ (460 nm) = $(2.04 \pm 0.05) \times 10^3 \text{ dm}^3 \text{ mol}^{-1} \text{ cm}^{-1}$369

Figure 158 Left: Beer-Lambert plot for 133 in CH₂Cl₂ at 378 nm. The dashed line is a linear fit giving ϵ (378 nm) = $(8.00 \pm .06) \times 10^3 \text{ dm}^3 \text{ mol}^{-1} \text{ cm}^{-1}$. Right: Beer-Lambert plot for 133 in CH₂Cl₂ at 314 nm. The dashed line is a linear fit giving ϵ (314 nm) = $(2.29 \pm .02) \times 10^4 \text{ dm}^3 \text{ mol}^{-1} \text{ cm}^{-1}$369

Figure 159 Left: Spectra of 134 in CH₂Cl₂ at the concentrations shown. Right: Beer-Lambert plot for 134 in CH₂Cl₂ at 486 nm. The dashed line is a linear fit giving ϵ (486 nm) = $(1.23 \pm 0.05) \times 10^3 \text{ dm}^3 \text{ mol}^{-1} \text{ cm}^{-1}$369

Figure 160: Beer-Lambert plot for 134 in CH ₂ Cl ₂ at 292 nm. The dashed line is a linear fit giving $\varepsilon(292 \text{ nm}) = (1.827 \pm .013) \times 10^4 \text{ dm}^3 \text{ mol}^{-1} \text{ cm}^{-1}$	370
Figure 161 Left: Spectra of 169 in CH ₂ Cl ₂ at the concentrations shown. Right: Beer-Lambert plot for 169 in CH ₂ Cl ₂ at 330 nm. The dashed line is a linear fit giving $\varepsilon(330 \text{ nm}) = (3.49 \pm 0.04) \times 10^4 \text{ dm}^3 \text{ mol}^{-1} \text{ cm}^{-1}$	370
Figure 162 Left: Spectra of 170 in CH ₂ Cl ₂ at the concentrations shown. Right: Beer-Lambert plot for 170 in CH ₂ Cl ₂ at 456 nm. The dashed line is a linear fit giving $\varepsilon(456 \text{ nm}) = (5.84 \pm .05) \times 10^3 \text{ dm}^3 \text{ mol}^{-1} \text{ cm}^{-1}$	370
Figure 163: Beer-Lambert plot for 170 in CH ₂ Cl ₂ at 378 nm. The dashed line is a linear fit giving $\varepsilon(378 \text{ nm}) = (2.166 \pm .008) \times 10^4 \text{ dm}^3 \text{ mol}^{-1} \text{ cm}^{-1}$	370
Figure 164 Left: Spectra of 171 in CH ₂ Cl ₂ at the concentrations shown. Right: Beer-Lambert plot for 171 in CH ₂ Cl ₂ at 578 nm. The dashed line is a linear fit giving $\varepsilon(578 \text{ nm}) = (1.254 \pm 0.005) \times 10^4 \text{ dm}^3 \text{ mol}^{-1} \text{ cm}^{-1}$	371
Figure 165: Beer-Lambert plot for 171 in CH ₂ Cl ₂ at 456 nm. The dashed line is a linear fit giving $\varepsilon(456 \text{ nm}) = (2.79 \pm .02) \times 10^4 \text{ dm}^3 \text{ mol}^{-1} \text{ cm}^{-1}$	371
Figure 166 Left: Spectra of 172 in CH ₂ Cl ₂ at the concentrations shown. Right: Beer-Lambert plot for 172 in CH ₂ Cl ₂ at 434 nm. The dashed line is a linear fit giving $\varepsilon(434 \text{ nm}) = (3.0 \pm 0.2) \times 10^3 \text{ dm}^3 \text{ mol}^{-1} \text{ cm}^{-1}$. Spectra recorded by Alice de Palo under my supervision.....	371
Figure 167: Beer-Lambert plot for 172 in CH ₂ Cl ₂ at 336 nm. The dashed line is a linear fit giving $\varepsilon(336 \text{ nm}) = (1.58 \pm .05) \times 10^4 \text{ dm}^3 \text{ mol}^{-1} \text{ cm}^{-1}$. Spectra recorded by Alice de Palo under my supervision.	372
Figure 168 Left: Spectra of 173 in CH ₂ Cl ₂ at the concentrations shown. Right: Beer-Lambert plot for 173 in CH ₂ Cl ₂ at 622 nm. The dashed line is a linear fit giving $\varepsilon(622 \text{ nm}) = (3.98 \pm .03) \times 10^3 \text{ dm}^3 \text{ mol}^{-1} \text{ cm}^{-1}$	372
Figure 169 Left: Beer-Lambert plot for 173 in CH ₂ Cl ₂ at 522 nm. The dashed line is a linear fit giving $\varepsilon(522 \text{ nm}) = (8.47 \pm .06) \times 10^3 \text{ dm}^3 \text{ mol}^{-1} \text{ cm}^{-1}$. Right: Beer-Lambert plot for 173 in CH ₂ Cl ₂ at 404 nm. The dashed line is a linear fit giving $\varepsilon(404 \text{ nm}) = (2.648 \pm .010) \times 10^4 \text{ dm}^3 \text{ mol}^{-1} \text{ cm}^{-1}$	372
Figure 170 Left: Spectra of 197 in CH ₂ Cl ₂ at the concentrations shown. Right: Beer-Lambert plot for 197 in CH ₂ Cl ₂ at 408 nm. The dashed line is a linear fit giving $\varepsilon(408 \text{ nm}) = (3.65 \pm 0.04) \times 10^4 \text{ dm}^3 \text{ mol}^{-1} \text{ cm}^{-1}$	373
Figure 171: Beer-Lambert plot for 197 in CH ₂ Cl ₂ at 264 nm. The dashed line is a linear fit giving $\varepsilon(264 \text{ nm}) = (4.13 \pm 0.09) \times 10^4 \text{ dm}^3 \text{ mol}^{-1} \text{ cm}^{-1}$	373

Figure 172 Left: TRIR spectra of [Mn(ppy)(CO) ₄] (88) photolyzed in THF under an atmosphere of CO to form solvent complexes 113 _{THF(σ)} and 113 _{THF(O)} . The triplet excited state bands are marked with asterisks. Right: Evolution of the 113 _{THF(σ)} 1912 cm ⁻¹ band and the 113 _{THF(O)} 1999 cm ⁻¹ band from 5 to 99 ps. The dashed lines are single exponential fits.	374
Figure 173 Left: TRIR spectra of 94 photolyzed in THF to form the corresponding C-H σ- and O-bound complexes. The triplet excited state bands are marked with asterisks. Right: Evolution of the σ- 1913 cm ⁻¹ band and the O-bound 1999 cm ⁻¹ band from 5 to 92 ps. The dashed lines are single exponential fits.	374
Figure 174 Left: TRIR spectra of 95 photolyzed in THF to form the corresponding C-H σ- and O-bound complexes. The triplet excited state bands are marked with asterisks. Right: Evolution of the σ- 1913 cm ⁻¹ band and the O-bound 1999 cm ⁻¹ band from 5 to 92 ps. The dashed lines are single exponential fits.	375
Figure 175: Kinetic profiles of selected TRIR bands for 173 on the picosecond timescale. The dashed lines are single exponential fits.	375
Figure 176: Kinetic profiles of selected TRIR bands for 173 on the nanosecond timescale. The dashed lines are single exponential fits.	376
Figure 177: Growth curves with <i>E. coli</i> BL21 in 50% LB media under the conditions shown. All cultures containing DMSO were 1% DMSO by volume. The TryptoCORM concentration used was 100 μM. Irradiation with a 2.4 W power 400 nm LED took place between 0 and 2 hours and comprised cycles of 3 minutes off, 2 minutes on.	377
Figure 178: Growth curves with <i>E. coli</i> BL21 in 10% LB media under the conditions shown. All cultures containing DMSO were 1% DMSO by volume. The TryptoCORM concentration used was 100 μM. Irradiation with a 2.4 W power 400 nm LED took place between 0 and 2 hours and comprised cycles of 3 minutes off, 2 minutes on.	377
Figure 179: Growth curves with <i>E. coli</i> BL21 under the conditions shown. All cultures containing DMSO were 1% DMSO by volume. The TryptoCORM concentration used was 100 μM. Irradiation with a 2.4 W power 400 nm LED took place between 0 and 2 hours and comprised cycles of 3 minutes off, 2 minutes on. This is a repeat of the experiment in Figure 135.	378
Figure 180: Growth curves with <i>E. coli</i> BL21 under the conditions shown. All cultures containing DMSO were 1% DMSO by volume. The concentration of 95 used was 100 μM. Irradiation with a 2.4 W power 400 nm LED took place between 0 and 2 hours and comprised cycles of 3 minutes off, 2 minutes on. This is a repeat of the experiment in Figure 137 with bacteria from a different plate.	378

Figure 181: A 400 MHz ^1H NMR spectrum of 87 in CDCl_3 .	379
Figure 182: A 126 MHz ^{13}C NMR spectrum of 87 in CDCl_3 .	380
Figure 183: A 500 MHz ^1H NMR spectrum of 88 in CDCl_3 .	380
Figure 184: A 126 MHz ^{13}C NMR spectrum of 88 in CDCl_3 .	381
Figure 185: A 400 MHz ^1H NMR spectrum of 138 in CDCl_3 .	381
Figure 186: A 101 MHz ^{13}C NMR spectrum of 138 in CDCl_3 .	382
Figure 187: A 400 MHz ^1H NMR spectrum of 139 in CDCl_3 .	382
Figure 188: A 101 MHz ^{13}C NMR spectrum of 139 in CDCl_3 .	383
Figure 189: A 400 MHz ^1H NMR spectrum of 140 in CDCl_3 .	383
Figure 190: A 101 MHz ^{13}C NMR spectrum of 140 in CDCl_3 .	384
Figure 191: A 400 MHz ^1H NMR spectrum of 141 in CDCl_3 .	384
Figure 192: A 126 MHz ^{13}C NMR spectrum of 141 in CDCl_3 .	385
Figure 193: A 400 MHz ^1H NMR spectrum of 46 in CDCl_3 .	385
Figure 194: A 126 MHz ^{13}C NMR spectrum of 46 in CDCl_3 .	386
Figure 195: A 400 MHz ^1H NMR spectrum of 143 in CDCl_3 .	386
Figure 196: A 101 MHz ^{13}C NMR spectrum of 143 in CDCl_3 .	387
Figure 197: A 400 MHz ^1H NMR spectrum of 135 in CDCl_3 .	387
Figure 198: A 101 MHz ^{13}C NMR spectrum of 135 in CDCl_3 .	388
Figure 199: A 700 MHz ^1H NMR spectrum of 132 in CDCl_3 .	388
Figure 200: A 176 MHz ^{13}C NMR spectrum of 132 in CDCl_3 .	389
Figure 201: A 400 MHz ^1H NMR spectrum of 82 in CDCl_3 .	389
Figure 202: A 101 MHz ^{13}C NMR spectrum of 82 in CDCl_3 .	390
Figure 203: A 400 MHz ^1H NMR spectrum of 148 in CDCl_3 .	391
Figure 204: A 101 MHz ^{13}C NMR spectrum of 148 in CDCl_3 .	391
Figure 205: A 700 MHz ^1H NMR spectrum of 133 in CDCl_3 .	392
Figure 206: A 176 MHz ^{13}C NMR spectrum of 133 in CDCl_3 .	392
Figure 207: A 700 MHz ^1H NMR spectrum of 149 in CD_2Cl_2 .	393
Figure 208: A 176 MHz ^{13}C NMR spectrum of 149 in CD_2Cl_2 .	393

Figure 209: A 700 MHz ^1H NMR spectrum of 134 in CD_2Cl_2 .	394
Figure 210: A 176 MHz ^{13}C NMR spectrum of 134 in CD_2Cl_2 .	395
Figure 211: A 400 MHz ^1H NMR spectrum of 167 in CDCl_3 .	395
Figure 212: A 126 MHz ^{13}C NMR spectrum of 167 in CDCl_3 .	396
Figure 213: A 400 MHz ^1H NMR spectrum of 169 in CDCl_3 .	396
Figure 214: A 126 MHz ^{13}C NMR spectrum of 169 in CDCl_3 .	397
Figure 215: A 500 MHz ^1H NMR spectrum of 174 in CDCl_3 .	397
Figure 216: A 126 MHz ^{13}C NMR spectrum of 174 in CDCl_3 .	398
Figure 217: A 400 MHz ^1H NMR spectrum of 176 in CDCl_3 .	398
Figure 218: A 126 MHz ^{13}C NMR spectrum of 176 in CDCl_3 .	399
Figure 219: A 400 MHz ^1H NMR spectrum of 170 in CDCl_3 .	399
Figure 220: A 126 MHz ^{13}C NMR spectrum of 170 in CDCl_3 .	400
Figure 221: A 500 MHz ^1H NMR spectrum of 171 in CDCl_3 .	400
Figure 222: A 126 MHz ^{13}C NMR spectrum of 171 in CDCl_3 .	401
Figure 223: A 500 MHz ^1H NMR spectrum of 172 in CDCl_3 .	401
Figure 224: A 126 MHz ^{13}C NMR spectrum of 172 in CDCl_3 .	402
Figure 225: A 500 MHz ^1H NMR spectrum of 173 in CDCl_3 .	402
Figure 226: A 126 MHz ^{13}C NMR spectrum of 173 in CDCl_3 .	403
Figure 227: A 400 MHz ^1H NMR spectrum of 187 in CDCl_3 .	403
Figure 228: A 126 MHz ^{13}C NMR spectrum of 187 in CDCl_3 .	404
Figure 229: A 400 MHz ^1H NMR spectrum of 188 in CDCl_3 .	404
Figure 230: A 126 MHz ^{13}C NMR spectrum of 188 in CDCl_3 .	405
Figure 231: A 500 MHz ^1H NMR spectrum of 189 in CDCl_3 .	405
Figure 232: A 126 MHz ^{13}C NMR spectrum of 189 in CDCl_3 .	406
Figure 233: A 400 MHz ^1H NMR spectrum of 192 in CDCl_3 .	406
Figure 234: A 101 MHz ^{13}C NMR spectrum of 192 in CDCl_3 .	407
Figure 235: A 400 MHz ^1H NMR spectrum of 193 in CDCl_3 .	407
Figure 236: A 101 MHz ^{13}C NMR spectrum of 193 in CDCl_3 .	408

Figure 237: A 400 MHz ^1H NMR spectrum of 195 in CDCl_3 .	408
Figure 238: A 400 MHz ^1H NMR spectrum of 196 in CDCl_3 .	409
Figure 239: A 101 MHz ^{13}C NMR spectrum of 196 in CDCl_3 .	409
Figure 240: A 500 MHz ^1H NMR spectrum of 197 in CDCl_3 .	410
Figure 241: A 126 MHz ^{13}C NMR spectrum of 197 in CDCl_3 .	410
Figure 242: A 400 MHz ^1H NMR spectrum of 198 in CDCl_3 .	411
Figure 243: A 101 MHz ^{13}C NMR spectrum of 198 in CDCl_3 .	411
Figure 244: A 400 MHz ^1H NMR spectrum of 199 in CD_2Cl_2 .	412
Figure 245: A 101 MHz ^{13}C NMR spectrum of 199 in CDCl_3 .	412

List of Schemes

Scheme 1: Metabolism of haem with the formation of CO.	41
Scheme 2: Formation of cGMP from GTP.	43
Scheme 3: How prodrugs can be used to release CO upon exposure to a trigger. M represents a transition metal with co-ligands L, whereas A and B are nonmetallic compounds.	50
Scheme 4: Decomposition of CORM-2, 1, in DMSO.	54
Scheme 5: Some aqueous chemistry of CORM-3, complex 5.	56
Scheme 6: Mechanism of CO release from esterase-targeting ET-CORMs.	63
Scheme 7: Generalised scheme for ET-CORM activation using amide bond cleavage catalyzed by proteases. ¹¹⁷	64
Scheme 8: Principle of photosensitisation to induce CO release.	68
Scheme 9: Modular synthesis of CORM-peptide conjugates using Sonogashira and ‘click’ chemistry.	70
Scheme 10: Conjugation of a Mn photoCORM with biotin using CuAAC.	71
Scheme 11: Carbon monoxide release from CORM-A1, compound 50.	73
Scheme 12: Diels-Alder cycloaddition reaction followed by extrusion of CO as a strategy for CO release. ¹⁴⁷	74
Scheme 13: General mechanism of the intramolecular ‘click and release’ methodology created by Wang and co-workers. ¹⁴⁸	74
Scheme 14: General mechanism for control of CO extrusion from complex 63 through E1cB elimination. ¹⁴⁹	75
Scheme 15: Two organic photoCORMs with visible light activation.	75
Scheme 16: Turn-on fluorescent probe for CO detection.	85
Scheme 17: Formation of paramagnetic species 75 and 76 in CORM degradation.	88
Scheme 18: Photochemical CO release from luminescent Re(I) photoCORM 77.	91
Scheme 19: Synthesis of the family of photoCORMs based on [Mn(ppy)(CO) ₄] and known derivatives.	92
Scheme 20: Reaction scheme for a Suzuki-Miyaura cross-coupling using mild conditions to functionalise a photoCORM.	93

Scheme 21: Species observed by mass spectrometry in a photochemical study by Fairlamb and co-workers. ¹⁵⁹	94
Scheme 22: The CO-release process from tpm complex 103 studied by TRIR spectroscopy.....	98
Scheme 23: Photochemical behavior of two chromium carbene CO-releasing molecules as determined by TRIR spectroscopy. ^{194,195}	100
Scheme 24: CORM-2 degrades in DMSO solution but further CO release can be prompted photochemically. Harris and co-workers used TRIR spectroscopy to show that degradation products 3 and 4 lose a CO ligand on the ultrafast timescale. ¹⁹⁶	100
Scheme 25: Illustration of the sequence of laser pulses in a TR ^M PS experiment. ²¹⁰	104
Scheme 26: Schematic representation of the setup used in TR ^M PS. ²¹⁰	105
Scheme 27: Photolysis of [Mn(ppy)(CO) ₄] in MeCN results in the formation of solvent complex [113 _{MeCN}]. The structures of three possible isomers of 113 _{MeCN} are shown along with their Free Energies at 298 K relative to the <i>fac</i> -isomer. For each isomer, the predicted infrared stretching frequency and scaled intensity of their vibrational modes in the metal carbonyl region are given at the D3-PBE0/def2-TZVPP//BP86/SVP(P) level with COSMO solvent correction in MeCN.	114
Scheme 28: Summary of the photochemical behavior of 88 in <i>n</i> -heptane.....	122
Scheme 29: Possible mechanism for decomposition of 113 _{OH₂} into Mn hydroxy clusters.....	125
Scheme 30: Summary of the reactions after CO loss from 88 in THF. Solvent coordination predominately occurs <i>via</i> a C-H bond to form 113 _{THF(σ)} before isomerisation to the more stable O-bound complex 113 _{THF(O)} . Note that the unsaturated complex in brackets is not observed. .	131
Scheme 31: Summary of the reactions after CO loss from 88 in DMSO. Solvent coordination predominately occurs <i>via</i> a C-H bond before isomerisation to the give the S- and O-bounds species.....	143
Scheme 32: Possible dimerization and cluster products formed in the continuous irradiation study.....	147
Scheme 33: Theisodesmic reaction used to calculate the relative energies of the complexes in Table 7.	148
Scheme 34: Intermolecular and intramolecular mechanisms for isomerisation of 113 _{THF(σ)} to 113 _{THF(O)}	157
Scheme 35: General catalytic cycle for a manganese carbonyl-catalysed alkenylation reaction. R = aryl.....	161

Scheme 36: The glutathione (GSH) and glutathione disulfide (GSSG) redox couple is the main intracellular redox buffer.	165
Scheme 37: Reaction of compound 125 with thiols leads to the formation of photoCORM 129. ²⁵⁵ An example reaction mechanism for the reaction of 125 with cysteine is shown.	166
Scheme 38: PhotoCORM 131 can be activated by reaction with H ₂ O ₂ as well as by visible light. ²⁵⁷	167
Scheme 39: Previously-used conditions for click chemistry with alkyne 46.....	170
Scheme 40: The triazole ring of compound 132 and synthetic equivalents needed for the retrosynthesis, 135 and 46.....	170
Scheme 41: Synthesis of the cyclometalating reagent [BnMn(CO) ₅].....	171
Scheme 42: Synthesis of ‘clickable’ alkyne complex 46. The yields are those achieved in this work.	171
Scheme 43: The two-step synthesis of azidoferrocene, compound 135, from ferrocene.....	172
Scheme 44: The final step in the synthesis of compound 132.	173
Scheme 45: Conditions for direct CORM functionalization with compound 133 unsuccessfully applied to ferroceneboronic acid.....	178
Scheme 46: The attempted application of palladium mesylate dimer pre-catalyst 97 to the synthesis of 133.....	179
Scheme 47: Possible retrosynthesis for a boronic acid CORM suitable for Suzuki-Miyaura couplings.....	180
Scheme 48: Previous synthesis of protonated ppy ligand 148 reported in the literature. ²⁸⁷	180
Scheme 49: Synthesis of CORM 133.	181
Scheme 50: Initial synthesis of protonated ligand 134 <i>via</i> a Suzuki-Miyaura reaction.....	183
Scheme 51: Synthesis of protonated ligand 149 <i>via</i> a Negishi coupling followed by cyclometallation with [BnMn(CO) ₅].....	184
Scheme 52: Decomposition of chloroform under ambient light and air.	205
Scheme 53: The coordination of THF following CO loss from complex 133, and subsequent isomerisation, shows the same behavior as [Mn(ppy)(CO) ₄]	212
Scheme 54: The CO loss from complex 132 results in a C-H σ-complex with the <i>n</i> -heptane solvent followed by displacement of <i>n</i> -heptane by water.....	214
Scheme 55: Oxidation of compound 132 to increase water solubility.....	216

Scheme 56: Synthesis of complex 161.	224
Scheme 57: Structures of the prodrug Sulfasalazine and its degradation products.	225
Scheme 58: Synthesis of azo ligands 167 and 169.	226
Scheme 59: Synthesis of complexes 170-173.	227
Scheme 60: Synthesis and cyclometallation of azobenzene 176.	232
Scheme 61: Formation of complex 179 _{THF(G)} . Dashed arrows have been used to reflect the lack of direct evidence for the mechanistic pathway.	248
Scheme 62: Formation of complex 180 _{THF(O)} . Dashed arrows have been used to reflect the lack of direct evidence for the mechanistic pathway.	252
Scheme 63: Literature redox behaviour of azobenzenes as determined by cyclic voltammetry in acetonitrile. Left: azobenzene. Right: 4,4'-nitroazobenzene.	255
Scheme 64: Summary of the formation of the species listed in Table 20 during infrared spectroelectrochemistry.	258
Scheme 65: Square scheme for complex 172 with proposed assignments of the species observed in the infrared spectroelectrochemistry.	259
Scheme 66: Species observed in the spectroelectrochemistry of 181 during formation of CO ₂ reduction catalyst 185.	260
Scheme 67: Relationship between the species observed in the UV-visible spectroelectrochemical experiment on 172.	262
Scheme 68: Summary of the synthesis of an azide CORM building block, compound 188.	268
Scheme 69: Possible radical cross-coupling side-reaction in the synthesis of 187. ³³²	268
Scheme 70: Demonstration of CuAAC conditions with novel azide 188.	271
Scheme 71: Synthesis of coumarin alkyne 196.	273
Scheme 72: CuAAC conditions for the synthesis of 197.	273
Scheme 73: Synthesis of compound 199.	287
Scheme 74: Cleavage of azo dyes with <i>p</i> -phenoxy substituents.	294
Scheme 75: Interconversion of catechol and 1,2-benzoquinone. Known metal carbonyls with catecholate co-ligands.	295
Scheme 76: PEGylation to produce more water-soluble [Mn(ppy)(CO) ₄] derivatives that retain synthetic flexibility.	296

Scheme 77: Possible arylation of the indole 2-position of TryptoCORM with aryldiazonium salts.³⁵¹297

List of Tables

Table 1: Reactivity of ET-CORMs towards two esterase enzymes.....	63
Table 2: Character table of the C_s point group showing the reducible representation of the carbonyl ligands of $[Mn(ppy)(CO)_4]$ underneath.....	107
Table 3: Character table of the C_{2v} point group showing the reducible representation of the carbonyl ligands of $[Mn(ppy)(CO)_4]$ underneath.....	108
Table 4: DFT-Calculated excitation wavelengths, intensities and orbital components for the low-energy allowed transitions of $[Mn(ppy)(CO)_4]$ in the weak shoulder from 425-325 nm.....	111
Table 5: Summary of kinetics of the isomerisation of complexes 88, 94 and 95 in THF.....	138
Table 6: Summary of data for the isomerisation reactions following CO loss from $[Mn(ppy)(CO)_4]$ in ether solvents.	141
Table 7: Assignment of the experimentally observed infrared bands and their unscaled DFT calculated wavenumbers. Relative changes to electronic energies (corrected for zero-point energy), ΔE and Gibbs energies at 298 K, ΔG_{298} , for the reaction in Scheme 33 are given at the D3-PBE0/def2-TZVPP//BP86/SVP(P) level with COSMO solvent correction in heptane. All calculations were performed by Dr Jason Lynam.....	149
Table 8: Summary of the lifetimes of the non-dissociative excited state.....	153
Table 9: Lifetimes of the C-H to O isomerisation of the three ether solvents reported in Section 2.3.5 with the ratio of the lifetime to the number of C-H bonds included for comparison.....	157
Table 10: How the current function varies with scan rate for complex 132. All solutions contained 1 mM 132 and 1 M electrolyte in CH_2Cl_2	188
Table 11: Summary of cyclic voltammetry data.	188
Table 12: Summary of the infrared stretching band positions of the neutral and cationic ferrocenyl Mn complexes studied by infrared spectroelectrochemistry.	190
Table 13: The increase in carbonyl stretching wavenumber upon formation of the cations of 132-134, relative to the neutral molecule, derived from the spectroelectrochemical experiment in Figure 69.	191
Table 14: Yield of isolated products for cyclometalation reactions with $[MeMn(CO)_5]$ and $[BnMn(CO)_5]$. Yields are based on the amount of azobenzene ligand used.....	228
Table 15: Comparison of metal carbonyl infrared stretching band wavenumbers in CH_2Cl_2 and THF between ppy complex 88 and azo complexes 172 and 173.....	229

Table 16: Comparison of the CO release experiments for a range of Mn(I) carbonyl complexes to compare the release profile of 172 with complexes 90, 91, 95, 133, 134 and 161. The starting concentration of CORM was 10 μM in all cases except for complex 133, where it was 40 μM	238
Table 17: Single exponential lifetime of the decay of $^3[172]-(1)$ and growth of $^3[172]-(2)$ with 95% confidence intervals.	245
Table 18: Single exponential lifetime of $^3[172]-(2)$ and concurrent bleach recovery with 95% confidence intervals.	246
Table 19: Single exponential lifetimes for the decay of the $^3[173]-(1)$ bands and growth of the $^3[173]-(2)$ band at 2054 cm^{-1} , with 95% confidence intervals.	250
Table 20: Single exponential lifetimes for the decay of the $^3[173]-(2)$ bands. The single exponential lifetimes for concomitant bleach recovery are also given. The fits are reported with 95% confidence intervals.	251
Table 21: Summary of the cyclic voltammetry data of complex 172.	255
Table 22: Summary of the infrared stretching bands observed in spectroelectrochemistry of 172.	258
Table 23: Stretching frequencies used to calibrate the TRIR spectra.	299
Table 24: Crystal data and structure refinement for compound 132.	353
Table 25: Crystal data and structure refinement for compound 133.	355
Table 26: Crystal data and structure refinement for compound 148.	357
Table 27: Crystal data and structure refinement for compound 170.	359
Table 28: Crystal data and structure refinement for compound 173.	361
Table 29: Crystal data and structure refinement for compound 188.	363
Table 30: Crystal data and structure refinement for compound 189.	365
Table 31: Crystal data and structure refinement for compound 197.	367

Additional Materials

The electronic submission of this Thesis is enclosed with additional files comprising X-ray crystal structure files, scans of mass spectra, raw and processed TRIR data, and spreadsheets showing how myoglobin assay data were processed.

Acknowledgements

Thank you to my supervisors Ian Fairlamb, Jason Lynam and Alison Parkin. They have each added support, insight and guidance throughout, while encouraging me to be creative and independent. I have learned a lot from them and I am grateful for the opportunity to undertake such a highly varied and stimulating programme of research under their supervision. I am grateful to the Engineering and Physical Sciences Research Council (EPSRC) for funding.

I have been just as fortunate to mentor to some incredibly talented, kind, and just plain hilarious students during my time in York. Work from some of them is included in this Thesis, where their contributions are highlighted. Helping them develop their skills and confidence has been a joy and they have given so much back to me. Thank you to Linna Wang, Will Evans, and Lisa Backwell (summer project students), Sam Andrew, Katie Fernandez and Claire Lancaster (final year undergraduates) Rachel Steen (MSc by research student), and Alice de Palo (undergraduate exchange student).

Thanks to the staff at the ULTRA facility at the Rutherford Appleton Laboratory (particularly Mike Towrie, Ian Clark, Igor Sazanovich and Emma Gozzard) for their considerable support facilitating the TR^{MPS} experiments. The time spent at RAL was a highly stimulating experience. I am also grateful to Dr Paul Scattergood and Professor Paul Elliott of the University of Huddersfield for providing an initial sample of the coumarin alkyne **196** used in this work.

I thank the technical staff in York for their support: Karl Heaton (MS); Heather Fish and Pedro Aguiar (NMR spectroscopy); Rachel Parker, Sam Hart, Jessica Milani and Adrian Whitwood (X-ray crystallography); Graeme McAllister (CHN); Peter O'Toole and Karen Hogg (microscopy). Thanks also to our lab technicians Charlotte Elkington, Naser Jasim and Julia Walton.

My thanks go to all members of the Fairlamb, Lynam and Parkin groups, where I have made lots of friends. Thank you to Tom, Alan, Lyndsay, Lucy and Josh who got me up and running when I started and to Richard, Harriet, Robin, Emily and Julia for helping me out in the microbiology lab. Thanks to Anders for somehow living with me for nearly three years, listening to my ramblings and making me laugh, George C for telling me when it's lunchtime, Lewis for our long chats, George P for Boycott Bingo, Lisa for board games and Steve Roggenbuck, Neil for teaching me to appreciate the finer things in life, Mark for emotional support during the World Cup, Mary for delightful African food, David for being called David, Will for bacon sandwiches, Lauriane for making me feel so old, Rachel for elderflower power, and Dan for our day out and Claire for encouragement and excellent parkin.

Finally, I would like to thank Mum, Dad, Emily, Bonnie and all my family for their constant support. I could not have done this without them.

Author's Declaration

I declare that this thesis is a presentation of original work and I am the sole author. The work was carried out at the University of York and the Rutherford Appleton Laboratory, Harwell between October 2014 and September 2018 and has not previously been presented for an award at this, or any other, University. All sources are acknowledged as References.

Part of this work has been reproduced in a publication, a copy of which is attached as Appendix 1:

B. J. Aucott, J. S. Ward, S. G. Andrew, J. Milani, A. C. Whitwood, J. M. Lynam, A. Parkin and I. J. S. Fairlamb, *Inorg. Chem.*, 2017, **56**, 5431–5440

Benjamin James Aucott

September 2018

1 Introduction

The toxicity of carbon monoxide (CO) is well-known. But CO is also produced endogenously in low concentrations by healthy mammals. It is now widely understood that CO is an important signalling molecule.

Administration of exogenous CO has been shown to have a wide range of beneficial effects but controlling the dose of CO gas in a meaningful way can be challenging. As a result, prodrugs termed CO-releasing molecules (CORMs), designed to display a well-defined and controlled CO release profile, have been developed. A range of delivery methods and CO-release triggers has been used. Mechanistic studies have also been employed to understand how to design CORMs with desirable properties.

This introduction begins by discussing the role of CO in biology and then provides examples of its therapeutic applications. Methods to administer CO, including the use of CORMs, will then be discussed. A summary of the techniques used for mechanistic insight into CO release is provided, and finally the aims and objectives of the work in this Thesis will be outlined.

1.1 Carbon Monoxide in Biology

1.1.1 Toxicity

The toxicity of carbon monoxide (CO) is well-known, having been studied since the 19th century. Headaches, confusion, hyperventilation, disturbed vision, and palpitations were among the symptoms of CO poisoning listed by John Scott Haldane in 1895, when he reported the effects of breathing different mixtures of air and “carbonic oxide” upon himself and mice.¹ Haldane showed that CO binds to the Fe-based O₂ carrier haemoglobin (Hb). Colourimetric assays on blood samples established that CO binds to Hb more strongly than O₂ by more than two orders of magnitude.² This work led to the introduction of CO safety measures: use of small animals as an early warning system in coal mines, where many workers died of CO poisoning.³ Safe levels of CO are currently considered to be exposure below 50 ppm over 8 hours.⁴

The early explanation of the toxicity of CO came from Haldane’s observations that CO binds to Hb. It was proposed that the resulting disturbance to the Hb O₂ transport mechanism was responsible for tissue hypoxia (O₂ starvation).¹ However, more recent research suggests that the level of carboxyhaemoglobin (CO-Hb) does not share a simple proportional relationship with the symptoms and outcomes experienced by patients,⁵ as would be predicted from Haldane’s proposal. For example, experiments to restrict O₂ availability in other ways have showed that simple lack of O₂ transport in the blood (hypoxaemic hypoxia) is insufficient to explain the effects

of CO poisoning. Okeda and co-workers performed experiments in the 1980s on anaesthetised cats, where blood oxygen content was controlled by breathing N₂/O₂ mixtures.⁶ The results showed that hypoxia alone was not enough to cause damage to brain tissue, as the circulatory system was able to adjust to the O₂ deficiency.⁶ Induction of an accompanying drop in blood pressure, an additional effect of CO poisoning, along with hypoxia, was required to cause damage to brain tissue.⁶ Earlier experiments suggested that inhalation of CO gas is considerably more toxic to dogs than receiving CO as CO-Hb in blood transfusions to reach the same CO-Hb levels.⁷ The extra toxicity of inhaled CO cannot be accounted for within Haldane's initial explanation.

The treatment for CO poisoning, however, has remained unchanged since the times of Haldane, who recommended the administration of oxygen.¹ Experiments in dogs showed that CO-Hb levels dropped faster in animals breathing O₂ or CO₂/O₂ mixtures compared to air, though this was before it was realised that CO-Hb levels are not always a reliable indicator of symptoms or outcome.⁸ Normal and hyperbaric pressures of oxygen are used to treat CO poisoning.⁹⁻¹¹ The success levels of treatment do not appear to have a simple relationship with the partial pressure of O₂.¹²

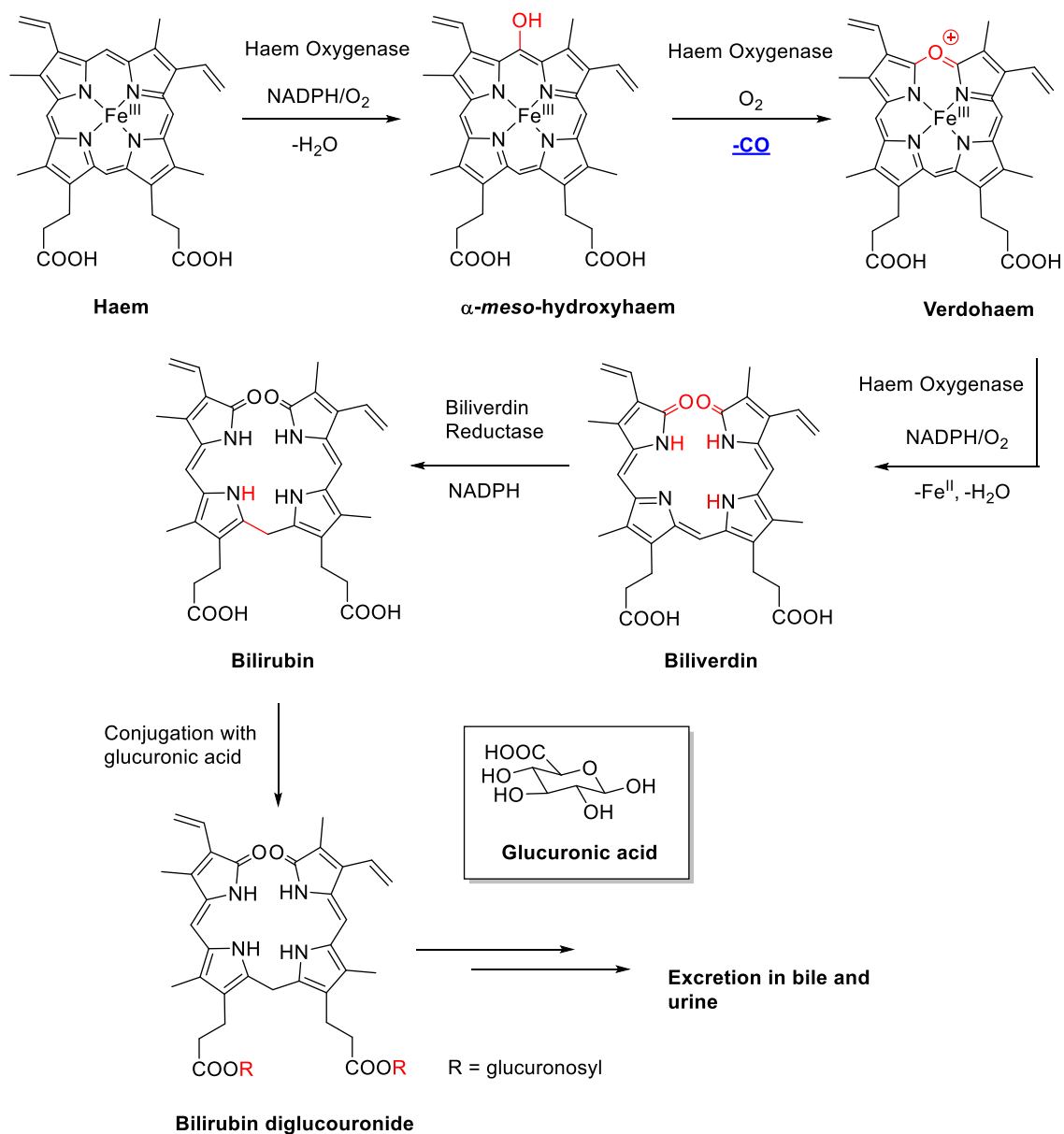
Another hypothesis for the toxicity of CO that has been examined is the inhibition of cytochrome c oxidase, another Fe-based protein, by CO. Just as with Hb, CO can bind to the iron of the haem group within cytochrome c oxidase, the terminal acceptor in the electron transport chain of aerobic respiration.¹³ This is in turn associated with an increase reactive oxygen species (ROS),¹⁴ which can cause further damage to DNA, proteins and cell membranes.¹⁴ Although the formation of, and damage caused by, reactive oxygen species has been implicated in the toxicity of CO in numerous studies,¹⁴⁻¹⁹ it is unclear how much the inhibition of cytochrome c oxidase contributes to the overall observed toxicity of CO.¹⁵ Experiments in which CO coordination to cytochrome c oxidase has been observed have typically been under high concentrations of CO and low concentrations of O₂ that are unlikely to be replicated *in vivo*.¹⁵

A full understanding of the mechanisms of CO toxicity remains elusive despite over a century of research.¹⁵ This is due in no small part to the discovery that CO is produced endogenously in healthy mammals and plays important roles as a signalling molecule, many of which are yet to be fully characterised.²⁰

1.1.2 Endogenous CO Production

In 1949, Sjöstrand discovered that CO is endogenously produced in humans.²¹ Subjects with diseases such as cancer, high blood pressure, and anaemia exhibited higher levels of CO in their breath than healthy people.²¹ The elevated CO levels returned to match those of healthy subjects upon recovery from disease.²¹ These observations were the first suggestion that this highly toxic gas plays an important physiological role in both healthy and diseased states.

Sjöstrand later provided the first evidence that endogenous CO production was linked to the metabolism of haem groups.²² Indeed the vast majority of endogenous CO production is accounted for by the oxidative metabolism of haem, catalysed by haem oxygenase (HO) enzymes (Scheme 1).²³



Scheme 1: Metabolism of haem with the formation of CO.

The first three steps in Scheme 1 are catalysed by haem oxygenases. The metabolism of haem begins with hydroxylation to generate α -meso-hydroxyhaem, which occurs *via* a peroxy intermediate.²⁴ Loss of CO from the α -carbon then occurs and the ring is cleaved open. Reduction by NADPH catalysed by cytochrome p450 results in formation of Fe(II), which is lost from the porphyrin and sequestered by ferritin, leaving the bile pigment biliverdin.²⁴ Biliverdin is subsequently reduced by NADPH in a reaction catalysed by a second enzyme, biliverdin

reductase, to yield bilirubin, which is solubilised by conjugation with glucuronic acid and excreted.²⁵

Three HOs have been identified, two of which are well-characterised.²⁶ Haem oxygenase 1 (HO-1) can be expressed by all mammalian cells.²⁷ Its expression may be induced by a very broad range of stresses including hypoxia,^{28–30} shear stress,³¹ heat shock³² H₂O₂ exposure,^{33,34} and UV irradiation.^{33–35} The observation that HO-1 is expressed under hypoxic conditions is particularly intriguing as CO produced from HO-1 activity would be expected to make the hypoxic stress worse. This point illustrates the importance of the various cellular targets in the biology of CO as opposed to simple effects on O₂ transport.

Haem oxygenase 2 (HO-2) is mainly found in the circulatory system.³⁶ It is the product of a different gene to HO-1, and constitutively expressed rather than being induced by stressful stimuli.³⁶ Less is known about the role of haem oxygenase 3 (HO-3). It shares > 90 % structural similarity with HO-2, but appears to be a poor catalyst for haem degradation, leading to the suggestion that it plays a regulatory role by binding haem.³⁷

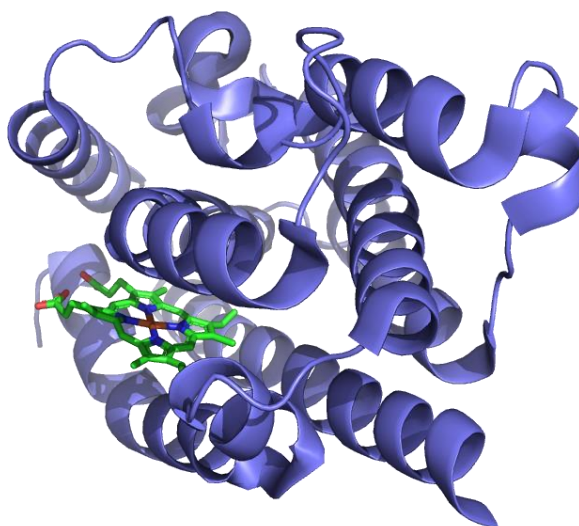


Figure 1: X-ray crystal structure of HO-1 with its haem substrate bound. Image produced from Protein Data Bank entry 1N45³⁸ using PyMOL.³⁹

Experiments studying the upregulation or knockout of the *hmx1* gene that codes for HO-1 have shown that the haem oxygenases are vital in responding to stress and preventing inflammation.⁴⁰ A study of *hmx1* gene-deleted mice exposed to a range of oxidants (including H₂O₂, paraquat and hemin), showed a much greater susceptibility to oxidative damage, suggesting that HO-1 activity can play a role as an antioxidant during oxidative stress.⁴¹ An *in vivo* study comparing wound healing rates in wild-type mice with HO-2 knockouts showed that the anti-inflammatory and injury reparative responses were severely depleted without HO-2.⁴² The products of haem

breakdown can induce expression of HO-1. It has therefore been suggested that the constitutively expressed HO-2 plays a regulatory role which can promote HO-1 production to increase haem degradation.⁴²

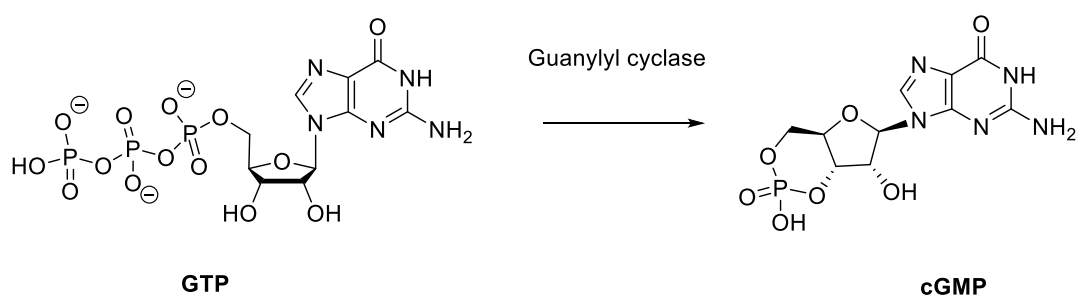
Many of the effects of HO activity can be replicated by the exogenous administration of one or more HO products.⁴³ For example, *in vitro* experiments with bile pigments biliverdin and bilirubin have shown their antioxidant properties and protective effects in models of cardiovascular and lung disease.⁴⁴ However, the therapeutic viability of bile pigments is relatively unexplored and represents another means of understanding and conveying the beneficial effects of HO activity. The therapeutic effects of administering exogenous CO have been studied far more widely and are discussed below.

1.1.3 Physiological and Therapeutic Effects of CO

Initially dismissed as a waste product of haem degradation, CO is now established as a signalling molecule of importance in numerous biochemical pathways. The following sections detail some examples of the interplay of CO signalling pathways and its relationship with physiological outcomes. The examples chosen are intended to display the wide range of physiological effects associated with CO.

1.1.3.1 Relationship of CO with Soluble Guanylyl Cyclase

One of the most significant mechanisms in CO signalling is through the activity of soluble guanylyl cyclase (sGC). This enzyme catalyses the conversion of guanosine triphosphate (GTP) into cyclic guanosine monophosphate (cGMP), as shown in Scheme 2.⁴⁵ Cyclic GMP is a ‘second messenger’, meaning that it is released by cells upon exposure to a ‘first messenger’ such as CO. Carbon monoxide can activate sGC to produce cGMP, as does NO – another highly toxic gas that acts as a gasotransmitter in lower concentrations.⁴⁶



Scheme 2: Formation of cGMP from GTP.

The role of cGMP is to trigger the activation of protein kinases which phosphorylate other proteins. Phosphorylation is often a trigger for the activation, transport or interaction of proteins, including enzymes, which can have significant physiological implications.⁴⁷ In particular, cGMP is associated with effects such as inhibition of platelet aggregation (preventing blood clots) and

Aerobic respiration uses electrons from the oxidation of sugars to reduce O_2 to H_2O . Energy released from this reaction is used to phosphorylate adenosine diphosphate (ADP) to form the adenosine triphosphate (ATP), the key energy carrier of the cell. Cytochrome c oxidase is a haem-containing protein that performs the reduction of O_2 to H_2O . Figure 3 shows a hypothesis for how CO interferes with this process to generate ROS. Inhibition of cytochrome c oxidase with CO slows down O_2 reduction and ATP production in the mitochondria, leading to a build-up of reduced electron carriers (Complex III in Figure 3).⁵⁷ This can in turn lead to an increased rate of side-reactions such as the partial reduction of O_2 , leading to the production of reactive oxygen species (ROS). The initial species produced is the superoxide radical, $[O_2^{\cdot-}]^-$, which can disproportionate to form O_2 and H_2O_2 catalysed by the enzyme superoxide dismutase (SOD).⁵⁷ The H_2O_2 is able to leave the mitochondria.⁵⁸ It has been shown that CO-induced production is not dependent on hypoxia but rather a build-up of reducing equivalents in the electron carriers in the mitochondria due to a reduced rate of O_2 reduction to H_2O . There is also evidence that CO induces expression of SOD.⁵⁷

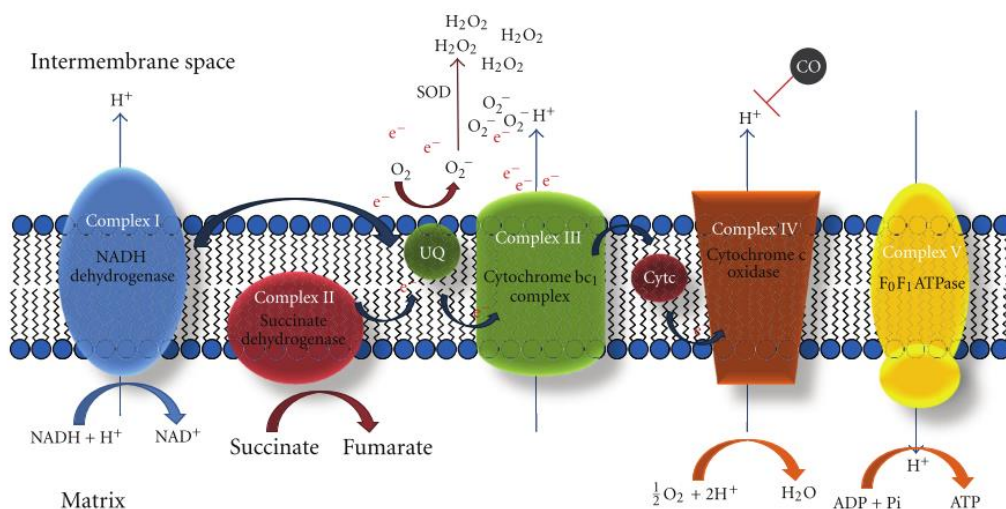


Figure 3: Mechanistic hypothesis for the CO-induced generation of ROS in the mitochondria by inhibition of cytochrome c oxidase. Adapted from C. S. F. Queiroga, A. S. Almeida and H. L. A. Vieira, *Biochem. Res. Int.*, 2012, Article ID 749845, 9 pages under a Creative Commons Attribution Licence.¹⁷

Reactive oxygen species are common and important components of signalling; for example some transcription factors and protein kinases are activated by the cellular redox environment.⁵⁷ Bursts of ROS from CO inhibition of cytochrome c oxidase could therefore lead to localised biochemical changes, for example CO-derived H_2O_2 is implicated in mitochondrial biogenesis: increasing the number of mitochondria allows cells to maintain high levels of respiration under stressful conditions.²⁰

1.1.3.3 Effect of CO on Inducible NO Synthase

The role of NO as a gasotransmitter has been extensively studied; it is known to be a neurotransmitter, vasorelaxant, and is generated as part of the inflammatory response.⁵⁹⁻⁶¹ The roles of CO and NO appear to be closely linked; having related signalling roles and mediating their effects in similar ways. For example, the two gases both act as neurotransmitters and may sometimes act as cotransmitters, meaning that release of both CO and NO is required for transmission of some nerve impulses in the brain.⁶² It has also been shown that CO is involved in regulating NO production, and *vice versa*.⁶³

Endogenous NO is produced from L-arginine in a reaction catalysed by a haem-containing enzyme called Nitric Oxide Synthase (NOS).⁶⁴ As with HO, NOS has both constitutively expressed and inducible (known as iNOS) isoforms.⁶⁰ It has been shown that CO can inhibit the activity of iNOS by binding to the haem group of the active site, thereby lowering the rate of NO production.⁶⁴ The involvement of NO in the inflammatory response suggests that iNOS inhibition by CO could be one mode of action for the anti-inflammatory effects induced by CO,⁴³ but more work is required to establish the relationship between CO and NO and to understand their respective biological roles. It is clear that CO and NO signalling are intricately related.

1.1.3.4 Effect of CO on Ion Channels

The effects of CO also extend to ion channels in the cell membrane. It has been shown that L-type Ca^{2+} ion channels, which are important in regulating vascular tone in the circulatory system, are a target for CO, which inhibits the channels.⁶⁵ This may play a role in the cardioprotective properties of CO. The effect may be mediated by mitochondria-generated ROS since antioxidants reversed the effect of CO.⁶⁵ This helps to explain HO-1 is upregulated and when the cardiovascular system is under stress, for example myocardial infarction. Exogenous CO has been shown to reduce injury from myocardial infarction in mice.⁴³

Carbon monoxide is also involved in activation of some ion channels, such as 'big-conductance' calcium-activated potassium (BK_{Ca}) channels. These channels excrete K^{+} ions when Ca^{2+} ions are detected, regulating the potential across the plasma membrane, and are linked to smooth muscle relaxation and vasodilation.⁶⁶ This shows how CO can play a role in blood pressure regulation. There is evidence to suggest that activation of BK_{Ca} channels mediated through several of the pathways discussed above, including release of ROS, direct binding to haem proteins associated with the channels, and sGC activity.⁶⁶

1.1.3.5 Role of CO in Mitrogen-Activated Protein Kinase Pathways

At least some of the anti-inflammatory properties of HO activity are known to derive from CO, based on experiments involving exogenous administration of CO. The way in which the CO mediates this effect appears to involve one of three important protein kinase signalling cascades

known as mitogen-activated protein kinase (MAPK) pathways. These pathways play significant roles in the inflammatory and immune response by increasing production of pro-inflammatory cytokines; compounds released as part of the immune response to potential pathogens. It is ultimately the overproduction of these molecules that results in the potentially fatal tissue damage caused by septic shock. The relationship of CO with MAPK pathways makes CO a promising anti-inflammatory agent.

The effect of CO was studied using *in vitro* and *in vivo* models of sepsis. The results showed that CO administration resulted in lower levels of three pro-inflammatory cytokines: tumour necrosis factor- α , interleukin-1 β , and macrophage inflammatory protein-1 β . Meanwhile, the CO led to an increased concentration of anti-inflammatory cytokine interleukin-10.⁶⁷

The *in vitro* experiment was performed with RAW 264.7 macrophages. Interestingly, the concentration of cGMP in the macrophages did not increase upon CO exposure, which suggested that the anti-inflammatory effect in this case was independent of the activation of sGC.⁶⁷ By comparison, an over 1000-fold increase in cGMP concentration was observed in the positive control experiment with smooth muscle cells (which relax in the presence of CO to cause vasodilation).

Instead of sGC activation, the study found an increase in the activity of MAPKs (particularly one of the three classes of kinase called p38) upon exposure to 250 ppm CO.⁶⁷ Mice without the ability to activate the p38 MAPK pathway did not receive the same beneficial effect in the presence of CO, confirming that p38 MAPK is a target for CO.⁶⁷

The examples discussed above rely on the ability of CO to bind to haem groups, yet in p38 MAPKs there are no haem groups for CO to interact with and no binding site for CO has been identified thus far.²⁰ It is therefore unclear how CO exerts its effect on this pathway. It is likely that CO has an indirect effect through other haem-based proteins, that can interact with both CO and a species involved in the p38 MAPK pathway. For example, it has been observed that antioxidants prevent CO activation of the p38 MAPK pathway.¹⁴ This suggests that ROS may play a role in this signalling pathway, perhaps derived from CO inhibition with cytochrome c oxidase.

The anti-inflammatory effects of CO are also mediated by other pathways. As discussed in Section 1.1.3.3, CO can influence NO production, which is involved in the inflammatory response. It has also been shown that CO can inhibit the function of toll-like receptors; proteins in the immune system that detect conserved molecular structures from pathogens to initiate the immune response and activate inflammatory pathways.⁶⁸

1.1.3.6 Applications of CO in Cancer

The extent of the therapeutic potential for CO treatment against cancer is still unclear as contrasting results have been obtained in different studies.⁶⁹ It appears that both HO-1 activity and CO can aid tumour growth under low CO concentrations, as CO can also be associated with a cytoprotective effect, cell proliferation and the development of new blood vessels (angiogenesis).⁶⁹ Yet these roles of CO may still be exploitable as a cancer therapeutic. Higher concentrations of CO can be used to cause metabolic exhaustion of the cancer cells by overstimulation of these pathways resulting in 'metabolic exhaustion'.⁷⁰ It has been shown that CO weakens prostate cancer cells towards chemotherapeutic agents without affecting normal cells.⁷¹ The addition of CO caused more consumption of O₂ by the mitochondria but also generated more reactive oxygen species.⁷¹ Human prostate cancer tumours grafted onto mice showed inhibited growth when mice were exposed to 250 ppm CO for 1 hour per day and was correlated with increased apoptosis of the tumour cells.⁷¹ A number of CO-releasing pro-drug systems have also been shown to cause apoptosis of cancer cells derived from the released CO.^{72,73}

The conflicting results obtained in different studies suggest that whether HO-1 or CO have anti-cancer effect may be highly dependent on the type of tumour and the dosage of CO.⁷⁰ More work is needed to understand the full impact of CO upon cancer cell metabolism. One thing that is clear is that exquisite control of dosage and localisation of CO is beneficial to the investigation of CO as a therapeutic agent and any subsequent development of pharmaceuticals will necessitate a delivery method with these properties.

1.1.3.7 Antimicrobial Properties of CO

Carbon monoxide is toxic to a range of pathogenic bacteria, typically at tens of micromolar concentrations.^{74,75} Studies in this area have been reviewed comprehensively; bactericidal effects on *Escherichia coli*, *Staphylococcus aureus*, and *Pseudomonas aeruginosa* have been observed.^{4,69,75} Bactericidal activity has been attributed mainly to the binding of CO to haemoproteins in the bacterial respiratory chain, preventing ATP synthesis.⁷⁵ These effects are promising given the escalating problem of antimicrobial resistance and the resulting need for new antimicrobials with novel modes of action. Carbon monoxide also induces dormancy of *Mycobacterium tuberculosis*, which could be used to slow infections down to enable the immune system to clear the infection. Carbon monoxide can bind to the haem-containing sensory proteins DosS and DosT which causes regulatory proteins to induce the dormancy response.⁷⁶

However, mechanisms by which CO acts are not always clear. This is because most antimicrobial experiments with CO have used prodrugs, called carbon monoxide-releasing molecules (CORMs), to deliver CO.⁴³ The use of CORMs could potentially cause the biological effects of CO to be accompanied by further effects of the by-products from CO release. The importance of this point is highlighted by the observation that some CORMs are considerably more toxic to

bacteria than CO gas.⁷⁵ This observation may be due to more effective localisation of CO into bacterial cells than can be achieved with CO gas, or it may be related to the effects of the CORM and its degradation products. The therapeutic properties of CO must therefore be clearly distinguished from the biological activity of the remaining fragments of the prodrug.

The application of CORMs, as opposed to just CO, as antimicrobials will be further discussed in Section 1.3.1.

1.1.4 Summary

The study of the biochemical mechanisms that constitute CO signalling in healthy humans, as discussed above, reveals the basis for a wide range of possible targets and therapeutic applications. The exploration of CO in breath as a tool for monitoring inflammation and oxidative stress also remains an active area of research.⁶⁸ Additional evidence of therapeutic effects has been found for a range of other disease states. This considerable body of research shows that CO is a promising therapeutic molecule with a range of possible targets.

1.2 Delivery Methods for CO

In many of the studies discussed above, CO was administered as a gas. However, for the last 20 years it has been apparent that greater localisation and control of CO delivery is required if this molecule is to realise its potential as a therapeutic agent. The goal is to provide well-defined, reproducible, and localised doses. Improvements in CO delivery aid studies of CO physiology and provide a starting point towards developing prodrugs that release CO in therapeutic doses.⁴³ This Section outlines the variety of possible methods available to deliver CO to biological targets.

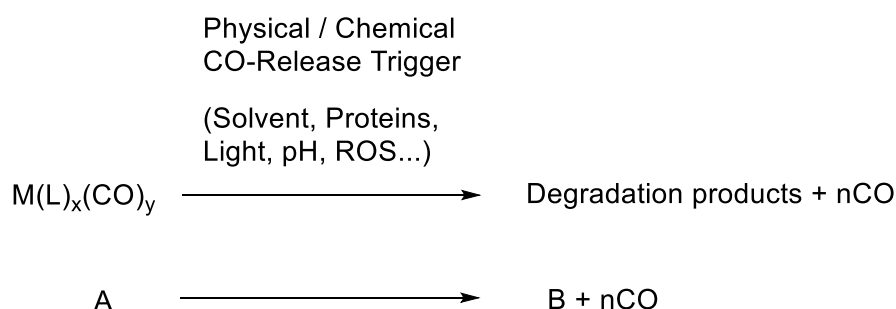
1.2.1 Inhalation of CO Gas

Commercialisation of a CO gas delivery system for spontaneous and ventilator breathing is currently being explored by CO therapeutics company Proterris.⁷⁷ Previously, some details have been published of the development of a medical device for the administration of CO gas called the Covox DS (delivery system). The Covox DS system has been used to deliver CO to human volunteers.⁴³ It gives precise control over the amount of CO inhaled and absorbed by allowing adjustments for the body weight and breathing rate of the subject. In trials on healthy volunteers the elevation of CO-Hb levels was reproducibly around 12 % when a dosage of 3 mg kg⁻¹ h⁻¹ was used for one hour.⁴³ However, as discussed in Section 1.1.1, it is unclear whether CO-Hb is a reliable measurement of CO dosage due to the other variability or symptoms and outcomes with CO-Hb levels, since CO interacts with many other targets in the body. This raises the question of how much CO is actually absorbed into the body when breathing CO gas and it is unclear whether a reliable method can be developed to quantify CO doses given to a population of patients.

Furthermore, CO gas delivery is unselective, as CO can be transported through the blood and hence spread throughout the body. As a result, treatment with CO gas is likely to require larger doses compared to delivery methods with greater selectivity to ensure the dose at the site of action is sufficient. This in turn requires careful monitoring and control of the CO administered in a clinical setting to monitor exposure over time following a given dose. Use of CO gas is therefore far less flexible and convenient compared to other CO release methods such as the use of prodrugs.⁷⁸

1.2.2 Metal-Based CORMs

The use of CORMs as prodrugs that release CO has been proposed as a more selective method of delivering a controllable, well-defined dose of CO compared to CO gas inhalation.²³ This has prompted study of triggered CO release from a diverse range of organic and organometallic compounds for therapeutic application.^{43,66,78,79} A CORM is designed to react when exposed to a physical or chemical trigger to release CO (Scheme 3).⁸⁰ Crucially, CORMs are able to replicate many of the physiological effects of CO and HO activity.⁴³ Due to the extensive coordination chemistry of CO with transition metals, most CORMs are metal carbonyl complexes,⁶⁹ although some non-metallic CORMs are known.⁷⁹



Scheme 3: How prodrugs can be used to release CO upon exposure to a trigger. M represents a transition metal with co-ligands L, whereas A and B are nonmetallic compounds.

The most common triggers for CO release from metal-based CORMs are ‘thermal’, photochemical, and enzymatic reactions.⁷⁸ Each method has its advantages over the others and will be discussed in turn.

1.2.2.1 Carbon Monoxide as a Ligand

The salient feature of the chemistry of CO in the coordination sphere of a metal is its ability to behave as a π -acid ligand.⁸¹ This property enables it to form strong M-CO bonds with electron-rich transition metals, including to the reduced form of haem groups in biological systems. Metal carbonyl complexes can therefore be exploited for the storage and controlled release of CO.

Carbon monoxide behaves as a Lewis base, typically acting as a two-electron donor to transition metals through the C atom. Terminal or bridging (μ_2 or μ_3) coordination modes through just the

C atom are the most common. Bridging can sometimes occur either through a second (and sometimes third) electron pair shared from the π -bond (Figure 4).

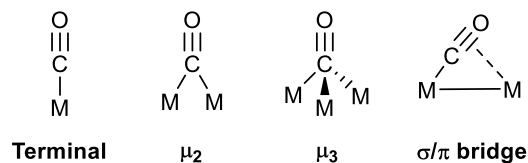


Figure 4: Common binding modes of CO to transition metals

Despite the electronegativity difference in the C and O atoms the dipole moment of CO is only 0.12 D,⁸² as the HOMO is based primarily on the C atom. As a result of this, CO is considered a soft ligand. The molecular orbital (MO) diagram for CO is shown in Figure 5.

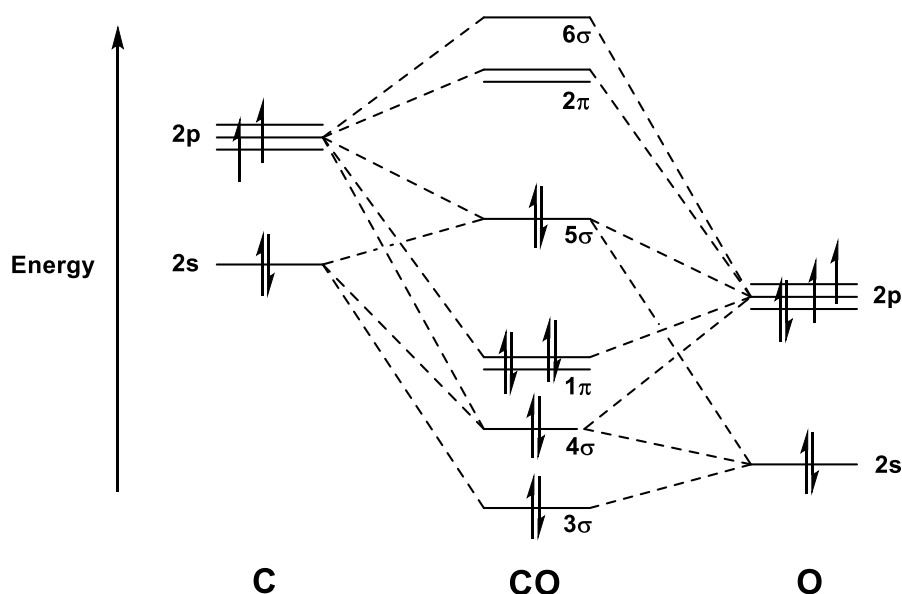


Figure 5: The MO diagram for CO.

The MO diagram shows that the Highest Occupied Molecular Orbital (HOMO) is the 5σ orbital. Historically, the 5σ orbital has been described as an antibonding orbital, as an explanation for why the infrared stretching frequency of non-classical metal carbonyls increases from that of CO. However, recent computational work has suggested that the 5σ orbital is slightly bonding in character,⁸³ and that the infrared stretching frequencies of non-classical metal carbonyls can be explained by the behaviour of the π -system.⁸⁴ The description of the 5σ orbital as weakly bonding is consistent with the absence of a node between the C and O nuclei (Figure 6). The 5σ orbital MO of CO can form a σ -bond to metal-based orbitals as shown below on the left of Figure 6. As a result, coordination to a metal centre to form an M-C bond would be expected to result in a strengthening of the C \equiv O bond due to the removal of antibonding electron density. However, the π -backdonation from occupied metal-based orbitals into the antibonding 2π orbitals of the CO ligand,⁸⁵ ensures that there is an overall weakening in the C \equiv O bond upon coordination to an

electron-rich metal centre, as shown in the centre of Figure 6. On the right of Figure 6 is shown a third interaction: π -donation from the occupied 1π orbitals into vacant metal-based orbitals. This effect is often overlooked as a more minor interaction but can strengthen or weaken the M-C bond depending on whether the π -electrons can interact with empty or filled metal-based orbitals.

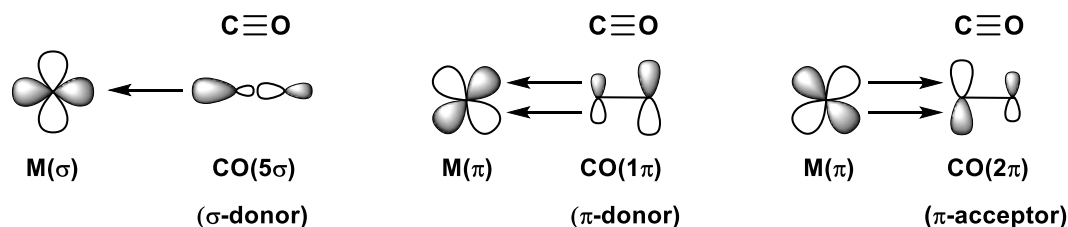


Figure 6: Interactions of CO MOs with transition metal orbitals.

1.2.2.2 ‘Thermal’ CORMs

Thermal CORMs have a simple, unselective release trigger, in which the metal complex releases CO upon dissolution in solution at 37 °C, the average normal body temperature. The term ‘thermal’ CORM is commonly interchanged with other terms such as ‘solvent-induced’ or ‘spontaneous’ CORM.⁸⁵ This is because the mechanism of degradation of thermal CORMs typically involves a ligand substitution reaction whereby a solvent molecule replaces CO. This Section describes the development of thermal CORMs.

A timeline of some of the developments and publications to be discussed in this Section is provided in Figure 7. The timeline shows how the initial testing of CORMs was based on verifying that the CO released by a metal carbonyl could mimic the effects attributed to CO gas, verifying the biological effect of CO and the strategy of using CORMs to deliver it. As the field has developed, the more recent work has focused on modulation of the CO release rate and the biological properties, such as water solubility, tissue localisation or specific therapeutic activity. There is now a wide range of thermal CORMs available and design strategies are based on derivatising existing complexes to confer desirable properties or release characteristics and there has been a shift in focus latterly towards the greater control over CO release rate and localisation provided by photoCORMs (Section 1.2.2.4).

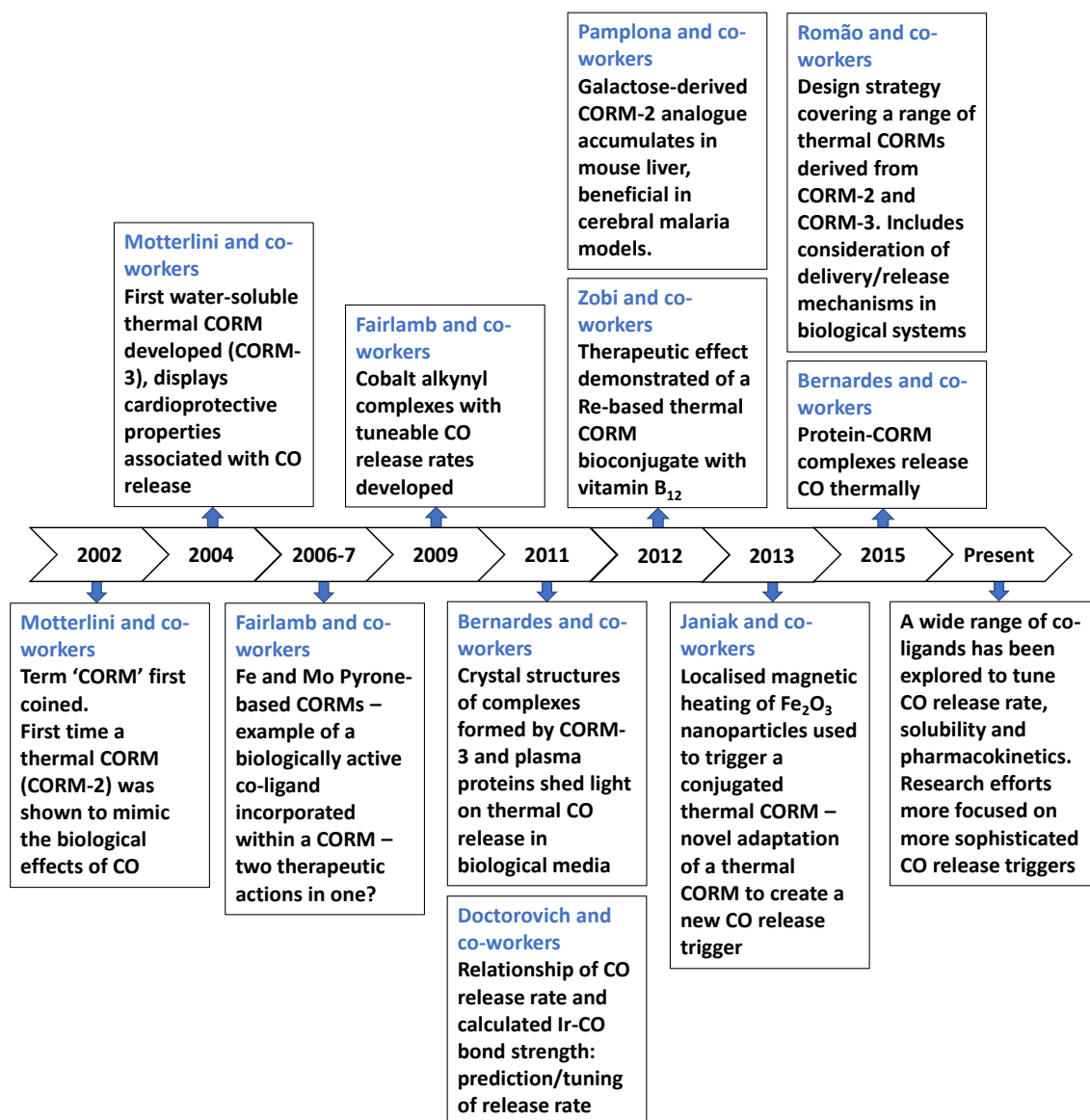
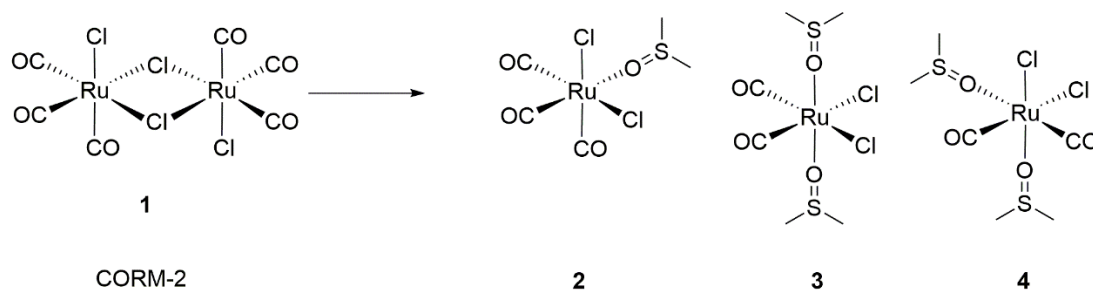


Figure 7: A timeline of some of the published developments in the field of thermal CORMs discussed in this Section, from the first CORMs paper in 2002 to the more recent shift to more sophisticated design strategies and CO release triggers.⁸⁶⁻⁹⁶

The first published example of a thermal CORM used for therapeutic CO release was complex **1**, [Ru(CO)₃Cl₂]₂, also known as CORM-2 (Scheme 4), in 2002.⁸⁶ As this complex displayed low water solubility it was solubilised in dimethyl sulfoxide (DMSO). Dissolution of CORM-2 in DMSO followed by mixing with an aqueous solution of deoxymyoglobin (deoxy-Mb) induced CO release, as detected by carboxymyoglobin (Mb-CO) formation in the UV-visible spectrum of the solution. The conversion of deoxy-Mb to Mb-CO is a very common technique to assess CO release and will be discussed in more detail in Section 1.3.2.1.

The mechanism for CO release from CORM-2 was also investigated by infrared and NMR spectroscopies. The DMSO complexes **2-4** were observed to form from a freshly-prepared sample

of **1**, confirming that CO release from CORM-2 is initiated by ligand substitution of the solvent to produce dicarbonyl and tricarbonyl complexes.⁸⁶ Although CORM-2 is often termed a ‘thermal’ CORM in the literature, it is more accurately a solvent-triggered CORM. The DMSO plays a much more significant role than a simple solubilising agent. It is possible that a similar mechanism could occur in water but CORM-2 was not soluble enough in water to test this hypothesis.



Scheme 4: Decomposition of CORM-2, 1, in DMSO.

It was then shown in the initial 2002 paper that the CO released from CORM-2 resulted in the vasodilation of precontracted rat aortas.⁸⁶ Control experiments showed that this was not caused by the decomposition products of CORM-2 or the DMSO used as a delivery vehicle, showing that the released CO was responsible for the effect. The mechanism of vasodilation was shown to occur *via* a cGMP-dependent pathway.⁸⁶ These experiments showed that CO released from a CORM can elicit a therapeutically relevant effect in the same way as CO gas. Low levels of cytotoxicity from CORM-2 and its degradation products were also observed.⁸⁶

The promising therapeutic results obtained for CORM-2 led to a search for a water-soluble alternative, and such an example was published in 2004.⁸⁷ Reaction of CORM-2 with glycine and sodium ethoxide yielded water-soluble complex **5**, also known as CORM-3, as shown in Figure 8.⁹⁷ An additional advantage of using an amino acid to confer water solubility as a CORM co-ligand is that glycine is already well-known in biological systems. Although the precise mechanism for CO loss from CORM-3 is not known, one of the degradation products of CO loss from CORM-3 is likely to be glycine, which the body’s own metabolism and excretory systems can remove.

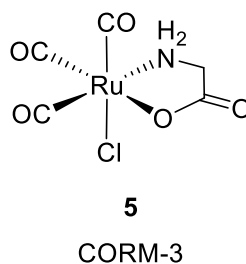
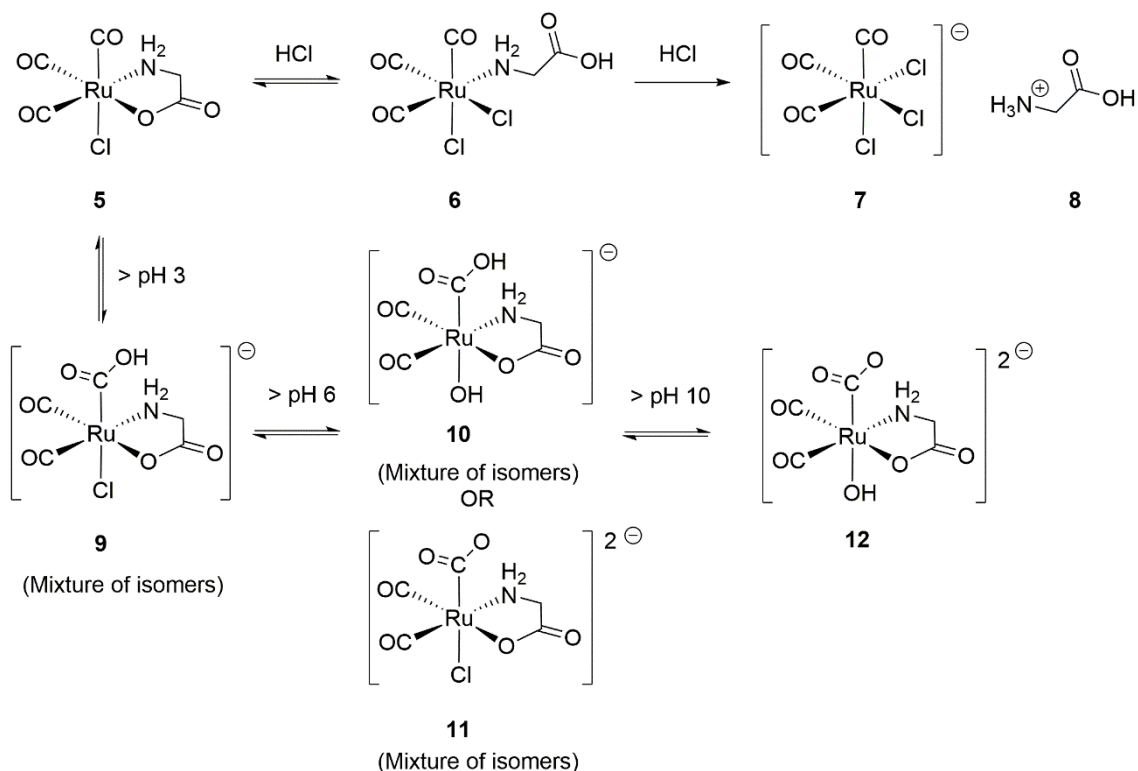


Figure 8: Structure of CORM-3, complex 5.

It was demonstrated that CO released from CORM-3 is able to mimic the cardioprotective properties associated with CO by increasing the resistance of cardiac muscle cells to oxidative stress and ischaemia-reperfusion (lack of O₂ followed by re-supply of O₂, which causes oxidative damage).⁹⁷ Another finding was that CORM-3 improved survival rates of transplanted hearts in a mouse model.⁹⁷ The development of CORM-3, the first water-soluble source of CO, represented an enormous opportunity for *in vitro* studies of the role of CO in biology and the development of therapeutics. There is now a large range of published applications for this compound in animal models.⁶⁹ These include improved outcomes in organ transplantation,^{98,99} reduced injury from myocardial infarction,¹⁰⁰ treatment of sepsis¹⁰¹, treatment of *Pseudomonas aeruginosa* infections,¹⁰² and reduction of inflammation in arthritis.¹⁰³ Indeed CORM-3 is now commercially available from Sigma-Aldrich (catalogue number SML0496).¹⁰⁴

However, purification of CORM-3 has been problematic and raises questions about the reliability of its synthesis for therapeutic application. In addition to the bands of CORM-3 (complex **5**), the infrared spectrum contains metal carbonyl bands at 2137, 2072 and 2058 cm⁻¹ that suggest a *facial* tricarbonyl impurity.¹⁰⁵ Further bands at 1985 and 2058 cm⁻¹ (the latter overlapping the tricarbonyl impurity) were also observed and suggest that a dicarbonyl impurity is also present.¹⁰⁵ The presence of impurities resulted in a study of the aqueous chemistry of CORM-3.¹⁰⁶ A key finding of this work was the formation of tricarbonyl complex **6** upon addition of HCl to CORM-3 (Scheme 5). Complex **6** matches the tricarbonyl impurity typically found in samples of CORM-3.¹⁰⁵ Subsequent loss of the glycine ligand can then take place to form **7**. It was also noted that CORM-3 underwent nucleophilic attack by water at low pH to produce isomer mixture **9** consistent with the dicarbonyl impurities observed in CORM-3 samples. Upon increasing the pH, two more equilibria were established. These were assigned to deprotonation and ligand exchange, although the order of these events was not conclusively assigned due to uncertainty of the approximate pK_a values in complex **9**.¹⁰⁶ It is unclear how, and to what extent, the impurities in CORM-3 affect the therapeutic effects observed. The equilibria in acidic and basic aqueous solutions shown in Scheme 5 makes the preparation of a pure sample of CORM-3 difficult. Instead, CORM-3 may be regarded as a mixture of compounds, where complex **5** is accompanied by impurities such as **6** and **9**.



Scheme 5: Some aqueous chemistry of CORM-3, complex 5.

A further point of interest is that CORM-3 only releases around one equivalent of CO to myoglobin despite being a tricarbonyl complex. It has been observed that CORM-3 can also participate in the water-gas shift reaction, in which CO from the CORM reacts with water to produce CO₂ and H₂ (Equation 1).⁹¹



This reactivity usually requires high temperatures and pressures, but direct detection of CO₂ and H₂ above the headspace of CORM-3 solutions provides evidence of that CORMs can participate in similar reactivity.⁹¹ Such side-reactions illustrate the importance of directly detecting CO release from metal carbonyl complexes, as it cannot be assumed that all CO ligands are lost, nor can it be assumed that loss of CO ligands from the metal actually results in release of CO gas. Common methods for direct CO detection are discussed in Section 1.3.2.

Although the aqueous chemistry of CORM-3 must be studied to understand its CO release properties, other CO release mechanisms are at work in biological systems. Results published by the Bernardes group in 2011 showed that, as well as being a thermal CORM, CORM-3 can react with common plasma proteins to product protein-CORM complexes which subsequently degrade.⁹¹ Figure 9 shows a crystal structure of a protein-CORM complex between lysozyme and CORM-3.⁹¹ The metal centre remains in the +2 oxidation state but the glycinate, chloride and one CO molecule have dissociated. The octahedral complex with the protein comprises two carbonyl ligands, three water molecules and a nitrogen lone pair from a histidine residue. One of the

carbonyl ligands in Figure 9 is bent – in the crystal structures of CORM binding sites the Ru-C-O angle ranged from 178° to 139°, the latter of which is unusually low, but not unheard of for a terminal metal carbonyl.⁹¹ No hypothesis, such as a specific interaction of the carbonyl ligand with the surrounding protein, was offered for such a small Ru-C-O angle. This kind of reactivity is also thought to have very poor selectivity, as reactions take place with other common plasma proteins such as myoglobin and albumin.¹⁰⁷ Therefore, in biological systems, the mechanism of CO release from CORM-3 may instead involve CO loss from the CORM-protein complex. It was later shown in 2015 that the CORM-3 protein complexes can spontaneously release CO. This work shows the importance of understanding CORM behaviour within the complex biological systems into which they are to be introduced, since different CO release mechanisms may become available.

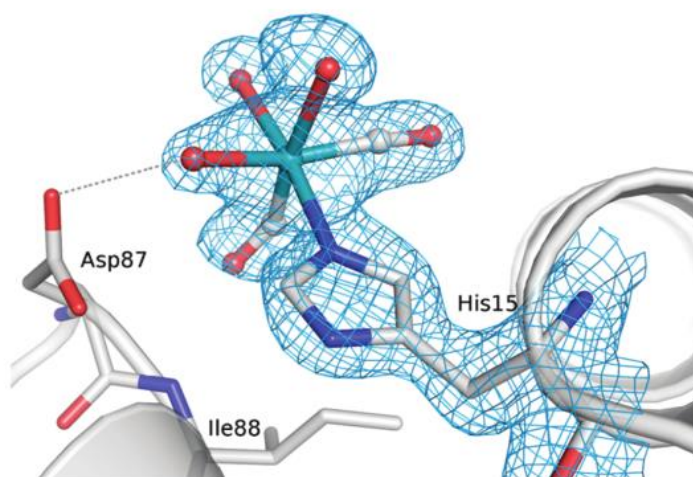


Figure 9: Crystal structure of the complex formed by CORM-3 and a histidine residue in hen egg white lysozyme. Reproduced with permission from T. Santos-Silva, A. Mukhopadhyay, J. D. Seixas, G. J. L. Bernardes, C. C. Romão and M. J. Romão, *J. Am. Chem. Soc.*, 2011, 133, 1192–5.

A disadvantage of ‘thermal’ or ‘solvent-triggered’ CORMs is that CO release begins immediately upon mixing with a solvent, as soon as the CORM solution is prepared. This can reduce the selectivity of CO release from the CORM. The choice of co-ligands can still provide some flexibility for tuning CO release rate, solubility, and the nature of decomposition products. An example of how CO release rate can be tuned by co-ligands is the work of Doctorovich and co-workers, who synthesised a series of Ir(III) tetrachlorocarbonyl CORMs in which they placed various substituents *trans* to the carbonyl ligand (Figure 10).⁹²

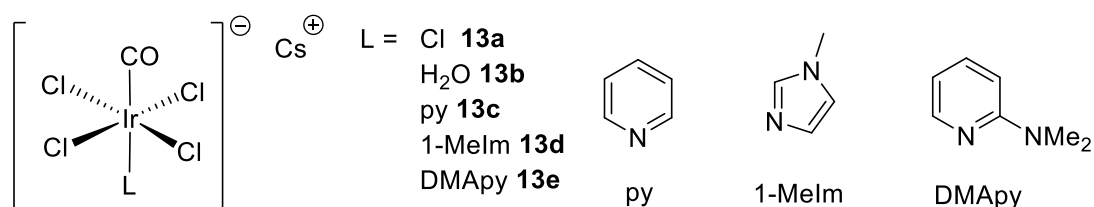


Figure 10: Thermal CORMs synthesized and tested by Doctorovich and co-workers.⁹²

The thermal CO release rates to Mb were shown to be independent of Mb concentration, so that the kinetics of thermal CO release could be measured. The CO is lost by ligand substitution with H₂O. Figure 11 shows the broad correlation between the DFT-calculated Ir-CO bond strength and the thermal CO release rate in this series of complexes.⁹² In turn, the Ir-CO bond strength is modulated by the *trans* effect of the ligand L. For example, the protonated DMApy ligand is a good π -acceptor ligand, which withdraws electron density from the metal and weakens the Ir-CO bond, whereas chloride and hydroxide can only behave as π -donors. However, an associative substitution mechanism (i.e. for CO loss is likely due to the negative entropy of activation of the reaction⁹² and the assignment of associative ligand substitution mechanisms to other Ir(III) complexes.¹⁰⁸ This means that although the M-CO bond is weakened by the strong donor ligand *trans* to CO, the substitution takes place by association of a water molecule to form a 7-coordinate intermediate, from which the CO is then lost. Despite the associative mechanism it is clear that the properties of the co-ligand L still affect the thermal CO substitution kinetics and can therefore be used to tune the rate of CO release.

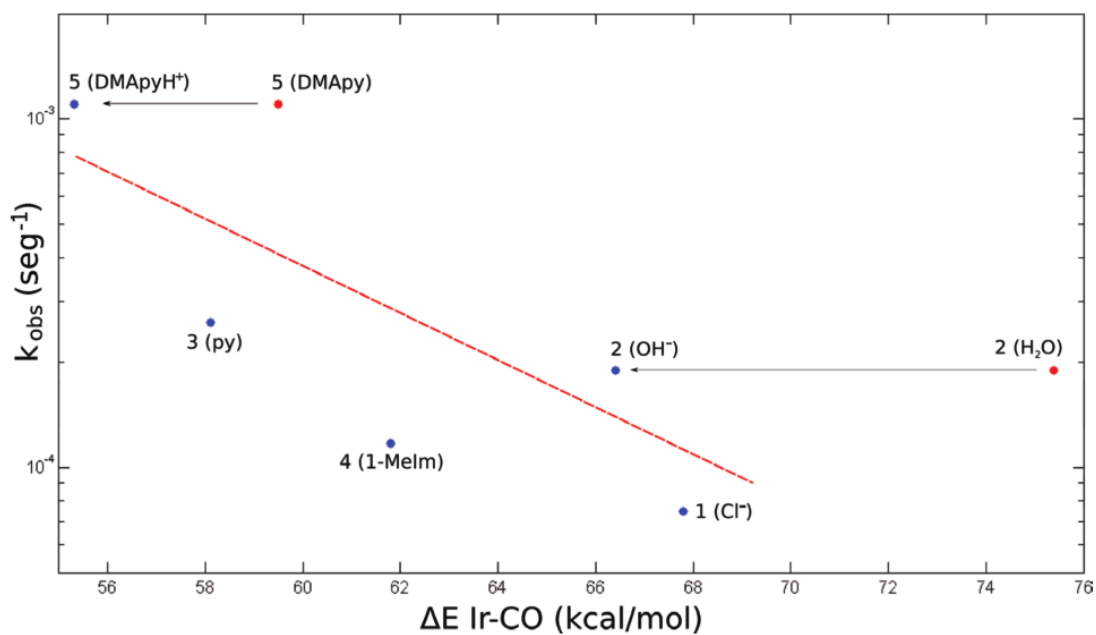


Figure 11: Relationship of DFT-calculated Ir-CO bond strength (in kcal/mol) and the observed rate constant for CO loss (plotted on a logarithmic scale in units of s⁻¹). The red line was added to show the qualitative trend. Reprinted with permission from D. E. Bikiel, E. G. Solveyra, F. Di Salvo, H. M. S. Milagre, M. N. Eberlin, R. S. Corrêa, J. Ellena, D. A. Estrin and F. Doctorovich, *Inorg. Chem.*, 2011, 50, 2334–2345. Copyright 2011 American Chemical Society.

Numerous other systems have been shown to release CO thermally; a selection of the diverse metal and co-ligand combinations that have been used is provided in Figure 12.

has been used *in vitro* to demonstrate some cardioprotective properties of CO, such as protection against ischaemia-reperfusion injury.⁹³

Release of CO from histidine complex **16** has also been shown to play a therapeutic role in ischaemia-reperfusion injury, in neuronal cells, by preventing apoptosis *via* the p38 MAPK pathway.¹⁰⁹ This complex also displays thermal CO release and uses a biocompatible co-ligand.⁴³ The number of equivalents of CO and the *in vitro* and *in vivo* toxicity were not published.

Fairlamb and co-workers synthesised a range of η^1 and η^4 pyrone complexes that purportedly release CO thermally.^{88,89} Pyrones are known to have their own biological activity, particularly as anti-cancer compounds.^{110,111} The incorporation of ancillary ligands with biological activity of their own raises the possibility of multiple modes of action within the same drug, where co-ligands liberated after CO release go on to have a further therapeutic effect. Halogen-substituted complexes **19c-e** showed thermal CO release whereas unsubstituted complexes did not.⁸⁸ A possible explanation for this is that the electron-withdrawing effect causes weaker coordination of the CO to the pyrone, though it is not known whether pyrone loss is the initial step in CO release. It is important to state that, although the term ‘thermal’ release was used for the pyrone complexes no control experiment in the absence of Mb or buffer solution was performed and CO release triggered by these species cannot be ruled out. The rate of CO release was slow if any at all, with less than one equivalent, and frequently less than 0.1 equivalents, of CO per CORM released within 60 minutes in all cases.^{88,89}

Numerous $\text{Co}_2(\text{CO})_6$ alkynyl complexes have been shown to have anti-cancer properties, including conjugates with nucleosides¹¹² and aspirin.¹¹³ The mechanism of the anti-cancer activity is unclear but the $\text{Co}_2(\text{CO})_6$ moiety is required as the alkynyl ligands are inactive on their own. It is unclear in these studies whether CO is released. A series of binuclear cobalt alkynyl complexes was also synthesised by Fairlamb and co-workers to investigate the CO-release properties of this family of compounds.⁹⁰ The substituents on the alkyne had a dramatic effect on the CO release rate. Complex **20b** released CO to myoglobin with a few minutes whereas **20c** took hours and **20d-f** did not release a detectable amount of CO in two hours.⁹⁰ Unusually, complex **20a** released only one equivalent of CO despite the presence of many more CO ligands, whereas **20b** was shown to release up to three equivalents of CO.⁹⁰ Unlike with the pyrone complexes, direct evidence of thermal CO release was obtained, through experiments in DMSO. Coordination of DMSO and CO loss leads to the cleavage of the Co-Co bond and formation of $[\text{Co}(\text{CO})_4]^-$.⁹⁰ A similar mechanism could be envisaged for water as DMSO is behaving as a 2-electron donor ligand. However, many of these complexes displayed poor cytotoxicity results on healthy human cell lines, suggesting that their therapeutic use may be limited.⁹⁰

Iron CORMs such as **21** and **22** are a popular choice due to the abundance of iron chemistry in biology. This can be helpful when considering clearance of CORM-derived by-products after CO

release, although the toxicity of each CORM must be assessed on a case-by-case basis. Complex **22** has been shown to be a vasorelaxant and releases CO thermally.¹¹⁴ Although **22** can release CO in anaerobic media, one of its related derivatives, in which the imine is replaced by an amide, only releases CO in aerobic media, and an oxo-bridged diiron species was detected as an intermediate in the decomposition, showing that O₂ can also trigger CO release.¹¹⁴ Complex **21** comprises an unusual dithiocarbamate ligand to convey water solubility.¹¹⁵ A major advantage is that it releases all three equivalents of CO, as each ligand is successively displaced by a water molecule.¹¹⁵ However, cytotoxicity studies on RAW 264.7 macrophages showed significant toxic effects at tens of micromolar concentrations and no therapeutic applications have been demonstrated thus far.

Finally, a recent innovation with the area of thermal CORMs has been the use of magnetic heating to cause CO loss. Janiak and co-workers attached a Ru(II) tricarbonyl thermal CORM complex to magnetic maghemite (Fe₂O₃) nanoparticles using a dihydroxyphenylalanine-derived ligand **23** (Figure 13).⁹⁵ In the presence of an alternating magnetic field, localised heating occurs at the nanoparticles which is sufficient to increase the rate of solvent-triggered CO release from the CORM. In this way, a slow-releasing thermal CORM can be converted into one with a completely different CO release profile using a different, controllable, CO release trigger.

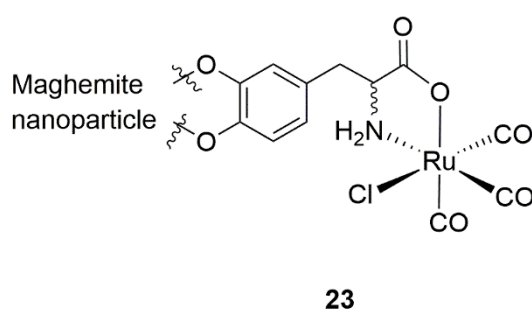


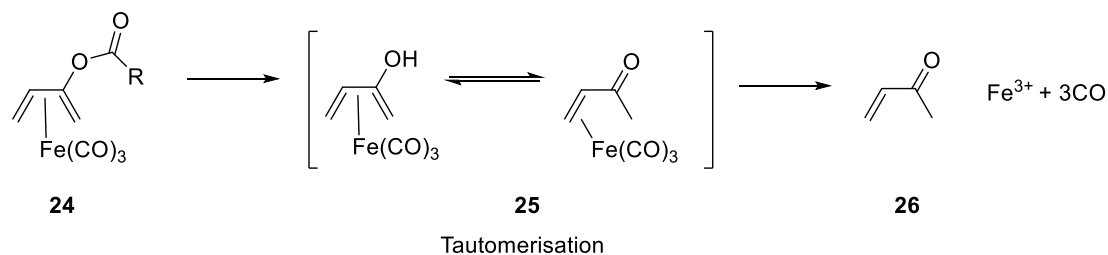
Figure 13: Thermal CORM 23 triggered by magnetic heating of maghemite nanoparticles.

Despite the possibility for selective accumulation in tissues and control of CO release rates, the lack of stability in water of thermal CORMs can lower the selective delivery of CO compared to a CORM triggered by another mechanism. If a CORM is not stable in water, it is inevitable that some CO will be released before the CORM reaches its target. More selectivity can be obtained through other CO-release triggers, but numerous thermal CORMs have been shown to have therapeutic effects derived from CO release, including *in vivo* studies.

1.2.2.3 Enzyme-Triggered CORMs

A method for gaining more selective CO release is to use CORMs that target enzymes. Such CORMs are stable in the presence of air, water and common plasma proteins but can be decomposed by enzymes localised in the target tissue or disease site. Such CORMs are described as ‘enzyme-triggered’ CORMs, or ET-CORMS.

One example of this is the use of acyloxybutadienyl iron carbonyl complexes as a method for targeting esterase enzymes, a strategy published in 2011.¹¹⁶ These compounds (Scheme 6) are stable in solution as dienylesters, but the corresponding dienol complexes are not stable in water. The ester complex **24** can be readily converted into the unstable dienol by the action of esterases that cleave specific ester bonds. Following ester hydrolysis, the resulting enol **25** tautomerises to the keto form and degrades rapidly to release CO.



Scheme 6: Mechanism of CO release from esterase-targeting ET-CORMs.

By altering the substitution patterns of a series of acyloxybutadienyl iron carbonyl complexes, different esterase enzymes can be targeted (Figure 14). Since different concentrations of esterase enzyme can be found in different tissues and disease states, CORMs can be designed with a much more specific target in mind. In this work, the ET-CORMs could be designed to be activated by pig liver esterase or by a lipase enzyme found in the fungal pathogen *Candida rugosa*, as shown in Figure 14 and Table 1. The release of CO to myoglobin was only observed when the appropriate esterase was present, showing that the CORMs are thermally stable and do not degrade upon reactivity with the myoglobin itself. As a control, complex **30**, which cannot tautomerise to the unstable enone form, was not activated by either esterase.

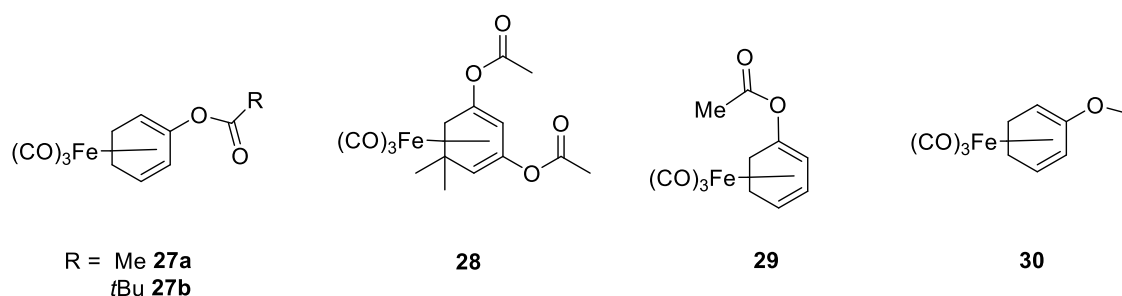


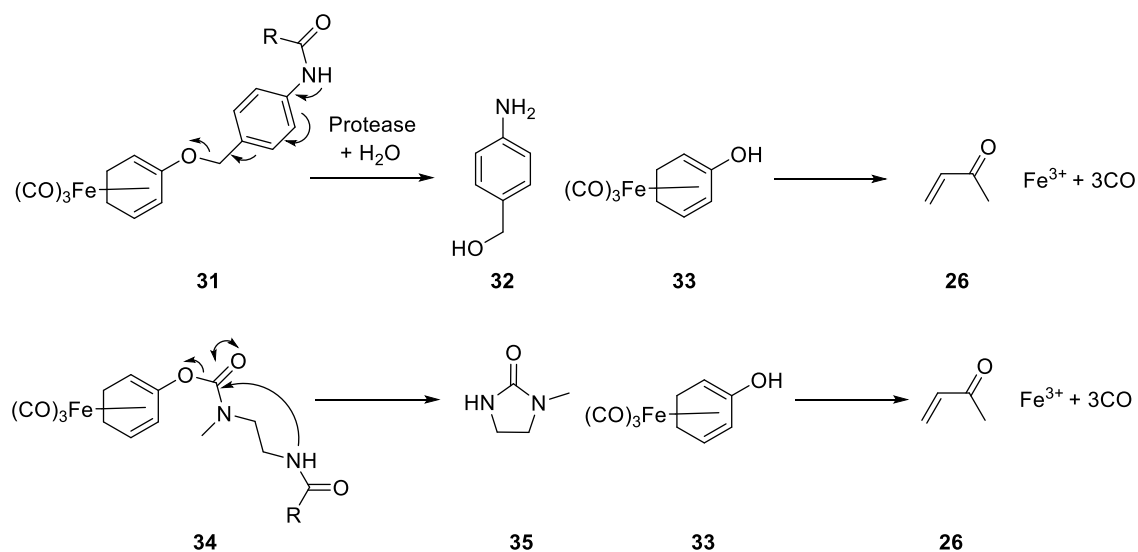
Figure 14: Esterase-triggered ET-CORMs.

Table 1: Reactivity of ET-CORMs towards two esterase enzymes.

Enzyme	27a	27b	28	29	30
Pig liver esterase	No	No	Yes	Yes	No
<i>C. rugosa</i> lipase	Yes	Yes	No	Yes	No

One drawback of this work is that the CORMs are synthesised as a racemate.¹¹⁶ Compelling evidence for the esterase-triggered CO release mechanism was obtained in the observation that the esterase carries out a kinetic resolution of the racemate. However, administering racemic mixtures as therapeutics can be impractical due to the high dosage required and possible detrimental effects of the undesired enantiomer, with separation of enantiomers often a challenging and expensive process. Furthermore, there could be significant issues with regulatory approval of a racemic mixture for therapeutic use. In the case of these compounds, the cytotoxicity was also high, with IC₅₀ values for the two CORMS shown above determined to be within the tens of micromolar range.¹¹⁶ Nevertheless, when stimulated by an appropriate esterase, this class of compounds displayed a striking inhibition of NO production at CORM concentrations as low as 5 μM.¹¹⁶ This series of compounds illustrates how modularity within the ancillary ligands of a CORM can be exploited to provide targeted CO release.

The same framework was later (2015) adapted to produce CORMs that are activated by proteases;¹¹⁷ increased production of proteases occurs in cardiovascular disease and cancer,^{118,119} for which CO may confer therapeutic benefits.⁴³



Scheme 7: Generalised scheme for ET-CORM activation using amide bond cleavage catalyzed by proteases.¹¹⁷

Recently, a similar strategy targeting esterases has been employed for the delivery of persulfides.¹²⁰ Hydrogen sulfide and persulfides are known to play a physiological role and the development of persulfide delivery agents will aid research into possible therapeutic applications.

1.2.2.4 Metal Carbonyl PhotoCORMs

A very common method of CORM activation is photolysis. Compounds used to release CO upon photolysis are termed photoCORMs. Such complexes must be stable in the dark in aqueous solution and in biological systems, only releasing CO when irradiation is supplied. This provides

selective CO release to a particular area and is especially applicable to surfaces. The vast array of compounds developed has been discussed in several recent reviews.^{66,121–123} Irradiation of metal carbonyls initially prepares metal-to-ligand charge transfer (MLCT) excited states in which electron density is transferred to carbonyl ligands from the metal ¹MLCT(CO). These excited states acquire CO-dissociative character by mixing with higher-energy d-d transitions, though the ligand field excited states themselves typically lie much higher in energy than the MLCT bands.¹²⁴ Further discussion of the photophysical and photochemical processes linked to CO photodissociation is provided in Section 2.1, where CO loss from low-energy excited states of ¹MLCT(bpy) character [Cr(bpy)(CO)₄] (bpy = bipyridyl) is discussed alongside the ¹MLCT(CO) states. It is important to study the primary photochemical processes involved in CO dissociation in order to understand how photoCORMs can be improved.

The early examples of photoCORMs were simple homoleptic carbonyls such as Fe(CO)₅ and Mn₂(CO)₁₀. In the same 2002 paper in which they coined the term ‘CORM’ and published the thermal releaser CORM-2, Motterlini and co-workers showed that light-induced CO release from Mn₂(CO)₁₀ resulted in vasodilation in rat hearts, in the first demonstration of a therapeutically relevant effect from a photoCORM.⁸⁶

Light-triggered loss of CO from many metal carbonyls may be achieved from using UV light.¹²³ However, CO release wavelengths in the visible region, preferably near-infrared (NIR) light represent the most therapeutically useful. This is because UV irradiation has inferior tissue penetration¹²⁵ and can cause tissue damage.¹²⁶ As a result, it is desirable to increase the CO release wavelength of photoCORMs. The choice of metal, oxidation state and ancillary ligands of a photoCORM can be used to tune the CO release wavelength. A successful approach taken by Mascharak and co-workers was to use π-acceptor co-ligands, which led low-energy CO-dissociative excited states in a series of Mn(I) tricarbonyls, leading to visible light CO release.¹²⁷ This strategy will be discussed in detail in Chapter 4, where a similar method is applied to a different family of compounds to tune the CO release wavelength of the compounds in this Thesis.

Comparable methodologies have been used by other groups (Figure 15). For example, Darensbourg and co-workers designed diazabutadiene complex **36**, which releases CO at 560 nm.¹²⁸ TD-DFT calculations suggested that CO release takes place by population of an MLCT excited state in which electron density is transferred from Mn-CO bonding orbitals into the low-lying imine π* manifold, which confirms that the presence of low-lying vacant orbitals can result in a lower-energy CO-dissociative transition.¹²⁸ However, CO release was not quantified from this complex and the only direct detection was a small peak in the infrared spectrum.

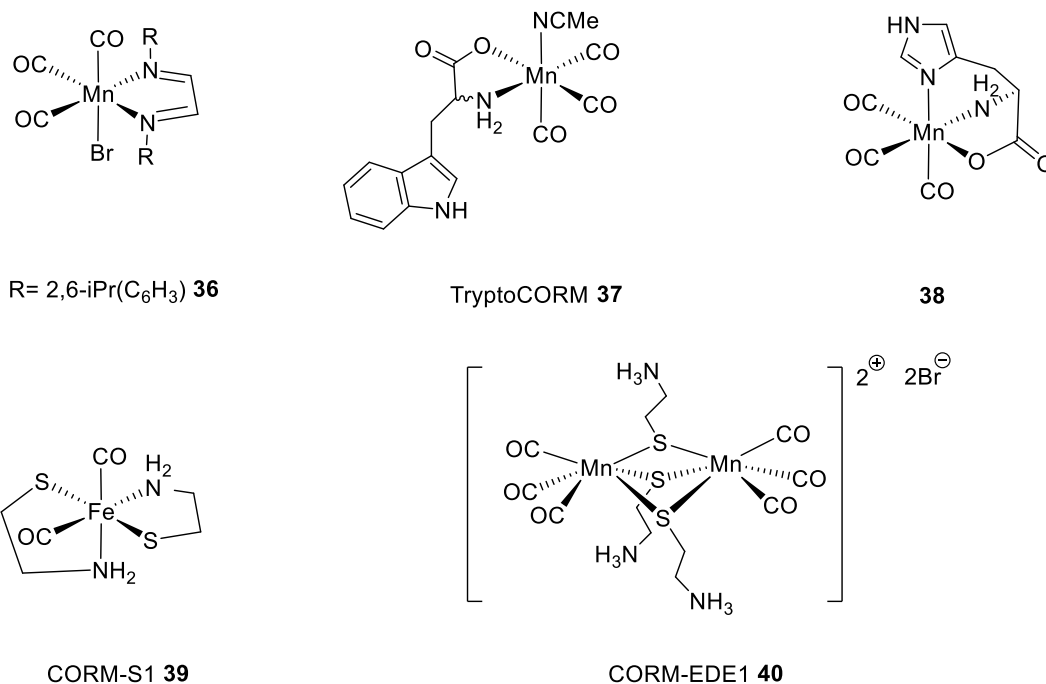


Figure 15: Recent photoCORMs.^{128–133}

Incorporation of amino acids as biocompatible co-ligands has also been employed, in conjunction with Mn(I) tricarbonyl complexes. Histidine (**38**) and tryptophan (**37**) have both been used as tridentate and bidentate photoCORM co-ligands respectively. Complex **38**, prepared by Schatzschneider and co-workers released only one equivalent of CO to Mb photochemically with 365 nm irradiation.¹²⁹ Complex **37**, synthesised by Fairlamb and co-workers, known in the literature as TryptoCORM, displayed visible light CO release to Mb at both 400 and 465 nm, although only 2.0 and 1.4 equivalents of CO were released from this tricarbonyl complex.¹³⁰ Low cytotoxicity to RAW 264.7 macrophages of both TryptoCORM and its degradation products was demonstrated, and light-triggered CO release prevented the growth of *E. coli* cultures.¹³⁰ Recently, it has been demonstrated that TryptoCORM can also elicit antimicrobial effects in the dark against *N. gonorrhoeae*.¹³¹

Two interesting examples are complexes **39** and **40**. Both complexes are thermally stable display photochemical CO release to Mb (irradiation above 400 nm), yet neither contains an extended π -system in the first coordination sphere of the metal carbonyl moiety. These systems show that it is possible to tune the CO photodissociation wavelength even in the absence of an unsaturated chromophore or π -acid ligand with a low-lying π^* orbital. Complex **39**, known as CORM-S1, released *ca.* 1.1 equivalents of CO after 15 minutes of continuous irradiation at (470 ± 10) nm with a 20 W LED.¹³² The therapeutic potential of CORM-S1 was demonstrated by showing that upon irradiation the released CO activates big-conductance potassium channels, showing that the CO-release profile from the CORM is compatible with biological activity.¹³²

Westerhausen and co-workers used cysteamine as a sulfur-bridging ligand to produce binuclear Mn(I) tricarbonyl complex **40** (CORM-EDE1).¹³³ Cysteamine is produced physiologically from the amino acid cysteine which makes it appealing as a biocompatible co-ligand.¹³³ The authors proposed the use of frozen aqueous stock solutions for storage and transport, however the complex is unstable in the presence of phosphate buffer solution, precipitating MnHPO₄.¹³³ One asset of this system is that CO release elicited from 365 nm or 470 nm irradiation yielded six equivalents of CO per dinuclear complex, which represents an excellent ratio of CO delivery for a relatively low molecular weight compound, such that lower concentrations of photoCORM can be used to deliver therapeutic doses of CO. The CO released from CORM-EDE1 was also shown to activate big-conductance potassium channels.¹³³

Another approach to achieve visible light CO release is to use a photosensitiser that absorbs a longer wavelength of light but induces CO dissociation from a photoCORM. Palladium complex **41**, Figure 16, was used as a photosensitiser to absorb 635 nm red light.¹³⁴ Such a methodology has recently been applied to improve the therapeutic viability of Mn₂(CO)₁₀ (**42**) by increasing the CO-release wavelength from UV to red light.¹³⁴

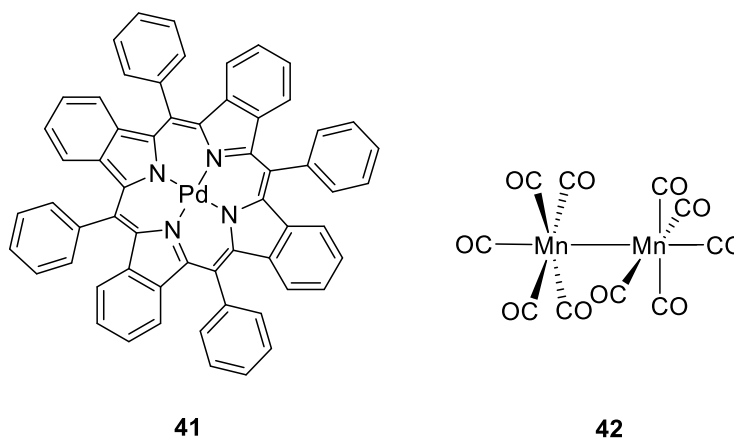
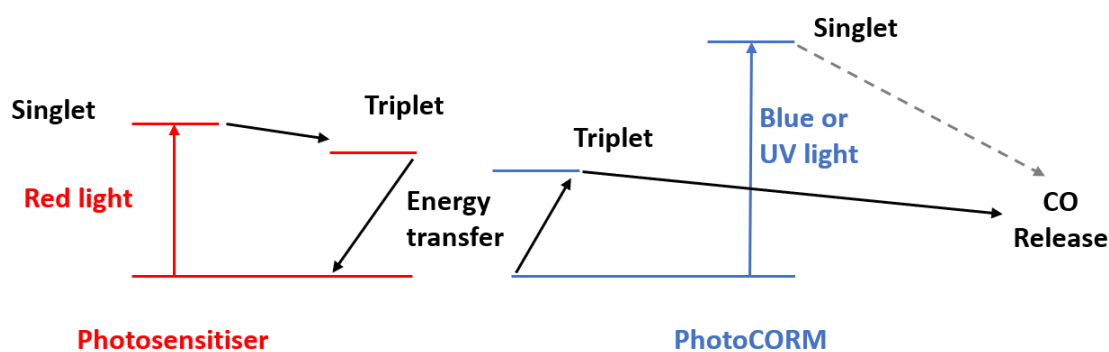


Figure 16: Photosensitiser complex 41.

Complex **41** absorbs at a longer wavelength than Mn₂(CO)₁₀ and after singlet excitation undergoes intersystem crossing to a triplet excited state that lives for hundreds of microseconds. The lifetime of this triplet excited state is sufficient for collisional energy transfer between this complex and Mn₂(CO)₁₀ to occur, generating a reactive triplet excited state from which CO loss can occur (Scheme 8).¹³⁴



Scheme 8: Principle of photosensitisation to induce CO release.

The practicality of using a photosensitiser in conjunction with a photoCORM does limit its use as both the CORM and photosensitiser need to be localised in the same place and the toxicity of two compounds and their by-products must now be considered. Schiller and co-workers addressed this problem in their work by incorporating complex **41** and $\text{Mn}_2(\text{CO})_{10}$ together in an electrospun polymer fabric.¹³⁴ This CO-releasing system could therefore be incorporated into fabrics such as bandages, where the anti-inflammatory and antibacterial properties of CO release could provide a beneficial effect. Irradiation with an LED gave good control of CO release depending on the power used.¹³⁴ However, therapeutic effects from such a system are yet to be demonstrated and it is unclear whether the formation of degradation products from CO release, such as MnO_2 , brings about any toxicity issues, depending on the toxicity of the compound and how well it is retained within the polymer. This would have to be investigated further by monitoring the release of complex **41** and any CORM degradation products.

1.2.2.5 Development of CORM Co-Ligands

The examples so far have shown how the choice of CORM co-ligands can be used to modulate CO release rate, wavelength, water solubility, biocompatibility and drug-like properties. This has led to a wide range of CORMs with different properties that are available for further adaptation and application. For example, it may be desirable to develop CORMs with slow CO release rates (half-lives of tens of minutes to hours) for some applications where the CORM is intended to mimic CO production by haem oxygenase enzymes, giving a low-level continuous supply of CO rather than a very large and short dose. On the other hand, applications such as antimicrobial activity appear to require CORMs with faster CO release rates.

As the CORMs field has developed over the last fifteen years, the design of the co-ligands around CORMs has become an increasingly important consideration.⁷⁸ This has led to development of targeted CORM systems through co-ligand design, moving away from simple broad-spectrum complexes like CORM-2 and CORM-3 towards complexes with specific targets and applications. Examples of this discussed above have been the localisation of sugar conjugate **14** in the liver and the active transport of vitamin B_{12} conjugate **15** into fibroblast cells. Given the large range of

possible therapeutic applications for CO, there is a very broad scope for designing many such targeted CORM systems where the co-ligands are optimised for a specific application of CO delivery. The modification of the ancillary ligands is part of designing the ‘drug sphere’ of CORMs: the outer coordination sphere of the metal, as coined by Romão *et al.*⁷⁸ The inner coordination sphere of the metal may be used to control the release rate, number equivalents of CO released and wavelength of CO release in the case of photoCORMs. However, several of these features, as well as the drug-like properties of metal-based CORMs can be designed by considering the outer drug sphere, to which medicinal chemistry principles can be applied more readily (Figure 17).⁷⁸

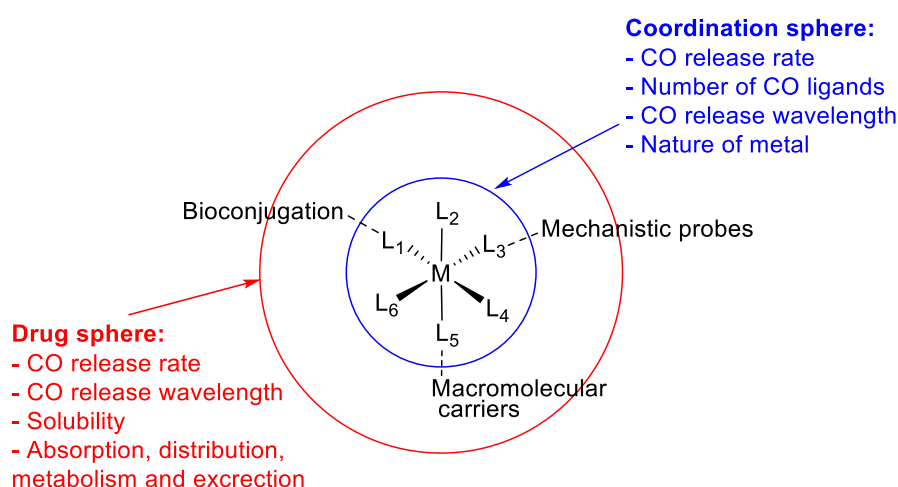
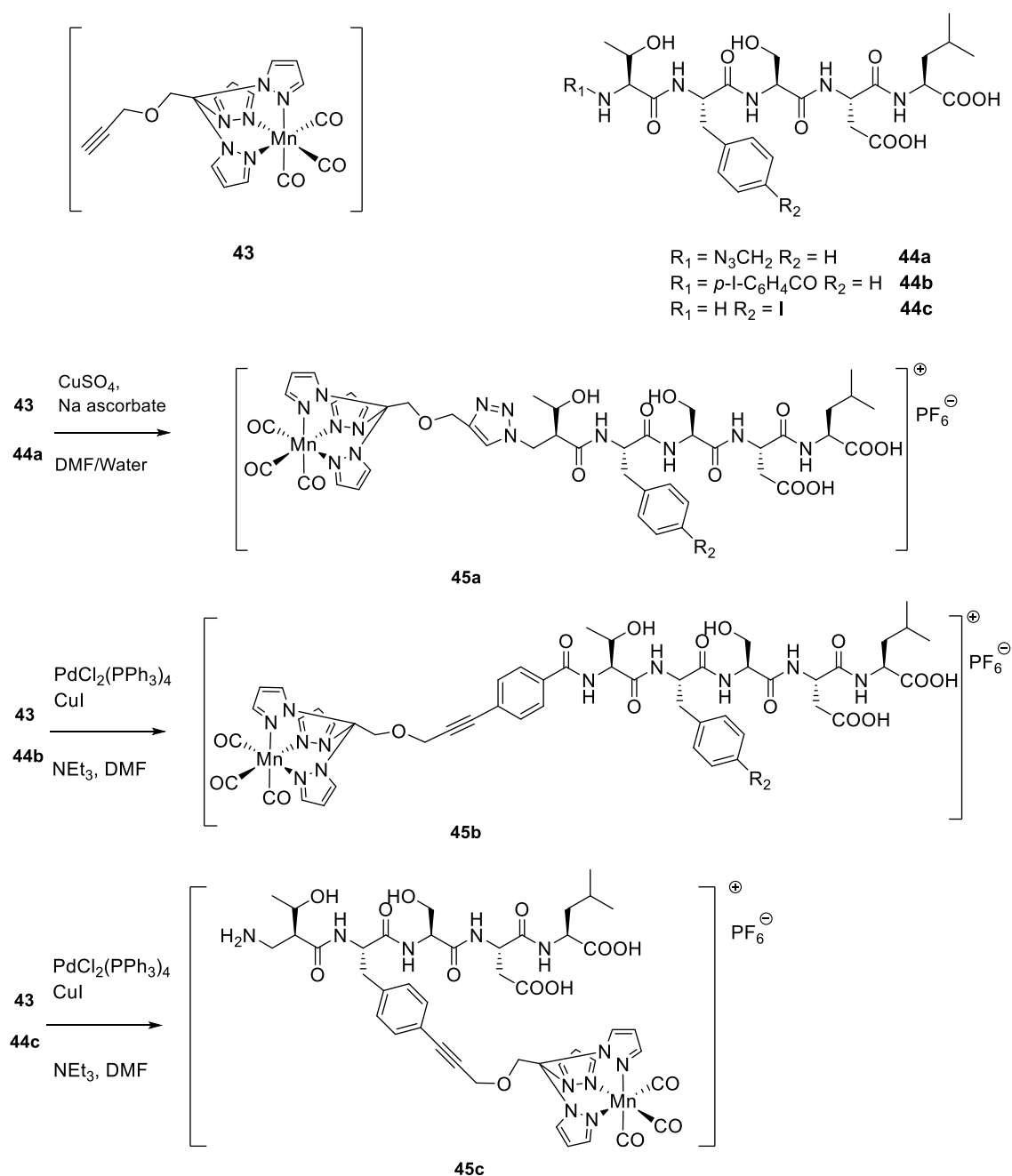


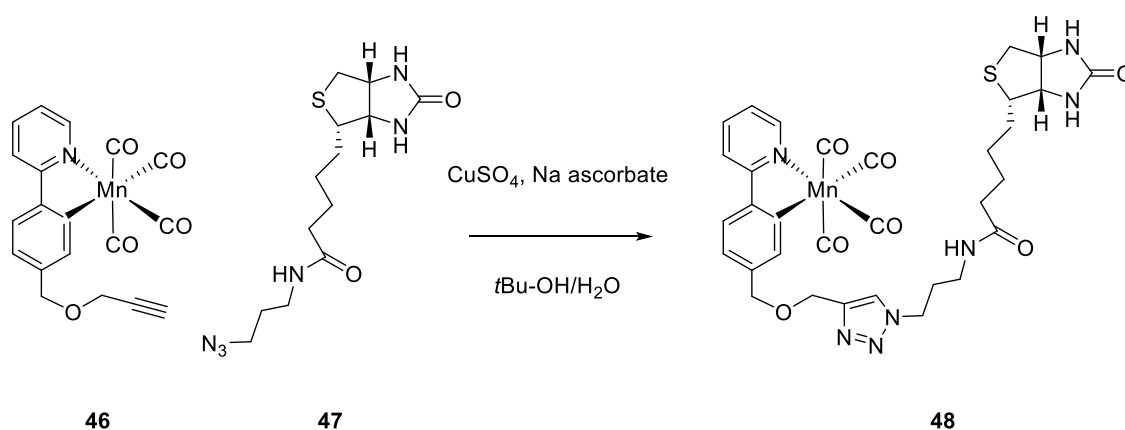
Figure 17: Coordination and drug spheres of a metal-based CORM as coined by Romão *et al.*

The idea of incorporating modularity into drug sphere CORM design has been explored by several different research groups. Schatzschneider and co-workers developed a tripodal Mn(I) photoCORM **43** so that the co-ligand contained a terminal alkyne, which could be functionalised with a Sonogashira coupling or a Cu-catalysed azide-alkyne cycloaddition (CuAAC).¹³⁵ The CuAAC reaction is one of the reactions described by Sharpless as ‘click’ chemistry, a robust group of reactions with high functional group tolerance, mild conditions, high yields, and simple purification.¹³⁶ These properties make the CuAAC reaction a highly appealing one for synthesising libraries of modular CORMs and to conjugate functional co-ligands into the drug sphere. To illustrate this idea, a peptide sequence was incorporated into a CORM to show the functional group tolerance of the reactions (Scheme 9). The peptide sequence chosen is part of the binding site of a transcription factor with anti-cancer properties. In future it may be possible to incorporate biologically active peptide sequences or make biomolecule conjugates so that CO release is accompanied by a second therapeutic effect from the conjugate.



Scheme 9: Modular synthesis of CORM-peptide conjugates using Sonogashira and ‘click’ chemistry.

Fairlamb and co-workers have used a click chemistry approach to incorporate biotin into a Mn(I) photoCORM (Scheme 10).¹³⁷ Biotin is an enzyme cofactor that binds exceptionally strongly to the proteins avidin (found in eggs) and streptavidin (produced by some strains of *Streptomyces* bacteria). The dissociation constant for the binding of biotin and avidin is of the order 10^{-15} , making this one of the strongest known noncovalent interactions.¹³⁸ As with Schatzschneider’s compounds, the Mn(I) centre in clickable alkyne **46** survives the CuAAC reaction conditions. Calorimetry experiments showed that compound **48** was able to bind to streptavidin, albeit less strongly than biotin itself.¹³⁷ With a robust CuAAC reaction and a modular system, other bioactive or therapeutic groups, and fluorophores to monitor CO release could be conjugated in the future.



Scheme 10: Conjugation of a Mn photoCORM with biotin using CuAAC.

Complex **49** (Figure 18) is another CORM conjugate with cobalamin, like thermal CORM **15**, but this compound is thermally stable and is conjugated through the ribose group of the B₁₂ cofactor rather than through the cyanide ligand bound to the cobalt centre.¹³⁹ In this example, the B₁₂ conjugate serves not only as a biocompatible co-ligand, but as part of a strategy to increase photoCORM uptake in cells. Zobi and co-workers were able to show accumulation of complex **49** in a single fibroblast cell using infrared microspectroscopy. This technique enables the production of images based on the absorption of infrared bands by the metal carbonyls. The results showed that thermal cobalamin CORM **15** did not accumulate in cells but photoCORM **49** was present in millimolar amounts.¹³⁹ This suggests that photoCORM **49** was actively transported into the cell (it entered the cell against a concentration gradient). Such a strategy opens up the possibility of a ‘Trojan horse’ type mechanism for CO delivery analogous to the methodology used in siderophore-conjugated antibiotics.¹⁴⁰ One idea for the future could be to produce a Trojan horse CORM-siderophore conjugate using the modular click chemistry discussed above.

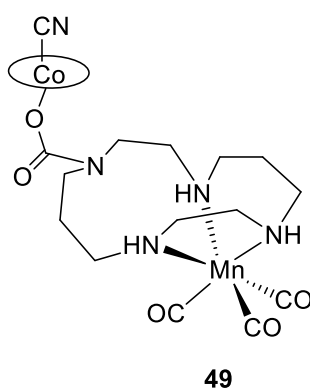


Figure 18: Conjugate of a Mn photoCORM with vitamin B₁₂, where the Co represents the cyanocobalamin.

Another strategy to improve cellular uptake of a CORM is extension of the drug sphere to include ‘carrier’ systems for CORMs. The iron storage protein ferritin has been used as a CORM ‘carrier’ system by Ueno and co-workers to improve uptake into human cell lines.¹⁴¹ Conjugation of

CORM-2 with ferritin produced *cis*-Ru(CO)₂ fragments coordinated to multiple binding sites of the ferritin. The amino acid residues primarily involved were histidine (N-donor), cysteine (S-donor) and glutamic acid (O-donor). This behaviour is much like the reactivity observed for CORM-3.⁹¹ Crystal structures of the bound Ru dicarbonyl fragments identified CORM binding sites and mutations to alter the electronic properties of the ligands were used to modulate the CO release rate.¹⁴¹ The ferritin conjugates showed slower CO release than CORM-2 itself (different mutants ranging from 8 to 18 times slower). This was attributed to the ferritin protecting the Ru centre from intracellular donors such as cysteine and glutathione, preventing the ligand substitution reactions that lead to thermal CO release.¹⁴¹ A four-fold increase in cellular uptake by two human cell lines was also observed when the ferritin conjugate was used. The slower CO release and greater cellular uptake led to greater CO-induced activation of the signalling molecule nuclear factor κ B than CORM-2.¹⁴¹ The ferritin carrier methodology was later extended to thermally stable Mn carbonyl complexes that produced a ferritin-caged photoCORM.¹⁴² However, it is not clear how reproducible the synthesis of these conjugates would be, given the many binding sites available for the metal centre; this could affect the reproducibility of the amount and rate of CO delivery. Although the use of a large protein as part of a drug presents challenges with handling, and toxicity of the degradation products from the Ru fragments have not been well-characterised, the authors suggest that the main application of this system is to provide CO release to biological systems for research into CO biology.¹⁴²

Similar strategies have also been applied using other nanoscale structures to deliver CORMs.¹⁴³ The glycinate amino acid side-chain in CORM-3 has been derivatised to incorporate poly(ethylene glycol) (PEG) units and a hydrophobic side-chain, which leads to formation of CORM-3-containing micelles of 30-40 nm in diameter.¹⁴⁴ The micelles displayed an enhanced anti-inflammatory effect compared to CORM-3 alone.¹⁴⁴

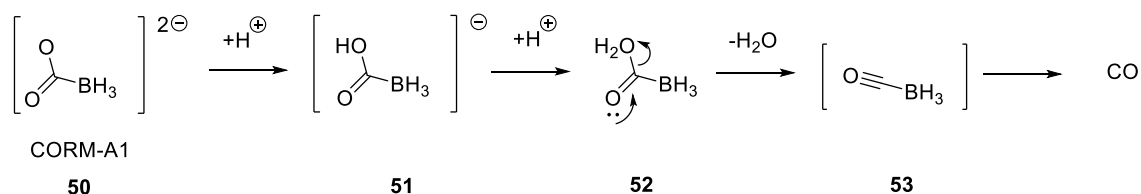
Attachment of CORMs to nanoparticles has also been investigated. Ford and co-workers showed how this can be particularly advantageous in the photoCORMs field; nanoparticles can take part in 'upconversion' of NIR light, absorbing a low-energy photon and emitting a visible light photon that can be absorbed by a photoCORM.¹⁴⁵ In this case, the photoCORM was encapsulated into a polymer matrix surrounding the nanoparticle. However, the use of a NIR laser was required in this system and it is unclear whether it would be practical to use such a high intensity of NIR light in a biological application. Although the polymer matrix is designed to reduce leaching of degradation products and aid solubility and excretion of the nanoparticles, the toxicity of the particles in a biological system was not assessed. These issues must be addressed before the system can be used as a therapeutic.

Despite the increasing development of the 'drug sphere' in the examples given above, the metal centre and its first coordination sphere remain relatively unchanged in most of these examples. It

is therefore important to also gain insight into the fundamental chemical processes involved in CO release in order to improve the efficiency of these CORMs.

1.2.3 Metal-Free CORMs

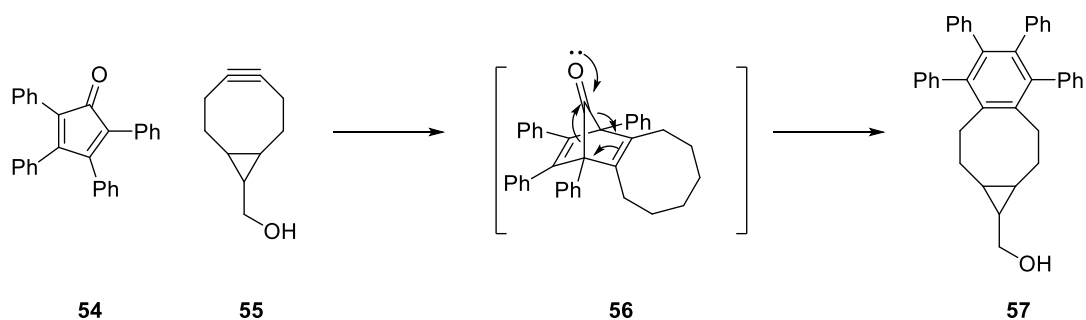
Although most CORMs are metal carbonyls, a smaller range of metal-free CORMs has also been exploited for therapeutic CO release. The first of these was $\text{Na}_2[\text{H}_3\text{BCO}_2]$, known as CORM-A1, shown in Scheme 11.



Scheme 11: Carbon monoxide release from CORM-A1, compound 50.

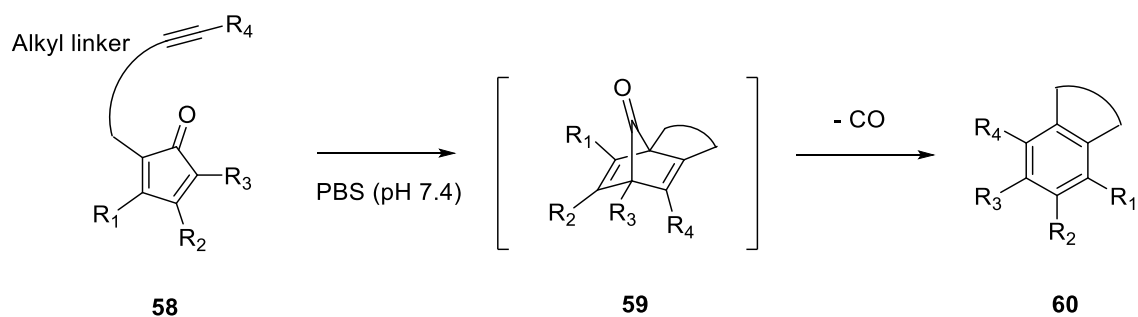
The rate of CO release from CORM-A1 is pH-dependent, CORM-A1 exhibiting rapid CO release to myoglobin under acidic conditions but releasing more slowly at physiological pH; the half-life, $t_{1/2}$ for CO release was 27 minutes at pH 7.4 but only 2 minutes at pH 5.5, both at 37 °C.¹⁴⁶ The relatively slow CO release from CORM-A1 compared to, for example, CORM-3, which has $t_{1.2} = 3.6$ minutes⁸⁷ in blood plasma was also reflected in the speed of the physiological response achieved: CORM-3 results in rapid vasorelaxation of rat aortas within the first few minutes after administration, whereas CORM-A1 had the strongest effect after 33 minutes.¹⁴⁶ This observation confirms that the development of CORMs with different CO release rates is important for controlling the therapeutic effect.

Many metal-free CORMs rely on the thermodynamic driving force of extrusion of CO from organic molecules. The loss of CO from bridged bicyclic systems such as **56** can form enthalpically-favourable aromatic products along with the entropically-favourable loss of CO. The first application of this in the CORMs field was by Wang and co-workers, who used a “click and release” strategy. A Diels-Alder reaction between compound **54** and strained alkyne **55** prepared intermediate **56**, which spontaneously extruded CO under physiological conditions (Scheme 12).¹⁴⁷



Scheme 12: Diels-Alder cycloaddition reaction followed by extrusion of CO as a strategy for CO release.¹⁴⁷

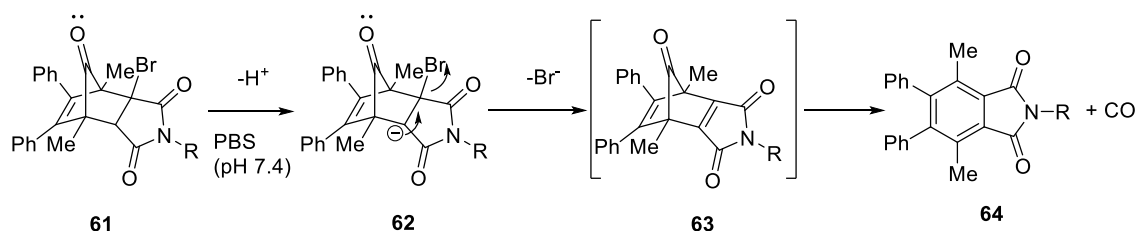
However, this is a poor strategy for therapeutic CO release as it relies upon the co-localisation of two compounds and the resulting intermediate **56**. Furthermore, the use of extended conjugated aromatic systems presents a challenge for water solubility; compounds such as **57** would need to be solubilised through further derivatisation to add more polar or H-bond donor/acceptor groups. It is also desirable to gain more control over the CO release rate. The “click and release” system was subsequently modified to involve an intramolecular cycloaddition based on structure **58** (Scheme 13), which eliminates the issue of co-localisation and provides greater control of CO release rate through the linker length and the alkyne substituent, which control the strain and steric properties upon forming the intermediate **59**.¹⁴⁸ In this case the drugs were solubilised by conjugation with glucose (R_4 in Scheme 13, other R groups are still aromatics). The solubility was sufficient to allow the therapeutic effect of this CORM family to be demonstrated using an animal model of colitis (inflammation of the intestine). A further advantage of this strategy is the formation of extensively conjugated fluorescent products which could be used in the future to track and monitor CO release using microscopy and flow cytometry techniques.¹⁴⁸ Examples of how this has been achieved in other systems is discussed in Section 1.3.3.6.



Scheme 13: General mechanism of the intramolecular ‘click and release’ methodology created by Wang and co-workers.¹⁴⁸

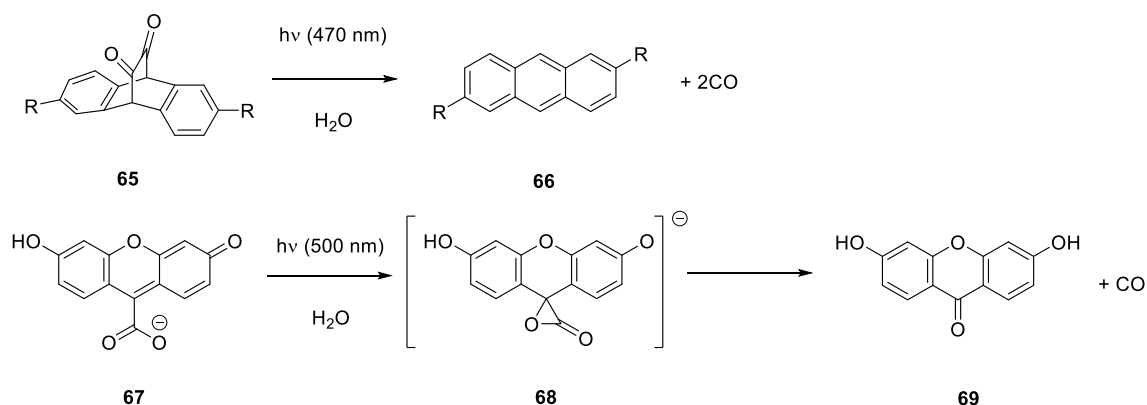
An alternative strategy for gaining for control over CO extrusion was published by Larsen and co-workers (Scheme 14).¹⁴⁹ In this methodology, pro-drugs derived from **61** contain an acidic proton and a good leaving group (bromide) such that E1cB elimination takes place to reveal the norbornadienone **63** which undergoes extrusion of CO. By controlling the nature of the R groups,

and the nature of the leaving group, the kinetics of the rate-determining E1cB elimination can be tuned to produce a series of thermal CORMs with different release rates.



Scheme 14: General mechanism for control of CO extrusion from complex 63 through E1cB elimination.¹⁴⁹

Another method to control CO extrusion is to perform the reaction photochemically; examples of metal-free photoCORMs are structures derived from **65** and **67** (Scheme 15). Complex **65** is unusual for a metal-free CORM in that it releases more than one equivalent of CO per molecule of pro-drug.¹⁵⁰ It was encapsulated by micelles to avoid precipitation of the poorly-soluble anthracene product **66**, and serves to prevent conversion of the ketones into the corresponding hydrates, which do not extrude CO.¹⁵⁰ Again, the fluorescence of the photoproducts in Scheme 15 is of interest for monitoring CORM localisation.



Scheme 15: Two organic photoCORMs with visible light activation.

Limited mechanistic work has been performed to understand how CO is extruded from these compounds. An isotopic labelling study in which the carboxylic acid of compound **67** was labelled with ¹⁸O, found that the ketone O atom in compound **69** is derived from the carboxylic acid, leading to the proposal of unstable intermediate **68**.¹⁵¹ The authors assumed that the CO released also comprised ¹⁸O from the labelled carboxylic acid, but this was not proven. Infrared spectroscopy of the headspace above a solution of complex could have been used to confirm this.

Mechanistic work on organic photoCORMs represents an underexplored area. The CO release wavelengths are in the visible light region of the spectrum, which an improvement on many UV-triggered metal photoCORMs but is still not as high as the optimal NIR wavelengths desired for

therapeutic use. More understanding of the CO release mechanism could lead to further improvements in the CO release wavelength through more informed design.

Metal-free photoCORMs can produce a therapeutic effect from CO release without the production of possibly toxic metal-based degradation products. However, the extended π -conjugated products formed from CO extrusion must also be tested for solubility and toxicity on their individual merits. Furthermore, the metal fragments from metal-based CORMs may have a role to play in enhancing the therapeutic effect of CORMs (Section 1.3.1.).

1.3 Understanding and Designing CORMs

A number of physiological experiments have been used to show that CO from CORMs has a therapeutic effect, including aortic ring relaxation;⁸⁶ disease models for sepsis,¹⁵² bacterial infections,¹⁰² ischaemia-reperfusion;¹⁵³ and ion channel activation.^{132,133} Although these experiments can be used to show how CORMs behave in a similar manner to CO, it is clear that mechanistic understanding of CO release is also necessary. Mechanistic insight requires direct methods to detect CO to establish CO-release profiles from CORMs. It also requires characterisation of CORM degradation products and an understanding of their effects on the physiological outcomes. In this Section, a case study of CORMs as antimicrobials is discussed to introduce the importance CORM degradation products and show how they can be understood. This is followed by discussion of and mechanistic tools to study the properties of CORMs and their degradation products, including methods to directly detect CO.

1.3.1 Effects of Metal Fragments – CORMs as Antimicrobials

The metal fragments derived from CORMs can have a substantial influence on both the toxicity profile and the therapeutic effect produced. It is widely recognised that the apparent antimicrobial effect of CO delivery from CORMs can be enhanced, or even overshadowed, by effects from the metal-based decomposition products.¹⁵⁴ An early indication of the striking effect that CORMs can have compared to CO gas administration was published by Saraiva and co-workers a decade ago.⁷⁴ The antimicrobial effect of a flux of CO gas (Figure 19) on cultures of *E. coli* and *S. aureus* was compared to CO release from CORM-2 (Figure 20). The percentage survival of bacteria was assessed by the ratio of the number of colonies grown from CO or CORM-treated cultures to untreated cultures, and plated serial dilutions were also used to illustrate the difference in survival rates. Similar results to CORM-2 were obtained when CORM-3 was used.⁷⁴

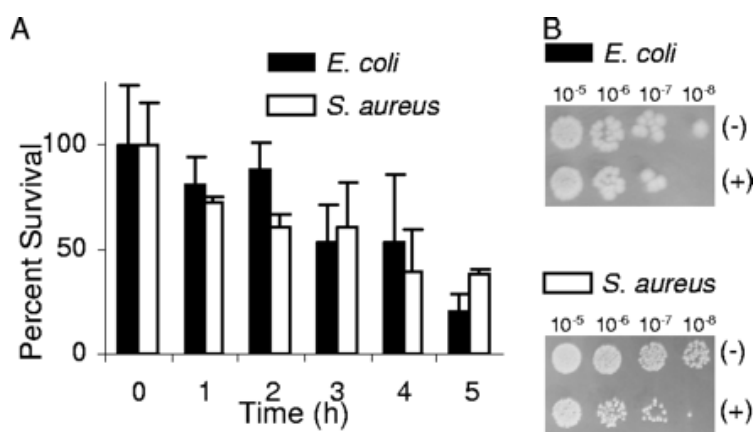


Figure 19 A: Effect of CO gas (15 min/hour) on survival of *E. coli* and *S. aureus* under microaerobic conditions. B: Plated serial dilutions of cultures after 4h of exposure to CO (+) or N₂ (-). Reproduced with permission from L. S. Nobre, J. D. Seixas, C. C. Romao and L. M. Saraiva, *Antimicrob. Agents Chemother.*, 2007, 51, 4303–4307. Copyright American Society for Microbiology 2007.

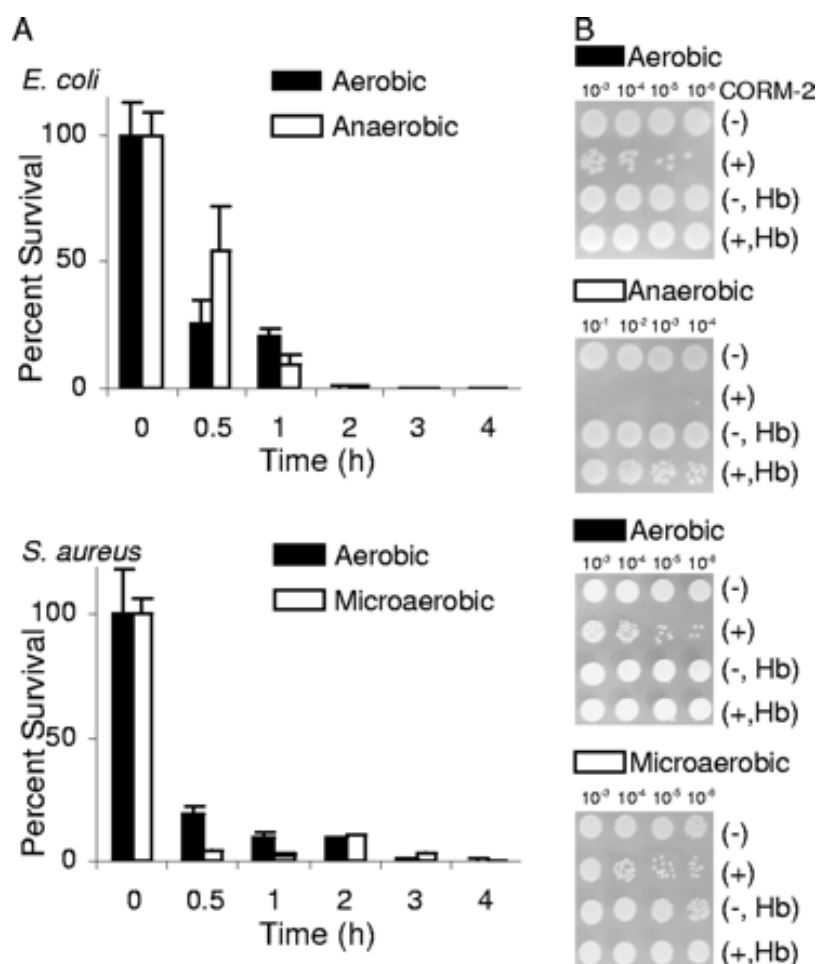


Figure 20 A: Effect of CORM-2 on survival rates of *E. coli* and *S. aureus*. B: Plated serial dilutions of cultures after four hours of exposure to CO (+) or N₂ (-) in the presence or absence of Hb. Reproduced with permission from L. S. Nobre, J. D. Seixas, C. C. Romao and L. M. Saraiva, *Antimicrob. Agents Chemother.*, 2007, 51, 4303–4307. Copyright American Society for Microbiology 2007.

The results showed that CO delivery from CORM-2 and CORM-3 had a far greater bactericidal effect than CO gas. When haemoglobin was added to the cultures to scavenge CO, the bactericidal effect of CORM-2 and CORM-3 against *S. aureus* was lost, confirming that CO release is the main cause of the observed antimicrobial effect, perhaps through inhibition of the respiratory chain and the production of reactive oxygen species.⁷⁴ It is difficult to compare how much CO gas was actually delivered to the cells from the above experiments, but it is clear that CORMs provide a practical, effective method of delivering CO in a way that can elicit a bactericidal effect. It is also known that *E. coli* cultures can survive CO levels close to the saturated concentration in water of ~1 mM; delivery from a CORM appears to increase the cytotoxicity.⁷⁵

A recent study by Poole and co-workers with CORM-3 has provided some thought-provoking results on CORM antimicrobial assays.¹⁵⁵ The CO-release profile of a CORM is generally determined by a CO scavenger such as Mb in the presence of a reductant (Section 1.3.2.1). But antimicrobial assays take place in growth media, which can expediate CORM-3 decomposition relative to the Mb assay conditions. As a result, most of the CO release occurs within the first few minutes of CORM addition to cultures in Poole's experimental conditions, but a bactericidal effect towards *E. coli* was still found.¹⁵⁵ Since the bactericidal effect of CORM-3 appears to persist over a period of hours, the question arises as to how much of a role the CO plays in the cytotoxicity in these experiments. It was also observed that the antimicrobial effect of CORM-3 was strongly dependent on the growth media employed. Surprisingly, media in which greater antimicrobial effects were observed also had some of the lowest levels of CO release.¹⁵⁵ This shows that for thermal CORMs such as CORM-3, caution must be taken in relating the CO release profile from a Mb assay to experiments in a growth medium where the CO release profile could be completely different. It was not investigated how the richness of the growth media also affected the susceptibility of the bacteria to CORM-3.

Experiments using NMR spectroscopy showed that the Ru(II) derived from CORM-3 can bind to thiols such as cysteine and reduced glutathione in a 1:1 ratio.¹⁵⁵ Addition of amino acids capable of complexing the Ru(II) to the growth medium was then shown to alleviate the antimicrobial effect of CORM-3 (Figure 21), and mass spectrometric measurement of Ru(II) content showed that the antimicrobial activity of CORM-3 correlated with Ru(II) content. Therefore, the cytotoxicity of CORM-3 in Poole's experiments was attributed to the Ru(II) fragment complexing thiols and disturbing the redox balance of the cell, an effect that could persist long after the released CO had dissipated.¹⁵⁵ It was already known that CORM-3 depletes free cellular thiol levels,¹⁵⁶ presumably due to formation of reactive oxygen species derived from CO inhibition of the respiratory chain.¹⁵⁷ However, using pre-degraded CORM-3, also known as the iCORM (inactive CORM), still caused a smaller but significant depletion in thiol levels, suggesting that Ru-derived products also play a role in this effect. It has already been shown that CORM-2 generates reactive oxygen species (ROS), including as the hydroxyl radical, in cell-free solutions.

Metal-derived ROS could therefore play a role in CORM toxicity. Under the same conditions, however, the iCORM does not produce ROS, and neither does CORM-2 when haemoglobin is used to scavenge CO; formation of ROS may still somehow depend on CO release.¹⁵⁷ More work is needed to study the formation of ROS from the metal fragments of CORMs to quantify these effects and understand how widespread they are within the different families of CORMs.¹¹⁵

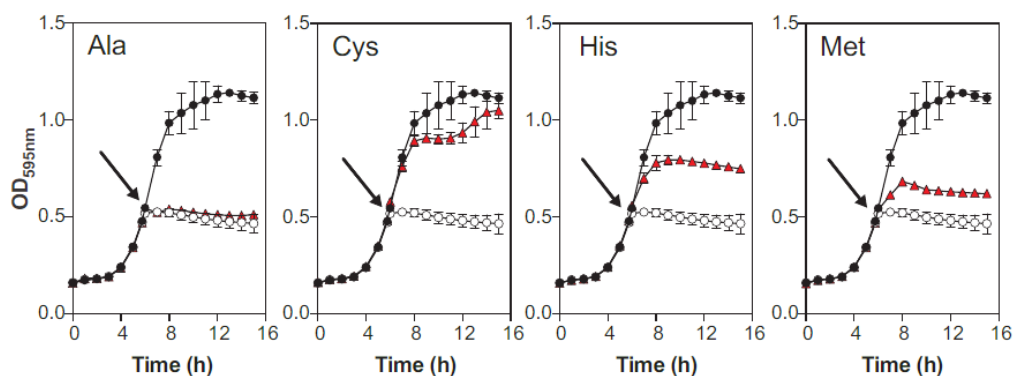


Figure 21: Addition of amino acids (arrows indicate the time of addition) protects *E. coli* from the cytotoxic effects of CORM-3. Black circles show no addition, white circles 60 μM CORM only and red triangles 60 μM CORM-3 and 120 μM of the amino acid. Adapted with permission from H. M. Southam, T. W. Smith, R. L. Lyon, C. Liao, C. R. Trevitt, L. A. Middlemiss, F. L. Cox, J. A. Chapman, S. F. El-Khamisy, M. Hippler, M. P. Williamson, P. J. F. Henderson and R. K. Poole, *Redox Biol.*, 2018, 18, 114–123.

The conflicting evidence uncovered in these experiments shows that the effects attributed to CORMs must be clearly distinguished from those of CO, because the metal ion and other degradation products can often play a role in the cytotoxic effects observed. Such an explanation could account for why CORM-2 and CORM-3 are so effective against *E. coli* cultures, whereas near saturation with CO gas can be tolerated.⁷⁵ However, the toxicity of the Ru(II) fragment from CORM-3 towards bacterial cells also affects mammalian cells,¹⁵⁵ so that Ru(II) binding to thiols is unlikely to provide a therapeutically viable effect in itself. It is still possible that a contribution to the antimicrobial effect of CORMs comes from the localised CO delivery from CORMs, which exposes the bacteria to higher intracellular concentrations than would be possible with CO gas, akin to a ‘Trojan horse’ type mechanism.¹⁵⁸

Strong evidence of antimicrobial activity has recently been obtained for TryptoCORM, complex **37**. Growth curves of the bacteria were monitored by the optical density at 600 nm (OD600) which increases with the number of bacteria through scattering and absorbance of the light by the cells. Control experiments with *E. coli* showed that the bacterial cultures grew in the dark in the presence of solubilising agent DMSO and that irradiation in the presence of CO has only a small effect. When TryptoCORM was added, the bacteria still grew when cultured in the dark, but the cells did not grow when 400 nm irradiation was used to induce CO release (Figure 22).

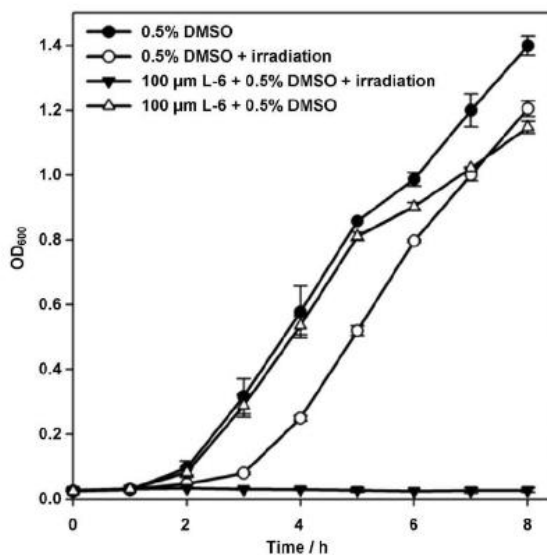


Figure 22: Antimicrobial effect of TryptoCORM, complex 37, on *E. coli*. Reproduced with permission from J. S. Ward, J. M. Lynam, J. Moir and I. J. S. Fairlamb, *Chem. Eur. J.*, 2014, 20, 15061–15068.¹³⁰

TryptoCORM is active against *E. coli* when CO release is triggered by light, but also displayed activity against *N. gonorrhoeae* in the dark.¹³¹ To determine whether the antimicrobial activity of TryptoCORM against *N. gonorrhoeae* was caused by CO, leghaemoglobin (LegHb) was used as a CO scavenger in cultures, and it was shown that LegHb protects the bacteria from the effects of TryptoCORM.¹³¹ Therefore, some CO release from TryptoCORM can take place in the dark in bacterial cultures, and this is sufficient to exert an antimicrobial effect. The mechanism of the dark CO release is likely to be thermal substitution, but the identity of the incoming ligand (e.g. water, buffer salts, or amino acid side chains) is unknown. It was already known that *N. gonorrhoeae* is one of the most sensitive pathogenic bacteria to CO, and given the development of antibiotic-resistant strains of *N. gonorrhoeae* it is a realistic antimicrobial target for CO. This work, along with the previously reported low cytotoxicity to mammalian cells,¹³⁰ is an example of a study that shows that there could be a place for CORMs as antimicrobials. The next stage for TryptoCORM would be to study its efficacy in animal models of infection.

The earlier experiments of Saraiva and co-workers showed that CO can be the primary cause of an antimicrobial effect,⁷⁴ because a CO scavenger alleviates the cytotoxicity, but the work of Poole and co-workers shows that extent of this effect can vary under different experimental conditions. Metal-based degradation products can sometimes dominate the apparent antimicrobial effects. This may be through the coordination thiols and amino acids as discussed above, or other mechanisms such as generation of reactive oxygen species by the reaction of O₂ or other oxygen species with the metal centre. Caution should therefore be exercised when CORMs show an antimicrobial effect if the cytotoxicity towards mammalian cells has not been assessed. Thermal CORMs that are unstable and degrade in buffer solutions or growth media, such cytotoxicity tests must occur under as similar conditions as possible with verification of the CO release profile of

the CORM. Control experiments involving the administration of the iCORMs are sometimes performed,⁶⁶ but even these experiments fail to capture all the intermediate species encountered during CO release since iCORMs are only the end products of CORM degradation. A clear distinction must therefore be made between the biological activity of CO and the biological activity of CORMs, and experiments with CORM-2 and CORM-3 must be evaluated carefully in light of the toxicity of the metal fragment.

1.3.2 Methods of CO Detection

Direct CO detection, to quantify the rate and amount of CO-release, is important to compare CORMs and to investigate the mechanisms of their decomposition. It is therefore imperative to have accurate, precise, and adaptable methods for the detection of CO. Indirect methods, such as measuring the decay of spectral features belonging to CORMs or formation of iCORMs is insufficient to demonstrate CO release because CORM degradation can result in side-reactions, including CO₂ production or CO migratory insertion.^{91,159} Degradation of a CORM is therefore not always indicative of CO release.

1.3.2.1 Myoglobin Assay

By far the most commonly-used method to directly detect CO release from CORMs is the myoglobin CO-release assay. This assay relies on the coordination of CO released from the CORM to deoxy-Mb, which causes a shift of the porphyrin electronic absorptions in the UV-visible spectrum (Figure 23). Quantification of the CO released can be achieved because the extinction coefficient of deoxy-Mb at 540 nm is known.¹⁶⁰

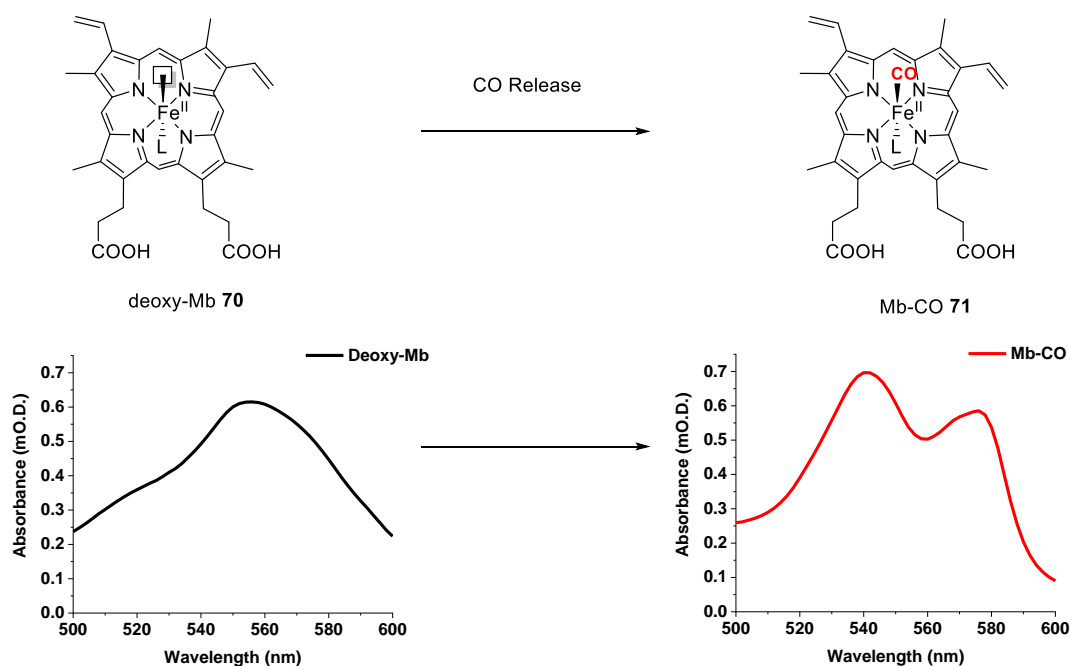


Figure 23: Spectral changes upon the binding of CO to deoxy-Mb, forming Mb-CO. The ligand L represents a histidine residue to which the haem cofactor is bound.

The assay relies on the myoglobin to capture all of the CO released. A layer of paraffin oil is placed on top of the myoglobin solution to prevent CO escape.¹⁶⁰ The concentrations of CORM are typically tens of μM , which means that the CO concentration in solution never approaches saturated levels (around 1 mM).¹⁶¹ Myoglobin degradation and CO escape mean that the assay is not normally continued beyond several hours.¹⁶⁰

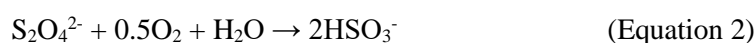
Quantification of CO release with myoglobin enables rates of CO release to be measured. However, caution should be taken with the fitting of oversimplified rate equations to the data as most CORMs contain multiple CO ligands, which will be released at different rates, and competing processes that do not release CO may also be taking place. As a result, it is difficult to directly relate observed rate constants to those of the fundamental CO release processes of interest. To provide a relative comparison for the rate of CO loss of different CORMs, the half-life, $t_{1/2}$, for CO release is often quoted.⁷⁸ The half-life is defined as the time taken for x moles of a CORM to release $0.5x$ moles of CO.⁷⁸ The value of x used can sometimes vary between different studies, and it is occasionally found for some compounds that the measured half-life varies with the value of x .¹⁶² Despite its limitations the half-life can be a useful comparative tool for comparing CO release rates in a series of CORMs.

One issue with the Mb assay that needs to be addressed is that the CORM being studied may also absorb at 540 nm, particularly as there is a drive towards producing visible light-absorbing photoCORMs. This can be corrected for using the isosbestic points of deoxy-Mb and Mb-CO to fit and subtract the absorbance of the CORM and its degradation products from the measured data.¹⁶⁰ Therefore, the sensitivity of the method is often limited by the size of the errors in the

isosbestic point correction. Errors in the correction compared to spectra generated from reference data are typically below, 1%, so that the method is able to distinguish concentrations to the nearest μM with acceptable precision in a typical assay when concentrations of tens of μM are reached. A step-by-step example of the isosbestic point correction is provided in Section 3.4.3.

Such a correction is not suitable for all CO-releasing molecules, however - poorly soluble CORMs, those containing strong absorbing groups, or nanoscale particles that could scatter light are all problematic. In such cases, two separate solutions can be used within a sealed vessel: one containing the CORM releasing CO and another containing aqueous Mb, such that CO release can be detected.⁸⁶ Henry's Law constants could be used to measure the total amounts of CO released in the sealed system, although this is not used: other tests for CO release are generally employed when the UV-visible spectrum of the Mb and CORM in the same solution cannot be recorded.⁸⁵

Another limitation of the myoglobin assay is that it must be performed under reducing conditions because the active site of the as-isolated form of myoglobin contains O_2 -bound to the iron centre to give an Fe^{3+} superoxide. The oxygen ligand must be removed by reduction of the iron centre with sodium dithionite.¹⁶⁰ Sodium dithionite produces an anaerobic environment in the assay by reducing the oxygen in solution¹⁶³ (Equations 2 and 3), and the solution is layered with paraffin oil to provide a barrier to CO and O_2 exchange with the atmosphere, minimising CO escape and reaction of deoxy-Mb with O_2 .



The use of sodium dithionite as a reductant means that CORMs that react with the reductant could appear to release CO when they would be stable in its absence. It is also not possible to separate out reactivity of the CORM with the Mb, water or buffer salts. Therefore, the Mb assay cannot be used to distinguish between thermal and protein-triggered CO release. An additional consequence of sodium dithionite use is that this assay is unable to identify CORMs that are triggered selectively by oxidising conditions. It is advantageous to design CORMs that release CO under oxidising conditions due to the role of reactive oxygen species in diseases states and oxidative stress, yet such activity cannot be tested for using the Mb assay. The assay can, however, be used to show stability of a CORM to all of these factors followed by photolytic CO release, and this makes the Mb assay a good choice for photoCORM activity.¹²³ However, the CO release kinetics are rarely comparable between studies due to different irradiation powers and path lengths being used.

Despite the limitations discussed above, the myoglobin assay remains the most popular method of CO detection employed to study CORMs.⁶⁶ The assay readily provides data on CO release rate

and stoichiometry in a way that lends itself to comparison with other CORMs, as long as the experimental setup is kept the same. The assay can be adapted to study photoCORMs by incorporating irradiation and provides a convenient means of confirming photoCORM stability in aqueous buffer solution and in the presence of a protein. The materials required for the assay are commercially available, and the equipment needed is commonly found in synthetic chemistry laboratories.

A synthetic Rh complex that binds CO has been developed for assaying CO release in organic solvents, in an analogous way to the myoglobin assay.¹⁶⁴ For studies of therapeutic or biological effects, the CO release profile in water is more relevant.

1.3.2.2 Electrochemical CO Detection

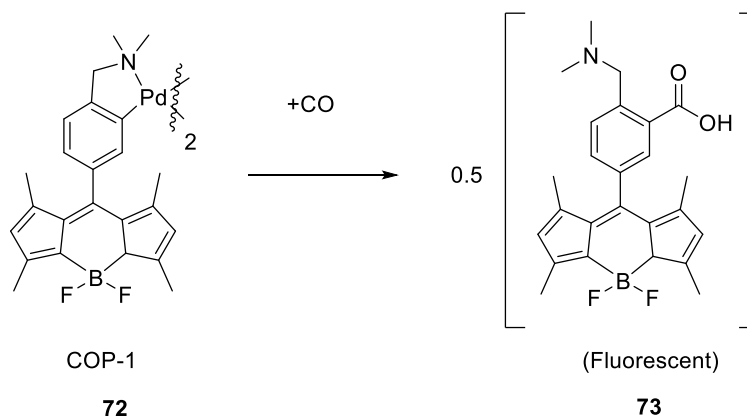
Some studies have used electrochemical oxidation of CO to CO₂ at an electrode to produce a measurable current.^{146,161} In 2005, a prototype electrochemical CO sensor, similar to a nitric oxide (NO) sensor, was used to detect CO release from CORM-A1.¹⁴⁶ The sensor contained a gas-permeable membrane through which the CO released by the CORM diffuses before oxidation occurs at the electrode. The membrane prevents solution interferences that may be produced during the decomposition of CORM-A1 from also being oxidised and contributing to the measured current. However, the selectivity of the electrode for CO over other gases was not discussed, and therefore this electrode would therefore be of limited use in a more complex system, such as a biological sample. In a biological sample, other gases (including NO) could also diffuse through the membrane and reach the electrode surface, where the interferent gas could lead to measurement of an increased or decreased current, leading to inaccurate measurement of the CO concentration.

A system with two working electrodes to separately detect CO and NO release both selectively and simultaneously.¹⁶¹ Two platinum disk electrodes were used, one of which was modified by the electrochemical deposition of tin on the surface, which was shown to provide greater selectivity for the oxidation of CO over NO.¹⁶¹ The different sensitivities to CO and NO at each electrode enabled accurate determination of CO and NO concentrations.¹⁶¹ This system was tested against numerous interferences likely to be present in biological samples: nitrite, ascorbic acid, uric acid, acetaminophenone and dopamine did not affect the sensor at concentrations below 500 μM .¹⁶¹ The selectivity and sensitivity of this system enabled it to be used to detect both CO and NO, two key signalling molecules, in biological systems: the sensor was used to detect CO and NO levels in live mouse kidney tissue.¹⁶¹

1.3.2.3 Turn-on Fluorescent Probes

Palladium dimer **72**, a fluorescent probe for CO known as COP-1, has been developed for use in microscopy experiments to study localisation of CO in cells.¹⁶⁵ Complex **72** constitutes a useful

tool for studying the mechanism of CO release in cells, undergoing carbonylation when exposed to CO, to fluorescent carboxylic acid **73**, which can be used in imaging (Scheme 16).



Scheme 16: Turn-on fluorescent probe for CO detection.

This probe has been used to image CO released from CORM-3 into live cells from the human cell line HEK293T. It can be used to detect the micromolar levels used in typical therapeutic doses of CO release and is highly selective for CO over common reactive oxygen, nitrogen and sulfur species commonly encountered in biology.¹⁶⁵ Another fluorescent probe is known as COSer; this is a biosensor which contains CO-binding haem protein CooA and yellow fluorescent protein. Upon CO coordination, a conformational change occurs which increases the fluorescence of the protein and this system can also sense micromolar concentrations of CO.¹⁶⁶ Detection of CO by fluorescent probes is an alternative imaging tool to the CORM-based fluorophores discussed in Section 1.3.3.6 and Chapter 5 of this Thesis, although this fluorescent CO detection method could in itself be incorporated into a CORM drug sphere.

1.3.2.4 Headspace Analysis

The release of CO gas can also be detected by analysis of the headspace above the CORM solution using a gas-tight cell. Common techniques for this include infrared spectroscopy and gas chromatography.¹⁶⁷ The very high sensitivity of CO detection by gas chromatography (down to 0.03 ppm) makes this a suitable technique for very low levels of CO, although therapeutically active levels of CO gas are typically of the order of hundreds of ppm so such a low detection limit is unlikely to be required.⁶⁹

The distinctive fundamental band in the infrared spectrum of gas-phase CO features P and R branches from its rotational fine structure and is centred at 2142 cm^{-1} . However, the intensity of the bands in gas phase infrared spectra are dependent on pressure due to intermolecular collisions which affect the line width. This means that aliquots need to be removed from the headspace above the solution, injected into a gas cell under vacuum and re-pressurised with an inert gas to

the same pressure each time to ensure consistent readings.¹⁶⁷ A calibration curve with known quantities of CO can be used to obtain quantitative data.

These methods have the additional benefit that if the concentration in the headspace can be quantified Henry's Law constants could be used to calculate the solution concentrations of CO. However, if the concentration of CO were to get too high this could affect the dissociation of CO from the CORM if CO loss is reversible; this is dependent on the CO release mechanism of the CORM.

1.3.3 Mechanistic Tools to Study CORMs

Monitoring the formation of degradation products spectroscopically does not provide evidence that a compound is releasing CO. The techniques described here are to characterise CORM degradation products and should be used in conjunction with other experiments that provide direct evidence of CO release. This is further complicated by the fact that the Mb CO release assay takes place under anaerobic conditions due to the presence of sodium dithionite, whereas many of the other techniques described (and biological CO release) take place under aerobic conditions. Different kinetics and speciation may therefore appear compared to the myoglobin assay.

1.3.3.1 Infrared Spectroscopy

As well as for direct detection of the CO released, infrared spectroscopy may be used as a means of understanding the mechanisms of CORM degradation, particularly for metal carbonyl photoCORMs. The studies on B₁₂-conjugated CORM **49** also showed that infrared spectroscopy can be used as an imaging tool in biological systems.¹³⁹

Carbonyl ligands exhibit strong infrared stretching vibrations, the wavenumbers and intensities of which are highly sensitive to the electronic environment and symmetry of the metal centre. Infrared spectroscopy is therefore very useful for detecting intermediates from CORMs that still contain carbonyl ligands. Metal carbonyl photoCORMs typically contain more than one CO ligand, yet only release a single CO in their solution photochemistry, leaving the other carbonyls as infrared reporter groups. The initial degradation products can therefore be studied with time-resolved spectroscopy using flash photolysis and pump-probe techniques. In this way, it is possible to use infrared spectroscopy to monitor CO release on timescales from picoseconds to days, providing insight from the fundamental photochemical steps involved in CO release through to the species formed over timescales relevant to biological systems. Ultrafast time-resolved infrared (TRIR) studies on photoCORMs will be discussed in detail in Section 2.1.1.

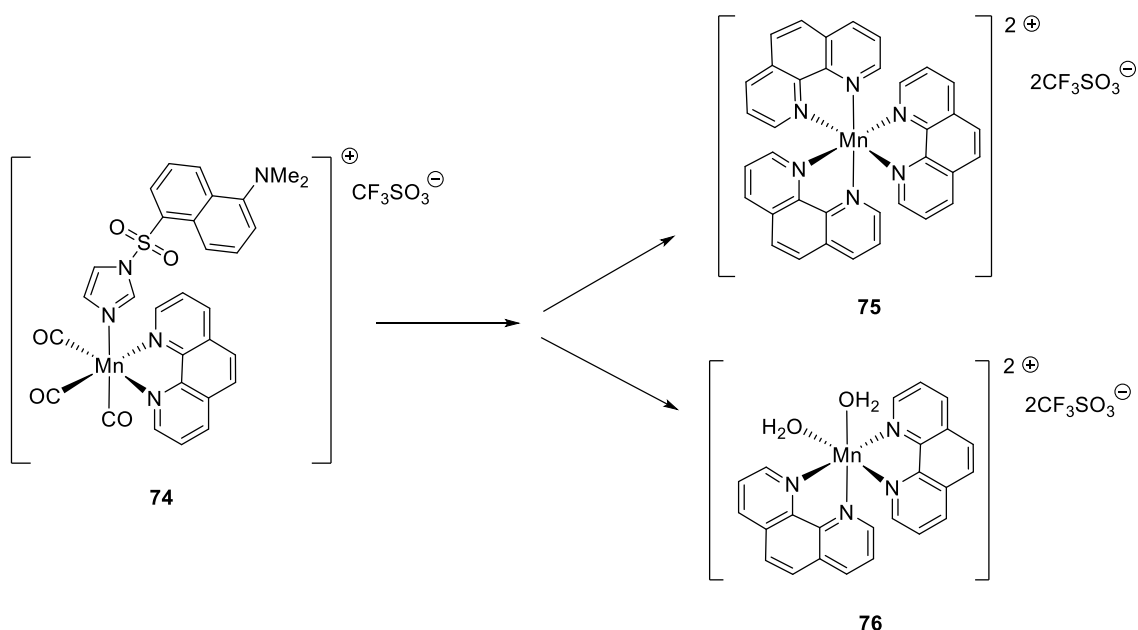
The assignments of such intermediates can be assisted by theoretical methods such as Density Functional Theory (DFT). Although DFT does not account for anharmonicity in vibrations and usually requires scaling factors to produce absolute values in line with the experimental

wavenumbers,¹⁶⁸ the main advantage of DFT is that it enables quantitative prediction of the differences in vibrational wavenumber between different compounds.

One of the disadvantages of infrared spectroscopy is that it is often unable to reveal the final fate of the metal fragment if all the CO ligands are released, since the carbonyl ligands are the main spectroscopic handle. Furthermore, bubbles of gas and precipitates can form during CO release, which can cause problems for *in situ* measurements, although use of an attenuated total reflectance (ATR) geometry can at least partially mitigate this.¹⁰⁵ Characterisation of metal carbonyl-containing solids is often more difficult to interpret compared to the solution phase due to packing effects which can alter the number and intensity of the bands. Furthermore, organic solvents or D₂O must typically be used, as an infrared band for liquid water overlaps with the metal carbonyl region from 1800-2200 cm⁻¹.

1.3.3.2 Magnetic Resonance

The use of NMR spectroscopy in studying CORM degradation is often limited by the formation of degradation products containing paramagnetic metal species, or by precipitation (also a problem for most other methods), both of which can affect the homogeneity of the magnetic field and lead to poor-quality spectra. Studies on several Mn(I) tricarbonyl photoCORMs by Mascharak and co-workers showed the formation of paramagnetic Mn(II) species, confirmed by electron paramagnetic resonance (EPR) spectroscopy – the same spectra could be acquired by mixing solutions of Mn(II) salts with their CORM co-ligands in buffer solution.⁷³ In one case X-ray crystal structures of two Mn(II) complexes, **75** and **76**, derived from photoCORM **74** were solved.¹⁶⁹ As the stoichiometry of these reactions is not balanced, it is unclear what happens to the remaining Mn ions, but it is clear that the presence of paramagnetic species can be a problem for NMR characterisation of CORMs, in which case EPR could be used instead.



Scheme 17: Formation of paramagnetic species 75 and 76 in CORM degradation.

However, as discussed above, NMR spectroscopy has been used to study CORM-2 and CORM-3 because the Ru(II) degradation products are diamagnetic, enabling the assignment of the mixture of dicarbonyl and tricarbonyl degradation products by NMR spectroscopy.⁹⁷ Binding constants for CORM-3 to reduced glutathione and several amino acids were obtained; the strength of this binding was used to account for the cytotoxicity of CORM-3-derived Ru(II) fragments.¹⁵⁵

1.3.3.3 UV-Visible Spectroscopy

The main use of UV-visible spectroscopy is in the study of photoCORMs, where the absorption spectrum of the CORM can be used to determine optimal wavelengths for CO release. The interpretation of these spectra is often accompanied by TD-DFT calculations to model the orbital components involved in each transition – this helps to determine which transitions are likely to be CO dissociative. The absorption bands can then be tuned by co-ligand design.¹²⁷

On the ultrafast timescale, transient absorption (TA) spectroscopy is a pump-probe technique that can be used to study excited state formation of metal carbonyl complexes by detecting electronic absorptions. This has been used to study the photochemistry of many organic and metal carbonyl systems,^{170–175} and provides a complementary spectroscopic technique to the structural information from TRIR spectroscopy (or other vibrational spectroscopy such as Raman).¹⁷⁶ However, specifically in the CORM field, the TRIR spectroscopy has been more commonly used to study ultrafast photochemistry due to the diagnostic metal carbonyl bands. Ultrafast spectroscopic measurements typically require greater amounts of sample due to the requirement for a flow system that avoids buildup of degradants in the sample, and the sensitivity may be limited, as with other spectroscopic methods, by the difference in absorption between the starting materials and products studied.

Changes in the electronic absorption spectrum may provide clues as to the nature of the CORM decomposition products formed, though little structural information can usually be obtained from just the electronic spectrum. Although it can be more difficult to assign the UV-visible bands of intermediate species compared to the diagnostic infrared spectroscopic analysis, UV-visible spectroscopy can be used in conjunction with other techniques to characterise CORM degradation products such as magnetic resonance and infrared spectroscopy; several groups have applied UV-visible spectroscopy as part of wider mechanistic studies.^{127,130,177} The loss of UV-visible absorption bands of a CORM and formation of intermediates can be monitored spectroscopically to provide kinetic profiles of CORM degradation, although care must be taken with comparing experiments under different conditions (e.g. different irradiation path lengths in photochemical experiments).

1.3.3.4 Mass Spectrometry

Mass spectrometry is sometimes used to study CO release mechanisms, usually with ‘soft’ ionization techniques to detect charged molecular ions or adducts with cations such as H⁺. These methods can be used to provide proposed structures for intermediates. Removing aliquots from a solution of the degrading CORM enables the intermediate species in CO release to be tracked over time, usually on the timescale of seconds to minutes. Fairlamb and co-workers previously used mass spectrometry to show that CO insertion can occur into a Mn-C bond during degradation of the photoCORM family derived from [Mn(ppy)(CO)₄] (ppy = 2-phenylpyridyl).¹⁵⁹ Side-reactions such as this account for why non-integer equivalents of CO are sometimes released from CORMs. More details are given in the background to the [Mn(ppy)(CO)₄] CORM family in Section 1.4.

However, in the absence of standards to calibrate the data these results do not provide quantitative information. As a result, it may sometimes be unclear whether the intermediates being observed are present in large enough amounts to significantly impact upon the overall CO release mechanism.

1.3.3.5 Quantum Yield

For photoCORMs, a comparatively useful measurement of the efficiency of CO release is the quantum yield for CO photodissociation, Φ , given by equation 4:

$$\Phi = \frac{\text{Moles of photoproduct formed}}{\text{Moles of photons absorbed}} \quad \text{Equation 4}$$

The quantum yield is an important parameter because it facilitates comparison between the efficiency of CO release from different photoCORMs. The myoglobin CO release assay does not lend itself well to comparison of CO release efficiency because of the different light sources and irradiation powers used in different experiments. Furthermore, the CO release profiles measured

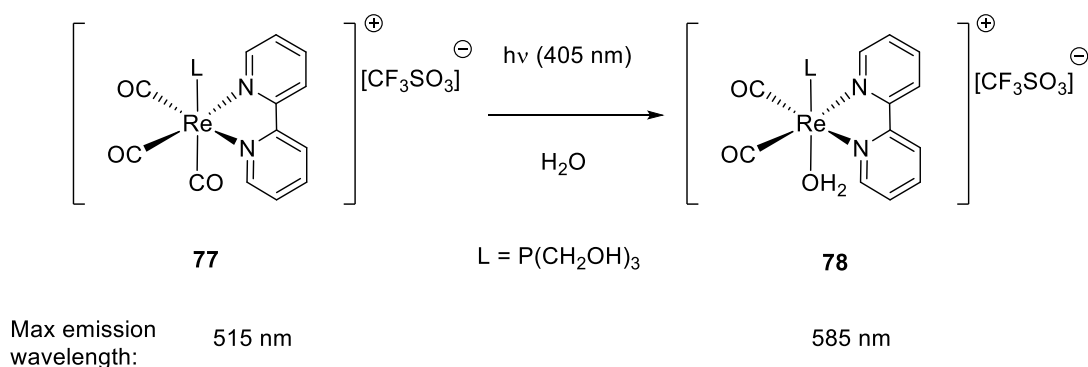
in the myoglobin assay may include the thermal release of a second or third CO ligand which cannot be distinguished from the photochemical behavior.

The value of Φ is usually strongly dependent on wavelength because of the changing nature of the transitions involved in different absorption bands and overlapping transitions within the same spectral features. As a result, a filter or other means of generating monochromatic light must be used to ensure that only a narrow region of the absorption spectrum is pumped. The intensity of the light is then calibrated using actinometry, where a process with a known quantum yield (such as ferrioxalate photoreduction) is studied so that the intensity of the light source can be measured.¹⁷⁸

Furthermore, the extinction coefficient of the photoCORM, and whether visible light can be used to induce CO loss, are also important considerations when thinking about the efficiency of photoCORMs. Measurements of quantum yield are complemented by time-resolved pump-probe experiments – such experiments can provide the mechanistic insight into the other ultrafast photochemical and photophysical processes occurring when a photoCORM absorbs a photon, such as formation of unreactive excited states or dissociation of the non-CO co-ligands. The setup required to measure quantum yields is not widely available in all synthetic laboratories, but understanding the balance of these processes informs the assessment and design photoCORMs.

1.3.3.6 Luminescence

A useful tool for studying CORMs biological systems is the ability to visualize the location of CO release at the same time as monitoring release rate. To this end, CORMs with fluorescent tags have begun to be developed, along with those displaying ‘turn-on’ luminescence, or changes in the wavelength of emission, when CO is released. A particularly fruitful area has been the study of Re(I) tricarbonyl carbonyl polypyridine photoCORMs, which display shifts in luminescence wavelength upon CO release, allowing distinction between the intact CORM and the photoproducts after irradiation.^{179,180} One of the first examples of this was the luminescent Re(I) CORM **77** developed by Ford and co-workers (Scheme 18).



Scheme 18: Photochemical CO release from luminescent Re(I) photoCORM 77.

The photoCORM **77** displayed luminescence with a maximum at 515 nm upon 405 nm excitation.¹⁸¹ Upon loss of a CO and coordination of a water molecule, photoproduct **78** formed, which was also luminescent but displayed a red-shifted emission. The different luminescence profiles of these two molecules enabled monitoring of CO-release inside prostate carcinoma cells using confocal fluorescence microscopy (Figure 24).

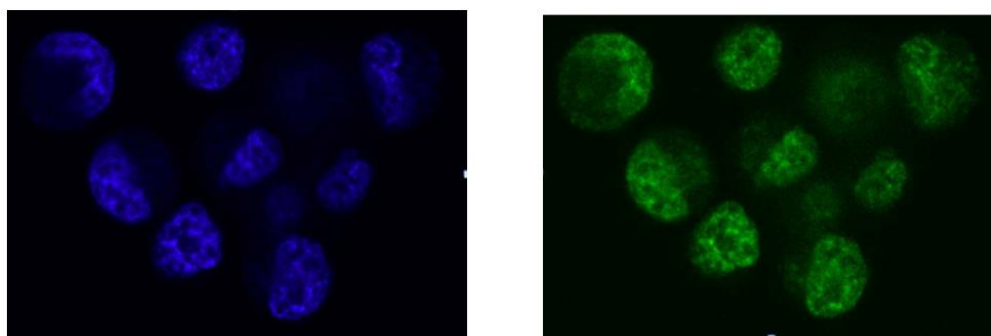


Figure 24: Confocal fluorescence microscopy images during CO release from photoCORM 77 inside cells. Left 465-496 nm emission from photoCORM 77. Right: The same sample after 405 nm photolysis showing emission above 660 nm. Adapted with permission from A. E. Pierri, A. Pallaoro, G. Wu and P. C. Ford, *J. Am. Chem. Soc.*, 2012, 134, 18197–18200. Copyright, American Chemical Society, 2012.

These results show that complex **77** enters cells intact before releasing CO photochemically inside the cells, confirming that this complex is stable to the cell culture conditions and the contents of the cytosol.

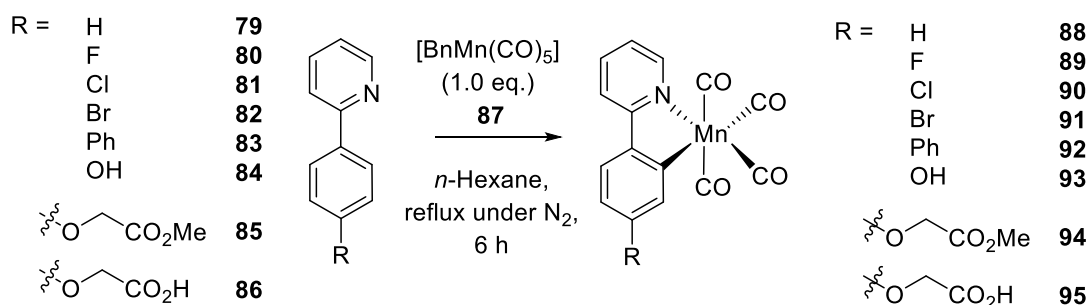
The use of luminescence has been extended further: experiments on a similar Re(I) tricarbonyl, this time with a benzothiazole-derived co-ligand, showed the same behavior as complex **77** in the microscopy experiments, entering the cells before photochemical uncaging of CO.¹⁸² Because of the change in luminescence wavelength upon CO release, flow cytometry was then used to sort cancer cells containing the luminescent CORM based on the extent of CO release. This was used to show that the cells that had been exposed to more photochemically released CO displayed

increased apoptosis.¹⁸² A chitosan-based Re(I) photoCORM has also been imaged in live cells and caused apoptosis of colorectal cancer cells.⁷²

1.4 PhotoCORMs Based on [Mn(ppy)(CO)₄]

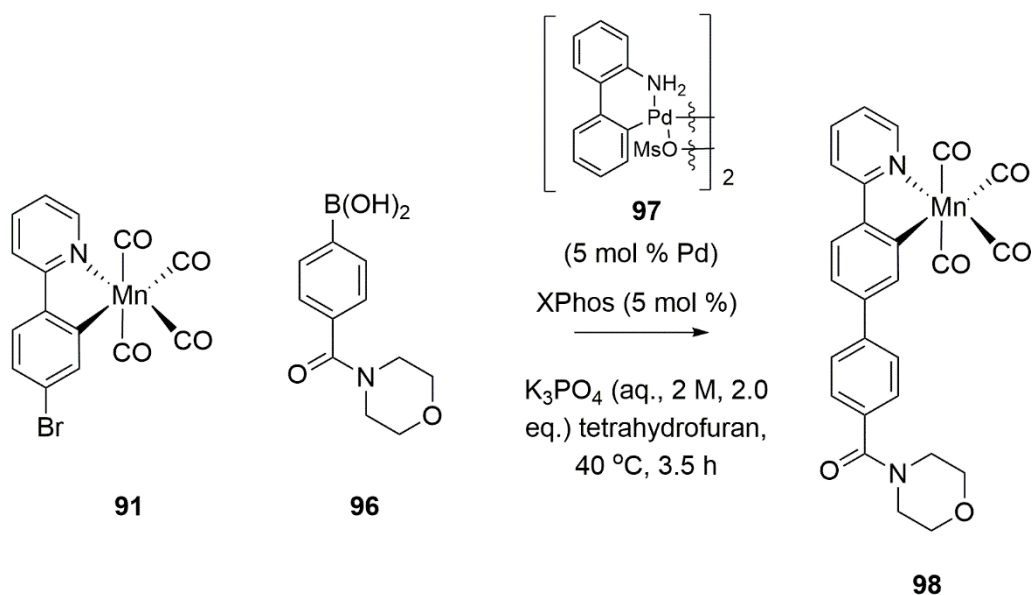
The CORMs studied in this Thesis are derived from [Mn(ppy)(CO)₄] (ppy = 2-phenylpyridyl), complex **79**. This Section summarises previous work on this family of compounds.

The synthesis of [Mn(ppy)(CO)₄], *via* the cyclomanganation of 2-phenylpyridine with [BnMn(CO)₅], was first reported in 1975 by Bruce and co-workers.¹⁸³ Based on this reaction, a library of complexes based on substituted ppy ligands was envisaged, with the substituents providing an opportunity to modulate the CO release and to confer drug-like properties. Recently, [Mn(ppy)(CO)₄] and derivatives bearing substituents on the 4' position of the ppy ligand have been investigated as photoCORMs (Scheme 19).^{159,184}



Scheme 19: Synthesis of the family of photoCORMs based on [Mn(ppy)(CO)₄] and known derivatives.

Derivatives of these complexes have included groups to accommodate further functionalisation or improve water solubility. For example, bromide **91** was further functionalised *via* a Suzuki coupling to produce complex **95** (Scheme 20).¹⁸⁴ This was made possible using a Buchwald pre-catalyst that works with only mild heating, avoiding thermal decomposition of solutions of **91** at higher temperatures.¹⁸⁵



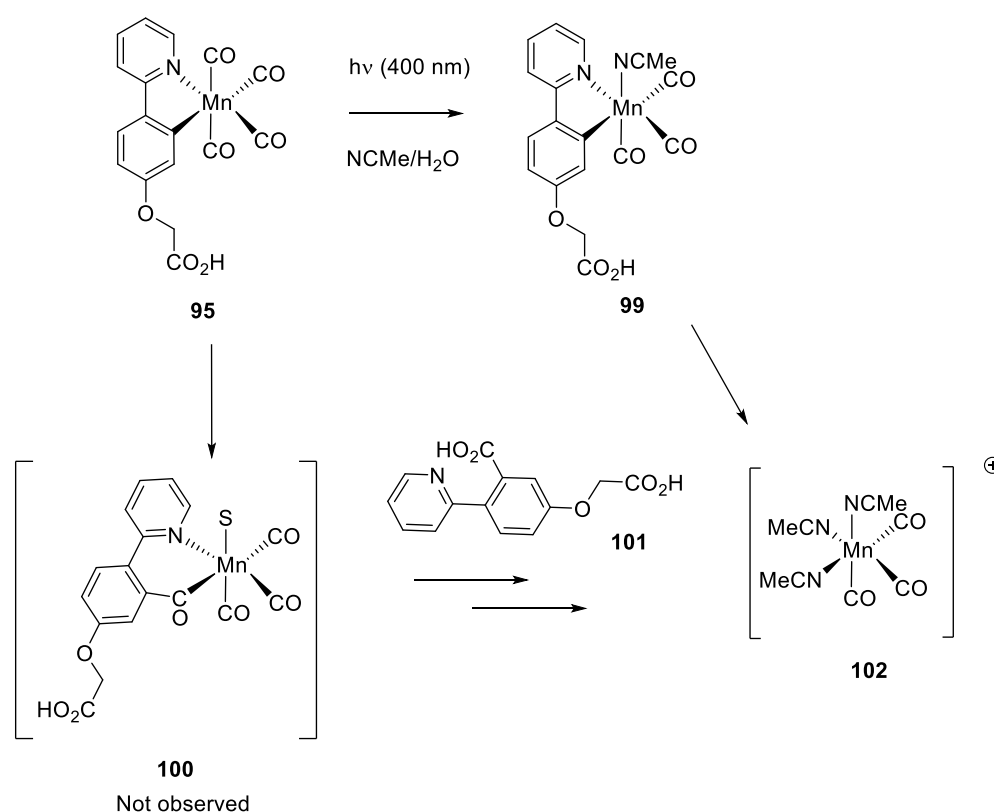
Scheme 20: Reaction scheme for a Suzuki-Miyaura cross-coupling using mild conditions to functionalise a photoCORM.

Compounds in this family are stable in the dark to myoglobin-containing buffer solution, but release CO upon irradiation with 365 nm or 400 nm LEDs.¹⁵⁹ Exhaustive photolysis in the presence of myoglobin led to the release of an average of *ca.* three equivalents of CO per molecule of CORM.¹⁸⁴ The extent and rate of release of the complexes appeared to change slightly when the substituent on the ppy ligand was changed, although any differences in water solubility of the complexes, which are not reflected in the myoglobin CO release assay, could also account for the different CO release rates.

Complexes **92-94** were subsequently tested in cell viability studies.¹⁵⁹ The alamarBlue assay was used to measure the reduction of a coloured redox indicator by living cells (in this case RAW 264.7 macrophages from mice), whilst lactate dehydrogenase (LDH) levels were also monitored to measure lysis of the cells. The results showed that the cells remained viable at 10 μM for each derivative, though compound **92** was highly toxic moving up to 50 μM . Cells exposed to complexes **93** and **94** on the other hand, retained good to excellent viability up to 100 μM . These two derivatives therefore showed promising results, but the results confirm that the toxicity of every photoCORM should be assessed on an individual basis. Following the success of the mammalian toxicity studies for complex **94**, its antimicrobial properties were also explored, and these will be discussed further in Chapter 5.

Finally, photochemical decomposition products from 400 nm irradiation of **94** were detected in an ESI mass spectrometry study (Scheme 21).¹⁵⁹ These results must be treated with a degree of caution as the experiment was not quantitative and so some of the species may only be minor decomposition products, whilst some species may be produced or fragment within the mass spectrometer. When a 50:50 $\text{H}_2\text{O}:\text{MeCN}$ solution of complex **94** was irradiated, ESI mass spectra

suggested that loss of a CO ligand is followed by replacement with MeCN to form tricarbonyl species **99**. The detection of the protonated form of the substituted ppy ligand, along with tricarbonyl complex $[\text{Mn}(\text{MeCN})_3(\text{CO})_3]^+$ indicates that loss of the ppy ligand may take place prior to further CO loss. Finally, the observation of carboxylic acid **101** has been attributed to CO insertion into the Mn-C bond to the ppy ligand. This is expected to occur through formation of a solvent complex such as **99** ($S = \text{MeCN}$ or H_2O) which blocks the vacant coordination site left by CO insertion. Such a side-reaction may help to explain why the tetracarbonyl prodrug releases only *ca.* three equivalents of CO. Other pathways such as the water-gas shift reaction or formation of a thermally stable monocarbonyl unreactive at the irradiation wavelength chosen could also explain why four equivalents of CO are not released, although no evidence was obtained for these alternatives in this preliminary study. Another hypothesis is that the final equivalent of CO is either not released or is released in a way that is not captured by the myoglobin assay. For example, the timescale of the myoglobin assay is restricted to several hours because of CO escape and myoglobin degradation and slower release would not be detected in a typical assay.¹⁶⁰



Scheme 21: Species observed by mass spectrometry in a photochemical study by Fairlamb and co-workers.¹⁵⁹

Although this preliminary study provides some understanding of the decomposition pathways of the $[\text{Mn}(\text{ppy})(\text{CO})_4]$ family of photoCORMs, the photoproducts on the ultrafast timescale have not been elucidated. Understanding and controlling the primary photochemical and photophysical

properties of these compounds will enable the evaluation of these complexes as photoCORMs and can then be used to inform the design of more efficient targets.

1.5 Aims and Objectives

Despite its well-known toxicity, the role of CO in biology is still not understood. One thing is clear: CO plays a role in cell signalling in mammalian cells, both healthy and diseased. The therapeutic potential of CO is clear but its administration is challenging. The development of CORMs as a delivery method for CO over the last 15 years has resulted in some key considerations for CORM design. Ideally, CORMs should be stable to ambient conditions for storage and transport but release a well-defined dose of CO upon exposure to a selective trigger. In the case of photoCORMs, visible or NIR light is preferable and CO release should be the main photoproduct (i.e. the quantum yield is high). Both the CORM itself and its degradation products need to be well-characterised and their toxicity, absorption, distribution, metabolism and excretion should be studied. Finally, tailored co-ligands should be incorporated to provide more than a scaffold for CO release. Depending on the purpose of the CORM, this could include modulation of CO release rate/wavelength, inclusion of a fluorophore for imaging, or a bioconjugate or drug molecule for a second therapeutic mode of action.

A range of mechanistic tools is available to capture CO release from CORMs, but just as important is understanding the nature of the degraded CORM fragments, as these can have substantial effects in biological systems. For photoCORMs, it is important to understand the fundamental photochemical steps involved in CO release so that more efficient, visible light-releasing compounds can be designed.

The aims and objectives of the work in this Thesis are:

- Study the photochemical CO release properties and degradation mechanisms of $[\text{Mn}(\text{ppy})(\text{CO})_4]$ and derivatives (Chapter 2).
 - Use time-resolved infrared (TRIR) spectroscopy to study the ultrafast photoproducts of MLCT excitation interpretation and understand the subsequent reactivity of the photoproducts (picoseconds to microseconds).
 - Interpret DFT calculations to help assign the species involved in the TRIR experiments.
 - Use *in situ* infrared spectroscopy to study the decomposition of $[\text{Mn}(\text{ppy})(\text{CO})_4]$ on longer timescales (minutes to hours).

- Synthesise, characterise, and assess redox-tagged CORMs based on $[\text{Mn}(\text{ppy})(\text{CO})_4]$. (Chapter 3).
 - Synthesise and characterise CORMs containing ferrocenyl co-ligands with different linker lengths between the Mn and Fe centres.
 - Study the electrochemical behaviour of the ferrocenyl CORM complexes with cyclic voltammetry and infrared spectroelectrochemistry.
 - Investigate the CO release properties of the complexes using *in situ* infrared and UV-visible spectroscopies and the Mb CO-release assay.

- Investigate and evaluate a method of increasing the wavelength of CO release of Mn(I) tetracarbonyl CORMs further into the visible region. The redox properties of these complexes will also be studied (Chapter 4).
 - Synthesise a series of Mn(I) tetracarbonyl complexes with azo co-ligands,
 - Assess the photochemical CO release wavelengths using the Mb assay.
 - Perform a spectroelectrochemical study to test for redox-triggered CO release.

- Synthesise a fluorescent $[\text{Mn}(\text{ppy})(\text{CO})_4]$ derivative for imaging in live cells, with a view to assessing its antimicrobial properties (Chapter 5).
 - Synthesise and characterise a fluorophore-tagged derivative of $[\text{Mn}(\text{ppy})(\text{CO})_4]$ using a click chemistry methodology.
 - Study the CO release properties of the fluorophore-tagged complex.
 - Image the complex in a human cell line.
 - Assess the toxicity of the fluorophore-tagged complex.

2 Ultrafast Time-Resolved Infrared Spectroscopy of [Mn(ppy)(CO)₄]

One of the main methods for initiating CO loss from CORMs is through photolysis (Section 1.2.2.4). Absorption of a photon by a metal carbonyl photoCORM initiates ultrafast photophysical and photochemical behaviour, such as formation of electronically excited states and CO dissociation.¹²⁴ Studying these ultrafast processes and the subsequent evolution of the photoproducts allows the photochemical properties, reactivity and CO release mechanisms of these compounds to be mapped, which is a requirement to inform the design of more efficient photoCORMs.

In this Chapter, the use of ultrafast Time-Resolved Infrared (TRIR) spectroscopy to study the photochemistry of the photoCORM [Mn(ppy)(CO)₄] (ppy = 2-phenylpyridyl) (complex **88**) is described. Changes in the infrared stretching frequencies of the carbonyl ligands of the photoproducts provide structural information about the photoproducts formed, supported by DFT calculations. The results reveal that the qualitative balance between photodissociation and non-dissociative triplet excited state formation is markedly different to the well-studied isoelectronic [Cr(bpy)(CO)₄] (bpy = bipyridyl) system. Complex **88** is subsequently demonstrated as a useful model system for studying metal-solvent interactions following CO photolysis.

All TRIR data were obtained at the Central Laser Facility (CLF) of the Rutherford Appleton Laboratory. Experiments were enabled by the assistance of Dr Ian Clark, Dr Igor Sazanovich and Professor Michael Towrie. All DFT calculations reported in this Chapter were performed by Dr Jason Lynam.

2.1 Background

2.1.1 Ultrafast TRIR Studies of PhotoCORMs

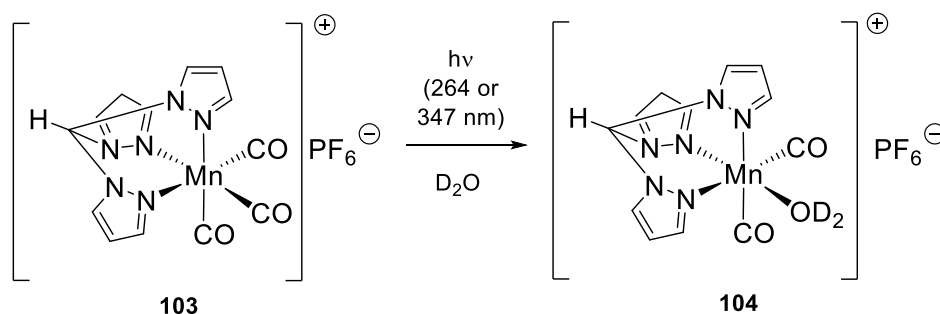
The key primary photochemical reactions of metal carbonyls often take place within femtoseconds to nanoseconds after the absorption of a photon.¹²⁴ Therefore, ultrafast spectroscopic techniques are powerful tools for investigating metal carbonyl photochemistry because they provide direct structural characterisation of the primary photoproducts whilst also enabling the evolution of the photoproducts to be monitored.

Ultrafast spectroscopic experiments typically involve a ‘pump-probe’ approach, in which an initial ‘pump’ pulse prompts a photochemical behaviour of interest and a subsequent ‘probe’ pulse is used to characterise the resulting products. Transient absorption (TA) spectroscopy, where photoproducts are characterised by a UV-visible probe pulse, and time-resolved infrared (TRIR)

spectroscopy, where an infrared probe is used, are often chosen to study metal carbonyl complexes.¹²⁴ The latter of these is particularly useful for structural characterisation because of the high sensitivity of carbonyl stretching frequencies to their electronic environment. These techniques, in conjunction with insight from theoretical calculations, have been used to characterise metal carbonyls comprising a range of metal and co-ligand combinations in the gas phase and in solution.^{124,176,186,187}

The photochemistry of simple early photoCORMs, such as $\text{Mn}_2(\text{CO})_{10}$, was already well-characterised before their therapeutic relevance was demonstrated. The primary ultrafast photochemical reactivity of $\text{Mn}_2(\text{CO})_{10}$ was studied both in the gas phase and a range of solvents (including alkanes and alcohols) using traditional flash photolysis experiments,¹⁸⁸ ultrafast TA spectroscopy,^{171,189} and ultrafast mass spectrometry.¹⁷⁰ This work revealed competing ultrafast pathways: Mn-Mn bond homolysis to form two $\text{Mn}(\text{CO})_5$ radicals, and CO loss to form $\text{Mn}_2(\text{CO})_9$.¹⁷⁰ Ultrafast TRIR spectroscopy was subsequently applied to study the 310 nm photolysis of $\text{Mn}_2(\text{CO})_{10}$ in cyclohexane,¹⁹⁰ providing the structural information to confirm that CO loss and Mn-Mn bond homolysis compete on the ultrafast timescale.

In one of the first ultrafast photochemical studies of a purpose-designed photoCORM, the groups of Nuernberger and Schatzschneider studied CO dissociation from the Mn(I) tricarbonyl species $[\text{Mn}(\text{tpm})(\text{CO})_3][\text{PF}_6]$ (tpm = Tris(2-pyrazolyl)methane) (**103**) in D_2O on the picosecond timescale with TRIR spectroscopy.¹⁹¹ Photochemical loss (at 264 or 347 nm) of one carbonyl ligand followed by D_2O solvent coordination to form $[\text{Mn}(\text{tpm})(\text{CO})_2(\text{OD}_2)]^+$ was the major photochemical process observed; this took place within the first few picoseconds after photolysis (Scheme 22).



Scheme 22: The CO-release process from tpm complex 103 studied by TRIR spectroscopy.

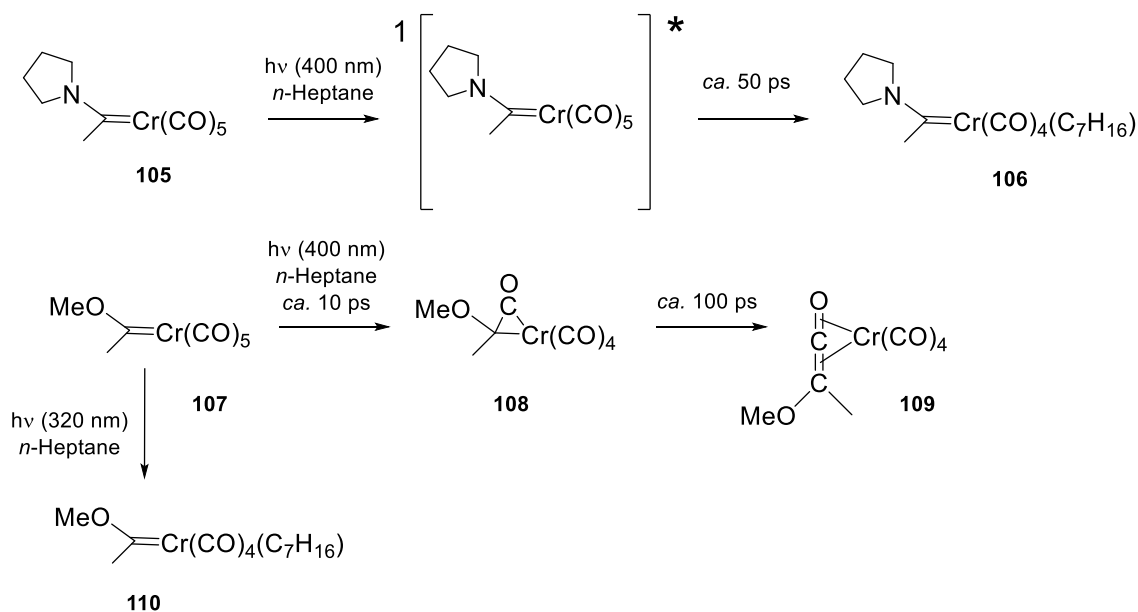
The infrared spectrum of the remaining carbonyl ligands of the photoproduct initially appeared broad. This broadness is due to vibrational excitation of the photoproduct which accompanies electronic excitation. Nuernberger and co-workers concluded that the vibrational energy does not cause excitation of the CO stretches themselves – if this were the case the photoproduct bands would move by much more than a few wavenumbers, as observed in the hot bands after photolysis of $[\text{M}(\text{CO})_6]$ ($\text{M} = \text{Cr}, \text{Mo}, \text{W}$).¹⁹² Therefore in $[\text{Mn}(\text{tpm})(\text{CO})_3]^+$, the vibrational excitation

involves low-frequency vibrations that couple to the CO stretches to give the broadening of the carbonyl bands. The bands sharpened over the first few tens of picoseconds, representing the vibrational relaxation or ‘cooling’ of the photoproduct as energy is transferred away by collisions with the solvent. Vibrational relaxation is also accompanied by a small shift of the bands to higher wavenumber due to a slight strengthening and shortening of bonds in the ground vibrational state. Geminate recombination of CO with the $[\text{Mn}(\text{tpm})(\text{CO})_2]^+$ fragment was also observed.¹⁹¹ Although this process took place faster than the ps time resolution of these experiments, its effect could still be observed in the ground state bleach bands. The slight recovery of the bleach bands on the ps timescale reflects the vibrational relaxation of $[\text{Mn}(\text{tpm})(\text{CO})_3]^+$ following geminate recombination within 1 ps. Rapid geminate recombination of this kind has been further studied in other systems such as the group 6 homoleptic carbonyls.¹⁹³

Another notable feature of this work was that two successive UV laser pulses (the first pump pulse followed by a ‘re-pump’ pulse at the same wavelength 200 ps later) did not initiate further photochemical degradation of the photoproduct.¹⁹¹ This observation led the authors to invoke previous work suggesting that subsequent photoCORM decomposition is non-photochemical and involves oxidation of the Mn.¹⁹¹ Although the absorption spectra of the photoproducts were not known, and so specific CO-dissociative transitions were not targeted in the ‘re-pump’ experiment, this work shows how TRIR spectroscopy can be adapted for use in mechanistic studies of photoCORMs.

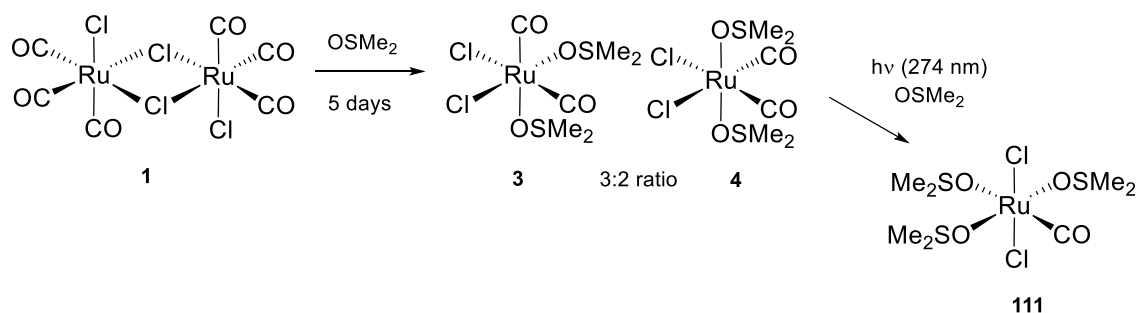
In another study, Pryce and co-workers used ultrafast TRIR spectroscopy to characterise the photochemistry of the chromium amino carbene complex $[\text{Cr}(\text{CO})_5\text{C}(\text{NC}_4\text{H}_4)(\text{Me})]$ **105**.¹⁹⁴ In this system, photoproduct bands assigned to an excited state appear within the first 3 ps after 400 nm laser photolysis in *n*-heptane. The bands for the excited state are replaced by those of a second set species over *ca.* 50 ps. This species was identified as the solvated complex **106**, in which a heptane solvent molecule is weakly bound to the coordination site vacated by one of the CO ligands (Scheme 23). The replacement of CO with a solvent molecule on the picosecond timescale is consistent with theoretical calculations predicting a small energy barrier to CO loss in the CO-dissociative excited state.

The related complex $[\text{Cr}(\text{CO})_5\text{C}(\text{OMe})(\text{Me})]$ (**107**) displays similar behaviour upon photolysis at 320 nm. However, this complex does not always lose a CO ligand to form a solvent complex. Instead, a metallaketene species is formed upon 400 nm excitation.¹⁹⁵ For chromium, this was proposed to occur through excitation to a singlet state, though in the analogous tungsten complex metallaketene (**109**) formation was proposed to occur through direct optical population of a triplet state.¹⁹⁵



Scheme 23: Photochemical behavior of two chromium carbene CO-releasing molecules as determined by TRIR spectroscopy.^{194,195}

Harris and co-workers used ultrafast TRIR spectroscopy when investigating the behaviour of CORM-2 derivatives (Scheme 24).¹⁹⁶ Since CORM-2 degrades when solubilised in dimethyl sulfoxide (DMSO), a solution of pre-degraded CORM-2 featuring the two DMSO complexes **3** and **4** in approximately 3:2 ratio was analysed. The dominant photoproduct in the infrared spectrum after 1.7 ns was assigned as the monocarbonyl species **111** on the basis DFT predictions. This suggests that the first step in the photochemical degradation of these complexes, as many of the other systems discussed above, is CO-loss.



Scheme 24: CORM-2 degrades in DMSO solution but further CO release can be prompted photochemically. Harris and co-workers used TRIR spectroscopy to show that degradation products **3 and **4** lose a CO ligand on the ultrafast timescale.**¹⁹⁶

The use of TRIR spectroscopy in the photoCORM field has revealed the primary photochemical behaviour of several classes of photoCORMs. The first step in the degradation of the complexes discussed above was CO-loss followed by solvation, which takes place in competition with formation of other excited states and vibrational relaxation. As the results of the studies above show, loss of CO is commonly the dominant photochemical pathway in metal carbonyl

photochemistry. However, this behaviour is not universal: the reaction or loss of co-ligands and formation of non-dissociative excited states can dominate in other complexes.¹²⁴

2.1.2 Photochemistry of [Cr(bpy)(CO)₄]

Although relatively little is known about the photochemistry of [Mn(ppy)(CO)₄], the isoelectronic complex [Cr(bpy)(CO)₄] (bpy = 2,2'-bipyridyl), **112** has been extensively studied and may provide an informative comparison. Ultrafast TRIR and TA spectroscopies and theoretical calculations have been used to understand the photochemistry of **112** and this system represents an interesting balance between the formation of non-dissociative excited states and CO loss.¹⁹⁷

According to quantum mechanical calculations by Daniel and co-workers, the three highest occupied molecular orbitals in [Cr(bpy)(CO)₄] are metal-based, arising from three of the Cr 3d atomic orbitals, while the three lowest-energy unoccupied molecular orbitals are ligand-based and have bpy π^*_{bpy} character.¹⁹⁸ As a result, the lowest-energy spin and symmetry-allowed transitions in [Cr(bpy)(CO)₄] produce singlet metal-to-ligand charge transfer (MLCT) states.¹⁹⁸ This leads to a broad, solvatochromic band of MLCT(bpy) absorptions in the visible part of the electronic absorption spectrum with a maximum at around 500 nm.¹⁹⁹ Transitions of a ¹MLCT(CO) nature, from the Cr 3d orbitals into the π^*_{CO} orbitals, were calculated to be weaker and slightly higher in energy (bordering the UV region) than the ¹MLCT(bpy) states.¹⁹⁸

Ultrafast TA and TRIR spectroscopy studies by Vlček and co-workers have characterised the photoproducts that arise from the different types of MLCT transitions. The major photochemical pathway in [Cr(bpy)(CO)₄] produces two non-dissociative excited states.²⁰⁰ Irradiation of the low-energy bands produces two ³MLCT states within 1 ps, which dominate the TRIR spectra for the first tens to hundreds of picoseconds before decaying to the ground state, as indicated by recovery of the bleached ground state bands.²⁰⁰ The ³MLCT states were found to have lifetimes of $\tau_1 = 8 \pm 3$ ps and $\tau_2 = 76 \pm 7$ ps in CH₂Cl₂ solution with 400 nm excitation.²⁰⁰ Since direct transitions to triplet excited states break the spin selection rule and are therefore extremely weak, the ³MLCT states observed are formed through intersystem crossing following initial excitation to the low-energy ¹MLCT(bpy) states. A recent TA spectroscopy study by Yartsev and co-workers showed that intersystem crossing took place within around 100 fs, with sequential population of the short-lived ³MLCT state followed by the second longer-lived, lower-energy ³MLCT state.¹⁷⁵

Excitation to the low-energy ¹MLCT(bpy) states also results in some CO dissociation as a minor photochemical pathway.^{200–202} Loss of CO leads to sub-picosecond formation of solvent complexes of the form *fac*-[Cr(bpy)(S)(CO)₃] (S = CH₂Cl₂ or pyridine).²⁰⁰ Daniel and co-workers calculated that the low-energy ¹MLCT(bpy) excited states are very weakly bound along the axial Cr-CO coordinate with only a small barrier to CO loss.²⁰³ At longer Cr-CO bond lengths there is

an avoided crossing between the $^1\text{MLCT}(\text{bpy})$ excited states and d-d excited states of the same symmetry, resulting in the mixing of some d-d transition character with the $^1\text{MLCT}(\text{bpy})$ states.²⁰³ Wavepacket dynamics simulations for $[\text{Cr}(\text{bpy})(\text{CO})_4]$ along the axial Cr-CO coordinate predicted excitation of the wavepacket onto the repulsive part of the $^1\text{MLCT}(\text{bpy})$ potential due to the longer equilibrium bond length in the excited state. This led to the prediction of complete photodissociation within 600 fs, in good agreement with the experimentally-observed timescale of CO loss.²⁰³

Although the potential energy surfaces for the slightly higher-energy $^1\text{MLCT}(\text{CO})$ excited states were not calculated, calculations on the isoelectronic complex $[\text{W}(\text{en})(\text{CO})_4]$ (en = 1,2-diaminoethane) show that the lowest-energy $^1\text{MLCT}(\text{CO})$ comprises charge transfer from the metal and equatorial carbonyls [the $\text{Cr}(\text{CO}_{\text{eq}})_2$ moiety] to the axial carbonyls $[\text{CO}_{\text{ax}}]$.²⁰⁴ The lack of π -acceptor ability makes this the lowest-energy excited state in $[\text{W}(\text{en})(\text{CO})_4]$.

The behaviour of the $^1\text{MLCT}(\text{CO})$ and $^1\text{MLCT}(\text{bpy})$ can be compared by examining the wavelength-dependence of $[\text{Cr}(\text{bpy})(\text{CO})_4]$ photochemistry. In CH_2Cl_2 at an excitation wavelength of 500 nm, only the $^1\text{MLCT}(\text{bpy})$ states are populated, whereas at 400 nm both $^1\text{MLCT}(\text{bpy})$ and $^1\text{MLCT}(\text{CO})$ transitions take place.²⁰⁰ Upon moving from 518 nm to 419 nm, the quantum yield for photodissociation increases approximately threefold from 3.83×10^{-2} to 1.07×10^{-1} .²⁰² The $^3\text{MLCT}$ states are still the major photoproducts. This suggests that the $^1\text{MLCT}(\text{CO})$ states of $[\text{Cr}(\text{bpy})(\text{CO})_4]$ behave in a similar manner to $^1\text{MLCT}(\text{bpy})$ but that the $^1\text{MLCT}(\text{CO})$ states result in more CO loss and less $^3\text{MLCT}$ formation compared to $^1\text{MLCT}(\text{bpy})$ states. The reactivity of $[\text{Cr}(\text{bpy})(\text{CO})_4]$ is summarised in Figure 25.

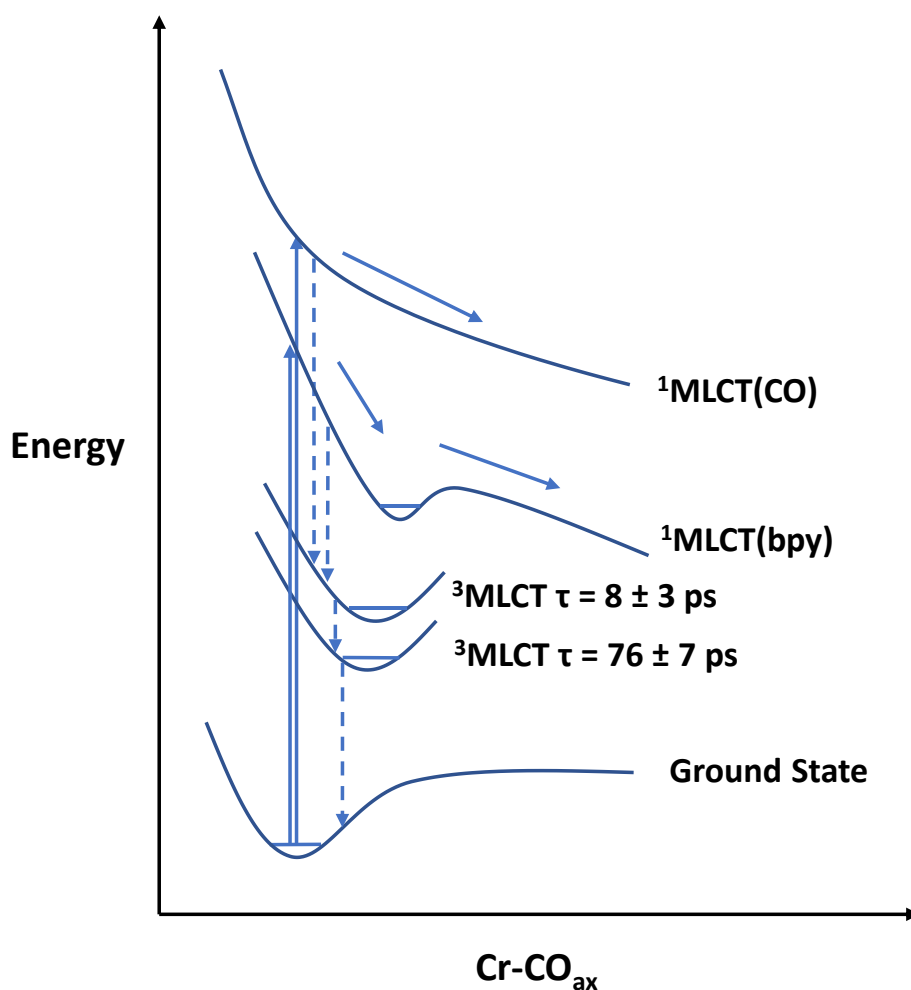


Figure 25: Schematic of key excited states in the photochemistry of $[\text{Cr}(\text{bpy})(\text{CO})_4]$, updated from the summary by Viček and co-workers²⁰⁰ to reflect sequential population of the $^3\text{MLCT}$ states.¹⁷⁵

The same rationale for the dissociative nature of $^1\text{MLCT}(\text{CO})$ states is used as was described above for the $^1\text{MLCT}(\text{bpy})$ states.²⁰⁵ Calculations on $[\text{Cr}(\text{CO})_6]$ predict low-energy $^1\text{MLCT}(\text{CO})$ excited states that are CO dissociative: axial elongation of M-CO bonds in leads to mixing with higher-energy dissociative d-d states, resulting in photodissociation from initial population of the $\text{MLCT}(\text{CO})$ state.^{172,206–208}

In contrast to $[\text{Cr}(\text{bpy})(\text{CO})_4]$, most other metal carbonyl complexes do not possess low-lying vacant orbitals from α -diimine co-ligands such as bpy, and as such the lowest-energy excited states are the $^1\text{MLCT}(\text{CO})$ states.¹⁹⁹ The unoccupied d-orbitals are again much higher in energy than the CO ligand-based orbitals. As a result, in most metal carbonyl complexes CO loss from $^1\text{MLCT}(\text{CO})$ excited states on the sub-ps timescale is the major photochemical pathway,²⁰⁹ as was the case for the photoCORM examples in Section 2.1.1. It is the presence of the low-lying bpy-based unoccupied orbitals that dictates the different photochemical behaviour of $[\text{Cr}(\text{bpy})(\text{CO})_4]$. The $^1\text{MLCT}(\text{bpy})$ absorbances, with a lower quantum yield for CO dissociation,²⁰⁰ compete with the $^1\text{MLCT}(\text{CO})$ states, and both types of excitations can lead to ‘trapping’ in unreactive $^3\text{MLCT}$

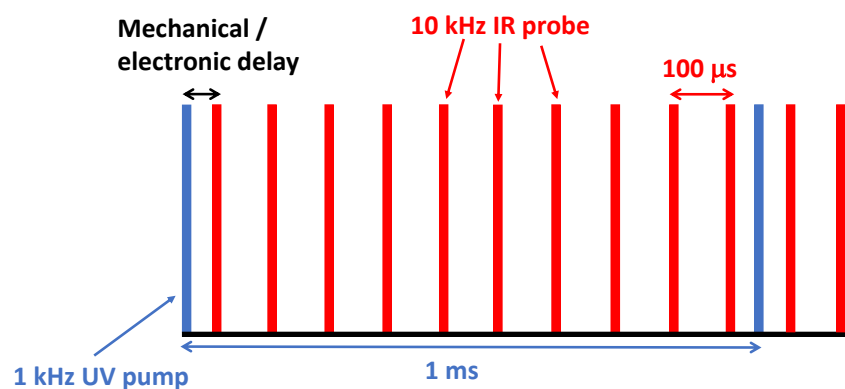
states. Thus, the example of $[\text{Cr}(\text{bpy})(\text{CO})_4]$ shows that the nature of the co-ligand can be hugely influential on the photochemical pathways observed when designing photoCORMs.

2.1.3 Time-Resolved Multiple Probe Spectroscopy (TR^MPS)

The TRIR spectroscopy method used in this Chapter is Time-Resolved Multiple Probe Spectroscopy (TR^MPS). Using TR^MPS, it is possible to study processes from sub-picosecond to millisecond timescales on the same spectrometer in a single experiment.²¹⁰

In the study of $[\text{Mn}(\text{ppy})(\text{CO})_4]$, a UV pump pulse must be used to excite the CO dissociative transition(s), because CO loss is known to take place at 365 and 400 nm. An infrared probe pulse then records the infrared spectrum of the photoproducts after the chosen delays. The time resolution is limited by the length of the pulses; in this work pump pulses of 100 fs duration and probe pulses of 50 fs were used.

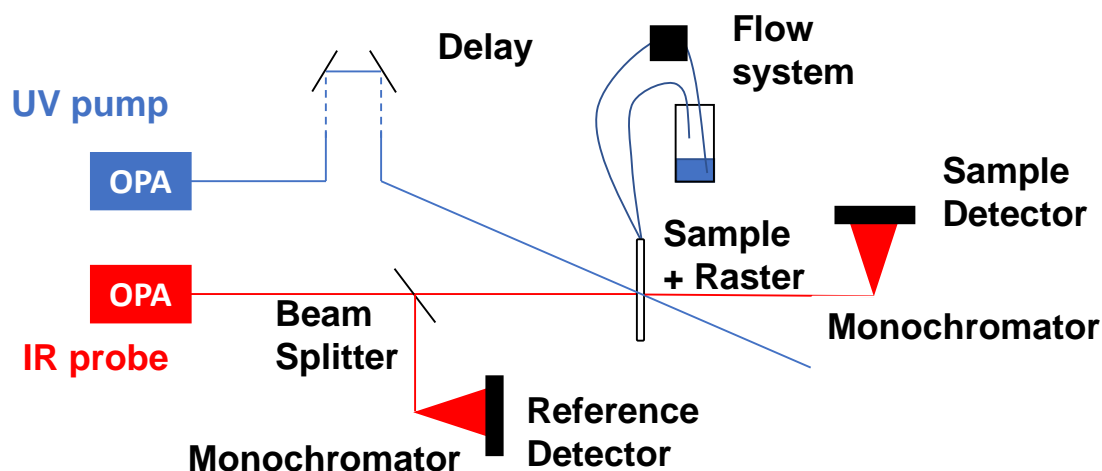
Unlike a typical ‘pump-probe’ experiment, TR^MPS uses a ‘pump-probe-probe-probe...’ sequence (Scheme 25).²¹⁰ The pump and probe lasers have different repetition rates such that multiple probe pulses (every 100 μs) occur in between each pump pulse (every 1 ms), providing a succession of ten infrared pulses after each pump pulse. This is useful for obtaining a series of relatively long delays. Further delays between the pump and probe lasers are achieved with either an optical delay line (ps to ns delays) or a combination of optical and electronic delays (ns to μs delays).²¹⁰



Scheme 25: Illustration of the sequence of laser pulses in a TR^MPS experiment.²¹⁰

A schematic of the TR^MPS setup is shown in (Scheme 26). The wavelength of the laser pulse is tuned using an optical parametric amplifier (OPA). The timing of the UV pump pulse is controlled using the optical and electronic delays before passing through the sample. The sample must be flowed and rastered to prevent a build-up of photoproducts in the cell. The infrared probe beam is split into two beams: one beam passes through the sample and the other is diverted to a reference detector. Subtraction of the reference detector readings from the data provides a way of correcting

data for shot-to-shot variation in the laser pulse intensities. The resulting spectra are typically presented as difference spectra with respect to the last spectrum in the ten-probe pulse sequence.



Scheme 26: Schematic representation of the setup used in TR^{MPS}.²¹⁰

In summary, a wide range of timescales can be investigated using TR^{MPS}, allowing the both the structural information about the primary photoproducts, and information about their subsequent reactivity to be studied. The method used to collect the data in this Chapter and details of the subsequent data processing are discussed in more depth in the experimental section (Section 7.1).

2.2 Spectroscopic Characterisation of [Mn(ppy)(CO)₄]

Before reporting the results of the TR^{MPS} experiments, it is necessary to introduce and discuss the vibrational and electronic spectroscopic characterisation of [Mn(ppy)(CO)₄].

The number and symmetry of carbonyl ligands at a metal centre can be determined using vibrational spectroscopy and group theory: this combination will also be used later to aid the assignment of photoproducts.

Experimental UV-visible spectra, combined with DFT calculations, will be used to understand the electronic transitions in [Mn(ppy)(CO)₄]. This provides insight into the nature of the low-energy electronic transitions to be probed in the TRIR experiments and facilitates comparison with other metal carbonyl systems.

2.2.1 Ground State Infrared Spectrum of [Mn(ppy)(CO)₄] (**88**)

Four metal carbonyl stretching bands¹⁸³ are observed in the ground-state infrared spectrum of [Mn(ppy)(CO)₄] **88**: in MeCN these are at 1933, 1976 (shoulder), 1989 and 2076 cm⁻¹. The spectrum is shown in Figure 26.

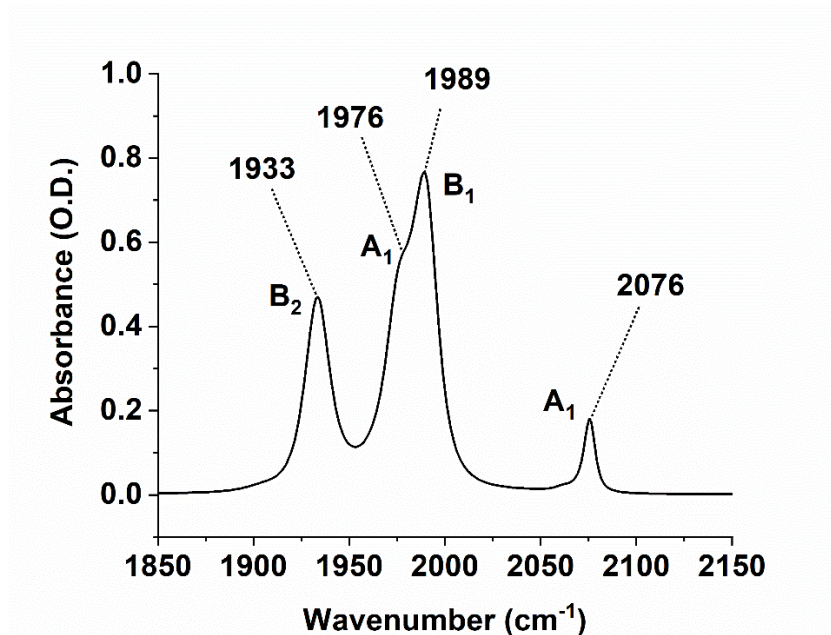


Figure 26: Infrared spectrum of [Mn(ppy)(CO)₄] in MeCN, recorded at 2 cm⁻¹ resolution. Assignments based on vibrational analyses of analogous *cis*-[ML₂(CO)₄] complexes.²¹¹

The appearance of the spectrum can be compared with a group theoretical vibrational analysis that predicts the number of infrared-active C≡O stretching bands. The point group of [Mn(ppy)(CO)₄] is C_s, though the molecule may also be considered to possess *pseudo*-C_{2v} symmetry if the differences in masses, bond lengths and angles for the C and N atoms of the ppy ligand are taken to be small. The C_{2v} point group contains the two elements in C_s [the identity E and mirror plane σ(yz)], plus two more: a C₂ axis and σ(yz) in which the C and N atoms of the ppy ligand are interconverted. The symmetry elements are shown in Figure 27.

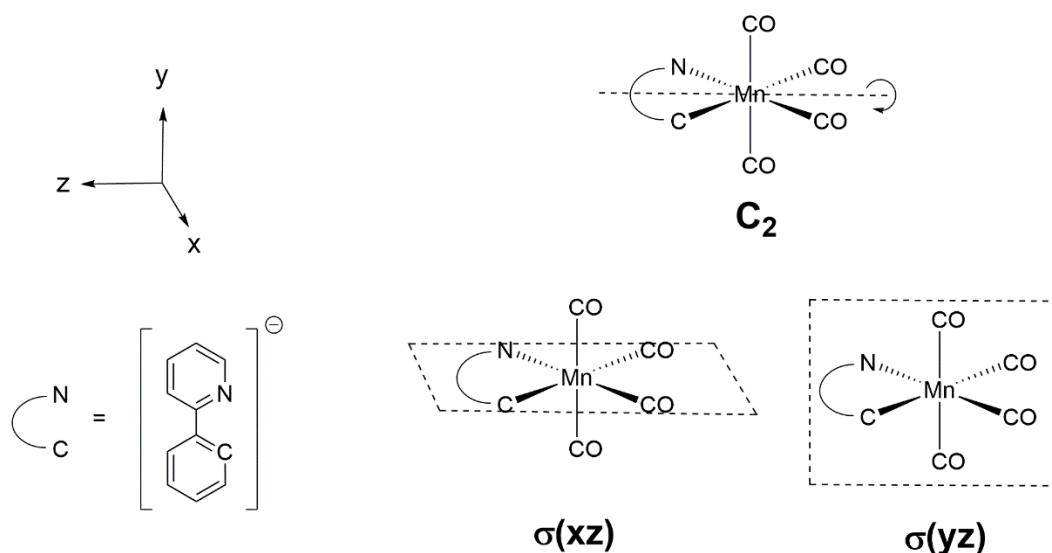


Figure 27: Symmetry elements (excluding the identity) of the C_{2v} point group superimposed on complex $[\text{Mn}(\text{ppy})(\text{CO})_4]$. The C_s point group features only the identity and $\sigma(\text{yz})$ symmetry elements. This molecule may be considered to have C_s or *pseudo- C_{2v}* symmetry.

Using vectors pointing in the directions of the four carbonyl ligands as a basis set in the C_s point group, the reducible representation $\Gamma_{\text{vib}}(\text{CO})$ in the bottom row of Table 2 is obtained.

Table 2: Character table of the C_s point group showing the reducible representation of the carbonyl ligands of $[\text{Mn}(\text{ppy})(\text{CO})_4]$ underneath.

C_s	E	σ_h	Linear Functions
A'	1	1	x, y
A''	1	-1	z
$\Gamma_{\text{vib}}(\text{CO})$	4	2	

Inspection of the character table shows that the reducible representation comprises $3A' + A''$. Only vibrational modes that transform in the same way as the linear (x,y or z) functions can be infrared-active, as they transform in the same way as the electric dipole moment operator. Since in this case the linear functions can transform as either of the two non-degenerate irreducible representations in the group, all four vibrational modes are predicted to be infrared-active.

An analysis using the *pseudo- C_{2v}* point group also predicts four bands. The reducible representation is shown with the character table in Table 3. Inspection of the character table for the C_{2v} point group reveals that the M-CO bond basis set spans the irreducible representations $2A_1 + B_1 + B_2$. As the linear functions transform as either A_1 , B_1 , or B_2 , all four of the stretching modes are again predicted to be infrared-active.

Table 3: Character table of the C_{2v} point group showing the reducible representation of the carbonyl ligands of $[\text{Mn}(\text{ppy})(\text{CO})_4]$ underneath.

C_{2v}	E	C_2	$\sigma(xz)$	$\sigma(yz)$	Linear Functions
A_1	1	1	1	1	z
A_2	1	1	-1	-1	
B_1	1	-1	1	-1	x
B_2	1	-1	-1	1	y
$\Gamma_{\text{vib}}(\text{CO})$	4	0	2	2	

Assignment of the observed bands to each symmetry mode, as shown above in Figure 26, may be made based on analyses of other *cis*- $[\text{ML}_2(\text{CO})_4]$ complexes.²¹¹ For example, the infrared spectrum of $[\text{Cr}(\text{bpy})(\text{CO})_4]$, which is isoelectronic to $[\text{Mn}(\text{ppy})(\text{CO})_4]$ and is C_{2v} symmetric, displays the same intensity pattern as $[\text{Mn}(\text{ppy})(\text{CO})_4]$.²¹² The B_1 mode involves the asymmetric stretch of the mutually *trans* carbonyl ligands, whilst the B_2 mode comprises the asymmetric stretch of the two mutually *cis* carbonyls in the plane of the ppy ligand. This ordering is consistent with the expectation of higher force constants for a carbonyl *trans* to a strong π -acceptor.²¹¹ The two A_1 modes involve totally symmetric vibrations comprising the symmetric stretches of the two carbonyls in the plane of the ppy ligand (of lower wavenumber and higher intensity) and the mutually *trans* carbonyl ligands (the weak, high-wavenumber band). As these two modes are of the same symmetry, there could also be some mixing between them. A visualisation of the vibrational modes is shown in

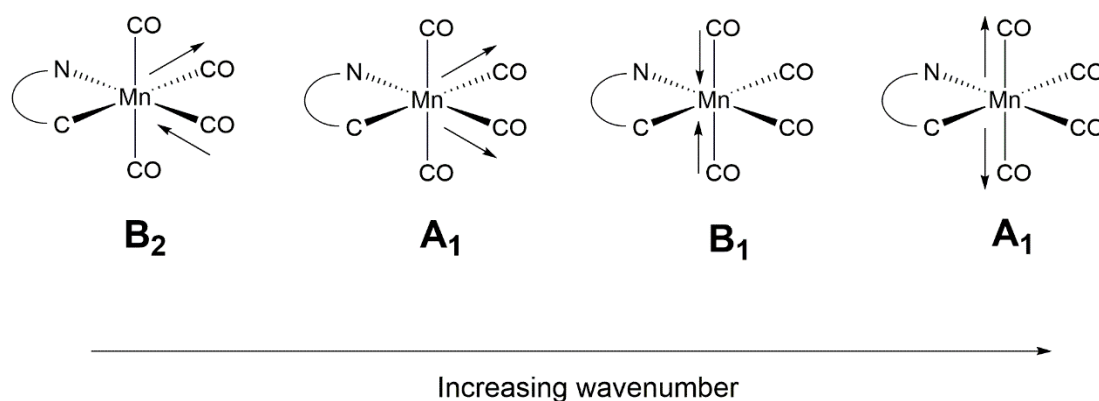


Figure 28: Visualisation of the vibrational modes for $[\text{Mn}(\text{ppy})(\text{CO})_4]$. Normal modes of the same symmetry may also participate in mixing.

2.2.2 Electronic transitions of [Mn(ppy)(CO)₄]

A series of UV-visible absorption spectra of [Mn(ppy)(CO)₄] at a range of concentrations in acetonitrile are shown in Figure 29. The most intense absorption [$\lambda_{\text{max}} = 230 \text{ nm}$, $\epsilon = (2.56 \pm 0.08) \times 10^4 \text{ dm}^3 \text{ mol}^{-1} \text{ cm}^{-1}$] is assigned to ligand-based $\pi\text{-}\pi^*$ transitions on the ppy ligand.

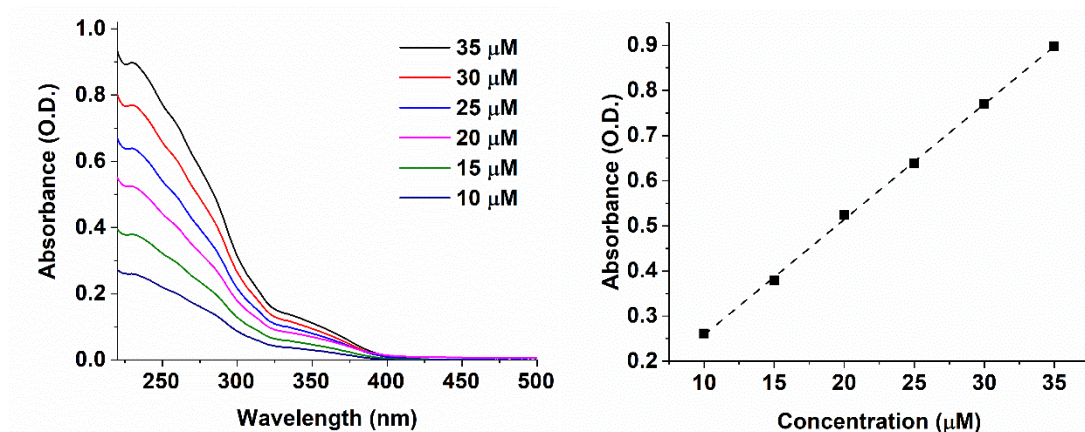


Figure 29: UV-visible spectra of [Mn(ppy)(CO)₄] in acetonitrile at low concentrations to show the intense $\pi\text{-}\pi^*$ ppy transitions. Left: Spectra at the concentrations shown. Right: Beer-Lambert plot with linear fit giving $\epsilon(230 \text{ nm}) = (2.56 \pm 0.08) \times 10^4 \text{ dm}^3 \text{ mol}^{-1} \text{ cm}^{-1}$.

However, since photochemical CO release takes place at 400 and 365 nm,^{159,184} it is excitation of the lower-energy shoulder, assigned to CO-dissociative MLCT transitions, between *ca.* 425-325 nm that is of greatest interest in this work. A photolysis wavelength of 355 nm [$\epsilon = (3.05 \pm 0.11) \times 10^3 \text{ dm}^3 \text{ mol}^{-1} \text{ cm}^{-1}$] was therefore selected for the subsequent TRIR studies outlined in Section 2.3.

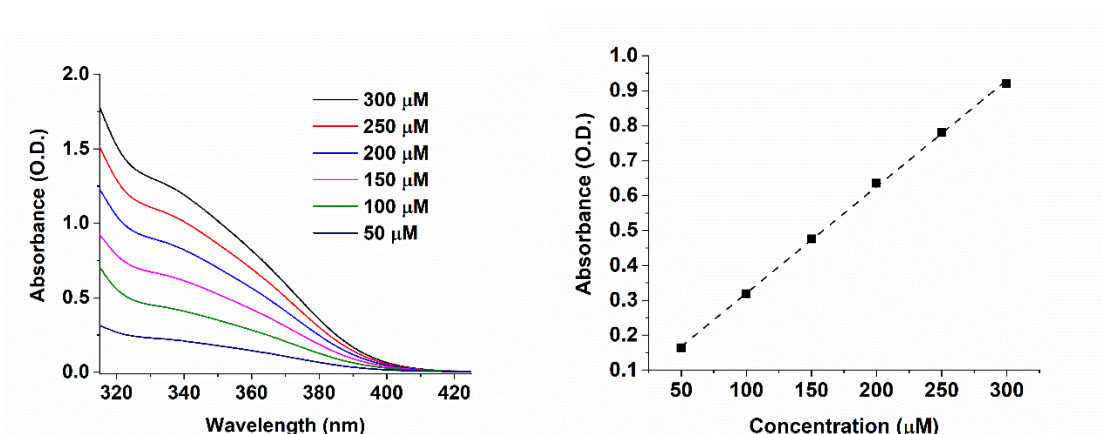


Figure 30: UV-visible spectra of [Mn(ppy)(CO)₄] in acetonitrile at higher concentrations to show the low-energy band. Left: Spectra at the concentrations shown. Right: Beer-Lambert plot with linear fit giving $\epsilon(355 \text{ nm}) = (3.05 \pm 0.11) \times 10^3 \text{ dm}^3 \text{ mol}^{-1} \text{ cm}^{-1}$.

The molecular orbitals of [Mn(ppy)(CO)₄] were calculated using DFT at the pbe0/def2-TZVPP level of theory, using C_s symmetry (Figure 31). Looking first at the highest occupied molecular

orbitals, the calculations show that both the HOMO and (HOMO – 1) are predominately based on the phenyl moiety of the ppy ligand, with a smaller contribution from Mn d-orbitals. This is consistent with the concept of the ppy ligand as an electron-rich formally anionic donor ligand. It is only when moving down to the (HOMO – 2) that an orbital with more d-character is found: this molecular orbital shows the Mn-CO π -backbonding interaction with the C \equiv O π^* orbitals of the two CO ligands in the plane of the ppy ligand. These results are in contrast to calculations on related complexes with neutral co-ligands, such as bpy in [Cr(bpy)(CO)₄] and tpm in [Mn(CO)₃(tpm)]⁺, in which all three of the highest occupied molecular orbitals are dominated by metal d-orbital contributions.^{191,198}

Turning to the lowest unoccupied molecular orbitals of [Mn(ppy)(CO)₄], the LUMO and (LUMO + 1) are located on the ppy ligand, mostly on the pyridyl ring. The character of the (LUMO + 2) orbital is very different as it does not involve the ppy ligand. Instead, it is spread across the metal and the mutually *trans* CO ligands, containing a large contribution of C \equiv O π^* character and a contribution from the Mn d_{z²} orbital. Complexes such as [Cr(bpy)(CO)₄] and other group six ‘diimine’ complexes have similar low-lying delocalised orbitals over the mutually *trans* CO ligands.²⁰⁴ Delocalisation over the Mn-CO moiety was also observed in calculated the low-lying virtual orbitals of [Mn(CO)₃(tpm)]⁺.¹⁹¹

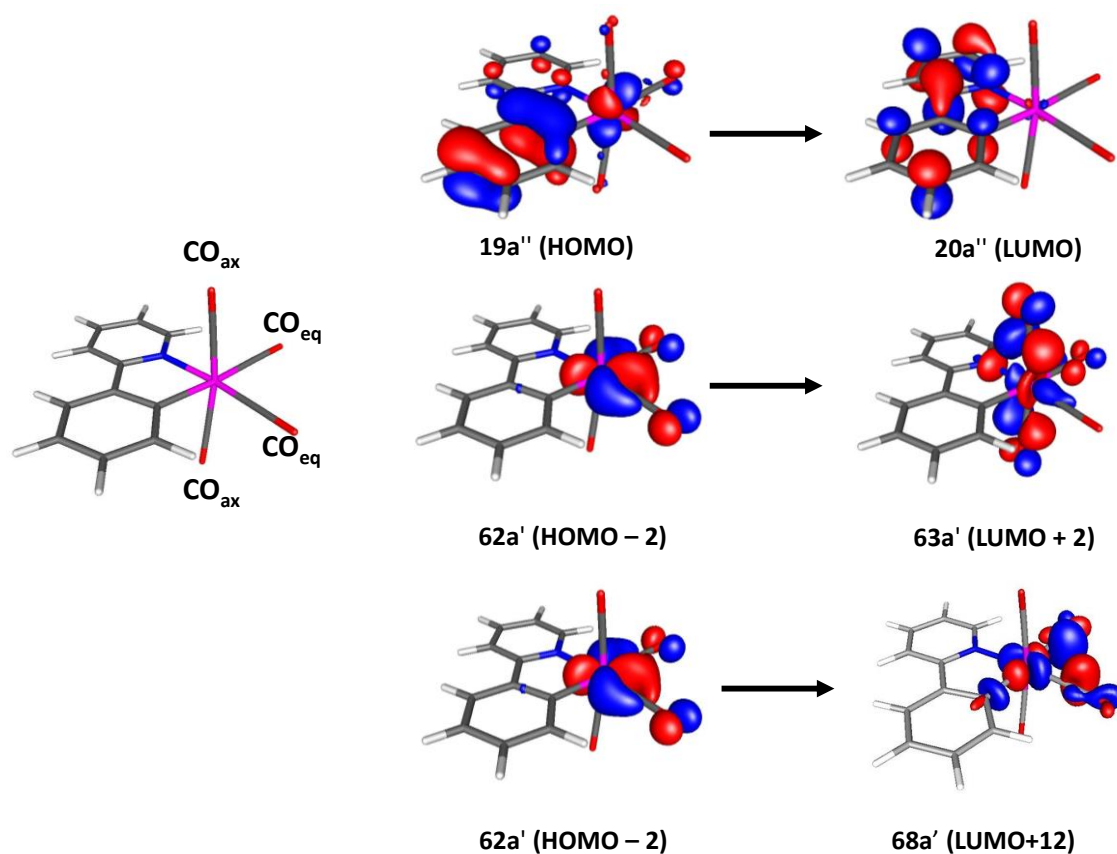


Figure 31: DFT-optimised structure and calculated molecular orbitals for [Mn(ppy)(CO)₄] (carbon grey, hydrogen white, manganese pink, nitrogen blue, oxygen red). Isosurfaces shown at 0.5 e Å⁻³.

The electronic absorptions of [Mn(ppy)(CO)₄] were also modelled by DFT calculations. The results suggest that the lowest-energy feature (425-325 nm) in the spectrum is dominated by two distinct absorptions with maxima at 345 and 342 nm. Both transitions feature substantial contributions from the same two components (Table 4).

Table 4: DFT-Calculated excitation wavelengths, intensities and orbital components for the low-energy allowed transitions of [Mn(ppy)(CO)₄] in the weak shoulder from 425-325 nm.

Energy / nm	Oscillator strength	Excitation Symmetry	Occupied orbital	Virtual orbital	Coefficient / %
345	0.345×10^{-1}	A'	19a''	20a''	75.9
			62a'	63a'	14.1
			62a'	68a'	2.3
342	0.180×10^{-1}	A'	62a'	63a'	56.3
			19a''	20a''	18.2
			62a'	68a'	11.3

The first component of importance is the HOMO-LUMO transition ($19a'' \rightarrow 20a''$). There is largely a ppy ligand-based $\pi\text{-}\pi^*$ transition, redistributing electron density from the phenyl to pyridyl moiety. There is also a small component of charge transfer from the Mn to the ppy ligand, similar to the predominant character of the ${}^1\text{MLCT}(\text{bpy})$ states of $[\text{Cr}(\text{bpy})(\text{CO})_4]$.¹⁹⁸ No such ligand-based transition is seen at low energy for $[\text{Cr}(\text{bpy})(\text{CO})_4]$ as the highest occupied molecular orbitals are all metal-based.¹⁹⁸ This reflects the more uneven distribution of electron density in the complexed ppy ligand compared to in bpy. As most of the transfer of electron density takes place within the ppy ligand in this component, it is unlikely that component ($19a'' \rightarrow 20a''$) confers strongly CO-dissociative character to the transitions at 342 and 345 nm.

The second contribution of note is from the component ($62a' \rightarrow 63a'$). In this case, electron density moves out of a metal d-orbital that is $\text{M}(\text{CO}_{\text{eq}})_2$ bonding into an orbital delocalised across the two CO_{ax} ligands. This is analogous to the CO-dissociative ${}^1\text{MLCT}(\text{CO})$ transitions studied previously in $[\text{W}(\text{en})(\text{CO})_4]$,²⁰⁴ and to the excitation from Mn d-orbitals to the delocalised Mn-CO orbitals in $[\text{Mn}(\text{CO})_3(\text{tpm})]^+$.¹⁹¹ Based on these comparisons, the ($62a' \rightarrow 63a'$) component is proposed to be the main mechanism for CO dissociation. As the excitations at 342 and 345 nm are both comprised of this component to different extents, they are both proposed to have CO-dissociative character. Finally, there is a small component in both orbital contributions that populates orbital $68a'$, which appears to be more of a dissociative CO_{eq} component, unlike the typical behaviour of metal carbonyls. However, the small contributions of these transitions suggests that they are unlikely to dominate the photochemical behaviour. These observations are a useful starting point to understand the fundamental photochemistry of $[\text{Mn}(\text{ppy})(\text{CO})_4]$, and through comparing to the different ligand spheres of known complexes an understanding of how the ligands, metal and oxidation state tune the photochemical behaviour is sought.

2.3 Ultrafast TRIR Spectroscopy of $[\text{Mn}(\text{ppy})(\text{CO})_4]$

Although the water solubility of $[\text{Mn}(\text{ppy})(\text{CO})_4]$ is adequate for CO release and toxicity studies, it is not sufficiently for the millimolar concentrations required by TRIR spectroscopy. The photochemical properties must therefore be probed in other solvents. The effects of the different physical properties and coordinating abilities of different solvents can provide insight into the reactivity and solvation of the photoproducts produced.

2.3.1 Acetonitrile

Photolysis of a solution of $[\text{Mn}(\text{ppy})(\text{CO})_4]$ at 355 nm in the polar coordinating solvent acetonitrile was studied by TR^MPS. The results are presented as difference spectra with reference to background spectra recorded at pump-probe delays of 900 to 1000 μs . For example, the background spectrum for a pump-probe delay of 10 μs was recorded at a pump-probe delay of

910 μs . The positive bands therefore represent photoproduct species, and the negative bands reflect bleaching of the ground state. The resulting spectra are presented in Figure 32, along with a spectrum of the ground state of $[\text{Mn}(\text{ppy})(\text{CO})_4]$ in MeCN (from Figure 26) for reference.

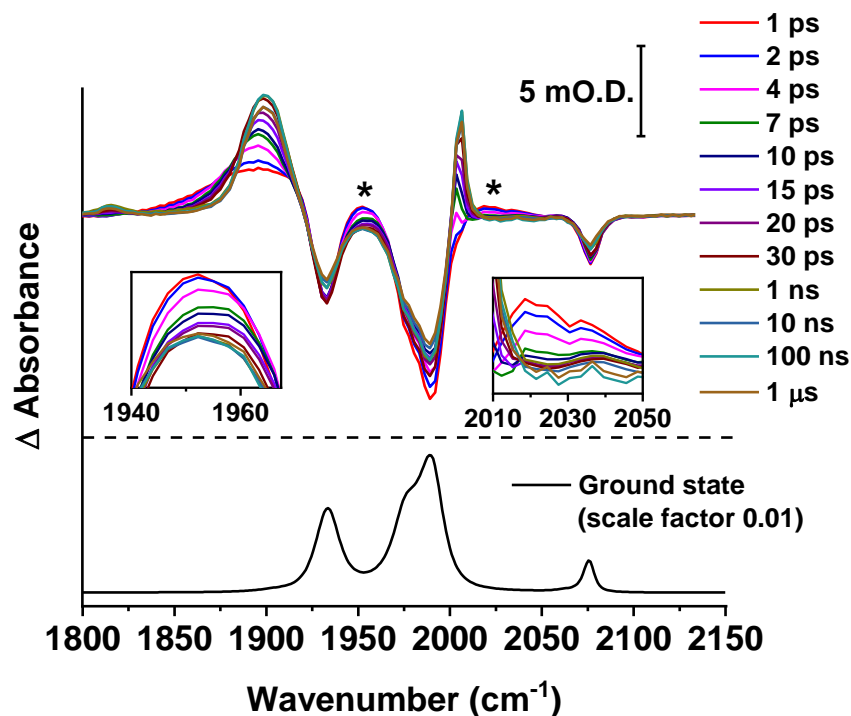


Figure 32: TRIR spectra of $[\text{Mn}(\text{ppy})(\text{CO})_4]$ in MeCN at selected pump-probe delays with a pump wavelength of 355 nm. The asterisks and insets show the triplet excited state. A spectrum of the ground state of $[\text{Mn}(\text{ppy})(\text{CO})_4]$ in MeCN is provided for reference, scaled by a factor of 100.

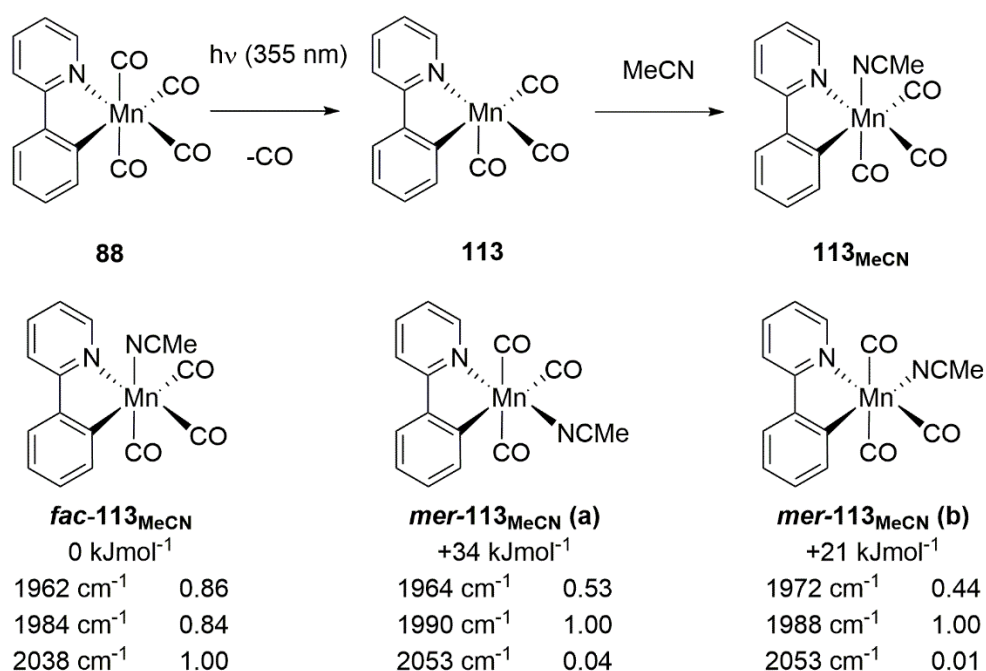
The difference spectra show a set of negative bands that match well to the position and intensity profile of the ground state of $[\text{Mn}(\text{ppy})(\text{CO})_4]$. This shows that the ground state of $[\text{Mn}(\text{ppy})(\text{CO})_4]$ is depleted during the experiment - due to absorption of the pump pulse and formation of the photoproducts (positive bands).

Two sets of photoproduct bands formed within the first few picoseconds. The major photoproduct exhibited a broad feature centred just below 1900 cm^{-1} and a band at around 2000 cm^{-1} on the edge of a bleach. Over the course of the first 20-30 ps, these bands sharpened and shifted to higher wavenumber, resulting in bands at 1898 cm^{-1} and 2006 cm^{-1} . These changes to the bands on this timescale are consistent with solvation of the photoproduct and subsequent vibrational cooling, as commonly seen in the first few ps after CO loss (previously discussed in Section 2.1.1). The small shift in the bands upon cooling suggests that the CO stretches themselves were not vibrationally excited. For comparison, photolysis of $[\text{W}(\text{CO})_6]$ in *n*-heptane to form $[\text{W}(\text{CO})_5(\text{C}_7\text{H}_{16})]$ gives a ‘hot’ photoproduct band, but there was a large shift of 27 cm^{-1} between the $\nu = 0 \rightarrow 1$ and $\nu = 1 \rightarrow 2$ bands.²¹⁰ The vibrational cooling behaviour observed in

[Mn(ppy)(CO)₄] more likely reflects coupling of the CO stretches to other excited vibrational modes as observed in [Mn(tpm)(CO)₃]⁺.¹⁹¹ After cooling, the bands for this photoproduct remained unchanged through the nanosecond and microsecond timescales.

The intensity pattern of the major photoproduct bands is characteristic of a *facial* tricarbonyl species, similar to the *fac*-[Cr(bpy)(S)(CO)₃] complexes observed by Vlček and co-workers,²⁰⁰ in which the two low-energy bands appear together as a broad feature, with a third sharper and more intense band at higher wavenumber. For *meridional* tricarbonyl species, three bands are also expected, but the band at higher wavenumber should appear much weaker relative to the other bands as it corresponds to the stretching of the mutually *trans* carbonyl ligands.²⁰¹ Furthermore, the separation of the two low-wavenumber bands is typically larger for *meridional* than for *facial* isomers.²⁰¹ In the experimental data, these two bands are so close together that they form a single broad band, supporting a *facial* tricarbonyl.

The infrared spectra and relative energies of the *facial* and two possible *meridional* isomers were also predicted using DFT (Scheme 27). The calculations were run at the D3-PBE0/def2-TZVPP//BP86/SVP(P) level with a COSMO solvent correction in acetonitrile.



Scheme 27: Photolysis of [Mn(ppy)(CO)₄] in MeCN results in the formation of solvent complex [113_{MeCN}]. The structures of three possible isomers of 113_{MeCN} are shown along with their Free Energies at 298 K relative to the *fac*-isomer. For each isomer, the predicted infrared stretching frequency and scaled intensity of their vibrational modes in the metal carbonyl region are given at the D3-PBE0/def2-TZVPP//BP86/SVP(P) level with COSMO solvent correction in MeCN.

The calculations confirm that the *facial* isomer is the most thermodynamically stable. This is to be expected for metal carbonyl complexes as the strong *trans* effect of CO has a destabilising

effect on mutually *trans* CO ligands. The predicted intensity patterns of the *meridional* isomers are in line with the above discussion and do not match the species observed, whereas the predicted intensities for the *facial* isomer match the experimental data much better. Based on this evidence, the major photoproduct species was assigned as *fac*-[Mn(ppy)(MeCN)(CO)₃]. This is consistent with the earlier mass spectrometry study with complex **95** in which a tricarbonyl acetonitrile complex **102** was observed.

Returning to Figure 32, much weaker bands (marked with an asterisk and shown in the insets) corresponding to the second photoproduct also appear within 1 ps, comprising a feature between the bleaches at 1950 cm⁻¹ and a broad band between 2010-2050 cm⁻¹. Unlike the major photoproduct, this species is not long-lived; instead it decays over the first 20 ps. The bands for this species closely resemble the appearance of the ³MLCT excited states of [Cr(bpy)(CO)₄] in TRIR studies in its broad features, the timescale of its decay, and its position relative to the bleaches.²⁰⁰ The upward shift of the carbonyl stretching bands in the excited state relative to the ground state is typical of charge transfer excited states.²¹³ The shift is consistent with a loss of electron density from the metal, as predicted by the DFT calculations in Section 1092.2.2. The broadness of the bands is also typical for charge transfer in an excited state.²¹³ This is because redistribution of the electrons in the excited state leads to relatively large bond length changes, affording access to a greater number of vibrationally excited states. Based these points, this photoproduct was assigned as one or more triplet excited states of [Mn(ppy)(CO)₄].

The lifetime(s) of the excited state(s) could be determined by monitoring the exponential decay of the feature at 2010-2050 cm⁻¹. A plot of change in absorbance over the first 50 ps for the maximum at 2019 cm⁻¹ is shown in Figure 33.

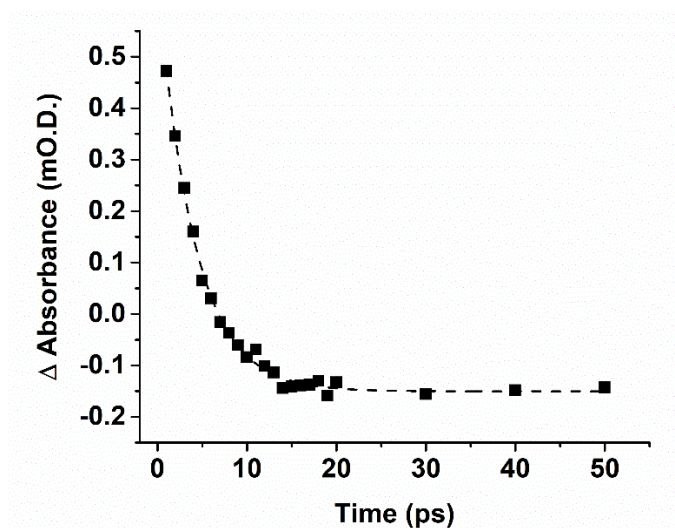


Figure 33: The change in absorbance of the excited state at 2019 cm^{-1} from 1 to 50 ps. The dashed line represents a single exponential fit with a lifetime of 4.1 ± 0.2 ps.

The decay of the excited state was modelled well by a single exponential fit with a lifetime of (4.1 ± 0.2) ps (the errors reported are 95% confidence intervals). Fitting to a bi-exponential function returned two identical lifetimes of (4.1 ± 0.2) ps. The same process was then performed at 2033 cm^{-1} to determine if another excited state was present elsewhere within the same broad band. The single exponential fit at 2033 cm^{-1} yielded a lifetime of (4.1 ± 0.3) ps, and the bi-exponential fit yielded lifetimes of (4.1 ± 0.3) ps and (13.1 ± 110) ps. The failure of the bi-exponential fits at both 2019 cm^{-1} and 2033 cm^{-1} suggests that a single excited state is formed in this experiment. Fitting of the feature at 1950 cm^{-1} was not undertaken due to its position between the bleaches, although decay over the first *ca.* 20 ps is qualitatively observed.

On the same timescale that the excited state decayed, a small recovery in the bleach bands was observed qualitatively (Figure 32, page 113). This suggests that the excited state molecules ultimately return to the ground state rather than undergoing CO dissociation. Single exponential fits to the bleach recovery displayed very large standard errors and could not be precisely quantified and compared to the decay of the excited state.

There are several reasons why the bleach recovery lifetime is not comparable to that of the excited state decay. Firstly, the molecules returning to the electronic ground state from the excited state may still be vibrationally excited, leading to broad bands in the ground state that sharpen as the ground state cools. Secondly, geminate recombination of the CO ligand would have a similar effect. Although geminate recombination for metal carbonyl complexes can occur faster than the picosecond timescale,^{191,193} which is not directly observable in this experiment, the subsequent vibrational relaxation of the ground state typically occurs on the picosecond timescale and would lead to a small recovery of the bleach bands, as was observed in the study of $[\text{Mn}(\text{tpm})(\text{CO})_3]^+$.¹⁹¹ Thirdly, the bleaches only undergo small changes and some are close in wavenumber to

photoproduct bands also undergoing vibrational relaxation, which further affects the bleach recovery kinetics. Together, these three effects convolute the bleach recovery kinetics. However, the small extent of overall bleach recovery does support the conclusion that the excited state is a minor photoproduct. Most of the intensity of the bleaches persists because CO loss is the major pathway. Similar triplet excited states were observed in a range of solvents: further discussion and a table of the lifetimes is included in Section 2.5.1.

A third photoproduct in Figure 32 (page 113) featuring a small band at 1815 cm^{-1} can be observed from *ca.* 30 ps (Figure 32, page 113). This band persists into the microsecond timescale. Several possibilities were considered for this species. Based on the earlier mass spectrometry work (Section 1.4) suggesting that CO insertion into the Mn-C bond of the ppy ligand can take place, a metal acyl species was considered. However, the infrared stretching frequencies for metal acyl species are typically much lower (appearing at *ca.* 1600 cm^{-1}) than the observed value of 1815 cm^{-1} .²¹⁴⁻²¹⁶ Similarly, thermal substitution of a second CO ligand by MeCN solvent may be ruled out based on the DFT-calculated infrared bands of the dicarbonyl; *cis*-[Mn(ppy)(MeCN)₂(CO)₂] was predicted to have $\nu(\text{CO})$ bands at 1942 and 1993 cm^{-1} , whilst the $\nu(\text{CO})$ band for [Mn(ppy)(MeCN)₃(CO)] was predicted to absorb at 1961 cm^{-1} . Therefore, the small band at 1815 cm^{-1} could not be assigned. This band was not observed in any of the other solvents used in this Chapter.

The dependence on pump pulse wavelength was investigated (Figure 34). Given the wavelength-dependent behaviour of [Cr(bpy)(CO)₄], it might be expected that less CO loss and more excited state formation takes place at longer pump wavelengths. Changing the pump pulse wavelength from 355 nm to 400 nm resulted in much smaller intensities for all bands due to the low extinction coefficient of [Mn(ppy)(CO)₄] at this wavelength. The key finding of this experiment was that qualitatively, the photochemical behaviour was still dominated by CO loss and formation of *fac*-[Mn(ppy)(MeCN)(CO)₃], with the excited state bands very weakly visible at early delays. It is also notable that the intensity of the bleach bands seems smaller relative to the photoproduct bands when compared to the 355 nm pump experiment in Figure 32 (page 113). One reason for this might be the different vibrational cooling dynamics of the photoproduct bands when 400 nm photolysis is employed.

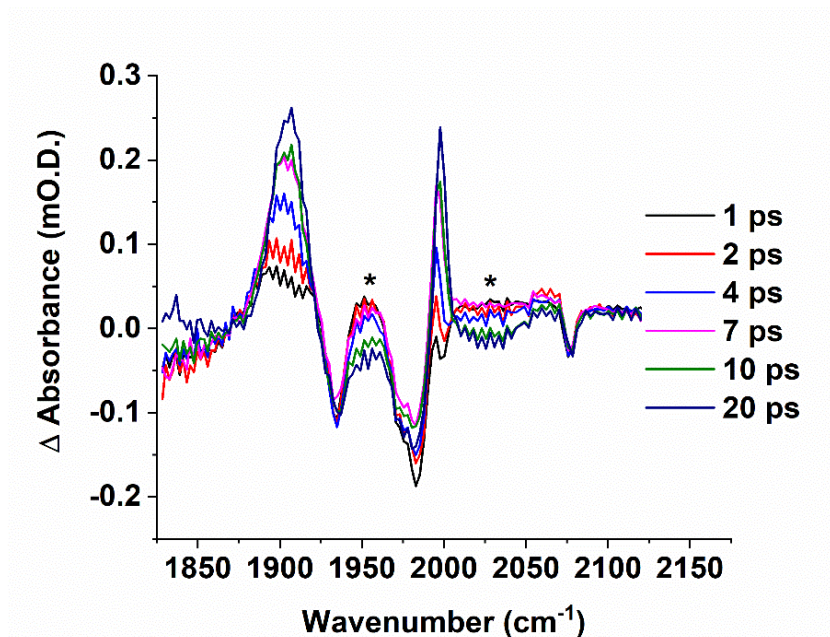


Figure 34: TRIR spectra showing the photolysis of [Mn(ppy)(CO)₄] at a pump wavelength of 400 nm. The asterisks show the positions of the triplet excited state bands.

The dominant *fac*-[Mn(ppy)(MeCN)(CO)₃] could also be prepared in a synthetic chemistry laboratory by irradiation with a 400 nm LED. Continuous irradiation of a solution of [Mn(ppy)(CO)₄] in acetonitrile produced the same photoproduct, observed by *in situ* infrared spectroscopy over a period of 30 minutes (Figure 35). The results are displayed as difference spectra with respect to a spectrum collected before irradiation started.

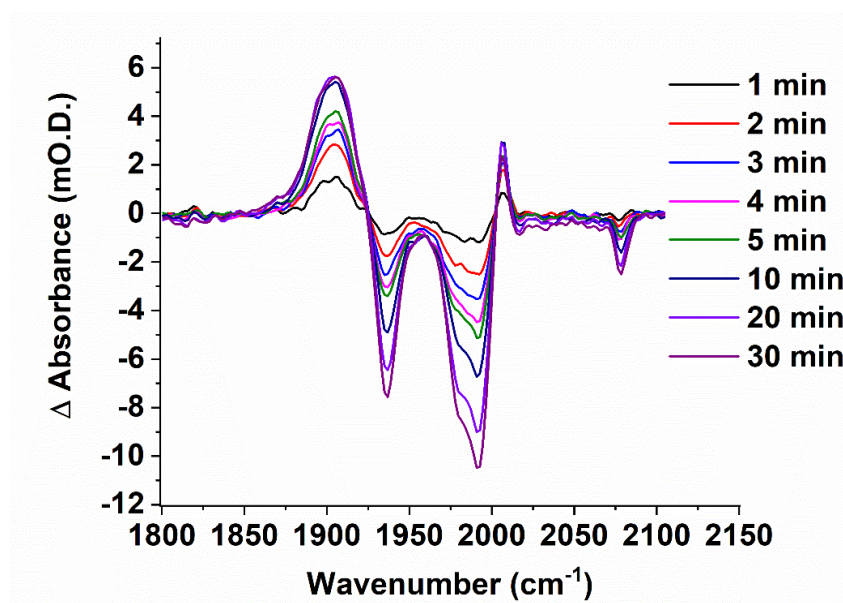


Figure 35: Continuous irradiation of an acetonitrile solution of $[\text{Mn}(\text{ppy})(\text{CO})_4]$, monitored by in situ infrared spectroscopy at a resolution of 4 cm^{-1} , with spectra collected after the irradiation times indicated. The solution was irradiated by a 400 nm LED drawing 6.0 W power. The difference spectra shown are relative to a reference spectrum recorded immediately before irradiation began.

The spectra show the progressive appearance of negative bands corresponding to the loss of $[\text{Mn}(\text{ppy})(\text{CO})_4]$ with the gain of the bands for *fac*- $[\text{Mn}(\text{ppy})(\text{MeCN})(\text{CO})_3]$. The C-N stretch of the bound acetonitrile ligand was either too weak to be observed or obscured by the MeCN solvent subtraction. From 10–30 minutes, the bleaches continued to grow whilst the tricarbonyl photoproduct bands remained constant. This shows that there was some loss of the photoproduct over this timescale. However, no new metal carbonyl bands appeared during this time suggesting that the subsequent decomposition was either too rapid to observe in this way or resulted in insoluble products. Due to the continuous irradiation employed in this experiment rather than the pump-probe approach used in TRIR spectroscopy, the decomposition of **113**_{MeCN} observed here may be due to absorption of a second photon, such as photolytic loss of a second CO ligand. The same process would not be possible in the TRIR experiment as only a single ‘pump’ laser pulse was used.

2.3.2 Alkane Solvents

To further probe the reactivity of $[\text{Mn}(\text{ppy})(\text{CO})_4]$ and its photoproducts, loss of CO followed by solvent coordination was studied in *n*-heptane, a much less polar, weaker-coordinating solvent than MeCN. Selected spectra obtained at short pump-probe delays (up to 100 ps) are presented in Figure 36. A spectrum of the ground state, scaled by a factor of 0.01, is also provided for reference.

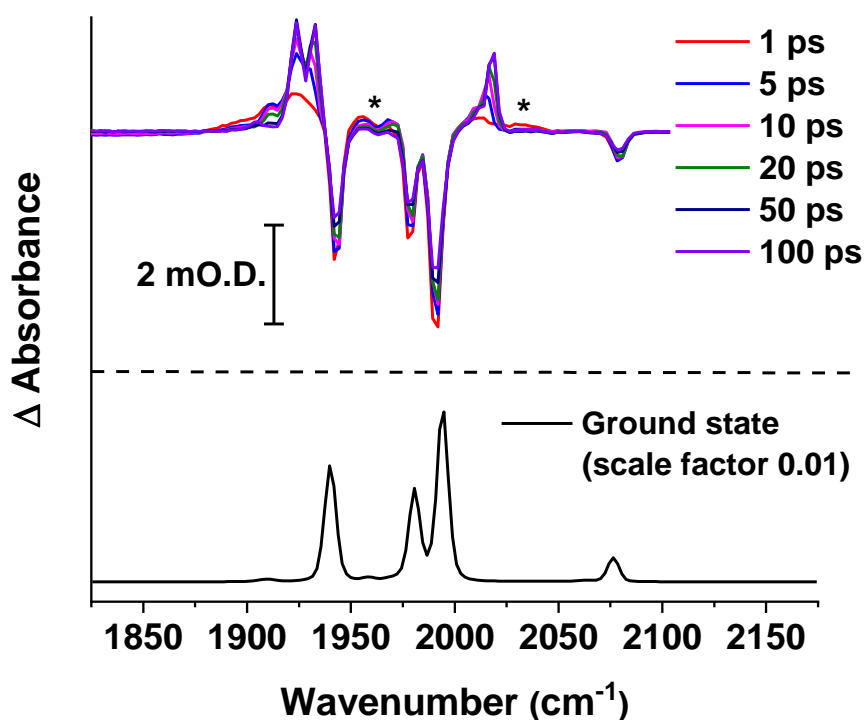


Figure 36: TRIR spectra of [Mn(ppy)(CO)₄] in *n*-heptane at selected pump-probe delays up to 100 ps, using a pump wavelength of 355 nm. The asterisks show the triplet excited state. An infrared spectrum of the ground state of [Mn(ppy)(CO)₄], recorded on an FTIR spectrometer, is included at 1 % scale for reference.

The major photoproduct bands in the first few ps are broad absorbances at 1912, 1924 and 2013 cm⁻¹. The spectral pattern is similar to that observed in MeCN and suggests formation of the solvated *facial* tricarbonyl complex, *fac*-[Mn(ppy)(C₇H₁₆)(CO)₃]. Formation of alkane complexes after photolysis of CO from metal carbonyls is very well established from TRIR and NMR spectroscopic studies.^{124,173,217-219} Due to relatively weaker intermolecular interaction between complexes and the solvent in *n*-heptane compared with MeCN, the bands in *n*-heptane are sufficiently sharp that the two low-wavenumber stretches can be individually resolved in the bleach bands. The ground state spectra provided as a reference with the MeCN and *n*-heptane spectra confirms that the different appearance of the bleaches is caused by the ground state spectrum, not due to photoproduct absorptions in this region. Indeed, four bands are observed in the bleaches for all other solvents discussed for the remainder of this Chapter, similar to *n*-heptane although a little less sharp: it is MeCN that is unusual in having such overlap of the two central bleaches. Ground state peak positions for all of the solvents are tabulated in Section 7.1.1.

Over the first few tens of ps, the photoproduct bands sharpen and shift to higher wavenumber, resulting in a set of bands at 1923, 1933 and 2019 cm⁻¹. This is similar behaviour to that observed in MeCN. This is most likely to be caused vibrational relaxation of the solvated tricarbonyl photoproduct. However, an alternative explanation for this shift was also considered: heptane could bind to the Mn centre as a σ -complex through either a terminal or an internal C-H bond and

it is therefore conceivable that interconversion of the two coordination isomers could be responsible for this change. Calculations to predict the relative energies and infrared spectra of both the terminal and internal heptane C-H complexes are discussed in Section 2.3.6.

The small, broad bands at short delays, marked with asterisks in Figure 36, were assigned to a triplet excited state [a single exponential fit gave $\tau = (3.7 \pm 0.8)$ ps at 2032 cm^{-1}] similar to the one observed in MeCN, the decay of which was accompanied by partial bleach recovery.

After the first 100 ps, the bands assigned to *fac*-[Mn(ppy)(C₇H₁₆)(CO)₃] (**113**_{hep}) began to decay, and were completely replaced by a new set of bands of the same symmetry within 10 ns (Figure 37).

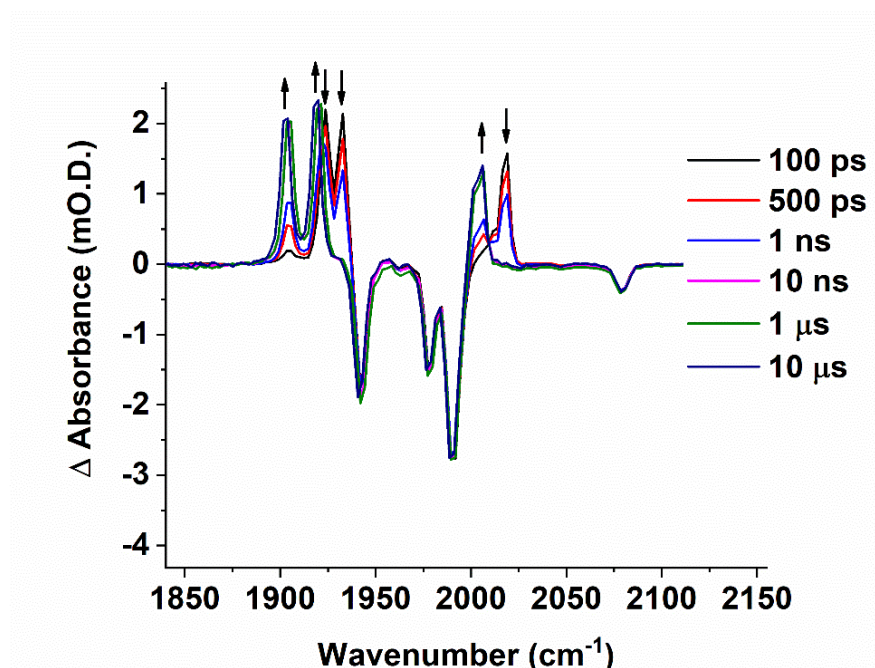
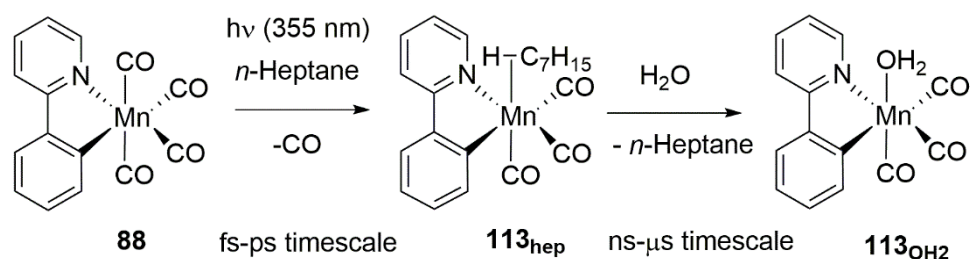


Figure 37: TRIR spectra of [Mn(ppy)(CO)₄] in *n*-heptane at selected pump-probe delays of 100 ps and longer, using a pump wavelength of 355 nm. The asterisks show the triplet excited state.

This new set of bands had lower C≡O stretching wavenumbers (1904 , 1919 and 2006 cm^{-1}) than the bands for *fac*-[Mn(ppy)(C₇H₁₆)(CO)₃]. The downward shift of 10-20 cm^{-1} for each band suggests that the coordinated solvent molecule has been substituted by a stronger donor ligand. As the spectra were run under ambient conditions, the solvent contained water and so the resulting complex was assigned as *fac*-[Mn(ppy)(OH₂)(CO)₃] (**113**_{hep}) (Scheme 28). This is analogous to the study by Nuernberger and co-workers where [Mn(tpm)(CO)₃]⁺ was photolysed in D₂O to form [Mn(tpm)(CO)₂(D₂O)]⁺ (Section 2.1.1).¹⁹¹ Substitution of alkane donor ligands by water impurities is known from previous TRIR studies on [Cr(CO)₆] (M = Cr, Mo, W).^{210,220,221} The displacement of alkane ligands by other stronger two-electron donors such as heterocycles has also been studied.^{222,223}



Scheme 28: Summary of the photochemical behavior of 88 in *n*-heptane.

A repeat of this experiment was then performed with a different batch of freshly-opened anhydrous *n*-heptane (Figure 38). The flow system was placed under an N₂ atmosphere and sealed.

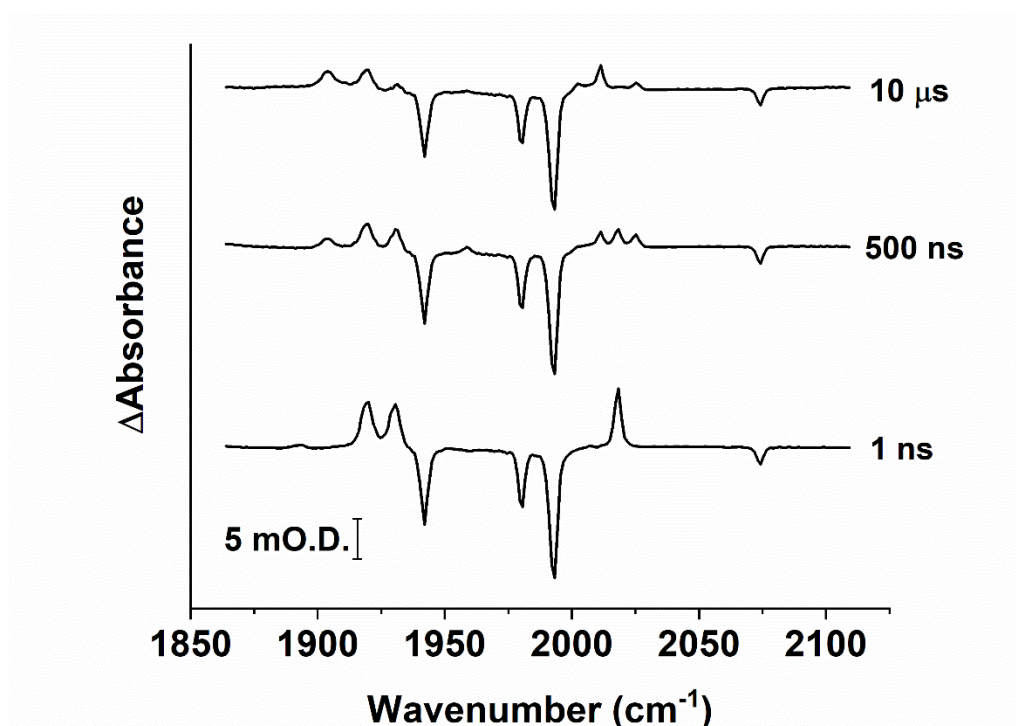


Figure 38: TRIR spectra of [Mn(ppy)(CO)₄] in *n*-heptane under an N₂ atmosphere at the pump-probe delays shown, using a pump wavelength of 355 nm. Conversion of 113_{hep} into 113_{OH2} is observed going from bottom to top. Experiment performed by Anders Hammarbäck.

The initial photoproduct formed (spanning ps to ns delays) was again complex 113_{hep}, but as with the experiment under air, the weakly-coordinating *n*-heptane ligand was displaced. Two sets of bands replaced complex 113_{hep}. One of these species corresponds to the thermodynamically-favoured complex 113_{OH2}, which once again persists into the μ s timescale. The use of an N₂ atmosphere and anhydrous *n*-heptane slowed the formation of 113_{hep} down. Under these conditions the water complex formed over hundreds of nanoseconds to microseconds, compared to a few nanoseconds in the experiment performed under air. The rate of the substitution of the *n*-heptane ligand with water is likely to be a reflection of the timescale of diffusion of water through

the solvent with different concentrations of water in the samples. Some variation in the rate might also be accounted for by a lack of temperature control of the flow system.

In addition to formation of **113**_{OH₂}, bands for a second species that also replaced **113**_{hep} were also present in (Figure 38). Two bands were observed, at 1959 and 2025 cm⁻¹. This species decayed on the microsecond timescale, appearing to convert to complex **113**_{OH₂}, which was the dominant product at 10 μs. Since this species appears to be formed from **113**_{hep} and decay into **113**_{OH₂}, another *facial* tricarbonyl complex was considered a possibility: the relatively small amount of this complex formed means that a further third band could be hidden by the bleach around 1940 cm⁻¹. The bands shift upwards in wavenumber relative to the decaying **113**_{hep} bands. If the new complex is a result of another ligand displacing the *n*-heptane, the resulting ligand must be either a weaker σ-donor or stronger π-acceptor than *n*-heptane. It is suggested that this complex could be formed through displacement of the *n*-heptane solvent by olefin impurities in the solvent. This hypothesis would also account for why the result is dependent on the batch of *n*-heptane used – in the ‘wet’ experiment there is more water and this outcompetes the impurities by diffusing on a faster timescale. Coordination of an alkene would also explain the increase in wavenumber of the carbonyl stretching bands, since the alkene can behave as a π-acceptor ligand when *n*-heptane and water cannot.

To examine how long-lived water complex **113**_{OH₂} is in an alkane solvent, a continuous irradiation experiment, this time in *n*-hexane, was performed in a synthetic chemistry laboratory. Irradiation of [Mn(ppy)(CO)₄] in was carried out using a 400 nm LED (Figure 39).

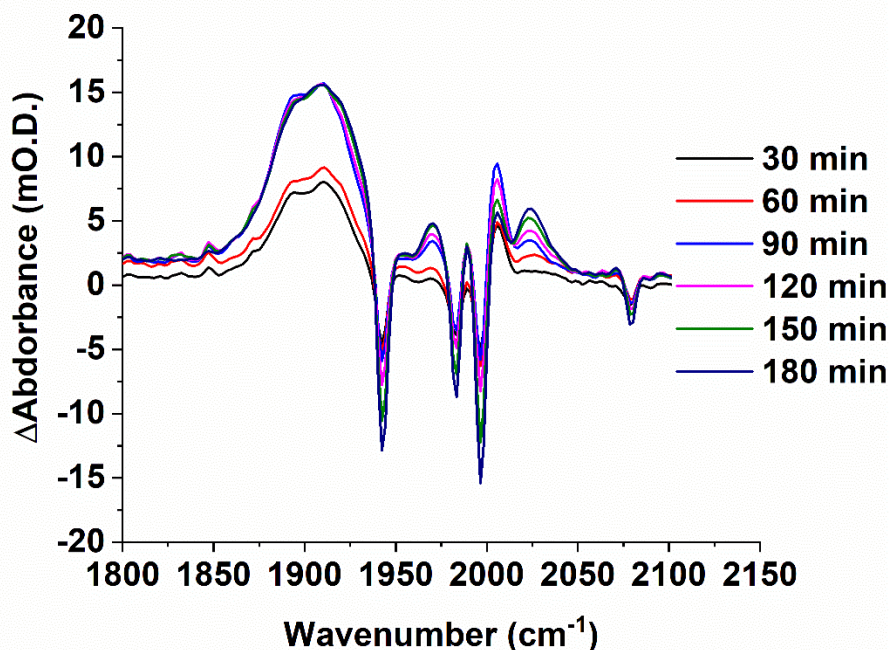


Figure 39: Continuous irradiation of an *n*-hexane solution of $[\text{Mn}(\text{ppy})(\text{CO})_4]$, monitored by *in situ* infrared spectroscopy at a resolution of 4 cm^{-1} , with spectra collected after the irradiation times shown on the graph. The solution was irradiated by a 400 nm LED drawing 6.0 W power. The difference spectra shown are relative to a reference spectrum recorded immediately before irradiation began.

The product bands in the spectrum after 30 minutes were dominated by a broad band from *circa* $1890\text{-}1920\text{ cm}^{-1}$ and a band at 2006 cm^{-1} , similar to complex **113**_{OH₂} from the TRIR experiments in *n*-heptane (1904 , 1919 and 2006 cm^{-1}). At later times, the broad low-wavenumber feature remained, but the band at 2006 cm^{-1} became less intense and another band at 2024 cm^{-1} grew in. Further peaks near to the bleaches at 1940 and 1981 cm^{-1} also appeared – it is unclear whether these are artifacts due to changes in the nearby bleaches or if they are additional products. The broad, low-wavenumber feature ($1890\text{-}1920\text{ cm}^{-1}$) with a single higher-wavenumber stretch (2024 cm^{-1}) suggests that another *facial* tricarbonyl complex formed. Returning to the mass spectrometry study of complex **85** (see Section 1.4) a mass corresponding to some isomer of the tricarbonyl complex $[\text{Mn}(\text{CO})_3(\text{MeCN})_3]^+$ was detected suggesting that loss of the ppy ligand, presumably through protonation of the Mn-C bond, can take place during the photochemical degradation. A complex of the form *fac*- $[\text{Mn}(\text{CO})_3(\text{OH}_2)_3]^+$ (Scheme 29) was therefore considered for the new species observed in Figure 39. The species *fac*- $[\text{Mn}(\text{CO})_3(\text{OH}_2)_3]^+$ itself is known but has bands at 1944 and 2051 cm^{-1} , too high to be the species seen in (Figure 39).²²⁴ High-nuclearity Mn^I carbonyl complexes with bridging hydroxide ligands are known. For example, $\{\text{fac}-[\text{Mn}(\text{CO})_3(\mu_3\text{-OH})_3]\}_4$ is readily accessible from oxidation of $\text{Mn}_2(\text{CO})_{10}$ with $\text{Me}_3\text{N}\cdot\text{O}\cdot 2\text{H}_2\text{O}$ at ambient temperature.²²⁵ This tetranuclear complex has infrared stretches at 1891 , 1932 and 2027

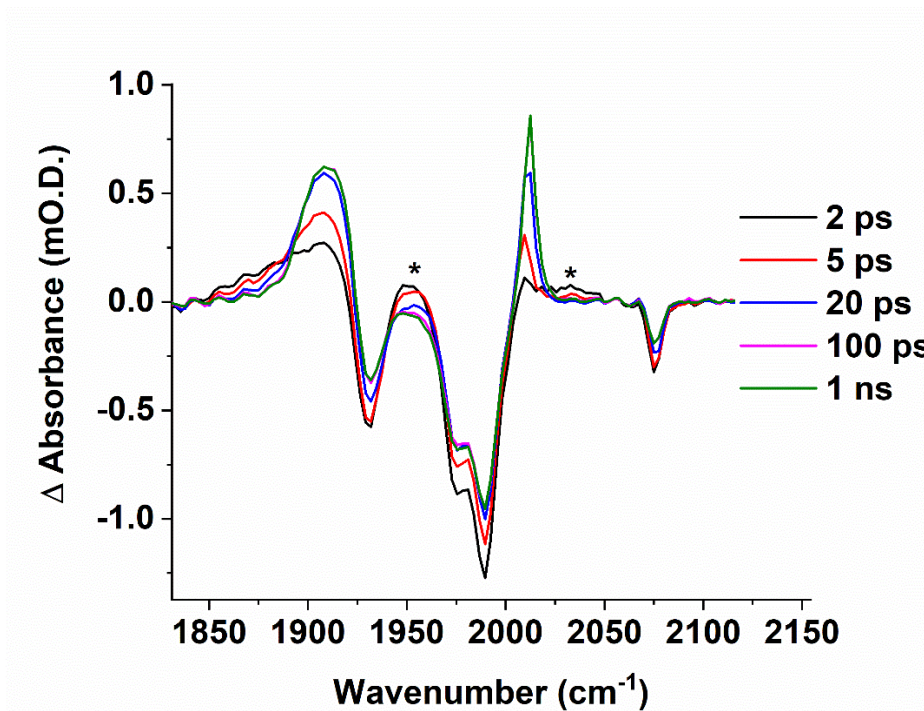


Figure 40: TRIR spectra of $[\text{Mn}(\text{ppy})(\text{CO})_4]$ in CH_2Cl_2 at selected pump-probe delays up to 1 ns. A pump wavelength of 355 nm was used. The asterisks show the triplet excited state.

The solvated tricarbonyl complex persists into the microsecond timescale. However, over tens of microseconds, the bands assigned to *fac*- $[\text{Mn}(\text{ppy})(\text{CH}_2\text{Cl}_2)(\text{CO})_3]$ were replaced by lower-wavenumber bands of the same symmetry at 1900 and 2004 cm^{-1} (Figure 41). It should be noted that the apparent slight bleach recovery on the tens of microseconds timescale as seen in Figure 41 is an artifact caused by flow of the pumped sample out of the probe area. A small loss of photoproduct intensity is also expected as a result of this effect, but this is more difficult to see in the spectra due to the other changes taking place with the photoproduct bands.

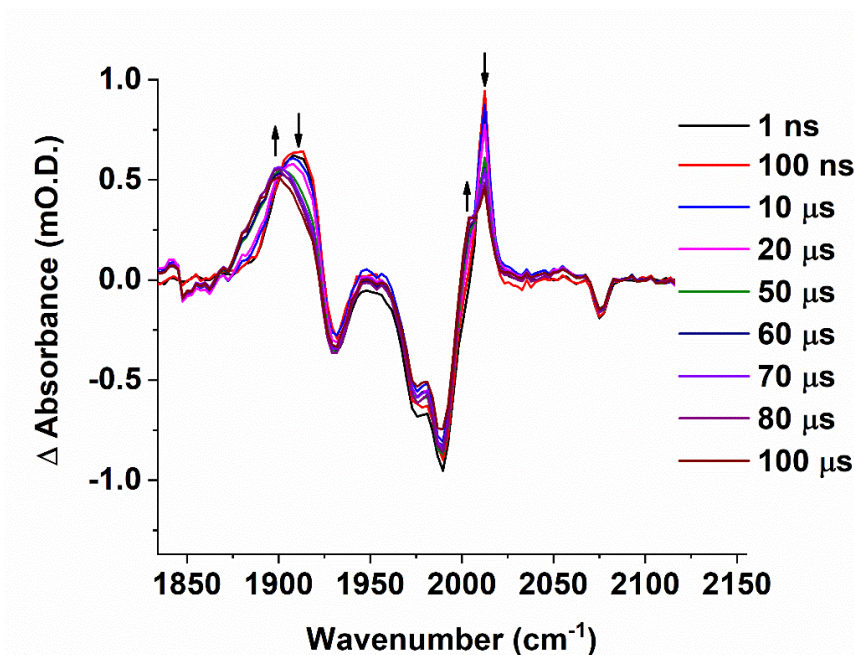


Figure 41: TRIR spectra of [Mn(ppy)(CO)₄] in CH₂Cl₂ at selected pump-probe delays of 1 ns and longer. A pump wavelength of 355 nm was used. The asterisks show the triplet excited state.

The bands for the species that formed over tens of microseconds are close in wavenumber to those seen for the aquo complex **113**_{OH₂} in *n*-heptane (Section 2.3.2). It was therefore concluded that **113**_{OH₂} also forms in dichloromethane depending on the water content of the solvent. The low-energy stretches for **113**_{OH₂} in CH₂Cl₂ and *n*-heptane appear at slightly different wavenumbers: 1904 and 1919 cm⁻¹ for *n*-heptane and a broader band with a maximum at 1898 cm⁻¹ for CH₂Cl₂. However, in the ground state infrared spectrum of [Mn(ppy)(CO)₄], the bands in *n*-heptane also appear at higher wavenumber. For example, the lowest-energy mode is at 1933 cm⁻¹ in CH₂Cl₂ and 1940 cm⁻¹ for *n*-heptane, showing the sensitivity of the infrared stretches to solvent environment. A full table of the ground state infrared bands in all solvents used is provided in Section 7.1.1.

2.3.4 Toluene

Spectra obtained in toluene solution showed comparable behaviour to CH₂Cl₂ and *n*-heptane. The initially-dominant *fac*-[Mn(ppy)(toluene)(CO)₃] complex (**113**_{tol}) exhibited bands at 1906 and 2007 cm⁻¹ and was observable into the nanosecond timescale (Figure 42).

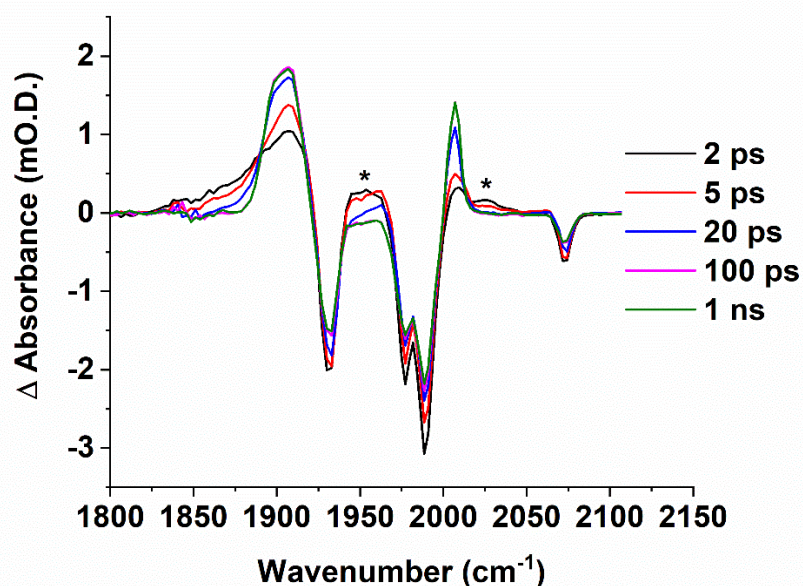


Figure 42: TRIR spectra of [Mn(ppy)(CO)₄] in toluene at selected pump-probe delays up to 1 ns. A pump wavelength of 355 nm was used. The asterisks show the triplet excited state.

Subsequent replacement of the bands for **113_{tol}** with bands at 1884, 1898 and 2001 cm⁻¹ took place between 100 ns and 2 μs (Figure 43). This species was again attributed to formation of complex **113_{OH2}** due to replacement of the toluene ligand with water in the solvent. The structure of **113_{tol}** is could comprise a C-H σ-complex or a C=C π-complex; either of these coordination modes would provide two electrons to form 18-electron solvent complexes analogous to those observed above in other solvents. These possibilities are discussed in conjunction with their DFT-calculated energies and infrared spectra in Section 2.4

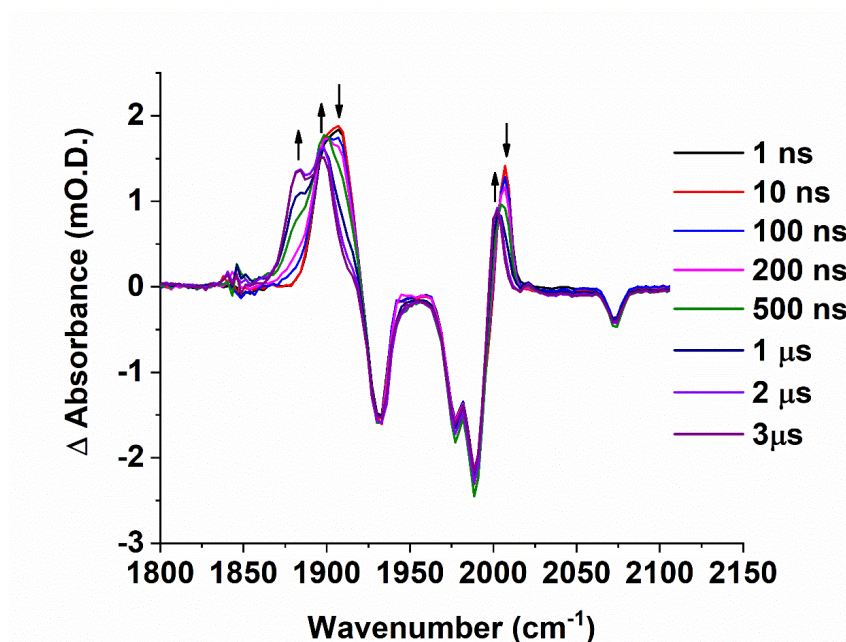


Figure 43: TRIR spectra of $[\text{Mn}(\text{ppy})(\text{CO})_4]$ in toluene at selected pump-probe delays of 1 ns and longer. A pump wavelength of 355 nm was used. The asterisks show the triplet excited state.

2.3.5 Ethers

2.3.5.1 Tetrahydrofuran

The photochemical behaviour of $[\text{Mn}(\text{ppy})(\text{CO})_4]$ in ether solvents was also studied. This class of compounds represents an interesting comparison to the *n*-heptane case in that ethers contain both C-H bonds and available O lone pairs, both of which are donors that coordinated to the metal centre in the *n*-heptane experiments in Section 2.3.2.

The first ether studied was tetrahydrofuran (THF), Figure 44.

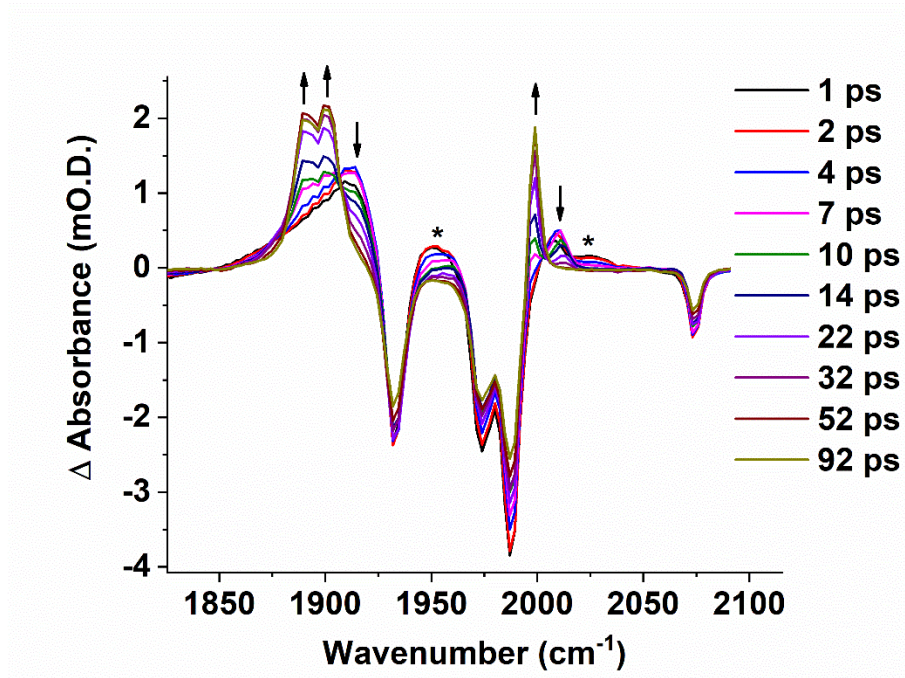


Figure 44: TRIR spectra of $[\text{Mn}(\text{ppy})(\text{CO})_4]$ in THF under air at selected pump-probe delays. A pump wavelength of 355 nm was used. The asterisks show the triplet excited state. The arrows indicate the direction of change in absorbance of the bands over time.

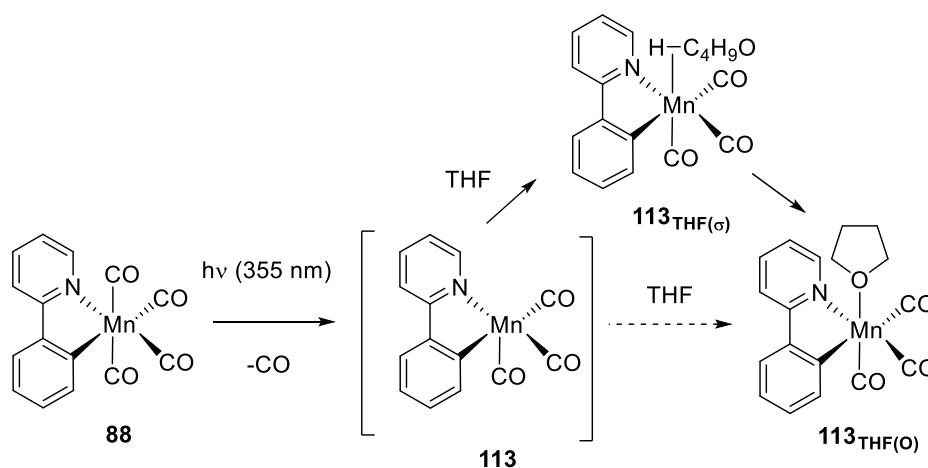
Spectra recorded at short pump-probe delays showed broad bands at 1912 and 2011 cm^{-1} , which were assigned to a *fac*- $[\text{Mn}(\text{ppy})(\text{THF})(\text{CO})_3]$ complex. These bands were then completely replaced within *ca.* 50 ps by another *facial* tricarbonyl complex. The wavenumbers of the bands for this second, later species are lower than the initial solvent complex (1889 , 1899 and 1999 cm^{-1}), close those of to the water complex **113**_{OH₂} observed in *n*-heptane, CH_2Cl_2 and toluene. This set of bands then persists for the remainder of the experiment (beyond the μs timescale).

The interconversion between the two tricarbonyl complexes observed in this experiment shows a different kind of reactivity to other solvents used so far. The timescale of the reaction, which is complete within 50 ps, is much too fast for even a diffusion-controlled reaction between a solvent complex and trace water in the solvent.²²⁶ The process in Figure 44 is also not solvation of the 16-electron unsaturated complex $[\text{Mn}(\text{ppy})(\text{CO})_3]$. Solvation is expected to take place within just the first few picoseconds, as seen in the other solvents tested in this Chapter. The timescale of solvation is in accordance with the previous studies photoCORMs^{191,194,196} (Section 2.1.2) and $[\text{Cr}(\text{bpy})(\text{CO})_4]$.²⁰⁰

Reaction on the picosecond timescale as observed in Figure 44 is suggestive of a unimolecular reaction or a further reaction with the solvent. The shift in the infrared bands to lower wavenumber suggests that the second species formed contains a stronger donor ligand that increases the electron density on the Mn centre, allowing greater π -backbonding to the CO ligands. This is consistent with a change in the coordination mode of the THF solvent complex from initial weak

binding *via* a C-H σ -complex $\mathbf{113}_{\text{THF}(\sigma)}$ to coordination through an oxygen lone pair, $\mathbf{113}_{\text{THF}(\text{O})}$, as shown in Scheme 30.

A comparable isomerisation reaction in alcohol solvents has been reported. Harris and co-workers studied the photolysis of $[\text{Cr}(\text{CO})_6]$ in alcohols and found that initial coordination *via* a C-H σ -complex precedes formation of the more stable O-bound species.²²⁷ The single exponential lifetimes of these reactions were highly dependent on the alcohol solvent used but were hundreds of picoseconds or longer.²²⁷



Scheme 30: Summary of the reactions after CO loss from 88 in THF. Solvent coordination predominately occurs *via* a C-H bond to form $\mathbf{113}_{\text{THF}(\sigma)}$ before isomerisation to the more stable O-bound complex $\mathbf{113}_{\text{THF}(\text{O})}$. Note that the unsaturated complex in brackets is not observed.

The mean lifetime for the interconversion between $\mathbf{113}_{\text{THF}(\sigma)}$ and $\mathbf{113}_{\text{THF}(\text{O})}$ was obtained by fitting the absorbances at 1912 cm^{-1} and 1999 cm^{-1} to single exponential fits (Figure 45). The fits were started from 5 ps because the first few ps are dominated by the rise of the solvated complex $\mathbf{113}_{\text{THF}(\sigma)}$ and its cooling. A function with both single exponential growth and decay components was considered to help model the growth at very early times, however there are very few points in the initial rise of $\mathbf{113}_{\text{THF}(\text{O})}$ and this was considered likely to affect the overall quality of the fitted data.

When choosing the time to begin fitting the data the dominance of vibrational cooling at early times must be balanced against the need to fit as much of the data from the interconversion of $\mathbf{113}_{\text{THF}(\sigma)}$ and $\mathbf{113}_{\text{THF}(\text{O})}$ as possible. Although the shifting and sharpening of the bands caused by vibrational relaxation takes place over a longer timescale than 5 ps and was not modelled in the analysis, the decay of $\mathbf{113}_{\text{THF}(\sigma)}$ and the rise of $\mathbf{113}_{\text{THF}(\text{O})}$ gave lifetimes of $(15.1 \pm 2.2) \text{ ps}$ and $(18.9 \pm 1.6) \text{ ps}$ respectively such that the 95 % confidence intervals just overlap, confirming that the two processes are taking place on the same timescale.

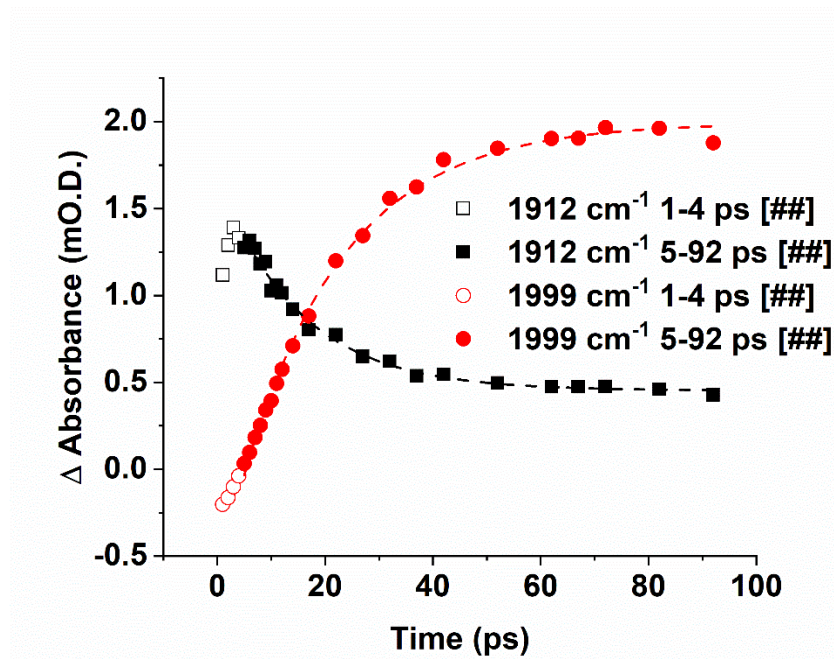


Figure 45: Kinetics of the isomerisation of $113_{\text{THF}(\sigma)}$ to $113_{\text{THF}(\text{O})}$ in THF under air. The bands at 1912 cm^{-1} for complex $113_{\text{THF}(\sigma)}$ (black squares) and 1999 cm^{-1} for complex $113_{\text{THF}(\text{O})}$ (red circles) were monitored over time. The dashed lines represent single exponential fits to the data giving mean lifetimes of $(15.1 \pm 2.2)\text{ ps}$ for $113_{\text{THF}(\sigma)}$ and $(18.9 \pm 1.6)\text{ ps}$ for $113_{\text{THF}(\text{O})}$. The open symbols represent the delays from 1-4 ps which were excluded from the single exponential fits due to the effect of initial vibrational cooling and solvation.

From the spectra above in Figure 44, it is difficult to determine the extent of competition between initial formation of σ -complex $113_{\text{THF}(\sigma)}$ and direct formation of O-bound species $113_{\text{THF}(\text{O})}$ [formation of the O-bound species $113_{\text{THF}(\text{O})}$ without the intermediate formation of $113_{\text{THF}(\sigma)}$] at very early delays. A qualitative comment on direct formation of $113_{\text{THF}(\text{O})}$ can be made. Direct formation of $113_{\text{THF}(\text{O})}$ would be expected to result in broad, vibrationally excited bands at lower wavenumber than the bands of the vibrationally relaxed molecules. For example, two of the ‘cooled’ bands of $113_{\text{THF}(\sigma)}$ are at 1889 and 1899 cm^{-1} , and if $113_{\text{THF}(\text{O})}$ were present at very short times a significant absorbance below 1889 cm^{-1} would be expected from the vibrationally excited bands. In the spectra in Figure 44 there is only a very low absorbance in this region and some of this will be caused by the broad vibrationally excited $113_{\text{THF}(\sigma)}$ bands. As such the dominant pathway is formation of $113_{\text{THF}(\sigma)}$ followed by isomerisation to $113_{\text{THF}(\text{O})}$ with little or no direct formation of $113_{\text{THF}(\text{O})}$.

To verify whether this result is reproducible, the experiment was repeated using a fresh bottle of commercially-available $>99.9\%$ anhydrous, inhibitor-free THF under an atmosphere of N_2 . Figure 46 shows a selection of the resulting spectra.

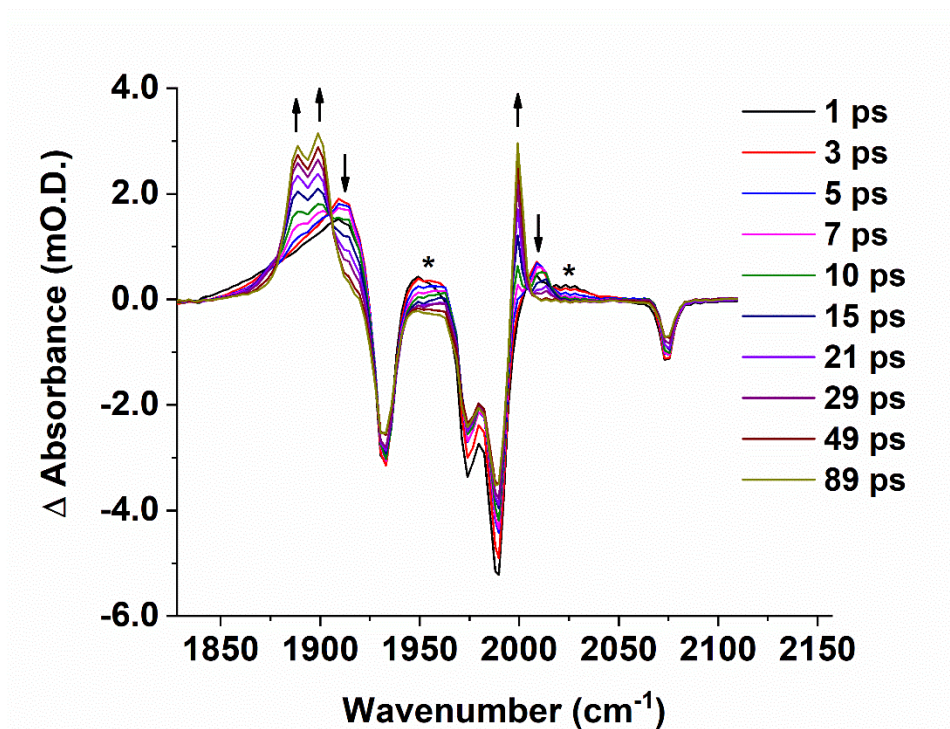


Figure 46: TRIR spectra of $[\text{Mn}(\text{ppy})(\text{CO})_4]$ in dry THF under N_2 at selected pump-probe delays. A pump wavelength of 355 nm was used. The asterisks show the triplet excited state. The arrows indicate the direction of change in absorbance of the bands over time.

The spectra show that essentially identical behaviour is observed in THF under an atmosphere of N_2 as under the ambient atmosphere. When the interconversion of $\mathbf{113}_{\text{THF}(\text{g})}$ to $\mathbf{113}_{\text{THF}(\text{o})}$ in the N_2 experiment was quantified, the bleach of $\mathbf{113}_{\text{THF}(\text{g})}$ at 1912 cm^{-1} and growth of $\mathbf{113}_{\text{THF}(\text{o})}$ at 1999 cm^{-1} gave single exponential mean lifetimes of $(17.6 \pm 1.3) \text{ ps}$ and $(18.7 \pm 0.8) \text{ ps}$ respectively (fitting delays from 5 to 92 ps, Figure 47). These values confirm that there is no significant difference to the behaviour under dry air-free conditions.

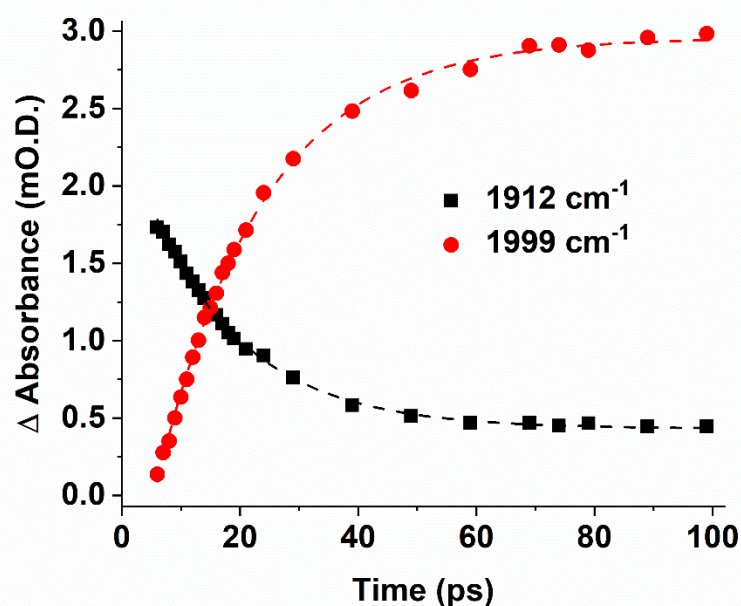


Figure 47: Kinetics of the isomerisation of $113_{\text{THF}(\sigma)}$ to $113_{\text{THF}(\text{O})}$ in dry THF under N_2 from 5 to 99 ps. The bands at 1912 cm^{-1} for complex $113_{\text{THF}(\sigma)}$ (black squares) and 1999 cm^{-1} for complex $113_{\text{THF}(\text{O})}$ (red circles) were monitored over time. The dashed lines represent single exponential fits to the data giving mean lifetimes of $(17.6 \pm 1.3) \text{ ps}$ for $113_{\text{THF}(\sigma)}$ and $(18.7 \pm 0.8) \text{ ps}$ for $113_{\text{THF}(\text{O})}$.

Another experiment was then performed in deuterated solvent, THF-*d*8, to test for a kinetic isotope effect. If a C-H or C-D bond is broken or made (primary kinetic isotope effect) in the rate-determining state of the interconversion of $113_{\text{THF}(\sigma)}$ and $113_{\text{THF}(\text{O})}$, the rate will change when THF-*d*8 is used.²²⁸ Spectra are shown in Figure 48 and the kinetic plots in Figure 49. Note that the high-wavenumber band of the ground state was not observable in THF-*d*8 as this region of the spectrum was obscured by C-D stretching modes.

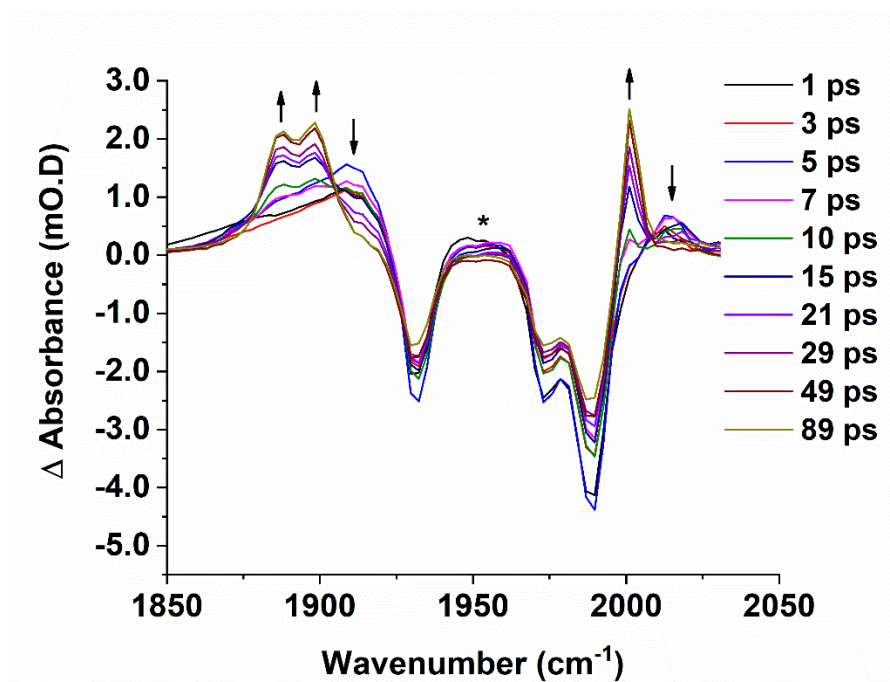


Figure 48: TRIR spectra of $[\text{Mn}(\text{ppy})(\text{CO})_4]$ in $\text{THF-}d_8$ at selected pump-probe delays. A pump wavelength of 355 nm was used. The asterisks show the triplet excited state. The arrows indicate the direction of change in absorbance of the bands over time. The high-wavenumber bleach at 2073 cm^{-1} was not observable due to absorbance by the solvent.

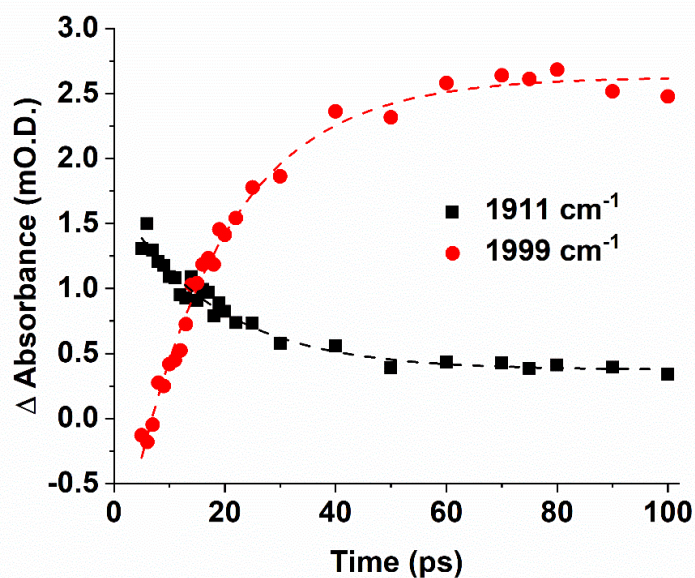


Figure 49: Kinetics of the isomerisation of $113_{\text{THF}(\sigma)}$ to $113_{\text{THF}(\text{O})}$ in $\text{THF-}d_8$ from 5 to 99 ps. The bands at 1911 cm^{-1} for complex $113_{\text{THF}(\sigma)}$ (black squares) and 1999 cm^{-1} for complex $113_{\text{THF}(\text{O})}$ (red circles) were monitored over time. The dashed lines represent single exponential fits to the data giving mean lifetimes of $(17.7 \pm 3.7) \text{ ps}$ for $113_{\text{THF}(\sigma)}$ and $(17.0 \pm 1.8) \text{ ps}$ for $113_{\text{THF}(\text{O})}$.

The lifetimes for the isomerisation reaction in $\text{THF-}d_8$ were $(17.7 \pm 3.7) \text{ ps}$ from the bleach of $113_{\text{THF}(\sigma)}$ and $(17.0 \pm 1.8) \text{ ps}$ for the growth of $113_{\text{THF}(\text{O})}$. There is therefore no significant

difference to the kinetics in THF-*d*8 compared to the experiments in the protio solvent. The lack of a kinetic isotope effect for the interconversion of **113**_{THF(σ)} and **113**_{THF(O)} suggests that there is no C-H or C-D bond breaking in the rate-determining state. This is consistent with a mechanistic pathway in which the C-H / O-bound isomerisation does not involve an oxidative addition and/or C-H bond cleavage.

Reaction of the photoproducts with CO to re-form [Mn(ppy)(CO)₄] was also studied. As mentioned in Section 2.1.1, the study on [Mn(tpm)(CO)₃]⁺ by Nuernberger and co-workers concluded that geminate recombination with CO occurs for this molecule on the sub-ps timescale.¹⁹¹ This was based on the partial recovery of the bleached bands on the ps timescale rather than direct recombination. It may be that [Mn(ppy)(CO)₃] undergoes similar recombination with CO on the sub-ps timescale.

However, since diffusion-controlled processes are typically limited to the nanosecond timescale,²²⁶ CO would not be able to diffuse through the solvent quickly enough to affect the isomerisation reaction of **113**_{THF(σ)} to **113**_{THF(O)} on the ps timescale and any CO recombination taking place on the sub-ps timescale must come from the CO ligand that has photodissociated. Displacement of the O-bound ligand by CO over a longer timescale could re-form [Mn(ppy)(CO)₄]. To test for re-formation of [Mn(ppy)(CO)₄] in THF, a TRIR experiment was performed under an atmosphere of CO (see Appendix 4 for results).

The single exponential fits for the loss of the **113**_{THF(σ)} band at 1911 cm⁻¹ and the gain of the **113**_{THF(O)} band at 1999 cm⁻¹ gave mean lifetimes of (17.3 ± 1.3) ps and (19.8 ± 0.8) ps respectively. Although in this case the 95 % confidence intervals did not overlap, these values are very close to the mean lifetimes for other experiments THF isomerisation experiments (Table 6) and suggests that there is no effect on the ps timescale upon the isomerisation caused by performing the experiment under CO.

The CO atmosphere does enable examination of the kinetics at longer delays, in order to observe whether CO gas can displace the O-bound complex. Spectra were recorded at longer pump-probe delays, under 1 atm CO. The exact concentrations of both CO and the photoproduct complex are not known in the experiment as they were not accurately measured. No measured solubility data for CO in THF could be found, but data for a range of organic solvents, including ethers, suggests millimolar concentrations would likely be achieved; for example, the solubility of 1,4-dioxane at 290 K and 1 bar was measured to be 5.5 mM.²²⁹ Given that [Mn(ppy)(CO)₄] is only present at around 15 mM in these experiments, and that only a fraction of the complex is photolysed (the photoproduct bands lead to mO.D.-scale absorbances but the [Mn(ppy)(CO)₄] ground state bands are around 2 orders of magnitude stronger), these estimates suggest that the CO is present in substantial excess, such that a pseudo-first order rate constant could be measured if a reaction were to be observed. The results of the experiment under 1 atm CO are shown in Figure 50.

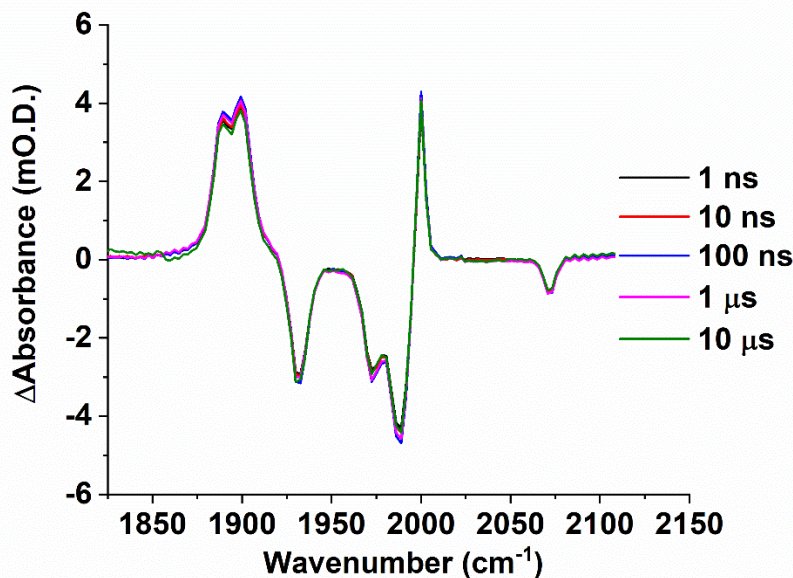


Figure 50: TRIR spectra of $[\text{Mn}(\text{ppy})(\text{CO})_4]$ in THF under a CO atmosphere at long pump-probe delays. A pump wavelength of 355 nm was used. The asterisks show the triplet excited state. The arrows indicate the direction of change in absorbance of the bands over time.

Over hundreds of microseconds, the pumped photoproducts are flowed out of the probe volume leading to loss of both the ground state bleaches and photoproduct bands. It would therefore be difficult to distinguish variation in flow rates with re-formation of $[\text{Mn}(\text{ppy})(\text{CO})_4]$ from $\mathbf{113}_{\text{THF}(\text{O})}$ on this timescale so 10 μs is the longest delay shown.

This experiment shows that any reaction of CO with $\mathbf{113}_{\text{THF}(\text{O})}$ to re-form $\text{Mn}(\text{ppy})(\text{CO})_4$ takes place slower than the microsecond timescale. Due to the ps-timescale isomerisation of $\mathbf{113}_{\text{THF}(\sigma)}$ to $\mathbf{113}_{\text{THF}(\text{O})}$, displacement of the σ -complex by CO cannot be studied - a similar experiment in *n*-heptane, where the σ -complex is much longer-lived, would be required to study such a process, although the presence of trace water in the flow system would again interfere (as in Section 2.3.2). Studies of the re-formation of solvent complexes after CO loss have shown that CO can displace weaker donors. For example, George and co-workers photolysed $[\text{CpRe}(\text{CO})_3]$ (Cp = cyclopentadienyl) in *n*-heptane to produce $[\text{CpRe}(\text{CO})_2(\textit{n}\text{-heptane})]$, which reacts to re-form $[\text{CpRe}(\text{CO})_3]$ under a CO atmosphere.²³⁰ However, these reactions took place on the millisecond timescale at two atmospheres of CO, showing that even alkane complexes can be somewhat stable to CO substitution.²³⁰

Further experiments using derivatised ppy complexes **94** and **95** (structures on page 92) were also performed (see Appendix 4 for spectra and kinetic plots) to verify that the isomerisation observed with **88** occurs with other ppy-derived ligands and compare the kinetics of the isomerisation. The results of the kinetics experiments in THF are summarised in Table 5.

Table 5: Summary of kinetics of the isomerisation of complexes 88, 94 and 95 in THF.

Complex	Solvent	Atmosphere	$\tau_{\text{THF}(\sigma)}$ / ps	$\tau_{\text{THF}(\text{O})}$ / ps
88	THF	Air	15.1 ± 2.2	18.9 ± 1.6
88	THF	N ₂	17.6 ± 1.3	18.7 ± 0.8
88	THF- <i>d</i> 8	Air	17.7 ± 3.7	17.0 ± 1.8
88	THF	CO	17.3 ± 1.3	19.8 ± 0.8
94	THF	Air	19.0 ± 1.6	19.8 ± 1.0
95	THF	Air	17.9 ± 0.9	22.2 ± 4.3

2.3.5.2 1,4-Dioxane

The isomerisation behaviour in THF was compared to another cyclic ether solvent: 1,4-dioxane (Figure 51).

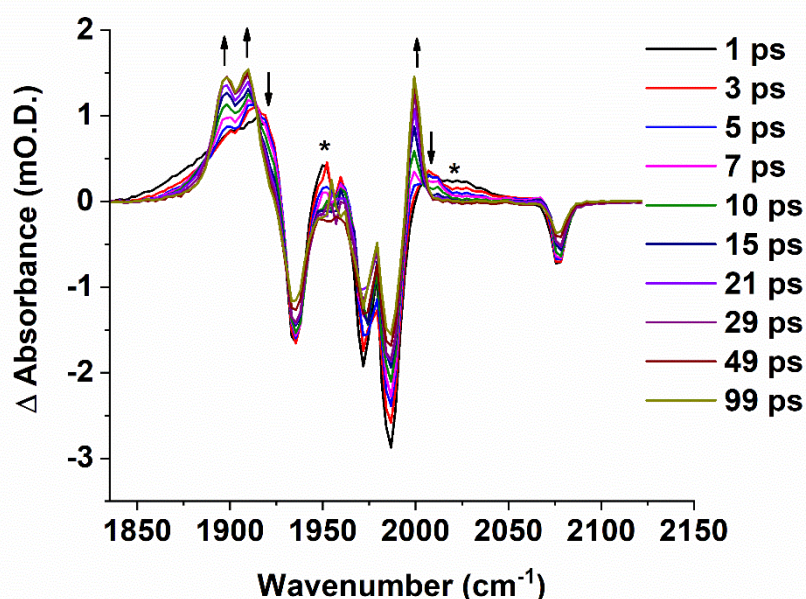


Figure 51: TRIR spectra of [Mn(ppy)(CO)₄] in 1,4-dioxane at selected pump-probe delays. A pump wavelength of 355 nm was used. The asterisks show the triplet excited state. The arrows indicate the direction of change in absorbance of the bands over time.

The results show a similar behaviour to the experiments performed in THF: initial broad bands at 1919 and 2011 cm⁻¹ are replaced over tens of picoseconds by bands at 1899, 1911 and 1999 cm⁻¹. This suggests that a similar isomerisation from a σ -complex **113**_{diox(σ)} to the O-bound species **113**_{diox(O)} also takes place in 1,4-dioxane. As with THF, at early times there is little evidence for

the vibrationally excited O-bound complex $\mathbf{113}_{\text{diox(O)}}$ suggesting that most of the tricarbonyl fragments produced by photolysis are initially solvated by binding to C-H bonds in the solvent before isomerisation, rather than by direct binding to the O atoms of the solvent. Formation of a σ -complex remains the major reaction pathway in spite of the lower ratio of C-H bonds to O atoms within 1,4-dioxane (4 C-H bonds per O atom) compared to THF (8 C-H bonds per O atom). The kinetics of the isomerisation are shown in Figure 52.

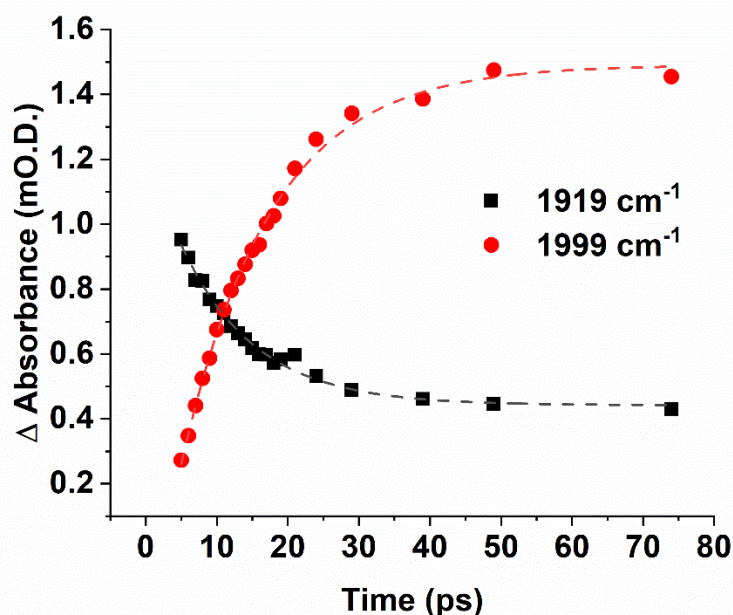


Figure 52: Kinetics of the isomerisation of $\mathbf{113}_{\text{diox}(\sigma)}$ to $\mathbf{113}_{\text{diox}(\text{O})}$ in 1,4-dioxane from 5 to 74 ps. The bands at 1919 cm^{-1} for complex $\mathbf{113}_{\text{diox}(\sigma)}$ (black squares) and 1999 cm^{-1} for complex $\mathbf{113}_{\text{diox}(\text{O})}$ (red circles) were monitored over time. The dashed lines represent single exponential fits to the data giving mean lifetimes of (10.8 ± 1.2) ps for $\mathbf{113}_{\text{diox}(\sigma)}$ and (12.8 ± 0.8) ps for $\mathbf{113}_{\text{diox}(\text{O})}$.

The bleach of the $\mathbf{113}_{\text{diox}(\sigma)}$ feature at 1919 cm^{-1} and the growth of the $\mathbf{113}_{\text{diox}(\text{O})}$ band at 1999 cm^{-1} both fit single exponential functions with lifetimes respective lifetimes of (10.8 ± 1.2) ps and (12.8 ± 0.8) ps.

2.3.5.3 *n*-Bu₂O

A similar experiment performed in the linear ether *n*-Bu₂O was also performed. The spectra (Figure 53) indicate a similar isomerisation to the two cyclic ethers examined so far. The early bands for $\mathbf{113}_{\text{nbu2o}(\sigma)}$ at 1916 and 2016 cm^{-1} are replaced by the O-bound species $\mathbf{113}_{\text{nbu2o}(\text{O})}$ with bands at 1891 , 1909 and 2004 cm^{-1} . However, the timescale of the interconversion is considerably slower than for both THF and 1,4-dioxane (Figure 54).

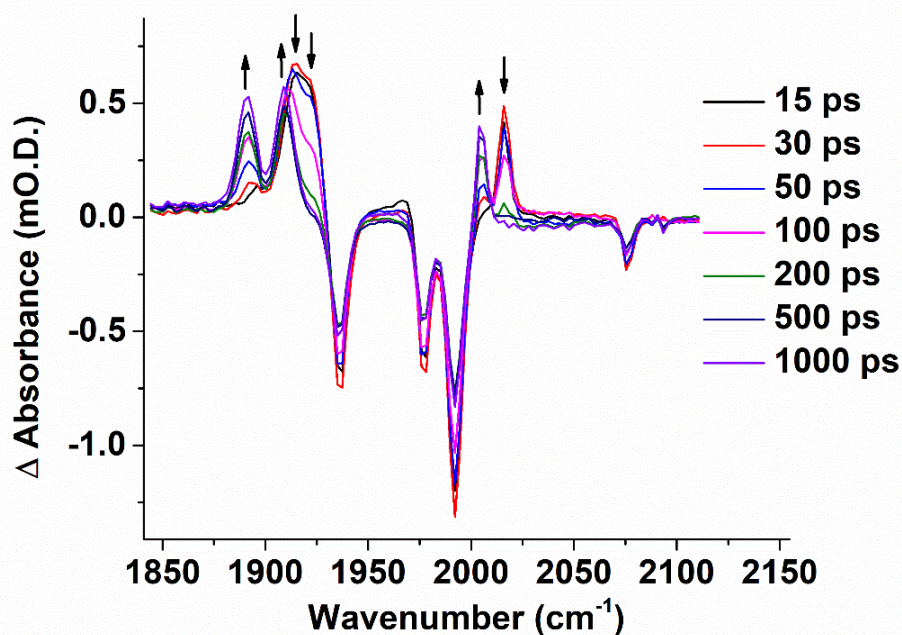


Figure 53: TRIR spectra of $[\text{Mn}(\text{ppy})(\text{CO})_4]$ in $n\text{-Bu}_2\text{O}$ at selected pump-probe delays. A pump wavelength of 355 nm was used. The asterisks show the triplet excited state. The arrows indicate the direction of change in absorbance of the bands over time.

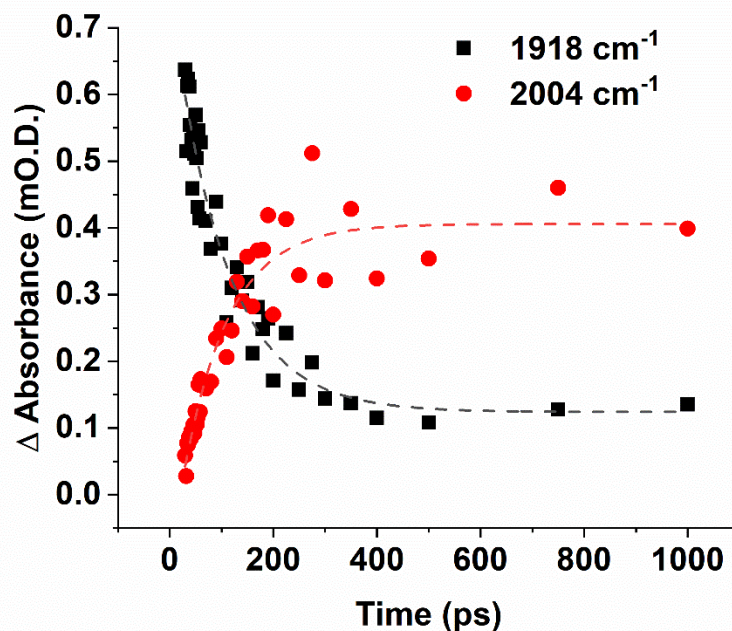


Figure 54: Kinetics of the isomerisation of $113_{\text{nbu}2\text{o}(\sigma)}$ to $113_{\text{nbu}2\text{o}(\text{O})}$ in $n\text{-Bu}_2\text{O}$ from 5 to 1000 ps. The bands at 1918 cm^{-1} for complex $113_{\text{nbu}2\text{o}(\sigma)}$ (black squares) and 2004 cm^{-1} for complex $113_{\text{nbu}2\text{o}(\text{O})}$ (red circles) were monitored over time. The dashed lines represent single exponential fits to the data giving mean lifetimes of (103 ± 26) ps for $113_{\text{nbu}2\text{o}(\sigma)}$ and (88 ± 29) ps for $113_{\text{nbu}2\text{o}(\sigma)}$.

The mean lifetimes for the isomerisation reactions of the three ether solvent complexes are summarised in Table 6.

Table 6: Summary of data for the isomerisation reactions following CO loss from [Mn(ppy)(CO)₄] in ether solvents.

Solvent (S)	Number of C-H bonds per O Atom	$\nu(\text{CO})$ $\mathbf{113}_{\text{S}(\sigma)}$ / cm^{-1}	$\nu(\text{CO})$ $\mathbf{113}_{\text{S}(\text{O})}$ / cm^{-1}	τ $\mathbf{113}_{\text{S}(\sigma)}$ / ps	τ $\mathbf{113}_{\text{S}(\text{O})}$ / ps
1,4-Dioxane	4	1919, 2011	1899, 1911, 1999	10.8 ± 1.2	12.8 ± 0.8
THF	8	1912, 2011	1889, 1899, 1999	15.1 ± 2.2	18.9 ± 1.6
<i>n</i> -Bu ₂ O	18	1916, 2016	1891, 1909, 2004	103 ± 26	88 ± 29

The data show a similar trend for all three ether solvents; the carbonyl stretches for the initial σ -complexes appear at similar wavenumbers in the three solvents, although the two low-wavenumber bands are not resolved due to vibrational excitation at early delays. The subsequent O-complex bands also appear at similar wavenumbers in the three solvents. The shift in wavenumber of the bands upon isomerisation is very similar in all three cases. The highest-wavenumber mode decreases by 12 cm^{-1} upon isomerisation. Comparing the mid-point of the two low-wavenumber modes in $\mathbf{113}_{\text{S}(\sigma)}$ with the low-wavenumber feature of $\mathbf{113}_{\text{S}(\text{O})}$ gives a downward shift of between $14\text{-}18 \text{ cm}^{-1}$ across the three solvents.

The timescale of the isomerisation is different in each case. The isomerisation in THF has a mean lifetime in the region of *ca.* 15-20 ps. The precision of this measurement was indicated by reproducibility of the kinetics in experiments under N₂, in THF-*d*8 and with derivatives **94** and **95**. Therefore, the mean lifetime of the σ -complex with 1,4-dioxane is significantly shorter than that with THF. In *n*-Bu₂O the mean lifetime of the σ -complex is much longer than both the cyclic ethers and is approximately an order of magnitude longer than the 1,4-dioxane complex.

The trend in the mean lifetimes of the σ -complexes correlates with the ratio of C-H bonds to O atoms in the molecule. The more C-H bonds per O atom, the longer the mean lifetime of the σ -complex. The implications of this trend on the possible mechanisms for interconversion of the σ -complexes to the O-bound isomers are discussed in Section 2.5.2.

2.3.6 Dimethyl sulfoxide

The final solvent investigated in this study was dimethyl sulfoxide (DMSO). This solvent has the potential for further complexity compared to the ether solvents as, in addition to six C-H bonds and an oxygen atom, there is also a sulfur atom in the molecule that may be capable of coordinating to the tricarbonyl metal fragment. The TRIR spectra in DMSO are shown in Figure 55.

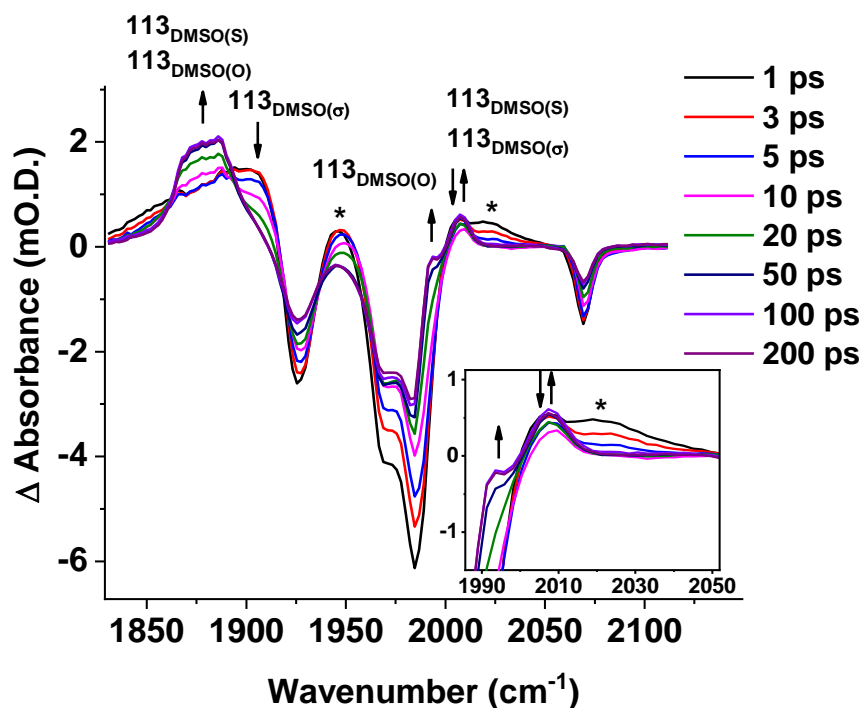


Figure 55: TRIR spectra of $[\text{Mn}(\text{ppy})(\text{CO})_4]$ in DMSO at selected pump-probe delays. A pump wavelength of 355 nm was used. The asterisks show the triplet excited state. The arrows indicate the direction of change in absorbance of the bands over time. Experiment conducted by Anders Hammarbäck.

The intensities of the positive bands are relatively low compared to the bleaches and the bands are much broader than the bleaches – this was assumed to be due to vibrational cooling and the mixture of different broad, overlapping bands of the different products formed. There also qualitatively appears to be a relatively strong excited state band, though the relative ratio of photoproduct to excited state or quantum yields have not been quantified for any of the complexes.

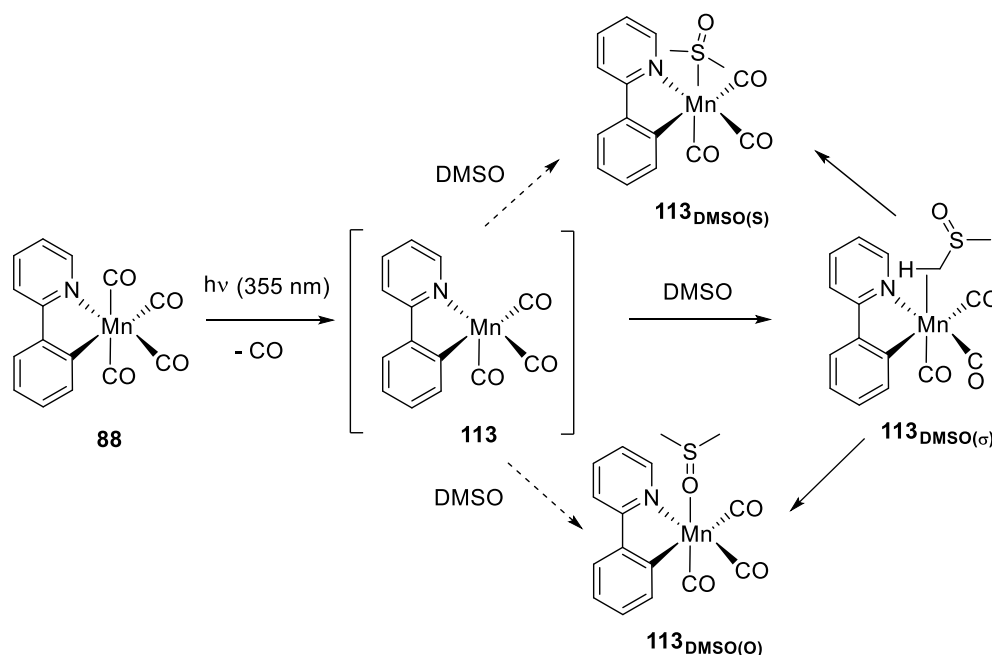
Considering the low-wavenumber region of the spectrum first, short delays show a very broad band with a maximum at around 1907 cm^{-1} . This feature is replaced on the picosecond timescale by a broad band centred at approximately 1880 cm^{-1} . These spectral changes resemble the σ -complex isomerisation observed in the ether solvents.

The region around 2000 cm^{-1} displayed different behaviour to the ether solvents. At short delays, a photoproduct band at 2007 cm^{-1} is observed. This band began to decay slightly in the first 10

ps, presumably at the same time as competing sharpening and shifting of the bands through vibrational relaxation. However, a feature at the same position grew in again from around 20 ps. The feature at 2007 cm^{-1} then persisted for the remainder of the experiment.

Additionally, a small photoproduct band grew in at 1994 cm^{-1} . This band only became prominent in the spectrum at around 50 ps but its proximity to the ground state bleach at 1987 cm^{-1} made subtler early changes difficult to see. The band at 1994 cm^{-1} also persisted for the remainder of the experiment.

The formation of the two bands at 1994 cm^{-1} and 2007 cm^{-1} on the ps timescale and their persistence into the μs timescale suggests that both S and O coordination to the *facial* tricarbonyl fragment occurred (Scheme 31). These two bands formed too rapidly to be complexation by water, oxygen or other impurities, and are too long-lived to be the σ -complex (based on the timescales of the ether isomerisations) or the unsaturated 16-electron complex. The initial photoproduct species with bands at 1907 cm^{-1} and 2007 cm^{-1} was assigned as the σ -complex $\mathbf{113}_{\text{DMSO}(\sigma)}$ due to the similar wavenumbers of the bands for this species compare to the ether solvent σ -complexes and because of the shift of the bands to lower wavenumber upon subsequent S or O coordination.



Scheme 31: Summary of the reactions after CO loss from 88 in DMSO. Solvent coordination predominately occurs via a C-H bond before isomerisation to the give the S- and O-bounds species.

The two low-energy bands for each of the S-bound species $\mathbf{113}_{\text{DMSO(S)}}$ and O-bound species $\mathbf{113}_{\text{DMSO(O)}}$ overlap, leading to a broad feature between $1870\text{--}1890\text{ cm}^{-1}$ containing these four bands. Distinction between $\mathbf{113}_{\text{DMSO(S)}}$ and $\mathbf{113}_{\text{DMSO(O)}}$ is therefore only possible using the highest

wavenumber stretch (i.e. 1994 or 2007 cm^{-1}). The assignment shown in Figure 55 was based on DFT predictions of their infrared spectra: this is discussed in Section 2.3.6.

The kinetics of the isomerisation from $\mathbf{113}_{\text{DMSO}(\text{G})}$ to $\mathbf{113}_{\text{DMSO}(\text{S})}$ and $\mathbf{113}_{\text{DMSO}(\text{O})}$ were investigated. The decay of the $\mathbf{113}_{\text{DMSO}(\text{G})}$ band at 1907 cm^{-1} was analysed from 5 to 100 ps (Figure 56). A single exponential fit yielded a mean lifetime of (11.9 ± 1.5) ps. As there is the possibility of conversion from $\mathbf{113}_{\text{DMSO}(\text{G})}$ to both $\mathbf{113}_{\text{DMSO}(\text{S})}$ and $\mathbf{113}_{\text{DMSO}(\text{O})}$, fitting to a bi-exponential decay was also attempted but this returned mean lifetimes of (19.3 ± 12.3) ps and (4.8 ± 4.8) ps. The better fit to the first-order exponential suggests that there are not two clearly distinguishable first order decay processes. If there are two separate first order processes taking place from formation of $\mathbf{113}_{\text{DMSO}(\text{S})}$ and $\mathbf{113}_{\text{DMSO}(\text{O})}$ it may be more likely that their individual lifetimes are similar and not distinguishable. This may be the case if the conversion to $\mathbf{113}_{\text{DMSO}(\text{S})}$ and $\mathbf{113}_{\text{DMSO}(\text{O})}$ takes place at similar rates.

When the formation of the bands for $\mathbf{113}_{\text{DMSO}(\text{O})}$ at 1994 cm^{-1} and $\mathbf{113}_{\text{DMSO}(\text{S})}$ at 2007 cm^{-1} (Figure 56) were analysed, the mean lifetimes were (19.6 ± 1.5) ps and (23.0 ± 7.9) ps respectively. Due to the decreasing absorbance of $\mathbf{113}_{\text{DMSO}(\text{G})}$ dominating at 2007 cm^{-1} at early times, the fit for this band was begun from 15 ps rather than 5 ps. This suggests that the O- and S-bound complexes do form at similar rates, contributing to the decay of $\mathbf{113}_{\text{DMSO}(\text{G})}$ which is approximately twice as fast as the growth of the two long-lived products.

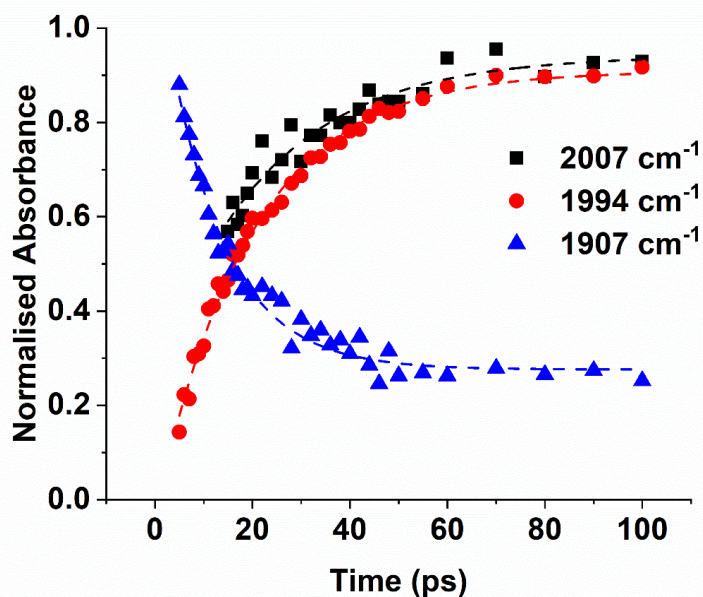


Figure 56: Kinetic plots to study the isomerisation of $113_{\text{DMSO}(\sigma)}$ to $113_{\text{DMSO}(\text{S})}$ and $113_{\text{DMSO}(\text{O})}$ in DMSO from 5 to 100 ps. The bands at 1907 cm^{-1} for complex $113_{\text{DMSO}(\sigma)}$ (blue triangles), 1994 cm^{-1} for complex $113_{\text{DMSO}(\text{O})}$ (red circles), and 2007 cm^{-1} (black squares) for $113_{\text{DMSO}(\text{S})}$ were monitored over time. The fit for $113_{\text{DMSO}(\text{S})}$ was started at 20 ps due to overlap with a decaying band of vibrationally hot $113_{\text{DMSO}(\sigma)}$ at early times. The dashed lines represent single exponential fits to the data giving mean lifetimes of (11.5 ± 1.5) ps for $113_{\text{DMSO}(\sigma)}$, (19.6 ± 1.5) ps for $113_{\text{DMSO}(\text{O})}$ and (23.0 ± 7.9) ps for $113_{\text{DMSO}(\sigma)}$.

As the bands at early times were extremely broad, a small amount of direct coordination through the S or O atoms rather than *via* the intermediate complex $113_{\text{DMSO}(\sigma)}$ (Scheme 31) cannot be ruled out. The broad absorbance of the low-energy bands at short times stretches below 1850 cm^{-1} and could contain a contribution from direct formation of vibrationally excited $113_{\text{DMSO}(\text{O})}$ and/or $113_{\text{DMSO}(\text{S})}$. However, much of this very broad feature at early times is at similar or higher wavenumber than the bands from vibrationally cooled $113_{\text{DMSO}(\text{O})}$ and $113_{\text{DMSO}(\text{S})}$. This shows that a significant contribution to this band must come from a different species to $113_{\text{DMSO}(\text{O})}$ and $113_{\text{DMSO}(\text{S})}$, i.e. complex $113_{\text{DMSO}(\sigma)}$, because vibrational cooling results in an increase in wavenumber. Hence a large proportion of the initial solvation of the *facial* tricarbonyl fragment is once again concluded be *via* a C-H σ -complex (Scheme 31), but direct coordination of S- and O-bound complexes cannot be ruled out.

Finally, an *in situ* infrared spectroscopy study, with continuous 365 nm LED irradiation, was performed to determine whether interconversion between the O-bound and S-bound complexes takes place. The results are shown in Figure 57.

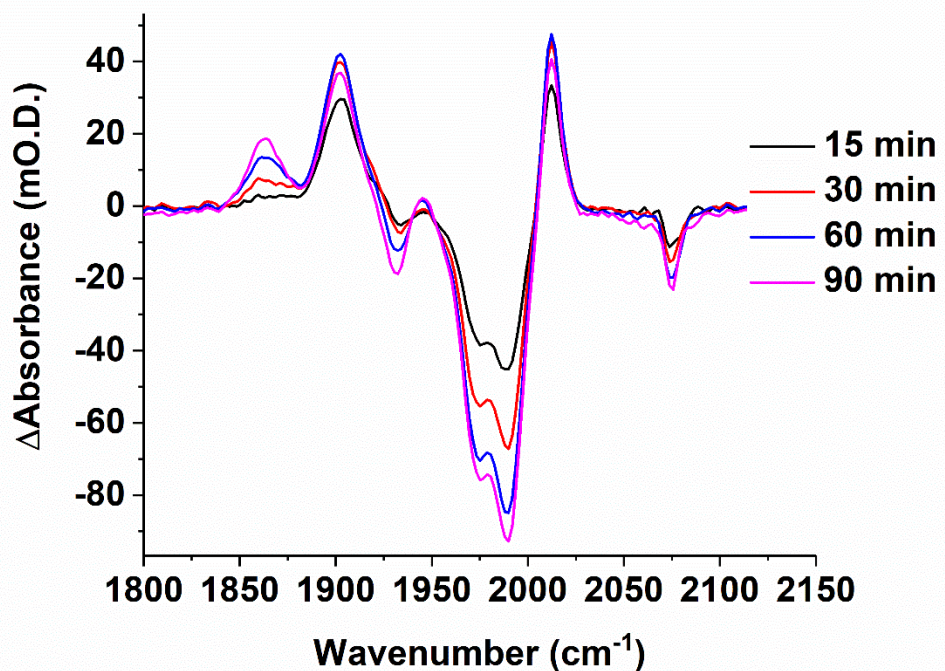
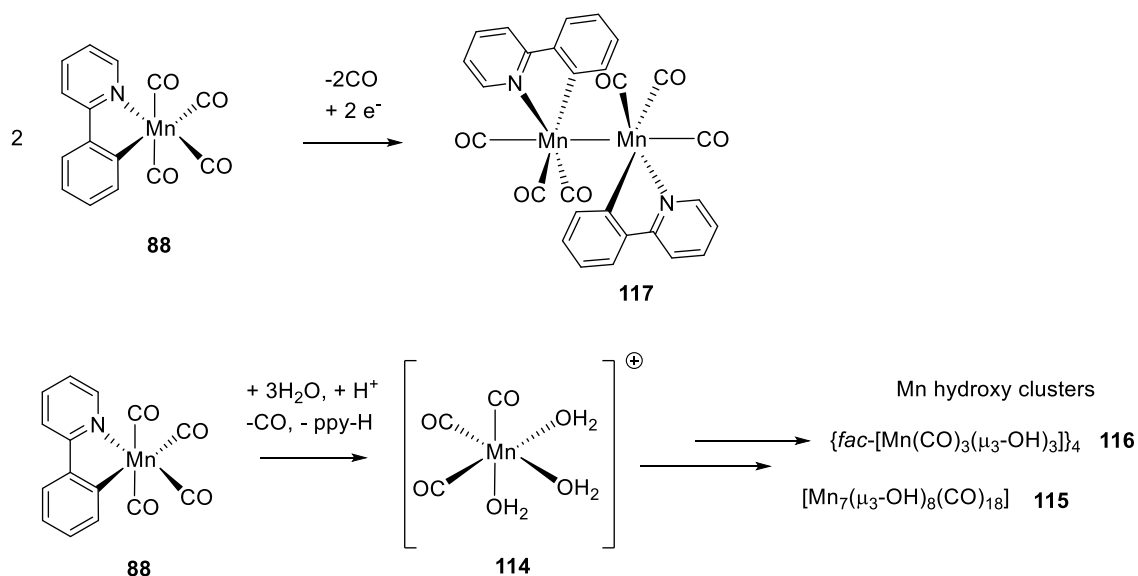


Figure 57: Continuous irradiation of a DMSO solution of $[\text{Mn}(\text{ppy})(\text{CO})_4]$, monitored by in situ infrared spectroscopy at a resolution of 4 cm^{-1} , with spectra collected after the irradiation times shown on the graph. The solution was irradiated by a 365 nm LED drawing 6.0 W power. The difference spectra shown are relative to a reference spectrum recorded immediately before irradiation began.

A similar experiment has previously been performed by Dr. Benjamin Moulton with similar results to those reported here.²³¹ Looking at the difference spectrum after 15 minutes, bands at 1902 and 2013 cm^{-1} have grown in, whilst the bleach at 1928 cm^{-1} appears much smaller than usual, suggesting the presence of a third product band in this region. This is consistent with a single *facial* tricarbonyl photoproduct at this timepoint, though the infrared bands do not match either $\mathbf{113}_{\text{DMSO(O)}}$ or $\mathbf{113}_{\text{DMSO(S)}}$: both these DMSO complexes observed in the TRIR experiments are presumed to degrade on the timescale of milliseconds to seconds. The product observed was again tentatively assigned to be a multinuclear Mn hydroxy cluster as discussed for alkane solvents in Section 2.3.2.²²⁵ However, there are many more possibilities for DMSO than in an alkane solvent. Not only could both DMSO or water-derived hydroxide act as bridging ligands, the redox behaviour of DMSO could lead to formation of reduced dimers such as **117** (Scheme 32).



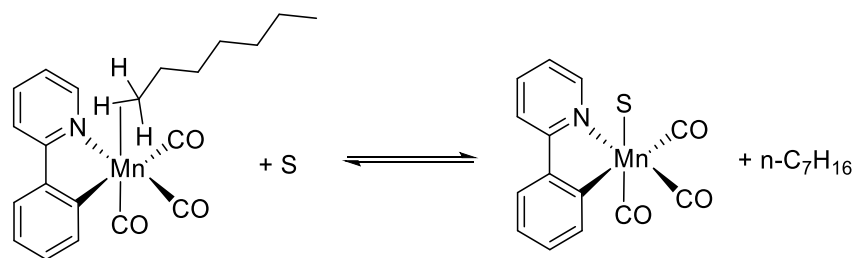
Scheme 32: Possible dimerization and cluster products formed in the continuous irradiation study.

Additionally, a band at 1870 cm⁻¹ begins to grow in after 30 minutes (Figure 57), accompanied by a small decline in the other photoproduct bands, suggesting that further decomposition is taking place. However, attempts in this work and in the previous work by Moulton to further isolate or characterise these species were not successful.²³¹ A small amount of a brown precipitate also formed on the ATR prism, which was found to be insoluble in all solvents tested and did not contain discernible metal carbonyl bands. No further characterisation of this solid was performed, but it would be useful in future work to identify it, as this may be the final Mn-based degradation product. It would be desirable to avoid the formation of precipitate in biological systems and so understanding what this product is and how it forms could be an important part in the evaluation of this CORM system.

In biological systems, the role of other two-electron donors such as N, O or S residues of amino acids should be considered – these could play a role in coordinating to the metal centre as opposed to the water molecules. No mechanistic studies have so far been performed on this family of complexes to study how the CORM degradation products react with amino acids/proteins, but it is known that thermal CORM degradation products do form complexes with proteins, as was discussed in Section 1.2.2.2.

2.4 DFT Calculations

To aid the assignments made for the tricarbonyl photoproducts following CO loss, the infrared spectra of the solvent complexes discussed in Section 2.3 were calculated using DFT. The relative energies of the photoproducts were also calculated relative to heptane complex **113**_{hep} using the isodesmic reaction shown in Scheme 33.



Scheme 33: The isodesmic reaction used to calculate the relative energies of the complexes in Table 7.

Table 7: Assignment of the experimentally observed infrared bands and their unscaled DFT calculated wavenumbers. Relative changes to electronic energies (corrected for zero-point energy), ΔE and Gibbs energies at 298 K, ΔG_{298} , for the reaction in Scheme 33 are given at the D3-PBE0/def2-TZVPP//BP86/SVP(P) level with COSMO solvent correction in heptane. All calculations were performed by Dr Jason Lynam.

Complex	Predicted Bands / cm^{-1}				Observed Bands / cm^{-1}				$\Delta E / \text{kJ mol}^{-1}$	$\Delta G_{298} / \text{kJ mol}^{-1}$
	IR (1)	IR (2)	IR (3)	IR (4)	IR (1)	IR (2)	IR (3)	IR (4)		
113 _{DMSO(σ)}	1960	1978	2039	-	1907		2007	-	3	3
113 _{hep} (terminal)	1951	1977	2039	-	1923	1933	2019	-	0	0
113 _{THF(σ)} (3 position)	1957	1976	2038	-	1912		2011	-	-1	-3
113 _{tol(σ)}	1958	1977	2039	-	-	-	-	-	-5	-4
113 _{hep} (central)	1954	1975	2037	-	1923	1933	2019	-	-11	-5
113 _{Dioxane(σ)}	1956	1976	2036	-	1919		2011	-	-12	-12
113 _{H₂O(σ)}	1957	1981	2051	-	-	-	-	-	-5	-14
113 _{THF(σ)} (2 position)	1954	1972	2034	-	1912		2011	-	-13	-14
113 _{nBu₂O(σ)} (terminal)	1960	1977	2039	-	1916		2016	-	-9	-15
113 _{tol(π)}	1949	1969	2030	-	1906		2007	-	-23	-15
113 _{CH₂Cl₂}	1952	1976	2037	-	1908		2012	-	-19	-16
113 _{nBu₂O(σ)} (2-position)	1952	1973	2035	-	1916		2016	-	-24	-18
113 _{H₂O(O)}	1958	1973	2036	-	1904	1919	2006	-	-26	-32
113 _{Dioxane(O)}	1945	1967	2032	-	1899	1911	1999	-	-43	-37
113 _{THF(O)}	1943	1966	2030	-	1889	1899	1999	-	-44	-37
113 _{DMSO(O)}	1929	1965	2026	-	?	?	1994	-	-46	-43
113 _{nBu₂O(O)}	1939	1968	2031	-	1891	1909	2004	-	-59	-49
113 _{MeCN}	1962	1984	2038	-	1898		2006	-	-60	-61
113 _{DMSO(S)}	1946	1978	2039	-	?	?	2007	-	-89	-81
88	1984	2011	2017	2087	1928	1972	1986	2071	-112	-114

The first point to note is that the DFT calculations systematically overestimate the CO stretching wavenumbers of all the photoproducts. This is typical of DFT-calculated vibrational spectra; the main cause is that the calculations do not model the anharmonicity of the vibrational modes.¹⁶⁸ As a result, scaling factors derived from experimental data are sometimes applied to correct the DFT-calculated band positions, though the scaling factors used vary according to the exact DFT method used.^{168,232,233} As such, it is more informative to study the relative shifts in the bands and the trends with different ligands, rather than the absolute values of the predicted infrared bands.

For example, the calculated spectra for THF capture the small downward shifts of each of the three carbonyl bands upon conversion of **113**_{THF(σ)} to **113**_{THF(O)}. This is replicated in the experimental data, consistent with coordination of the more strongly-donating O-centred ligand. Similar shifts are observed in both the experimental and computational spectra for both the 1,4-dioxane and ⁿBu₂O complexes.

In the cases of THF and ⁿBu₂O, C-H bonds from more than one chemical environment are available to coordinate to the metal. In THF, σ -complexes involving coordination of a C-H bond from the C2 or C3 positions of the ring were calculated, but the predicted infrared bands of two σ -complexes are only 3-4 cm⁻¹ apart, rendering the two coordination modes indistinguishable in the broad, vibrationally hot early spectra (the full width half maximum of the THF band at 2011 cm⁻¹ was 9 cm⁻¹ after 10 ps). Similarly, coordination through C-H bonds from different positions on the alkyl chains of ⁿBu₂O were not distinguishable.

Looking at the calculated free energy changes, reactions to form the ether solvent σ -complexes are much less thermodynamically favourable than formation of their O-bound isomers. This is consistent with the σ -complexes being the kinetic products of solvation of the *facial* tricarbonyl fragment, followed by ultrafast isomerisation to the thermodynamically favoured coordination mode. Different C-H bonds in the same solvent did not always have similar energies when coordinated as σ -complexes. For example, THF bound through a C2 C-H bond is calculated to be around 10 kJ mol⁻¹ lower in energy than the corresponding C3 complex, although as discussed above isomerisation of the σ -complexes was not observable experimentally.

In DMSO, the lower bands for both **113**_{DMSO(O)} and **113**_{DMSO(S)} are significantly lower in wavenumber than in **113**_{DMSO(σ)}, in line with experimental data. The assignment of the O-bound and S-bound species can be made by looking at the band at highest wavenumber for each species. Experimentally, for the initial photoproduct **113**_{DMSO(σ)}, this band appears at 2007 cm⁻¹ and in the two subsequent complexes it appears at 2007 cm⁻¹ and 1994 cm⁻¹. In the calculations, this band is predicted to be in the same position for **113**_{DMSO(σ)} and **113**_{DMSO(S)}, consistent with the overlap observed experimentally, with the band for **113**_{DMSO(O)} at lower wavenumber, and the assignments of **113**_{DMSO(S)} and **113**_{DMSO(O)} were made on this basis. The difference in the Gibbs free energy changes for the formation of complexes **113**_{DMSO(O)} and **113**_{DMSO(S)} is quite large, with **113**_{DMSO(S)}

the more stable complex by around 40 kJ mol⁻¹. However, as reported in Section 2.3.6, the bands for both **113**_{DMSO(S)} and **113**_{DMSO(O)} persisted into the μ s timescale, suggesting that there is a sufficient kinetic barrier to prevent isomerisation on this timescale. Further discussion is provided in Section 2.5.2.

Moving on to the photoproducts in weaker-coordinating solvents such as *n*-heptane, CH₂Cl₂ and toluene, the experimental data summarised in (Table 7) show a shift to lower wavenumber upon displacement of the solvent and formation of complex **113**_{OH₂}. The magnitude of this shift appears quite small in CH₂Cl₂ and toluene with the bands shifting downwards by only a few wavenumbers, though in *n*-heptane the experimental shift is 10-20 cm⁻¹. The DFT calculations predict that the bands for complex **113**_{OH₂} will in fact be quite close in wavenumber to the initial solvent complexes, with only a small decrease or indeed a small increase in wavenumber of the bands upon forming **113**_{OH₂}. The σ -complex **113**_{OH₂(σ)} was also calculated and the predicted infrared bands are very similar to the **113**_{hep} species, at much higher wavenumbers than for **113**_{OH₂}.

As with the ether solvents, multiple binding modes are possible for toluene, CH₂Cl₂, and *n*-heptane. The infrared spectra and energies of the different coordination modes available were calculated using DFT. In *n*-heptane, a similar situation occurs as for the ether solvents: even though the bands are relatively sharp in this solvent, the stretching wavenumbers of the different C-H σ -complexes are unlikely to be distinguishable because they are predicted to lie within 2-3 cm⁻¹ of one another. As a result, it was concluded that the sharpening and shifting of the bands at early times seen in the *n*-heptane spectra is more likely to be due to vibrational relaxation, as seen in all other solvents, than redistribution of different C-H bond coordination isomers.

When the relative energies of coordination complexes via different C-H bonds in *n*-heptane were considered, the results depended on the DFT methodology employed. At the PBE0/def2-TZVPP//BP86/SVP(P) level with COSMO solvent correction in heptane, coordination through a C-H bond on one of the terminal carbon atoms was more stable than through an internal C-H bond by 13 kJ mol⁻¹. However, when a dispersion correction was applied to account for non-covalent interactions, the opposite trend was observed, with the ‘internal’ form predicted to be 5 kJ mol⁻¹ lower in energy than the ‘terminal’ complex. Given the small energy differences involved, conclusive determination of the thermodynamically preferred binding mode in *n*-heptane σ -complex was not possible computationally. Previous NMR spectroscopic studies of transition metal alkane complexes have revealed that a mixture of isomeric C-H bound complexes are observable, suggesting that the energy difference between different C-H coordination modes is likely to be small.^{234–236}

Toluene can act as a two-electron donor to the metal centre as a σ -complex *via* a C-H bond **113**_{tol(σ)} or through an η^2 (C=C) π -complex *via* a double bond **113**_{tol(π)}. The DFT-calculated infrared spectrum for **113**_{tol(σ)} is a close match to the other σ -complexes, such as *n*-heptane, whereas the

bands in **113**_{tol(π)} were predicted to be *ca.* 10 cm⁻¹ lower in wavenumber. The experimental data resemble the latter case – the bands for the toluene complex are lower than those of σ -complexes formed in other solvents. On this basis the product in toluene was assigned as **113**_{tol(π)}.

In CH₂Cl₂, the initial solvent complex could conceivably occur through a σ -complex or coordination of a Cl lone pair. Comparison of the experimental band positions with other σ -complexes shows that the broad absorbance containing the two low-wavenumber bands is lower than other σ -complexes, but the higher band is approximately in the same place. The geometry optimisations performed resulted only in the Cl-bound solvent complex, leading to the tentative assignment of **113**_{CH₂Cl₂} as a Cl-bound solvent complex.

The calculated energies of the solvent complexes in *n*-heptane, CH₂Cl₂ and toluene help to explain why complex **113**_{OH₂} forms in these solvents, but not in ether solvents or in DMSO. The calculated free energy changes of ligand substitution show that **113**_{OH₂} is predicted to be more thermodynamically stable than **113**_{hep}, **113**_{tol(π)}, and **113**_{CH₂Cl₂} but less stable than **113**_{MeCN}, **113**_{THF(σ)}, **113**_{DMSO(S)} and **113**_{DMSO(O)}, consistent with the experimentally-observed formation of **113**_{OH₂} only in *n*-heptane, CH₂Cl₂ and toluene.

2.5 Discussion

2.5.1 Triplet Excited State

Bands assigned to a short-lived triplet excited state were observed in all solvents, although the relative amounts formed in each case were not quantified. In each case, this feature decayed rapidly in the first few picoseconds as a single exponential, suggesting that only one excited state is present. As discussed in Section 2.3.1, the ground state bleach bands recover partially on the picosecond timescale, which indicates that the molecules forming this excited state do not dissociate but return to the ground state, as happens for the two ³MLCT states in [Cr(bpy)(CO)₄].

The triplet excited state lifetimes in a range of solvents are compiled in Table 8. Note that photolysis at 400 nm in MeCN and at 355 nm in *n*-Bu₂O did produce small changes in the region expected for the excited state bands but these were too weak to quantify precisely with a single exponential fit. The excited state lifetime in all the solvents are statistically identical.

Table 8: Summary of the lifetimes of the non-dissociative excited state.

Complex	Solvent	Atmosphere	τ (excited state) (ps)
88 [Mn(ppy)(CO) ₄]	MeCN	Air	4.1 ± 0.2
88	<i>n</i> -Heptane	Air	3.7 ± 0.8
88	CH ₂ Cl ₂	Air	3.6 ± 0.9
88	Toluene	Air	4.6 ± 0.5
88	1,4-Dioxane	Air	5.2 ± 0.5
88	DMSO	Air	3.8 ± 0.3
88	THF	Air	5.6 ± 0.8
88	THF	N ₂	5.1 ± 0.7
94 (ester derivative)	THF	Air	6.3 ± 0.7
95 (COOH derivative)	THF	Air	6.1 ± 0.7

This can be compared with the isoelectronic complex [Cr(bpy)(CO)₄], in which the photoproduct distribution is reversed: the dominant photoproducts are two non-dissociative triplet excited states and CO dissociation is a minor pathway.²⁰⁰ In the previous work on [Cr(bpy)(CO)₄], pump wavelengths of 500 nm [to study ¹MLCT(bpy) excitations only] and 400 nm [both ¹MLCT(bpy) and ¹MLCT(CO) excitations] were employed. The low-energy ¹MLCT(bpy) transitions dominant in [Cr(bpy)(CO)₄] are less CO-dissociative than ¹MLCT(CO) excited states, resulting instead in more intersystem crossing and excited state formation.²⁰⁰ Lowering the pump wavelength increased the population of ¹MLCT(CO) excitations and led to more CO dissociation, although the majority of the bleached intensity still recovered at 400 nm.²⁰² Vlček and co-workers suggested that the ¹MLCT(CO) states are more CO-dissociative than the ¹MLCT(bpy) states but that they still lead to some intersystem crossing causing non-dissociative triplet excited state formation.²⁰⁰

The calculations in Section 2.2.2 on page 109 for [Mn(ppy)(CO)₄] showed two transitions at 345 and 342 nm. Due to the proximity of these two bands to one another it was not possible to distinguish their different characters from the experimental data obtained at 355 and 400 nm pump wavelengths. The 342 nm band was dominated by an orbital transition involving removal of electron density from Mn-CO bonding orbitals in the plane of the ppy ligand and population of Mn-CO antibonding orbitals of the mutually *trans* carbonyl ligands. This is similar to the CO-dissociative ¹MLCT(CO) excited states calculated for [W(en)(CO)₄] and is likely to contribute to the strong observed preference for CO dissociation.

It is interesting to consider the role of the other major orbital component implicated in the DFT calculated absorption spectrum of $[\text{Mn}(\text{ppy})(\text{CO})_4]$, which dominates the character of the 345 nm excitation in the DFT-predicted spectrum. It is mainly a $\pi \rightarrow \pi^*$ transition on the ppy ligand but features some transfer of electron density from the Mn to the ppy ligand. Since the DFT calculations suggest that this is a prominent contributor to the low-energy excitations of $[\text{Mn}(\text{ppy})(\text{CO})_4]$, it appears that this component also plays a role in the strongly CO dissociative photochemistry observed. If this were the case, it would imply that CO dissociation also outcompetes intersystem crossing for the excitation dominated by the ppy $\pi \rightarrow \pi^*$ orbital transition. Calculations of the potential energy surface for this excitation could be used to help determine whether this predominately ligand-based excitation is bound along the $\text{Mn}-\text{CO}_{\text{ax}}$ coordinate and thereby influences CO dissociation. It is known that the $^1\text{MLCT}(\text{bpy})$ transitions have a small barrier to CO loss as indicated by the temperature dependence of the quantum yield for CO dissociation. Similar experiments on $[\text{Mn}(\text{ppy})(\text{CO})_4]$ could be used to determine whether CO dissociation has an energy barrier.

Similarly, an understanding of the relative energies and orbital characters of the triplet excited states may help to explain why only a single non-dissociative triplet excited state is accessed in $[\text{Mn}(\text{ppy})(\text{CO})_4]$ when two are sequentially populated in $[\text{Cr}(\text{bpy})(\text{CO})_4]$.¹⁷⁵ The short-lived triplet excited state decays to produce a longer-lived triplet and it is this second triplet state that decays back to the ground state.¹⁷⁵ Calculations of the triplet excited states of $[\text{Cr}(\text{bpy})(\text{CO})_4]$ did indeed predict two low-lying triplet excited states close together in energy, originating from excitation of electrons from the $\text{Cr}(d_{xy})$ and $\text{Cr}(d_{z^2-y^2})$ orbitals into the bpy π^* manifold.¹⁹⁸ In $[\text{Mn}(\text{ppy})(\text{CO})_4]$ (*circa* 5 ps), the lifetime of the triplet excited state is close to the shorter of the two lifetimes for $[\text{Cr}(\text{bpy})(\text{CO})_4]$, but appears to decay to the ground state, suggesting that this is already lowest-energy triplet excited state.

Although the behaviours of these two major orbital transitions cannot be deconvoluted in the spectra due to the very similar predicted transition energies (342 nm for the predominately $^1\text{MLCT}(\text{CO})$ transition and 345 nm for the mostly ppy $\pi \rightarrow \pi^*$ transition), it appears that in $[\text{Mn}(\text{ppy})(\text{CO})_4]$ both these transitions result in CO dissociation outcompeting intersystem crossing. It is important to investigate the sub-ps dynamics of $[\text{Mn}(\text{ppy})(\text{CO})_4]$ photochemistry in future work, in order to understand the balance between ultrafast intersystem crossing to produce the triplet excited state and CO dissociation.

Quantum yield measurements would be required to quantify the balance between the excited states and its wavelength dependence. These results could then be compared with the $[\text{Cr}(\text{bpy})(\text{CO})_4]$ case. Pryce and co-workers estimated the quantum yield for CO loss in $[\text{Cr}(\text{CO})_5\text{C}(\text{NC}_4\text{H}_4)(\text{Me})]$ based on the extent of recovery of the bleached bands.¹⁹⁴ In this work the bleached bands recovered by around 25 % in MeCN giving a very crude estimate of 0.75 for

the overall quantum yield for CO loss.¹⁹⁴ A problem with estimating quantum yield in this way is that the vibrational excitation of the bleached bands, due to relaxation of the excited states and geminate recombination, distorts the bleaches. A global fitting approach was considered, but the variation in the bleach band shapes during the early times makes it difficult to separate the excited state contribution from the other processes – it would be necessary to model how the vibrational relaxation and geminate recombination evolve over time to estimate the extent of excited state recovery, and such a detailed analysis due to lack of data on these processes.

2.5.2 Binding Mode and Reactivity of Solvent Complexes

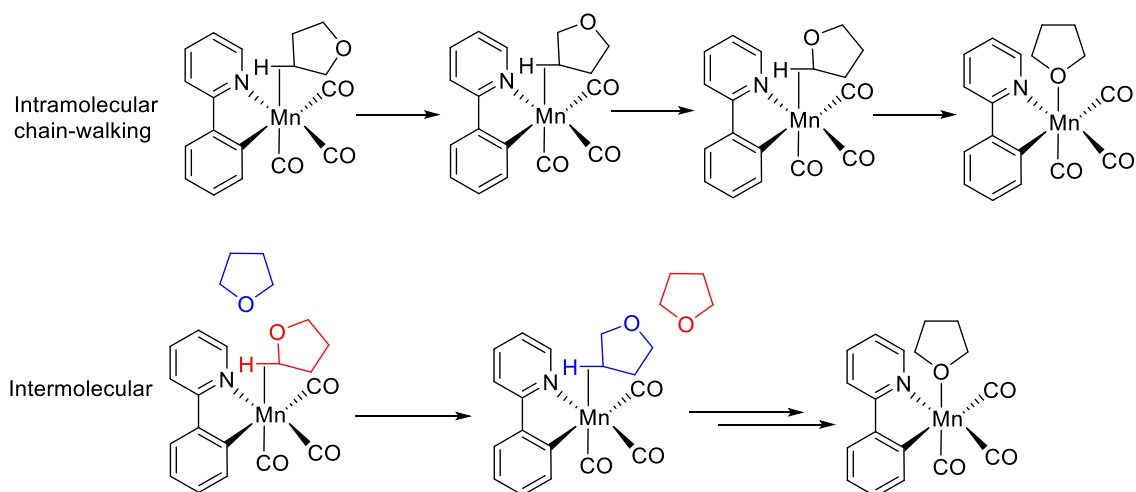
Using TR^MPS in conjunction with DFT calculations, the binding modes of different solvents to the *facial* tricarbonyl moiety and subsequent reactivity have been probed. The assignment of the ether solvent and DMSO isomerisations, as well as the toluene binding modes, show how vibrational spectroscopy can distinguish different binding modes of many ligands. However, a limitation of TRIR spectroscopy apparent in this work is that it is not possible to distinguish the different possible C-H σ -complexes formed by the same solvent molecule due to the very similar positions of the carbonyl stretching bands in these complexes.

Low-temperature NMR spectroscopy has proved to be an insightful technique for studying metal carbonyl alkane complexes.¹²⁴ When TRIR studies by George and co-workers showed that [CpRe(CO)₂(*n*-heptane)], formed from photolysis of [CpRe(CO)₃] in *n*-heptane, had a lifetime on the millisecond timescale at 298 K, the use of NMR spectroscopy to study alkane complexes became a possibility, as at lower temperatures the complexes had long enough lifetimes for NMR measurements.²³⁰ Ball and co-workers incorporated a continuous irradiation system within an NMR spectrometer at 180 K, characterising [(Cp)Re(CO)₂(cyclopentane)] by its highly shielded environment (¹H chemical shift of -2.32 ppm) and the reduction in the magnitude of the ¹J_{C-H} coupling constant compared to the free ligand.²³⁷ This was followed up by a similar study in *n*-pentane, which showed that all three C-H environments can bind to the dicarbonyl, with a slight preference for the internal CH₂ C-H bonds compared to the terminal CH₃ C-H bonds.²³⁴ Very rapid exchanging of the geminal C-H bonds was observed, and intramolecular isomerisation of the different C-H environments (sometimes called ‘chain-walking’) also took place but was much slower, on the timescale 1-10 s⁻¹ at 173 K.²³⁴ An energy barrier for chain-walking consistent with this timescale (~30 kJ mol⁻¹) was measured for Rh and Ir complexes with ethane prepared by low-temperature protonation.²³⁸ The NMR spectroscopic studies have also been extended to the less stable [CpMn(CO)₂(alkane)] complexes, with a mixture of three of the four possible C-H bound isomers forming in isopentane: the C-H bond on the tertiary carbon was too sterically hindered to coordinate.²³⁵ Any chain-walking was again slow on the NMR timescale at low temperature (130 K).^{235,236}

It is therefore likely that similar studies on $[\text{Mn}(\text{ppy})(\text{CO})_3(n\text{-heptane})]$ would show that a mixture of C-H σ -complexes is formed, eventually equilibrating with one another through chain-walking. If the barriers to interconversion of the $[\text{Mn}(\text{ppy})(\text{CO})_3(n\text{-heptane})]$ σ -complexes by chain-walking are comparable to those measured at low temperature for the 4d and 5d metals Rh, Re and Ir discussed above, the half-life for the chain-walking reaction would be on the order of 10 ns at 300 K. However, as 3d metals typically form weaker alkane complexes,²¹⁷ the barrier to chain-walking may be expected to decrease. If the barrier to chain-walking decreased to $\sim 10 \text{ kJ mol}^{-1}$ for $[\text{Mn}(\text{ppy})(\text{CO})_4]$ derivatives, chain-walking would occur on the picosecond timescale at 300 K. Since the metal-carbon bond strengths are greater at the bottom of a triad it is expected that the $[\text{Mn}(\text{ppy})(\text{CO})_3(n\text{-heptane})]$ σ -complexes may be more labile than the examples in the literature where chain-walking barriers have been measured. As a result, and in the absence of NMR data for the barrier in $[\text{Mn}(\text{ppy})(\text{CO})_3(n\text{-heptane})]$, chain-walking on the picosecond timescale in $[\text{Mn}(\text{ppy})(\text{CO})_3(\text{alkane})]$ complexes remains a possibility.

In ether solvents and DMSO, most or all initial solvent coordination took place *via* C-H σ -complexes, followed by isomerisation to the thermodynamically more stable O-bound isomer (and S-bound isomer in the case of DMSO) on a timescale strongly dependent on the solvent. Initial solvation occurred within the first few ps. Coordination of the solvent on this timescale could be considered a stochastic process or dependent on the structure of the first solvation sphere of the $[\text{Mn}(\text{ppy})(\text{CO})_4]$ prior to photolysis – more specifically on the orientation of the solvent molecules with respect to the newly-formed Lewis acidic site on the metal. In many of the solvents, it is difficult to tell whether the initial solvation is stochastic or not because there are many more C-H bonds in the solvents tested than O or S atoms, and the broadness of the vibrationally excited early bands makes small amounts of the O- or S-bound photoproducts difficult to detect. In 1,4-dioxane the ratio of C-H bonds to O atoms is just 2:1, and the lack of significant absorption at lower wavenumbers than the band positions of $\mathbf{113}_{\text{THF}(\sigma)}$ suggests that very little $\mathbf{113}_{\text{THF}(\text{O})}$ is directly formed.

Several possible mechanisms for the isomerisation of the C-H bound complexes to their O or S-bound forms were considered and these are shown in Scheme 34. An intramolecular isomerisation could be envisaged, in which the same solvent molecule that coordinated to the metal as a σ -complex undergoes a migration to coordinate through the O atom. For C-H bonds that are remote from an O atom, a chain-walking mechanism of the sort discussed above is invoked, with intramolecular isomerisation to a series of σ -complexes until the O atom coordinates to the metal. Intermolecular substitution pathways were also considered: these rely on stochastic complexation of the photolysed tricarbonyl fragments with different solvent molecules to form labile σ -complexes in different C-H environments. Again, this sampling of the different coordination modes would end when the thermodynamically most stable O-bound complex forms.



Scheme 34: Inter-molecular and intra-molecular mechanisms for isomerisation of $113_{\text{THF}(\sigma)}$ to $113_{\text{THF}(\text{O})}$.

In the case of purely random binding of solvent molecules, it would be expected that the lifetime of each σ -complex would simply be proportional to the number of C-H bonds in the solvent molecule. However, the ratio of the lifetime of the σ -complex and number of C-H bonds for THF is only around half that of *n*-Bu₂O (Table 9), so purely random solvent binding does not account for the differences in observed lifetimes. It is possible that energetic or conformational preferences in the different solvents prevent solvent complex formation from being completely random.

Table 9: Lifetimes of the C-H to O isomerisation of the three ether solvents reported in Section 2.3.5 with the ratio of the lifetime to the number of C-H bonds included for comparison.

Solvent (S)	Number of C-H bonds per O Atom	τ $113_{\text{S}(\sigma)}$ / ps	τ $113_{\text{S}(\text{O})}$ / ps	τ $113_{\text{S}(\sigma)}$ / Number of C-H bonds	τ $113_{\text{S}(\text{O})}$ / Number of C-H bonds
1,4-Dioxane	4	10.8 ± 1.2	12.8 ± 0.8	2.7	3.2
THF	8	15.1 ± 2.2	18.9 ± 1.6	1.9	2.4
<i>n</i> -Bu ₂ O	18	103 ± 26	88 ± 29	5.7	4.8

Attempts to calculate a transition state for the ‘chain-walking’ isomerisation of C2-bound to $113_{\text{THF}(\sigma)}$ could not $113_{\text{THF}(\text{O})}$ locate a transition state for this pathway. However, both the intermolecular and chain-walking isomerisation mechanisms have been investigated computationally by Harris and co-workers for the analogous isomerisation of alcohol solvent complexes after photolysis of $[\text{Cr}(\text{CO})_6]$.²²⁷ Simulations of the kinetics of the intermolecular and intramolecular pathways showed that the two mechanistic pictures are very difficult to

distinguish, even when binding energies of the different σ -complexes are taken into account to ‘bias’ the chain-walk mechanism. The difficulty in distinguishing the mechanisms arises because the distribution of the different σ -complexes becomes random in both the chain-walk and intermolecular mechanisms.²²⁷

It is interesting to note that Harris and co-workers did not observe a C-H σ -complex in MeOH or EtOH.²²⁷ Instead, the vibrationally excited bands cooled over the first 30 ps to give the O-bound solvent complex, compared to lifetimes of the longer-chain alcohol σ -complexes of greater than 100 ps.²²⁷ These results were interpreted in terms of fast isomerisation compared to the timescale of vibrational relaxation, so that the isomerisation is obscured by the broad bands at early times.²²⁷ In the ether solvents measured in this Chapter, the overall isomerisation reaction takes place up to an order of magnitude faster (lifetime of *ca.* 10 ps in 1,4-dioxane) than for the fastest isomerisations observed in alcohol solvents.²²⁷ Meanwhile, the methyl groups in DMSO did form C-H σ -complex at short times, which decays with a lifetime of around 10 ps, in agreement with the observations of Harris and co-workers that σ -complex coordination and isomerisation takes place for alcohols such as propan-2-ol, the most similar structural analogue to DMSO that was studied.²²⁷ It is therefore surprising that little or no σ -complex with the [Mn(ppy)(CO)₃] fragment appeared to form to the methyl group in MeCN or to the two C-H bonds in CH₂Cl₂. For the isomerisation to be completely obscured by vibrational cooling in these experiments, isomerisation would have to be extremely fast, with a lifetime of only a few picoseconds. However, it could also be the case that initial solvation yields direct formation of **113**_s as the major pathway in MeCN and CH₂Cl₂, rather than an initial C-H σ -complex. Indeed, DFT calculations did not return a σ -complex for these complexes, only **113**_{MeCN} and **113**_{CH₂Cl₂}.

Although a transition state was not located for σ -complex migration, calculations on the migration of DMSO from **113**_{DMSO(O)} to the more thermodynamically-favoured **113**_{DMSO(S)} found the transition state as shown in Figure 58.

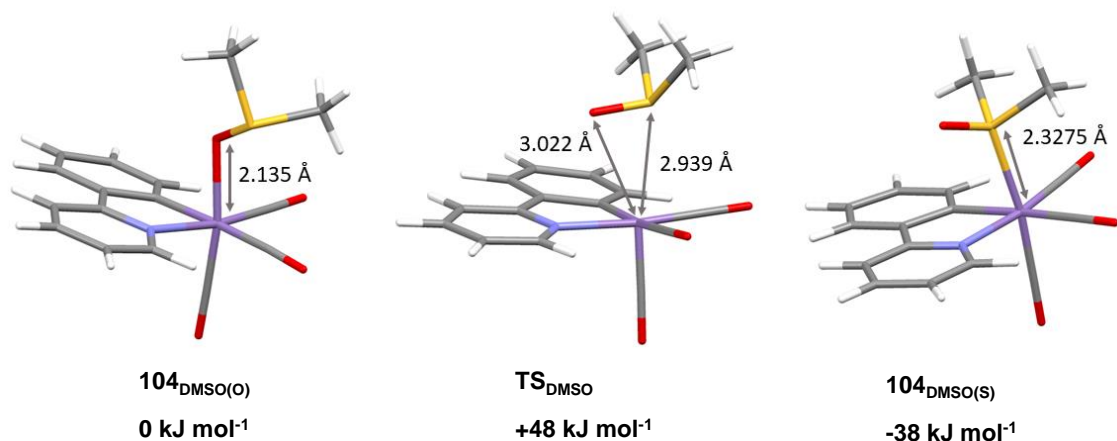


Figure 58: Structure of $113_{\text{DMSO(O)}}$, $113_{\text{DMSO(S)}}$ and $[\text{TS}_{\text{DMSO}}]$ showing Mn-O and Mn-S bond lengths. Atom colours: carbon grey, hydrogen white, manganese pink, nitrogen blue and oxygen red. Energies are Gibbs energies at 298 K at the D3-PBE0/def2-TZVPP/BP86/SVP(P) level with COSMO solvent correction in DMSO.

The transition state for conversion of $113_{\text{DMSO(O)}}$ to $113_{\text{DMSO(S)}}$ lies 48 kJ mol^{-1} higher in energy than $113_{\text{DMSO(O)}}$. The Mn-O and Mn-S distances increase considerably in the transition state compared to the bound complex, such that DMSO is only weakly bound to the metal in the transition state. This suggests that an intramolecular shift from $113_{\text{DMSO(O)}}$ into $113_{\text{DMSO(S)}}$ has a somewhat dissociative character rather than being a ‘slip’ from the O to S atom. This could also be interpreted as an intermolecular mechanism where a second DMSO ligand comes in to coordinate after elongation of the Mn-O distance. The barrier of 48 kJ mol^{-1} suggests a half-life for the interconversion of $113_{\text{DMSO(O)}}$ to $113_{\text{DMSO(S)}}$ on the timescale of tens of microseconds. Experimentally, however, the interconversion of $113_{\text{DMSO(O)}}$ to $113_{\text{DMSO(S)}}$ was not observed: in the TRIR experiment the bands for $113_{\text{DMSO(O)}}$ and $113_{\text{DMSO(S)}}$ were still visible at $800 \mu\text{s}$, whilst in the continuous irradiation experiments both $113_{\text{DMSO(O)}}$ and $113_{\text{DMSO(S)}}$ decayed too rapidly to build up in concentration and be observed.

In the future, it would be interesting to ‘spike’ the THF or DMSO isomerisation experiments with water (or D_2O to avoid overlap with the metal carbonyl region) as a competitor to solvent binding and to assess whether the water complex of **113** can form at short times. In such an experiment, it might be expected that the solvent σ -complex (and possibly the O/S-bound forms) would form in competition with the water complex at short times. As discussed in this Section, there is unlikely to be a water σ -complex as no such complex was seen for MeCN or CH_2Cl_2 , but a ‘spiked’ organic solvent experiment would be a useful method to test for this, circumventing the low solubility of $[\text{Mn}(\text{ppy})(\text{CO})_4]$ in water. This kind of experiment may also provide more information about whether the solvent binding at early times is truly statistical or whether the composition of the solvation sphere around the metal leads to a bias towards one or the other of the competing types of solvent molecules.

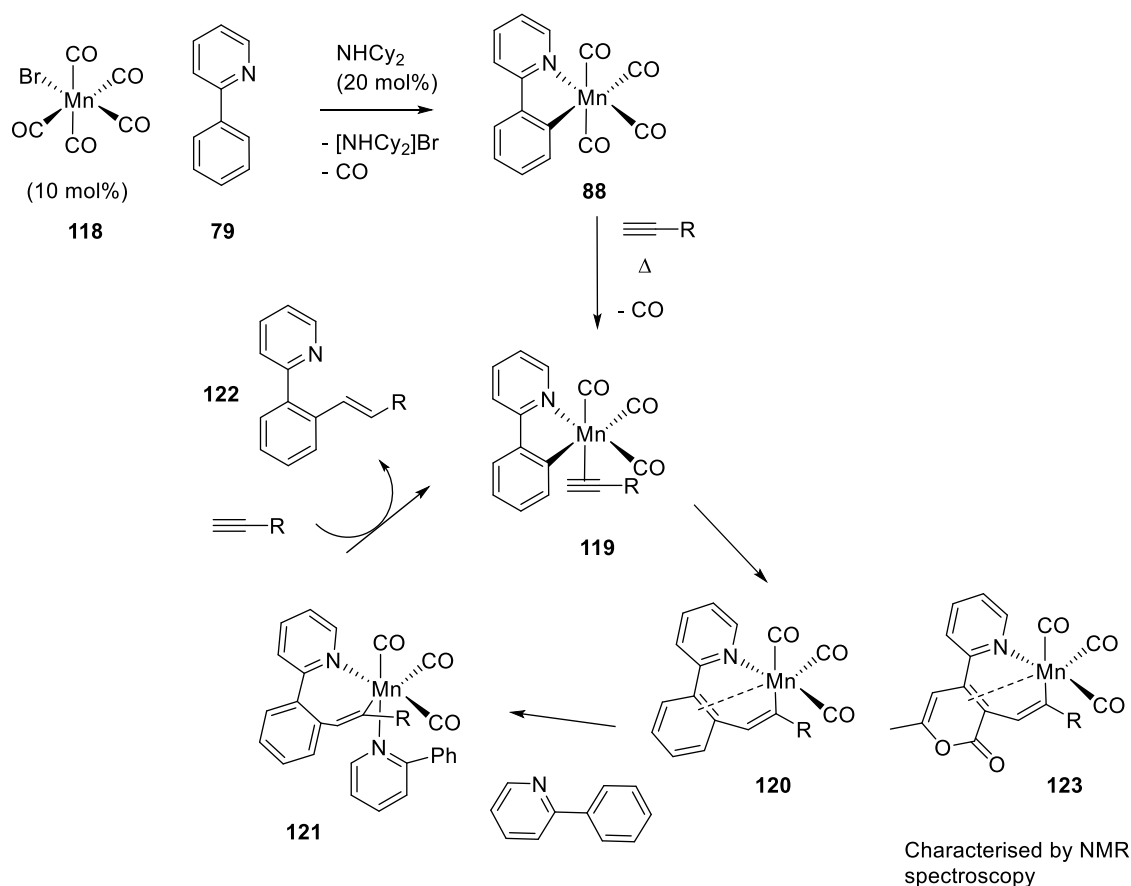
2.5.3 PhotoCORM Design

The comparison of the TRIR studies on $[\text{Mn}(\text{ppy})(\text{CO})_4]$ in this Chapter with previous work on $[\text{Cr}(\text{bpy})(\text{CO})_4]$ illustrates how changes to the metal, oxidation state, and nature of the co-ligands can result in large changes to the fundamental photochemical behaviour of photoCORMs, in a pair of isoelectronic complexes. The dominance of CO dissociation over non-dissociative excited state formation in $[\text{Mn}(\text{ppy})(\text{CO})_4]$ is a desirable behaviour for a photoCORM as it can reduce the intensity of irradiation required. Further study of the ultrafast intersystem crossing measurement of the quantum yield for CO loss from $[\text{Mn}(\text{ppy})(\text{CO})_4]$ and derivatives may be informative in controlling this balance.

In all solvents tested, CO loss is followed by solvation to form *fac*- $[\text{Mn}(\text{ppy})(\text{CO})_3(\text{S})]$. For a CORM in aqueous solvent, direct formation of *fac*- $[\text{Mn}(\text{ppy})(\text{CO})_3(\text{OH}_2)]$ is therefore expected, similar to the $[\text{Mn}(\text{tpm})(\text{CO})_2(\text{OD}_2)]^+$ observed by Nuernberger and co-workers.¹⁹¹ Complex **113**_{OH₂} was prepared by substitution of an alkane ligand by trace water in this work but the low solubility of $[\text{Mn}(\text{ppy})(\text{CO})_4]$ in aqueous solvent precluded study of its direct formation in water. This tricarbonyl water complex is stable at least into the microsecond timescale from the TRIR experiments, whilst the analogous acetonitrile complex is also stable. No other photoproducts from the prior mass spectrometry study in Section 1.4 were observed to form on the microsecond timescale or faster. Indeed, the bands for **113**_{OH₂} appeared to persist for minutes to hours in *n*-heptane in continuous LED irradiation experiments monitored by *in situ* infrared spectroscopy, and the bands for **113**_{MeCN} were also observable on this timescale when the experiment was performed in MeCN. Subsequent degradation of the tricarbonyl species may therefore be slow after initial CO loss under these conditions. The *in situ* irradiation experiments also suggested that thermodynamically favourable multinuclear OH-bridged Mn tricarbonyl clusters may form when **113**_{OH₂} degrades. The study of the photochemistry and chemical reactivity of these clusters may prove informative for understanding the degradation method of this family of photoCORMs. Such clusters were not within the mass range of the detector in the ESI mass spectrometry studies¹⁵⁹ and were not isolated in this work or a previous study where similar bands were observed in DMSO.²³¹

2.5.4 Implications of TRIR Results for Catalysis

The photochemistry of $[\text{Mn}(\text{ppy})(\text{CO})_4]$ is of additional interest due to its relevance to catalysis. The Mn-catalysed alkenylation of sp^2 centres is thought to involve $[\text{Mn}(\text{ppy})(\text{CO})_4]$ in catalyst activation, and is a desirable synthetic transformation due to its use of an Earth-abundant metal catalyst to directly activate a C-H bond (Scheme 35).^{239–241}



Scheme 35: General catalytic cycle for a manganese carbonyl-catalysed alkenylation reaction. R = aryl.

The proposed mechanism, based on DFT calculations and NMR spectroscopic characterisation, involves cyclometallation of the substrate 2-phenylpyridine to produce $[\text{Mn}(\text{ppy})(\text{CO})_4]$.²⁴¹ The catalyst activation is completed by loss of an axial CO ligand and coordination of an alkyne substrate molecule. Insertion of the alkyne into the Mn-C bond of the ppy ligand can then take place giving intermediate **120**, an analogue which has been characterised by NMR spectroscopy.²⁴² Coordination of a second 2-phenylpyridine ligand is then followed by protonation of the alkene by the alkyne starting material to product.

In the current catalytic methodologies, high temperatures are required to encourage CO dissociation to activate the catalyst.²⁴³ However, a photochemical method for catalyst activation could also be envisaged, and the characterisation of some $[\text{Mn}(\text{ppy})(\text{CO})_4]$ photochemistry in this Chapter has led to investigations in this area.²⁴⁴ Further, TRIR studies of $[\text{Mn}(\text{ppy})(\text{CO})_4]$ have since been performed with a focus on alkyne solvents: the wide range of timescales encompassed by a TR^{MPS} experiment allows structural characterisation of the alkyne π -complex and its insertion into the Mn-C bond to the ppy ligand, providing experimental validation of the proposed mechanism in Scheme 35.²⁴⁴

The results of this work also suggest that wider implications for solvation of transition metal catalysts can be probed using complex $[\text{Mn}(\text{ppy})(\text{CO})_4]$. In many catalytic processes, pre-catalysts are activated by ligand loss and the catalytic cycles involve steps in which ligand dissociation leads to coordinatively unsaturated complexes.²⁴⁵ In such cases, it is likely that weak interactions with solvent molecules occur, even though such unsaturation is formally described as a ‘vacant’ coordination site.

One example where solvation is believed to play a critical role in is the isomerisation of allyl alcohol to propanal using the photochemically-activated precatalyst $[\text{Fe}(\text{CO})_5]$. The isomerisation reaction works well in alkane solvents but poorly in stronger donors such as alcohols or pyridine.²⁴⁶ Strongly-coordinating solvents such as alcohols or pyridine were proposed to compete with the alkene substrate to bind to the $^1[\text{Fe}(\text{CO})_4]$, forming stable $[\text{Fe}(\text{CO})_4(\text{S})]$ solvent complexes that inhibit the formation of the on-cycle intermediate $[\text{Fe}(\text{CO})_3(\eta^2\text{-alkene})]$ complex.²⁴⁶

Understanding the structure and reactivity of catalyst solvent complexes may therefore assist in designing new catalysts and rationalising their reactivity. The complex featured in this work, $[\text{Mn}(\text{ppy})(\text{CO})_4]$, could be a useful tool in understanding how solvent molecules interact with Lewis acidic ‘vacant’ metal coordination sites. The structural information from, and sensitivity to electronic environment of, the carbonyl reporter ligands in TRIR spectroscopy provides a handle to characterise the nature of metal-solvent complexes. It is also advantageous for studying metal-solvent interactions that photodissociation is the major photoproduct for $[\text{Mn}(\text{ppy})(\text{CO})_4]$ and the excited state bands only complicate the spectra for a few ps, allowing the chemistry of the solvent complexes to be assessed without convolution of the spectra from other photoproducts.

2.6 Conclusions

The study of the ultrafast photochemical behaviour of $[\text{Mn}(\text{ppy})(\text{CO})_4]$ in this Chapter has provided insight into the primary photochemistry of this family of photoCORMs. The qualitative balance of CO loss and non-dissociative excited state formation is reversed compared to the isoelectronic $[\text{Cr}(\text{bpy})(\text{CO})_4]$. The orbital contribution involved in the relevant transitions were studied by DFT calculations to rationalise this: the band irradiated for $[\text{Mn}(\text{ppy})(\text{CO})_4]$ contains a transition resembling a strongly CO-dissociative $^1\text{MLCT}(\text{CO})$ whereas the lowest-energy excited states for $[\text{Cr}(\text{bpy})(\text{CO})_4]$ are less CO-dissociative $^1\text{MLCT}(\text{bpy})$ states.

The chemistry of the photoproducts after CO loss was studied from ps to μs timescales using TRIR spectroscopy and using *in situ* infrared spectroscopy in continuous irradiation experiments. In weakly-coordinating solvents such as *n*-heptane, toluene and CH_2Cl_2 , initial solvent coordination was followed by substitution with a water ligand to form *fac*- $[\text{Mn}(\text{ppy})(\text{CO})_3(\text{OH}_2)]$.

In ether solvents and DMSO isomerisation reactions form C-H σ -complexes to the more stable O- and S-bound forms were observed, with lifetimes of 10-100 ps. This work shows how TRIR studies of $[\text{Mn}(\text{ppy})(\text{CO})_4]$ can provide fundamental insight into metal carbonyl photochemistry and metal complex-solvent interactions with applications for photoCORMs and in catalysis.

3 Synthesis and Evaluation of CO-Release from a Series of Ferrocenyl CORMs

Many of the CORMs synthesised and examined in the wider field can be broadly categorised as displaying one of three release mechanisms: thermally triggered (i.e. unstable in aqueous solution), protein-triggered and photochemically triggered (Chapter 1).^{107,247} However, it is desirable to develop CORMs that can release CO in response to other triggers, for example the redox state of target cells, to gain new methods for selectivity in CO release.

This Chapter outlines the synthesis and characterisation of three novel Mn(I) tetracarbonyl CORMs containing the redox-active group ferrocene. The impact of using a redox-active co-ligand in a CORM is evaluated by studying the electrochemistry and CO release properties of the Mn(I) complexes.

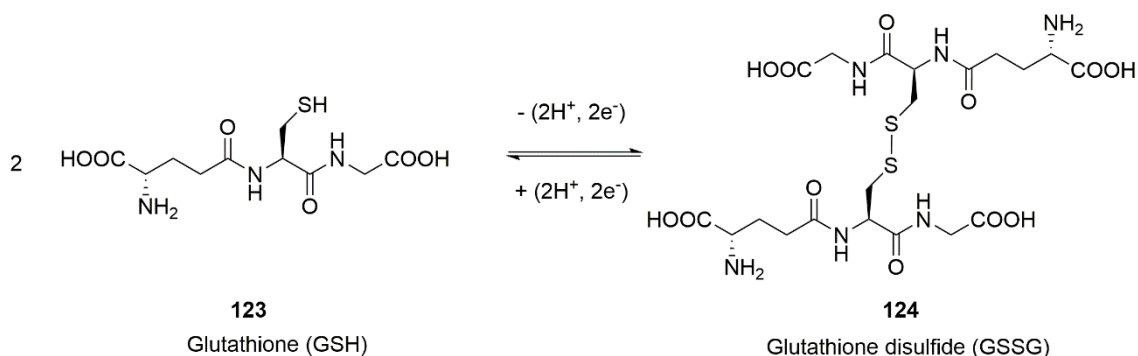
The synthetic route to complex **134** was developed in collaboration with Samuel Andrew, an MChem student whom I mentored in the laboratory, and the DFT calculations on complex **134** were performed by Professor Ian Fairlamb.

3.1 Background

The redox environment within a cell can be characterised by the concentrations of the redox-active compounds, e.g. glutathione (GSH) and glutathione disulfide (GSSG) (Scheme 36).²⁴⁸ The 2GSH/GSSG couple is connected to other key redox-active molecules within the cell through its reactivity. For example, the reduced form of the cofactor nicotinamide adenine dinucleotide phosphate (NADPH) reduces GSSG to 2GSH using the enzyme glutathione reductase, whilst GSH can be oxidised back to GSSG by reactive oxygen species such as peroxides.²⁴⁸ The redox chemistry of thiols is important in many proteins due to the thiol group present in the amino acid cysteine. Disulfide linkages between cysteine residues are critical for the structure and function of proteins.²⁴⁹

However, it is the 2GSH/GSSG couple that is often considered the ‘redox buffer’ of mammalian cells, as its two components are present in millimolar concentrations, much higher than other individual redox-active molecules.²⁵⁰ The concentrations of the two components of the 2GSH/GSSG couple can therefore be used to gauge the redox environment of the cell. Different potentials are associated with the status of the cell.^{248,251} Proliferation occurs in a reducing environment (*ca.* -240 mV vs NHE), whilst differentiation (*ca.* -200 mV) and apoptosis (*ca.* -170 mV) take place at successively higher potentials.²⁴⁸ The concentrations also vary within different compartments of the cell, so that there is highly localised control of the redox environment.²⁴⁸ For example, in the endoplasmic reticulum, where protein synthesis takes place, the redox couple

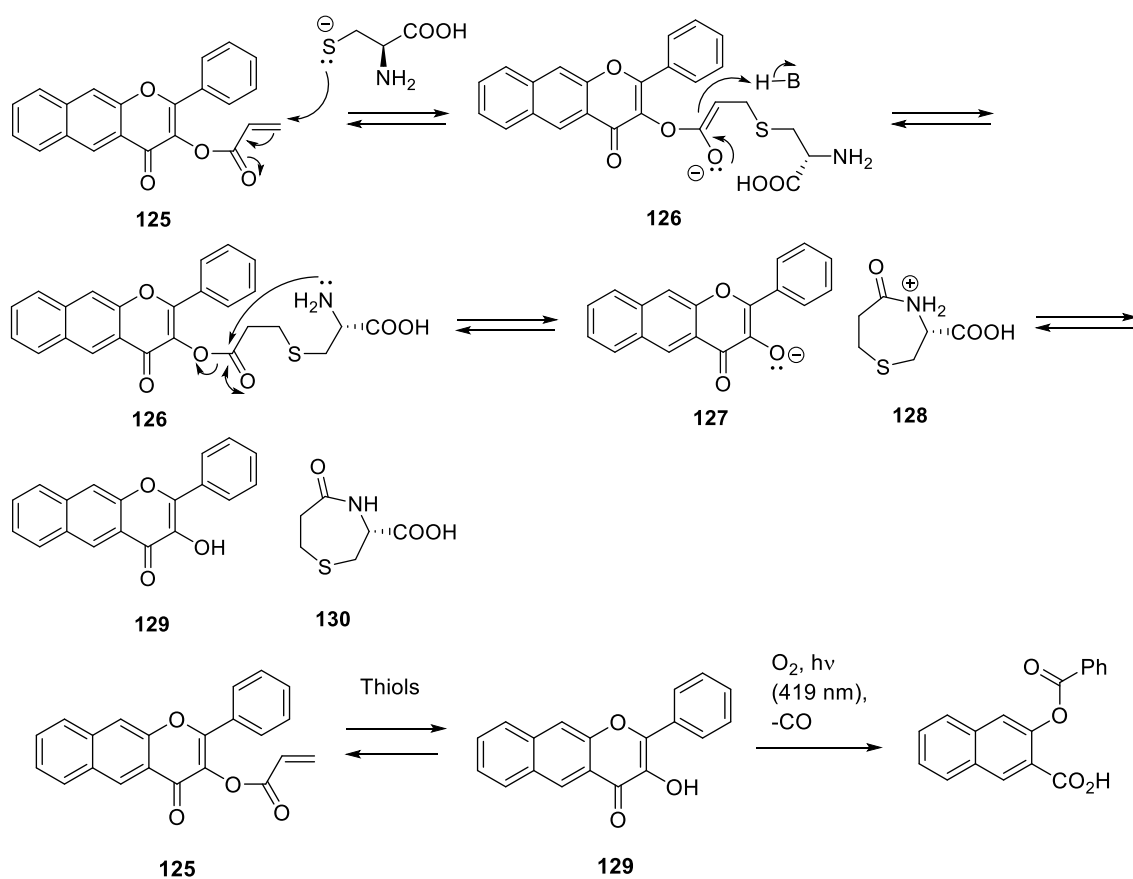
2GSH/GSSG reflects a more oxidising environment than the cytosol, which has been attributed to the need for disulfide bond formation in the endoplasmic reticulum during protein synthesis.²⁵²



Scheme 36: The glutathione (GSH) and glutathione disulfide (GSSG) redox couple is the main intracellular redox buffer.

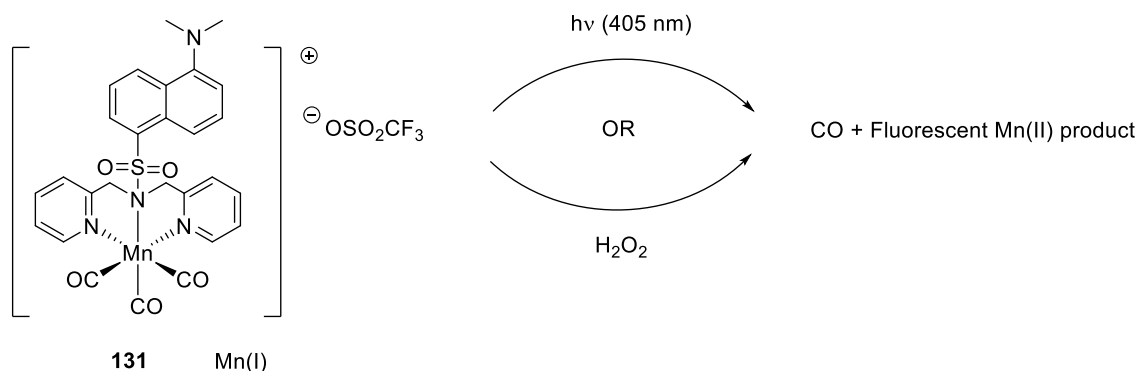
As well as being indicative of the status of healthy cells, changes in redox state are important in disease. A wide range of disease states are associated with the production of reactive oxygen species which are then involved in redox signalling,²⁵³ including in cardiovascular disease and cancer, for which CO may be a future treatment. Whether the production of reactive oxygen species is a cause, a symptom of, or a response to a disease, these changes in the redox environment may be exploitable in drug design, including CORMs. The immune system itself also uses redox potentials: for example, phagocytes can respond to pathogens by engulfing them and producing superoxide anions (which are converted into hydrogen peroxide) to destroy the pathogenic organism.²⁵⁴ This inherent oxidative response of the immune system could be exploited to achieve selective CO release, the CORM acting alongside the immune response.

The importance of the redox environment in which CO release takes place is beginning to be investigated and exploited. Studies on non-metal photoCORM **129** (Scheme 37) exploited the redox buffer of the cell by demonstrating the thiol-sensing properties of this compound, resulting in CO release sensitive to the cellular environment.²⁵⁵ PhotoCORM precursor **125** reacts with thiols to generate photoCORM **129**, which is fluorescent, enabling sensing of this common redox-active functional group.²⁵⁵ The thiols are soft nucleophiles and attack the Michael acceptor, followed by attack of a second nucleophile at the carbonyl (e.g. an amine for amino acids such as cysteine)²⁵⁶ to hydrolyse the ester, forming **129** and cyclic by-product **130**. Subsequent CO loss could then be monitored as CO release results in the formation of non-fluorescent products.²⁵⁵ The concentrations of GSH and GSSG are several orders of magnitude higher inside the cell than in extracellular environments and therefore represent a target for obtaining CO release within cells.²⁴⁸ Meanwhile, more reducing environments will be reflected by higher concentrations of GSH.²⁴⁸



Scheme 37: Reaction of compound 125 with thiols leads to the formation of photoCORM 129.²⁵⁵ An example reaction mechanism for the reaction of 125 with cysteine is shown.

Additionally, it has been shown that CO loss from photoCORM 131 (Scheme 38) may be triggered not only photochemically, but also by chemical reaction with the strong oxidant H₂O₂, a constituent of cellular reactive oxygen species.²⁵⁷ However, more than two equivalents of the very reactive H₂O₂ were used to garner CO release - it was unclear whether such a ratio of CORM to oxidant would occur physiologically. To further extend this work, it would be desirable to gain greater control of the redox potential leading to CO release by altering the metal and co-ligands. Controlling the potential of redox-triggered CO release could then lead to specific targeting of disease states or cellular environments.



Scheme 38: PhotoCORM 131 can be activated by reaction with H₂O₂ as well as by visible light.²⁵⁷

It is well-known that weaker σ -donors and stronger π -acceptors result in higher redox potentials required to oxidise metal centres,²⁵⁸ a principle explained by the lower electron density present on the metal in the presence of such ligands. This point illustrates the compromise that must be struck between the number of equivalents of CO contained within a CORM and achieving a redox potential that is biologically relevant, which makes direct redox-triggered CO release at the metal carbonyl centre challenging. For example, the studies on the amino carbene complex [(CO)₅CrC(NC₄H₈)CH₃] showed a small amount of CO release upon oxidation, but again at a strongly oxidising potential of +360 mV vs Fc/Fc⁺.¹⁹⁴

The introduction of a redox active co-ligand to promote CO release may help to circumvent this problem by promoting reactivity at more relevant redox potentials. The incorporation of a well-studied electrochemical tag into a CORM also provides a mechanistic reporter group that could be used to study CORM degradation.

A good example of a redox-active moiety that can be introduced is ferrocene. Ferrocene is stable in air and water. It has low chronic toxicity in mammals,²⁵⁹ and many of its derivatives have low toxicity to healthy cells.²⁶⁰ The extensive synthetic chemistry of ferrocenyl compounds has allowed a range of ferrocenyl drug candidates to be synthesised and studied. Functionalisation of the ferrocene co-ligand could be exploited to modulate the redox potential and influence CO release. Ferrocenyl derivatives have already been shown to be effective against cancer cells,²⁶¹ malaria,²⁶² and as broad-spectrum antimicrobials.^{263–266}

One of the biggest successes to date in the development of ferrocenyl drugs has been the development of the antimalarial drug ferroquine.²⁶⁷ This ferrocenyl derivative of the antimalarial chloroquine and is used as a racemate (Figure 59). Ferroquine has yielded promising results in phase II clinical trials.²⁶⁸ Combination therapy with another antimalarial agent, eliminated the parasite within 28 days in 97% of the 284 patients studied.²⁶⁹

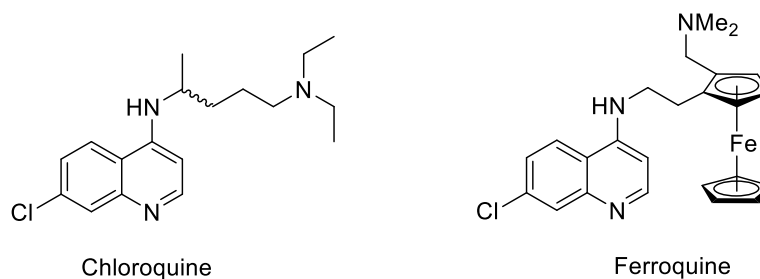


Figure 59: Structures of Chloroquine and Ferroquine.

Two modes of action are believed to contribute to the effects of ferroquine. The first is binding through the quinoline moiety to the protein haematin, preventing aggregation of this protein into haemazoin.²⁷⁰ This is a key step in how the *Plasmodium* parasites dispose of toxic free haem groups and inhibiting the disposal of haem kills the parasite. The second effect is attributed to the ferrocenyl moiety.²⁷⁰ The highly oxidising environment inside the parasite's digestive vacuole, used by eukaryotic cells for digestion and excretion, causes oxidation of the ferrocenyl group to form ferricenium cations.²⁷⁰ The ferrocene/ferricenium couple enables ferrocenyl compounds to participate in Fenton-type chemistry²⁷¹ where the Fe^{II}/Fe^{III} centre catalyses the disproportionation of hydrogen peroxide into hydroxide and hydroperoxide radicals:



In this way, the ferrocenyl group affects the oxidative environment around it by producing damaging radical reactive oxygen species. It was recently observed that ferroquine also possesses anti-cancer activity, inhibiting the growth of prostate cancer tumours in an *in vivo* study.²⁷²

Ferrocifen and its derivatives serve as another example of a well-studied family of ferrocenyl therapeutic compounds.²⁷³ This family of compounds is based on analogues of the breast cancer drug 4-hydroxytamoxifen (Figure 60). Incorporation of the ferrocenyl moiety still enables the compound to bind to its oestrogen receptor target, albeit less strongly than 4-hydroxytamoxifen.²⁷³ The ferrocenyl moiety is associated with cytostatic activity preventing tumour growth.^{274,275} Many structural analogues have since been synthesised, including varying the length of both alkyl chains, replacing the phenol functional group with other hydrogen-bonding moieties, and using other metallocenes in place of ferrocene, giving a diverse family comprising hundreds of compounds. These compounds are currently undergoing further preclinical studies.

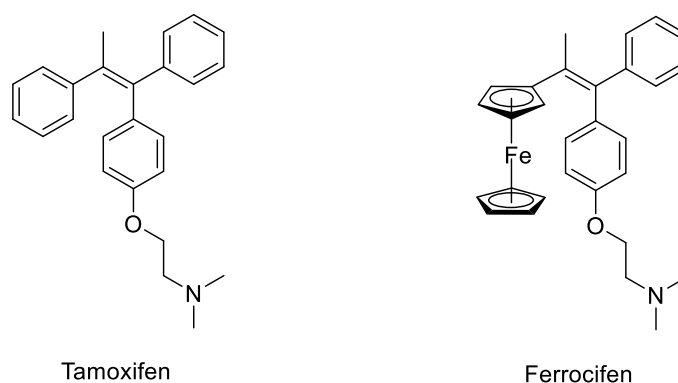


Figure 60: The replacement of a phenyl group in the active anti-cancer compound tamoxifen with a ferrocenyl group gives ferrocifen, the parent compound of a family of anti-cancer drug candidates.

The aim of the work in this Chapter was to synthesise and characterise ferrocenyl CORM complexes **132-134**. Complexes **132** and **133** are based on the air- and water-stable Mn(I) 2-phenylpyridyl (ppy) tetracarbonyl framework. As introduced in Section 1.4, the Mn(I) ppy complexes are typically air- and water-stable and some of the Mn(I) ppy complexes and their degradation products have favourable toxicity profiles.¹⁵⁹ Stability to air and water is advantageous when developing new CO release triggers as it means that the background degradation of the complex is slow, making any other CO release triggers more selective.

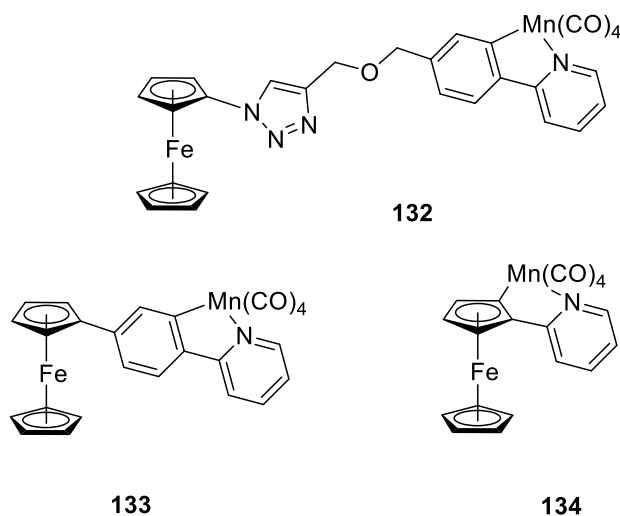


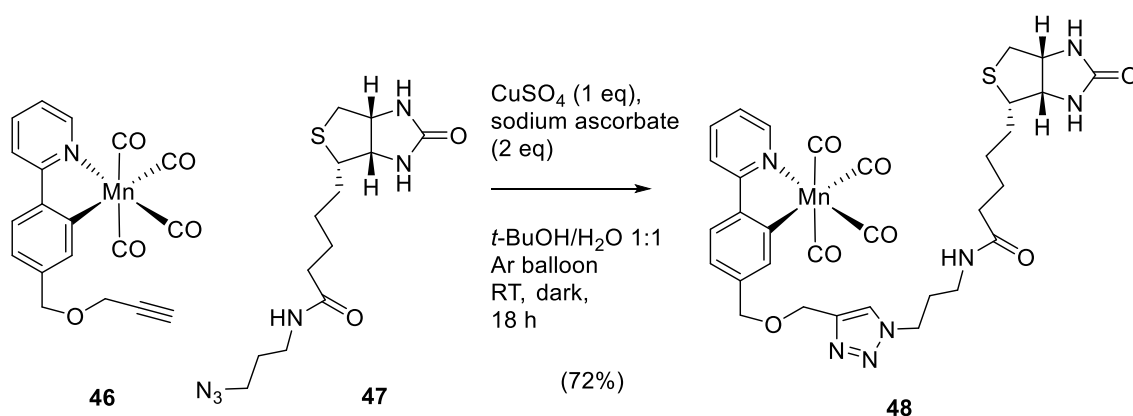
Figure 61: Three ferrocenyl CORM targets for synthesis and characterization.

The synthesis of Mn(I) ppy complexes **132-134** was to be followed by an evaluation of their thermal, photochemical, and electrochemical CO release properties. The effect of different linker lengths between the Fe and Mn centres in the Mn(I) ppy three complexes can be studied. Complexes with a large separation of the Mn tetracarbonyl and ferrocenyl units could be attractive if CO release could be accompanied by additional therapeutic benefits from the ferrocene. On the other hand, incorporating the ferrocenyl group closer to the site of the CO release would be expected to increase the likelihood of a direct redox-triggered CO release process.

3.2 Synthesis of Ferrocenyl CORMs

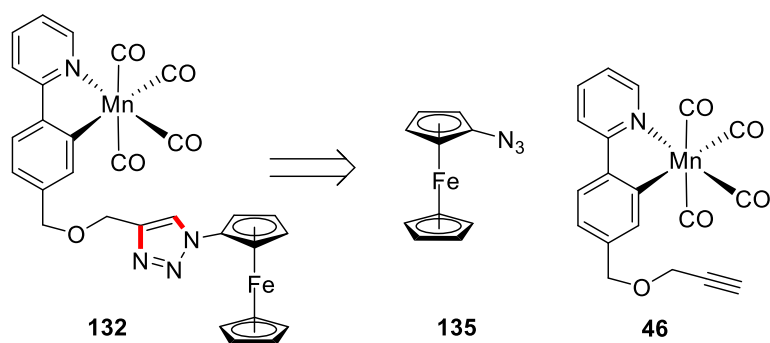
3.2.1 Synthesis of Compound 132

The synthetic route to compound **132** is similar to previous structurally-related CORMs that use the same modular design. Previous work on the synthesis of biotinylated CORM **48** (Section 1.2.2.5), led to a synthetic pathway to alkyne **46**.¹³⁷ The triazole ring of **48** was then produced in the final step using a copper(I)-catalysed variant of the Huisgen [3+2] dipolar cycloaddition reaction (Scheme 40).¹³⁷



Scheme 39: Previously-used conditions for click chemistry with alkyne **46**.

The same synthesis can be applied to Mn(I) ppy complex **132** to install a ferrocenyl group that is remote to the Mn carbonyl moiety (Scheme 40).



Scheme 40: The triazole ring of compound **132** and synthetic equivalents needed for the retrosynthesis, **135** and **46**.

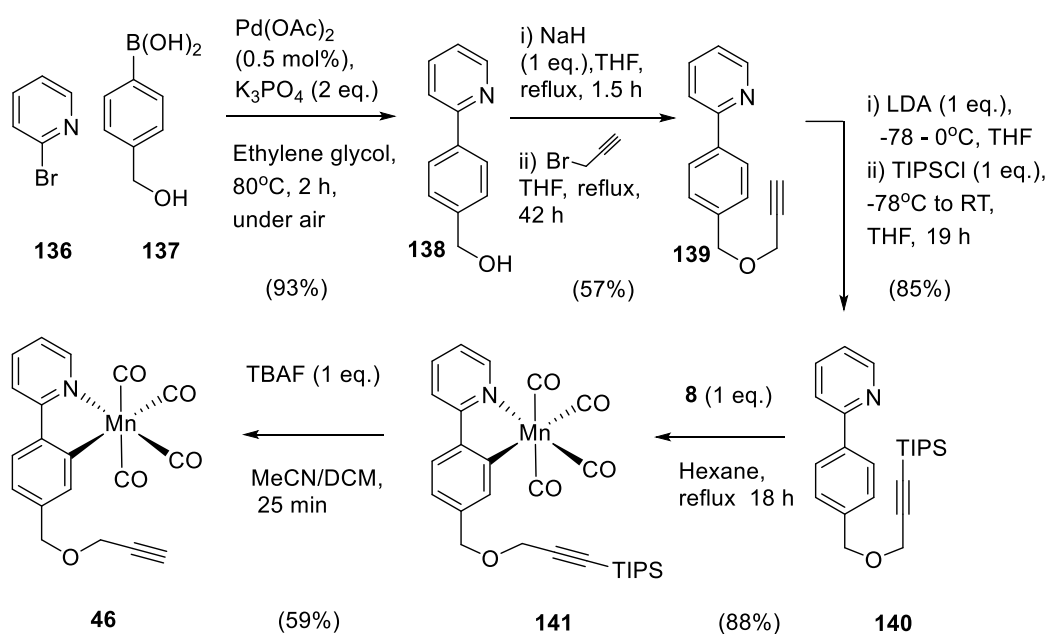
The manganese (I) centre in the product is derived from dimanganese decacarbonyl, **42** (Scheme 41). Reduction in a sodium amalgam produces $\text{Na}^+[\text{Mn}(\text{CO})_5]^-$ which readily undergoes nucleophilic substitution with benzyl chloride to produce NaCl and $[\text{BnMn}(\text{CO})_5]$, **87**, a well-known precursor to manganese-based CORMs.¹⁸⁴ The bromide-containing analogue of this species, $[\text{BrMn}(\text{CO})_5]$, which can be synthesised by adding Br_2 to oxidise $[\text{Mn}_2(\text{CO})_{10}]$,²⁷⁶ could also have been used to perform the cyclometalation, although the reaction is less clean and

additionally requires a base due to the ‘ σ -complex-assisted metathesis’ mechanism of this reaction.²⁴¹



Scheme 41: Synthesis of the cyclometalating reagent [BnMn(CO)₅].

Alkyne intermediate **46**, a convenient building block for a modular approach to CORM design, was synthesised in good yield using a previously developed synthetic route.¹³⁷ The steps involved in the preparation of alkyne **46** are summarised in Scheme 42.



Scheme 42: Synthesis of ‘clickable’ alkyne complex **46. The yields are those achieved in this work.**

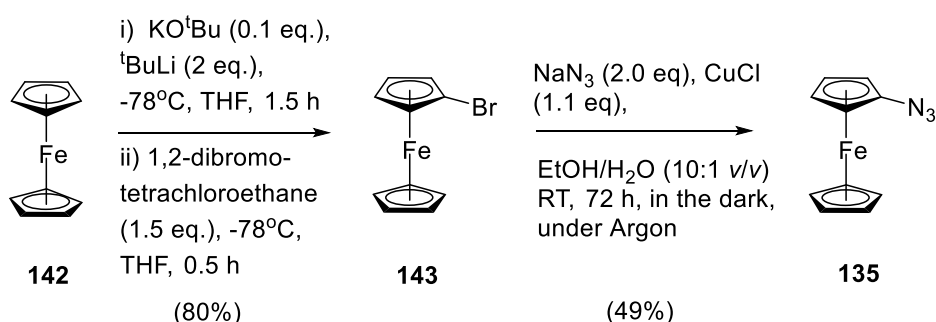
The first step in the synthesis was to construct the 2-phenylpyridine moiety, beginning with the Suzuki-Miyaura coupling of 2-bromopyridine, **136**, with 4-hydroxybenzeneboronic acid, **137**, catalysed by Pd and mediated by base. Subsequent deprotonation of the alcohol **138** with sodium hydride, followed by nucleophilic substitution with propargyl bromide produced alkyne **139**.

Typically, the cyclometalation step would be performed by simply heating the phenylpyridine ligand together with benzyl pentacarbonyl manganese(I) in a hydrocarbon solvent. However, in the case of alkyne-containing species **139**, there is a complication: the alkyne must first be protected with a triisopropylsilyl (TIPS) group for the cyclometalation to produce the desired product. Cyclometalation of **139** did not proceed cleanly, giving multiple products. This may be

because unprotected alkyne can bind to the Mn centre in an undesired side reaction that leads to insertion of the alkyne into the Mn-C bond of the ppy.¹³⁷ Such insertion reactions play a key role in the application of Mn carbonyl complexes in catalysis.²⁴¹

However, installation of the bulky TIPS group prevents the undesired addition of the alkyne to the manganese centre. Similar reactions are known in the literature; the yields of these reactions are minimised when the alkynes are TIPS-protected.²⁷⁷ Following the cyclometalation, deprotection was achieved in good yield with tetra *n*-butylammonium fluoride (TBAF) trihydrate. Despite this reaction inducing some dissociation of the phenylpyridine from the manganese, TBAF trihydrate in a CH₂Cl₂/acetonitrile mixture was previously found to be a superior deprotecting agent to KOH, KF, and dry TBAF in THF.¹³⁷ In any case, the desired product and the traces of free ligand from deprotection reaction were separable by flash column chromatography on silica gel.

The second component of the Huisgen cycloaddition, azidoferrocene, **135**, was made from ferrocene in two steps (Scheme 43) using literature reactions.^{278,279}



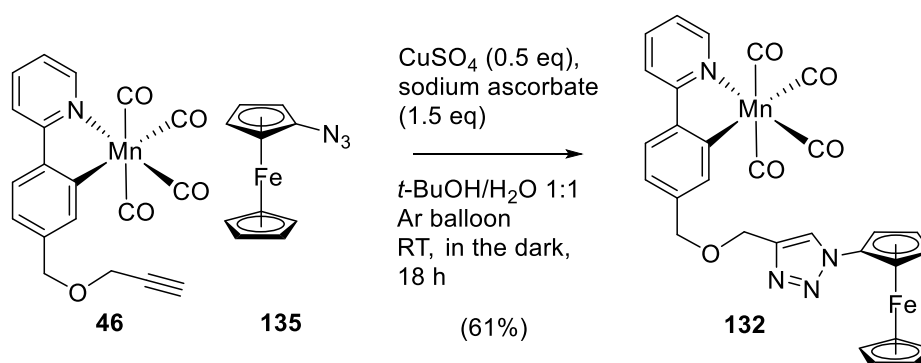
Scheme 43: The two-step synthesis of azidoferrocene, compound 135, from ferrocene.

In the first step, ferrocene was lithiated using *t*-butyl lithium and then brominated with 1,2-dibromotetrachloroethane to produce bromoferrocene. *When working with ^tBuLi it is critical that appropriate safety precautions are taken to protect against the highly pyrophoric nature of this reagent.*

It is often difficult to separate ferrocene, mono- and dihalogenated ferrocenes by conventional techniques. A novel purification protocol developed by Long and co-workers allows the brominated product to be separated from unreacted ferrocene based on the redox potentials of the two compounds.²⁸⁰ The redox potential for the oxidation of bromoferrocene lies some 170 mV above that of the ferrocene/ferricenium couple, allowing removal of the ferrocene under moderately oxidising conditions.²⁸⁰ The crude mixture suspended in hexane was repeatedly washed with an aqueous solution of 200 mM FeCl₃ to oxidise the ferrocene. The resulting ferricenium ions partitioned into the aqueous layer whilst the unoxidised bromoferrocene remained in the hexane layer.

The second step in the synthesis of **132** is a copper (I)-catalysed substitution reaction with sodium azide, which produced azidoferrocene in moderate yield.²⁷⁹ The low yield was attributed to decomposition of the azidoferrocene product in solution during the reaction, but sufficient material for the final step was obtained.

Finally, target molecule **132** was synthesised from the two fragments using the copper(I)-catalysed Huisgen cycloaddition (Scheme 44). The procedure for the synthesis of analogous compounds by Ward¹³⁷ was adapted for this work; reactions were performed at twice the catalyst and reductant loadings, reducing the reaction time from 40 h to 18 h and resulting in a yield of 61%.



Scheme 44: The final step in the synthesis of compound 132.

Monitoring of the reaction by TLC analysis showed azidoferrocene degrading faster than the alkyne **46**. Some of the unreacted alkyne **46** was recovered during purification of the target by column chromatography. This suggests that using even larger amounts of CuSO_4 and sodium ascorbate may improve the yield further as more of the azide will react before it degrades. An additional improvement in the yield would be worth the use of these comparatively inexpensive reagents. However, the good yield of 61% in this experiment provided an adequate amount of material for further study.

Complex **132** was extensively characterised. The carbonyl region of the infrared spectrum closely resembles that of alkyne **46** and ppy parent compound **88**, showing four strong carbonyl bands at 2076, 1991, 1977 and 1931 cm^{-1} consistent with the C_s and pseudo- C_{2v} symmetries discussed in Chapter 2. The carbonyl stretches are essentially unchanged from the starting material, which is expected given the distance from the carbonyls to the site of the reaction. This confirms that the Mn(I) tetracarbonyl centre was carried through the reaction and purification steps intact. No loss of axial CO ligands or coordination of the triazole to the Mn(I) centre took place during the reaction or purification. The terminal alkyne C-H stretch at 3302 cm^{-1} has also been lost during the reaction. The strong azide stretch at around 2100 cm^{-1} seen in the azidoferrocene starting material was also lost, whilst new bands at 1567 and 1519 cm^{-1} in the product may be attributed to stretches within the triazole ring in the product.

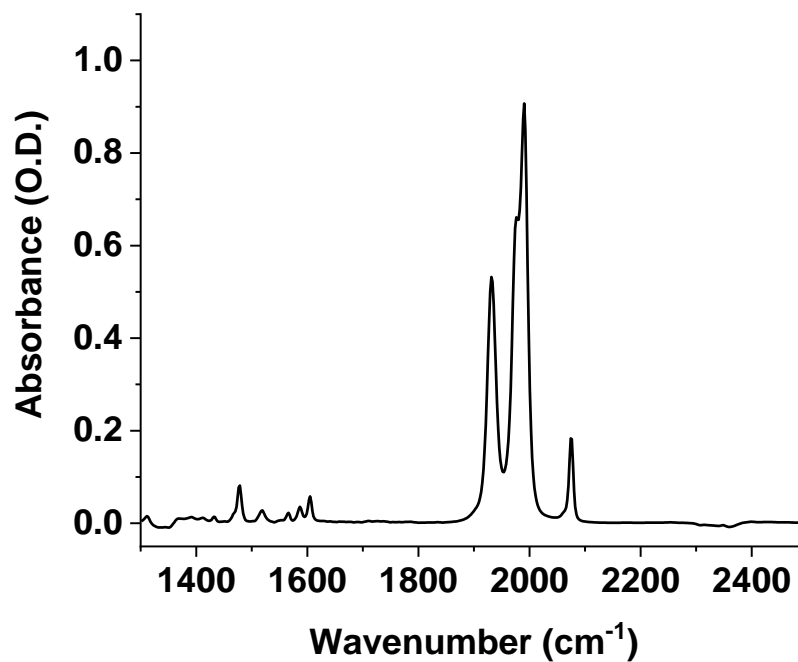


Figure 62: Infrared spectrum of complex 132 recorded in CH₂Cl₂ solution.

Characterisation by NMR spectroscopy allowed full assignment of the proton NMR spectrum consistent with the target molecule, supported by ¹³C, HMBC, HSQC, COSY and NOESY experiments.

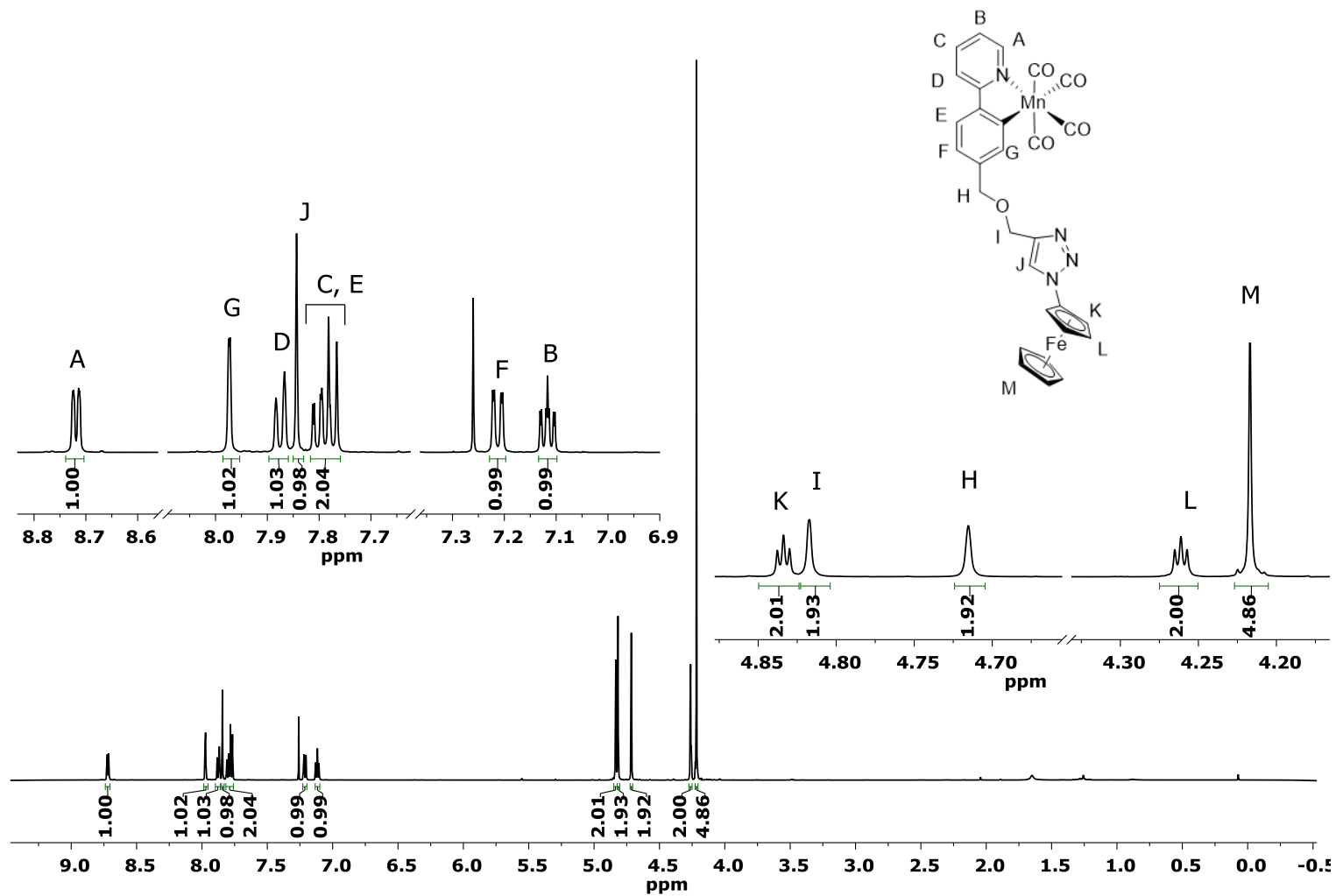


Figure 63: A 700 MHz ¹H NMR spectrum of complex 132 in CDCl₃ at 298 K. Expansions of the spectrum are shown in the insets.

Proton A was assigned on the basis of its high chemical shift of 8.72 ppm; a deshielded doublet from this position on the ring is a distinguishing feature of 2-phenylpyridines.²⁸¹ By using the ¹H-¹H COSY spectrum, B, C and D were then assigned by following the correlations around the pyridyl ring. Nuclear Overhauser effects were observed between the pairs of protons F and H, and G and H, suggesting that these protons are spatially close (within *ca.* 5 Å). Given that G is a singlet, protons F and G can be assigned, leaving E as the remaining aromatic resonance in the ppy moiety.

In addition to H, three other two-proton resonances are seen between 4 and 5 ppm. One of these three is a singlet at 4.82 ppm and must be the isolated CH₂ protons I as it is the only other expected two-proton singlet. The other two are triplets from protons K and L of the ferrocene ring. A key finding was the presence of a nuclear Overhauser effect between the triazole proton J (the remaining singlet in the aromatic region at 7.84 ppm, formerly the terminal alkyne proton) and the pair of protons K on the ferrocene ring (4.83 ppm), showing that these protons from the two reagents are now in the same region of the same molecule. The other remaining triplet at 4.26 ppm is therefore L, and M is clearly the five-proton singlet at 4.22 ppm.

The accurate mass ESI mass spectrum shows the pseudo molecular ion corresponding to protonated [**132**]⁺ with an *m/z* value of 617.0292. Interestingly, a small set of peaks for the protonated **132** with the loss of one molecule of CO is also seen, though this degradation may be occurring within the spectrometer and no evidence for a tricarbonyl species has been noted in the other characterisation methods.

Crystals of **132** were obtained by layering *n*-pentane on top of a chloroform solution of **132** in an NMR tube. Yellow needle-like crystals were obtained from which a suitable single crystal for X-ray diffraction was found. The structure is shown in Figure 64. Comparison with other Mn(I) phenylpyridine complexes indicates a slight distortion from the idealised octahedral structure, for example the C(1)-Mn(1)-N(1) bond angle is 80.04(18)° due to the rigidity of the 2-phenylpyridine system. There is also distortion of the trans-carbonyls at 168.8(2)° for the C(14)-Mn(1)-C(15) angle. These angles are very close (within one degree) of other known Mn(I) ppy complexes.^{184,282} The bond lengths within the first coordination sphere of the Mn in complex **132** are also essentially identical to structures of [Mn(ppy)(CO)₄] and related complexes with derivatised ppy ligands.^{184,282} As expected, the Mn-C bonds *trans* to the N and C donors of the ppy ligand are shorter than those *trans* to CO ligands, reflecting the stronger donor properties of the N and C atoms of the ppy and the π-acceptor properties of the CO ligands.

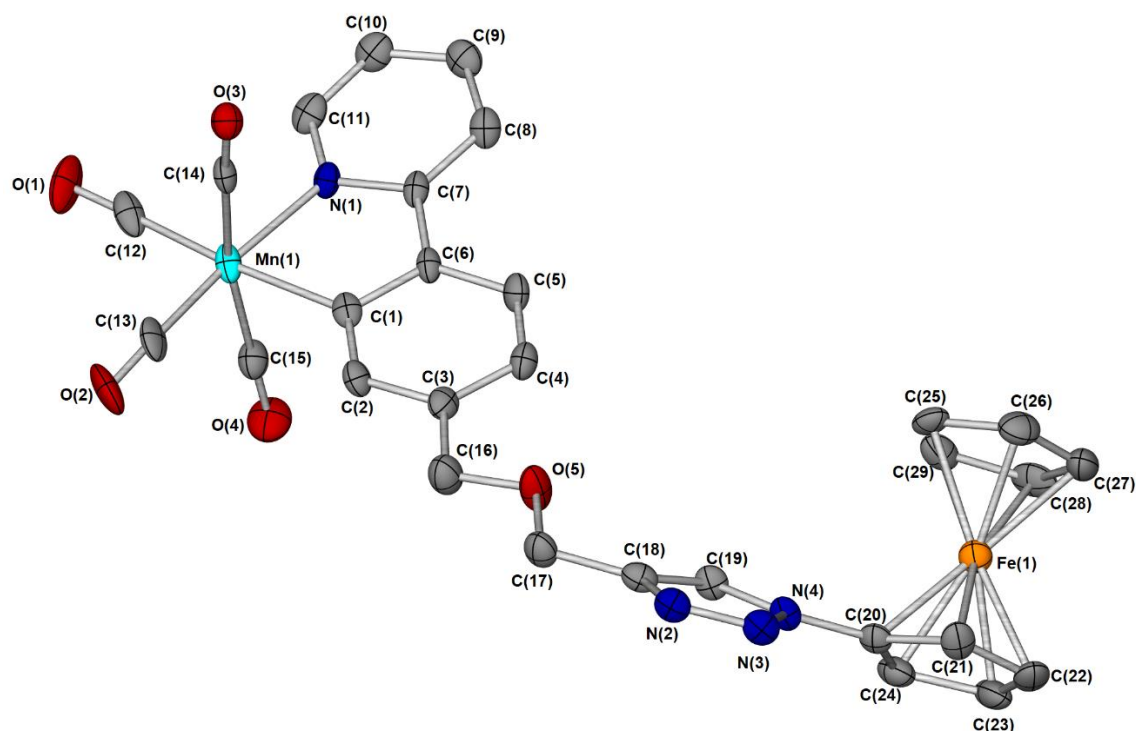
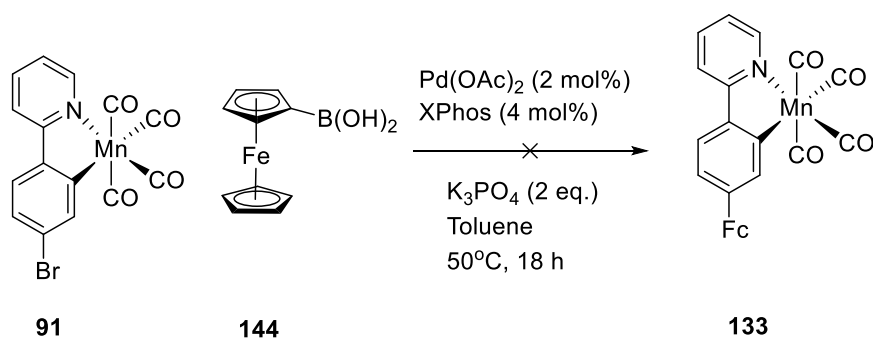


Figure 64: An X-ray crystal structure of compound **132** with hydrogen atoms omitted for clarity. Atoms are displayed as thermal ellipsoids at 50% probability. Selected bond lengths (Å): C(1)-Mn(1) = 2.056(5), C(12)-Mn(1) = 1.836(6), C(13)-Mn(1) = 1.805(6), C(14)-Mn(1) = 1.853(5), C(15)-Mn(1) = 1.867(5), N(1)-Mn(1) = 2.059(4). Selected bond angles (°): C(1)-Mn(1)-N(1) = 80.04(18), C(12)-Mn(1)-C(1) = 174.9(2), C(14)-Mn(1)-(C15) = 168.8(2), C(13)-Mn(1)-N(1) = 172.65(19), C(13)-Mn(1)-C(12) = 92.3(2), C(15)-Mn(1)-(C1) = 84.1(2)

3.2.2 Synthesis of **133**

Bromo-substituted CORM **133** has previously been demonstrated as a competent coupling partner in Suzuki-Miyaura cross-coupling reactions with arylboronic acids, as discussed in Section 1.4.¹⁸⁴ Direct functionalisation of CORMs is synthetically appealing to facilitate access to a wide range of structures, so similar chemistry was attempted to synthesise compound **132**.

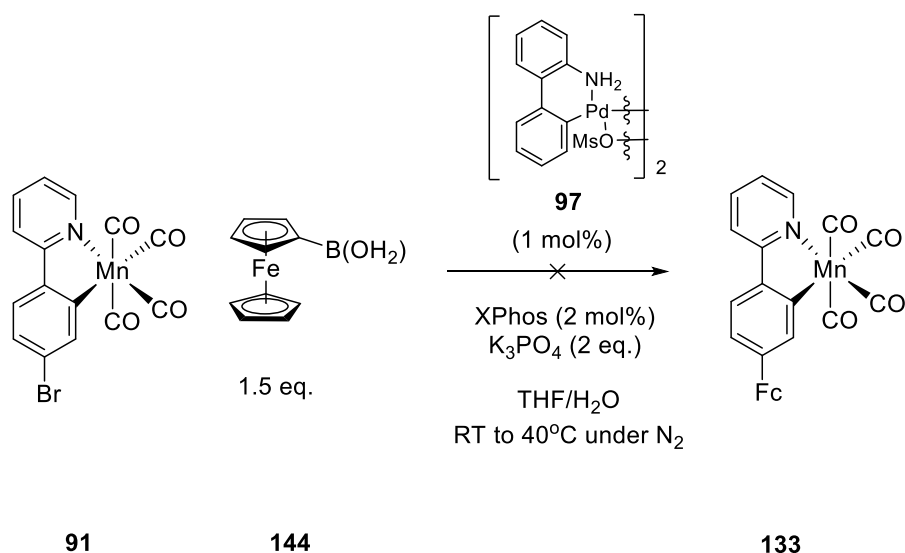
A Suzuki-Miyaura cross-coupling was performed on cyclometalated bromide **91** to test whether **132** could be synthesised directly. The initial reaction conditions developed for functionalisation with phenylboronic acid were applied to this reaction with ferroceneboronic acid (Scheme 45).¹⁸⁴



Scheme 45: Conditions for direct CORM functionalization with compound 133 unsuccessfully applied to ferroceneboronic acid.

Using the conditions shown in Scheme 45, no trace of product was detected by proton NMR or IR spectroscopy, nor by ESI mass spectrometry. Ferroceneboronic acid is a more challenging substrate for a Suzuki-Miyaura coupling than many arylboronic acids due to its increased susceptibility to electrophilic aromatic substitution.²⁸³ This leads to rapid protodeboronation, which causes ferroceneboronic acid to degrade to ferrocene – the rate of deboronation is at least 10^6 times faster for FcB(OH)_2 compared to PhB(OH)_2 .²⁸³ Ferrocene was observed in the crude ^1H NMR spectrum after the reaction in Scheme 45. Furthermore, the literature procedures for Suzuki-Miyaura cross-couplings with ferroceneboronic acid generally require temperatures of 70 °C or above.^{284–286} Such high temperatures are not feasible when using starting material **87**, as the ‘Mn-phenylpyridine’ moiety begins to degrade when heated above 70 °C, yielding the protonated ppy ligand.¹⁸⁴

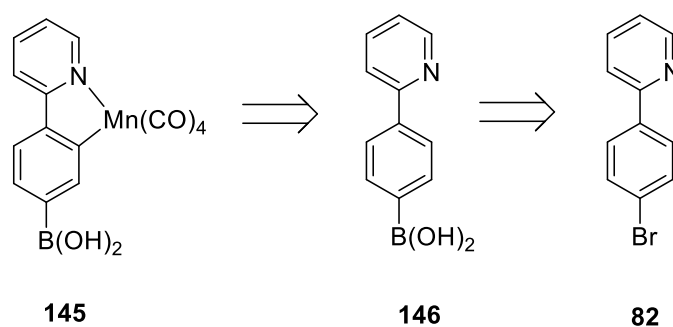
A low-temperature catalytic system to couple starting materials **91** and **144** was required. An excellent candidate for this is Buchwald’s dimeric palladium mesylate pre-catalyst **97** (Scheme 46).¹⁸⁵ This pre-catalyst is apparently activated more rapidly than traditional palladium precatalysts and its use has been demonstrated with substrates such as furanboronic acid that are prone to protodeboronation and traditionally considered difficult substrates. Crucially, the procedure requires only mild temperatures, typically proceeding in less than one hour at room temperature or 40 °C.¹⁸⁵ Buchwald’s conditions were therefore applied to the synthesis of **133**.



Scheme 46: The attempted application of palladium mesylate dimer pre-catalyst **97 to the synthesis of **133**.**

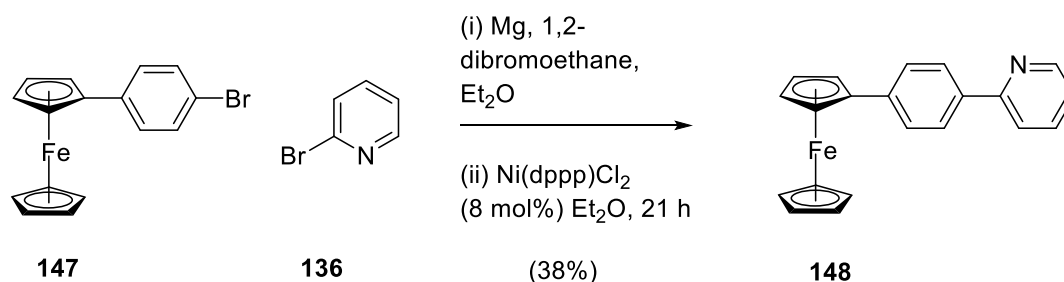
After 3 hours at 40°C, a faint new spot was visible on the TLC plate, matching the R_f of the free phenylpyridine ligand. Again, no product **133** could be identified using TLC, NMR or mass spectrometry. Indeed, experiments at both 40 and 60 °C with pre-catalyst **97** did not yield any conversion to product by ^1H NMR spectroscopy or ESI mass spectrometry, suggesting along with the nature of the successful reactions in the literature that a higher temperature is required for ferroceneboronic acid, above that at which the Mn carbonyl moiety degrades.

Inversion of the functional groups on the starting materials was considered for the Suzuki-Miyaura reaction. In this case, the CORM would be functionalised with a boronic acid (**144**) for coupling with bromoferrocene (Scheme 47). However, the Mn carbonyl moiety may not tolerate the acidic conditions used to unmask the boronic acid (see Section 3.4.3), so instead the boronic acid functional group would have to be carried through the cyclometalation, a further challenge in functional group tolerance. The synthesis of bromide **91** in good yield, in fewer steps, makes it a generally more useful building block for CORM functionalisation, when less challenging boronic acids are used. Although further catalysts and conditions tolerant to the $\text{Mn}(\text{CO})_4$ moiety could be screened, the main focus of this project was the synthesis of the target CORM.



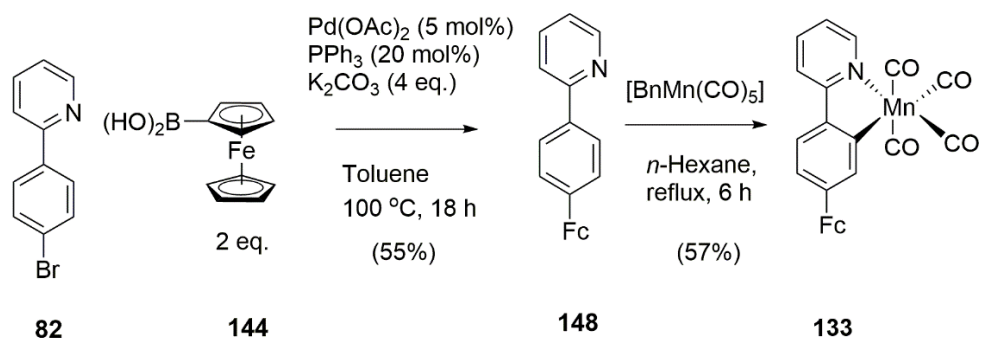
Scheme 47: Possible retrosynthesis for a boronic acid CORM suitable for Suzuki-Miyaura couplings.

As a result, the more straightforward synthetic route of preparing protonated ligand **148** and then cyclometalating was attempted. This removes the temperature constraints in the Suzuki-Miyaura cross-coupling as the Mn centre is installed after the cross-coupling. Compound **148** has been previously synthesised using a Grignard reagent in a modest yield of 38%²⁸⁷ (Scheme 48) with starting material **147** accessible by Suzuki-Miyaura coupling of 4-bromophenylboronic acid with iodoferrocene.²⁸⁸



Scheme 48: Previous synthesis of protonated ppy ligand 148 reported in the literature.²⁸⁷

An improvement in the yield of compound **148** was achieved using a Suzuki-Miyaura coupling of ppy derivative **82** and ferroceneboronic acid **144** to afford the product in a reasonable 55% yield (Scheme 49). The conditions used were based on previous Suzuki couplings of ferroceneboronic acid with an aryl bromide.²⁸⁹ Further optimisation of this reaction could be carried out by a screening of catalyst, solvent and base combinations, and microwave heating could also be employed to decrease the reaction time. However, the reaction provided sufficient product for the subsequent cyclometalation.



Scheme 49: Synthesis of CORM 133.

The characteristic four strong metal carbonyl stretching bands at 2074, 1990, 1975, 1931 cm^{-1} in the infrared spectrum of **133** in CH_2Cl_2 solution indicated that the synthesis was successful (a spectrum is shown in Section 3.3.1). The metal carbonyl stretching band positions are the same as for complex **132** within the 2 cm^{-1} spectrometer resolution. Proton NMR spectra (Figure 65) also confirmed that the cyclometalation reaction had taken place. Comparison of the spectra of protonated ligand **148** with cyclometalated complex **133** confirms the deprotonation and the desymmetrisation that takes place upon cyclometalation. The two sets of two protons on the phenyl ring in compound **148** that formed a pair of doublets were lost upon cyclometalation, giving three separate resonances. There was also a small shift in the ferrocenyl protons upon installation of the Mn tetracarbonyl moiety,

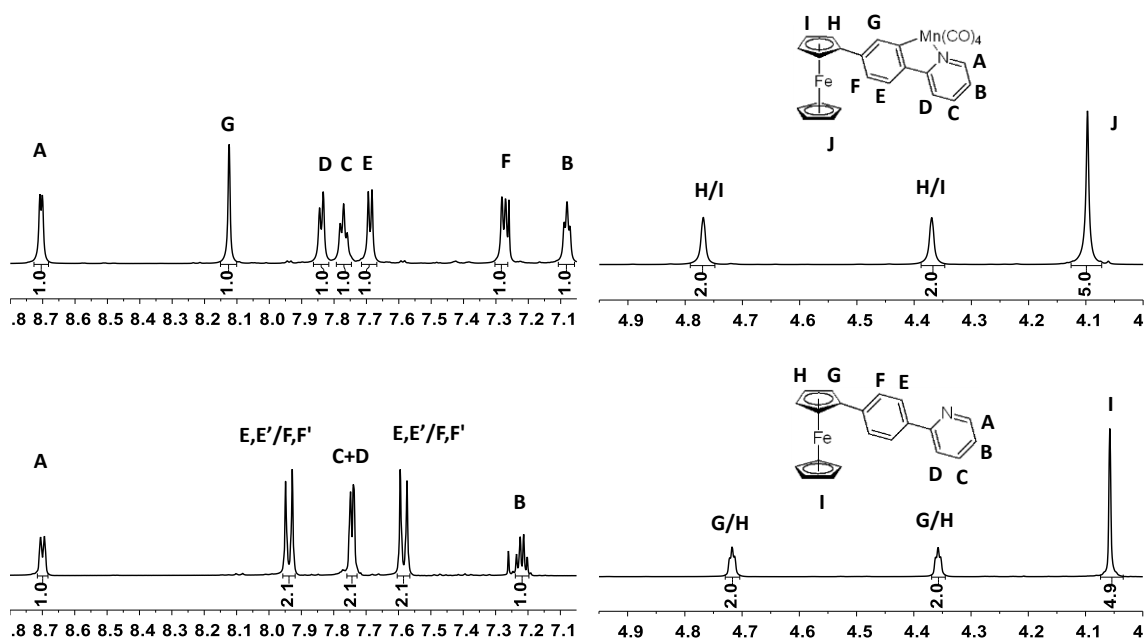


Figure 65: Stack of 700 MHz NMR of complex **133 (top) and protonated ligand **148** (bottom) recorded in CDCl_3 at 298 K.**

Single crystals of protonated ligand **148** and complex **133** were grown enabling X-ray structures to be obtained (Figure 66 and Figure 67).

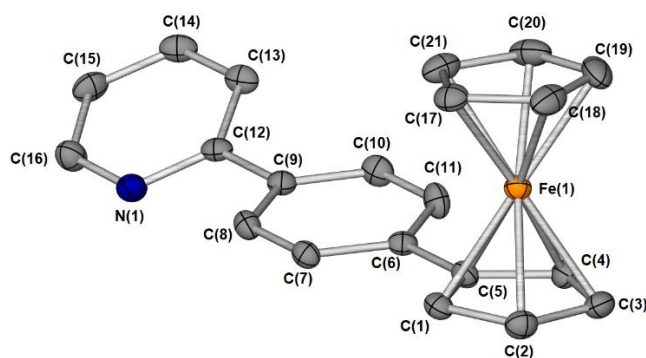


Figure 66: X-ray crystal structure of protonated ligand 148 with hydrogen atoms omitted for clarity. Atoms are displayed as thermal ellipsoids at 50% probability. Selected bond lengths (Å): C(9)-C(12) = 1.485(5), C(5)-C(6) = 1.472(5), C(16)-N(1) = 1.366(5), C(7)-C(8) = 1.383(5), C(3)-C(4) = 1.421(5), C(1)-Fe(1) = 2.037(4) Selected bond angles (°): C(6)-C(5)-C(1) = 124.0(3), N(1)-C(12)-C(9) = 116.8(3) Selected torsion angles (°): C(8)-C(9)-C(12)-N(1) = 21.6(5), C(1)-C(5)-C(6)-C(7) = 8.9(6).

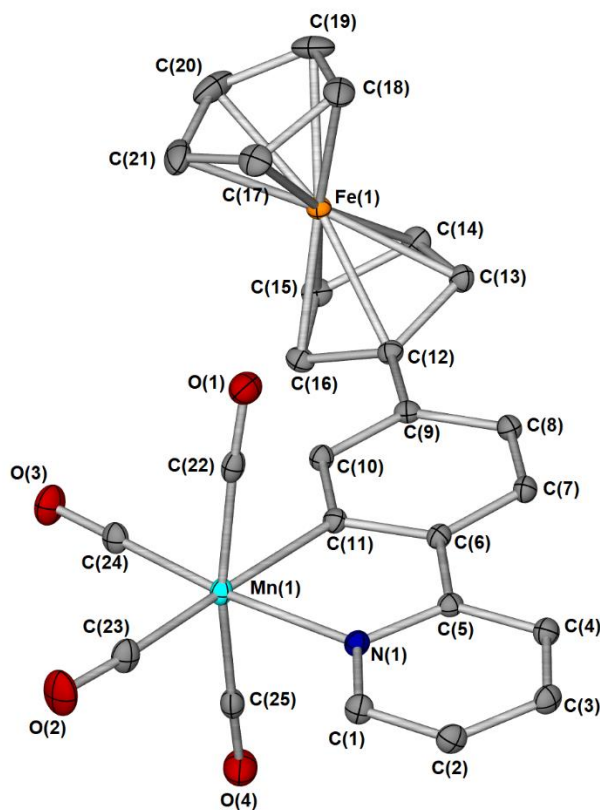
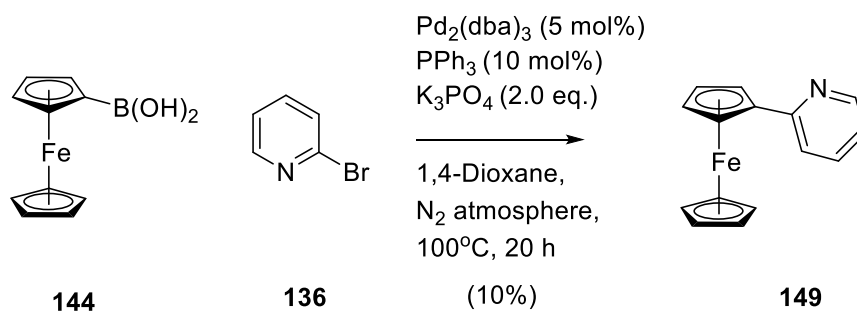


Figure 67: An X-ray crystal structure of compound 133 with hydrogen atoms omitted for clarity. Atoms are displayed as thermal ellipsoids at 50% probability. Selected bond lengths (Å): C(11)-Mn(1) = 2.0538(13), C(22)-Mn(1) = 1.8622(15), C(23)-Mn(1) = 1.8344(14), C(24)-Mn(1) = 1.8048(14), C(25)-Mn(1) = 1.8541(15), N(1)-Mn(1) = 2.0694(12) Selected bond angles (°): C(11)-Mn(1)-N(1) = 79.83(5), C(24)-Mn(1)-N(1) = 172.14(5), C(23)-Mn(1)-C(11) = 176.65(6), C(25)-Mn(1)-C(22) = 167.63(6), C(23)-Mn(1)-N(1) = 97.07(6), C(24)-Mn(1)-C(23) = 90.79(6). Selected torsion angles (°): N(1)-C(5)-C(6)-C(11) = 0.49(17), C(10)-C(9)-C(12)-C(13) = 20.3(2).

As with complex **132**, there is a slight distortion of the octahedral geometry at the Mn due to the rigid bidentate ppy ligand as is common for Mn(I) ppy complexes. The torsion angle between the phenyl and pyridyl rings changes upon cyclometalation, from $21.6(5)^\circ$ in protonated ligand **148** to $0.49(17)^\circ$ in complex **133** reflecting the requirement for a more planar ring system in order for ppy to coordinate to the metal. This observation is inverted in the torsion angle between the phenyl and ferrocenyl Cp ring: in **148** the two rings are nearly planar with a torsion angle of $6.7(6)^\circ$ but upon cyclometalation this increases to $20.3(2)^\circ$.

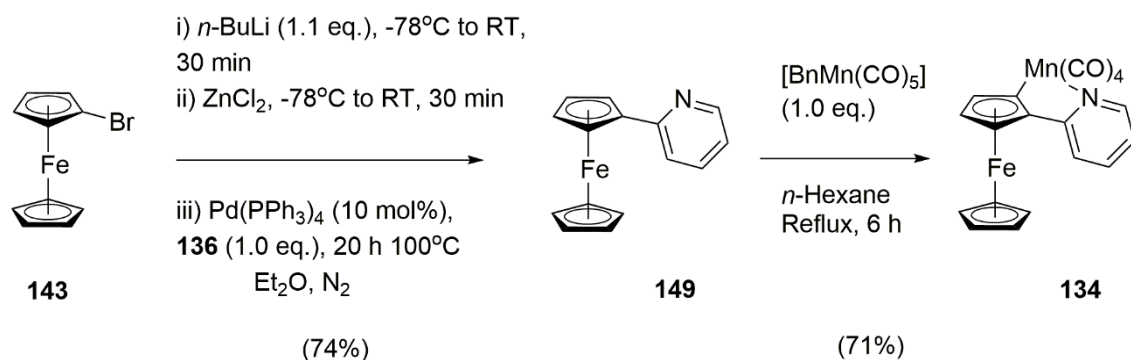
3.2.3 Synthesis of **134**

Target complex **134** exhibits planar chirality and was synthesised as a racemate. The conditions in this Section were developed by Samuel Andrew, an MChem student, under my mentorship.²⁹⁰ The synthetic route to complex **134** requires cyclometallation of protonated ligand **149**. Initial attempts so synthesise **134** involved a Suzuki-Miyaura cross-coupling (Scheme 50).



Scheme 50: Initial synthesis of protonated ligand **134 via a Suzuki-Miyaura reaction.**

The poor yield of this reaction was again attributed to protodeboronation taking place during the reaction; the crude NMR spectrum in CDCl_3 revealed an intense singlet at 4.15 ppm corresponding to ferrocene, which was not present in the boronic acid starting material spectrum. As a result of this, an alternative synthetic route was employed involving a Negishi coupling. Rather than rely on the use of boronic acid **144**, Negishi couplings utilise a zincated intermediate that can be prepared from bromoferrocene (Scheme 51).



Scheme 51: Synthesis of protonated ligand **149 via a Negishi coupling followed by cyclometallation with [BnMn(CO)₅].**

The Negishi coupling afforded 2-pyridylferrocene, **149**, in good yield. The subsequent cyclometallation to produce target **134** also proceeded in good yield, despite the deprotonation of a cyclopentadienyl ring in this reaction compared to a phenyl ring in other cases (Figure 68).

A crystal structure of complex **134** could not be obtained as the complex degraded over time to produce protonated ligand **149**. The NMR spectra of precursor **149** and complex **134** are shown in Figure 68. The NMR spectra show only small changes in chemical shift to the protons on the pyridyl ring, but more diagnostic of a successful reaction is the desymmetrisation of the Cp ring upon cyclometallation. The two sets of two protons in starting material **149** were replaced by three different chemical environments in **134** confirming that the expected substitution pattern had been achieved.

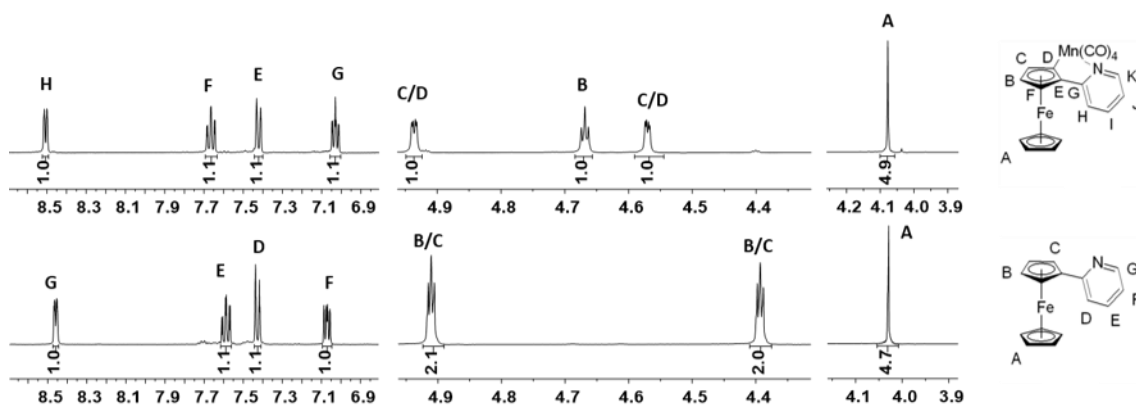


Figure 68: Stack of 700 MHz NMR spectra of complex **134 (top) and protonated ligand **149** (bottom) in CD₂Cl₂ at 298 K.**

The infrared spectrum of complex **134** (see Section 3.3.1) in the metal carbonyl region showed bands at 1932, 1976, 1988 and 2077 cm⁻¹. The positions and relative intensities of the bands are similar to the ppy complexes, confirming that cyclometallation took place to afford complex **134**.

3.3 Electrochemistry of Complexes 132-134

An electrochemical study was carried out to understand the redox properties of compounds **132-134** and compare them to their corresponding ppy or fcpy protonated ligands. This study also provides guidance for spectroelectrochemical experiments, where structural information will be elucidated under potential control.

As all compounds were readily soluble in CH_2Cl_2 ; this solvent was selected for the first electrochemical experiments. The electrolyte was present in relatively high concentration (1 M) during the experiment because of the high solution resistance of CH_2Cl_2 .^{291,292} This causes two undesirable effects. Firstly, it increases the size of the Ohmic potential drop – the change in potential caused by a current flowing through the cell. Although it is possible to correct for this,^{291,293} using additional electrolyte can avoid this. Secondly, it increases the peak separation in cyclic voltammograms away from the theoretical peak separation for a reversible couple of $59/n$ mV (where n is the number of electrons transferred).²⁹³ This can give the illusion of slow interfacial electron transfer when in fact this is not the case. Both the above effects were minimised by using a high concentration of electrolyte. Blank voltammograms were recorded with solvent and electrolyte to verify that the electrolyte concentration did not cause any artifacts in the baseline.

Cyclic voltammetry was used to establish that all compounds displayed a reversible one-electron redox couple based on oxidation of the ferrocenyl moiety. The midpoint potential, $E_{1/2}$, provides an estimate of the redox potential of the compound. An example with compound **132** is given in Figure 69.

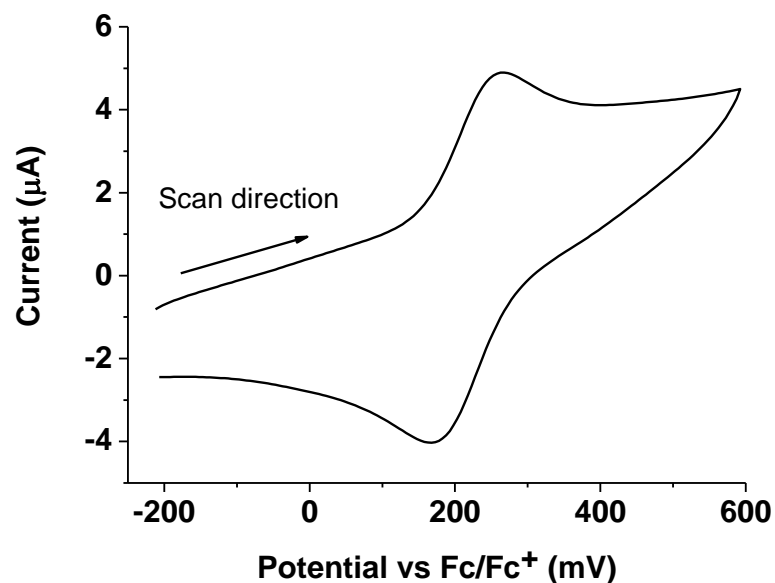


Figure 69: Cyclic voltammogram of complex 132. Scan rate: 100 mV s^{-1} , solvent: CH_2Cl_2 , electrolyte: 1 M tetra *n*-butylammonium hexafluorophosphate, analyte concentration: 5 mM .

The redox potential was measured against a silver pseudo-reference electrode, which was calibrated using ferrocene as an internal standard (Figure 70). When the redox potential of the complex to be measured was too similar to the Fc/Fc^+ couple, the acetylferrocene/acetylferricenium couple was used ($+270 \text{ mV vs Fc}/\text{Fc}^+$).²⁹⁴ The potential scale has been set such that the midpoint potential of the Fc/Fc^+ couple is at 0 V .

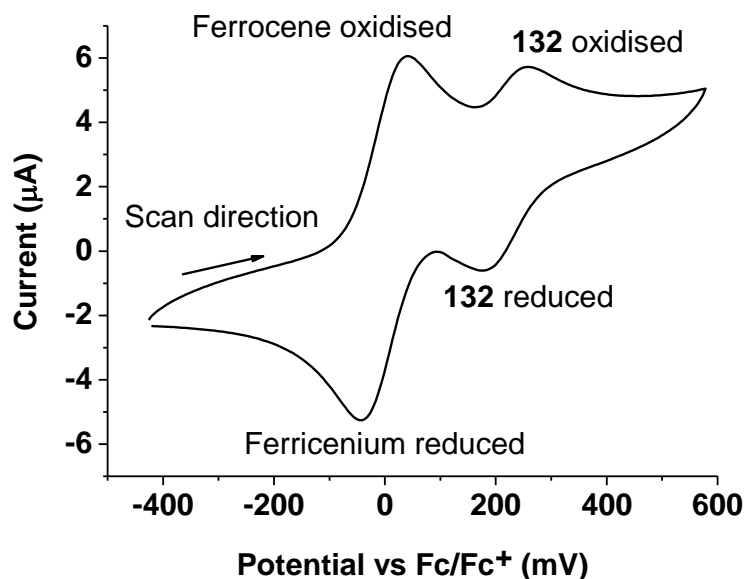


Figure 70: Cyclic voltammogram of a CH_2Cl_2 solution of 5 mM of both compound **132** and ferrocene. The electrolyte concentration was 1 M tetra *n*-butylammonium hexafluorophosphate and the scan rate was 100 mV s^{-1} .

The potential window from -1 V to +600 mV vs Fc/Fc⁺ was investigated and only a single redox couple was found within this range, corresponding to the ferrocenyl group in each compound. No reaction of the Mn(I) centre was observed within the potential window of the experiments. Recent work on Mn(I) tricarbonyl complexes has shown that an irreversible oxidation can occur above +1 V vs Fc/Fc⁺ in these complexes.²⁹⁵ Addition of a fourth tricarbonyl ligand is likely to increase this potential even further in complex **132** due to the additional π back-donation of the CO ligand stabilising the lower oxidation state of the metal.²⁵⁸ Such activity is unlikely to have a therapeutic relevance because of the extremely high redox potential required to effect the oxidation.

Although the peak separation between the oxidative and reductive peaks, ΔE , of complex **132** was 74 mV compared to the theoretical value of 59 mV, the peak separation for the Fc/Fc⁺ couple internal standard was 80 mV. Since the Fc/Fc⁺ couple is known to be a fully reversible one-electron couple, the behaviour of **132** was deduced to also be a one-electron reversible couple. Repeated scans showed the identical redox behaviour to the first scan.

An additional measurement of the reversibility was obtained by plotting the ‘current function’, $\frac{i}{\sqrt{v}}$ where i is peak current and v is the scan rate. For a reversible redox couple in solution, the current function should remain constant as the scan rate is changed.²⁹³ The result for compound **132** is shown in Table 10. The current function remains roughly constant across this range of scan rates, again supporting the reversibility of this redox couple.

Table 10: How the current function varies with scan rate for complex 132. All solutions contained 1 mM 132 and 1 M electrolyte in CH₂Cl₂.

Scan rate (mV s ⁻¹)	50	100	150	200
$\frac{i}{\sqrt{v}}$ (μA s ^{1/2} mV ^{-1/2})	0.29	0.28	0.29	0.30

Electrochemical measurements were extended to complexes **133** and **134** as well as protonated ligands **148** and **149**. The peak positions and separations are shown in Table 11.

Table 11: Summary of cyclic voltammetry data.

Compound	E_{ox} (mV, vs Fc/Fc ⁺)	E_{red} (mV, vs Fc/Fc ⁺)	ΔE (mV)	$E_{1/2}$ (mV, vs Fc/Fc ⁺)	i_a/i_c
132	+257	+183	74	+220	1.05
133	+90	-27	117	+31	0.94
148 (ligand)	+105	-10	115	+48	1.03
134	-82	-194	112	-138	1.04
149 (ligand)	+125	+27	98	+76	0.97

The data show that the peak separations between the anodic and cathodic waves, ΔE , are consistently higher than the theoretical maximum value of 59 mV due to solution resistance; this was verified by the similar peak separation of the ferrocene internal standard. The ratio of the anodic and cathodic peak currents, $\frac{i_a}{i_c}$, was close to one in all cases, confirming the reversibility of the oxidations in all of the compounds tested.

Complex **132** is rather difficult to oxidise in comparison to ferrocene and the other ferrocene-containing complexes in this work. Ferrocenyl triazoles appear to be electron-deficient according to the literature: the redox potentials of other triazole-conjugated ferrocenes are above 200 mV vs Fc/Fc⁺.²⁷⁹ Table 11 also shows the effect of cyclometalation upon the redox potential of the ferrocene when comparing complexes **133** and **134** with their respective protonated ligands **148** and **149**. Cyclometalation causes the redox potential of the ferrocenyl moiety to decrease, making oxidation more favourable. This is consistent with the coordination to the Mn(I) tetracarbonyl moiety having an overall electron-donating effect upon the ligand. For complex **134**, where a Cp ring of the ferrocene forms part of the first coordination sphere of the Mn, the effect is much more dramatic than for the distantly conjugated ferrocene in complex **132**. This illustrates how changes in redox behaviour in these complexes could be used to sense changes in the environment of the

ligand during CO release, although this would be a much more powerful analytical technique if the CO release were itself redox-triggered. Future work could involve irradiating the CORM in solution during repeated cyclic voltammetry scans to observe CORM degradation.

3.3.1 Infrared Spectroelectrochemistry

The response of the infrared stretches of the carbonyl stretches to oxidation of the ferrocenyl moiety in complexes **132-134** were assessed by infrared spectroelectrochemistry. The results illustrate the importance of the linker length in determining the extent of communication between the iron and manganese centres.

As with the electrochemistry, complexes **132-134** were studied in dichloromethane due to their high solubility in this solvent. For each complex, an infrared initial spectrum was recorded at the Open Circuit Potential (OCP). An oxidising potential step to +1 V versus the silver wire *pseudo*-reference electrode was then applied and infrared spectra were recorded at 30 second intervals until no further change was observed (600 seconds). A reducing potential step to -500 mV versus the silver wire *pseudo*-reference electrode was then applied and infrared spectra were again recorded every 30 seconds until no further change was observed (600 seconds). Key spectra for each compound are shown in panels A-C of Figure 71, and panel D provides an example of successive spectra after a potential step. The band positions of the species depicted in Figure 71 are summarised in Table 12.

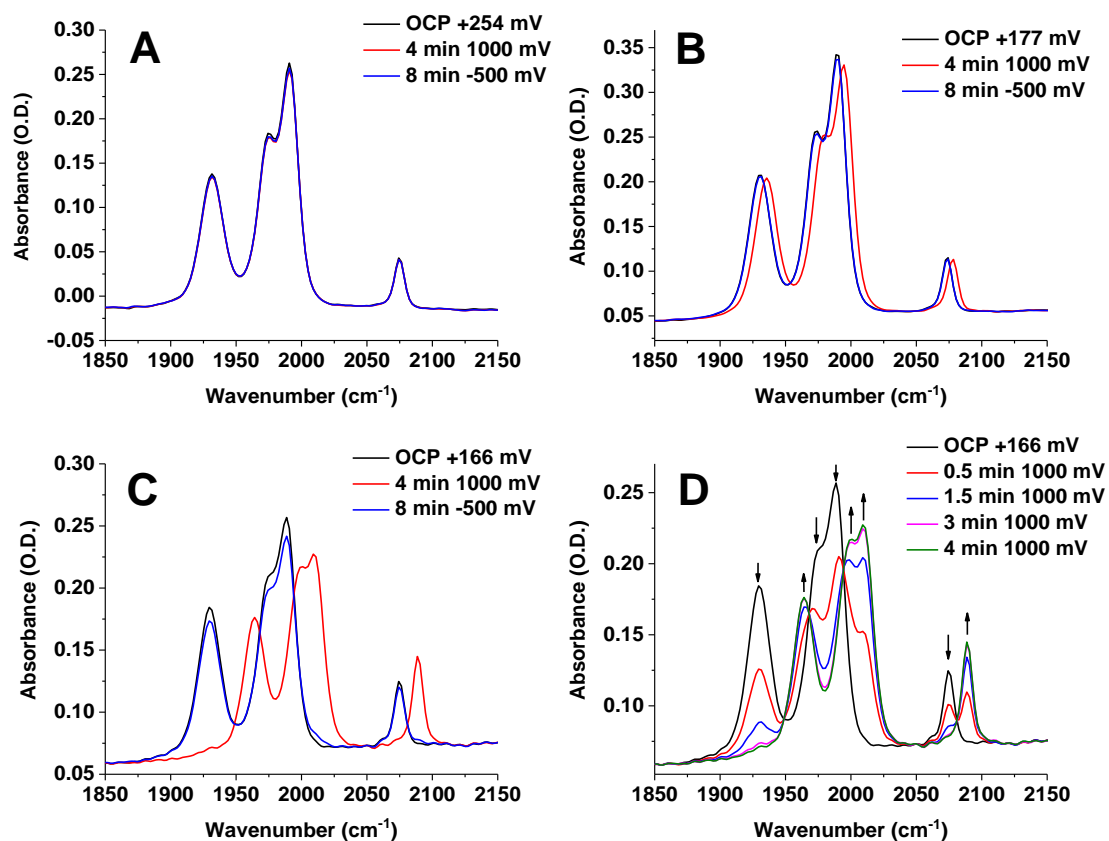


Figure 71: Infrared spectroelectrochemistry of complexes 132-134 (panels A–C, respectively). Initial spectra before the potential steps are shown at the Open Circuit Potential (OCP). Experiments were performed in CH₂Cl₂ at a concentration of 5.0 mM in the presence of 1.0 M tetra *n*-butylammonium hexafluorophosphate as the electrolyte. All spectra are subject to a single point baseline correction at 2050 cm⁻¹. (D) Selected spectra from the oxidation step of panel C showing the isosbestic points upon oxidation.

Table 12: Summary of the infrared stretching band positions of the neutral and cationic ferrocenyl Mn complexes studied by infrared spectroelectrochemistry.

Compound	$\nu(\text{CO})$ (1) (cm ⁻¹) B₂	$\nu(\text{CO})$ (2) (cm ⁻¹) A₁	$\nu(\text{CO})$ (3) (cm ⁻¹) B₁	$\nu(\text{CO})$ (4) (cm ⁻¹) A₁
132	1931	1977	1991	2076
[132] ⁺	1931	1977	1991	2076
133	1931	1975	1990	2074
[133] ⁺	1936	1980	1995	2078
134	1932	1976	1988	2077
[134] ⁺	1964	2000	2010	2089

Triazole **132** (Table 12, bottom) shows no response of the carbonyls to oxidation. Complex **133** (Table 12, centre) shows a slight increase in wavenumber of the carbonyls (approximately 5 cm⁻¹), Complex **134** (Table 12, top) showed a significant shift of approximately 30 cm⁻¹ in the metal carbonyl stretches for all four peaks when an oxidizing potential is applied. The increase in stretching frequency is consistent with a removal of electron density from the manganese, resulting weaker pi-backbonding to the carbonyl groups. The increase in the infrared band positions upon the oxidation of complexes **132-134** is tabulated for each vibrational mode in Table 13.

Table 13: The increase in carbonyl stretching wavenumber upon formation of the cations of 132-134, relative to the neutral molecule, derived from the spectroelectrochemical experiment in Figure 71.

Compound	$\nu(\text{CO})$ (1) (cm ⁻¹) B₂	$\nu(\text{CO})$ (2) (cm ⁻¹) A₁	$\nu(\text{CO})$ (3) (cm ⁻¹) B₁	$\nu(\text{CO})$ (4) (cm ⁻¹) A₁
[132] ⁺	0	0	0	0
[133] ⁺	5	5	5	4
[134] ⁺	32	24	22	12

The Table shows that for complex **134** and its cation, the shift in the stretching wavenumber is strongly dependent on the nature of the vibrational mode. It is noteworthy that the band that shows the greatest shift in wavenumber is the B₂ band, the asymmetric stretch of the two carbonyls in the plane of the ppy ligand, whereas the smallest shift in wavenumber is exhibited by the high-wavenumber A₁ band involving the mutually *trans* carbonyl ligands, while the other two modes showed an intermediate shift. This suggests that oxidation may have a greater electron-withdrawing effect upon the two carbonyl ligands in the plane of the ppy ligand. The DFT calculations shown for the parent ppy complex **88** in Figure 31: DFT-optimised structure and calculated molecular orbitals for [Mn(ppy)(CO)₄] (carbon grey, hydrogen white, manganese pink, nitrogen blue, oxygen red). Isosurfaces shown at 0.5 e Å⁻³. Figure 31 (as discussed in Section 2.2.2) show that the HOMO of **88** is based largely on the ppy ligand, in particular on the phenyl ring. Oxidation therefore removes electron density from the ppy ligand, which would weaken π-backbonding to the CO ligands in the plane of the ppy ligand, particularly the CO ligand *trans* to the electron-rich phenyl ring, causing the infrared stretching wavenumber to increase more than for other modes. Although in the case of complex **134** a ferrocenyl(pyridyl) ligand is present rather than ppy, calculations on **134** confirmed an analogous structure of the HOMO to that of **88**, with much of the electron density residing on the ferrocenyl moiety of the ligand (the calculations and discussion are presented in Section 3.4.3).

The trend observed from complexes **132-134** is consistent with a through-bond communication between the two metal centres and suggests that redox-active ligands should be incorporated into

the first coordination sphere of the manganese carbonyl for the redox behaviour to have a significant effect upon the reactivity of the Mn centre. Consistent with the reversibility of this process in the electrochemical results, the spectroelectrochemistry shows that the oxidized ferricenium cation of each complex can be repeatedly oxidised and then reduced back to the neutral form. The presence of numerous isosbestic points in the conversion between the oxidised and reduced species also helps to support the conclusion that no other species are present during the experiment. This means that these compounds are unlikely to be useful for redox-triggered CO release, but their redox-active groups may provide a secondary application as a mechanistic reporter group or as a way of studying the effect of a redox event adjacent to a neighbouring carbonyl group.

3.4 Photochemistry and CO Release

3.4.1 Monitoring Photolysis By UV-Visible Spectroscopy

The photochemical CO release properties of complexes **132-134** were also tested for comparison to the previously-studied Mn(I) tetracarbonyl complexes containing a ppy ligand.¹⁸⁴

Compound **132** was assessed for photochemical degradation using 400 nm light. This wavelength, on the boundary of the visible spectrum, is on the tail of the metal-to-ligand charge transfer band observed in $[\text{Mn}(\text{ppy})(\text{CO})_4]$. Photochemical degradation and CO release at 400 nm has been demonstrated for other manganese(I) tetracarbonyl ppy complexes, as discussed in Chapter 2. The UV-visible absorption spectrum of complex **132** is shown in Figure 72 and closely resembles that of $[\text{Mn}(\text{ppy})(\text{CO})_4]$ (see Section 2.2.1). No band associated with the ferrocenyl group of **132** was observed in the visible region; the lowest energy band tails off at 400 nm. However, complex **133**, where the ferrocene is conjugated to a phenyl ring rather than a triazole ring, does display the expected low-energy band for ferrocene (see Appendix 3).

Irradiation was performed using a 400 nm LED embedded within a cuvette lid using a power supply developed by the workshops in the chemistry department at the University of York. Further details are given in the Experimental section of this thesis. Irradiation was performed in a cycle of 2 min on, 3 min off, and UV-visible spectra were recorded every 5 min, with the LED off, to monitor degradation. A typical experiment is shown below (Figure 72), where the power used was 2.4 W.

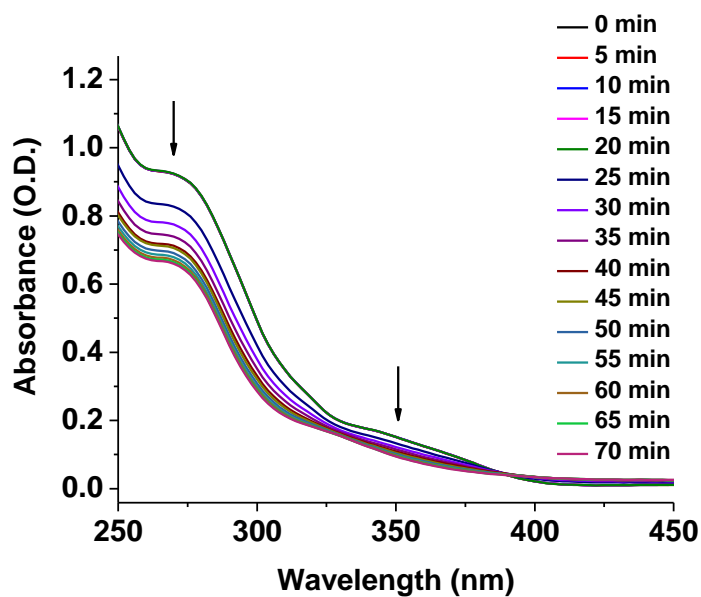


Figure 72: UV-visible monitoring of the degradation of compound 132 in CH₂Cl₂ when irradiated with 400 nm light at a power of 2.4 W, beginning at 23 min. The final three spectra were the result of 20 W irradiation. The concentration of 132 was 33 μ M. Arrows show the changes in the bands over time.

The first five spectra were recorded before any irradiation and are all coincident, proving the short-term stability of **132** in the dark. Upon irradiation, a clear change in the spectrum is seen as the absorbance of the peak around 270 nm decreases. The absorbance at 270 nm was monitored over time. Below (Figure 73) is a comparison of 2.4 and 6.0 W power 400 nm irradiation. A significantly faster degradation is seen when the power is increased.

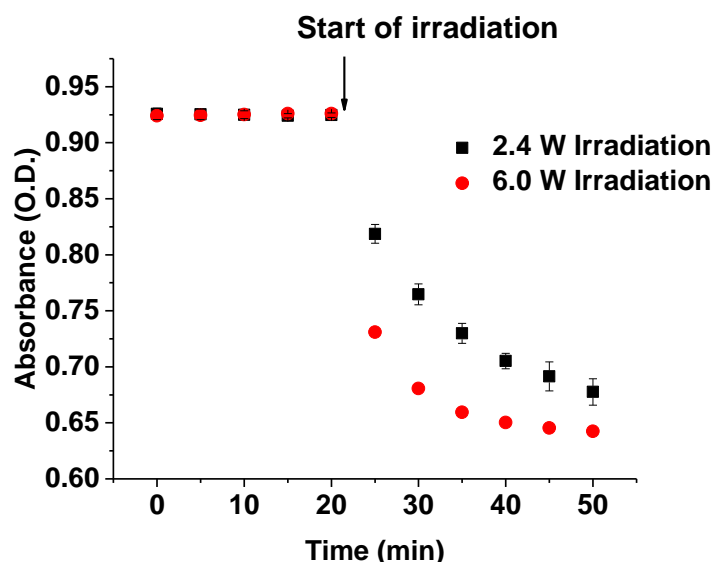


Figure 73: Comparison of 2.4 and 6.0 W irradiation of a solution of 33 μM compound 132 at 400 nm. Error bars are shown on the 2.4 W run. Three repeats were performed – the median data set was plotted with error bars corresponding to one standard deviation.

Three repeats were performed at 2.4 W, which showed comparable results. A control experiment with a solution stored in the dark showed the same absorbance as the first five spectra after the end of the experiment. The degradation appears to tail off well before the absorbance reaches zero; the degradation product likely has a similar spectrum to the starting material. Confirmation of this was obtained by irradiating at a high power of 20 W for the final three cycles – further degradation was minimal in the following UV-vis spectra suggesting the photochemical degradation was complete. A band at around 270 nm appears to be retained in the photoproducts, although this is to be expected as the transition is assigned as a ppy ($\pi \rightarrow \pi^*$) transition. It was not possible to conclude whether the ppy ligand has been lost from the metal on this information alone.

The similarity of the spectra is unsurprising as the band at 270 nm is due to the phenylpyridine moiety.¹³⁰ The higher-wavelength metal-to-ligand charge transfer band might be used to monitor this process instead, but the absorbance is low at the concentration used. The ferrocene moiety absorbs in this region too, which may further complicate the use of this band. Regardless, a clear change in the absorbance spectrum is indicated upon irradiation, showing that a photochemical reaction takes place, and matching the degradation profile of structurally similar compounds.^{137, 130,159}

3.4.2 In situ Infrared Spectroscopic Studies of CORM Degradation

Photochemical degradation was also studied using *in situ* ATR-IR spectroscopy, to compare the results to studies on the continuous irradiation experiments in Chapter 2. It was also anticipated that the structural information from the infrared spectra could help to determine whether the

triazole moiety in complex **132** can coordinate to the manganese centre after axial CO dissociation. Initially, the behaviour of complexes **132** and **133** will be discussed. Experiments with complex **134** be then be reported in Section 3.4.3.

The results for complex **132** will be discussed first. A 365 nm LED was used continuously at a power of 6.0 W – a shorter wavelength was used compared to the 400 nm LED in the UV-visible study in Section 3.4.1. This wavelength was chosen as it is nearer to the centre of the CO-dissociative band of the Mn(I) tetracarbonyl ppy complexes, so this wavelength is expected to speed up the photolysis so that large quantities of photoproduct could be observed. The results for complex **132** irradiated in DMSO solution are shown in Figure 74 and Figure 75. The spectra shown are difference spectra against a spectrum recorded just before the start of the LED irradiation: no decomposition was observed in the dark for complex **132** over 30 minutes.

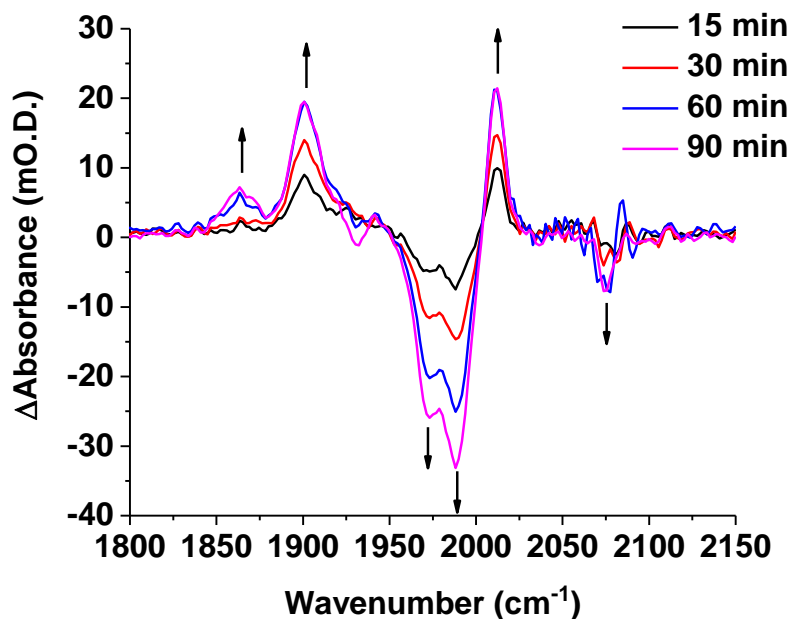


Figure 74: Selected *in situ* infrared spectra of a 12 mM DMSO solution of complex 132 showing the changes upon LED irradiation (6.0 W, 365 nm). The results are presented as difference spectra with reference to a spectrum recorded immediately before irradiation began. The resolution used was 2 cm⁻¹. The times given are the time since the irradiation began.

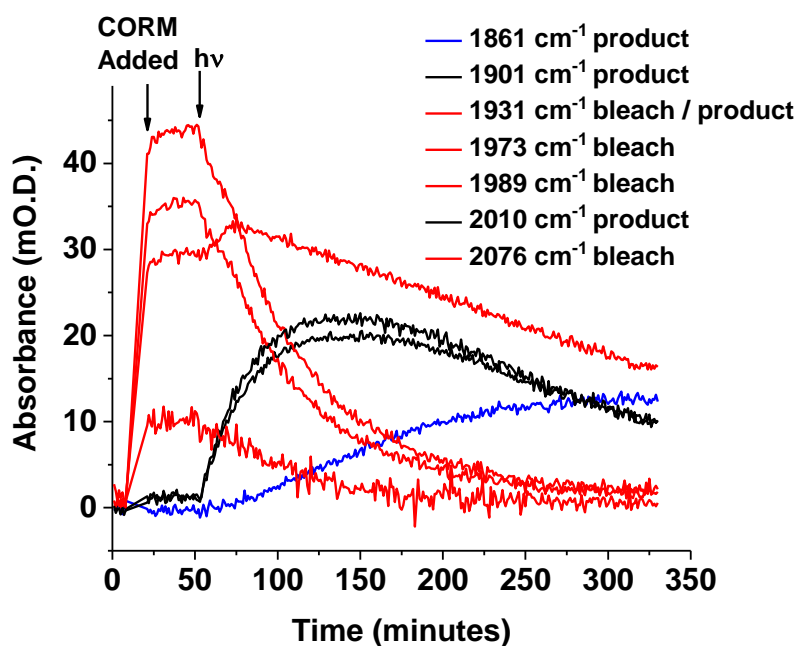


Figure 75: Peak heights of selected wavenumbers over the course of the irradiation experiment with 12 mM complex 132 in DMSO.

The spectra show that complex 132 displays very similar photochemical decomposition to [Mn(ppy)(CO)₄] (complex 88, Section 2.3.6). The complex was stable in the absence of irradiation for over 30 minutes. The only photoproduct visible after 15 minutes of irradiation was

a species with bands at 1901, 1931 (overlapping with a bleach), and 2010 cm^{-1} . This is essentially identical to the behaviour observed for **88** in Chapter 2, where the tricarbonyl photoproduct bands were observed at 1902, 1928 and 2013 cm^{-1} and were assigned to *facial* tricarbonyl dimer or cluster species. In later spectra, these three bands began to decay away and a small band at 1861 cm^{-1} slowly grew in, compared to a band that grew in at 1870 cm^{-1} for $[\text{Mn}(\text{ppy})(\text{CO})_4]$. The degradation pathway of substituted ppy complex **132** therefore appears to be the same as its parent complex, which could implicate the formation of tricarbonyl dimers or clusters in the degradation of these complexes.

Another photochemical *in situ* infrared degradation study was performed on complex **133**, also in DMSO. Selected spectra and a trace of peak heights over time are shown in Figure 76 and Figure 77 respectively. The results indicate that compound **133** has the same CO release mechanism as compounds **88** and **132** - the photoproduct bands appear to be the same in the three DMSO experiments. Therefore, the effect of any triazole coordination to the Mn centre was not observable on this timescale.

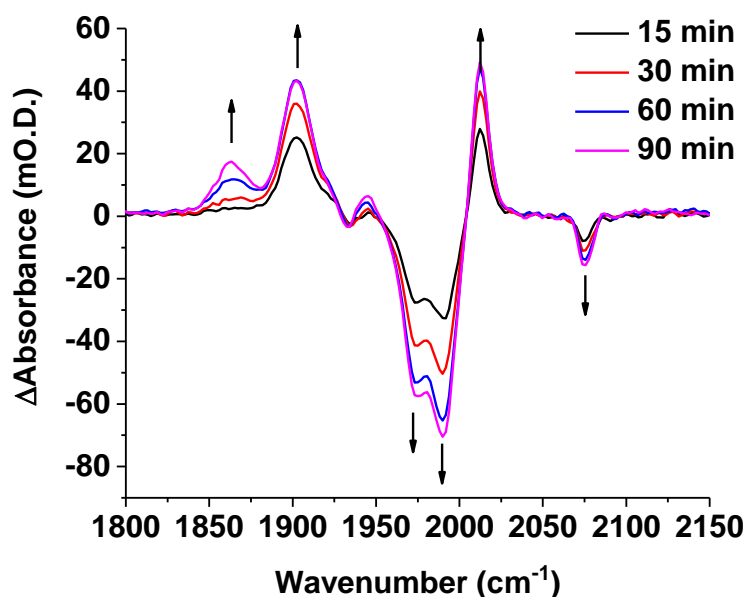


Figure 76: Selected *in situ* infrared spectra of a 20 mM DMSO solution of complex **133** showing the changes upon LED irradiation (6.0 W, 365 nm). The results are presented as difference spectra with reference to a spectrum recorded immediately before irradiation began. The resolution used was 2 cm^{-1} . The times given are the time since the irradiation began.

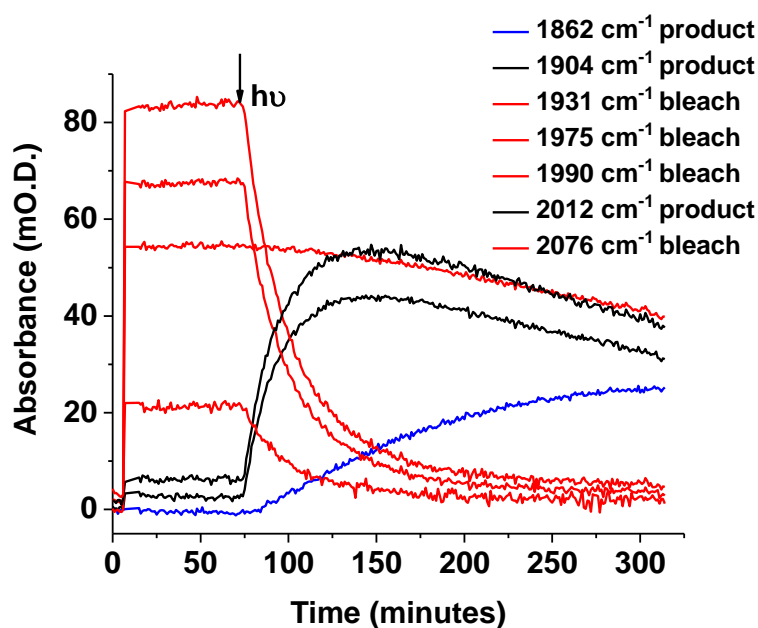


Figure 77: Peak heights of selected wavenumbers over the course of the irradiation experiment of 20 mM **133** in DMSO.

3.4.3 CO Release to Myoglobin

To directly verify that the photochemical degradation of the ferrocenyl complexes results in CO release, a UV-visible spectroscopic assay was performed with myoglobin (Mb). An example is shown with complex **133**. The CO release profile of the complexes was tested in the dark and upon irradiation with 400 nm light. When CO is released by a CORM, it binds to the haem group of deoxymyoglobin (deoxy-Mb), yielding carboxymyoglobin (Mb-CO). The distinct UV-visible spectra of deoxy-Mb and Mb-CO enable quantification of the CO lost (Figure 78).

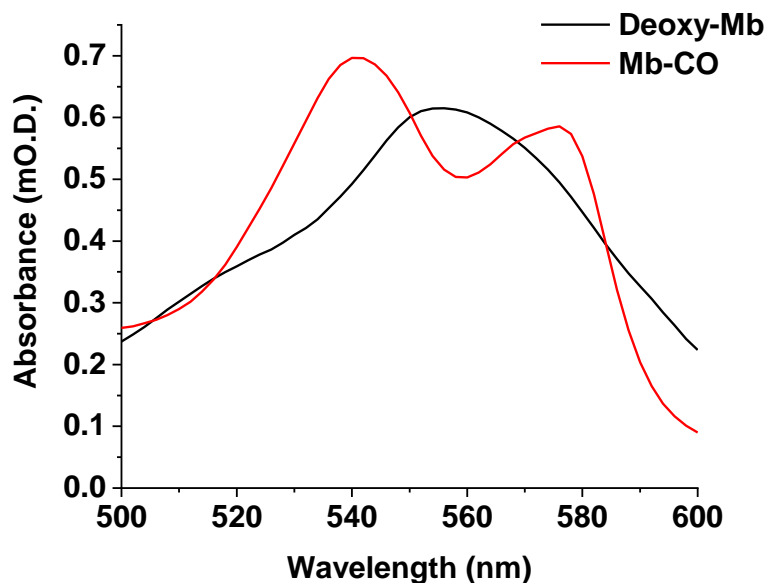


Figure 78: UV-visible spectra of standard samples of deoxy-Mb and Mb-CO.

When the compound was administered to the buffered deoxy-Mb solution in DMSO (to a final DMSO concentration of 0.5%), some precipitation of the complex occurred: the upwards translation of the deoxy-Mb spectrum in the presence of complex **133** is indicative of turbidity of the solution (Figure 79).

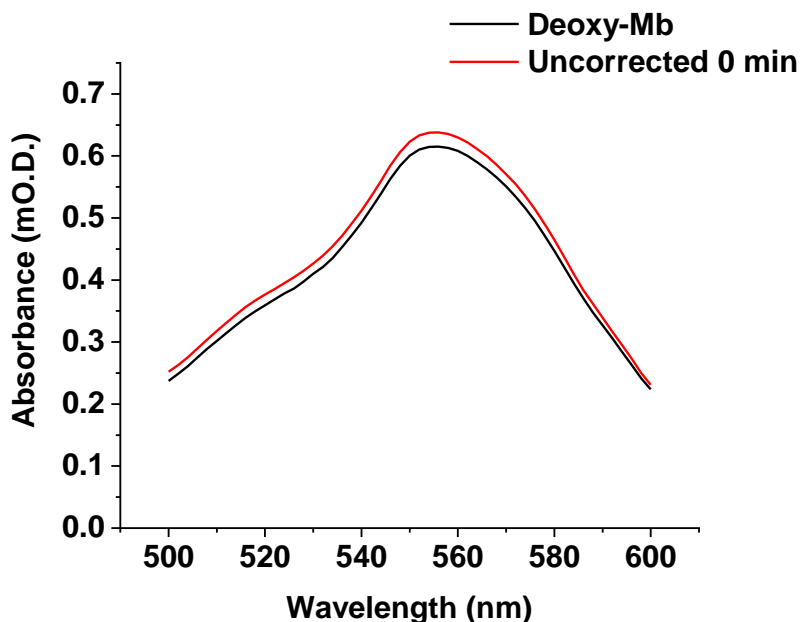


Figure 79: UV-visible standard spectrum of deoxy-Mb (black) compared to the spectrum at the start of Mb assay when complex **133 has been added to give a 40 μ M solution containing 0.5% DMSO (red).**

Relatively poor water solubility has also been observed for other substituted ppy tetracarbonyl CORMs - derivatisation to install ester or carboxylic acid groups has been used to address this.

Additionally, the 40 μM concentration of **133** used in this assay was selected to match the ~ 60 μM deoxy-Mb concentration, which is needed to give a sufficiently intense absorbance spectrum, rather than because 40 μM is proposed as a therapeutic concentration. For instance, concentrations of CORM-3 as low as 1 μM have been shown to completely inhibit growth of *Pseudomonas aeruginosa* cultures.¹⁰² A commonly-employed correction method, based on the isosbestic points of deoxy-Mb and Mb-CO, was applied to correct the spectra for CORM absorbance and scattering. A translation to match the spectra at the 510 nm isosbestic point was applied to correct for the turbidity (Figure 80).

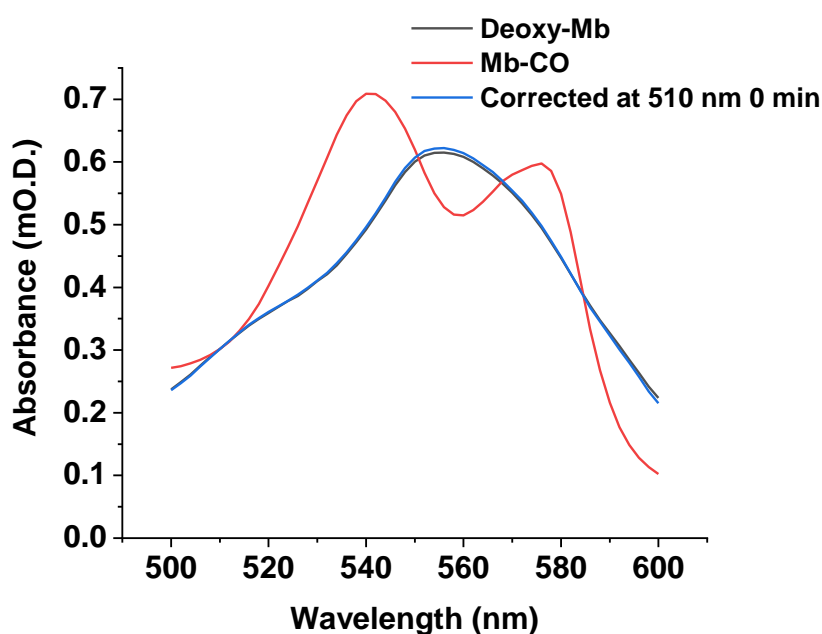


Figure 80: Standards and experimental spectra corrected based on the isosbestic point at 510 nm.

The corrected spectrum at 510 nm now appears similar to the deoxy-Mb standard, but the absorbance or scattering caused by complex **133** is not uniform across the wavelength range of 500-600 nm. As a result, a 'spectrum' for the dissolved complex and any scattering caused by precipitation can be extracted from the data by fitting the absorbances at the four isosbestic points (Figure 81).

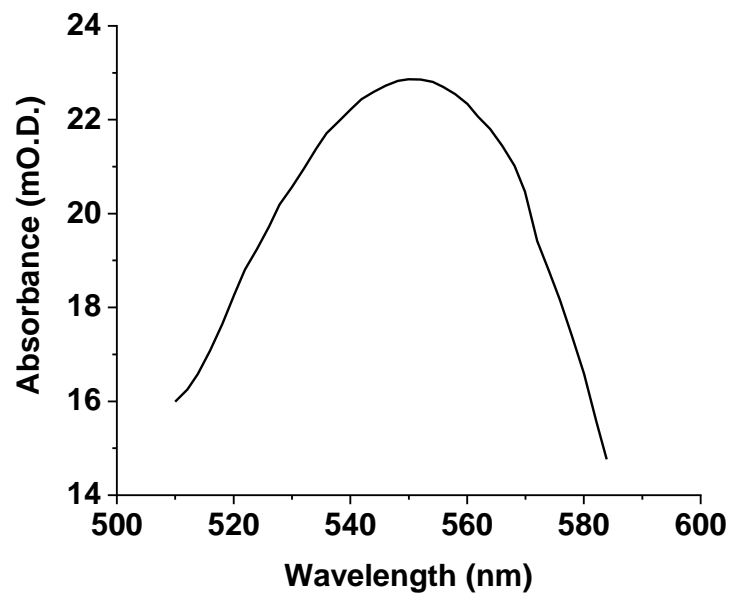


Figure 81: A spectrum due to CORM absorbance and scattering from precipitation, generated from the four isosbestic points of deoxy-Mb and Mb-CO.

Over time, the composition of the solution changes as a complex releases CO, and degradation products form. To account for the changes over time, the fitting process described must be performed on each spectrum individually so that a spectrum similar to that in Figure 81 is obtained from the raw data for each timepoint. Subtraction of this spectrum from the 510 nm corrected spectrum then results in the fully-corrected data (Figure 82).

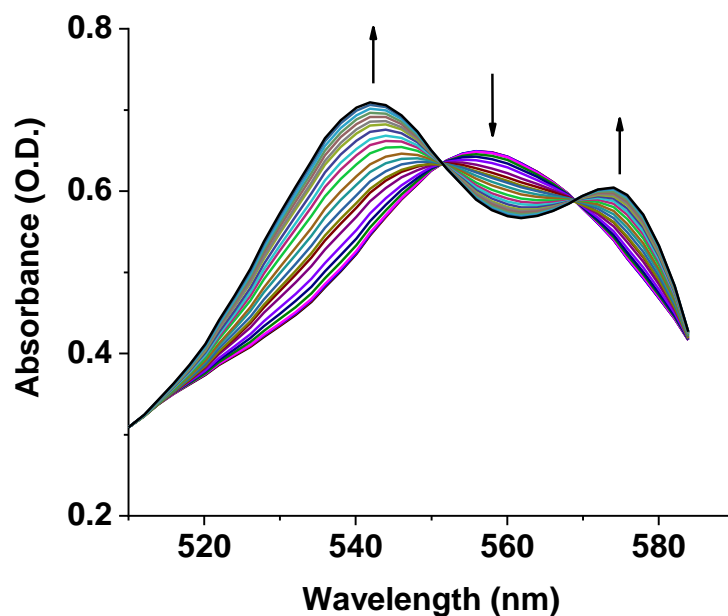


Figure 82: Experimental spectra after the isosbestic point correction for a Mb assay featuring irradiation of 40 μ M complex 133. Spectra recorded every 10 minutes.

The errors in the fitting can be estimated by generating spectra from the deoxy-Mb and Mb-CO standards for given deoxy-Mb and Mb-CO concentrations, then comparing them to the corrected spectra. An example is shown in Figure 83, showing that the generated spectra match the corrected ones well and that there is no systematic error across the wavelength range.

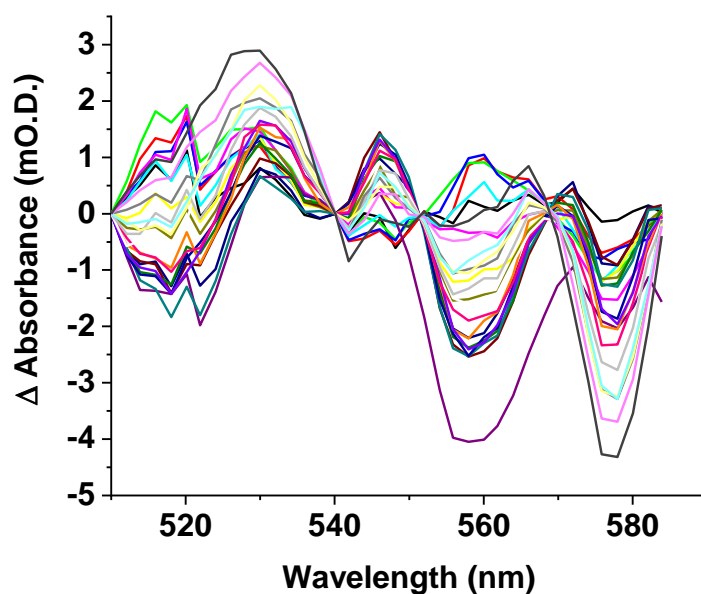


Figure 83: The error from the four-point correction of each experimental spectrum assessed by the difference between the corrected experimental spectrum and spectra of the appropriate concentration generated from the deoxy-Mb and Mb-CO standards.

Based on the change in absorbance at 540 nm throughout the experiment, the concentration of Mb-CO can be quantified (see Experimental Section for further details). For complex **133**, this leads to the CO release profile shown in Figure 84. Upon 400 nm LED irradiation of a 40 μ M solution of complex **133**, CO release was observed to take place. Irradiation took place inside the UV-visible spectrometer, with cycles of 2 minutes on, 3 minutes off to prevent the LED from heating the solution.

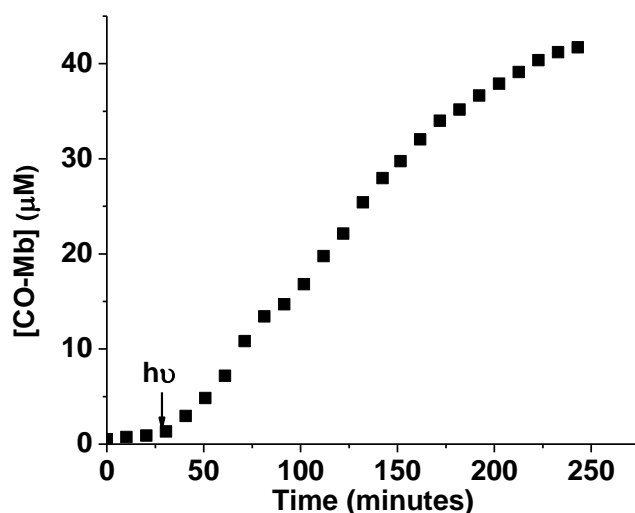


Figure 84: The release of CO to deoxy-Mb by a 40 μM solution of complex **133**. The experiment was run in the dark until irradiation with a 400 nm LED at a power of 5.0 W began where indicated. Irradiation was performed in cycles of 2 minutes on, 3 minutes off.

The spectrum shows that complex **133** behaves similarly to other Mn(I) tetracarbonyl ppy complexes by displaying stability towards buffered deoxy-Mb in the dark ($<1 \mu\text{M}$ Mb-CO after 25 min in the dark) and releasing CO to deoxy-Mb when irradiated with 400 nm light. The CO release was relatively slow compared to related ppy derivatives: the irradiation may have been hindered by the turbidity of the solution concentration of complex **133**. The assay was stopped after 4 hours before it went to completion, as degradation of the myoglobin and CO escape from the solution can cause problems beyond this point. Despite its poor solubility, complex **133** has been demonstrated as a photoCORM similar to other derivatives with substituted ppy ligands.

Complex **134** was also tested with a myoglobin assay, the results are shown in Figure 85.

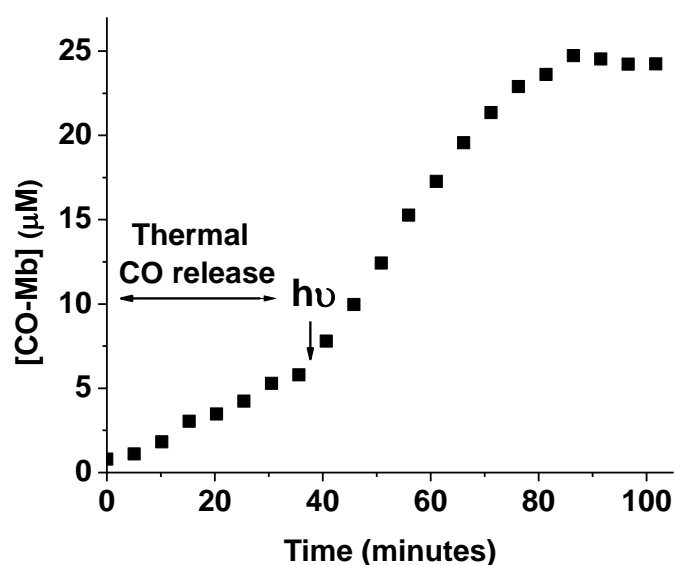
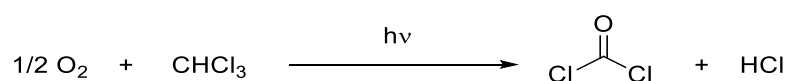


Figure 85. The release of CO to deoxy-Mb by a 10 μM solution of complex **134**. The experiment was run in the dark until irradiation with a 400 nm LED at a power of 5.0 W began where indicated. Irradiation was performed in cycles of 2 minutes on, 3 minutes off. Experiment performed in collaboration with Samuel Andrew.

In this case, complex **134** appeared to release CO to myoglobin in the dark (thermal CO release). Although it is not known which CO ligand would be lost, the strong *trans* effect of the CO ligands would suggest that the mutually *trans* CO ligands are labile to ligand substitution. When irradiation was started, as indicated on the graph, the rate of CO release was accelerated further. The CO release tails off at a [CO-Mb] concentration of 25 μM , suggesting that 2.5 equivalents of CO were released per molecule of **134**. Although complex **134** displayed photochemical CO release at the same wavelength as its ppy analogues, this was far less selective than the ppy-based CORMs.

The reason for the lower thermal stability of complex **134** was considered. Unlike for the ppy-based derivatives, old NMR samples of **134**, especially in CDCl_3 solvent, were observed to contain protonated ligand **149**. This was hypothesised to be the result of trace acid formed by decomposition of the chloroform (Scheme 52), which could promote the protonation of the Mn-C bond to release protonated ligand **149**.



Scheme 52: Decomposition of chloroform under ambient light and air.

To test the sensitivity of complex **134** to protonation, a solution of the complex was exposed to non-coordinating acid $[\text{HNMe}_2\text{Ph}]\text{BF}_4$. Successive injections of the proton source were made

(Figure 86) and the changes in intensity of the starting material and any degradant infrared stretching bands were monitored (Figure 87).

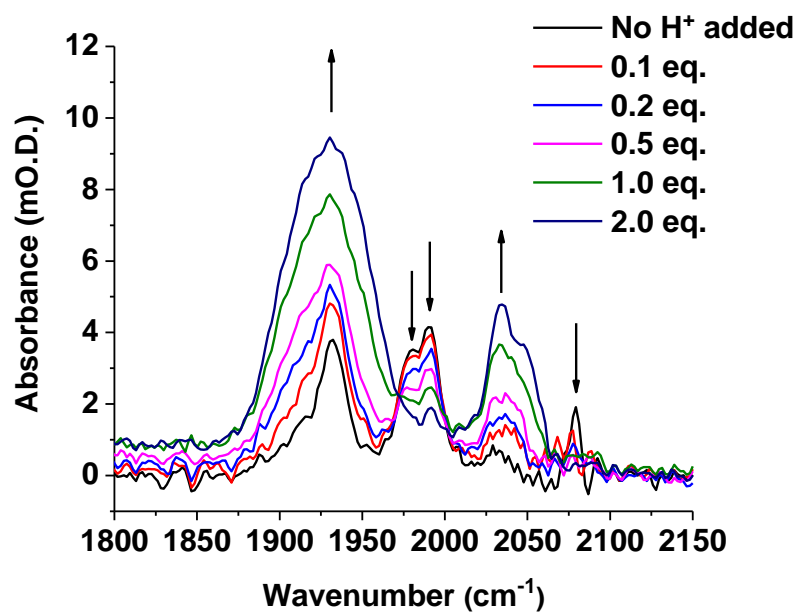


Figure 86: Effect of successive additions of the proton source [HNMe₂Ph]BF₄ to a 20 mM solution of 134 in CH₂Cl₂ as monitored by *in situ* infrared spectroscopy of the carbonyl bands. Experiment performed in collaboration with Samuel Andrew.

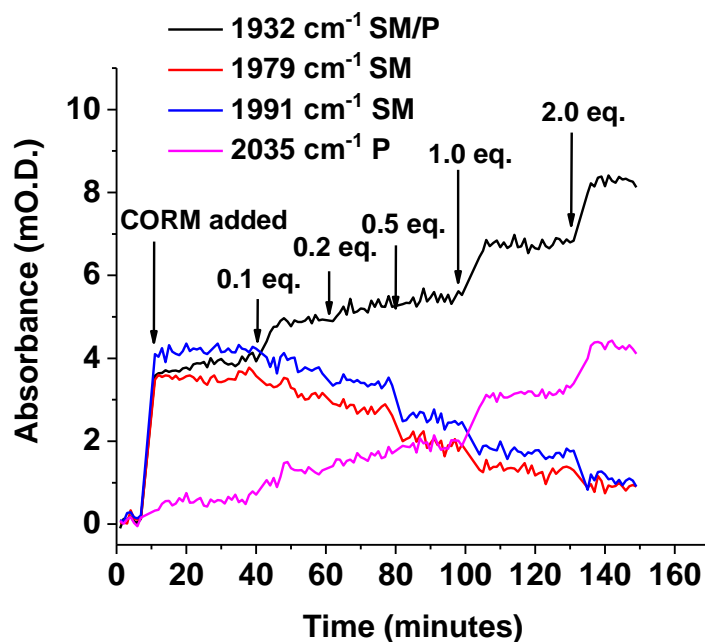


Figure 87: Effect of successive additions of the proton source $[\text{HNMe}_2\text{Ph}]\text{BF}_4$ to a 20 mM solution of **134** in CH_2Cl_2 as monitored by *in situ* infrared spectroscopy of the carbonyl bands. The changes to selected bands are shown. Experiment performed in collaboration with Samuel Andrew.

The data show that complex **134** does not degrade in ambient conditions in CH_2Cl_2 over *ca.* ten minutes under ambient conditions, having showed no change in the infrared spectrum over this period before any acid was added. This is consistent with the spectroelectrochemical data in Section 3.3, where no degradation was observed by infrared spectroscopy or cyclic voltammetry during the *ca.* ten minutes taken to prepare and run the experiments.

Upon successive injections of the non-coordinating proton source $[\text{HNMe}_2\text{Ph}]\text{BF}_4$, a clear change in the infrared spectrum was observed immediately. Decay of starting material bands at 1979 cm^{-1} and 1991 cm^{-1} as each addition is made show that the acid is degrading compound **134**. Of the other two carbonyl stretching bands of **134**, the 2085 cm^{-1} band was too weak to reliably track, while the 1932 cm^{-1} band grew in intensity when $[\text{HNMe}_2\text{Ph}]\text{BF}_4$ was added. A broad band at 2035 cm^{-1} also grew in upon additions of the acid, suggesting that a metal carbonyl-containing degradation product may form from this reaction.

The results for photochemical degradation of **132** and **133** in Section 3.4.2 presented the possibility of a *facial* tricarbonyl complex or cluster species, based on two low-wavenumber bands between $1900\text{--}1950\text{ cm}^{-1}$ followed by a higher-wavenumber band at around 2010 cm^{-1} (though these wavenumbers are in DMSO). A similar complex could be present in Figure 86, although the data is not conclusive. The broadness and intensity of the 1932 cm^{-1} feature suggest that multiple bands may be present, but due to overlap with the starting material it is difficult to discern whether two bands are present. Since the 1932 cm^{-1} feature gets broader as more acid is added, difference spectra after acid addition against the solution before acid addition would show

a peak either side of the starting material band at 1932 cm^{-1} . However, this would be a misleading way to present the data as it is far from clear that there are two degradant bands in that region of the spectrum. Therefore, this experiment does not rule out that similar *fac* tricarbonyl species to those proposed for **88**, **132** and **133** are present, but it is not conclusive evidence on its own.

The only degradation product that is confirmed for complex **134** is protonated ligand **149** as observed by NMR spectroscopy. A future experiment could involve an NMR study, similar to this *in situ* infrared study, to observe **149** forming as a proton source is added. However, if any paramagnetic degradation products or precipitation occurs, these could present problems for such an experiment.

To aid interpretation of why **134** appears more sensitive to protonation than **132** and **133**, the molecular orbitals for complex **134** were calculated by DFT (Figure 88) in order to make a comparison with the ppy-based complexes.

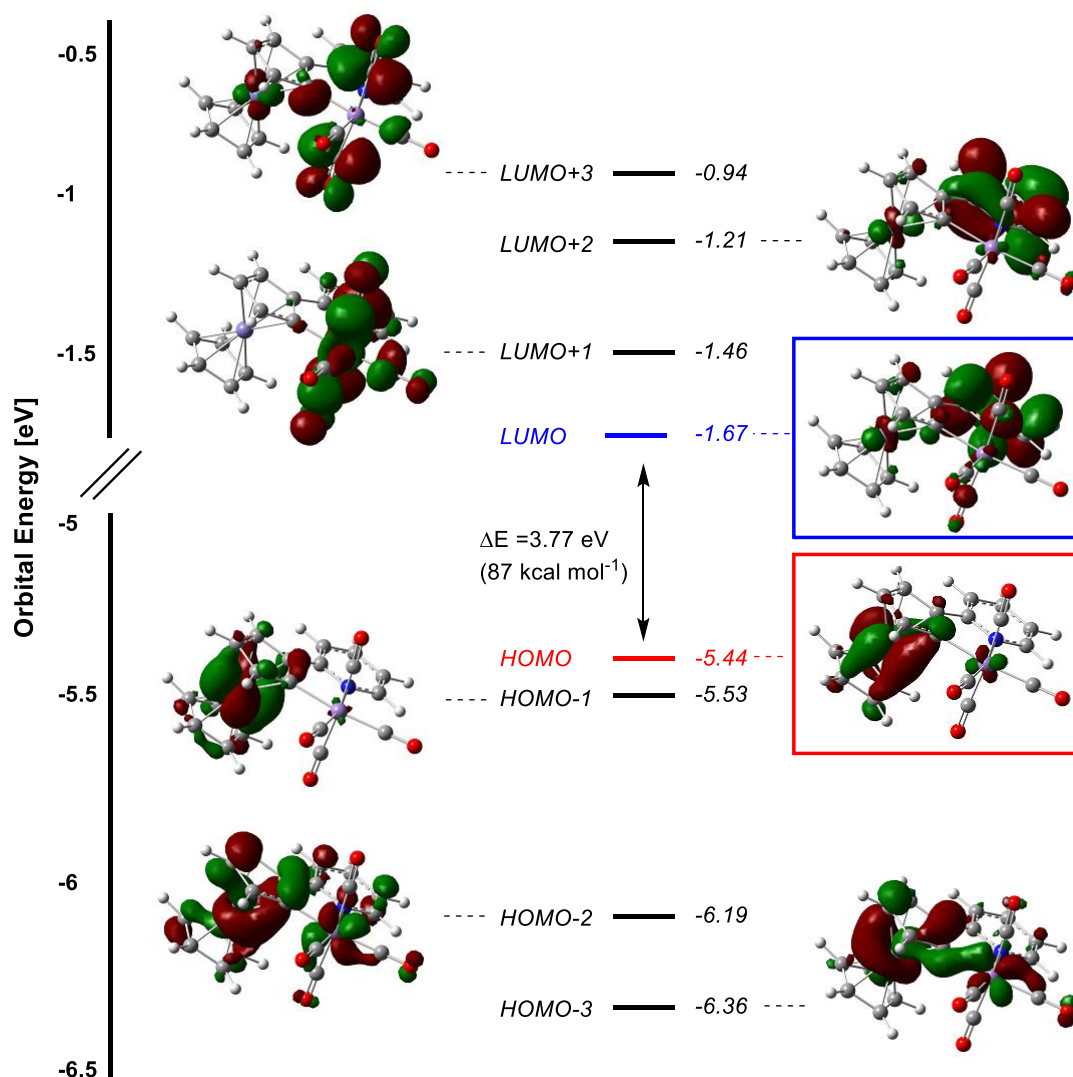


Figure 88: Frontier molecular orbitals of complex 134 as calculated by DFT (PBE0/DGTZVP/DEF2TV level of theory).

The calculations show that the electron density within each of the four highest occupied molecular orbitals is mainly located on the ferrocenyl group, with the lowest unoccupied molecular orbitals located on the pyridyl ring. This finding can be compared to the calculations on $[\text{Mn}(\text{ppy})(\text{CO})_4]$ in Chapter 2, in which the electron density in the highest occupied molecular orbitals had most electron density on the phenyl ring and Mn centre, and the lowest unoccupied molecular orbitals were located on the pyridyl ring. Therefore, the Fc_{py} and ppy ligands have a similar distribution of the electron density within the cyclometalated ligand. The experimental evidence shows that the ppy complexes are stable to buffer solution in the dark but that complex **134** degrades. This suggests that the Mn-C bond to the Cp ring in complex **134** is even more susceptible to protonation than the complexes featuring the ppy ligand.

In the case of triazole **132**, substantial precipitation from the 0.5% DMSO water solution prevented the measurement of any CO release. The myoglobin assay experiment was performed

in the dark for the first 30 minutes and with cycles of 2 minutes 365 nm LED irradiation per 5 minutes after that. As shown in Figure 89, the only change in the spectra over time was a steady increase in the absorbance across all wavelengths, without any change in shape from deoxy-Mb to Mb-CO. This shows that the dominant process occurring was a large increase in the turbidity of the solution – it was concluded that this was caused by scattering from precipitate of complex **132**. So little of the complex is present in solution that the CO release was negligible. However, given the similar photochemical behaviour observed for **133-134**, it would be expected that solubilisation of **132** would lead to measurable CO release in buffer solution.

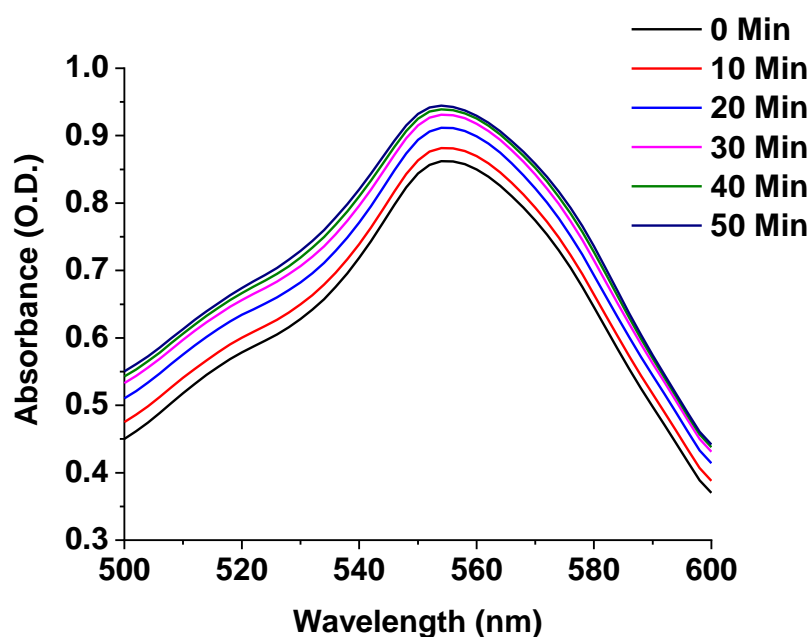


Figure 89; Precipitation of complex **132** when a 40 uM solution in phosphate buffer 0.5% DMSO was made. Irradiation at 400 nm and a power of 5 W in cycles of 2 minutes on, 3 minutes off from 30 min did not lead to CO release.

3.4.4 TRIR Studies

Since complex **133** displayed thermal stability and photochemical CO release at 400 nm, its ultrafast photochemical behaviour was also studied to compare it to the results with $[\text{Mn}(\text{ppy})(\text{CO})_4]$ and derivatives in Chapter 2. Difference spectra at selected picosecond delays after a 355 nm pump pulse are shown in Figure 90.

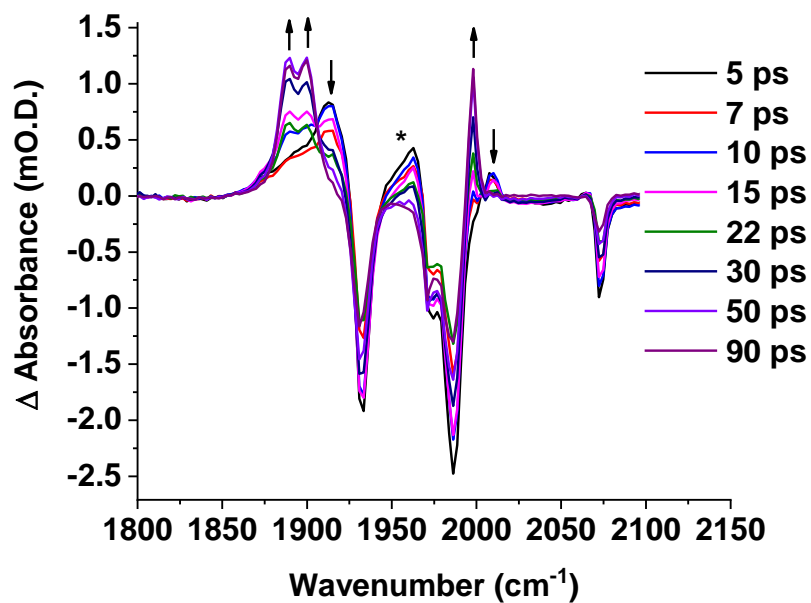
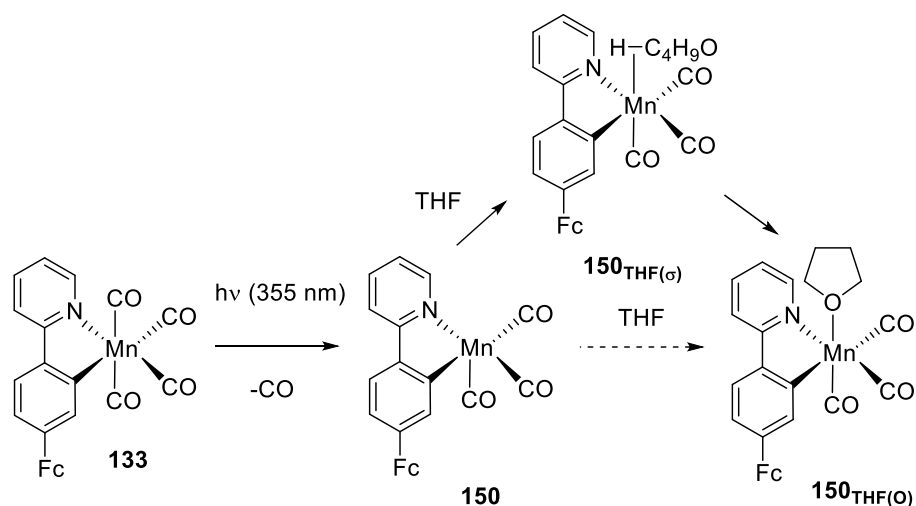


Figure 90: A TR^MPS experiment with ferrocenyl CORM 133 in THF. A pump wavelength of 355 nm was used.

The results show essentially identical behaviour the other complexes in the family of [Mn(ppy)(CO)₄]. Small bands corresponding to a short-lived triplet excited state decayed within the first few ps and were too weak to be quantified. Loss of CO is the dominant photochemical process and the isomerisation from complex **150**_{THF(σ)} to **150**_{THF(O)} was again observed Scheme 53). The kinetics of the isomerisation are shown in Figure 91.



Scheme 53: The coordination of THF following CO loss from complex 133, and subsequent isomerisation, shows the same behavior as $[\text{Mn}(\text{ppy})(\text{CO})_4]$

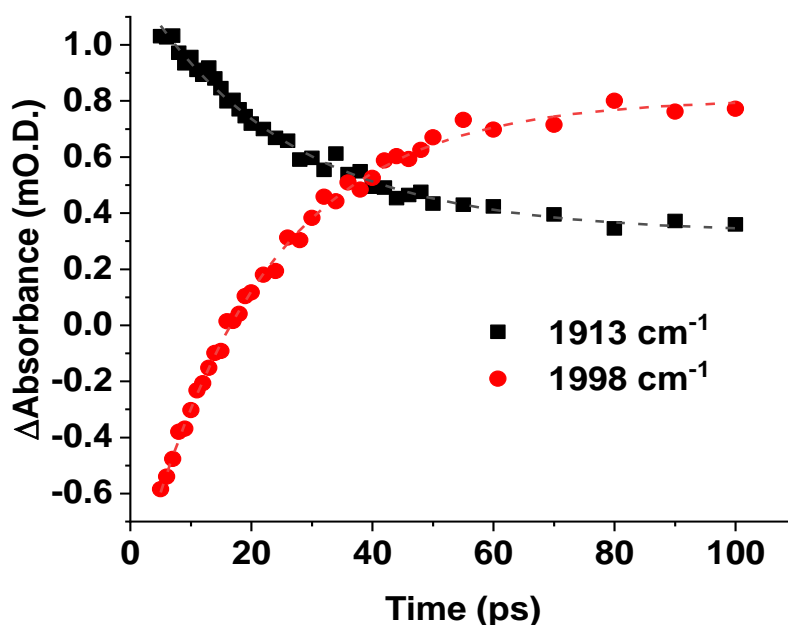


Figure 91: Kinetic plots from 5 to 100 ps to monitor the isomerisation of $150_{\text{THF}(\sigma)}$ to $150_{\text{THF}(\text{O})}$ using the $150_{\text{THF}(\sigma)}$ band at 1913 cm^{-1} and the $150_{\text{THF}(\text{O})}$ band at 1998 cm^{-1} . The dotted lines represent single exponential fits with lifetimes of (21.0 ± 1.1) ps and (25.1 ± 2.6) ps for the growth of the 1998 cm^{-1} band and loss of the 1913 cm^{-1} band respectively.

The single exponential lifetimes for the growth of $150_{\text{THF}(\text{O})}$ and decay of $150_{\text{THF}(\sigma)}$ were measured to be (21.0 ± 1.1) ps and (25.1 ± 2.6) ps respectively. This is a marginally slower lifetime than the other ppy ligands tested which were around 16–18 ps and could suggest that the additional steric bulk of the ferrocenyl moiety impedes movement or access of THF solvent molecules to the first coordination sphere.

The behaviour of **132** was also studied to examine whether triazole coordination to the Mn centre competes with solvent coordination after CO dissociation, a feature embedded in the original

design of this CORM. In order to allow the maximum amount of time for the triazole to coordinate, a weakly-coordinating solvent was used: *n*-heptane. This means that even if *n*-heptane coordinates before the triazole, it may be possible for ligand substitution to occur before the expected formation of the tricarbonyl aqua complex on the microsecond timescale. The results are shown in Figure 92.

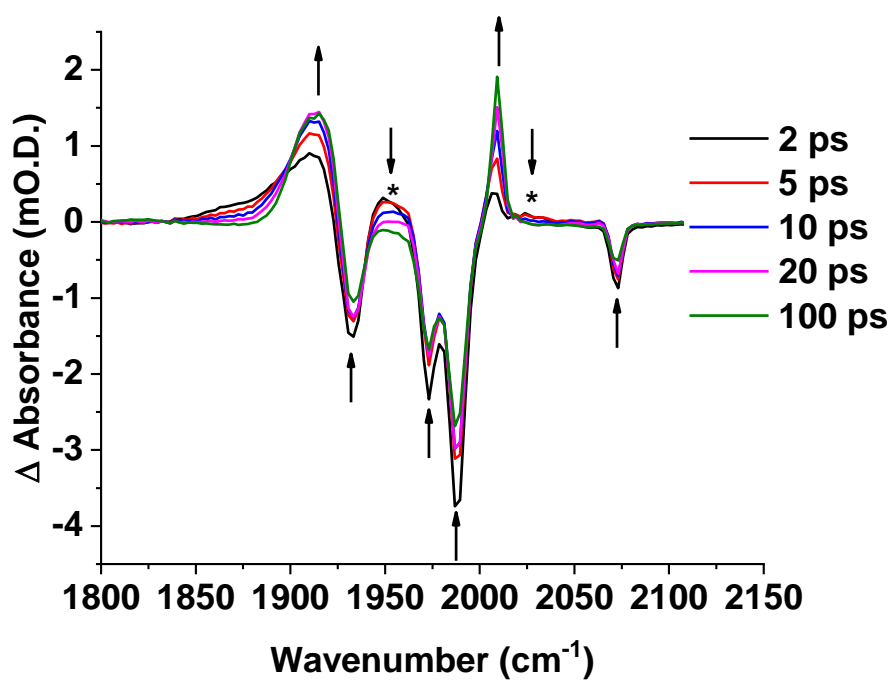


Figure 92: A TR^MPS experiment with ferrocenyl CORM 132 in *n*-heptane showing short pump-probe delays. The asterisks denote the excited state bands. A pump wavelength of 355 nm was used.

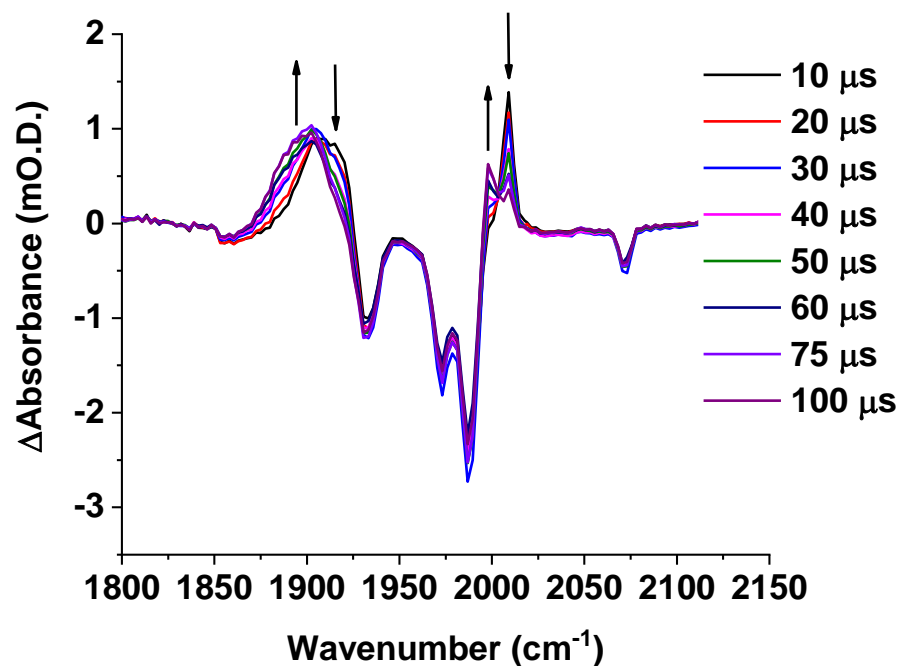
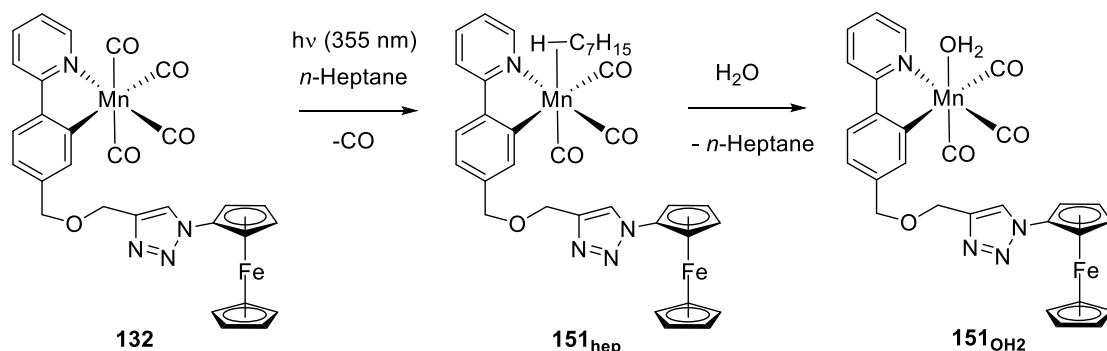


Figure 93: A TR^{MPS} experiment with ferrocenyl CORM **132** in *n*-heptane showing long pump-probe delays. A pump wavelength of 355 nm was used.

The spectra show formation of a tricarbonyl species that persists for tens of microseconds. The two low-wavenumber bands coalesce to give a feature with a maximum at 1908 cm⁻¹ with the other bands at 2009 cm⁻¹. After 10 μs, this species begins to be replaced by a tricarbonyl species with lower-wavenumber bands at 1902 and 1997 cm⁻¹, analogous to the events observed with [Mn(ppy)(CO)₄]. The timescale of the reaction and shift of the bands is characteristic of the formation of **151**_{hep} followed by intermolecular reaction with water to form **150**_{OH₂}. Therefore, the presence of the triazole moiety in complex **132** has no effect on its photochemical behaviour, even on the ultrafast timescale (Scheme 54).



Scheme 54: The CO loss from complex **132** results in a C-H σ -complex with the *n*-heptane solvent followed by displacement of *n*-heptane by water.

3.5 Solubilisation of **132** by Oxidation

In the case of **132**, the CORM was not soluble enough to study in water, precipitating out of solution (Section 3.4.3). To address the poor water solubility of **132**, oxidation to the corresponding ferricenium salt was attempted. The resulting cationic compound in combination with a water-soluble counterion could be used to solubilise **132**. Compounds containing the ferricenium moiety, coupled with water-soluble counterions such as trichloroacetate, tetrachloroferrate and picrate (Figure 94), have previously been shown to possess anti-cancer activity, due to the production of reactive oxygen species.²⁹⁶ The ferrocene analogue was able to infiltrate tumour cells but did not exhibit the toxicity of the ferricenium cation.²⁹⁶ As a result, it could be advantageous to use complex **132** as a ferricenium salt rather than as a neutral complex.

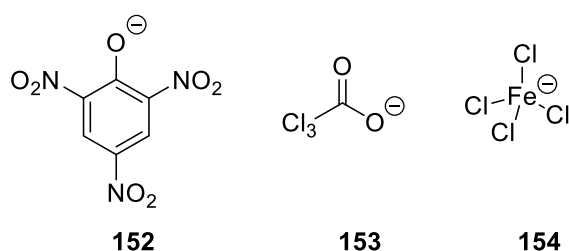
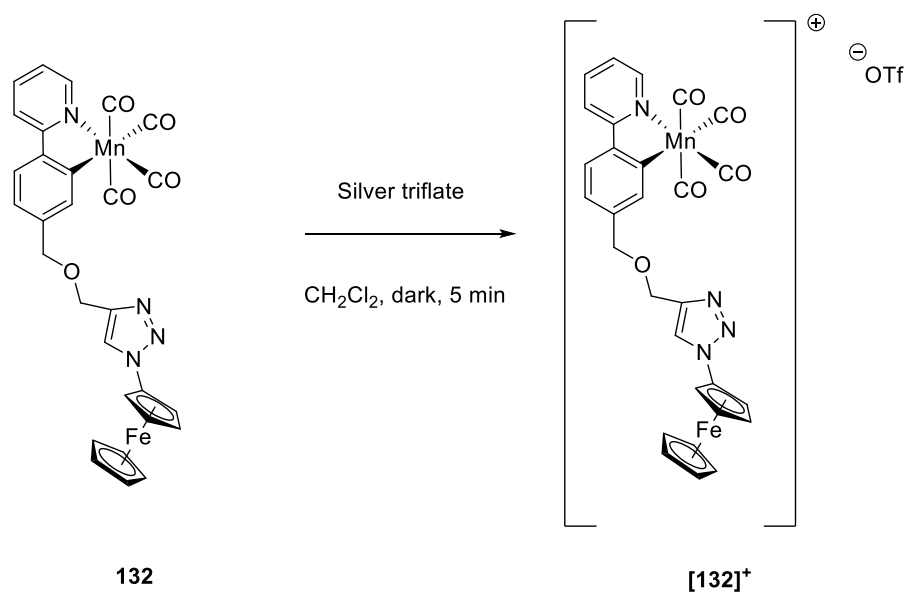


Figure 94: Water-compatible anions used with the ferricenium cation in anti-cancer studies.

Oxidation of the ferrocenyl group is frequently performed under harsh conditions, combining oxidants such as DDQ or benzoquinone with strong acid.²⁹⁴ When the milder of these two oxidants, benzoquinone, was tried with compound **132**, in conjunction with HPF_6 , some degradation of the metal carbonyl moiety was observed by infrared spectroscopy in the crude mixture. Given the stability of **132** over a wide potential window and the proven sensitivity of complex **134** towards protonation, it would appear that the Mn phenylpyridine group is not stable to the acid added. It is also unfeasible to perform the oxidation step earlier in the synthesis as the CuAAC reaction demands the use of reducing conditions. Alternative, acid-free conditions, incorporating a water-compatible anion, were sought.

Silver (I) was considered as a milder method to oxidise **132**. Because silver(I) possesses a reduction potential of +650 mV vs. the ferrocene/ferricenium couple in dichloromethane, there is a strong thermodynamic driving force to oxidise **132** (+220 mV in dichloromethane vs. the ferrocene/ferricenium couple, *vide supra*, Figure 70, page 187). Silver (I) triflate was chosen as the triflate anion is soluble in water. The conditions are shown below in Scheme 55.



Scheme 55: Oxidation of compound 132 to increase water solubility.

Upon combination of **132** with silver(I) triflate, a deep green solution immediately formed, indicative of oxidation of the yellow starting material to the ferricenium salt. The ferricenium cation $[\mathbf{132}]^+$ was detected by ESI mass spectrometry (see Appendix 7), instead of the protonated ion seen in the mass spectra of the neutral compound, showing that oxidation took place. An infrared spectrum of $[\mathbf{132}]^+$ was recorded and showed that the carbonyl groups were intact after this reaction, mirroring the spectroelectrochemical results and showing that the Mn carbonyl moiety remained intact during exposure to the oxidant. Further characterisation proved difficult due to the small scale of the reaction and the paramagnetism of the product. A ^1H NMR spectrum was recorded but due to the paramagnetism of the product the peaks were extremely broad, and nothing was seen in the typical chemical shift region for a ferricenium cation (around 30-40 ppm due to paramagnetic Fe^{III}).

The oxidation of **132** to improve the solubility could facilitate studies in aqueous solution, including biological activity and toxicity studies. However, the standard myoglobin CO release assay remains inaccessible for this compound due to the presence of the reductant sodium dithionite during the assay, which would be expected to reduce the oxidised complex. Other methods would be required to study CO release, and options such as headspace analysis by gas chromatography, in situ infrared spectroscopic studies and mass spectrometric detection of degradation products can be explored. The cationic ferricenium group could serve as a good mass spectrometry tag to monitor CO degradation products.

Future experiments to work towards solubilising complex **132** by oxidation should focus on trialling the oxidations with complex **133**, as this complex is more stable than **134** and displays a small shift of *ca.* 5 cm^{-1} upon oxidation. Although this complex has better water solubility than

complex **132**, testing the oxidation on this complex would allow more conclusive confirmation that all of the material had been chemically oxidised.

3.6 Conclusions

A series of ferrocenyl CORMs, complexes **132-134**, has been synthesised, characterised and evaluated for CO release properties through thermal, photochemical and redox triggers. Infrared spectroelectrochemistry has shown how the redox-active ferrocenyl moiety communicates with the Mn tetracarbonyl centre when the length of linker between them is varied.

Although direct redox-triggered CO release was not observed in this work, the spectroelectrochemical measurements show that significant changes to the metal carbonyl electronic environment can only be achieved with a ligand in the first coordination sphere of the metal carbonyl. However, in complex **134** where the ferrocenyl moiety is closest to the Mn centre, sensitivity towards protonation induces slow thermal CO release. This method of decomposition was supported by DFT calculations showing that the HOMO of complex **134** is located on the ferrocenyl moiety.

All three of the complexes in this work displayed photochemical CO release with 400 nm irradiation. This was detected directly using myoglobin for the more water-soluble complexes **133** and **134**. The photochemical behaviour of dark-stable complexes **132** and **133** was monitored with both *in situ* infrared spectroscopy and ultrafast TRIR spectroscopy. Similar photochemical behaviour was observed to $[\text{Mn}(\text{ppy})(\text{CO})_4]$ on timescales from picoseconds to minutes. The dominant ultrafast behaviour is CO loss to form a solvated tricarbonyl species, with a small proportion of a short-lived triplet excited state. Upon continuous irradiation over longer timescales, *in situ* infrared spectroscopy suggested that the solvated tricarbonyls react further to form species tentatively assigned as multinuclear Mn cluster species as was assigned for $[\text{Mn}(\text{ppy})(\text{CO})_4]$. The triazole moiety of complex **132** did not coordinate to the Mn centre upon CO loss.

Since all three ferrocenyl complexes synthesised in this work could still display CO release, they could be considered as possible dual mechanism drug compounds due to the combination of photochemical CO release and the therapeutic properties of the ferrocenyl moiety. Solubilisation of **132** in water may be achievable in the future by oxidation to the ferricenium salt with a suitable counterion.

Part of the work described in this Chapter has been reported in a recent publication (see Appendix 1).²⁹⁷

4 Characterisation of Cyclometalated Azo Mn(I) CORMs

The Mn(I) tetracarbonyl ppy complexes investigated so far in this Thesis display photochemical CO release when UV light or 400 nm visible light is used.^{159,184,297} As discussed in Chapter 1, it is important to develop photoCORMs that release CO using low-power visible or near-infrared wavelengths of light. In the literature, replacement of pyridyl N-donor ligands with π -accepting azo ligands has been shown to increase the CO release wavelength in a different series of Mn(I) photoCORMs.¹²⁷ The work in this Chapter investigates the effect on the CO release properties when the nitrogen donor of the ppy ligand is replaced with an azo functional group in Mn(I) tetracarbonyl complexes. The photochemical CO release to myoglobin and the ultrafast photochemistry of azo complexes are compared to the ppy analogues. The redox behaviour of the cyclometalated azo complexes is also briefly explored with a view to designing reductively-activated CORMs.

4.1 Background

4.1.1 Using Azo Ligands to Make Visible Light-Activated PhotoCORMs

The superior tissue penetration and reduced toxicity of visible and near infrared light relative to UV irradiation has led to a demand for photoCORMs that release CO at these wavelengths.¹²⁵ Recent research by Mascharak and co-workers has focussed on increasing the CO release wavelength of Mn(I), Re(I) and Ru(II) photoCORMs from the UV into the visible by varying the nature of the co-ligands. The outcomes from this work led Mascharak and co-workers to propose the use of π -acceptor co-ligands to increase the wavelength of CO release.¹²⁷ This previous work was considered in the design of the novel complexes described in this Chapter.

The initial work by Mascharak's group on Mn(I) tricarbonyl complexes **155-157** (Figure 95) revealed that the use of pyridyl and amine N donor groups led to CO-dissociative MLCT bands with maxima in the UV region, with λ_{max} values of 330 nm for complex **155** (Figure 95, left) and 350 nm for complex **156** (Figure 95, centre).²⁹⁸ Additional conjugation in the co-ligand was achieved by replacing the pyridyl ring with a quinoline (Figure 95, right). This change had a small effect, increasing the λ_{max} value of the CO-dissociative band to 360 nm.²⁹⁸ The extinction coefficient of the CO-dissociative MLCT band in complex **157** was also higher than in complexes **155** and **156**. In conjunction with quantum yield for CO loss, a large extinction coefficient could be advantageous in lowering the power of irradiation required to achieve appreciable CO release.

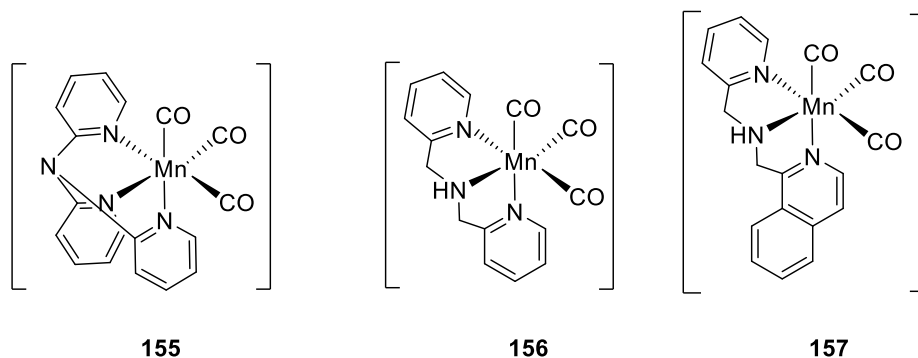


Figure 95: Pyridyl and amine Mn(I) tricarbonyl complexes studied by Mascharak and co-workers.²⁹⁸

Subsequent work on the conjugated imine complexes shown in Figure 96 led to large red-shifts of the CO-dissociative MLCT bands.²⁹⁹ The UV wavelengths required to excite the CO-dissociative MLCT bands in complexes **155-157** was shifted in complexes **158a** and **158b** to give λ_{max} values of 500 and 535 nm respectively.²⁹⁹ This significant increase in CO release wavelength was attributed to the low-lying π^* orbital of the imine ligand donor compared to pyridyl and amine ligands yielding a lower-energy LUMO in the imine complexes.²⁹⁹ Calculations using TD-DFT were used to study the orbitals involved in the CO-dissociative transition (not necessarily the HOMO and LUMO). The calculations showed that the LUMO is involved in the CO-dissociative MLCT transition, so lowering the LUMO by incorporating a π -acceptor co-ligand increases the transition wavelength.²⁹⁹ The occupied orbital involved in the CO-dissociative transition in these complexes was predominately the HOMO-2; like the HOMO these orbitals are based primarily on the metal and carbonyl ligands.²⁹⁹

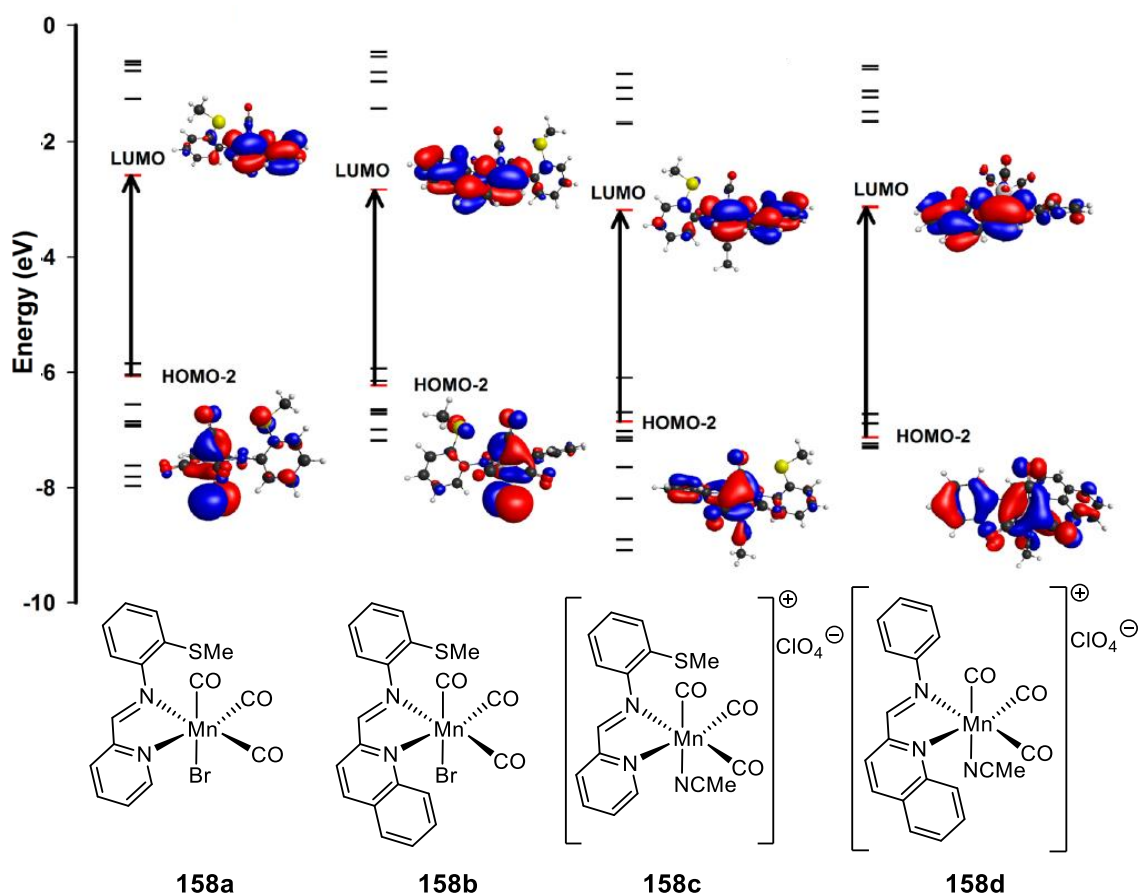


Figure 96: Energy differences between the metal-based occupied orbitals and the LUMO involved in the MLCT transition of Mn(I) tricarbonyls with different N-donor and bromide/MeCN co-ligands. Image adapted with permission from *Acc. Chem. Res.*, 2014, 47, 2603–2611.¹²⁷ Copyright 2014 American Chemical Society.

The calculations, shown in Figure 96, confirmed that the increased conjugation on the imine co-ligand upon going from complex **158a** to **158b** lowers the energy of the ligand-based LUMO and lowers the overall transition energy. This illustrates how conjugated systems can be utilised and tuned to alter the CO release wavelength. The occupied metal-based HOMO-2 also experiences a slight lowering in energy in **158b** relative to **158a** but this is counteracted by the even greater stabilisation of the LUMO, which is the dominant effect.¹²⁷

The effect of CORM co-ligands on tuning occupied metal-based orbital energy levels was also considered by Mascharak's group. In this case it is desirable to raise the energy of the occupied orbitals, thus lowering the transition energy. Comparing complexes **158b** and **158c**, replacement of the bromide ligand with the moderate π -acceptor ligand MeCN resulted in the MLCT band blue-shifting to below 450 nm (Figure 96), in large part because the occupied HOMO-2 orbital was raised in energy (though a slight lowering of the LUMO was also predicted).²⁹⁹ The σ -donor bromide ligand raised the HOMO-2 energy substantially compared to use of MeCN, so that the bromide complexes had the more desirable (longer) CO release wavelengths. This led to the

conclusion that stronger σ -donor co-ligands with poor π -acceptor properties are ideal co-ligands for visible light CO release as these types of ligands raise the energy of metal-based orbitals depopulated by MLCT transitions.^{127,299} This point, however, must be weighed against the advantages of including multiple CO ligands on a metal centre. Release of multiple equivalents of CO per photoCORM is a desirable property, but additional CO ligands may lower the wavelength of activation.

The imine complexes had a higher quantum yield for CO loss than the pyridyl and amine complexes. Cations **158c** and **158d** displayed quantum yields for CO loss of (0.130 ± 0.005) and (0.208 ± 0.005) respectively, whereas complexes **155-157** all had quantum yield values of < 0.1 near the maxima of their MLCT bands.²⁹⁹ A reason for the significantly higher quantum yield of complex **158c** compared to complex **158d** was not proffered. The difference between these complexes is the presence of a sulfide substituent on the imine ligand. Although coordination of the sulfide group to the metal centre was not observed, this shows that even distant substituents can have a notable influence on the photochemistry observed.

Another strong π -acceptor ligand that was assessed was 2-phenylazopyridine (azpy).³⁰⁰ One of the complexes synthesised that featured the azpy ligand was complex **159** in Figure 97. TD-DFT calculations showed that CO release was initiated by MLCT excitation of the HOMO-1, an orbital with substantial M-CO bonding character, into the ligand-based LUMO.³⁰⁰ Replacement of the imine functional group with an azo group led to an even greater red-shift of the MLCT band to give a λ_{max} value of 586 nm. Furthermore, the quantum yield for CO dissociation within the MLCT band further increased to (0.48 ± 0.01) .³⁰⁰ The key conclusion of the studies by Mascharak and co-workers was that the wavelength at which photoCORMs can release CO can be dramatically increased by careful choice of co-ligands; π -acceptor ligands lead to a low-lying LUMO in the complex which in turn increases the wavelength of the CO-dissociative transition.

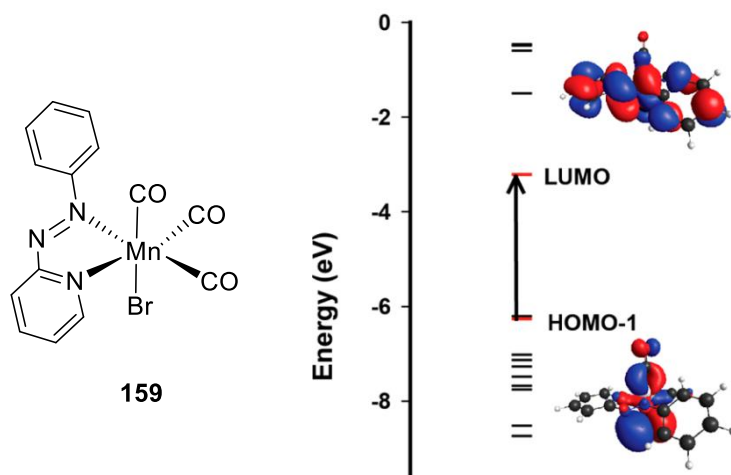


Figure 97: Mn(I) tricarbonyl complex featuring an azo group as one of the N-donors, developed by Mascharak and co-workers. Image adapted with permission from *Acc. Chem. Res.*, 2014, 47, 2603–2611.¹²⁷ Copyright 2014 American Chemical Society.

Further improvements to the CO-release wavelength in a related system were reported in a study by Zobi and co-workers, who introduced electron-withdrawing substituents to 2,2'-azopyridines to tune the λ_{\max} wavelength for the visible light CO-dissociative band. (Figure 98).³⁰¹ These complexes released CO to myoglobin upon visible light irradiation, but complexes **160c-e** also released CO in the dark with a half-life for CO release of less than an hour.³⁰¹

Complex	X	Y	λ_{\max} (nm)
160a	Me	H	625
160b	H	H	630
160c	Br	H	661
160d	CF ₃	H	678
160e	CF ₃	Cl	693

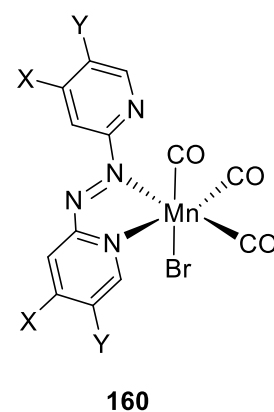


Figure 98: General structure of complexes synthesised by Zobi and co-workers.³⁰¹

The large extinction coefficients and red-shifted MLCT bands observed in metal carbonyl compounds through use of N-donor ligands with low-lying π^* orbitals raises the question of whether a similar methodology could be employed to increase the CO-release wavelength of [Mn(ppy)(CO)₄] derivatives. Cyclomanganated complexes of substituted azobenzenes with Mn(I) carbonyls have been known since the 1960s, having been synthesised by Heck³⁰². Bruce and co-workers have cyclomanganated a variety of substituted azobenzenes.³⁰³ However, the photochemical properties of this class of complexes has not been studied in detail and only one compound has been evaluated as a photoCORM: complex **161** (Figure 99).¹³⁷

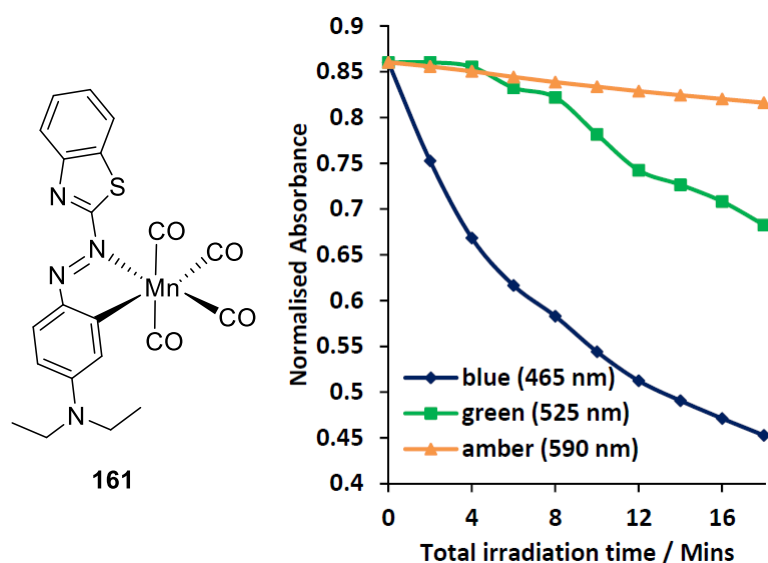
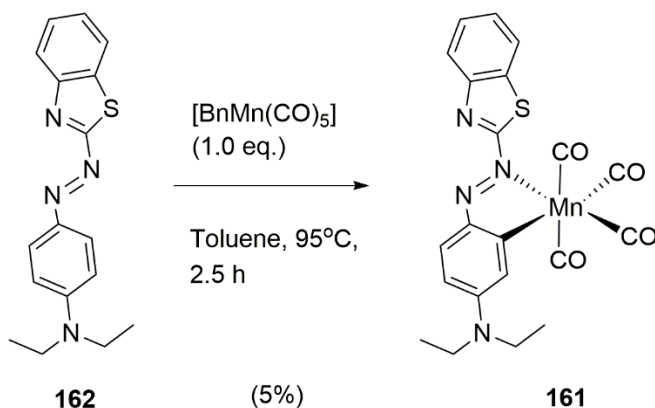


Figure 99: Visible light azo dye photoCORM **161 synthesised and tested by Fairlamb and co-workers. The graph is from the PhD thesis of Jonathan Ward and shows the decomposition of **161** upon irradiation with 2.4 W power LED light, as assessed by UV-visible spectroscopy.¹³⁷**

Complex **161** displayed promising initial results as a photoCORM due to its photochemical decomposition at 465 nm, with slower degradation at 525 nm also observed.¹³⁷ Direct evidence that decomposition of **161** resulted in CO release was also obtained through a myoglobin assay.¹³⁷ As previously shown in Section 2.2.2, [Mn(ppy)(CO)₄] itself shows no absorption bands above ~400 nm and therefore cannot release CO photochemically further into the visible spectrum. The CO release from complex **161** at 465 nm suggests that, as with Mascharak's complexes, replacement of a pyridine donor with an azo group increases the CO-release wavelength.

Unfortunately, complex **161** also degrades slowly in buffered myoglobin in the dark, which reduces the selectivity of the CO release, and it must be stored under an inert atmosphere to prevent decomposition.¹³⁷ The synthesis of complex **161** (Scheme 56) is also problematic: the cyclometalation is low-yielding and results in the production of a large number of impurities that are challenging to separate from the desired product. It is known that azo dyes can degrade photochemically through radical chemistry to form compounds such as anilines, phenols and hydroxyhydrazines.^{304,305} Azobenzenes are also known to isomerise between the *cis* and *trans* isomers, both photochemically with visible light and thermally above 70 °C.³⁰⁶ It is therefore possible that isomerisation of the free azobenzene product is also a problem in the purification. Any isomerisation at the high cyclometalation reaction temperature is less likely to be an issue in the Mn geometry locks the geometry of the azobenzene such that only the *trans* azobenzene-derived ligand can complex to the metal. The array of coloured impurities suggests that decomposition involves substantial structural changes to the strongly-absorbing azo ligand. The

resulting chromatographic separation resulted in further decomposition leading to a 5% yield.¹³⁷ As a result, an improved synthetic route to complex **161** is required. It would also be useful to develop stable alternatives to complex **161** that are easier to handle and store. Therefore, the synthesis of some photoCORMs related to complex **161**, bearing azo co-ligands, will be carried out in this Chapter and their CO-release properties will be evaluated in light of the ligand systems already developed in the literature.¹²⁷



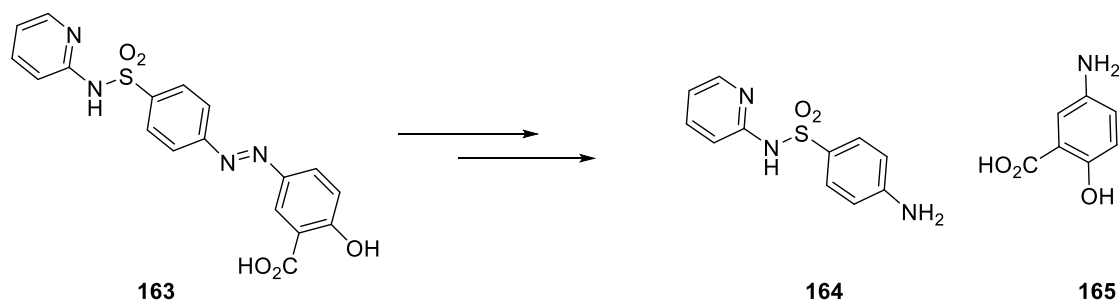
Scheme 56: Synthesis of complex 161.

4.1.2 Redox Properties of Azo Compounds

In addition to its photochemical properties, the azo ligand also represents a redox-active co-ligand that could be used to promote redox-activated CO release. The Mn(I) tetracarbonyl system remains a desirable system from which to initiate redox-triggered CO release due to its stability, the facile installation of organic co-ligands and the typically low toxicity of analogous complexes. In the earlier work on ferrocenyl CORMs (Chapter 3), some requirements for redox activation CORMs *via* co-ligands were considered. Spectroelectrochemistry of the ferrocenyl compounds showed that such a co-ligand should be placed directly in the first coordination sphere of the metal for a redox event to have a significant effect upon the electron density at the manganese centre. Azo dye co-ligands fulfil the requirements of a biologically-relevant redox couple that could be installed directly into the metal centre. The N=N double bond can be reduced to form the corresponding hydrazine, which can be reduced further to the anilines in which the azo bond has been cleaved. The electrochemistry of the azo complexes synthesised will therefore be studied to evaluate reduction as an additional method of triggering CO-release.

There are examples of azo-containing redox-active pro-drugs. Sulfasalazine (**163** Scheme 57) is one such example. This drug is used to treat arthritis, ulcerative colitis and inflammatory bowel disease and is featured in the World Health Organisation “List of Essential Medicines”.³⁰⁷ The active ingredient is the metabolite mesalazine, **164**, which is formed by reductive cleavage of the azo bond within the anaerobic environment of the small intestine and colon.³⁰⁸ It is conceivable that the redox properties of the azo group could be adapted for the delivery of carbon monoxide.

Reduction of the azo moiety would be expected to weaken the π -backbonding to the azo co-ligand and therefore weaken its coordinating ability. Loss of the co-ligands has been shown to play a role in activation of CORMs for CO release, as shown in the literature mass spectrometry study described in Section 1.4 and the experimental data revealing possible formation of Mn tricarbonyl clusters in Chapter 2.

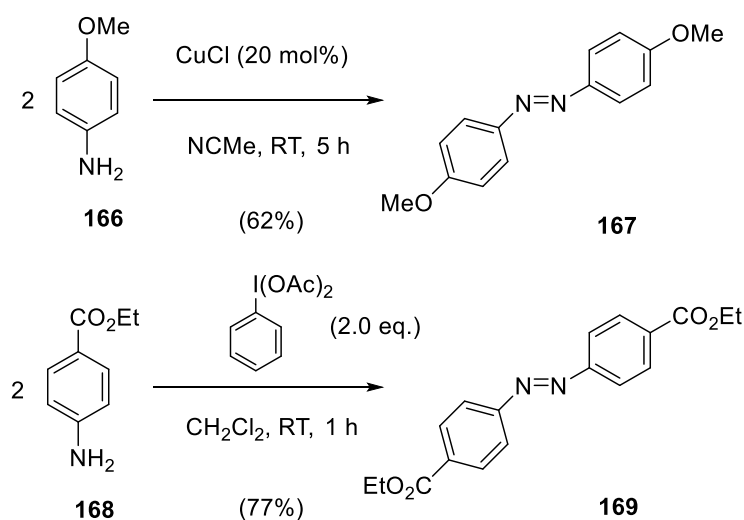


Scheme 57: Structures of the prodrug Sulfasalazine and its degradation products.

4.2 Synthesis of Azo Dye Complexes

The cyclomanganation of a variety of electron-rich and electron-poor substituted azobenzenes is known.³⁰⁹ Electron-rich azobenzene **167** and electron-poor azobenzene **169** were synthesised to exploit the robustness of the cyclomanganation reaction. If the preliminary studies on the visible light-triggered or redox-activated CO-release of these compounds were successful, it would then be possible to synthesise a series of substituted complexes to study the effect of substituents on CO release wavelength, extinction coefficient, CO release rate and redox potential.

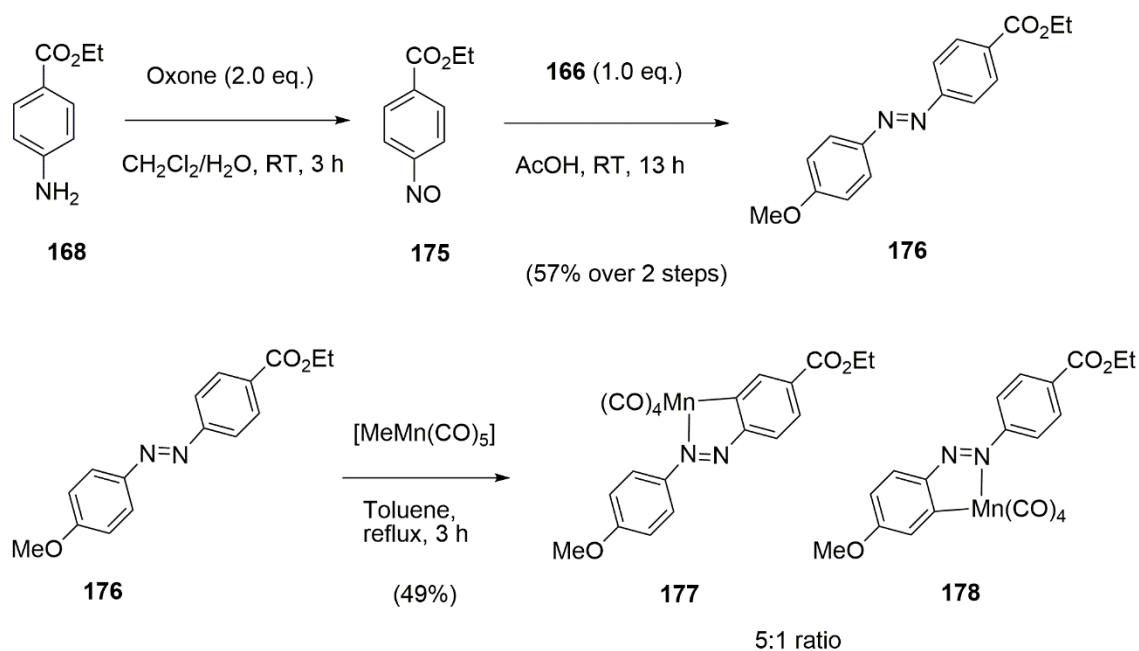
The electron-rich and electron-poor azobenzenes **167** and **169** were synthesised by literature methods by oxidation of the corresponding anilines: **167** by copper-catalysed aerobic oxidation³¹⁰ and **169** using iodobenzene diacetate as a stoichiometric oxidant.³¹¹



Scheme 58: Synthesis of azo ligands 167 and 169.

Earlier work by Bruce and co-workers showed that cyclometalation of azobenzene with one equivalent of $[\text{MeMn}(\text{CO})_5]$ yielded the mononuclear Mn tetracarbonyl complex.³¹² Subsequent reaction of the mononuclear complex with a second equivalent of $[\text{MeMn}(\text{CO})_5]$ enabled the formation in 7% yield of a dinuclear complex in which two cyclometalations occurred on the same azobenzene ligand.³¹³ In contrast, the use of $[\text{BnMn}(\text{CO})_5]$ to cyclometalate azobenzene produced the dinuclear complex in much greater yield initially, even when only one equivalent of $[\text{BnMn}(\text{CO})_5]$ was used.³¹⁴ The dinuclear complex was isolated in >80% yield when two equivalents of $[\text{BnMn}(\text{CO})_5]$ were used and it was shown that the dinuclear complex reacted with free azobenzene to produce the mononuclear complex.³⁰³

Cyclometalation of the protonated azo ligands **167** and **169** was performed using either $[\text{MeMn}(\text{CO})_5]$ (**174**) or $[\text{BnMn}(\text{CO})_5]$ (**87**) (Scheme 59). The use of one equivalent of $[\text{MeMn}(\text{CO})_5]$ was anticipated to deliver a relatively clean conversion of ligand into the mononuclear complexes whereas two equivalents of $[\text{BnMn}(\text{CO})_5]$ were used to promote formation of dinuclear complexes. This means that some of the CORMs synthesised in this work could deliver up to eight equivalents of CO per molecule - the number of equivalents of CO released is assessed with a myoglobin assay in Section 4.3.2.



Scheme 59: Synthesis of complexes 170-173.

The results of the syntheses are summarised in Table 14. A solution of the azobenzene and $[\text{MeMn}(\text{CO})_5]$ in degassed toluene at reflux gave the expected mononuclear Mn tetracarbonyl complexes **170** and **172**. In agreement with previous observations on other azobenzenes by Bruce and co-workers, only one $\text{Mn}(\text{CO})_4$ fragment was transferred to the product when one equivalent of $[\text{MeMn}(\text{CO})_5]$ was used.³¹² This provided a clean method of generating dinuclear complexes **171** and **173**.

The synthesis of dinuclear complexes **171** and **173** was achieved with two equivalents of $[\text{BnMn}(\text{CO})_5]$. The reaction was run until all of the $[\text{BnMn}(\text{CO})_5]$ was consumed (3 hours, monitored by infrared spectroscopy) and this provided a mixture of both the mono- and dinuclear complexes. The major products after 3 hours were the mononuclear complexes. The mono- and dinuclear complexes were isolable by column chromatography on silica gel. The synthesis with $[\text{BnMn}(\text{CO})_5]$ is therefore convenient for generating both the mononuclear and dinuclear complexes in a single reaction and purification, provided the two complexes are readily separable. Based on Bruce's earlier observations, a shorter reaction time could be used in the future to optimise for a greater yield of the dinuclear complex, although in this case the yields of both complexes were sufficient to provide the material needed for further study.

Table 14: Yield of isolated products for cyclometalation reactions with [MeMn(CO)₅] and [BnMn(CO)₅]. Yields are based on the amount of azobenzene ligand used.

Ligand	Product	Yield With [MeMn(CO) ₅] (1 eq.) (%)	Yield With [BnMn(CO) ₅] (2 eq.) (%)
167	170	58	66
	171	0	22
169	172	52	62
	173	0	21

The infrared spectra of complexes **172** and **173** are shown in Figure 100.

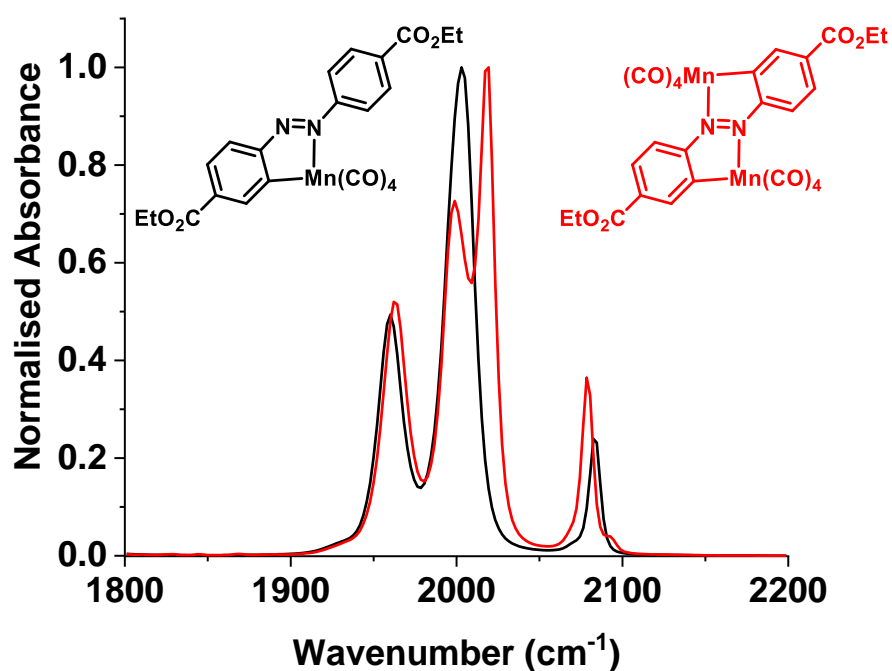


Figure 100: Normalised infrared spectra of complexes 172 (black) and 173 (red) in CH₂Cl₂ solution recorded at 2 cm⁻¹ resolution.

Unlike the related ppy complexes in Chapters 2 and 3, which exhibit four infrared stretching bands, mononuclear complex **172** displayed only three bands. Though many of the cyclometalated azo complexes in the literature possess four infrared stretching bands in the metal carbonyl region, the central two bands at *ca.* 2000 cm⁻¹ are typically only spaced by approximately 5 cm⁻¹, compared with > 10 cm⁻¹ for the ppy complexes. It is therefore likely that the central two bands are coalescent for complex **172**. The infrared spectrum of cyclometalated azo dye CORM **161** was previously found to have only three infrared bands in the metal carbonyl region with an intense, asymmetrical central band. In dinuclear complex **173**, the four different stretching modes

of the tetracarbonyl moiety can each be observed, and the spectrum resembles that of the ppy complexes derived from **88**. A comparison of the band positions is provided in Table 15. The Table reveals that the force constants for the vibrations in the azo complexes are larger for the azo complexes than for ppy complex **88**, consistent with the increased π -acceptor ability of the azo ligand compared to ppy. There is some variation in how much the bands shift by depending on the nature of the vibrational mode. Upon with moving from complex **88** to complexes **172** and **173**, the respective bands responded in an analogous fashion to oxidation of ferrocenyl CORM **134** (Section 3.3.1). As was the case in the infrared spectroelectrochemistry of **134**, the smallest shift on moving from ppy to azo ligands is in the high-wavenumber A_1 band, as this vibration involves the two mutually *trans* carbonyl ligands, whereas the low-wavenumber B_2 normal modes involving ligands trans to the ppy/azo ligands showd the largest increase in wavenumber. Also mirroring the spectroelectrochemistry of **134**, the two central bands $\nu(\text{CO})$ (2) and $\nu(\text{CO})$ (3) shifted by similar values to one another, despite involving the mutually *cis* and mutually *trans* carbonyls respectively. It is interesting that the impact on the infrared bands of moving from a ppy-based ligand to an azo ligand is similar to that of oxidation of complex **134**. The infrared spectra of **88**, **172** and **173** in THF are essentially identical to the CH_2Cl_2 spectra.

Table 15: Comparison of metal carbonyl infrared stretching band wavenumbers in CH_2Cl_2 and THF between ppy complex **88 and azo complexes **172** and **173**.**

Compound	Solvent	$\nu(\text{CO})$ (1) (cm^{-1}) B_2	$\nu(\text{CO})$ (2) (cm^{-1}) A_1	$\nu(\text{CO})$ (3) (cm^{-1}) B_1	$\nu(\text{CO})$ (4) (cm^{-1}) A_1
88	CH_2Cl_2	1932	1975	1990	2075
88	THF	1932	1974	1989	2073
172	CH_2Cl_2	1960	2003 (bands coalescent)		2084
172	THF	1959	2001 (bands coalescent)		2082
173	CH_2Cl_2	1963	1999	2019	2079
173	THF	1964	1998	2017	2078

The aromatic region of the ^1H NMR spectra for azobenzene **169** and its corresponding mononuclear **172** and dinuclear **173** complexes are shown in Figure 101.

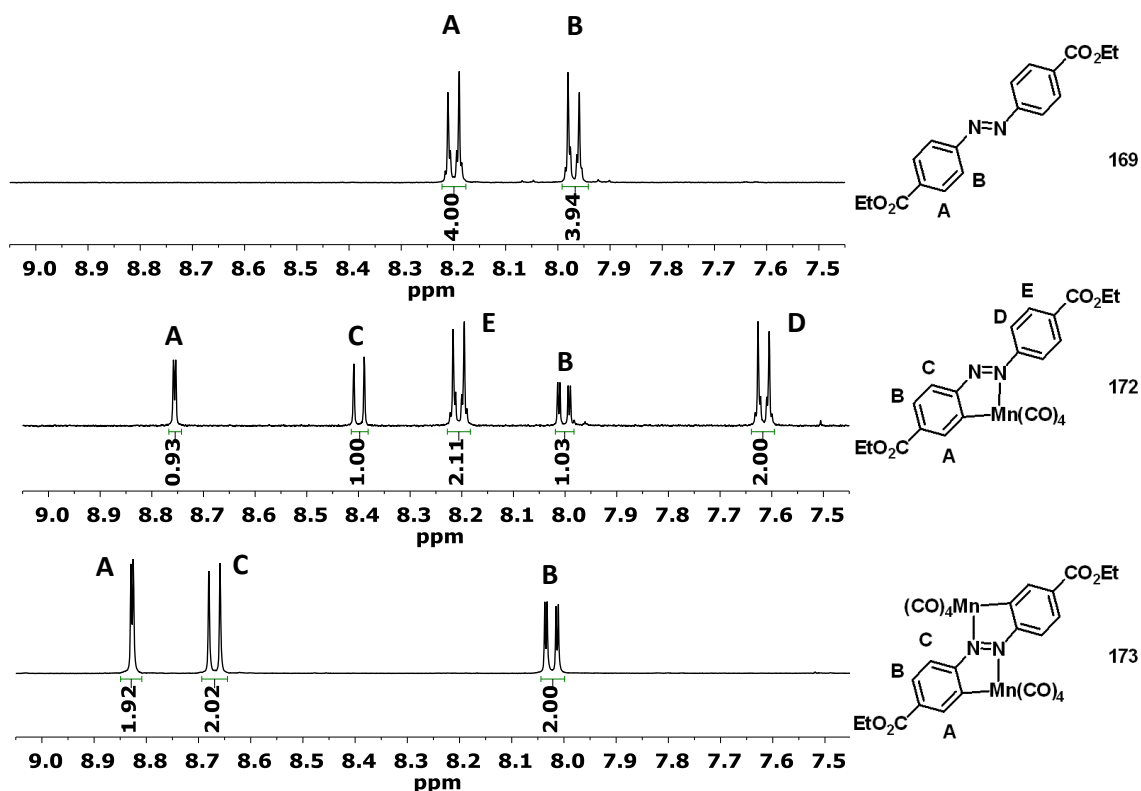


Figure 101: 400 MHz NMR spectra of compounds **169**, **172** and **173** in CDCl_3 at 298 K.

The aromatic protons in the free azobenzene **169** appear as two multiplets displaying second-order effects resulting from the AA'XX' spin system. Upon cyclometalation to form the mononuclear complex **172**, the molecule is desymmetrised; only one of the two rings displays the AA'XX' multiplets. The protons on the cyclometalated ring comprise very deshielded proton A, with a small 'W' coupling to proton B, which in turn displays a larger coupling to proton C on the adjacent carbon atom. After a second cyclometalation to form dinuclear complex **173**, desymmetrisation of the second ring takes place, leading to a similar pattern of resonances for the desymmetrised ring in mononuclear complex **172**.

Crystal structures of complexes **170** and **173** were obtained to confirm the structure of these compounds (Figure 102 and Figure 103 respectively). In the mononuclear complex **170**, the planarity of the aromatic system is disturbed to accommodate the five-membered manganacycle. The structure of dinuclear complex **173** is almost planar due to the additional geometric constraints of the second manganese centre. As expected, consistent with the ppy complexes reported in the literature^{137,184,282} and Chapter 2, in both azo complexes the Mn-C bonds *trans* to the N and C donors of the ppy ligand are shorter than those *trans* to CO ligands.

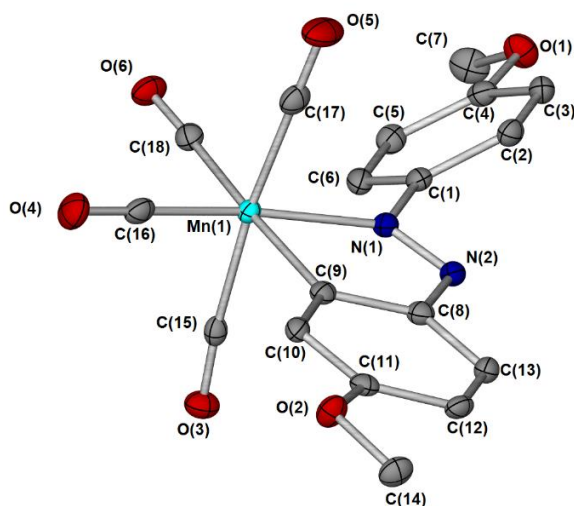


Figure 102 An X-ray crystal structure of compound 170 with hydrogen atoms omitted for clarity. Atoms are displayed as thermal ellipsoids at 50% probability. Selected bond lengths (Å): N(1)-N(2) = 1.278(2), C(9)-Mn(1) = 2.0346(19), C(15)-Mn(1) = 1.869(2), C(16)-Mn(1) = 1.815(2), C(17)-Mn(1) = 1.858(2), C(18)-Mn(1) = 1.846(2), N(1)-Mn(1) = 2.0505(16) Selected bond angles (°): C(9)-Mn(1)-N(1) = 77.92(7), C(16)-Mn(1)-N(1) = 168.53(8), C(18)-Mn(1)-C(9) = 176.45(8), C(17)-Mn(1)-C(15) = 173.45(8), C(18)-Mn(1)-N(1) = 98.56(7), C(16)-Mn(1)-C(18) = 92.82(8).

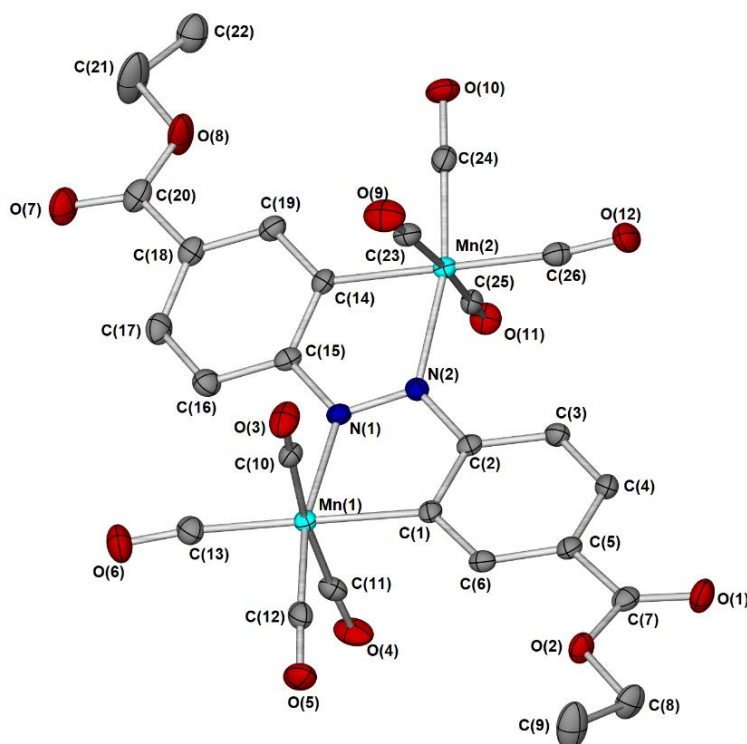
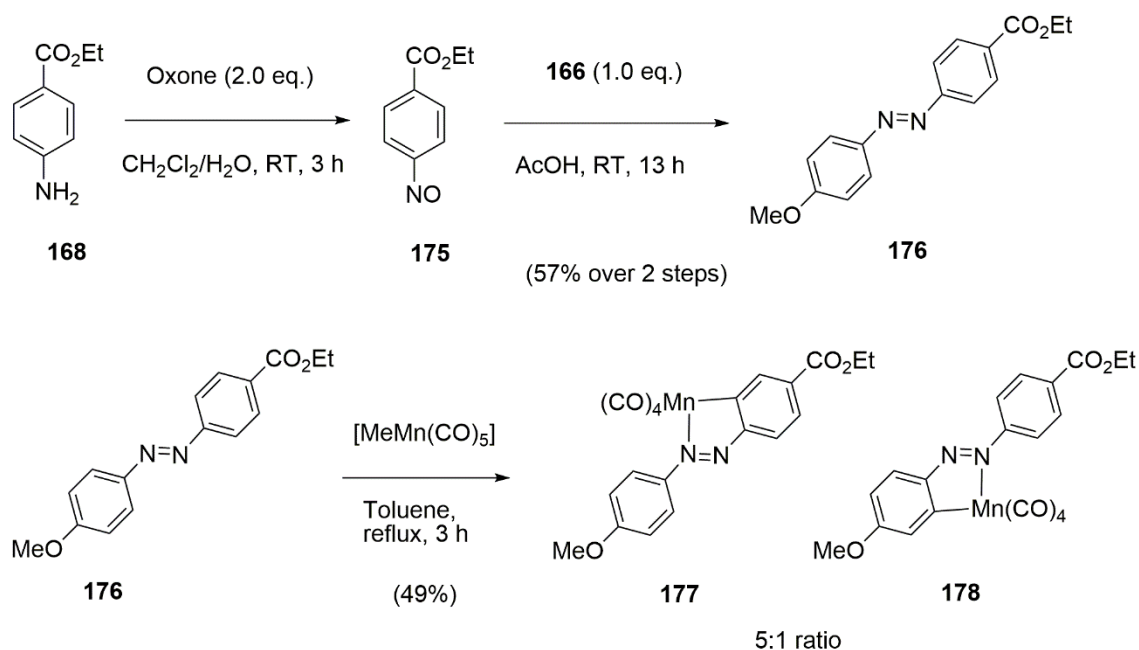


Figure 103: An X-ray crystal structure of compound 173 with hydrogen atoms omitted for clarity. Atoms are displayed as thermal ellipsoids at 50% probability. Selected bond lengths (Å): N(1)-N(2) = 1.299(3), C(1)-Mn(1) = 2.018(2), C(10)-Mn(1) = 1.877(3), C(11)-Mn(1) = 1.861(3), C(12)-Mn(1) = 1.801(3), C(13)-Mn(1) = 1.849(3), N(1)-Mn(1) = 2.083 (2) Selected bond angles (°): C(1)-Mn(1)-N(1) = 77.74(9), C(12)-Mn(1)-N(1) = 167.63(10), C(13)-Mn(1)-C(1) = 177.44(11), C(10)-Mn(1)-C(11) = 173.17(11), C(13)-Mn(1)-N(1) = 104.11(10), C(13)-Mn(1)-C(12) = 88.19(12).

The N=N bond of dinuclear complex **173** shows a significant lengthening from that of the corresponding free azobenzene³⁰⁹ **169**, from 1.250(2) Å to 1.299(3) Å. The lengthening of the azo bond upon cyclometalation reflects the π back-donation from the metal into the azo π^* and is therefore indicative of the nature of the bonding. A similar lengthening of the N=N bond was reported for the double cyclometalation of unsubstituted azobenzene itself.³¹⁵ Although complex **173** possesses different substituents on the azobenzene, the N=N bond length of this mononuclear complex lies in between these two values at 1.278(2) Å.

Ligand **176** (Scheme 60) was also synthesised in an effort to develop a ‘push-pull’ chromophore ligand. Incorporation of electron-rich donors and electron-poor acceptors in chromophore molecules is a well-known strategy to lower the energy gaps between frontier molecular orbitals, leading to intense visible light absorption, as summarised in a recent comprehensive review.³¹⁶ ‘Push-pull’ azobenzene **176** was synthesised by oxidation of aniline to nitroso compound **175**, which was then converted to azo dye **175** using aniline **166**.³¹⁷



Scheme 60: Synthesis and cyclometallation of azobenzene 176.

A preliminary attempt to cyclometalate ligand **176** with $[\text{MeMn(CO)}_5]$ resulted in the formation of the two regioisomers **177** and **178**. However, the regioisomers were not separable by silica gel or alumina column chromatography. The regioisomers were observed in the crude material by ^1H NMR spectroscopy (Figure 104).

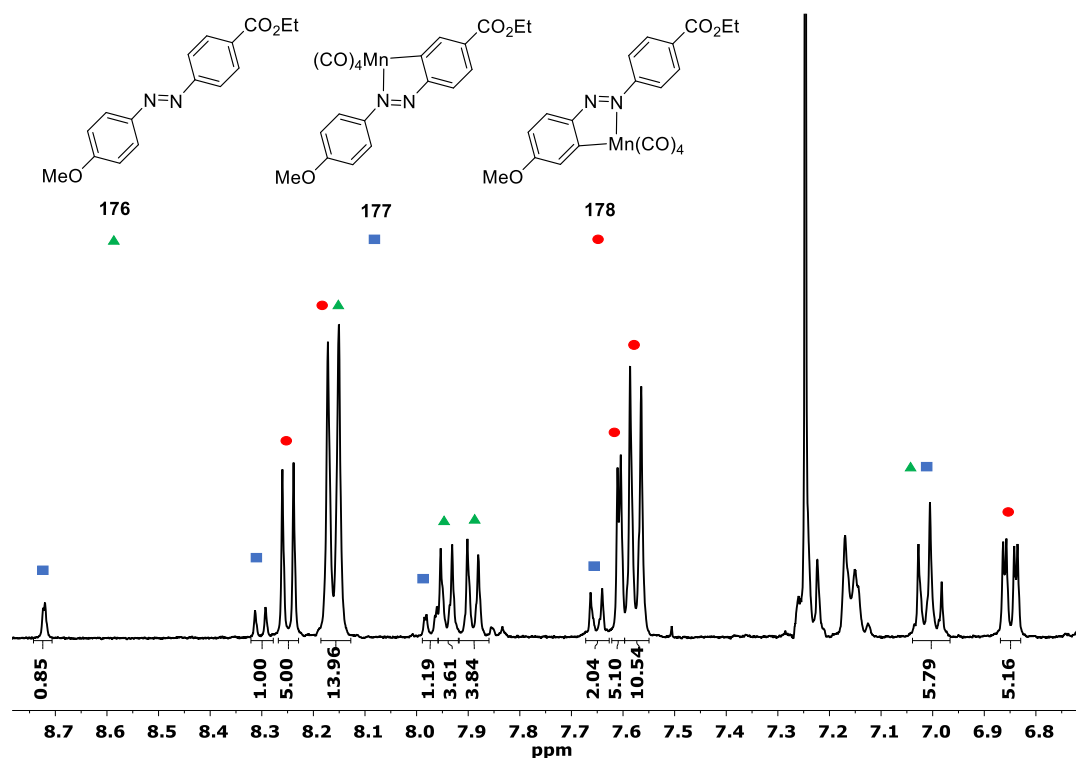


Figure 104: A 400 MHz spectrum of the crude material after cyclometalation of azobenzene **176** with $[\text{MeMn}(\text{CO})_5]$ recorded at 298 K in CDCl_3 .

The NMR spectrum contained some unreacted azobenzene starting material **176** (green triangles) despite complete consumption of the $[\text{MeMn}(\text{CO})_5]$ having been indicated by infrared spectroscopy during reaction monitoring. This may be due to a difference in sensitivity of the two techniques or decomposition of the $[\text{MeMn}(\text{CO})_5]$. Since metal carbonyls are strong absorbers of infrared light, infrared spectroscopy is expected to be a more sensitive technique than NMR spectroscopy in this case, suggesting that the $\text{MeMn}(\text{CO})_5$ degraded through a side-reaction during the cyclometalation. The non-integrated peaks near the CHCl_3 peak (from 7.1–7.3 ppm) correspond to the residual toluene reaction solvent. The two regioisomers appeared in approximately a 5:1 ratio and were assigned based on the spectra of complexes **170** and **172**. The highly deshielded single-proton resonance at 8.72 ppm, from the desymmetrised $-\text{CO}_2\text{Et}$ substituted ring, is diagnostic of desymmetrisation of the benzene ring in complex **172**, closely resembling the 8.76 ppm resonance from the similar proton in complex **172**.

Although the two possible sites for cyclometalation of **176** are *meta* to either the $-\text{CO}_2\text{Et}$ or $-\text{OMe}$ substituents, the electronic properties of these substituents clearly still have an influence on the regioselectivity of the reaction. Earlier work by Bruce and co-workers on the regioselectivity of the cyclomanganation of substituted azobenzenes showed that cyclometalation is typically selective towards electron-poor sites of aromatic rings.³⁰³

An indication of the electron-donating or electron-withdrawing influence of a substituent can be obtained by considering the Hammett parameters for *meta*-substituted aromatics, σ_m . The σ_m

values are +0.12 for -OMe and +0.37 for -CO₂Et.³¹⁸ Less positive values indicate superior electron-donating groups, meaning that the position *meta* to the -OMe group is more electron rich than the carbon atom *meta* to the -CO₂Et group. However, cyclometalation *meta* to the -OMe group is preferred on cyclometalation of azobenzene **176**. This cyclometalation reaction therefore appears to display an unusual regioselectivity for a more electron-rich site.

Preparative HPLC may be employed in future work in order to separate the two regioisomers. It may be possible to purify a single 'push-pull' complex by using an excess of [BnMn(CO)₅]. This would ensure that all the monocyclometalated complexes were converted into the dicyclometalated complex, which may then be chromatographically separable.

Given the successful synthesis and purification of the initial mono- and dinuclear complexes **170-173**, these complexes were evaluated as photoCORMs before further synthetic work. The idea of a 'push-pull' azo photoCORM could then be re-evaluated in light of these tests on the photoCORM and redox properties of cyclometalated azo Mn tetracarbonyl complexes.

4.3 Photochemical CO release

4.3.1 Calculated and Experimental UV-Visible Absorption Spectra

Before assessing the CO release of the complexes, UV-visible spectra were recorded to assess where the compounds absorb. This was intended to inform the choice of LED used for irradiation if specific transitions were identifiable. The ethoxy derivatives **172** and **173** were taken forward for study as a test system to assess the photochemical properties of the azo-derived complexes. The ester-substituted compounds were initially chosen due to the likelihood of the ester or corresponding carboxylic acid affording high water solubility for biological studies and easy functionalisation. Success with this group of compounds could then lead to a new modular CORM design based on functionalising the ester. Figure 105 shows an overlay of the UV-visible spectra of ester-substituted azobenzene **169** with cyclometalated complexes **172** and **173**. The spectrum of complex **172** was recorded by Alice de Palo under my supervision.

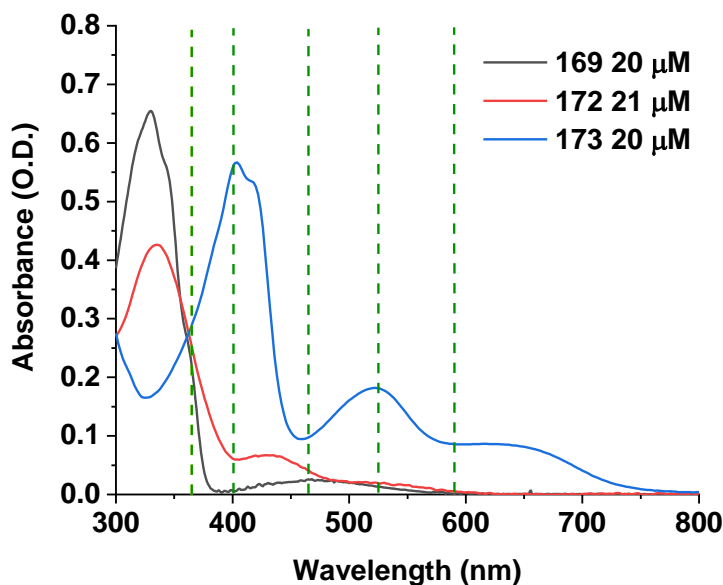


Figure 105: UV-visible spectra in CH_2Cl_2 of azo compound **169**, and cyclometalated complexes **172** and **173**. The dashed lines represent the LED wavelengths used for irradiation of the complexes to probe CO dissociation.

The spectra show that ligand **169** has only a relatively weak visible absorption band centred at around 500 nm, with the stronger azo π - π^* occurring mainly in the UV region of the spectrum. Upon cyclometalation to form complex **172**, another band with a λ_{max} value of 434 nm appears in the spectrum with $\epsilon(434 \text{ nm}) = (3.0 \pm 0.2) \times 10^3 \text{ dm}^3 \text{ mol}^{-1} \text{ cm}^{-1}$. The position, appearance, and extinction coefficient of this band resemble the MLCT band for $[\text{Mn}(\text{ppy})(\text{CO})_4]$ in Section 2.2.2, except the wavelength has undergone a bathochromic shift of around 80 nm into the visible region. This is an encouraging result as this irradiation of the MLCT band for $[\text{Mn}(\text{ppy})(\text{CO})_4]$ provides efficient CO release. This transition therefore warrants further investigation of its CO-release properties.

Complex **173** exhibits bands throughout the visible region and appears to show a further bathochromic shift of all bands compared to **172**. However, the relative intensities of the bands has also changed and so this result should be treated with caution; it may be that the transitions being observed in **173** are very different to those in **172**. To probe this, TD-DFT calculations could be employed to predict the orbital transitions involved within each band. However, a practical method to determine which transitions are CO-dissociative is to irradiate the complexes with several different wavelengths of UV or visible LED lights in the presence of myoglobin. The wavelengths of LED used are overlaid on the spectrum in Figure 105.

4.3.2 Photochemical CO Release to Myoglobin

To test the thermal stability and confirm the wavelength range of the photochemical CO-dissociative transitions, CO release to myoglobin was quantified. Incubation in the dark was followed by LED irradiation with various wavelengths of UV or visible light. As discussed in Section 1.3.2.1, the CO release assay relies on the change in absorbance of myoglobin at 540 nm upon binding CO. However, the azo dye CORMs synthesised in this Chapter also absorb at this wavelength. It is also likely that any degradation products containing the azo ligand would also absorb in this region of the spectrum. As a result, only low concentrations (10 μM) of the complexes were used compared to myoglobin (50-60 μM) and a full isosbestic point correction to the spectra (as described in Section 3.4.3) was performed. The results for complex **172** are summarised in Figure 106 and Table 16.

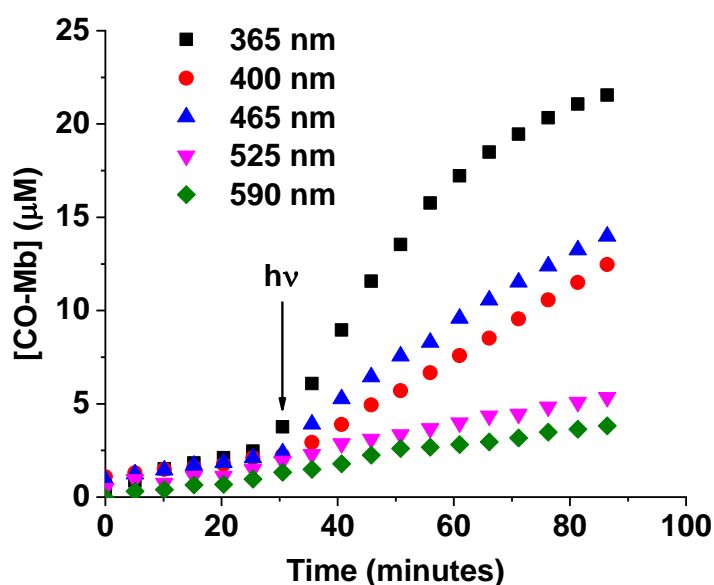


Figure 106: The CO release profiles of **172** in the dark and upon LED irradiation. A concentration of 10 μM **172** was used for all assays, with 50-60 μM myoglobin. Irradiation was performed at a power of 6.0 W in cycles of 3 minutes off, 2 minutes on from 30 minutes onwards.

The results show that slow CO release from complex **172** takes place in the dark during the first 30 minutes of the experiment, with 1-4 μM [CO-Mb] forming within this time. This could be due to reactivity such as protonation of the cyclometalated azo ligand, reaction with the phosphate buffer, water, Mb or the reducing agent sodium dithionite. After establishing this slow background level of CO release, the data show that LED irradiation at either 365, 400 or 465 nm accelerates the rate of CO release. This indicates photochemical irradiation enhances CO release within this wavelength range (365-465 nm). Irradiation with 525 nm and 590 nm LEDs did not result in an enhancement in the rate of CO release compared to the initial 30 minutes in the dark – the slow, linear profile of the early dark CO release continues throughout the experiment.

Although a full-length control with no irradiation was not performed to confirm this, the experiments with 525 and 590 nm were concluded to effectively measure the slow ‘background’ of CO release observed in the dark, since no enhancement is seen of the initial dark CO release and because the traces are very similar for both wavelengths. In any case, any such enhancement would be extremely small and unlikely to be useful for CORM applications.

The observation of some photochemical CO release at 465 nm represents a success of the CORM design. The 465 nm release shows that incorporation of an azo dye co-ligand has shifted the CO release wavelength further into the visible region compared to the family of ppy complexes $[\text{Mn}(\text{ppy})(\text{CO})_4]$, which display no electronic absorption bands at 465 nm (Section 4.1.1). This is the desired effect predicted from the work on analogous complexes by Mascharak and co-workers.¹²⁷ However, the rates of CO release at both 400 and 465 nm for complex **172** were still relatively slow given the high power of irradiation used when compared to complex **161** (Table 16). At the end of the experiment, after 30 minutes in the dark and 12×5 -minute on/off cycles of irradiation (24 minutes of irradiation in total), the 365 nm experiment resulted in the release of 2.2 equivalents of CO to myoglobin per Mn, whereas 1.3 equivalents per Mn were released at 400 and 465 nm. Thus, although the experiments at 400 and 465 nm gave an increase from the background ‘thermal’ CO release seen in the ineffective 525 and 590 nm experiments, the data show that UV irradiation at 365 nm was still the most efficient method of triggering CO release from complex **172**.

Table 16: Comparison of the CO release experiments for a range of Mn(I) carbonyl complexes to compare the release profile of 172 with complexes 90, 91, 95, 133, 134 and 161. The starting concentration of CORM was 10 μ M in all cases except for complex 133, where it was 40 μ M.

Complex	Wavelength / nm	Power / W	Eq. CO Released After 12 Irradiation Cycles per Mn
172	365	6.0	2.2
172	400	6.0	1.3
172	465	6.0	1.3
172	525	6.0	0.5
172	590	6.0	0.5
161	465	2.4	2.3 ¹³⁷
90	400	2.4	2.6 ¹⁸⁴
91	400	2.4	2.6 ¹⁸⁴
95	400	2.4	2.9 ¹⁵⁹
133	400	5.0	1.0 (Chapter 3)
134	400	5.0	2.5 (Chapter 3)

When considering the data in Table 16, it should be remembered that complex **172** displayed slow background CO release without irradiation and that the 0.5 eq. CO was released at 525 and 590 nm was thermal release. It is likely that a similar number of CO equivalents was released thermally in conjunction with the successful photochemical release at 365-465 nm, and so only a proportion of the total equivalents released were photochemically-triggered. Complex **161** also displayed thermal release to some extent, but caution should be taken in quantitatively comparing the background ‘thermal’ release rates of the two complexes as neither Ward’s study or this work included a full control over the entire length of an assay; the only test for thermal CO release was the initial 30-minute incubation in the dark.

Table 16 also shows a comparison with **172** and some CORMs derived from complex **88**, [Mn(ppy)(CO)₄]. The ppy-based derivatives were all stable to the experimental conditions in the dark and it is known that all CO release is photochemically triggered.¹⁵⁹ Although there is no comparable data for the equivalents of CO released by complex **88** itself at 10 μ M, several of its derivatives (Cl and Br labelled complexes **90** and **91** and carboxylic acid derivative **95**) have been tested and yielded 2.6-2.9 equivalents of CO per Mn at 400 nm, far more than **172** and at a lower

irradiation power.^{159,184} Therefore, despite an apparent shift of the CO release wavelength into the visible, the ppy-derived complexes appear to release CO much more rapidly than **172** at 400 nm. Similarly, complex **161** releases more CO at 465 nm than does **172**.

Finally, Table 16 shows the ferrocenyl complexes **133** and **134** that were discussed in Chapter 3. The CO release from complex **172** is comparable to the very slow CO release from ferrocenyl complex **133** at high power and 400 nm wavelength. However, as discussed in Chapter 3, complex **133** appeared to have poor water solubility compared to the other complexes, so the value of 1.0 equivalents per Mn is likely to be an underestimate and accounts for the difference with the other ppy derivatives. No such solubility issues were identified for complex **172** – there was no sign of any wavelength-independent increase in absorbance throughout the assay as had been observed in all experiments with complexes **132** (insoluble) and **133** (partially soluble). Complex **134**, which was water soluble, released 2.5 equivalents of CO per molecule, through both thermal and photochemical release. It is notable that despite there being two CO release mechanisms at work, complex **134** (and **161**) still release around 2.3-2.5 equivalents of CO, only slightly less than the ppy derivatives. This supports the hypothesis that the poor CO release rate observed for **172** is inherently a feature of this complex rather than as result of the mixed thermal/photochemical release mechanism.

The number of equivalents of CO released by exhaustive photolysis of **172** was evaluated by allowing the 365 nm irradiation experiment to run until no further change in the myoglobin spectra could be seen. The full CO release trace is shown in Figure 107.

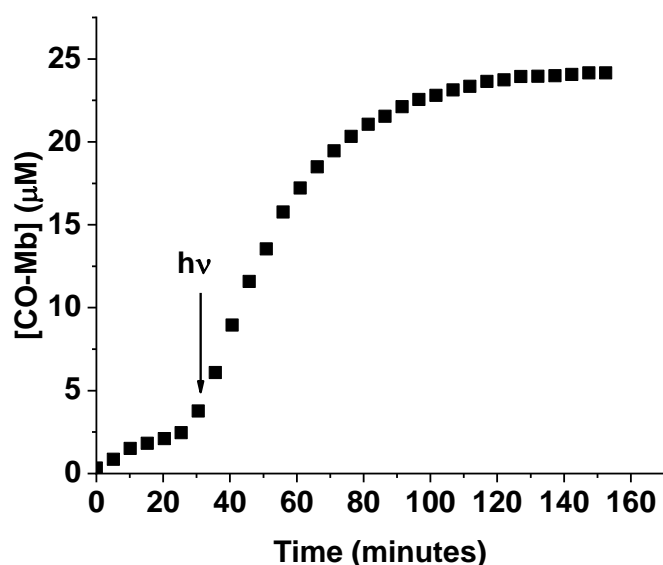


Figure 107: Exhaustive CO release from 10 μM **172 using 365 nm LED irradiation. Irradiation was performed at a power of 6.0 W in cycles of 3 minutes off, 2 minutes off from 30 minutes onwards.**

The data shows exhaustive CO release after 30 minutes of incubation with myoglobin in the dark followed by two hours of irradiation. The graph levels off at a [CO-Mb] concentration of 24 μM , so that 2.4 equivalents of CO were released per molecule of **172**. This is similar to the tetracarbonyl ppy complexes, which appear to release 2.5-3 equivalents of CO per molecule of photoCORM as reported in Section 3.4.3 and in the literature.¹⁸⁴ Non-integer values for CO can be understood based on side-reactions such as CO insertion into the Mn-C bond of the ppy¹⁵⁹ and the possible formation of cluster species detected in this Thesis. It is also possible that not all of the CO released by CORMs gets captured by the myoglobin assay.

The CO release profile of doubly-cyclometalated complex **173** was also studied. Thermal CO release and irradiation with 590, 525, and 400 nm LEDs was performed. The results, shown in Figure 108, showed little photochemical CO release at these wavelengths.

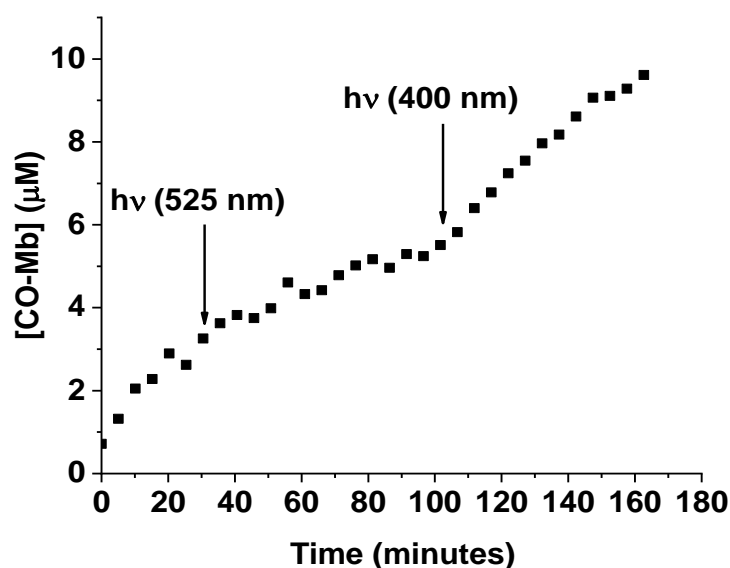


Figure 108: The CO release behavior of 10 μM **173** in the dark and upon LED irradiation. Irradiation at 525 and 400 nm was performed at a power of 6.0 W in cycles of 3 minutes on, 2 minutes off from 30 minutes onwards.

The data in Figure 108 highlights the instability of complex **173** in the dark leading to a small amount of slow CO release and shows that irradiation with 525 nm LED did not accelerate the CO release. When the 525 nm LED was replaced by a 400 nm LED, a slight acceleration in the CO release was observed indicating that at shorter wavelengths complex **173** does exhibit some photochemical CO release. However, the rate of the CO release at 400 nm for complex **173** appeared to be slower than for **172** at the same wavelength. This observation and the lack of sensitivity to visible light suggests that the CO-dissociative transitions for the doubly-cyclometalated complex **173** lie at shorter wavelengths than **173**.

4.3.3 Ultrafast Time-Resolved Infrared Spectroscopy of **172** and **173**

The ultrafast photochemistry of complexes **172** and **173** was studied using TR^MPS, the same type of pump-probe experiment employed in Chapter 2. The aim of the study was to gain an understanding of the primary photochemistry of these complexes to understand why they display such inefficient photochemical CO release compared to the analogous ppy complexes. As with the ppy complex **88** in Chapter 2, it was not possible to perform TRIR spectroscopy on the azo complexes in aqueous solution due to the tens of millimolar concentrations required for the experiment, several orders of magnitude higher than would be anticipated for a therapeutically relevant effect.⁷⁴

4.3.3.1 Complex 172

Based on the irradiation experiments in the myoglobin assays, which indicated that the most efficient CO loss occurs with 365 nm LED irradiation, a pump wavelength of 355 nm was used. Spectra at short pump-probe delays for complex **172** in THF solution are shown in Figure 109. A scaled ground state spectrum of **172** is provided as a reference, and the band positions for all ground states and solvents used are tabulated in Section 7.1.1. For clarity, the spectra at 2 and 100 ps are also compared individually in Figure 110.

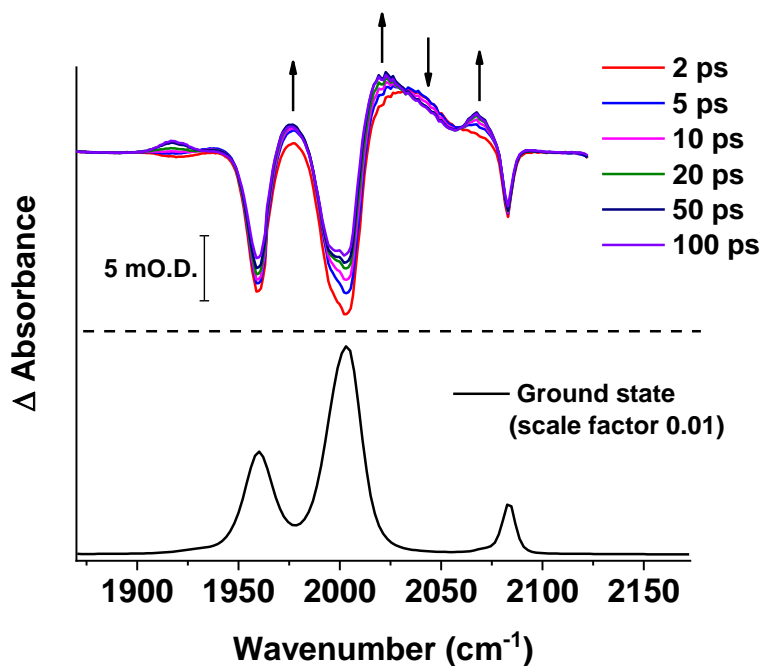


Figure 109: TRIR spectra of complex 172 in THF under air at picosecond pump-probe delays. A pump wavelength of 355 nm was used. The arrows indicate the direction of change in absorbance of the bands over time. A scaled spectrum of the ground state of complex 172 in THF is shown for reference.

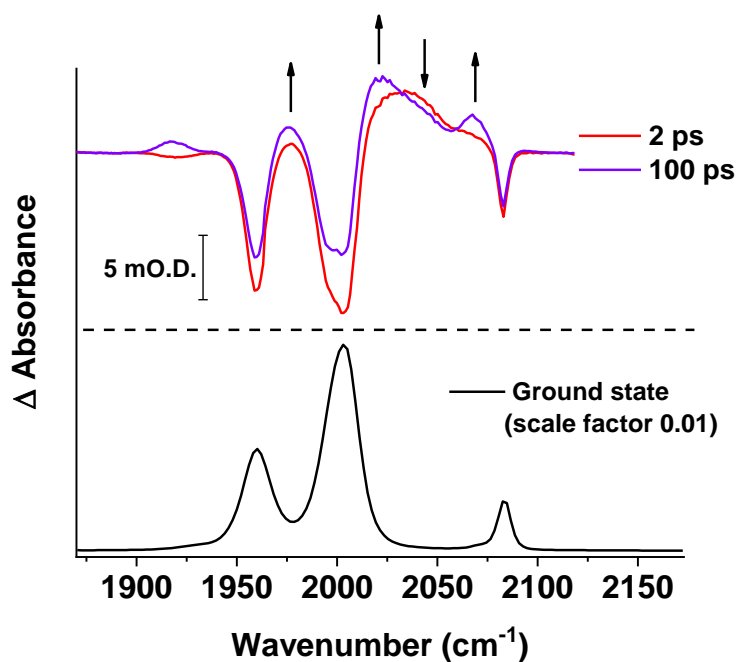


Figure 110: TRIR spectra of complex 172 in THF under air at picosecond pump-probe delays comparing the delays at 2 and 100 ps – the data are from the same experiment as that in Figure 109. A scaled spectrum of the ground state of complex 172 in THF is shown for reference.

The TRIR difference spectra at short pump-probe delays appeared very different to those of $[\text{Mn}(\text{ppy})(\text{CO})_4]$. The dominant photoproduct in the difference spectra at short pump-probe delays exhibited broad bands with apparent maxima at around 1976 cm^{-1} and 2040 cm^{-1} that appeared within the first 1-2 ps. The bands of this species did not resemble the solvated *facial* tricarbonyl species observed in the related experiments with $[\text{Mn}(\text{ppy})(\text{CO})_4]$. Instead, this photoproduct closely resembled the minor photoproduct $^3[\text{Mn}(\text{ppy})(\text{CO})_4]$: the short-lived non-dissociative triplet excited state. The predominant photoproduct observed in Figure 109 was therefore assigned as a triplet excited state, $^3[\mathbf{172}]\text{-(1)}$.

The reasons for the assignment of this excited state as a triplet are its lifetime (between *ca.* 5-10 ps, Table 17), and the resemblance of the spectra to the $^3\text{MLCT}$ states of $[\text{Mn}(\text{ppy})(\text{CO})_4]$ and the isoelectronic $[\text{Cr}(\text{bpy})(\text{CO})_4]$. In all cases the initial excitation is assumed to be to a singlet excited state (or states), since direct transitions to triplets are spin-forbidden and therefore much weaker. However, the lifetime of the excited state of complex **172** in Figure 109 is much longer than would be expected for the $^1\text{MLCT}$ state. For comparison, the singlet excited state in $[\text{Cr}(\text{bpy})(\text{CO})_4]$ decays within 100 fs due to the competing processes of CO loss and triplet excited state formation.¹⁷⁵ Given the behaviour of $[\text{Cr}(\text{bpy})(\text{CO})_4]$ and $[\text{Mn}(\text{ppy})(\text{CO})_4]$ it is likely that ultrafast CO dissociation, and intersystem crossing to form the $^3\text{MLCT}$ excited state, occur in <1 ps from the $^1\text{MLCT}$ state in complex **172**. Dissociation of CO in <1 ps was observed in $[\text{Mn}(\text{ppy})(\text{CO})_4]$ but the same cannot be confirmed for complex **172** with the data in Figure 109 due to the overlap of the weak solvated tricarbonyl bands with other bands. For $[\text{Mn}(\text{ppy})(\text{CO})_4]$ and

[Cr(bpy)(CO)₄], the MLCT nature of the excitation was apparent from TD-DFT calculations (Section 2.2.2); similar calculations could in future be performed to compare the charge transfer in azo complex **172**.

The band for ³[**172**]-**(1)** at around 2040 cm⁻¹ decayed on the ps timescale and was replaced with a new set of bands corresponding to a second photoproduct with bands at 2023 and 2068 cm⁻¹ (Figure 112). The small positive absorbance at 1976 cm⁻¹ remained essentially unchanged on the picosecond timescale but there were changes to the nearby bleach bands in this region as the first photoproduct was consumed and the second grew in, suggesting that both photoproducts also had bands in this region. The second photoproduct was also assigned as an excited state, ³[**172**]-**(2)**, because the bands were broad and did not resemble the solvated *facial* tricarbonyl species observed with [Mn(ppy)(CO)₄]. For example, the high-wavenumber band at 2068 cm⁻¹ in this excited state was far higher than the carbonyl stretches of any of the CO dissociation products observed so far. The lifetime of the initial photoproduct ³[**172**]-**(1)** was measured based on the absorbance at 2040 cm⁻¹, and this was compared to the growth of ³[**172**]-**(2)** (Table 17).

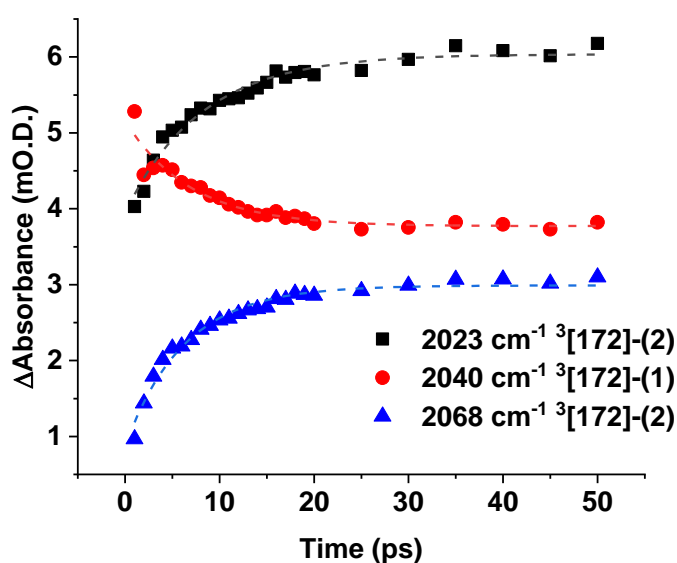


Figure 111: Kinetic profiles of selected TRIR bands for **172 on the picosecond timescale. The dashed lines are single exponential fits.**

The single exponential lifetimes for the loss of ³[**172**]-**(1)** and growth of ³[**172**]-**(2)** are the same within the 95% confidence intervals of the fits. This evidence supports the hypothesis that consecutive population of the two excited states takes place, as opposed to re-population of the ground electronic state upon decay of the short-lived excited state.

Table 17: Single exponential lifetime of the decay of $^3[172]-(1)$ and growth of $^3[172]-(2)$ with 95% confidence intervals.

Wavenumber / cm^{-1}	τ / ps
2040 (growth)	6.9 ± 2.0
2023 (decay)	8.1 ± 1.5
2068 (decay)	6.3 ± 1.0

Spectra at ns pump-probe delays from the same experiment as the data in Figure 109 are shown in Figure 112. The data show that the $^3[172]-(2)$ persisted for the first few tens of nanoseconds before decaying. The kinetics of the decay compared to the recovery of the bleach bands is shown in the first order exponential fits in Figure 113, and the lifetimes are subsequently tabulated in Table 18.

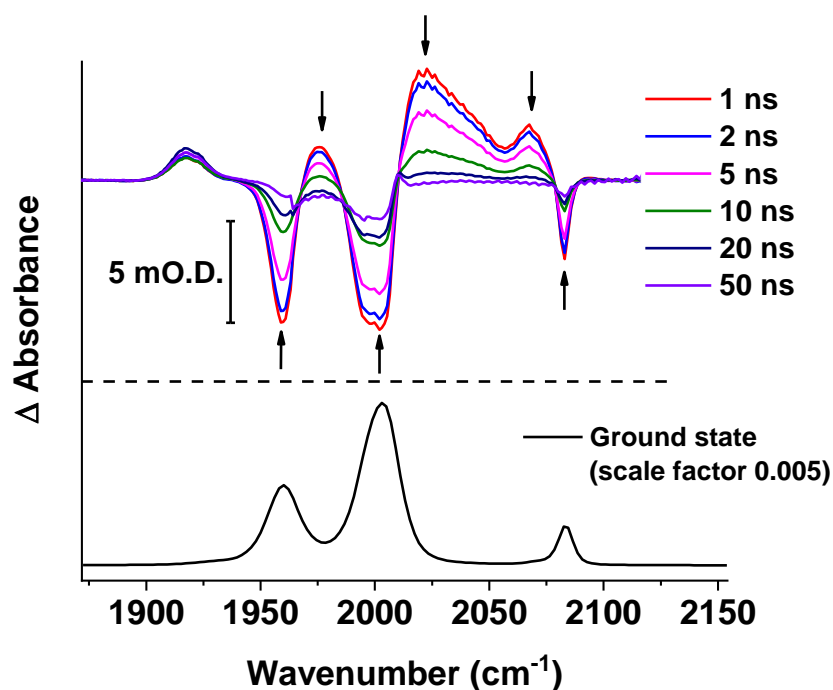


Figure 112: TRIR spectra of complex 172 in THF under air at nanosecond pump-probe delays. A pump wavelength of 355 nm was used. The arrows indicate the direction of change in absorbance of the bands over time. A scaled spectrum of the ground state of complex 172 in THF is shown for reference.

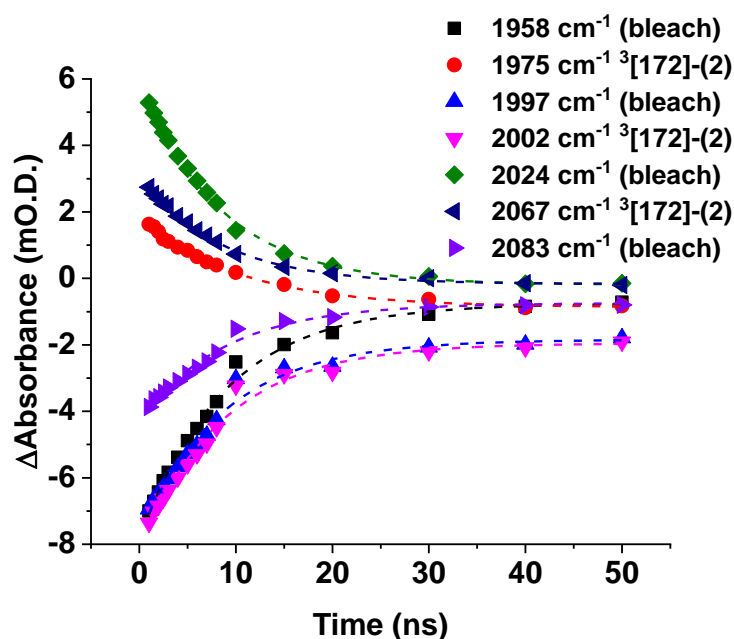


Figure 113: Kinetic profiles of selected TRIR bands for 172 on the nanosecond timescale. The dashed lines are single exponential fits.

Table 18: Single exponential lifetime of $^3[172]-(2)$ and concurrent bleach recovery with 95% confidence intervals.

Wavenumber / cm^{-1}	τ / ns
1975	10.3 ± 1.1
2024	8.3 ± 0.6
2067	8.4 ± 0.6
1958 (bleach recovery)	8.9 ± 1.1
1997 (bleach recovery)	8.8 ± 1.7
2002 (bleach recovery)	8.8 ± 1.7
2083 (bleach recovery)	8.8 ± 1.6

The loss of $^3[172]-(2)$ was accompanied by near-complete recovery of the ground state bleach bands, all with the same single exponential lifetime. Compared to $[\text{Mn}(\text{ppy})(\text{CO})_4]$, there was a much better match of the bleach bands to the decaying excited state bands – this could be because vibrational relaxation was complete by the nanosecond timescale, whereas the excited state in $[\text{Mn}(\text{ppy})(\text{CO})_4]$ decayed on the picosecond timescale and may have been convoluted by the effects of vibrational relaxation and geminate recombination.

The final band to discuss in the difference spectra in Figure 109 and Figure 112 is the small, low-wavenumber band at 1917 cm^{-1} . The 1917 cm^{-1} band was assigned to *facial* tricarbonyl complex **179**_{THF(O)} (Scheme 61). The assignment was confirmed by looking at the difference spectrum after a pump-probe delay of $1\ \mu\text{s}$, when the excited state bands had decayed away (Figure 114). An additional band at 2010 cm^{-1} , overlapping a bleach, is visible in the spectrum, consistent with the pattern of two closely spaced (in this case coalescent) low-wavenumber bands separated from a single band at high-wavenumber as observed for the *facial* tricarbonyl complexes in Chapter 1 and in the literature.²⁰⁰ This photoproduct persists into the microsecond timescale before being removed by the flow system. Studying its reactivity at longer times would require an *in situ* infrared experiment with LED irradiation such as those in Section 3.4.2, although the continuous irradiation in such an experiment may prevent the distinction of thermal and photochemical reactivity. If it could be made in adequate yield, would be desirable in future work to isolate this species for further characterisation and to assess its thermal and photochemical reactivity.

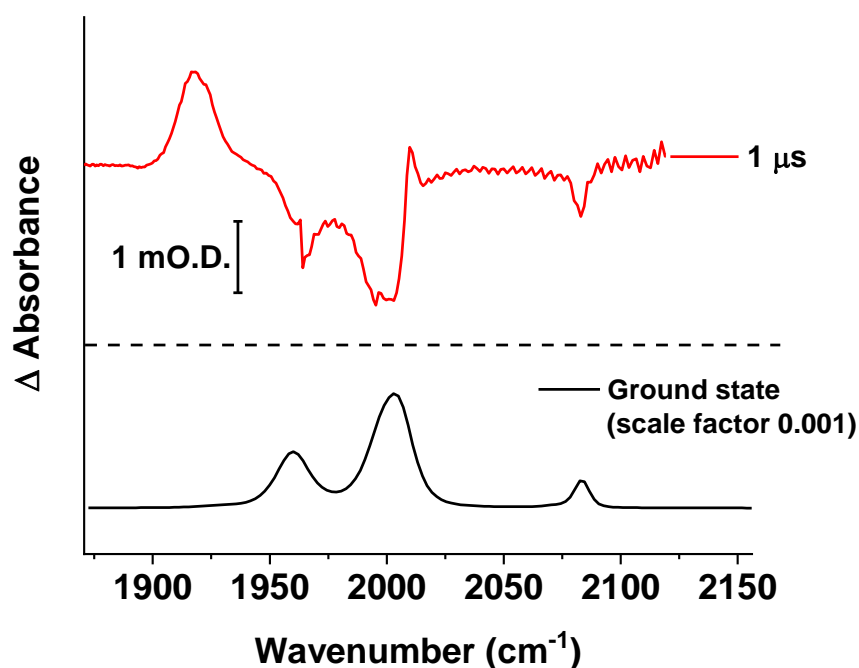
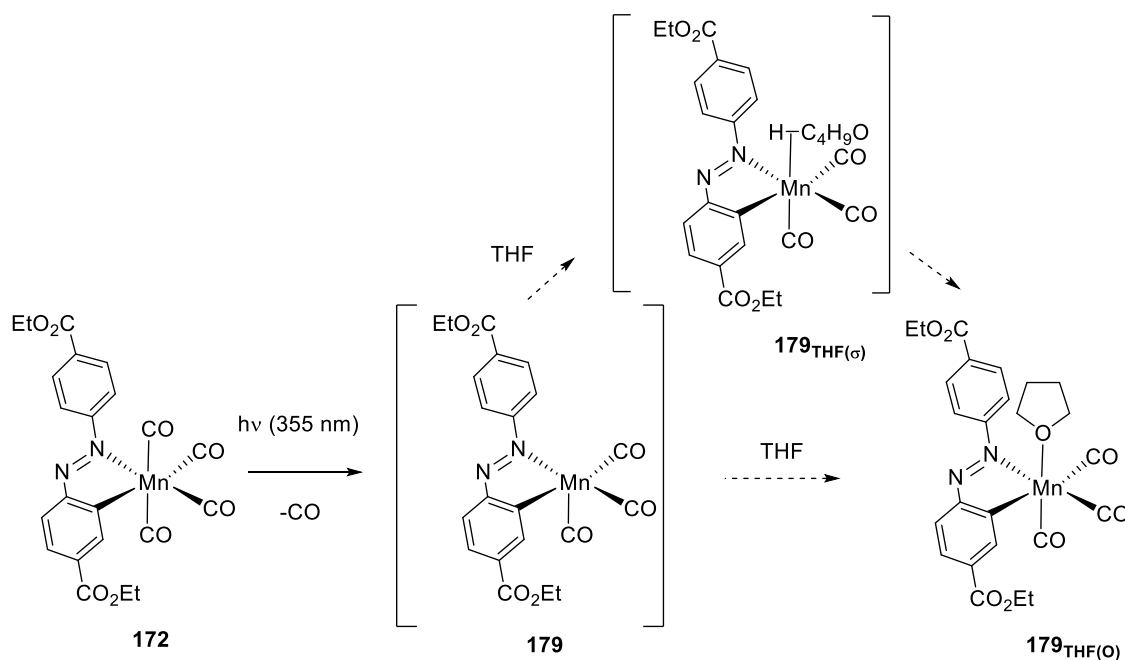


Figure 114: TRIR spectrum of **172** in THF under air at a pump-probe delay of $1\ \mu\text{s}$. A pump wavelength of 355 nm was used. A scaled spectrum of the ground state of complex **172** in THF is shown for reference.

The 1917 cm^{-1} band grew in with a single exponential lifetime of $(24.2 \pm 3.9)\text{ ps}$, showing that it was not part of the excited states, discussed above, that dominate the photochemistry of **172**. The time taken for the **179**_{THF(O)} band to initially grow in may be dictated by vibrational relaxation causing the band to sharpen, or by isomerisation from C-H σ -complex **179**_{THF(σ)} to produce **179**_{THF(O)} (Scheme 61). Vibrational relaxation is typically accompanied by a small shift of the band to higher wavenumber,³¹⁹ but this was not observed in the spectra in Figure 109. However, if isomerisation from **179**_{THF(σ)} to **179**_{THF(O)} were taking place, a broad band at higher wavenumber

corresponding to $179_{\text{THF}(\sigma)}$ should be present at short pump-probe delays, and no such band was observed in Figure 109. It would seem unlikely that THF coordinates selectively through the O atom in this case given the isomerisations observed in Chapter 2. It is possible that the band for $179_{\text{THF}(\sigma)}$ was masked by overlaps with the 1958 cm^{-1} bleach band and the excited state photoproducts that also absorb in this region, particularly because the bands for the excited states dominate the spectra with photodissociation seemingly only a minor pathway.



Scheme 61: Formation of complex $179_{\text{THF}(\sigma)}$. Dashed arrows have been used to reflect the lack of direct evidence for the mechanistic pathway.

4.3.3.2 Complex 173

The behaviour of the dinuclear complex **173** was also studied using TR^MPS. Similar behaviour was observed to that of complex **172**. At short pump-probe delays (Figure 115 and Figure 115), a short-lived excited state like the one observed for **172** was observed, denoted $^3[\mathbf{173}]\text{-(1)}$ decaying with a lifetime of *circa* 10 ps (Table 19). By 100 ps, a second excited state $^3[\mathbf{173}]\text{-(2)}$ dominated the spectrum. Excited state $^3[\mathbf{173}]\text{-(2)}$ grew in with a lifetime of (9.0 ± 1.0) ps measured at 2053 cm^{-1} , matching the decay of $^3[\mathbf{173}]\text{-(1)}$. Again, one only one bleach band (at 2017 cm^{-1}) showed any recovery as $^3[\mathbf{173}]\text{-(1)}$ decayed, and this most likely due to absorption $^3[\mathbf{173}]\text{-(1)}$ that forms on this timescale. A feature at low wavenumber with a maximum at around 1945 cm^{-1} was observed in these spectra, which was not observed in the spectra for **172**. This is likely to be the tail of the larger band at 1975 cm^{-1} rather than a separate band: excited states with MLCT character are expected to result in an increase in the wavenumber of the carbonyl bands.³²⁰

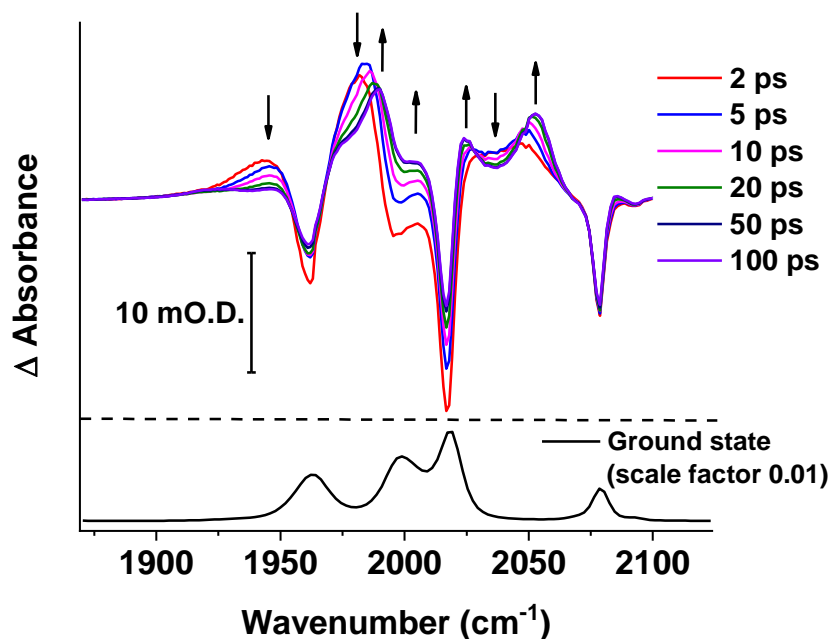


Figure 115: TRIR spectra of 173 in THF under air at picosecond pump-probe delays. A pump wavelength of 355 nm was used. The arrows indicate the changes of the photoproduct bands over time. A scaled spectrum of the ground state of complex 173 in THF is shown for reference.

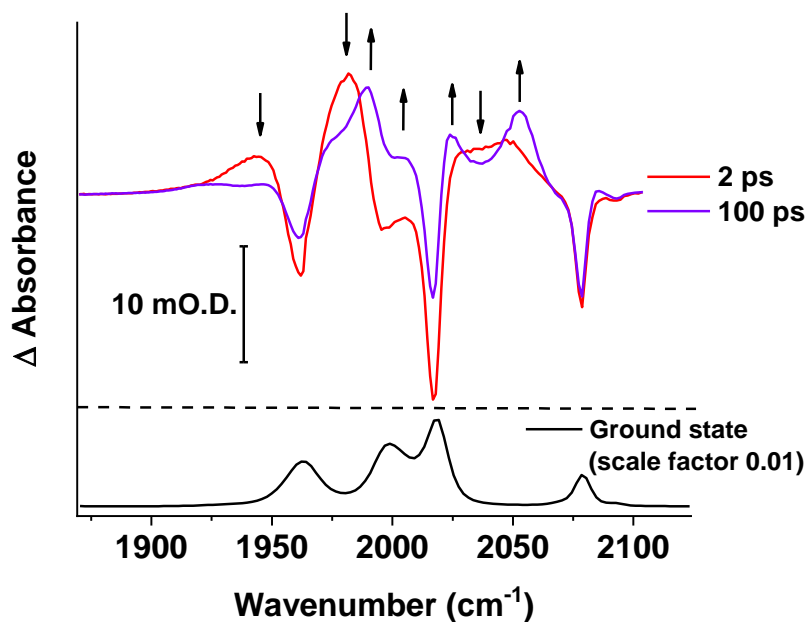


Figure 116: TRIR spectra of 173 in THF under air comparing 2 and 100 ps pump-probe delays for clarity. The arrows indicate the changes of the photoproduct bands over time. The graph shows the same data as Figure 115.

Table 19: Single exponential lifetimes for the decay of the $^3[173]$ -(1) bands and growth of the $^3[173]$ -(2) band at 2054 cm^{-1} , with 95% confidence intervals.

Wavenumber / cm^{-1}	τ / ps
1945	10.6 ± 0.9
1975	9.9 ± 0.9
2035	9.5 ± 0.6
2054 (growth of second excited state)	9.9 ± 0.6

As was the case for **172**, the long-lived excited state decayed on the nanosecond timescale with concomitant recovery of the bleaches, as shown in Figure 117 and Table 20. The lifetime was longer than for **172** at $\sim 30\text{ ns}$ compared to $\sim 10\text{ ns}$.

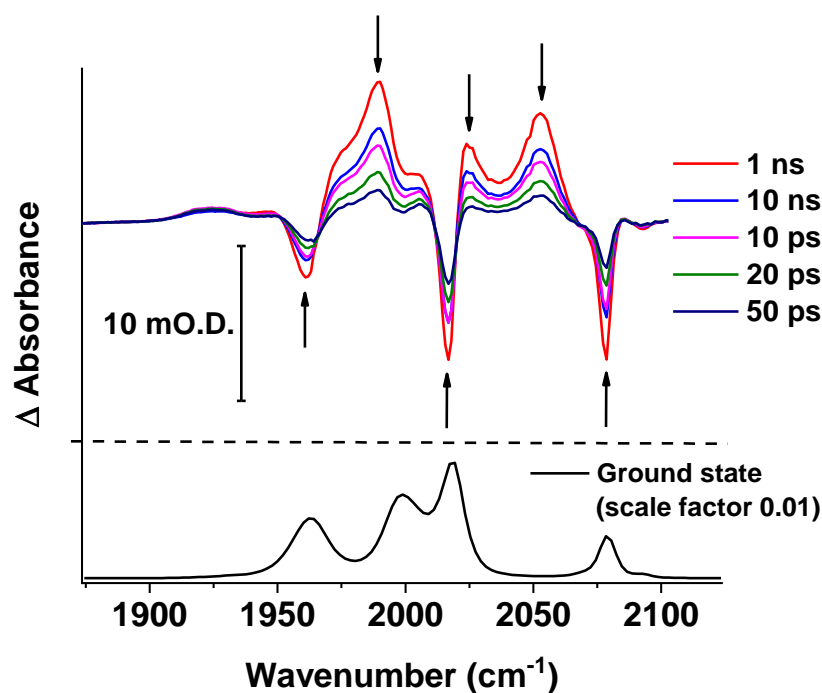


Figure 117: TRIR spectra of 173 in THF under air at nanosecond pump-probe delays. A pump wavelength of 355 nm was used. The arrows indicate the changes of the photoproduct and bleach bands over time. A scaled spectrum of the ground state of complex 173 in THF is shown for reference.

Table 20: Single exponential lifetimes for the decay of the $^3[173]-(2)$ bands. The single exponential lifetimes for concomitant bleach recovery are also given. The fits are reported with 95% confidence intervals.

Wavenumber / cm^{-1}	τ / ns
1990	28.4 ± 3.6
2024	28.1 ± 3.4
2054	27.6 ± 3.5
1961 (bleach recovery)	26.8 ± 5.4
2017 (bleach recovery)	29.3 ± 9.1
2079 (bleach recovery)	29.9 ± 5.2

Following the decay of $^3[173]-(2)$, a small set of bands resembling a solvated *facial* tricarbonyl species was observed, confirming that CO dissociation takes place in the UV for complex **173** to give $\mathbf{180}_{\text{THF(O)}}$ Scheme 62. No additional bands carbonyl stretching bands were observed compared to $\mathbf{180}_{\text{THF(O)}}$. This suggests that the infrared stretching bands of the remaining “ $\text{Mn}(\text{CO})_4$ ” moiety in the molecule did not shift in wavenumber by a sufficient amount to be detected.

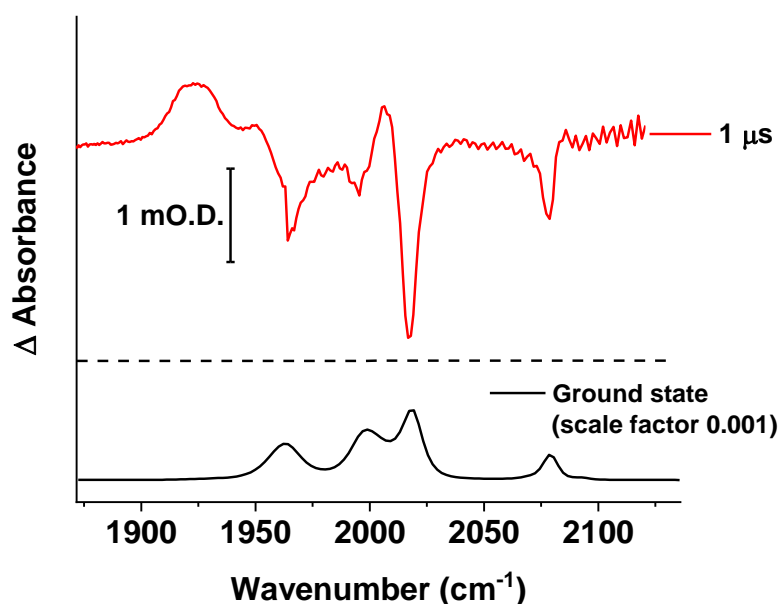
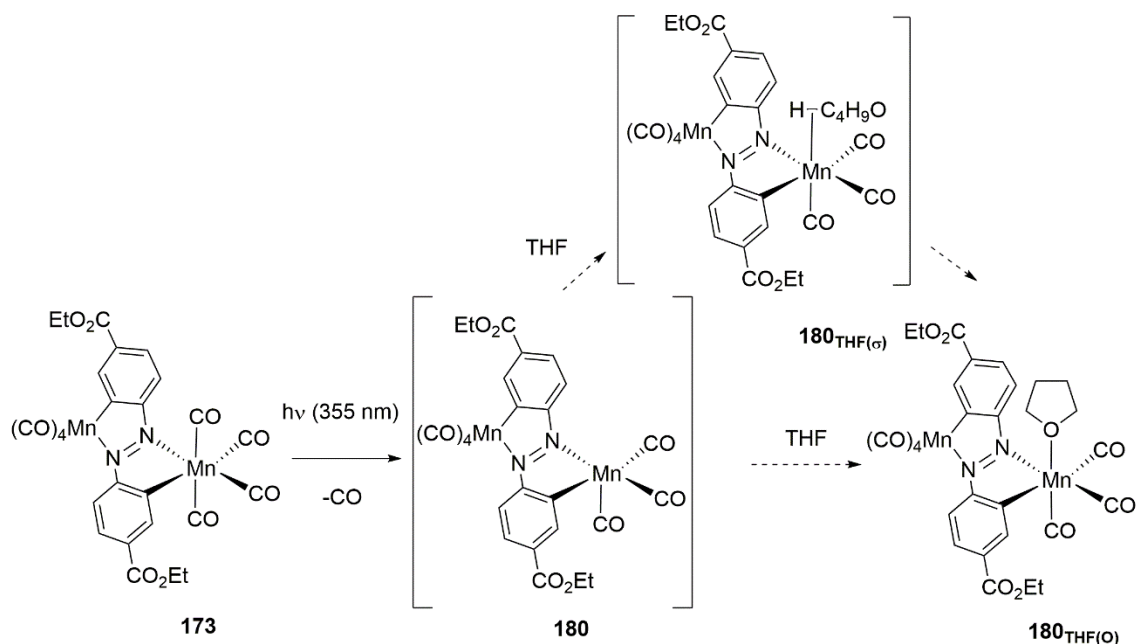


Figure 118: TRIR spectrum of 173 in THF under air at a pump-probe delay of 1 μs . A pump wavelength of 355 nm was used. A scaled spectrum of the ground state of complex 173 in THF is shown for reference.



Scheme 62: Formation of complex $180_{\text{THF(O)}}$. Dashed arrows have been used to reflect the lack of direct evidence for the mechanistic pathway.

4.3.3.3 Discussion of Ultrafast Results

The ultrafast photochemical behaviour observed for the two complexes **172** and **173** is strikingly different to the behaviour of $[\text{Mn}(\text{ppy})(\text{CO})_4]$ (Chapter 2) and more closely resembles $[\text{Cr}(\text{bpy})(\text{CO})_4]$. Photochemical CO loss is the dominant process for $[\text{Mn}(\text{ppy})(\text{CO})_4]$ but in **172** and **173** the major photoproducts are two consecutively populated excited states, representing a significant change in the balance of the fundamental primary photochemical steps. The balance between $^3\text{MLCT}$ formation and CO loss in the azo complexes **172** and **173** is skewed much more in favour of excited state formation compared to $[\text{Mn}(\text{ppy})(\text{CO})_4]$ and its derivatives. This qualitative comparison explains why photochemical CO release from the azo complexes to myoglobin was slower than for the ppy analogues, since CO release from the azo complexes appears to be very inefficient. Quantum yield measurements for CO dissociation would enable quantification of this comparison.

Like $[\text{Mn}(\text{ppy})(\text{CO})_4]$, which displayed one excited state with a lifetime that decayed on the ps timescale, the azo complexes **172** and **173** exhibited short-lived excited states - $^3[\mathbf{172}]-(1)$ and $^3[\mathbf{173}]-(1)$ respectively - on the ps timescale. Rather than the short-lived excited state decaying back to the ground state as observed for $[\text{Mn}(\text{ppy})(\text{CO})_4]$, in both azo complexes the short-lived excited state was replaced by a second excited state, $^3[\mathbf{172}]-(2)$ $^3[\mathbf{173}]-(2)$ respectively. It was this second state that decayed back to the ground state on the ns timescale, as confirmed by the kinetic profiles of the product bands. This is consistent with a hypothesis in which, after excitation to the unobserved singlet state, intersystem crossing occurs to a triplet that is above the lowest-energy

triplet state. Subsequent internal conversion would then enable relaxation to the lowest-energy triplet state, which would be the longer-lived state that decays on the ns timescale.

The hypothesis proposed above is analogous to the $[\text{Cr}(\text{bpy})(\text{CO})_4]$ system where two sequentially populated ‘trapping’ triplet excited states compete with CO dissociation, and $[\text{Mn}(\text{ppy})(\text{CO})_4]$ where one triplet excited state was seen. Studies using femtosecond TA spectroscopy were used to show consecutive population of the two excited states in $[\text{Cr}(\text{bpy})(\text{CO})_4]$. In this Chapter, the excellent spectral resolution of the TRIR experiments (compared to the UV-visible TA experiments) provides compelling evidence supporting similar behaviour to $[\text{Cr}(\text{bpy})(\text{CO})_4]$ in an isoelectronic system. The transfer between the two triplet states in **172** and **173** takes place with a lifetime of ~ 10 ps, comparable to the analogous process in $[\text{Cr}(\text{bpy})(\text{CO})_4]$. However, the second, lowest energy, triplet excited state in $[\text{Cr}(\text{bpy})(\text{CO})_4]$ decays with a lifetime of < 100 ps,³¹⁹ whereas with the azo complexes the analogous lifetime is on the ns timescale. The assignments proposed for the states in this study, essentially analogous to $[\text{Cr}(\text{bpy})(\text{CO})_4]$, are summarised in a Jablonski diagram, Figure 119.

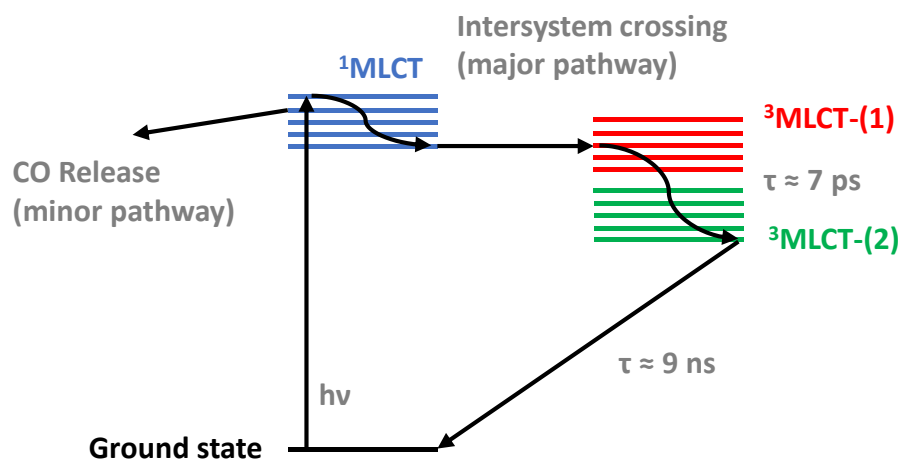


Figure 119: Jablonski diagram summarising the behavior of azo complexes 172 and 173.

The reason for the longer lifetime of the low-energy triplet excited state in the azo complexes compared to $[\text{Cr}(\text{bpy})(\text{CO})_4]$ is unclear. Calculations from TD-DFT or quantum mechanical methods would enable the orbital character of the triplet states of the azo complexes - and the relative intensities of the transitions between them - to be investigated. However, the much shorter lifetime of $^3[\mathbf{172}]-(1)$ and $^3[\mathbf{173}]-(1)$ compared to $^3[\mathbf{172}]-(2)$ and $^3[\mathbf{173}]-(2)$ can be readily explained by considering the spin state of each species: when the second triplet state decays back to the ground state, this process is spin-forbidden, whereas when first triplet state is converted into the second triplet, the process is spin-allowed.

4.4 Investigation of the Redox Properties of Complex 172

The slow CO release in the dark displayed by complexes **172** and **173** (Section 4.3.2) could be caused by the presence of the reductant sodium dithionite, which is used to generate deoxy-Mb. The electrochemistry of complex **172** was therefore studied to probe the redox properties of a cyclometalated azo dye CORM. A cyclic voltammogram in the presence of ferrocene as an internal standard (to calibrate the pseudo-reference electrode) was recorded to obtain an overview of the redox chemistry of complex **172** (Figure 120). The experiment was performed in a glovebox to avoid the baseline signal from O₂ reduction at the working electrode.

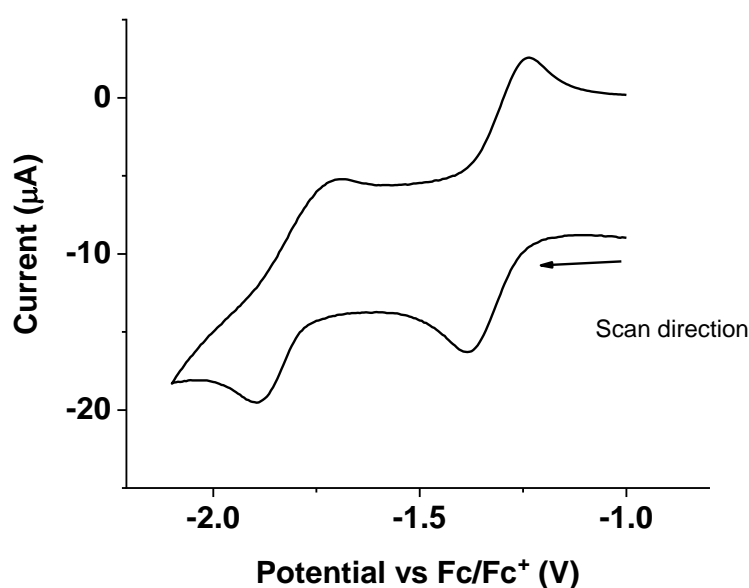


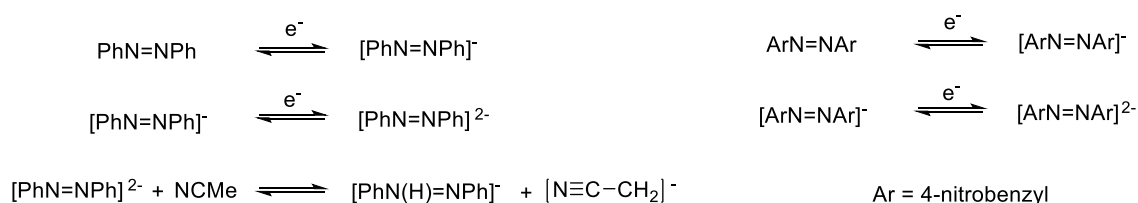
Figure 120: Cyclic voltammogram of a 1.0 mM solution of complex **172** in CH₂Cl₂ under Ar. The electrolyte was 100 mM tetrabutylammonium hexafluorophosphate. A scan rate of 100 mV s⁻¹ was used.

The results of the electrochemistry are summarised in Table 21. Complex **172** displayed two reversible reductions at low potentials with $E_{1/2}$ values of -1.311 and -1.792 V vs Fc/Fc⁺. As was observed for the compounds studied in Chapter 3, the peak separations, ΔE , were higher than the theoretical value of 59 mV, but this is likely due to solution resistance. The peak current ratios for both sets of peaks is close to one, suggesting reversible behaviour under these conditions.

Table 21: Summary of the cyclic voltammetry data of complex 172.

$E_{1/2}$ (V, vs Fc/Fc ⁺)	E_{ox} (V, vs Fc/Fc ⁺)	E_{red} (V, vs Fc/Fc ⁺)	ΔE (V)	i_a/i_c
-1.311	-1.241	-1.381	0.140	0.93
-1.792	-1.692	-1.891	0.199	1.00

The reversible electrochemical behaviour of azobenzene and its substituted derivatives has been well-studied (Scheme 63). Azobenzene reduction in dimethylformamide (DMF) or MeCN solvent results in two one-electron reductions followed by rapid protonation of the dianion from the acetonitrile solvent.³²¹ Subsequent re-oxidation of the protonated dianion afforded azobenzene in a two-electron oxidation.³²¹ Study of 4-nitroazobenzene revealed two reversible one-electron reductions without formation of a protonated dianion, presumably due to additional stabilisation of the dianion by the electron-withdrawing nitro groups.³²²

**Scheme 63: Literature redox behaviour of azobenzenes as determined by cyclic voltammetry in acetonitrile. Left: azobenzene. Right: 4,4'-nitroazobenzene.**

The behaviour in Figure 120 is similar to the behaviour observed for 4-nitroazobenzene in MeCN, where two reversible reductions form a non-protonated dianion.³²² In the literature, the two reductions for 4-nitroazobenzene occurred in MeCN at -0.870 and -1.195 V vs the saturated calomel electrode (SCE).³²³ The Fc/Fc⁺ couple lies at +400 mV vs SCE in MeCN,³²⁴ giving reductions of -1.270 and -1.595 V vs Fc/Fc⁺, similar to the potentials observed for complex **172** in CH₂Cl₂.

Structural information about the two reductions was sought using infrared and UV-visible spectroelectrochemistry.

4.4.1 Infrared Spectroelectrochemistry

Infrared spectroelectrochemistry was performed in CH₂Cl₂ solvent. The infrared spectroelectrochemistry experiment for complex **172** is shown in Figure 121. All data in Figure 121 were recorded in the same experiment which comprised measurement of the spectrum of **172** at the open circuit potential (OCP) followed by a potential step to -1 V for 600 s, then followed by a potential step to +1 V which was applied for 240 s. The potentials were measured with respect

to a Ag wire pseudo-reference electrode. The infrared spectroelectrochemistry was performed in a sealed cell in an air-purged spectrometer.

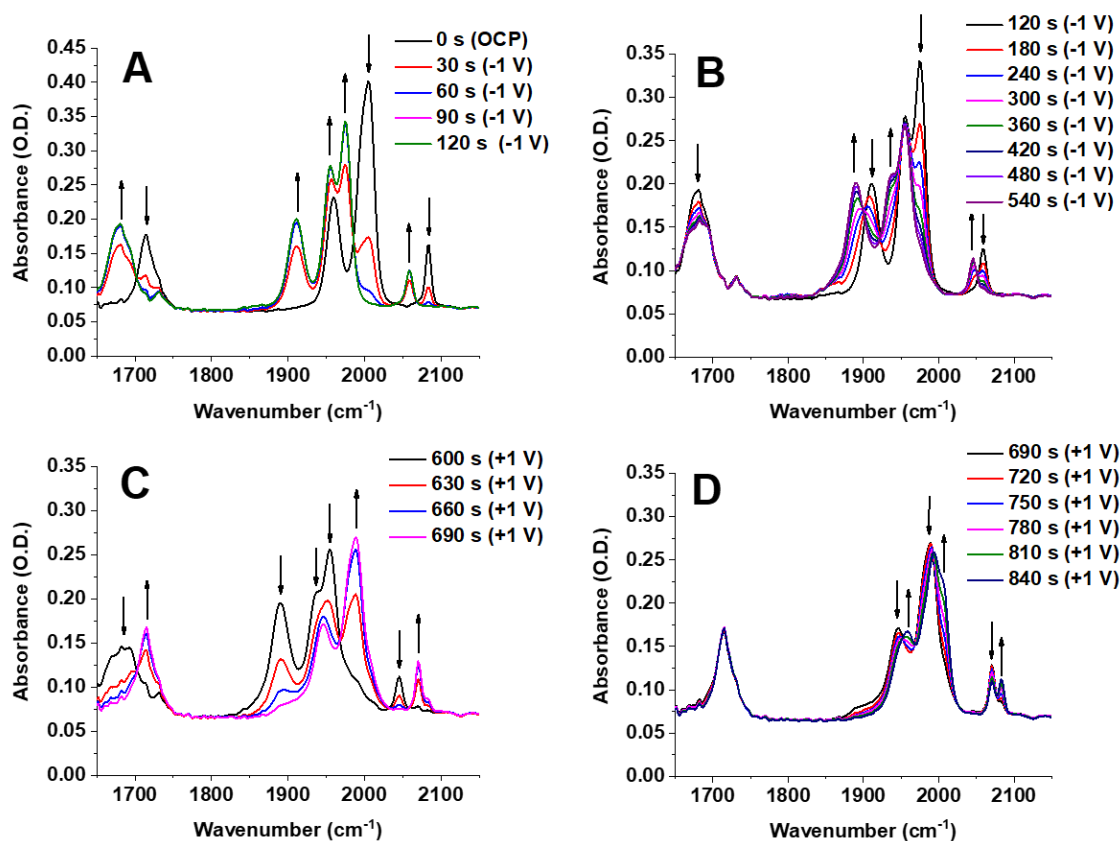


Figure 121: Infrared spectroelectrochemistry experiment with complex 172 in CH_2Cl_2 at a concentration of 5.0 mM in the presence of 1.0 M tetra n-butylammonium hexafluorophosphate. Panel A: Complex 172 at the open circuit potential of +446 mV vs the Pt pseudo-reference electrode, followed by a potential step to -1 V. Panel B: Further spectra after longer times at -1 V. Panel C: Initial spectra after the potential step to +1 V. Panel D: Further spectra after longer times at +1 V.

In panel A of Figure 121, the spectrum at the OCP (before the application of a potential step) shows the three metal carbonyl bands (2084 , 2004 and 1960 cm^{-1}) and ester carbonyl band (1715 cm^{-1}) of complex **172**, with the central metal carbonyl band containing the coalescence of one of the A_1 modes with the B_1 mode. Within 120 s of stepping from an open circuit potential of +446 mV down to -1 V vs Fc/Fc^+ , the bands for starting species **172** were completely replaced by those of a second species **172a**. Species **172a** had four stretching bands in the metal carbonyl region (2059 , 1975 , 1955 and 1911 cm^{-1}) and a single ester carbonyl band (1682 cm^{-1}). The pattern of positions and intensities in the metal carbonyl resembled the spectrum of other tetracarbonyl cyclomanganated spectra where the central two bands are no longer coalescent. The carbonyl bands for **172a** were shifted downwards relative to starting material **172**, consistent with **172a** being a more reduced species than **172**. Further changes in the infrared spectrum occurred within 10 minutes of the reductive -1 V potential step (Figure 121, panel B). The bands for species **172a**

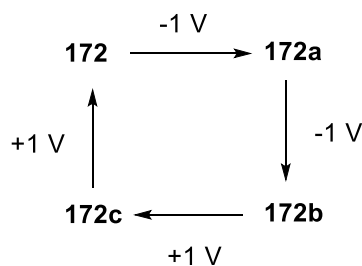
were replaced by a second reduced tetracarbonyl species **172b** with the bands shifted to even lower wavenumber (2045, 1954, 1938 and 1890 cm^{-1}). This suggests that this new species retains the same structure of the first coordination sphere around the Mn, albeit with much more electron density available for backbonding.

When no further changes were observed in the spectrum at -1 V (10 minutes), a potential step to +1 V vs Fc/Fc⁺ was performed to assess the reversibility of the reduction (Figure 121, panel C). The spectra show loss of **172b** and formation of a previously unseen species **172c**. Three metal carbonyl stretching bands (at 2071, 1988 and 1946 cm^{-1}) were observed but it is possible that the A₁ and B₁ modes overlap as was the case in neutral complex **172**. The metal carbonyl bands are shifted upwards by 25-45 cm^{-1} compared to the second reduced species, consistent with an oxidation reaction having taken place. The ester band shifted back up to 1715 cm^{-1} in the oxidation product, the same wavenumber as in starting complex **172**.

As the potential was held at +1 V vs Fc/Fc⁺ for even longer (Figure 121, panel D) the bands of the **172c** decayed to be replaced by the neutral starting complex **172**. This suggest that species **172c** is most probably a tetracarbonyl species as well, given the ease of re-formation of **172**. The use of such a high potential to re-oxidise the reduced species back to complex **172** also confirms that the reduced species and the neutral complex **172** cannot be oxidised further using strongly oxidising potentials. As with the ferrocenyl CORMs discussed in Section 3.3, it is anticipated that a very high potential would be needed to affect oxidation of the Mn(I) tetracarbonyl centre.

Both the cyclic voltammogram and the infrared spectroelectrochemistry show reversible behaviour overall, as **172** is re-formed upon oxidation. Importantly, CO release is not achievable by reduction of the azo moiety. Repeats of the spectroelectrochemistry experiment with 200 mV potential steps in an attempt to access the first reduced species without forming the second reduced species were not successful despite the 500 mV gap between their redox potentials in the cyclic voltammogram. This may be due to drifting of the potential applied over time due to the use of a silver wire pseudo-reference electrode in this experiment.

The infrared spectroelectrochemistry shows different intermediates upon oxidative and reductive potential steps, whereas the cyclic voltammogram appears to show two reversible one-electron steps. The same observations were made in a repeat experiment in EtOH. Including starting material **172**, four species were observed in the infrared spectroelectrochemistry. The simplest scheme to relate the species observed is summarised in Scheme 64. The infrared stretches of the species observed in the spectroelectrochemistry of **172** are summarised in Table 22.



Scheme 64: Summary of the formation of the species listed in Table 22 during infrared spectroelectrochemistry.

Table 22: Summary of the infrared stretching bands observed in spectroelectrochemistry of **172**.

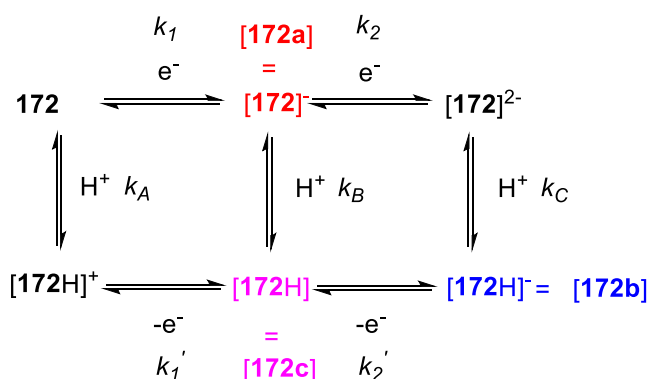
Species	Mn(CO) ₄ ν ₁ / cm ⁻¹	Mn(CO) ₄ ν ₂ / cm ⁻¹	Mn(CO) ₄ ν ₃ / cm ⁻¹	Mn(CO) ₄ ν ₄ / cm ⁻¹	ν(CO ₂ Et) / cm ⁻¹
172	1960	2004 (bands coalescent)		2084	1715
172a	1911	1955	1975	2059	1682
172b	1890	1938	1954	2045	1686
172c	1946	1988 (bands coalescent)		2071	1715

Possible assignments for species **172a-c** were considered. An explanation of the observed behaviour is aided by considering possible chemical steps using a square scheme (Scheme 65). The first reduction of **172** led to a large negative shift in the wavenumber of the metal carbonyl bands, suggestive of formation of an anionic species, so that **172a** would be assigned as [**172**]⁻. The second reduction step resulted in a further, but considerably smaller, decrease in wavenumber. Also, the ester carbonyl band changed little during the second reduction. A possible explanation for these observations is that the dianion has undergone rapid protonation after its formation ($k_c \gg k_2$ in Scheme 65). This would decrease the electron richness of the doubly-reduced species consistent with the smaller shifts in the metal carbonyl and ester bands upon the second reduction. As such, the second reduced species **172b** was tentatively assigned as [**172H**]⁻ in Scheme 65. The second reduction would therefore be described as an ‘EC’ process: an electron transfer (E) preceding a chemical (C) step. This reduction product appeared to be unreactive under the reducing conditions, even with a protic impurity such as water present. This suggests that any formation of arylhydrazine species [**172H₂**] is slow, as is the case in non-cyclometalated azo compounds.^{321,322}

When an oxidising potential was applied to **172b** (or [**172H**]⁻), regeneration of **172** was observed *via* an intermediate different to the one observed in the reductive step. This species, **172c**, could therefore be [**172H**], the product of the one-electron oxidation of [**172H**]⁻. As such, it is the

protonated form of intermediate observed during the reduction, [172]⁻. Comparison of the infrared bands of [172]⁻ and [172H] (Table 22) shows that the carbonyl bands for [172]⁻ are at lower wavenumber than for [172H]. This confirms that the metal centre is more electron-rich in [172]⁻ compared to [172H], consistent with the assignments made. The final step would then involve deprotonation and oxidation of [172H] then occurred to yield 172. The lack of an observed deprotonated intermediate prior to re-oxidation suggests another ‘EC’ process where a rapid deprotonation follows the oxidation.

It should be noted that the possible mechanism described by Scheme 65 still obeys the principle of microscopic reversibility, despite different mechanisms for the forward and reverse reactions. This is because the principle of microscopic reversibility operates under identical conditions for the forward and reverse reactions, whereas in the spectroelectrochemical data reported here the potential is changed between the reductive and oxidative steps, constituting a change in conditions. The square scheme shown in Scheme 65 is a common way of representing how the sweep direction can alter the reaction pathway. For example, Compton and co-workers recently used a nine-membered square scheme to illustrate the proton-coupled electron transfer reactions involved in catechol oxidation.³²⁵

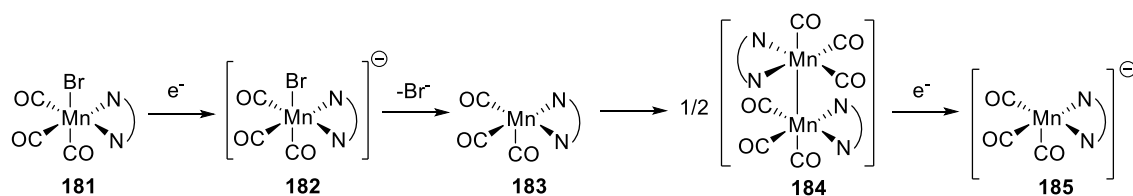


Scheme 65: Square scheme for complex 172 with proposed assignments of the species observed in the infrared spectroelectrochemistry.

Though the explanation suggested in Scheme 65 represents a plausible explanation of the behaviour, different assignments to the species cannot be ruled out. Square schemes containing alternative pathways could be envisaged. Given the very large potential steps made in the spectroelectrochemical experiment and the different k experimental conditions, it is possible that species 172a could be the doubly-reduced species [172]²⁻ or [172H]⁻, i.e. the two reductions from the cyclic voltammogram take place before spectra of [172]⁻ can be recorded. A subsequent chemical step, such as a rearrangement, could then account for formation of species 172b. Re-oxidation would then form species 172c before the reverse of the chemical step upon the second oxidation. However, it is unclear how the reduced species [172]²⁻ or [172H]⁻ would reversibly react as analogous species for other azobenzene derivatives are reported to be stable.^{322,323} The

cis-trans isomerisation often associated with azobenzenes³²⁶ also seems unlikely due to the photoactivation required for this reaction (the infrared spectroelectrochemistry was performed in the dark) and because the five-membered cyclometalated ring would become badly strained.

Ligand loss followed by radical dimerisation was also considered as an alternative pathway. Such dimers have been observed in spectroelectrochemical studies on the reduction of $[\text{Mn}(\text{bpy})(\text{CO})_3\text{Br}]$ (**181**), during investigations of the catalytic CO_2 reduction properties of Mn(I) complexes (Scheme 66).^{327–330} However, reductive radical dimerisation to form **184** in these complexes is reliant on the loss of the labile Br^- ligand to create a vacant coordination site on the metal and no such labile ligand is present in complex **172**, making this chemistry unlikely in complex **172**. As a result, the protonation behaviour described in Scheme 64 seems the most likely explanation for the behaviour seen.



Scheme 66: Species observed in the spectroelectrochemistry of 181 during formation of CO_2 reduction catalyst 185.

The difference in behaviour between the infrared spectroelectrochemistry and cyclic voltammetry could be attributed to the presence of water in the infrared spectroelectrochemical experiment. The cyclic voltammetry was performed in a dry Ar glovebox whereas the spectroelectrochemical cell could only be used outside of a glovebox. The dianion $[\mathbf{172}]^{2-}$ would be expected to be basic enough to deprotonate water, but not basic enough to deprotonate CH_2Cl_2 , possibly leading to the difference in behaviour under the different experimental conditions. This also explains why a repeat of the spectroelectrochemical experiment in EtOH yielded essentially identical behaviour. Further experiments could be performed to test this, such as performing the spectroelectrochemistry in dry solvent. Repeating the voltammogram while titrating in water or another proton source could confirm the mechanism as it would affect the peak current ratio of the second reduction if the protonation behaviour above were taking place. The scan rates of the cyclic voltammogram could also be changed to check whether any further reaction of the two reduced species occurs – this would help compensate for the differences in timescale between the cyclic voltammetry and spectroelectrochemistry experiments. However, given that the goal of this experiment was to look for CO-release, a more detailed mechanistic investigation to confirm this hypothesis was not carried out in this project.

4.4.2 UV-Visible Spectroelectrochemistry

The behaviour of complex **172** was also studied with UV-visible spectroelectrochemistry. As with the infrared experiment, a spectrum at the open circuit potential (OCP, in this case measured as +0.01 V vs the Ag/AgCl reference electrode) and then a potential step to -1.00 V vs Ag/AgCl was used to prepare the reduced species. Following this, a potential of +1.00 V vs Ag/AgCl was applied to re-oxidise the reduced species. The experiment was performed under air and under an Ar atmosphere, with the same behaviour observed in both cases. The results, under air in CH₂Cl₂ solution, are shown in Figure 122.

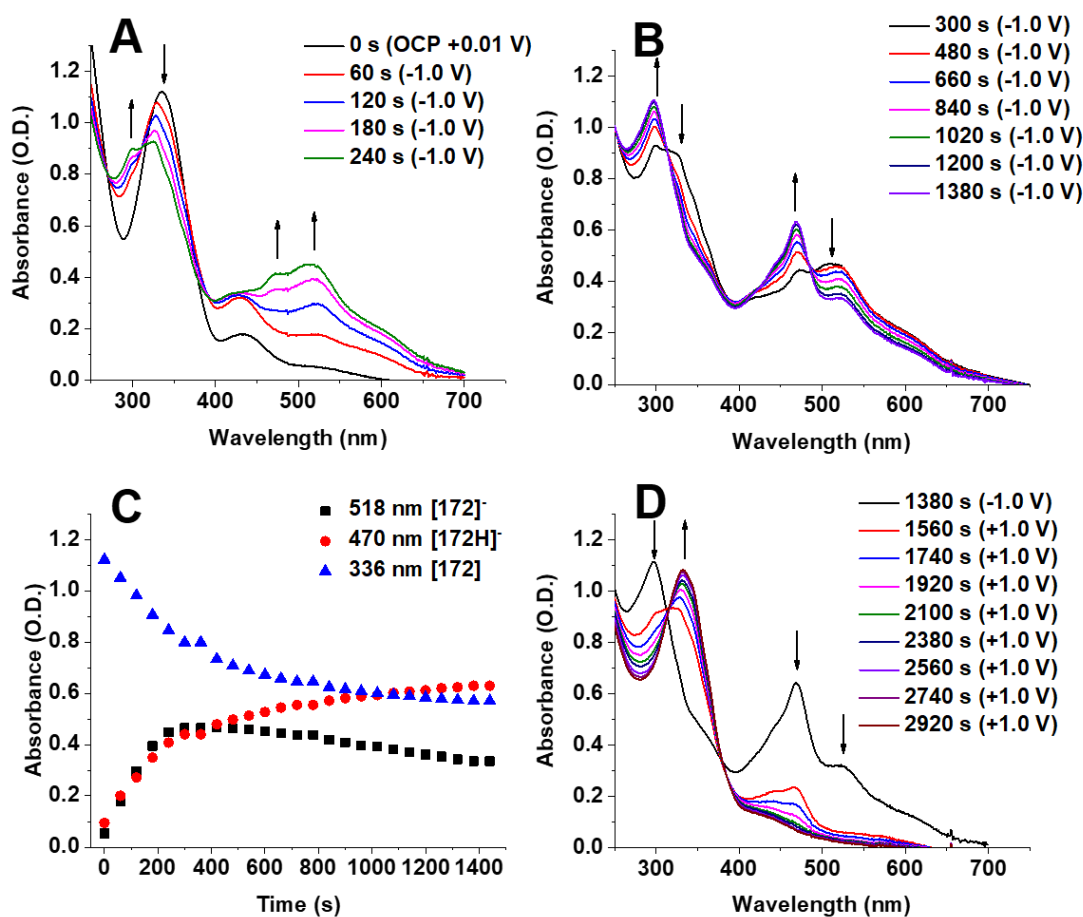
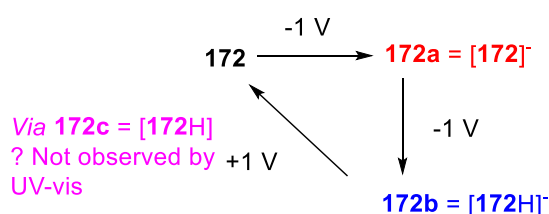


Figure 122: UV-visible spectroelectrochemistry experiment with complex **172** in CH₂Cl₂ at a concentration of 100 μ M in the presence of 500 mM tetra n-butylammonium hexafluorophosphate. Panel A: Complex **172** at the open circuit potential of +0.01 V vs Ag/AgCl, followed by a potential step to -1 V vs Ag/AgCl. Panel B: Further spectra after longer times at -1 V vs Ag/AgCl. Panel C: Time evolution of the bands observed in panels A and B. Panel D: Spectra after a potential of +1 V vs Ag/AgCl was applied.

In the first five minutes after the reductive potential was applied (Figure 122, panel A), the starting band at 336 nm for complex **172** decayed and the growth of new bands with maxima at 298, 470 and 518 nm grew in. At later times after the reduction began (Figure 122, panel B), the band at 470 nm continued to grow in whilst the band at 518 nm began to decay, as indicated by the plot

in Figure 122, panel C. This observation is consistent with the formation of two species and these are assumed to be the same species observed in the infrared spectroelectrochemistry, $[172]^-$ and $[172H]^-$.

When the potential was stepped from -1.0 V up to +1.0 V to re-oxidise $[172H]^-$, the spectrum of **172** was regenerated (Figure 122, panel D). No intermediate species could be observed in the re-oxidation experiment, whereas an intermediate, assigned as $[172H]^-$ was observed in the infrared spectroelectrochemistry. It may be that species $[172H]^-$ was not observed because its electronic absorption spectrum is too similar to either **172** or $[172H]^-$. Infrared spectroscopy was used to probe the metal carbonyl environment whereas the electronic transitions in UV-visible spectroscopy primarily reflect the π -system of the azo ligand, which could explain the discrepancy. A summary of the observations of the UV-visible spectroelectrochemistry is provided in Scheme 67.



Scheme 67: Relationship between the species observed in the UV-visible spectroelectrochemical experiment on **172.**

The key conclusion of this experiment is that regeneration of **172** was again observed upon oxidation, indicating that reduction does not lead to appreciable electrochemical CO release.

4.5 Conclusions

The success of a previous Mn(I) photoCORM design strategy of achieving visible light CO release by replacing pyridyl donor groups with azo donors prompted an analogous study for cyclometalated tetracarbonyls in this Chapter. Mononuclear and dinuclear cyclometalated azo dye complexes **172** and **173** were investigated as visible photoCORMs both by assessing CO release to deoxy-Mb and by studying their primary photochemistry with ultrafast TRIR spectroscopy. The electrochemical properties of complex **172** were also studied to test for reductively-activated decomposition of **172** which may lead to CO release.

The small family of novel cyclometalated complexes reported were synthesised using the same methods as their known analogues. Unusual regioselectivity was observed when unsymmetrical azo ligand **176** was cyclometalated, with the more electron-rich position being the site of cyclomanganation. This reaction may be of further interest for synthetic applications and

mechanistic investigations into cyclometalation reactions due to the role of cyclometalated complexes as pre-catalysts in alkenylation reactions.

Visible light CO release was observed up to 465 nm for complex **172**, which is higher than can be used for $[\text{Mn}(\text{ppy})(\text{CO})_4]$. Despite this observation, the approach of using azo ligands was not successful in improving the photoCORM properties overall. Unlike their ‘ppy’ analogues, the azo complexes **172** and **173** displayed slow degradation in the dark. The fastest wavelength for CO release was still in the UV part of the spectrum for both complexes **172** and **173**. Furthermore, the photochemical CO release was far slower than for many $[\text{Mn}(\text{ppy})(\text{CO})_4]$ derivatives even with higher-power irradiation, suggesting that the CO release from the azo complexes is relatively inefficient. This relatively inefficient CO release was probed by measuring their ultrafast photochemical behaviour. Unlike $[\text{Mn}(\text{ppy})(\text{CO})_4]$, where CO loss is the dominant process, complexes **172** and **173** mainly form non-dissociative triplet excited states, which internally convert to a lower-energy state on the ps timescale and decay back to the ground state on the ns timescale. This explains the inefficient photochemical release from the azo complexes in the myoglobin assay in this Chapter.

When applied in this Chapter, the design strategy of Mascharak and co-workers proved effective at moving the CO-dissociative band further into the visible region, since CO-release was observed at 465 nm for complex **161**, well above where $[\text{Mn}(\text{ppy})(\text{CO})_4]$ absorbs. However, the rate of CO loss at all wavelengths tested (365, 400, 465, 525 and 590 nm) was slower than the pyridyl donor analogues. This highlights the importance of considering the changes in the primary photophysical and photochemical steps, not just CO release wavelength, when changing the nature of the N-donor ligand. Changing the ppy ligand for an azobenzene-derived alternative did enable CO-release above 400 nm but it dramatically altered the branching ratio between loss of CO and excited state formation. The design principles from Mascharak and co-workers cannot therefore be applied universally to photoCORMs because even if the wavelength of the MLCT band increases, there is no guarantee of efficient CO release at the higher wavelength. The effect on the efficiency of CO release must therefore be considered along with the increase in photolysis wavelength.

The key result from the electrochemical investigations on complex **172** is that the reductions of complex **172** do not activate it towards irreversible reactivity or activate CO release. The voltammetric redox behaviour of **172** in dry CH_2Cl_2 comprises two reversible reductions, similar to the behaviour of azobenzene and its derivatives in MeCN. The resulting dianion may be protonated depending on the availability of a proton source. When very strongly reducing potentials were applied to complex **172** any decomposition was slow. The infrared spectroelectrochemistry in wet CH_2Cl_2 and in EtOH, shows that even reduction in the presence of protic species does not result in significant decomposition of the azo moiety or the Mn

tetracarbonyl centre on the timescale of several minutes, although protonation may accompany reduction.

5 Synthesis, Imaging, and Antimicrobial Testing of a Coumarin-Tagged CORM

Previous studies have indicated that photochemical CO-release from [Mn(ppy)(CO)₄] derivatives can reduce the growth rates of cultures of *E. coli* and *S. aureus*.¹³⁷ Greater understanding of the antimicrobial action of this class of photoCORMs could be gained by imaging them in mammalian and bacterial cells. This Chapter describes the installation of a fluorophore into a [Mn(ppy)(CO)₄]-derived photoCORM for applications in imaging and cytometry. Studies on the toxicity of the CO released by this fluorophore-tagged CORM towards *E. coli* are also reported and compared to other related photoCORMs.

The confocal microscopy work in this Chapter was performed in collaboration with Dr Karen Hogg and Dr Peter O'Toole of the Imaging and Cytometry Technology Facility, Department of Biology, University of York. The reader is referred to the digital file in any cases where the microscopy image contrast has been lost in the printing process. An initial supply of coumarin alkyne **196** for preliminary synthetic work was provided by Dr Paul Scattergood and Professor Paul Elliott of the University of Huddersfield before further quantities were synthesised by myself at the University of York.

5.1 Background

The impact of photochemical CO-release from carboxylic acid-substituted [Mn(ppy)(CO)₄] derivative **95** on the growth of wild-type *E. coli* W3110 and *S. aureus* 8325-4 cells was assessed by Dr Jonathan Ward in his PhD work.¹³⁷ Culturing *E. coli* or *S. aureus* with **95** in the presence of 400 nm irradiation reduced the growth rate of bacteria in liquid cultures compared with dark and CORM-free controls. The results for *E. coli* are shown in Figure 123. The OD₆₀₀ (optical density, i.e. absorbance / scattering, at 600 nm) increases proportionally with the number of bacterial cells and is therefore a measure of the extent of bacteria growth in each culture. It should be noted that the CORM-free controls were still performed in the presence of CORM solubilising agent DMSO because it is known that *E. coli* can use DMSO as an energy source through the DMSO reductase enzyme.³³¹

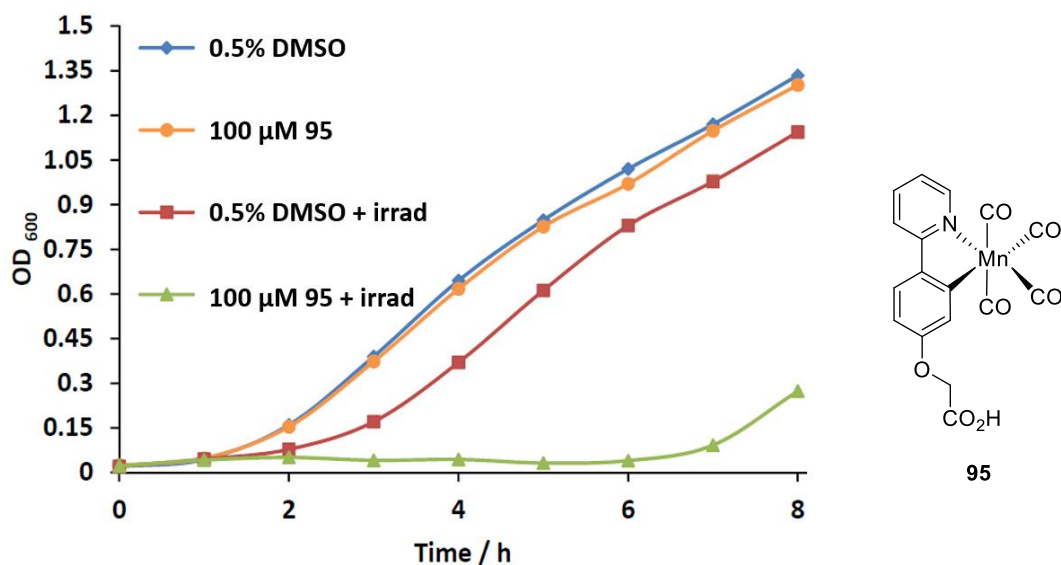


Figure 123: Growth curves for *E. coli* showing the effect of complex 95 both in the dark (orange circles) and in the presence of irradiation (green triangles). Control experiments with no CORM in the dark (blue diamonds) and with irradiation (red squares) are also overlaid. Where irradiation took place, a 400 nm LED drawing 2.4 W power was used for 3 minutes off, 2 minutes on between 1-3 hours. This data is taken from the PhD thesis of Jonathan Ward.¹³⁷

When media containing CORM 95 was irradiated before the addition of *E. coli*, to exhaustively release CO prior to bacterial growth, the antimicrobial effect was alleviated (Figure 124). This important control experiment shows that it is the release of CO that is having the antimicrobial effect. The concentration of complex 95 used in these assays was 100 μM. The effective concentration of CO throughout the experiment was not measured but the release profile from myoglobin assays can be used as a guide.¹⁸⁴ In cells, it is possible that localisation of the CORM leads to spatial variations in CO concentration as well as temporal variations. In separate experiments it was shown that such a concentration has only low cytotoxicity towards a mammalian cell line (murine RAW 264.7 macrophages).¹⁵⁹

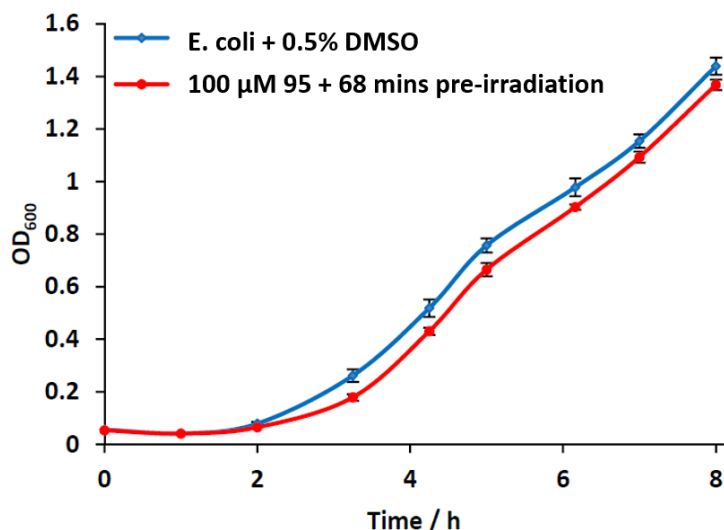


Figure 124: Growth curves for *E. coli* showing the effect of pre-irradiated complex 95. The blue triangles represent no addition of CORM or irradiation, the red squares show the effect of adding CORM 95 after pre-irradiation. Error bars represent the standard deviation from three measurements. This data is taken from the PhD thesis of Jonathan Ward.¹³⁷

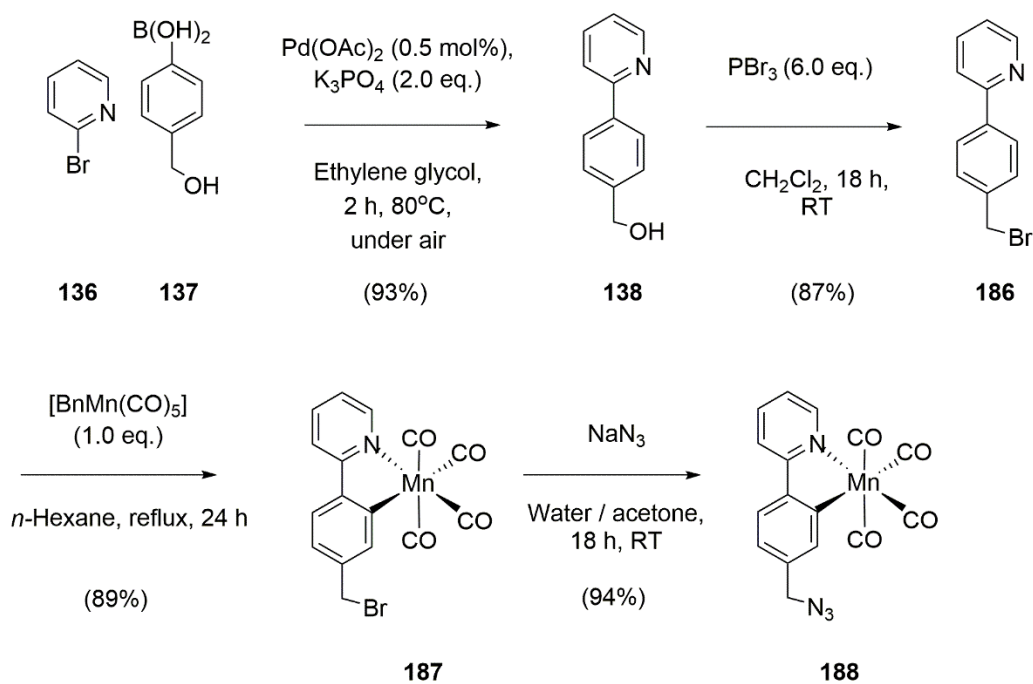
The way in which CORMs act as antimicrobials is not well-understood. Some Re(I)-based CORMs can enter cells before releasing CO, which may lend weight to the ‘Trojan horse’ theory of antimicrobial action by CO.^{181,182} However, it is unknown whether the Mn(I) CORMs studied in this Thesis can pass intact through the cell membrane to release CO inside cells, or if CO release instead takes place outside cells and CO diffuses in. The question of localisation is also important in enabling us to exploit interactions of CORMs with intracellular targets.⁵⁶

To study the entry of CORMs into cells, photoCORMs with luminescent properties have been developed to allow imaging by confocal fluorescence microscopy and flow cytometry, as discussed in Section 1.3.3.6. This enables the localisation of CORMs, and sometimes, their degradation products, to be studied so that the location of CO-release can be established.¹⁸⁰ Flow cytometry is also a useful tool as it can be used to sort cells based on multiple factors, such as fluorophore uptake and live-dead stains.¹⁸² These techniques provide a powerful method for correlating the localised CO-release from a CORM with antibacterial effects.

5.2 Synthesis of a Functionalisable Azide-Containing CORM Building Block

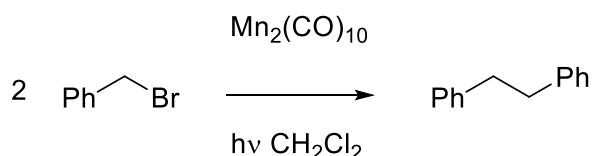
The use of modularity in CORM design through click chemistry, described in Section 1.2.2.5, provides a convenient strategy for introducing a fluorophore into the ligand of a photoCORM. To increase the range of CORMs that can be made using the stable [Mn(ppy(CO)₄)] moiety, it is desirable to make an azide-functionalised analogue of alkyne **46**. This would make the click

chemistry-derived modular design of $[\text{Mn}(\text{ppy}(\text{CO})_4)]$ derivatives more flexible, because the CORM could then be conjugated with either azide- or alkyne-containing reagents depending on the most convenient synthesis of the other component. Indeed, the CORM azide may well prove to be easier to access as the addition of the alkyne into the manganese is no longer a problem. This would eliminate the need for protection and deprotection, which should be advantageous in shortening the synthesis and working to increase the overall yield. A synthetically straightforward choice is benzyl azide **188** (Scheme 68).



Scheme 68: Summary of the synthesis of an azide CORM building block, compound 188.

Azide **188** can be made by building on the Suzuki reaction previously employed to make alcohol **138**. This alcohol is readily converted into the corresponding bromide, **187**, using PBr_3 . The cyclometalation and azidation reactions could conceivably be performed in either order. The decision to cyclometalate before the addition of the azide was initially taken to open up the possibility of making the azidation and CuAAC reactions a one-step transformation, avoiding the need to routinely isolate azide **188**.



Scheme 69: Possible radical cross-coupling side-reaction in the synthesis of 187.³³²

However, $[\text{Mn}(\text{CO})_5]^\cdot$ radical precursors such as $\text{Mn}_2(\text{CO})_{10}$ and $\text{BrMn}(\text{CO})_5$ can behave as pre-catalysts for radical cross-coupling reactions with benzyl bromides such as **186**.³³² A similar side-reaction could take place in the synthesis of compound **186**. However, it appears that

[BnMn(CO)₅] is a poor catalyst for the radical cross-coupling reactions as only cyclometalated complex **187** was obtained, and this was synthesised in good yield. The aromatic region of the ¹H NMR spectrum of cyclometalated complex **187** matched up well with the other 2-phenylpyridine complexes discussed in this Thesis, showing the loss of one proton and desymmetrisation of the AA'XX' phenyl ring upon cyclometalation. The NMR spectral evidence was combined with the strong metal carbonyl IR stretching bands at 2074, 1990, 1975 and 1931 cm⁻¹ in CH₂Cl₂, in agreement with analogous compounds. A low-resolution LIFDI mass spectrum showed two peaks of close to 1:1 intensity at 412.94 and 414.94 mass units, consistent with the formation of the molecular cation. These two intense peaks are due to the similar isotopic abundance of ⁷⁹Br and ⁸¹Br, and confirms that the benzyl bromide group has been carried through the reaction intact. Elemental analysis also corroborated this empirical formula and confirmed that complex **187** could be made with satisfactory purity. The cyclometalation therefore proceeded successfully without the formation of radical coupling products. This shows that relatively sensitive substrates can be used in this chemistry as long as the manganese reagent is chosen carefully with radical side-reactions in mind. Following cyclometalation, a simple S_N2 reaction of benzyl bromide **187** with NaN₃ affords azide **188** in excellent yield. Based on the initial amount of 2-bromopyridine starting material, the overall yield across this four-step synthesis is 67%, highlighting the excellent yields obtained throughout the route. A suitable single crystal was obtained by slow evaporation from a saturated solution in *n*-pentane and the structure was solved, Figure 125. The bond lengths and angles reflect a very similar geometry around the Mn centre to the other complexes discussed in in this Thesis and elsewhere.^{137,282}

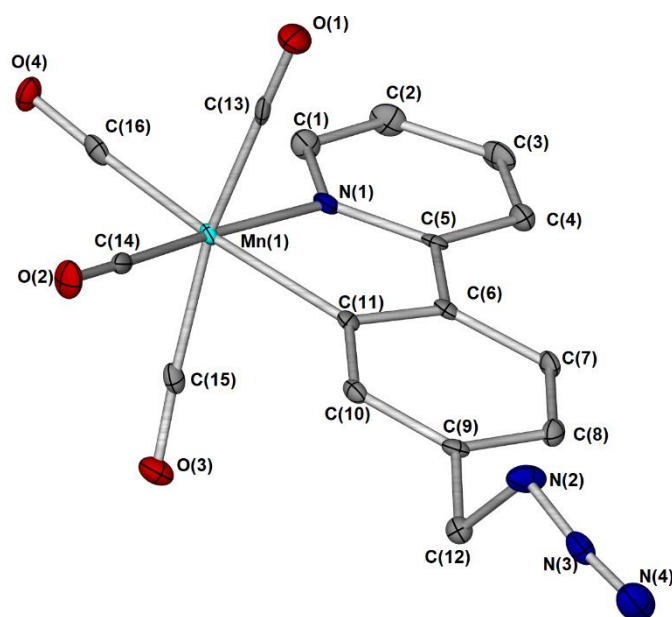
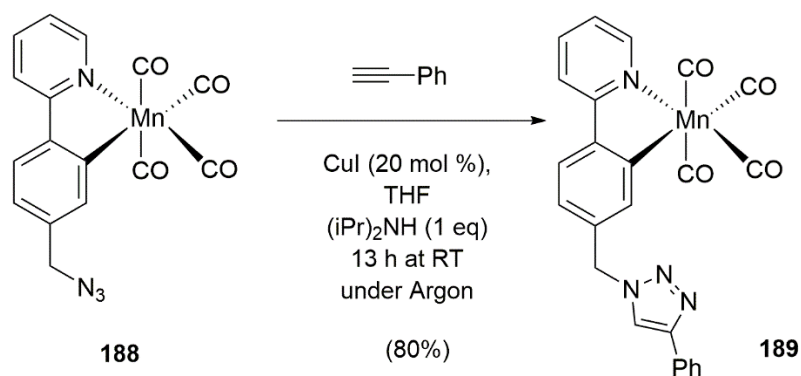


Figure 125: An X-ray crystal structure of compound 188 with hydrogen atoms omitted for clarity. Atoms are displayed as thermal ellipsoids at 50 % probability. Selected bond lengths (Å): C(11)-Mn(1) = 2.054(3), C(13)-Mn(1) = 1.841(3), C(14)-Mn(1) = 1.796(3), C(15)-Mn(1) = 1.857(3), C(16)-Mn(1) = 1.842(3), N(1)-Mn(1) = 2.073(2). Selected bond angles (°): C(11)-Mn(1)-N(1) = 79.53(11), C(16)-Mn(1)-C(11) = 172.33(12), C(13)-Mn(1)-(C15) = 166.55(12), C(14)-Mn(1)-N(1) = 172.93(12), C(14)-Mn(1)-C(16) = 93.50(13), C(15)-Mn(1)-(C11) = 81.79(12).

A test CuAAC reaction was then performed using phenylacetylene to show that the metal carbonyl framework can survive the reaction conditions. An organic solvent system³³³ was utilised in order to solubilise both components; this necessitated the use of a CuI catalyst as opposed to the copper(II) and ascorbate system previously used in the aqueous conditions (Section 3.2.1). The 80% yield of the isolated triazole **189** suggests that **188** could be a useful building block for conjugating CORMs with click chemistry. The high yields through this relatively straightforward synthesis, and the lack of a requirement for protecting group chemistry, represents an improved modular system for making [Mn(ppy)(CO)₄] derivatives and introduces extra flexibility for CORM conjugate synthesis.



Scheme 70: Demonstration of CuAAC conditions with novel azide 188.

A suitable single crystal of **189** was grown and the structure solved. Unsurprisingly, the geometry around the Mn centre experiences little change compared to azide **188**. The organic backbone of the compound conforms to a “V” shape due to the two planar pi-systems separated by the benzyl carbon. Intermolecular pi-stacking interactions were also observed between the aromatic planes.

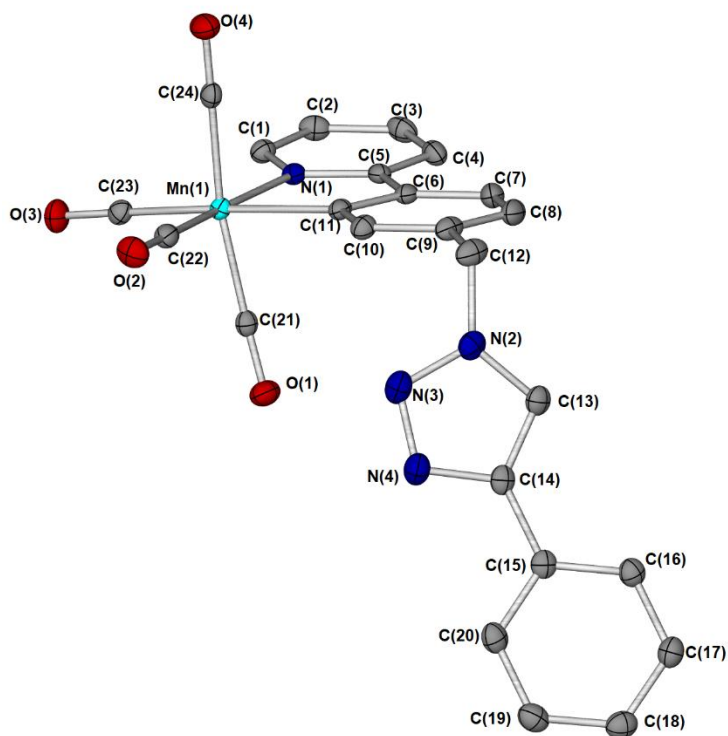


Figure 126: An X-ray crystal structure of compound 189 with hydrogen atoms omitted for clarity. Atoms are displayed as thermal ellipsoids at 50 % probability. Selected bond lengths (Å): C(11)-Mn(1) = 2.0574(14), C(21)-Mn(1) = 1.8595(14), C(22)-Mn(1) = 1.8025(15), C(23)-Mn(1) = 1.8303(15), C(24)-Mn(1) = 1.8476(14), N(1)-Mn(1) = 2.0661(11). Selected bond angles (°): C(11)-Mn(1)-N(1) = 79.64(5), C(23)-Mn(1)-C(11) = 173.00(6), C(24)-Mn(1)-(C21) = 168.48(6), C(22)-Mn(1)-N(1) = 173.35(6), C(22)-Mn(1)-C(23) = 92.02(6), C(21)-Mn(1)-(C11) = 80.95(5).

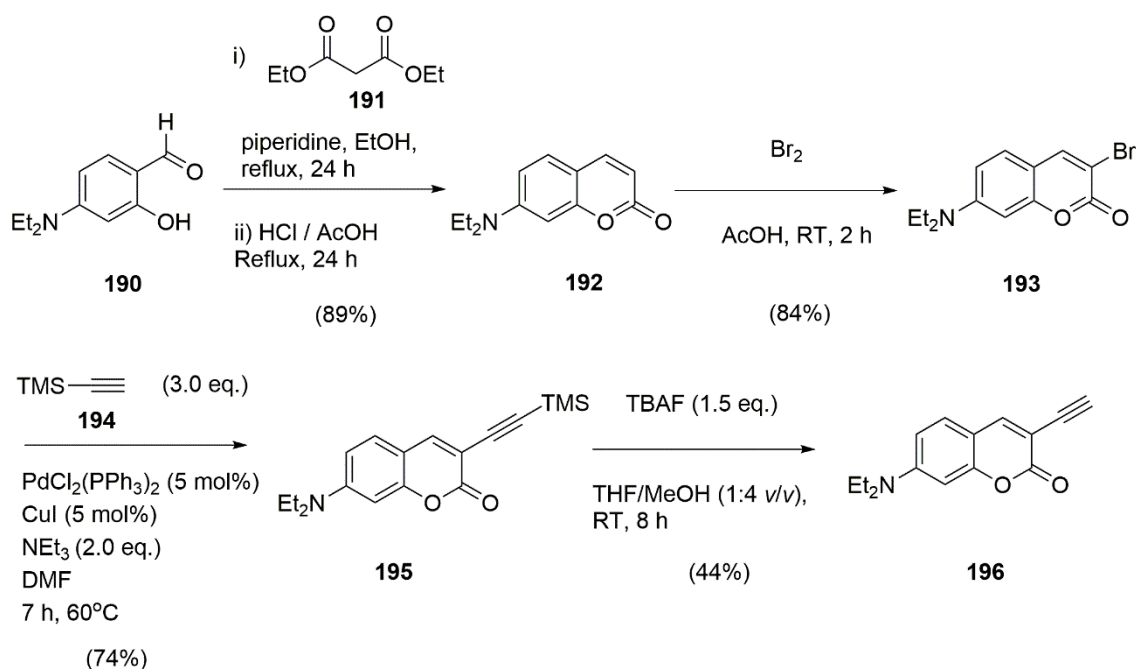
5.3 Synthesis of a Coumarin-Tagged CORM

Having demonstrated the stability and reactivity of azide **188** in suitable click chemistry conditions, a conjugate incorporating a fluorescent alkyne was synthesised. Alkynyl coumarin **196** was selected as the fluorescent tag (Scheme 71). The fluorophore in the resulting conjugate complex would be too remote to undergo a change in fluorescence emission wavelength that would be diagnostic of CO release, but the fluorescent tag was anticipated to allow monitoring of $[\text{Mn}(\text{ppy})(\text{CO})_4]$ derivatives inside cells.

There were several reasons for the choice of alkyne **196**. Firstly, the 7-diethylammcoumarin fluorophore is a relatively small fluorescent tag, which helps to avoid the properties of the fluorophore completely dominating those of the product and influencing the observed localisation of the CORM. Ideally, the fluorophore itself should have a minimal effect compared to the rest of the $[\text{Mn}(\text{ppy})(\text{CO})_4]$ -derived click product, so that the result can be related to other click product derivatives.

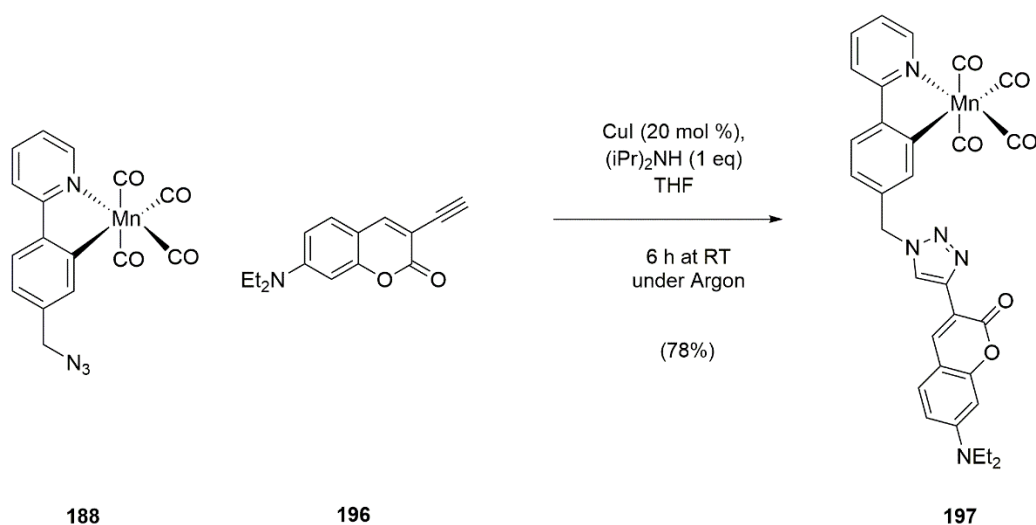
Secondly, the coumarin fluorophore has a λ_{max} value at a longer wavelength than the dissociative MLCT band that causes CO release in $[\text{Mn}(\text{ppy})(\text{CO})_4]$. The maximum of the fluorophore absorption band (408 nm) lies on the outer edge of the $[\text{Mn}(\text{ppy})(\text{CO})_4]$ CO-dissociative band (which tails off beyond 400 nm). This is important because it means that imaging of the fluorophore can take place without photolysing the CO ligands. Localisation of the CORM and its effect upon the cells could therefore be monitored through fluorescence microscopy both before and after photochemical CO release.

Thirdly, alkyne **197** is readily accessible through a robust synthetic method from the literature,³³⁴ as summarised in Scheme 71. Briefly, 7-(diethylamino)coumarin, (**192**) was synthesised by the condensation of commercially-available salicylaldehyde (**190**) with diethyl malonate (**191**) followed by ester hydrolysis and decarbonylation to give **192**. Bromination in the 3-position with Br_2 afforded **193**, which was used to install an alkyne through a Sonogashira coupling with trimethyl(silyl) (TMS) acetylene to give TMS-protected alkyne **195**. Deprotection with TBAF then provided the alkyne **196**.



Scheme 71: Synthesis of coumarin alkyne 196.

With alkyne **196** in hand, the copper-catalysed azide-alkyne cycloaddition with azide-functionalised CORM derivative **197** was performed, Scheme 72. The same conditions for this reaction were used as for the test reaction with phenylacetylene described above in Scheme 70.



Scheme 72: CuAAC conditions for the synthesis of 197.

The reaction proceeded to completion (consumption of starting materials by TLC) in 6 hours, and purification by silica gel flash column chromatography gave target complex **197** in a good yield of 78%. The infrared spectrum of the product has the same four metal carbonyl bands as observed for azide **188** and click product **189**, confirming that the [Mn(ppy)(CO)₄] moiety was carried through the synthesis intact. The crystal structure of **197** was also obtained using CH₂Cl₂/*n*-pentane layering. The structure shows a similar “V” shaped organic backbone to triazole **189** due to the planarity of the aromatic rings. The structure is shown in Figure 127.

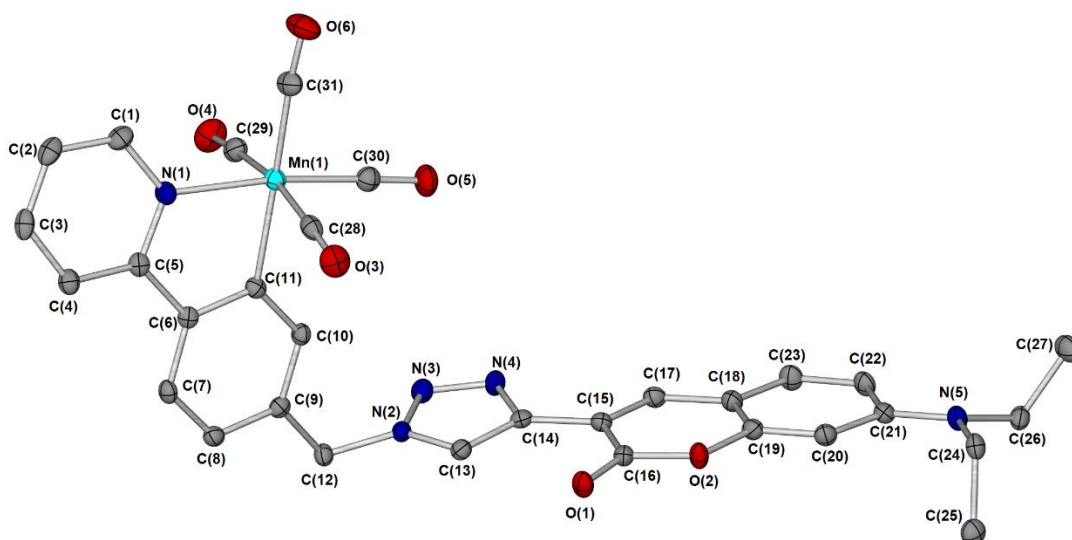


Figure 127: An X-ray crystal structure of compound **197** with hydrogen atoms omitted for clarity. Atoms are displayed as thermal ellipsoids at 50 % probability. Selected bond lengths (Å): C(11)-Mn(1) = 2.048(2), C(28)-Mn(1) = 1.853(3), C(29)-Mn(1) = 1.864(3), C(30)-Mn(1) = 1.8310(3), C(31)-Mn(1) = 1.8451(3), N(1)-Mn(1) = 2.065(2). Selected bond angles (°): C(11)-Mn(1)-N(1) = 79.45(9), C(31)-Mn(1)-C(11) = 174.82(10), C(28)-Mn(1)-(C29) = 168.69(12), C(30)-Mn(1)-N(1) = 171.61(10), C(30)-Mn(1)-C(31) = 90.66(12), C(28)-Mn(1)-(C11) = 81.32(10).

The UV-visible spectrum of **197** was recorded in CH₂Cl₂ to assess where the excitation band of the coumarin fluorophore lay. Two strong absorption bands were observed in the spectrum, with λ_{\max} values of 408 and 264 nm (Figure 128).

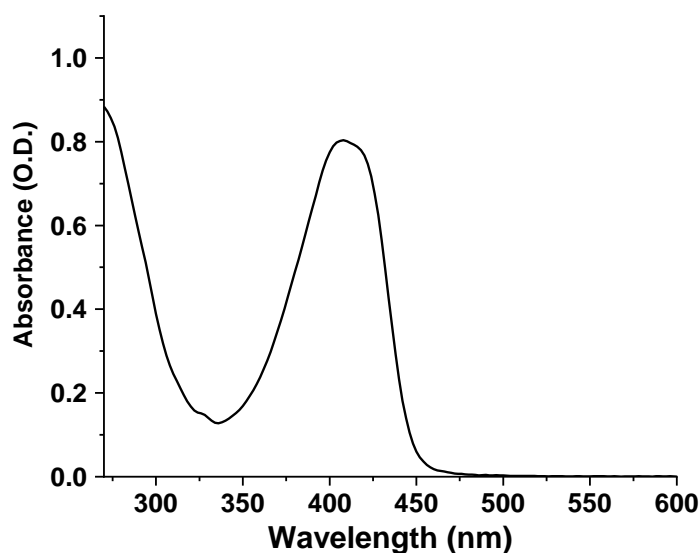


Figure 128: UV-Visible spectrum of **197** in CH₂Cl₂ at a concentration of 26.2 μ M.

The higher-energy band was assigned to the 2-phenylpyridine aromatic system (π - π^*) – a similar band is observed in ppy parent complex **88** (as was shown in Figure 29). The band at 408 nm was assigned to the coumarin-derived fluorophore. The 7-diethylaminocoumarin moiety has been used extensively as a fluorescent tag in other studies and so absorption and emission spectra of

several different derivatives are already known, including triazole ‘click’ products derived from complex **196**.^{335–338} In this group of previously-known compounds, the coumarin peak has been observed between 400–430 nm depending on the derivative,^{335–338} consistent with that observed in Figure 128. It is notable that changing the solvent from CH₂Cl₂ to phosphate-buffered saline did not significantly shift the wavelength of the coumarin triazole moiety,³³⁸ suggesting that the coumarin moiety of complex **197** will have an excitation maximum at approximately 408 nm in the phosphate-buffered saline solution used for imaging in this work. Another way to confirm this assignment might have been to compare the UV-visible spectrum of complex **189** with that of **197** to observe the effect of incorporation of the coumarin fluorophore.

The emission spectra of coumarin triazole analogues to **197** have also been well-studied. Excitation of the coumarin absorption maximum in 7-diehtylaminocoumarin-conjugated triazoles complexes related to **197** has been shown to result in fluorescence with a maximum intensity in the region of *ca.* 480–500 nm.^{335–338} The parent compound, **192**, exhibits slightly higher-energy coumarin excitation/fluorescence, absorbing at 350–380 nm and fluorescing at 390–445 nm.³³⁹ The exact wavelengths were solvent-dependent, but there was little change in wavelengths upon moving from halogenated solvents such as chloroform to polar protic solvents such as ethanol.³³⁹ The lengthening of the excitation and emission wavelengths of the coumarin fluorophore in click products are expected due to conjugation with the triazole moiety. For further comparison, coumarin alkyne **196** has an excitation maximum at 425 nm and the fluorescence maximum is at 488 nm in phosphate-buffered saline, and therefore its properties resemble the conjugated triazole products more than parent fluorophore **192**.³⁴⁰ The click chemistry in synthesising **197** was therefore expected to alter the properties of the fluorophore in a predictable manner.

If this study is taken forward in future work, it will be necessary to perform a detailed study of the emission spectrum of **197**, rather than simply relating its properties to those of previously-known analogues. Optimal imaging will be obtainable if the exact excitation wavelength in the media to be used is used and the emission spectrum is recorded. The emission spectrum may be wavelength-dependent, and this would be valuable information for the imaging study. Measuring the emission spectrum will allow more optimised collection of the emission wavelength range of the fluorophore. A control with complex **189**, which contains the same metal carbonyl moiety and triazole linker, could also be performed. For the initial preliminary studies described here, the similarity of the UV-visible absorption spectrum to known compounds with well-studied emission properties was enough to provide guidance on the excitation and emission wavelengths. However, the emission spectrum of complex **197** itself should be recorded to guide any future, more comprehensive, imaging studies with complex **197** than the work described here. As an example, it may be desirable to irradiate the cells and observe whether the CORM degradants enter/leave the cells after CO release – this could help inform toxicity studies of the degradants. In order to do this, the emission spectrum over time would need to be studied.

The CO-dissociative MLCT band, typically observed between 350-400 nm (based on Figure 30 and literature data)¹⁵⁹ is obscured by the coumarin band in Figure 128, but by analogy to [Mn(ppy)(CO)₄] this band is expected to exist in the region 350-400 nm. The spectrum confirms that excitation of the coumarin fluorophore could be performed at wavelengths longer than those that would cause CO release from the MLCT band.

A myoglobin CO release assay of **197** is shown in Figure 129. The assay confirms that this compound behaves as a CORM. An assay using 10 μM **197** with *ca.* 47 μM deoxy-Mb revealed similar properties to the other 2-phenylpyridine based manganese tetracarbonyl CORMs: stable in the dark with the release of approximately 2.7 equivalents of CO per molecule of CORM upon irradiation with a 400 nm LED. This number of CO equivalents is comparable to the literature studies of halogen-substituted ppy complexes discussed in Chapter 1,¹⁸⁴ and summarised in Table 16. As with other [Mn(ppy)(CO)₄] derivatives, the CO-release is relatively slow at 400 nm, most likely because the very edge of the MLCT band is being irradiated, although the release is still considerably faster than the 400 nm release from azo compounds **172** and **173** described in Chapter 4. The rate of release of **197** at 400 nm is comparable to the fastest CO release achieved by azo complex **172**, although for the azo complex a lower wavelength of 365 nm and a higher power had to be used to achieve this. As the LEDs used also contain a range of wavelengths up to a range of around 10 nm, it may be that the broadness of the LED irradiation introduces some CO release from wavelengths slightly below 400 nm. This will be similar for all the complexes where LEDs were used, but when comparing LED irradiation to laser excitation in TRIR spectroscopy or confocal microscopy, this could be an important distinction. Although the coumarin fluorophore does not absorb in the region of the Mb studied, a 4-point correction was needed due to some precipitation of the CORM and/or its degradation products throughout the assay.

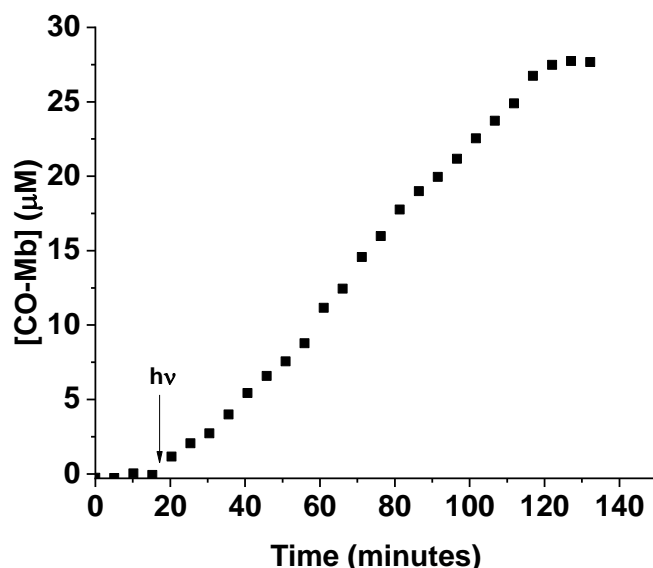


Figure 129: Myoglobin CO release assay with 10 μM compound **197** and *ca.* 47 μM myoglobin. Irradiation with a 400 nm LED at a power of 4.8 W began at 18.3 min and was provided in cycles of 3 minutes off, 2 minutes on.

5.3.1 Confocal Microscopy with Human 293T Embryonic Kidney Cells

Having assessed the CO release properties of **197**, preliminary confocal fluorescence microscopy experiments were performed, in order to assess whether CORM **197** could be imaged in live cells. Solutions of **197** (in a $\gg 99:1$ v/v PBS:DMSO solvent mixture to aid solubility of the CORM) were added to cultures of 293T embryonic kidney cells. The cells were incubated at 37 °C for 30 min before being placed onto a slide and imaged. Figure 130 shows the CORM at a final concentration of 50 nM using a 405 nm laser to excite the fluorophore.

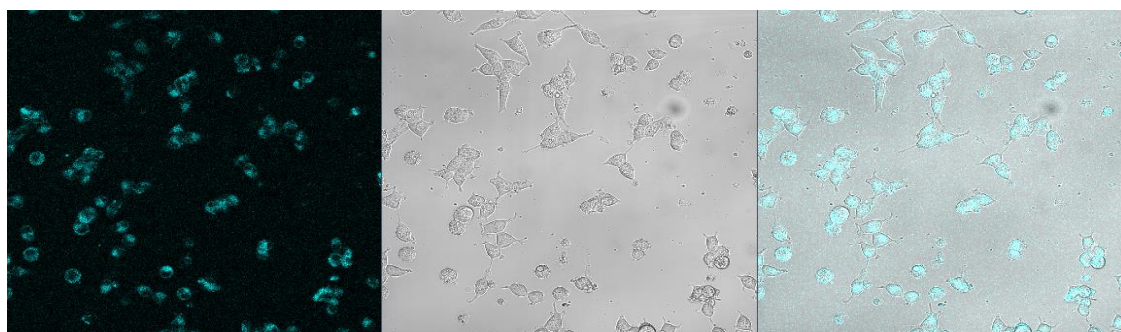


Figure 130: T293 cells after incubation with 50 nM **197** for 30 min. Left: Fluorescence response of **197** - emission collected between 410 nm to 597 nm. Centre: Image recorded of the cells in the same region, using white light. Right: Overlay of the emission and white light images. Each image is 425 x 425 μm .

Figure 130 shows that the coumarin fluorophore has entered the cells. This may be due to the whole of CORM **197** entering the cells or just a fluorescent fragment of the molecule following degradation. Although CORM **197** was stable in the dark in a myoglobin assay, there is no direct evidence that the tetracarbonyl centre fluorophore has remained intact in these experiments. In

antimicrobial studies where $[\text{Mn}(\text{ppy})(\text{CO})_4]$ derivatives were incubated with bacterial cells in media, the CO-derived antimicrobial effect required light for the *E. coli* to experience a detrimental effect. This suggests that the tetracarbonyl moiety is stable in biological systems, including when growth media is present.

The fluorescence appears to originate mainly in the cytoplasm of the cells, with the nucleus visible as a darker spot. In this image, only some nuclei can be seen – this is because the “Z” slice taken by the microscope does not contain the nuclei of all cells (*vide infra*).

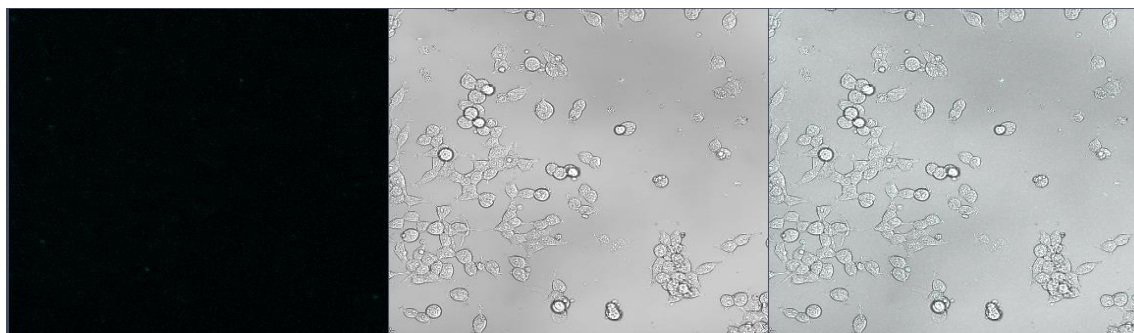


Figure 131: CORM-free control experiment using T293 cells. Each image is 425 x 425 μm . Left: Fluorescence response from the cells and solution - emission collected between 410 nm to 597 nm. Centre: Image recorded of the cells in the same region, using white light. Right: Overlay of the emission and white light images. Each image is 425 x 425 μm .

A control experiment, in which an equal amount of CORM-free DMSO/PBS solution was administered, confirmed that the administration of CORM **197** (Figure 131) results in greater fluorescence in the cytoplasm. Note that the same image recording and processing setting were used for both images. This experiment provides a measurement of the background level of autofluorescence by the cells for comparison to images in which the fluorophore is present.

Although the cytoplasmic and nuclear membranes appear intact in most of the cells, the number of living and dead cells cannot be determined from these images alone. It is crucial to know whether or not the cells in the culture are still alive; if the cells are dead it is likely that their membranes are no longer intact, so that all compounds in the surrounding medium appear to have been taken up.

A propidium iodide stain was used to discriminate live and dead cells. Propidium iodide (PI) is able to unselectively intercalate nucleic acids, upon which the fluorescence of the stain is enhanced. Ordinarily, PI is excluded from viable cells and is unable to bind to the nucleic acids that they contain. However, in necrotic and apoptotic cells, the stain can enter the cells and the enhanced fluorescence can be ‘switched on’. Figure 132 shows the effect of adding propidium iodide to the cells incubated with 50 nM **197**. Note that the slide was removed from the microscope to add PI, so the field of view is different to Figure 130. However, both images are from the same well of the same experiment.

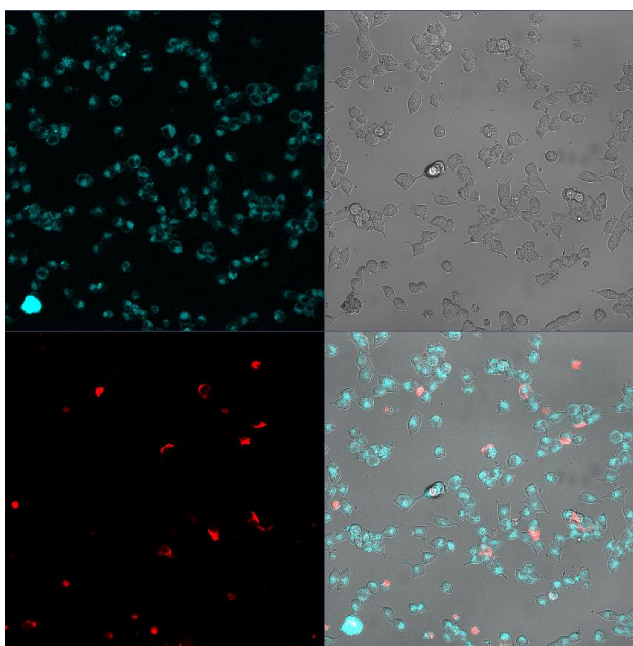


Figure 132: Addition of PI (2 μL of 400 μg / mL stain added to a 350 μL well) as a live/dead stain. Top left: CORM 197 fluorescence (50 nM, excitation 405 nm, emission 410-597 nm). Top right: white light image of the cells. Bottom left: PI fluorescence (excitation 561 nm, emission 569-740 nm). Bottom right: Overlay of all three images. Each image is 425 x 425 μm .

The images show that most of the cells appear to be alive after taking up the fluorophore. Some red nuclear staining is seen on some of the cells, suggesting that a small proportion are dead. There are also some other unusually-shaped ‘PI stains’ that do not appear to show nuclear staining, the origin of which is not certain. However, crucially the experiment shows that most of the cells are viable as they exclude PI. More detailed viability studies could be performed on human cell lines to understand the toxicity of this compound to human cells but overall these results correlate well with other mammalian cell toxicity screens of $[\text{Mn}(\text{ppy})(\text{CO})_4]$ -derived complexes, which show the compounds to be non-toxic.¹⁵⁹

A series of “Z-stack” images was also recorded, whereby the thin “Z slice” (in the plane of t sampled by the microscope is changed slightly between each image to move up through the cells. In Figure 133, 24 images are shown, each separated in Z by 0.76 μm . During the series, the cytoplasm and nuclei of all cells are seen, so that coumarin fluorophore and PI uptake can be examined in every cell. The images show that all cells have taken up the coumarin fluorophore, but far fewer are stained with PI, suggesting that the fluorescent material from **197** is taken up by viable cells. The detection of fluorescence inside the cells through the course of the Z stack confirms that the fluorophore is inside the cells rather than localising on the outside of the cell membrane.

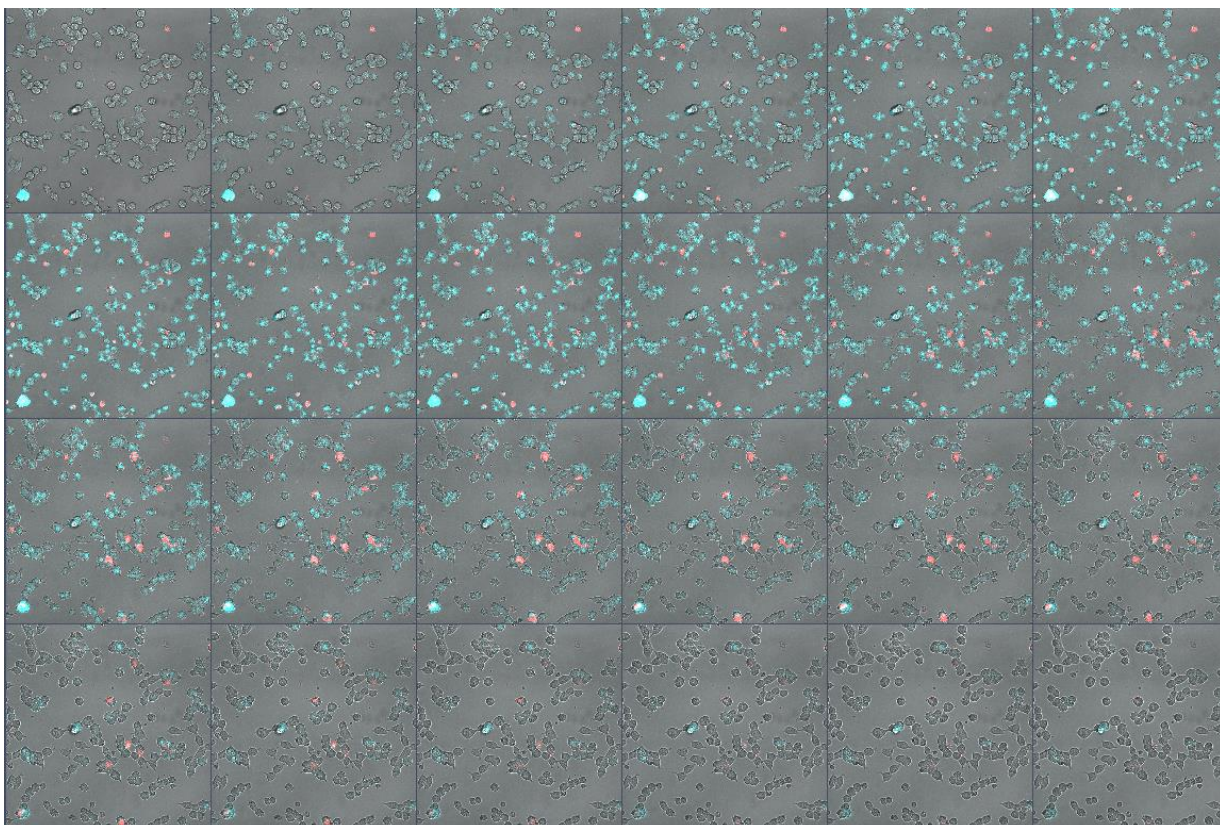


Figure 133: Z-stack images using the same conditions as Figure 132.

5.3.2 Confocal Microscopy with *E. coli*

Having established the feasibility of conducting fluorescence microscopy of mammalian cells using CORM **197**, preliminary imaging was then carried out with W3110 *E. coli* cultures to assess uptake of complex **197** in bacteria. Figure 134 shows an initial CORM-free control experiment where a DMSO/PBS solution was incubated with the cells. This shows the low background autofluorescence from the *E. coli* cells.

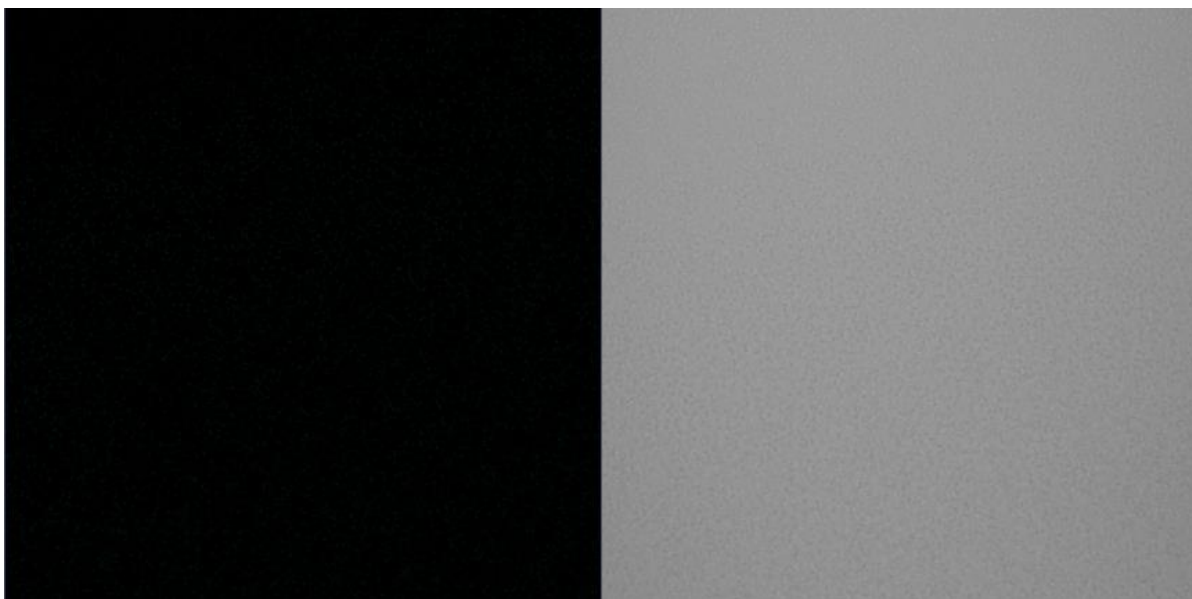


Figure 134: Autofluorescence control images after a CORM-free PBS/DMSO solution was added to the culture and incubated for 30 min. Left: 405 nm excitation with 410-627 nm emission. Right: Image recorded with white light. Image sizes are 135 x 135 μm .

Figure 135 shows the effect of incubating the *E. coli* in the presence of 10 μM **197** for 30 min. A high concentration was chosen to ensure that any fluorescence inside the cells was discernible above the autofluorescence background – it is more difficult to obtain high-quality images due to the much smaller size of bacterial cells than mammalian cells. The motion of the bacterial cells also means that shorter acquisition times must be used for the images of bacterial cell.

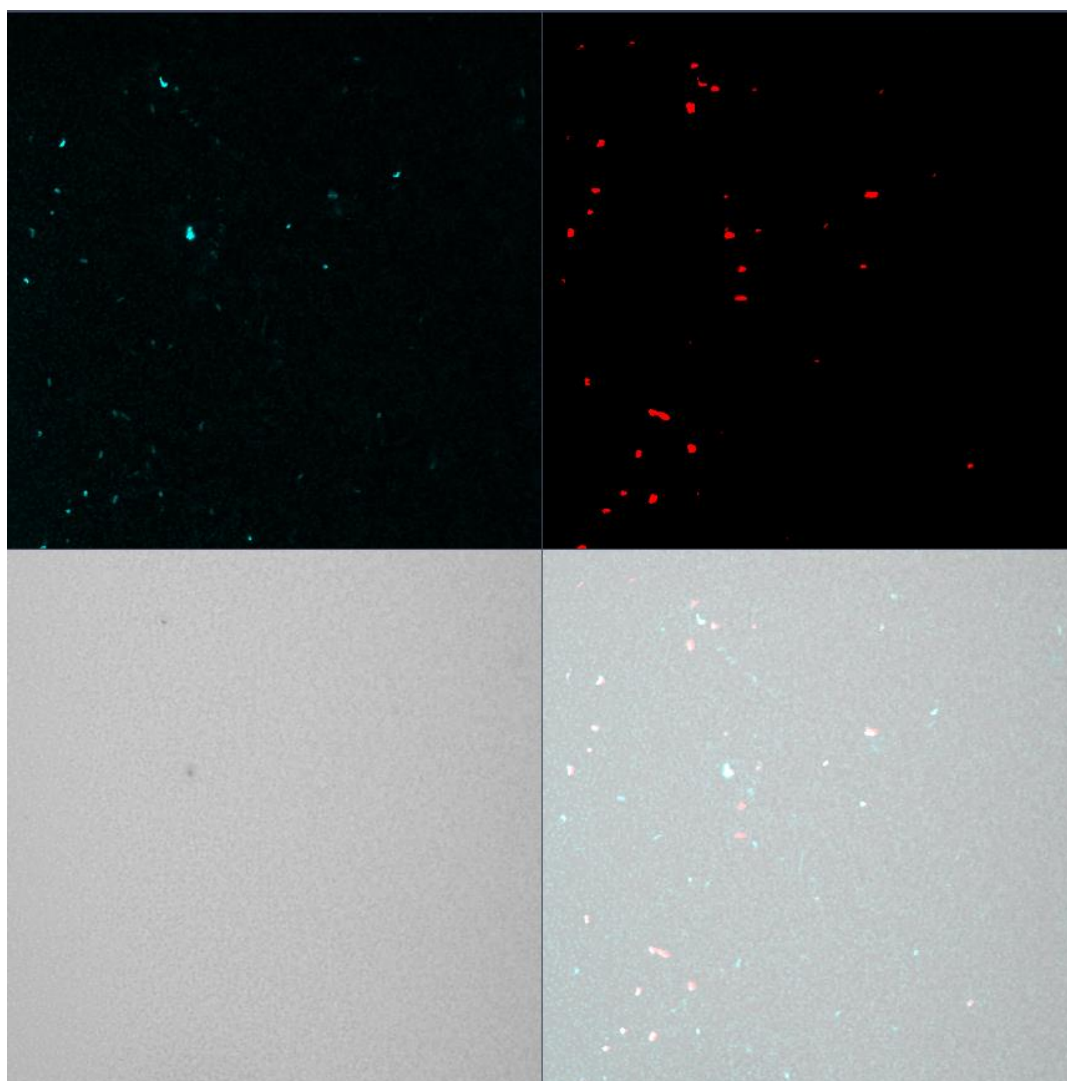


Figure 135: Addition of 10 μ M CORM 197 to an *E. coli* culture. Top left: Coumarin fluorescence (excitation 405 nm, emission 410-556 nm). Top right: PI fluorescence (excitation 561 nm, emission 566-719 nm). Bottom left: White light. Bottom right: Overlay of all three images. Image sizes are 135 x 135 μ m.

Live-dead PI staining was again carried out and the images in Figure 135 show some uptake of the fluorophore with apparent exclusion of PI. Larger, brighter spots visible in the images could be due to a small amount of CORM precipitation. More DMSO could be added to reduce this problem, since the culture only contains 0.01% DMSO due to the serial dilutions of the CORM stock. Cultures should not exceed 1% DMSO as DMSO-induced inhibition and stimulation of growth have been reported in mammalian cells have been reported and *E. coli* possess DMSO reductases.^{331,341} These effects will be examined in more detail in the toxicity studies in Section 197.

These preliminary results suggest that the coumarin-tagged CORM 197 may enter viable bacterial cells. The next step would be the use of flow cytometry to correlate fluorophore uptake into the cells with death after irradiation. However, before the commencement of such studies, it was first

necessary to check the toxicity of CORM **197** to *E. coli* using growth curves similar to those described in the Introduction.

5.4 Toxicity Studies With Mn(I) PhotoCORMs

With the preliminary imaging results in hand, it was necessary to assess whether CO-release from CORM **197** was toxic to bacteria. Antimicrobial assays were performed with BL21 *E. coli* cells as a model organism. Although large numbers of *E. coli* are present in gut flora, this well-studied bacterium can also act as a pathogen. It has already been shown (Section 1.3.1) that CO-release from several CORMs leads to greater toxicity than CO gas in *E. coli*.^{74,130} The intention of these experiments was to use growth curve experiments similar to those performed by Ward for complexes **37** and **95** (TryptoCORM). Control experiments were used to show that both fresh CORM addition and irradiation were necessary for an antimicrobial effect.¹³⁷

Before discussing the results of the studies on compound **197**, an important point about the method should be highlighted. In earlier *E. coli* growth curve experiments by Ward, bacteria used for the growth curves were removed from agar plates that had been stored at 4°C for between several days and several weeks.¹³⁷ An increased antimicrobial effect was noted when older plates were used in these studies with TryptoCORM.¹³⁷ A plating study confirmed that the number of *E. coli* colonies able to form from each culture decreased as the age of the plate increased.¹³⁷ This led to the hypothesis that the antimicrobial effect of TryptoCORM towards *E. coli* appeared more potent when older plates were used because fewer cells were alive on the older plates. Changes in the biochemistry of the *E. coli* over the storage period were also considered and may also contribute to the age effect observed. For example, the level of expression of haem-containing proteins that constitute targets for CO may change depending on the age and stress of the bacteria. Even when the cells from older plates were allowed to grow to a comparable OD600 to cultures from the newer plates, the effect of TryptoCORM on bacteria derived from the older plates were still much more pronounced, which suggests that the number of living cells alone may not account fully for the age effect.¹³⁷ Regardless of the origins of the age effect, previous work suggests that older plates made *E. coli* more susceptible to the antimicrobial effects of CO release.

For the experiments reported in this Chapter, a different method was used to prepare the bacteria. The bacteria used in the antimicrobial assays reported in this Thesis were freshly cultured in media in an incubator at 37°C for ~16 hours and were then diluted into fresh media immediately before the antimicrobial assay. Using fresh starter cultures every day provides a way of standardising the preparation of the bacteria used in the assay. However, the bacteria used in the starter culture experiments had less time to be weakened towards the effects of CO-release compared to cultures prepared by the first method. It is unclear to what extent either of the above methods relate to a

real bacterial infection; these studies were envisaged as a proof-of-concept and a mechanistic tool, rather than as an infection model.

The first growth curve experiments performed were used to examine the effect of DMSO and 400 nm irradiation on the cultures and assess the reproducibility of the new starter culture method; the results are shown in Figure 136.

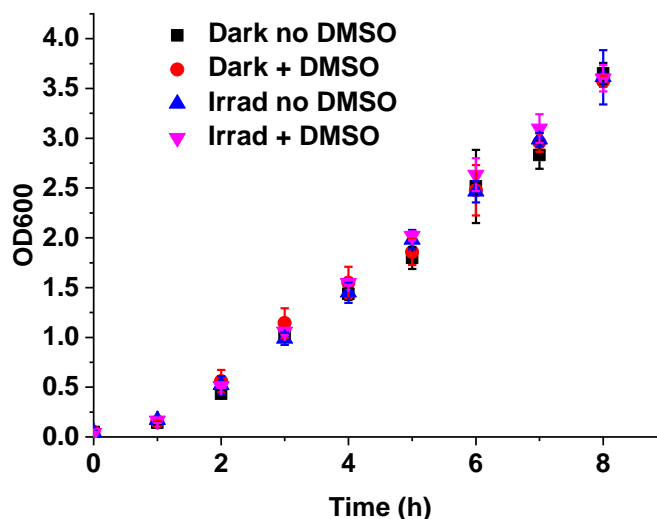


Figure 136: Growth curves with *E. coli* BL21 under the conditions shown. Each point is the mean of three separate repeats from different cultures, and the error bars show standard deviation. Irradiation with a 2.4 W power 400 nm LED took place between 1 and 3 hours and comprised cycles of 3 minutes off, 2 minutes on.

To test the conditions of the assay, L-TryptoCORM was added to the cultures and irradiated, since this compound is known to have an antimicrobial effect. Initially, a starting OD600 of 0.05 was used to match the starting OD600 in Ward's experiment.¹³⁷ A low concentration of 25 μ M TryptoCORM was initially used to test the limits of the assay and in case of poor solubility for **197**. The results are shown in Figure 137.

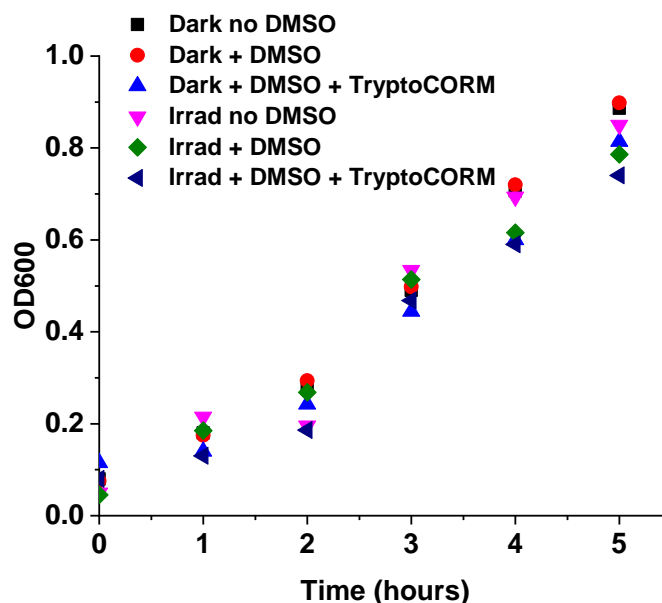


Figure 137: Growth curves with *E. coli* BL21 under the conditions shown. All cultures containing DMSO were 1% DMSO by volume. The TryptoCORM concentration used was 25 μ M. Irradiation with a 2.4 W power 400 nm LED took place between 1 and 3 hours and comprised cycles of 3 minutes off, 2 minutes on.

The growth curves show that L-TryptoCORM did not have an antibacterial effect under these conditions. Ward showed that 100 μ M TryptoCORM led to no growth whatsoever of *E. coli* over an 8-hour culture.¹³⁷ Numerous other variables were tested with these conditions. Modifications included increasing the CORM concentration to 100 μ M, irradiating from 0-2 hours in the assay rather than 1-3 hours in order to prevent the bacteria from growing too quickly and blocking out the irradiation. Other variables altered included changing the shaking rate from 180 to 90 rpm to reduce oxygenation of the culture and slow the growth of the cultures, and diluting the LB media to 50%, which still did not lead to any antimicrobial effect when starter cultures were used. The use of 10% LB resulted in growth that was too slow to discern any effect of the CORM. These results are provided in Appendix 5.

It was hypothesised that the lack of any antimicrobial effect in this experiment could be due to the use of a starter culture, resulting in more bacteria being alive and growing at the start of the experiment compared to Ward's experiments. To account for this, a growth curve was performed using a lower starting OD600 value (lowered from 0.05 to 0.001). These results are provided in Appendix 5. Although the bacteria grew significantly in the dark over the 8-hour experiment, all the experiments where irradiation was used failed to grow, suggesting that the 400 nm irradiation is damaging to the bacteria at low OD600 values. Finally, when a starting OD600 of 0.005 was used, the results from Ward's study of TryptoCORM were replicated, Figure 138.

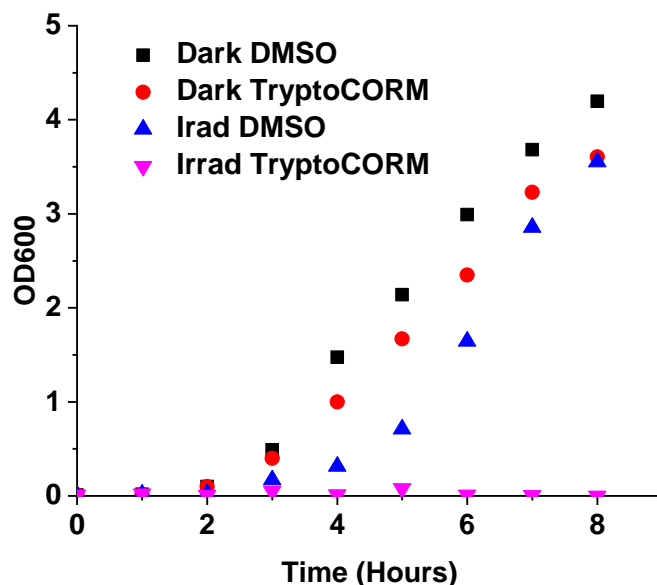
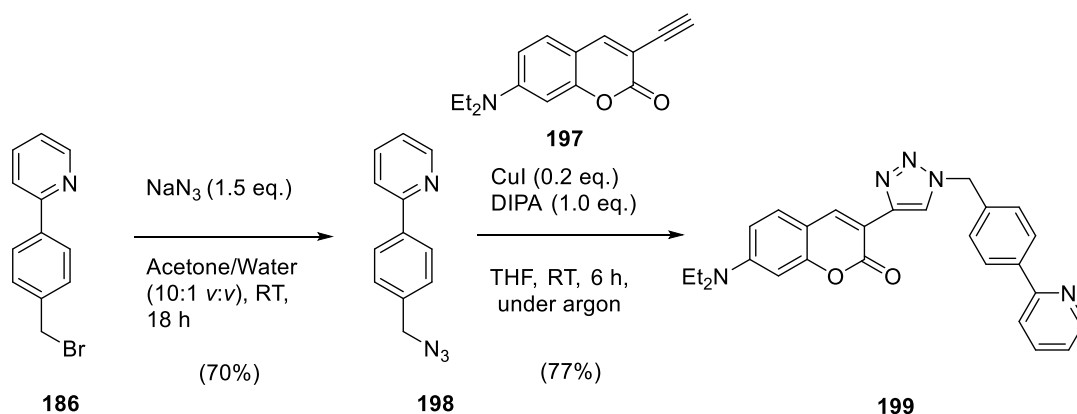


Figure 138: Growth curves with *E. coli* BL21 under the conditions shown. All cultures containing DMSO were 1% DMSO by volume. The TryptoCORM concentration used was 100 μ M. Irradiation with a 2.4 W power 400 nm LED took place between 0 and 2 hours and comprised cycles of 3 minutes off, 2 minutes on.

The results show a very clear antimicrobial effect of TryptoCORM when the lower starting OD600 was used. A combination of both irradiation and the addition of TryptoCORM was required to have the antimicrobial effect. A repeat of the same experiment with a starter culture derived from a fresh plate produced similar results, confirming that the observed effect can be reproduced (see Appendix 5). In the previous experiments with higher OD600 values, either not enough light could penetrate through the culture, or enough bacteria survived the CO-release to continue growing. It seems that using a lower starting OD600 with a starter culture compensates for the increased number of live, growing cells compared to Ward's method.¹³⁷

The toxicity of compound **197** was then studied. The use of L-TryptoCORM now serves as a useful positive control. As mass spectrometry studies on complex **95** have shown that the protonated ppy ligand is a possible by-product of CO-release, the Mn-free coumarin protonated ppy compound **199** was also synthesised for use as a negative control (Scheme 73). If an antimicrobial effect were to be observed, the appropriate iCORM control (using pre-irradiated CORM **197** to release all of the CO before adding to the cultures) could also be performed, both in the dark and with irradiation.



Scheme 73: Synthesis of compound 199.

The results of the growth curves with CORM **197** and Mn-free control compound **199** are shown in Figure 139. A control experiment with both DMSO and irradiation would usually be performed but this control did not grow at all in this experiment. This was excluded as an anomalous result since there is little difference between the irradiated cultures with or without DMSO in the other experiments performed throughout this Chapter.

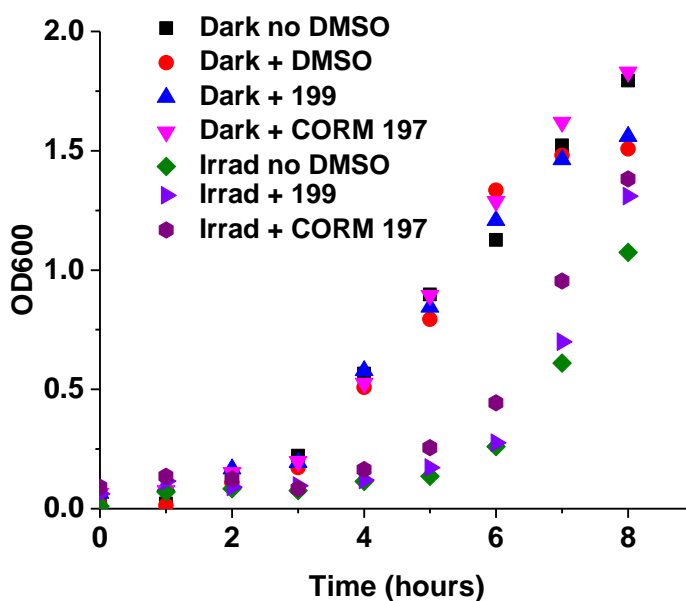


Figure 139: Growth curves with *E. coli* BL21 under the conditions shown. All cultures containing DMSO were 1% DMSO by volume. The concentrations of **197 and **199** used were 100 μM . Irradiation with a 2.4 W power 400 nm LED took place between 0 and 2 hours and comprised cycles of 3 minutes off, 2 minutes on.**

The high concentrations (100 μM) of compounds **197** and **199** led to some precipitation even when 1% DMSO was used to solubilise the complexes. The results in Figure 139 show that irradiation has a slightly detrimental effect upon the growth of the bacteria, and the presence of

CORM **197** or control compound **199** in DMSO has no additional killing effect compared to irradiation of the culture with no additives.

When the same experimental conditions were used to test another $[\text{Mn}(\text{ppy})(\text{CO})_4]$ derivative **95**, a small antimicrobial effect was observed, Figure 140. Complex **95** is highly soluble in water and does not form any precipitate at 100 μM concentration.

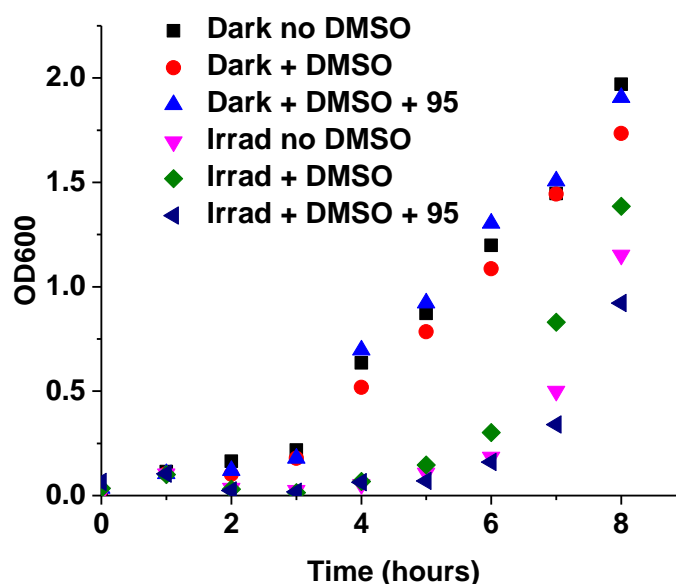


Figure 140: Growth curves with *E. coli* BL21 under the conditions shown. All cultures containing DMSO were 1% DMSO by volume. The concentration of **95 used was 100 μM . Irradiation with a 2.4 W power 400 nm LED took place between 0 and 2 hours and comprised cycles of 3 minutes off, 2 minutes on.**

There was a slight lag in the growth of the bacteria compared to the irradiated DMSO control culture when CORM **95** and irradiation were both added. A repeat of the experiments in Figure 140 with a starter culture from a different plate also showed only a small effect of irradiation of CORM **95** compared to the DMSO controls (Appendix 5). This shows that there was a small antimicrobial effect for complex **95**, but it was far less pronounced than for L-TryptoCORM under the same conditions (Figure 138). Therefore, a reproducible, but only very small, antimicrobial effect was observed for complexes **197** and **95**. Not only is complex **197** a poor CORM, but other $[\text{Mn}(\text{ppy})(\text{CO})_4]$ derivatives appear to have low antimicrobial activity.

The control experiments in this Thesis, and those performed by Ward with iCORMs of L-TryptoCORM, provide strong evidence that the antimicrobial effects that were observed were related to CO-release.¹³⁰ Yet the data show that the $[\text{Mn}(\text{ppy})(\text{CO})_4]$ derivatives appear to have a smaller antimicrobial compared to TryptoCORM at the same concentration. This is an intriguing result given that the $[\text{Mn}(\text{ppy})(\text{CO})_4]$ derivatives release 2.7-3.2 equivalents of CO per molecule to myoglobin under 400 nm irradiation whilst TryptoCORM releases only 2.1 equivalents of CO

per molecule. Myoglobin assays have shown that TryptoCORM releases CO much more rapidly at 400 nm than $[\text{Mn}(\text{ppy})(\text{CO})_4]$ derivatives.^{130,137,159} It is possible that CO-release rate is more influential than the overall quantity of CO released by a CORM. A faster rate of CO-release would give a higher concentration of CO for a shorter time, which could be to be more effective at killing bacteria than exposure to lower concentrations of CO over longer times.

If the CO release does indeed occur intracellularly, different uptake levels of the tetracarbonyl ppy CORMs and TryptoCORM could also account for the different extents of the antimicrobial effect through differences in the localised CO concentrations. It may be that the biologically-derived co-ligand in TryptoCORM improves uptake either through mimicking tryptophan in entering cells through membrane transporter proteins,³⁴² or by conveying a suitable balance of water solubility and lipophilicity to increase entry into the cell.

5.5 Conclusions

The use of Click chemistry has been extended in this Chapter with the synthesis of complex **188**. A flexible, modular system for CORM synthesis based on $[\text{Mn}(\text{ppy})(\text{CO})_4]$ derivatives is now available which, unlike the synthesis of alkyne **46**, does not require protecting group chemistry.

Coumarin-tagged photoCORM **197** was imaged in the presence of live mammalian and bacterial cells using confocal microscopy. The remote nature of the fluorophore makes it difficult to confirm from these experiments alone whether the Mn(I) tetracarbonyl moiety remained intact upon entry to the cells. However, irradiation is required in other $[\text{Mn}(\text{ppy})(\text{CO})_4]$ derivatives in order to cause the CO-induced antimicrobial effect,¹³⁷ suggesting that, at least in the case of *E. coli* **197** enters the cells without releasing CO.

The preliminary imaging results reported here suggest that **197** behaves similarly to the luminescent Re(I) photoCORMs studied in the literature.^{169,181,182} The growing number of imaging studies showing that CORMs can enter cells before releasing CO lends weight to the 'Trojan horse' picture of CORM antimicrobial activity in which CO-release takes place within the cell. It is unclear how much of a role is played by transfer of extracellular CO into cells, but the increased toxicity of CORMs compared to CO gas⁷⁴ suggests that entry of CORMs into cells before CO release could be important in creating high intracellular concentrations of CO.

However, the antimicrobial activity of **197** and related derivative **95** was poor compared to the known antimicrobial TryptoCORM. The antimicrobial effects of all compounds were smaller than those observed in previous work due to the use of starter cultures.¹³⁷ Given the lack of antimicrobial activity towards *E. coli* of CO released by **197**, a follow-up to the preliminary imaging and cytometry study was not justified.

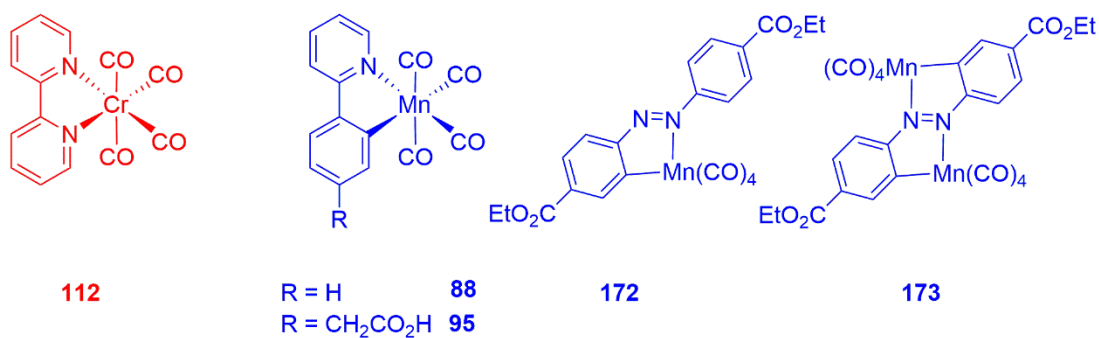
6 Conclusions and Future Work

6.1 Photochemical CO-release from $[\text{Mn}(\text{ppy})(\text{CO})_4]$ and related complexes

6.1.1 TRIR Studies for PhotoCORM Design

As described in the Introduction, metal carbonyl complexes capable of light-induced CO-release (photoCORMs) have been previously shown to hold promise in therapeutic applications ranging from vasorelaxation to antibiotic drug design. However, it has been difficult to develop compounds in which the CO-release is activated by NIR or visible light irradiation rather than UV which has unwanted toxic side-effects and a limited tissue penetration depth. The challenge in the production of such photoCORMs can be at least partially attributed to the fact that there was limited experimental insight into the mechanism of light-activated CO release, a problem which this Thesis has sought to rectify. The ultrafast TRIR studies in Chapters 2 and 4 show how this powerful technique can be used to understand the behaviour of photoCORMs. In conjunction with TD-DFT calculations the structural information provided by such infrared spectroscopy measurements has allowed the nature of the initial photoproducts to be determined.

In Chapter 2, the formation and stability into the μs timescale of tricarbonyl solvent complexes formed by loss of one CO from $[\text{Mn}(\text{ppy})(\text{CO})_4]$ compound **88** proves the mechanism of the start of the photo-activated CO release degradation pathway. These measurements were complemented by solution *in situ* IR experiments that probed the products generated after several minutes, enabling the tentative assignment of *facial* tricarbonyl Mn hydroxy clusters. In the future it would be desirable to investigate the timescale in between those spanned by these two IR techniques. Modern FTIR spectrophotometers could be used to record scans every few seconds across a small wavenumber range to probe the mechanism that converts *fac*- $[\text{Mn}(\text{ppy})(\text{S})(\text{CO})_3]$ to the final degradation products. It would also be helpful if follow-on work from this Thesis modified the flow system used in the TRIR experiments. At the moment the experimental setup is designed to remove the photoproducts following the first ‘pump’ pulse.²¹⁰ However, it is desirable to understand what happens when the products of initial CO loss absorb a second photon because in assays like the myoglobin experiment CO release is usually induced by continuous irradiation. Nuernberger and co-workers¹⁹¹ employed two consecutive pump pulses to address this question but found that the initial photoproduct $[\text{Mn}(\text{tpm})(\text{CO})_2(\text{OD}_2)]^+$ was unreactive. If **113**_{MeCN} and **113**_{OH₂} can be isolated in the future, their stability could be exploited to afford a mg-scale synthesis of these complexes for future photochemical studies.



Vlcek and co-workers

This Thesis

Figure 141: Key photoCORMs studied and compared in this Thesis.

This Thesis also reports how the TRIR studies have been extended to study the photochemical reactivity of less efficient CO-releasing molecules complexes **172** and **173** (Figure 141). The spectral resolution provided by infrared spectroscopy of the carbonyl bands again provides a useful way of distinguishing the photoproducts. Compared to [Mn(ppy)(CO)₄] the azo complexes more closely resembled the behaviour of [Cr(bpy)(CO)₄] by forming two consecutively-populated unreactive excited states as the major photoproducts, with little CO photodissociation. In the future, these results could prompt more extensive theoretical calculations on [Mn(ppy)(CO)₄] and complexes **172** and **173** to try and explain the differences in behaviour. Comparing the rates of CO dissociation versus intersystem crossing of the different complexes would be particularly informative. Quantum yield measurements for CO loss and quantification of the branching ratios between excited state formation and CO dissociation would also provide a useful method of comparing the complexes discussed in this Thesis with one another and with other studies.¹²⁷ Quantum yield measurements would require use of a monochromatic light source and an actinometer for calibration purposes.

The incorporation of azo ligands into Mn tetracarbonyl complexes was inspired by Mascharak and colleagues' work on visible light-activated tri-carbonyl CORMs.¹²⁷ Unfortunately, the use of azo ligands in place of a pyridyl N-donor in complex **88** increased the CO-release wavelength at the expense of efficient CO release. This result emphasises that to develop practically useful light-triggered CO-releasing molecules there must be a consideration of more factors than just the CO-release wavelength, whilst this principle provides a starting point for rational photoCORM design they are not comprehensive enough to guarantee success. Based on the work in Chapter 4 it is now suggested that a different method of attaining CO-release at longer wavelengths would be to use a photosensitiser in a similar manner to Schiller and co-workers.¹³⁴ Rather than use two separate molecules, the synthetically flexible click chemistry described in this Thesis with previously-known alkyne **46**, or novel azide **188**, could be used to append a photosensitiser to a photoCORM (Figure 142). The effect of combining the photosensitiser and CORM could be

compared to co-administration of distinct photoCORM and photosensitiser molecules to explore how photosensitisation may best be applied to photoCORMs in the solution phase.

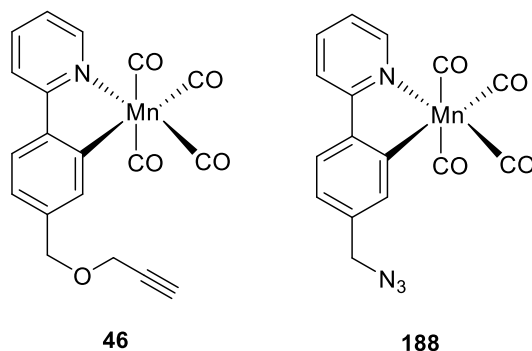


Figure 142: Alkyne **46** developed by Jonathan Ward and used in this Thesis, and complementary novel azide **188**, developed in this Thesis.

6.1.2 Isomerisation of ether and DMSO solvent C-H σ -complexes

The ether solvent and DMSO results show that ‘vacant’ or ‘solvated’ coordination sites on metals can play host to ultrafast isomerisations, providing an interesting example of fleeting C-H activation despite stronger donor ligands being present. This has implications for our understanding of metal-solvent complexes, which are ubiquitous in catalysis. Other than alcohol solvent (S) isomerisations observed by Harris and co-workers with $[\text{Cr}(\text{CO})_5(\text{S})]$, which are at least an order of magnitude slower than the THF and 1,4-dioxane isomerisations observed in this Thesis, there appears to be relatively little published data on such reactions. It would be interesting to test the behaviour of $[\text{Mn}(\text{ppy})(\text{CO})_4]$ in alcohol solvents to compare the rates of isomerisation with those observed by Harris and co-workers. The rate of isomerisation is clearly highly solvent-dependent but the effect of different metal complexes has not been explored. A vast range of metal carbonyl complexes displaying photochemical CO-release is available to study, including many of the photoCORMs discussed in this Thesis.

The mechanism by which the isomerisation occurs could not be identified. Future experiments could focus on performing photolysis at low temperatures for NMR studies that could distinguish a ‘chain-walk’ mechanism from an intermolecular mechanism. The dependence of the lifetimes associated with the isomerisations upon temperature could also be examined to obtain activation parameters which may reveal more about the mechanism.

6.2 Redox-Tagged CORMs

The synthesis and characterisation of three novel ferrocenyl CORMs was performed, incorporating two organometallic therapeutic groups within the same molecule. Electrochemical and infrared spectroelectrochemical measurements showed that the redox-active ferrocenyl group

must be located in the first coordination sphere of the Mn if ferrocene oxidation is to have a significant effect upon the Mn-CO bonds. However, no redox-triggered CO-release was observed for any of the complexes. Photochemical release from complex **133**, and both thermal and photochemical release from complex **134**, were quantified using the myoglobin CO-release assay. Taking these results into account, azo complex **172** was also investigated as a possible reductively-triggered CORM since the complex comprises a redox-active group in the first coordination sphere of a metal carbonyl. Despite very large changes in the metal carbonyl bands upon reduction, no redox-triggered CO-release occurred. This work may be able to guide future studies in the area of redox-activated CO-release.

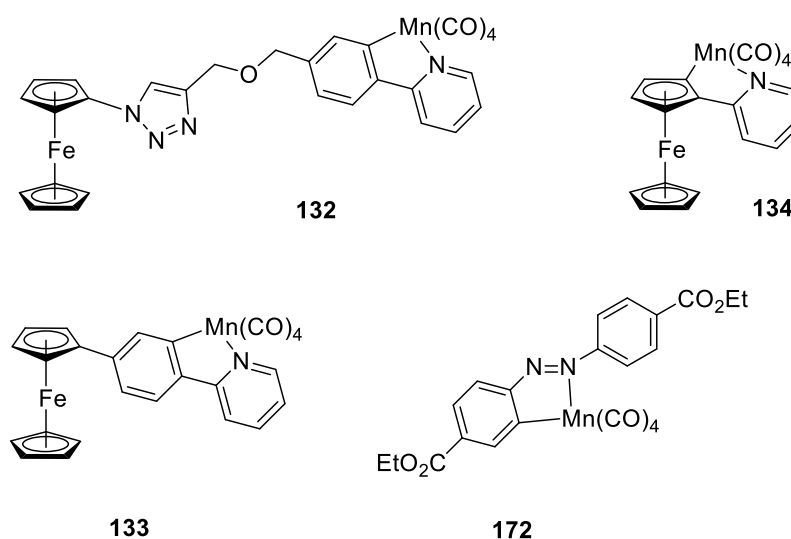
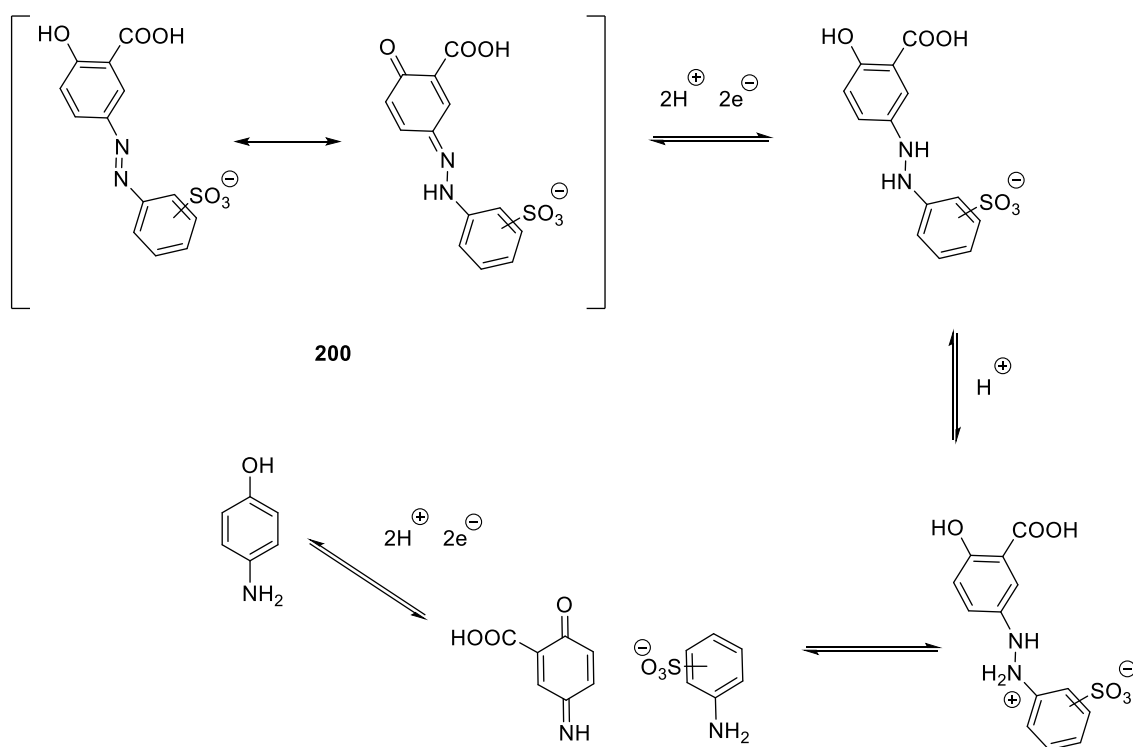


Figure 143: Novel redox-active CORMs tested for redox-triggered CO-release in this Thesis.

Although electrochemical reduction was unsuccessful, the metabolism of complex **172** and other azo CORMs by azoreductase enzymes could also be assessed. Azoreductases present in bacteria in the gut and on skin have been shown to reduce a variety of azo dyes including sulfasalazine,^{308,343,344} and if these enzymes could be used to cleave the azo bond in **172** then this could lead to CO release in the gut.

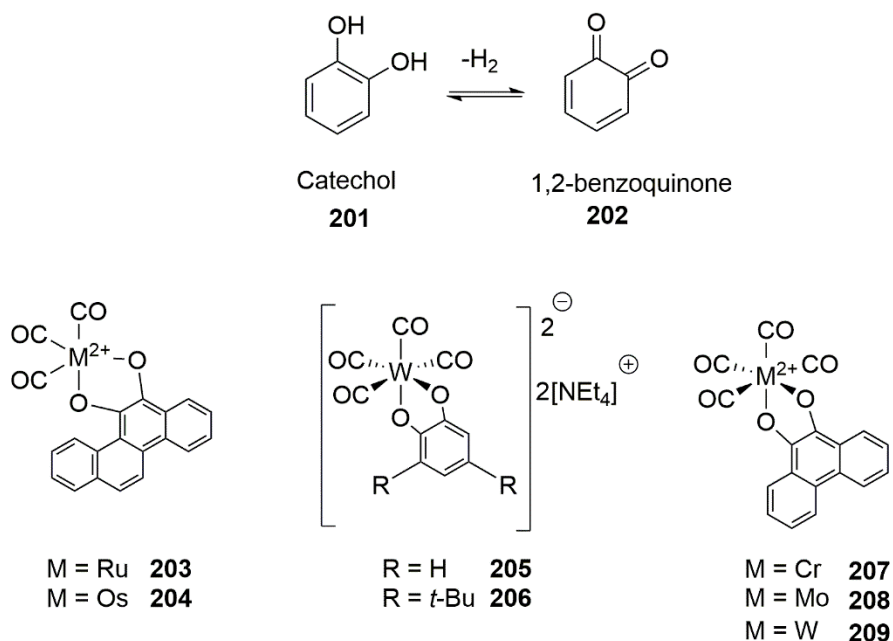
Future work on reductive activation of azo dye CORMs could take inspiration from the mechanism of reduction of the prodrug sulfasalazine. Tautomerization of the azo group to form a hydrazone, promoted by the *para* phenoxy substituent, can be used to assist the reductive cleavage of the azo bond, as has been shown by electrochemical studies on the reduction of sulfasalazine analogue 200, Scheme 74).³⁴⁵



Scheme 74: Cleavage of azo dyes with *p*-phenoxy substituents.

This is because the hydrazone tautomer is more easily reduced than the azo tautomer, yielding the corresponding hydrazine after protonation. Subsequent reduction of the hydrazine to yield two aniline products can then take place resulting in complete cleavage of the azo bond. The effect of complete cleavage of the azo bond upon the stability of the Mn(I) tetracarbonyl moiety could then be investigated.

A possible redox-tagged co-ligand system for future investigation would be catecholates. Catechol is converted into 1,2-benzoquinone upon 2-electron oxidation (Scheme 75). Quinone/hydroquinone redox couples are commonly encountered in biology and represent biocompatible ligands.³⁴⁶ There is some precedent in the literature for metal carbonyl catecholate complexes. For example, the tungsten complex $[\text{Et}_4\text{N}]_2[\text{W}(\text{CO})_4-(\text{O}_2\text{C}_6\text{H}_4)]$ **204** was shown to release one equivalent of CO upon dissolution in MeCN.³⁴⁷ A di-*tert*-butyl-substituted catecholate **205** was then used in order to stabilise the tricarbonyl degradation product so that it could be crystallised.³⁴⁷ A thermally stable complex would be advantageous for gaining more selective CO-release. Changes in the bonding to the metal centre upon oxidation to the benzoquinone could be investigated as a way to labialise the catecholate and initiate decomposition of the complexes. Some examples of known complexes are shown below in Scheme 75.³⁴⁷⁻³⁴⁹ Many of the known complexes were produced via photolysis, as these ligands have been used to trap the products of photolysis or metal carbonyls and other organometallic species. However, there are examples of thermal reactions too. However, complexes shown would likely require further functionalisation with solubilising groups because of their nonpolar extended fused aromatic systems.



Scheme 75: Interconversion of catechol and 1,2-benzoquinone. Known metal carbonyls with catecholate co-ligands.

6.3 Antimicrobial and Imaging Studies

Coumarin-tagged photoCORM **197** was imaged in the presence of live mammalian and bacterial cells using confocal microscopy. The results suggested that **197** behaves similarly to the luminescent Re(I) photoCORMs studied in the literature.^{169,181,182} Confirmation of whether the manganese centre survived entry into the cells could have been tested by synthesising other coumarin CORMs. Complex **209** (Figure 144) was synthesised in York, where the Mn is in the first coordination sphere of the fluorophore, with scope for performing imaging.³⁵⁰ In complex **209** it is more likely that CO-release would result in changes in the fluorescence properties of the coumarin, though the coumarin may also affect the CO-release properties. Given the poor toxicity results against *E. coli* for $[\text{Mn}(\text{ppy})(\text{CO})_4]$ derivatives this study was not continued. However, the question of whether $[\text{Mn}(\text{ppy})(\text{CO})_4]$ could enter mammalian cells remains of significant interest as CO has many other applications apart from being an antimicrobial.

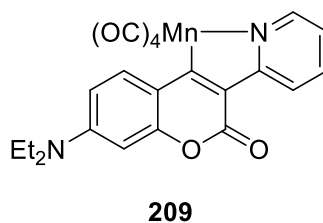
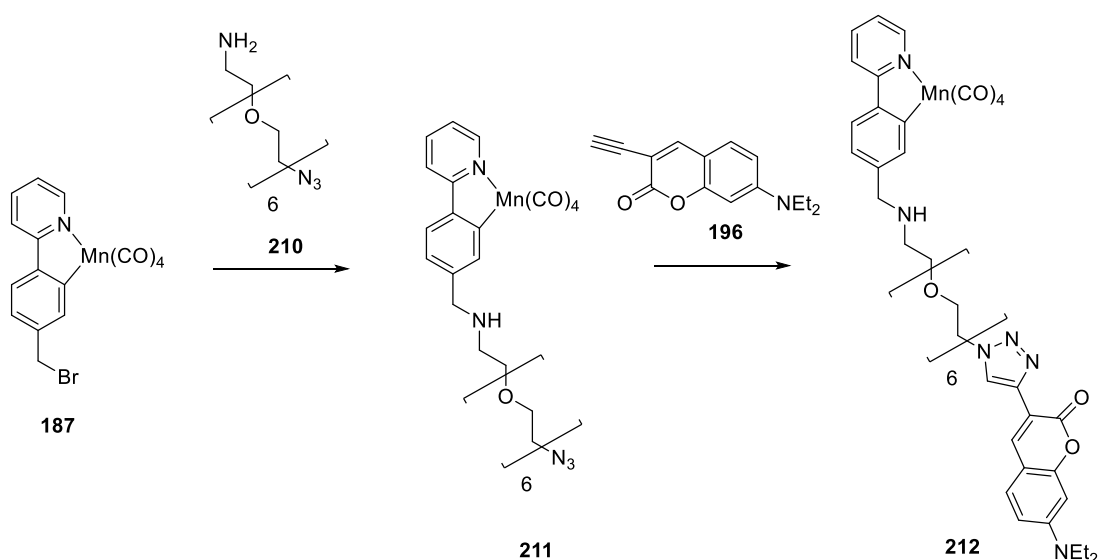


Figure 144: Structure of complex 209.

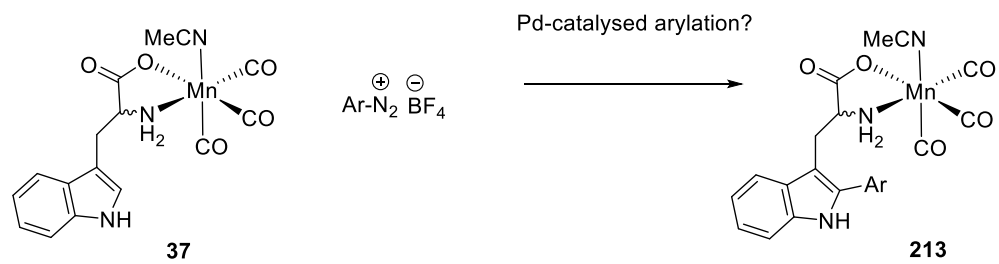
A suggestion for future work would be modulating the CO-release rates from $[\text{Mn}(\text{ppy})(\text{CO})_4]$ derivatives, or from TryptoCORM, to study the effect on the antimicrobial properties. The simplest way to do this would be to use different irradiation powers in growth curve experiments and assess how the antimicrobial activity is affected. Control experiments for the effect of the irradiation would be critical. Such experiments could then be used to test whether the rate of CO loss is more influential than the number of CO ligands lost per molecule of CORM. If this hypothesis were upheld this would allow a focus to be placed on faster CO release rates for CORMs intended as antimicrobials.

The solubility of some of the $[\text{Mn}(\text{ppy})(\text{CO})_4]$ CORMs could also be improved so that higher concentrations could be used without precipitation. One strategy would be to use click chemistry to PEGylate the drug sphere of the CORM, which could be achieved using **187** and commercially-available reagent **210** (Scheme 76).



Scheme 76: PEGylation to produce more water-soluble $[\text{Mn}(\text{ppy})(\text{CO})_4]$ derivatives that retain synthetic flexibility.

Future work could also focus instead on TryptoCORM, which appears to have several desirable properties: visible light CO release, a pronounced antibacterial effect against *E. coli*, and scope for further functionalisation for imaging. In the future it may be possible to use room-temperature tryptophan arylation reactions³⁵¹ to functionalise TryptoCORM and produce fluorescent derivatives, so that TryptoCORM could be imaged in live cells as opposed to complex **37**.



Scheme 77: Possible arylation of the indole 2-position of TryptoCORM with aryldiazonium salts.³⁵¹

7 Experimental

7.1 TR^MPS

The TRIR measurements were performed at the ULTRA³⁵² facility using the Time-Resolved Multiple Probe Spectroscopy mode of operation,²¹⁰ (TR^MPS) at the Central Laser Facility (STFC Rutherford Appleton Laboratories, Oxfordshire, UK). The experiments were driven by a 10 kHz repetition rate Ti:Sapphire amplifier (Thales) as a probe source, producing 40 fs pulses at 800 nm. The Ti:Sapphire laser output was used to pump an Optical Parametric Amplifier (TOPAS, Light Conversion Ltd.) followed by a AgGaS Difference Frequency Mixing stage which produced tuneable mid-IR probe beam of $\sim 500\text{ cm}^{-1}$ useable bandwidth. The IR probe beam was split to form reference and probe beams, which were passed through spectrographs onto MCT array detectors (IR Associates). The probe beam spot size at sample was *ca.* $80 \times 80\ \mu\text{m}^2$. High speed data acquisition systems (Quantum Detectors) allowed 10 kHz acquisition and processing of the probe and reference pulses to generate a pump-on pump-off infrared absorption difference signal. The excitation source for the TRIR experiments was the output of the 1 kHz titanium sapphire amplifier (Spectra Physics Spitfire XP, 100 fs pulse length) equipped with another TOPAS OPA, pulse energy at sample attenuated down to 1 μJ and focused down to *ca.* $150 \times 150\ \mu\text{m}^2$ spot). Both ULTRA amplifier and Spitfire amplifier were optically synchronised by sharing the same seed from 68 MHz Ti:Sapphire oscillator. The seed beam was delayed with an optical delay line before the 1 kHz amplifier to accommodate for the 100 fs -14.7 ns time delays between pump and probe. To go beyond 14.7 ns and up to 100 μs , subsequent seed pulses are selected from the 68 MHz seed pulse train accompanied by the appropriate setting of the optical delay line. The polarisation of the excitation beam at sample was set to be at 54.7° with respect to the probe.

Solutions of the manganese complexes were prepared at a concentration of *ca.* 15-20 mM in the appropriate solvent and flowed through a Harrick cell for the duration of the experiment. Experiments were performed under air at room temperature unless otherwise stated. Atmospheres of CO or N₂ were achieved by evacuating and backfilling the vessel using a Schlenk line.

The order in which the different pump-probe delays were collected was randomised, and three cycles of the experiment were run to generate an averaged dataset at each delay. The spectra were also normalised using the reference detector to account for shot-to-shot noise. Spectra were then viewed as averaged, normalised difference spectra against background spectra recorded at pump-probe delays of 900-1000 μs . The resulting data were then manipulated by firstly subtract the reference data to obtain a difference spectrum and then a first- or second-order polynomial fitting to the baseline was performed. The data were then exported as comma-separated variable files and imported into Origin 2018. Spectral calibration was then performed, either using a 190 μm

polystyrene standard or by using the known positions of the bleach bands. This allowed for detector pixels to be allocated to specific frequencies. The overlap in detection frequency between the two detectors was then removed manually. Data were then analysed in Origin 2018 and kinetic fits performed with the *ExpGro* and *ExpDec* functions with the errors reported as 95% confidence intervals.

7.1.1 Calibration of Spectra

The spectrograph provides a linear relationship between the pixel number and wavelength which can be used to fit the data, and the wavelengths were then converted into wavenumbers. Specific detector pixels were assigned to vibrational wavenumbers by fitting the data to the bleach bands of the starting material. The wavenumber of the bleach bands used, determined at a 2 cm⁻¹ resolution with a Unicam Research Series FTIR spectrometer, are given in Table 23.

Table 23: Stretching frequencies used to calibrate the TRIR spectra.

Compound	Solvent	IR stretching frequency (cm ⁻¹)			
88	MeCN	1933	1976	1989	2076
88	Toluene	1933	1976	1990	2074
88	CH ₂ Cl ₂	1932	1975	1990	2075
88	<i>n</i> -Heptane	1940	1981	1994	2077
88	1,4-Dioxane	1933	1975	1990	2074
88	ⁿ Bu ₂ O	1937	1977	1992	2075
88	DMSO	1927	1970	1987	2073
88	THF	1932	1974	1989	2073
94	THF	1933	1975	1990	2074
95	THF	1933	1975	1990	2074
133	THF	1931	1973	1988	2072
172	THF	1959	2001		2082
173	THF	1964	1998	2017	2078

7.2 Myoglobin CO-Release Assay

Myoglobin (from equine heart, ~10 mg) was dissolved in 10 mL phosphate-buffered saline solution (10 mM, pH 7.4). Sonication in an Ultrawave SFE590 sonic bath (full power, 25 kHz

frequency, *circa* 5 seconds) was used to aid dissolution. The resulting solution was filtered through cotton wool.

To a 1 mL PMMA disposable cuvette, was added 1 mL of the myoglobin solution. Sodium dithionite (1 mg) was added and the solution was mixed with a pipette. A UV-visible spectrum was recorded and this was taken to be the standard spectrum for deoxymyoglobin.

Immediately after the recording of the deoxymyoglobin spectrum, the same sample was bubbled with CO gas for *ca.* 30 seconds. The UV-visible spectrum recorded after bubbling with CO was taken as the standard spectrum for carboxymyoglobin. This solution was then discarded.

A stock solution of the CORM to be tested was prepared. The solvent was typically DMSO in order to solubilise the complex. The stock solution was 200 times the final concentration of CORM desired for the experiment. The stock solution (5 μ L) was added to 995 μ L myoglobin solution, so that only 0.5% DMSO was used in the experiment.

A cuvette containing 1 mL myoglobin solution was incubated within the spectrometer for 15 minutes to ensure the temperature inside the cuvette reached 37.5°C. Once this was achieved, sodium dithionite (1 mg) was added, followed by 5 μ L of the CORM stock solution. The solution was mixed with a pipette after each addition. A layer of paraffin oil (0.5 mL) was then added above the myoglobin solution to prevent CO escape. It is best to complete these additions quickly and begin recording spectra as soon as possible as thermal CO release may start immediately.

For photochemical CO release, an irradiation control unit, developed by workshops staff in the chemistry department at the University of York, was used. The control unit enables the power drawn by the LED irradiation source to be set, and has a timer that allows cycles of irradiation to repeatedly take place. The LEDs used were installed into plastic lids that fit over the top of the disposable PMMA cuvettes. This ensures that samples can be irradiated with well-defined wavelength ranges, power, and time in a reproducible manner.



Figure 145: Irradiation control unit developed at the University of York. On the left side is a dimmer switch and power readout to control the power drawn by the LED. On the right side is a programmable timer function that allows repeated on/off cycles.

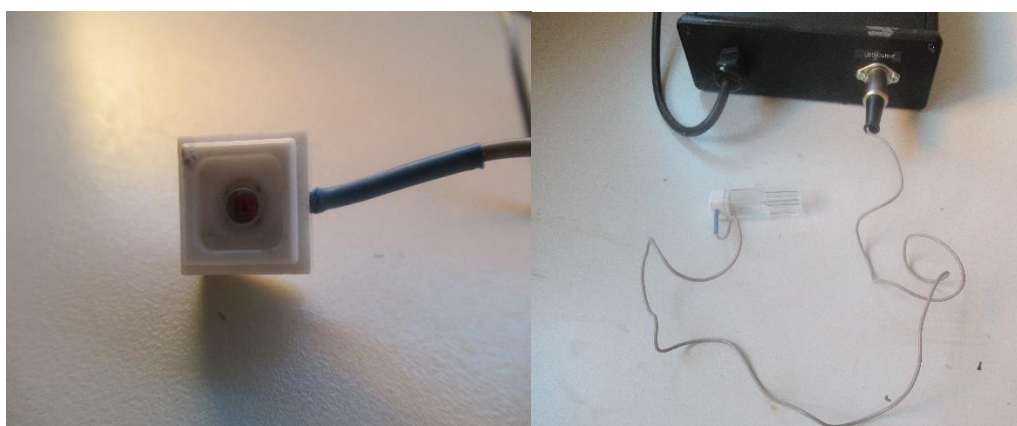


Figure 146 Left: LED embedded in a cuvette lid to irradiate samples inside a UV-visible spectrometer during myoglobin CO release assays. Right – The LED lid attaches to a PMMA cuvette and plus into the back of the irradiation control unit, which is in turn powered by the mains.

The data were processed according to the procedures outlined by Fairlamb and co-workers.¹⁶⁰ The four isosbestic points shared by deoxymyoglobin and carboxymyoglobin were used to correct the data for absorbance or precipitation of the CORM or its degradation products. Firstly, the raw spectra were corrected at the isosbestic point at 510 nm by translating the spectra at all wavelengths. Any differences in the absorption at the other three isosbestic points compared to the standard spectra was assumed to be caused by the CORM or its degradation products. The absorbances at the isosbestic points were fitted using nonlinear regression to produce a spectrum of the CORM absorbance, which can then be subtracted from the experimental data.

The concentration of carboxymyoglobin was extracted from the spectra based on the absorbance at 540 nm. From the standard spectrum of carboxymyoglobin, it is possible to calculate the

saturated carboxymyoglobin concentration, Mb-CO_{max}, using Equation 7, where OD₅₄₀ is the absorbance at 540 nm of the Mb-CO standard spectrum and ε₁ is the extinction coefficient of Mb-CO at 540 nm [ε₁ = 15.4 mM⁻¹ cm⁻¹].

$$\text{Mb-CO}_{\text{max}} = \frac{\text{OD}_{540} \times 1000}{\varepsilon_1}$$

[Equation 7]

In order to measure the Mb-CO concentration from the OD₅₄₀ in the experimental spectra, a second extinction coefficient is needed, as both deoxymyoglobin and carboxymyoglobin are present in the solution in the intermediate spectra. The second extinction coefficient, ε₂, accounts for the change in absorbance at 540 nm (ΔOD₅₄₀) as Mb-CO grows in. A reference point, the change in absorbance at the 510 nm isosbestic point ΔOD₅₁₀, is used to ensure that the change in absorbance at 540 nm is caused only by conversion of deoxymyoglobin to carboxymyoglobin (Equation 8).

$$\varepsilon_2 = \frac{(\Delta\text{OD}_{540} - \Delta\text{OD}_{510}) \times 1000}{\text{Mb-CO}_{\text{max}}}$$

[Equation 8]

Using the modified extinction coefficient ε₂, it is now possible to calculate the Mb-CO concentration in any of the sample spectra run in the assay using Equation 9.

$$\text{Mb-CO} = \frac{(\Delta\text{OD}_{540} - \Delta\text{OD}_{510}) \times 1000}{\varepsilon_2}$$

[Equation 9]

7.3 Electrochemistry

The electrode potential, *E*, of a redox couple at equilibrium is given by the Nernst equation (Equation 10),³⁵³ where *n* is the number of electrons, *a*_{red} and *a*_{ox} are the activities of the reduced

and oxidised species respectively, and x and y are the stoichiometric coefficients of the reduced and oxidised species in the cell half-reaction respectively.

$$E = \text{constant} - \frac{RT}{nF} \ln \frac{a_{red}^x}{a_{ox}^y} \quad [\text{Equation 10}]$$

However, the potential of one redox couple alone cannot be measured without reference to another. When two redox processes are coupled in an electrochemical cell, the Nernst equations for each redox process may be combined to give the more common Nernst equation: Equation 11, where E° is the standard reduction potential. In the equation, the oxidised form of species ‘a’ oxidises the reduced form of species ‘b’.³⁵³

$$E = E^\circ - \frac{RT}{nF} \ln \frac{a_{red}^x b_{ox}^y}{b_{red}^x a_{ox}^y} \quad [\text{Equation 11}]$$

In an equilibrium electrochemical cell, a net current flows between the two electrodes and a reaction occurs until equilibrium is reached and the potential difference between the electrodes reaches zero. In dynamic electrochemistry, however, a potentiostat sets a potential difference chosen by the user, forcing the composition of the solution near the electrode to change.³⁵³

The experiments carried out in this project employ the dynamic electrochemical technique of cyclic voltammetry.²⁹³ In one scan, the potential of the working electrode is swept in a linear fashion between two potentials E_1 and E_2 , and then back to E_1 . The current, proportional to the number of electrons transferred, is measured as a function of potential. Peak shapes arise from redox reactions; this is because the electron transfer rate is a function of potential. Initially the electron transfer rate increases as the potential does, but once the concentration of a species at the electrode surface is depleted, diffusion begins to limit the rate, causing a peak after which the current decreases.

A ‘blank’ scan is recorded without the species of interest present to identify the capacitive current. This current contribution arises from the migration of charged species in solution in response to the changing potential of the electrode rather than the net transfer of any electrons across the electrode-solution interface.

The cell used for these experiments comprises three electrodes. These are termed the ‘working’ (where the reaction of interest happens), ‘counter’ (which passes an opposite and equal current to the working electrode) and ‘reference’ (which contains another redox couple and provides a stable reference potential) electrodes. The potentiostat sets a potential difference between the working electrode and the counter electrode such that the potential difference between the working and reference electrodes is equal to the desired value. This setup is preferable over a two electrode system as it enables most of the current to pass between the working and counter electrodes, so that no reactions take place at (or within) the reference electrode. The three electrode system also

minimises the Ohmic potential drop between the working and reference electrodes (in accordance with Ohm's law this is linearly proportional to the current).²⁹³

The non-aqueous solvents used in this project necessitate the use of a 'pseudo-reference' electrode; most reference electrodes are usually compatible only with aqueous solutions. A pseudo-reference electrode differs from a standard reference electrode in that it does not contain another redox couple (a platinum wire was used in this work). The system is calibrated against the reversible ferrocene/ferrocenium couple (Fc/Fc^+) under the conditions of the experiment with either an internal or external standard.

7.3.1 Spectroelectrochemistry

Infrared spectroelectrochemistry was performed using an Optically Transparent Thin Layer Electrochemical (OTTLE) cell comprising a liquid IR cell with a Pt grid working electrode, Pt wire counter electrode and an Ag wire pseudo-reference electrode.

UV-visible spectroelectrochemistry was performed using an OTTLE cell composed of a quartz cuvette (path length 1 mm), a Pt grid working electrode, a Pt wire counter electrode and an Ag/AgCl reference electrode.

Experiments could be performed under an Argon atmosphere by flowing Ar over the solution to be studied.

7.4 *E. coli* Growth Curves

7.4.1 Media and Agar Plates

Luria broth (LB) growth media was made up containing a solution of 10 g/L tryptone, 5 g/L yeast extract and 10 g/L NaCl in deionised water from a Milli-Q purification system. The media was diluted accordingly if a less nutrient-rich media was required. The media was sterilised in an autoclave.

To make LB agar, the same concentrations a solution of 10 g/L tryptone, 5 g/L yeast extract, 10 g/L NaCl and 15 g/L agar was made in deionised water from a Milli-Q purification system. Once the LB agar was sterilised in an autoclave and had cooled, but not set, the agar was poured out into a petri dish and allowed to set. The plate was left to set in a sterile laminar flow hood to avoid contamination. Once the plate had set, the *E. coli* were streaked out onto the plate with a loop and allowed to grow at 37°C for between 16-24 h. Subsequent to this, the plates were stored at 4°C. New plates were made every four weeks to reduce the risk of contamination.

7.4.2 *E. coli* Growth Curve Experiments

Safety: This work was performed in a microbiology laboratory. Although the E. coli used in this work present a minimal risk to healthy humans, microbiological safety precautions were taken. Work surfaces were sanitised with 70% ethanol before and after work took place. Personal protective equipment (goggles, lab coat, and non-sterile gloves sanitised with 70% ethanol) was worn and as is standard good practice in any laboratory handwashing was always undertaken after leaving the laboratory.

A starter culture was prepared the night before the growth curve experiment. In a sterile laminar flow hood using aseptic technique, cells from a single colony on an agar plate were transferred into an 8 mL plastic bijou tube containing 3 mL LB and grown overnight (16 hours) in a shaker/incubator (180 rpm, 37°C).

Immediately before the start of the growth curve experiment, the OD600 of the starter culture was measured. An aliquot of the starter culture was removed, diluted into LB in a 1 mL PMMA cuvette, and the OD600 was measured using a nanodrop spectrophotometer (Thermo Scientific). The measured OD600 of the starter culture was then used to calculate the volume of starter culture to add to each experiment for the desired starting OD600.

The cultures for the growth curves were also performed as 3 mL cultures in 8 mL plastic bijou tubes. In a sterile laminar flow hood using aseptic technique, LB media (3 mL minus the required volume of *E. coli* stock) was initially added into each tube by pipette. For the DMSO controls, 15 µL DMSO was then added to the cultures, and for experiments where a CORM was added, 15 µL of a DMSO stock solution was added. The concentration of the CORM stock was calculated to give the desired final concentration in a 3 mL culture. The required amount of *E. coli* stock from the starter culture was then added to the bijou tubes, the cultures were mixed, and aliquots were removed to measure the starting OD600. Finally, the tubes were covered in aluminium foil and sterile plastic caps. For the cultures where irradiation was carried out, LEDs were embedded in the caps, and these were wiped with ethanol and left to dry in a laminar flow cabinet prior to use to ensure sterility. The cultures were grown in a shaker/incubator (usually 180 rpm unless otherwise stated) at 37°C.

Bacterial growth was monitored by taking aliquots every hour in a sterile laminar flow hood and measuring the OD600. Prior to measurement the aliquots were diluted as appropriate in LB in 1 mL PMMA cuvettes to avoid measured OD600 values above 1. The measured OD600 was then multiplied by the dilution factor to give the final value. The suspensions in the cuvettes were gently mixed immediately prior to measuring the OD600 to ensure that the suspended cells were dispersed in a homogenous manner.

7.5 Confocal Microscopy

Confocal microscopy was performed using a Zeiss LSM 780 multiphoton confocal microscope on an Axio Observer.Z1 invert. Excitation was provided by 458, 488 or 514 nm laser lines depending on the fluorophore. Images were viewed and processed using the Zen Lite or Zen 2010 software packages (Zeiss).

7.6 Single Crystal X-Ray Diffraction

Diffraction data was collected at 110 K on an Agilent SuperNova diffractometer with Mo-K α radiation ($\lambda = 0.71073 \text{ \AA}$). Data collection, unit cell determination and frame integration were carried out with CrysAlisPro. Absorption coefficients were applied using face indexing and the ABSPACK absorption correction software within CrysAlisPro. Structures were solved and refined using Olex2³⁵⁴ implementing SHELX algorithms and the Superflip³⁵⁵⁻³⁵⁷ structure solution program. Structures were solved by Patterson, charge flipping, or direct methods and were refined with the ShelXL³⁵⁸ package using full-matrix least squares minimisation. All non-hydrogen atoms were refined anisotropically. Hydrogen atoms were placed using a “riding model” and included in the refinement at calculated positions.

7.7 Reagents, Conditions and Solvents

Reactions in O₂ free or anhydrous conditions were performed with dry, degassed solvents under an inert atmosphere, effected using either standard Schlenk techniques (under N₂) or a balloon (of argon), as specified in the relevant procedures. For reactions performed at ‘room temperature’, the temperature was between 13-25°C, but usually 21°C.

Commercial chemicals were purchased from either Acros Organics, Alfa Aesar, Fluorochem or Sigma-Aldrich and were used without further purification unless otherwise stated. Dry Et₂O, tetrahydrofuran, toluene, CH₂Cl₂ and *n*-hexane were dispensed from a Pure Solv MD-7 solvent machine and stored in oven-dried ampoules under N₂. Dry tetrahydrofuran and Et₂O were then degassed by bubbling with N₂ and sonication. Water, EtOH and *t*BuOH were degassed by vigorous bubbling of N₂ through the solution for at least 1 h.

“Petrol” in the procedures below is used to mean the constituents of petroleum ether with boiling points between 40-60 °C.

7.8 Nuclear Magnetic Resonance Spectroscopy

Solution ¹H and ¹³C NMR analysis was carried out at 298 K (295 K for CH₂Cl₂) on Jeol ESC400/ESX400 and Bruker AV500/AV700 spectrometers. The spectra were processed in MNova software (version 11.0.3-18688, 2017). All coupling constants are quoted to the nearest

0.5 Hz. All chemical shifts in are reported in ppm and are referenced to the residual NMR solvent:³⁵⁹

¹H: CDCl₃: 7.26 ppm, DMSO-*d*₆: 2.50 ppm, MeOH-*d*₄: 3.31 ppm, CD₂Cl₂: 5.32 ppm

¹³C: CDCl₃: 77.36 ppm, DMSO-*d*₆: 39.52 ppm, MeOH-*d*₄: 49.00 ppm, CD₂Cl₂: 53.49 ppm).

For the ¹³C NMR spectra of some of the tetracarbonyl manganese(I) complexes, the metal carbonyl peaks were not observed due to the long relaxation times of metal carbonyls. Infrared spectroscopy confirms the presence of these metal carbonyls.

7.9 Infrared Spectroscopy

Spectra were recorded on a Bruker Alpha IR spectrometer, usually at a resolution of 4 cm⁻¹. Details of the method (ATR, transmission cell, solvent etc.) are given next to the data. Peak intensities are grouped qualitatively as very strong (vs), strong (s), medium (m) and weak (w), according to common convention.³⁶⁰

7.10 Mass Spectrometry

Electrospray Ionisation (ESI) mass spectrometry was carried out using a Bruker Daltronics microTOF spectrometer in positive ion mode with an Agilent Series 1200 liquid chromatography system. Liquid Injection Field Desorption Ionisation (LIFDI) was performed with a Waters GCT Premier mass spectrometer with an Agilent 7890A gas chromatograph. High resolution ESI data is within 5 ppm error of the theoretical value unless otherwise stated. All LIFDI data is within 120 ppm error.

Unless otherwise stated, the isotopes stated for the observed and calculated peaks are based on the mass of the isotope of highest abundance for each element: ¹H, ¹²C, ¹⁴N, ¹⁶O, ²³Na, ²⁸Si, ⁵⁵Mn, ⁵⁶Fe and ⁷⁹Br.

7.11 Elemental Analysis

Elemental analyses were performed on an Exeter Analytical CE-440 Elemental Analyser. The quoted percentages composition of C, H and N were the average of two experiments.

7.12 UV-Visible Spectroscopy

All UV-visible spectra were recorded with a Jasco V-560 spectrometer using Quartz or PMMA cuvettes. Extinction coefficients (ϵ) were calculated by fitting measured absorbances to the Beer-Lambert Law using at least five different concentrations. A baseline was recorded using the appropriate solvent.

7.13 Melting Point Determination

Melting points were measured on a Stuart SMP30 apparatus. Ramp rates of 2 or 3 °C min⁻¹ were used.

7.14 Chromatography

Thin layer chromatography (TLC) was carried out using aluminium-backed TLC plates (5554, Merck). Visualisation was by quenching of fluorescence using a lamp with $\lambda_{\text{max}} = 254$ nm.

Unless otherwise stated, flash column chromatography was performed using silica gel 60 (Fluorochem or Merck, particle size 40-63 μm).

7.15 Synthesis

The synthetic procedures are reported in the order they are referred to in the main body of the Thesis.

7.15.1 General Synthetic Procedures

General Procedure 1: Cyclometalation of 2-phenylpyridines with BnMn(CO)₅

An oven-dried Schlenk tube containing a stirrer bar, BnMn(CO)₅ (1 eq.) and the ligand to be cyclometalated (1 eq.) was evacuated and backfilled with N₂ three times. Dry, degassed hexane (16 mL per mmol of BnMn(CO)₅) was added *via* syringe and the solution was heated to reflux for 6-24 h. The Schlenk tube was covered in aluminium foil to exclude light. Reaction progress was monitored by IR spectroscopy by taking aliquots from the reaction mixture.

When the reaction was complete, the reaction mixture was allowed to cool to room temperature and filtered through a pipette packed with cotton wool. Any solid product that precipitated out of solution was dissolved in a small amount of CH₂Cl₂. The solvent was removed under reduced pressure to yield the product. If required, further purification was performed using flash column chromatography.

General Procedure 2: Cyclometalation of Azo Compounds with BnMn(CO)₅

To an oven-dried Schlenk tube, with stirrer bar, under a nitrogen atmosphere, were added the desired azo compound BnMn(CO)₅ (2.0 eq., 1.0 mmol, 184 mg) and the desired azo compound (1.0 eq, 0.5 mmol). Dry toluene (5 mL) was added via syringe. Aluminium foil was placed around the Schlenk tube, which was then heated to reflux.

To monitor the progress of the reaction, aliquots were removed from the reaction mixture and analysed by infrared spectroscopy. Complete consumption of BnMn(CO)₅ was usually observed

after around 3 hours. At this point, the reaction mixture was allowed to cool to room temperature, diluted with CH₂Cl₂ and filtered through Celite™. The solvent was removed under reduced pressure. Flash column chromatography was performed using silica gel and either *n*-hexane/CH₂Cl₂ or CH₂Cl₂/MeOH solvent systems as stated below.

General Procedure 3: Cyclometalation with MeMn(CO)₅

To an oven-dried Schlenk tube, with stirrer bar, under a nitrogen atmosphere, were added the desired azo compound MeMn(CO)₅ (1.0 eq., 0.2 mmol, 42 mg) and the desired azo compound (1.0 eq, 0.2 mmol). Dry toluene (2 mL) was added via syringe. Aluminium foil was placed around the Schlenk tube, which was then heated to reflux.

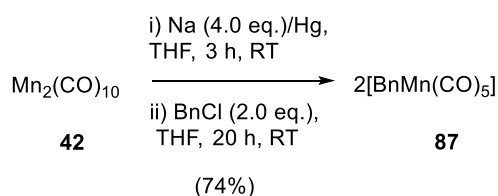
To monitor the progress of the reaction, aliquots were removed from the reaction mixture and analysed by infrared spectroscopy. Complete consumption of MeMn(CO)₅ was usually observed after 3-5 hours. At this point, the reaction mixture was allowed to cool to room temperature, diluted with CH₂Cl₂ and filtered through Celite™. The solvent was removed under reduced pressure. Flash column chromatography was performed using silica gel and either *n*-hexane/CH₂Cl₂ or CH₂Cl₂/MeOH solvent systems as stated below.

7.15.2 Compound Synthesis and Characterisation

For known compounds, where literature procedures were followed, the appropriate references are given next to the name of the *title compound*. Additional references are given next to the characterisation data if:

- (i) Appropriate characterisation data are not provided in the same reference(s) as the procedure, or
- (ii) The *title compound* is known but was made *via* an alternative route.

Benzyl pentacarbonyl manganese(I) (87)¹⁵⁹



In the first step of the reaction, a sodium amalgam was made. To an oven-dried Schlenk tube containing a magnetic stirrer was added mercury (3 mL). Sodium metal (4.4 eq., 11.7 mmol, 270 mg) was added to the stirring mercury under a positive pressure of nitrogen. The sodium must be added slowly in small pieces to prevent the amalgam from getting excessively hot. In a separate oven-dried Schlenk tube, dimanganese decacarbonyl (1.0 eq., 2.68 mmol, 1.04 g) was dissolved

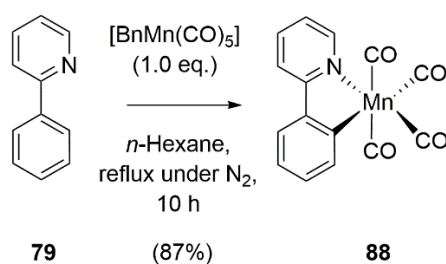
in dry, degassed tetrahydrofuran (40 mL). This solution was then added to the amalgam by cannula transfer, and the reaction mixture was stirred for 3 h. In another Schlenk tube, benzyl chloride (2.0 eq., 5.43 mmol, 625 μ L) was dried under vacuum with stirring for 1 minute at 0 $^{\circ}$ C. The tetrahydrofuran solution was transferred into the benzyl chloride at ambient temperature using a cannula filtration.

The mixture was stirred at ambient temperature for 20 h, then filtered through CeliteTM and washed with diethyl ether (5 \times 20 mL). The filtrate was loaded onto silica and placed onto a 3 cm diameter pad of silica of approximately 3 cm depth. The pad was washed with petrol (3 \times 40 mL) and the solvent was removed on the rotary evaporator. The remaining benzyl chloride was removed by placing the product under vacuum at room temperature for several hours. The *title compound* was obtained as pale brown crystals (1.14 g, 74% yield).

MP: 38 $^{\circ}$ C (lit 37-39 $^{\circ}$ C);³³² 1 H NMR (400 MHz, CDCl_3): δ (ppm) = 7.21-7.14 (m, 4H, Ar-H), 6.97 (m, 1H, Ar-H), 2.40 (s, 2H, CH_2); 13 C NMR (101 MHz, CDCl_3): δ (ppm) = 212.7, 210.2 (Mn-C \equiv O); 152.1, 129.0, 128.7, 126.2, 123.8 (Ar); 11.45 (CH_2); IR (tetrahydrofuran, cm^{-1}): 2107 (s), 2044 (m), 2005 (vs), 1988 (vs), 1716 (m), 1646 (w), 1596 (w), 1489 (w), 1362 (w), 1261 (w), 1219 (w).

Lab book reference: BJA-1-005

Tetracarbonyl (2-(phenyl κ ,C₂-pyridine- κ ,N) manganese(I) (**88**)¹³⁷



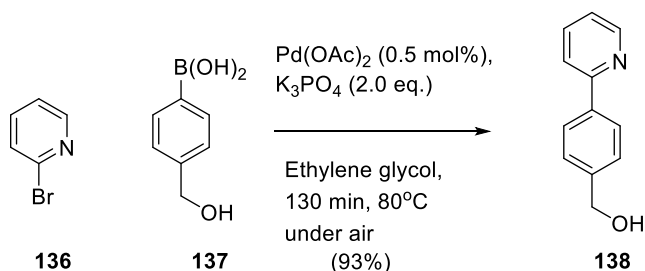
The reaction was performed using General Procedure 1 with $\text{BnMn}(\text{CO})_5$, (1.0 eq., 0.70 mmol, 202 mg), 2-phenylpyridine (1.0 eq., 0.70 mmol 100 μ L) and hexane (10 mL). Traces of grease were removed with an MeCN/*n*-hexane partition and the MeCN was removed under vacuum. The *title compound* was isolated as a yellow solid, 204 mg (87% yield).

M.P.: 120 $^{\circ}$ C (decomp.); 1 H NMR (500 MHz, CDCl_3): δ (ppm) = 8.73 (d, J = 5.5 Hz, 1H, Ar-H), 8.00 (dd, J = 7.5, 1.0 Hz, 1H, Ar-H), 7.79 (d, J = 8.0 Hz, 1H, Ar-H), 7.82-7.77 (m, 2H, Ar-H), 7.29 (apr, td, J = 7.5, 1.0 Hz, 1H, Ar-H), 7.19 (apr, td, J = 7.5, 1.0 Hz, 1H, Ar-H), 7.11 (ddd, J = 7.0, 5.5, 1.5 Hz, 1H, Ar-H); 13 C NMR (126 MHz, CDCl_3) δ = 220.4, 214.3, 175.1, 166.7, 154.2, 146.5,

141.95, 138.1, 130.6, 124.4, 124.3, 122.7, 119.6 (Ar-H); IR (CH₂Cl₂, cm⁻¹): 2076 (s), 1989 (vs), 1977 (vs), 1934 (vs), 1605 (m), 1578 (w), 1480 (m).

Lab book reference: BJA-1-063

2-(4'-Hydroxybenzyl)pyridine (138)¹⁵⁹



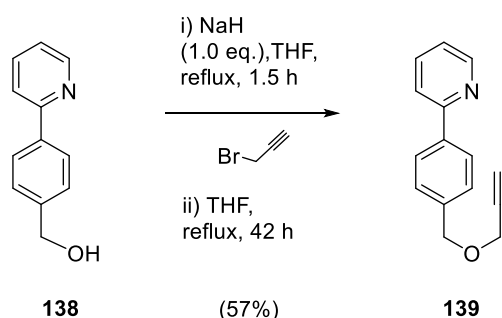
To a round-bottomed flask was added a magnetic stirrer bar, 2-bromopyridine (1.0 eq., 9.96 mmol, 1.57 g, 950 μ L), 4-hydroxybenzeneboronic acid (1.5 eq., 15.0 mmol, 2.28 g), Pd(OAc)₂ (0.005 mol%, 0.05 mmol, 11.8 mg), K₃PO₄ (2 eq, 20 mmol, 4.29 g), and ethylene glycol (60 mL). The reaction was heated in an oil bath to 80 °C for 130 min, when the reaction was adjudged to be complete by TLC.

The reaction mixture was then allowed to cool to room temperature before water (75 mL) and saturated brine (75 mL) were added and the product was extracted using CH₂Cl₂ (4 \times 100 mL). The CH₂Cl₂ layers were dried with MgSO₄, filtered, and the solvent removed on a rotary evaporator. The crude product was purified using flash column chromatography, beginning with petrol/EtOAc 2:3 v/v and moving to 1:1 v/v to elute the product. The solvent was removed to afford the *title compound* as a yellow oil (1.71 g, 93% yield).

¹H NMR (400 MHz, CDCl₃): δ (ppm) = 8.65 (ddd, J = 5.0, 2.0, 1.0 Hz, 1H, Ar-H), 7.90 (d, J = 8.5 Hz, 2H, Ar-H), 7.73 (apr. td, J = 7.5, 2.0 Hz, 1H, Ar-H), 7.68 (apr. dt, J = 8.0, 1.0 Hz, 1H, Ar-H), 7.40 (d, J = 8.0 Hz, 2H, Ar-H), 7.21 (ddd, J = 7.5, 5.0, 1.5 Hz, 1H, Ar-H), 4.69 (s, 2H, CH₂), 3.13 (s, 1H, OH); ¹³C NMR (101 MHz, CDCl₃): δ (ppm) = 157.8, 150.0, 142.5, 138.8, 137.3, 127.6, 127.4, 122.4, 121.0 (Ar); 64.7 (CH₂); IR (CH₂Cl₂, cm⁻¹): 3608 (m), 3330 (broad), 3050 (w), 2925 (w), 2880 (w), 1702 (w), 1591 (w), 1562 (w), 1472 (s), 1441 (s), 1415 (m), 1386 (m), 1044 (m), 1021 (m); HRMS (ESI⁺): m/z = 186.0913 [MH]⁺ (C₁₂H₁₂NO requires 186.0919).

Lab book reference: BJA-1-002

2-(4'-[(prop-2-ynyloxy)methyl]phenyl)pyridine (139)¹³⁷



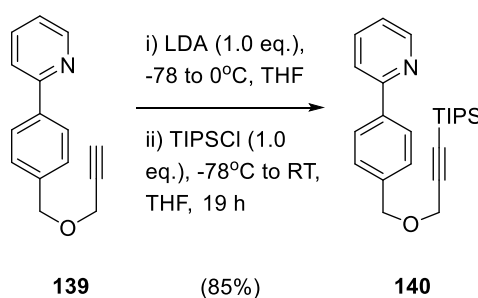
A suspension of 60% (wt.) NaH (1.0 eq., 10 mmol, 398 mg) in mineral oil was added to an oven-dried Schlenk tube with magnetic stirrer bar. The suspension was washed with dry *n*-hexane, which was removed by cannula filtration to yield pure NaH. The NaH was dissolved in dry, deoxygenated tetrahydrofuran (40 mL) and a solution of 2-(4'-hydroxyphenyl)pyridine (1.0 eq., 10 mmol, 1.95 g) in tetrahydrofuran (40 mL) was added slowly by cannula transfer. The solution was refluxed in the Schlenk tube for 90 mins. Propargyl bromide (1.0 eq., 10 mmol, 1.49 g, 1.12 mL) was added as an 80% (wt.) solution in toluene and the solution was refluxed for a further 40 h, at which time TLC indicated completion of the reaction.

After the orange-brown reaction mixture was allowed to cool to room temperature, water (40 mL) was added and the product was extracted using CH₂Cl₂ (4 × 50 mL). The organic layers were washed with saturated sodium carbonate (2 × 50 mL) and water (2 × 50 mL), before being dried with MgSO₄ and filtered. The solvent was removed under reduced pressure to give the crude product. This was subsequently loaded onto silica using CH₂Cl₂ and purified using flash column chromatography with petrol/Et₂O 7:3 *v/v* moving to 2:3 *v/v* to elute the product. Caution should be taken during dry loading so that the silica does not bump. The solvent was removed to give the *title compound*, a very viscous yellow oil (1.28 g, 57% yield).

¹H NMR (400 MHz, CDCl₃): δ (ppm) = 8.69 (ddd, *J* = 5.0, 2.0, 1.0 Hz, 1H, Ar-H), 7.98 (apr. dt, *J* = 8.5, 2.0 Hz, 2H, Ar-H), 7.76-7.69 (m, 2H, Ar-H), 7.47 (d, *J* = 8.0 Hz, 2H, Ar-H), 7.22 (ddd, *J* = 5.5, 5.0, 2.0 Hz, 1H, Ar-H), 4.66 (s, 2H, CH₂), 4.19 (d, *J* = 2.5 Hz, 2H, CH₂), 2.48 (t, *J* = 2.5 Hz, 1H, C≡C-H); ¹³C NMR (101 MHz, CDCl₃): δ (ppm) = 157.6, 150.1, 139.4, 138.5, 137.1, 128.8, 127.4, 122.5, 120.8 (Ar); 79.6 (C≡C-H); 74.8 (C≡C-H); 71.2 (benzylic CH₂), 57.1 (propargylic CH₂); IR (CH₂Cl₂, cm⁻¹): 3305 (s), 3052 (m), 2941 (m), 2864 (s), 1986 (m), 1940 (m), 1594 (s), 1558 (m), 1469 (s), 1434 (m), 1357 (m), 1086 (s); HRMS (ESI⁺): *m/z* = 224.1801 [MH]⁺ (C₁₅H₁₄NO requires 224.1075).

Lab book reference: BJA-1-003

2-(4'-[(3''-triisopropylsilyl-prop-2-ynyl-oxy)methyl]phenyl)pyridine (**140**)¹³⁷



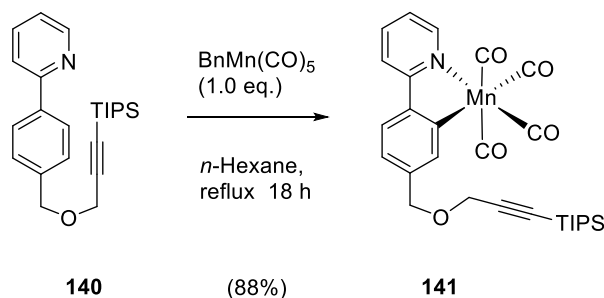
To an oven-dried Schlenk tube containing a solution of 2-(4'-[(prop-2-ynoxy)methyl]phenyl)pyridine (1.0 eq., 3.87 mmol, 0.865 g) in dry, degassed tetrahydrofuran (40 mL) at -78°C was added a solution of LDA (1.0 eq., 3.87 mmol, 9.6 mL) in tetrahydrofuran *via* syringe over five minutes. The LDA was freshly prepared by lithiation of freshly distilled diisopropylamine using *n*-BuLi. After the addition of LDA was complete, the Schlenk tube was placed in an ice/water bath at 0°C for 10 minutes before being cooled back to -78°C for the addition of TIPS-Cl (1.0 eq., 3.87 mmol, 0.84 mL). The reaction mixture was then allowed to warm to room temperature and left for 19 h, at which point TLC indicated completion of the reaction.

The reaction was quenched using saturated NH_4Cl (30 mL) and extracted with Et_2O (3×50 mL). The combined organic layers were washed with water (30 mL) and brine (30 mL), before being dried with MgSO_4 and filtered. The solvent was removed to give the crude product, which was purified by flash column chromatography on silica, starting with petrol and moving to petrol/ Et_2O 4:1 *v/v*. The solvent was removed to give the *title compound* as a yellow oil (1.25 g, 85% yield).

^1H NMR (400 MHz, CDCl_3): δ (ppm) = 8.69 (ddd, $J = 5.0, 2.0, 1.0$ Hz, 1H, Ar-H), 7.99 (d, $J = 8.5$ Hz, 2H, Ar-H), 7.77-7.71 (m, 2H, Ar-H), 7.47 (d, $J = 8.0$ Hz, 2H, Ar-H), 7.22 (ddd, $J = 5.5, 5.0, 2.5$, 1H, Ar-H), 4.70 (s, 2H, CH_2), 4.23 (s, 2H, CH_2), 1.09 (m, 21 H, CH and CH_3 from TIPS); ^{13}C NMR (101 MHz, CDCl_3) δ (ppm) = 157.7, 150.2, 139.4, 138.8, 137.2, 129.0, 127.4, 122.5, 120.9 (Ar); 103.4 ($\text{C}\equiv\text{C}-\text{Si}$); 88.4 ($\text{C}\equiv\text{C}-\text{Si}$); 70.7 (benzylic CH_2); 57.8 (propargylic CH_2), 18.4 (TIPS CH_3); 11.0 (TIPS CH); IR (CH_2Cl_2 , cm^{-1}): 2950 (s), 2870 (s), 2171 (w), 1977 (w), 1925 (w), 1702 (w), 1590 (m), 1561 (w), 1469 (s), 1441 (w), 1354 (m), 1083 (s), 1031 (m), 1010 (m), 997 (s); HRMS (ESI⁺): $m/z = 380.2391$ [MH]⁺ ($\text{C}_{24}\text{H}_{34}\text{NOSi}$ requires 380.2410).

Lab book reference: BJA-1-004

Tetracarbonyl 2-(4'-[(3''-triisopropylsilyl-prop-2-ynyl)oxy]methyl]phenyl) κ ,C²-pyridine- κ ,N) manganese (I) (141)¹³⁷

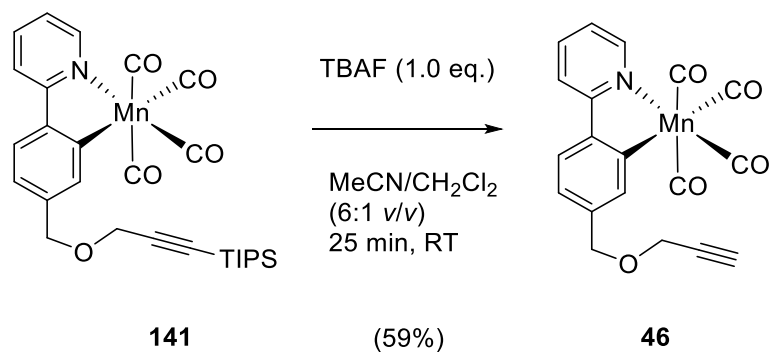


The reaction was performed using General Procedure 1 with $\text{BnMn}(\text{CO})_5$, (1 eq., 2.93 mmol, 840 mg), 2-(4'-[(3-triisopropylsilyl-prop-2-ynyl)oxy]methyl]phenyl)pyridine (0.96 eq., 2.82 mmol, 1.07 g) and hexane (40 mL). The *title compound* was isolated as a yellow solid (1.35 g, 88% yield) with no additional purification required.

MP: 78°C (lit.: 82°C);¹³⁷ ¹H NMR (500 MHz, CDCl_3): δ (ppm) = 8.72 (d, J = 5.5 Hz, 1H, Ar-H), 7.92 (s, 1H, Ar-H), 7.87 (d, J = 8.0 Hz, 1H, Ar-H), 7.82-7.75 (m, 2H, Ar-H), 7.20 (dd, J = 8.0, 1.5 Hz, 1H, Ar-H), 7.11 (ddd, J = 7.5, 5.0, 1.5 Hz, 1H, Ar-H), 4.70 (s, 2H, CH_2), 4.30 (s, 2H, CH_2), 1.11 (m, 21H, CH and CH_3 from TIPS); ¹³C NMR (126 MHz, CDCl_3): δ (ppm) = 220.2, 215.5, 214.2 (Mn-C \equiv O); 175.4, 166.4, 154.2, 146.1, 141.5, 139.9, 138.14, 124.5, 124.4, 122.6, 119.6 (Ar); 103.7, ($\text{C}\equiv\text{C}$ -Si); 88.3 ($\text{C}\equiv\text{C}$ -Si); 71.7 (benzylic CH_2); 58.4 (propargylic CH_2); 19.0 (TIPS CH_3); 11.5 (TIPS CH); HRMS (ESI⁺): m/z = 568.1327 [MNa]⁺ ($\text{C}_{28}\text{H}_{32}\text{MnNNaO}_5\text{Si}$ requires 568.1328); IR (CH_2Cl_2 , cm^{-1}): 3685 (vw), 3157 (vw), 2961 (m), 2946 (m), 2927 (m), 2893 (m), 2866 (m), 2076 (s), 1991 (vs), 1976 (vs), 1933 (vs), 1605 (m), 1587 (m), 1567 (m), 1479 (m), 1467 (m), 1351 (s).

Lab book reference: BJA-1-006

Tetracarbonyl 2-(4'-[(prop-2-ynyl)oxy]benzyl) κ ,C²-pyridine- κ ,N) manganese (I) (46)¹³⁷



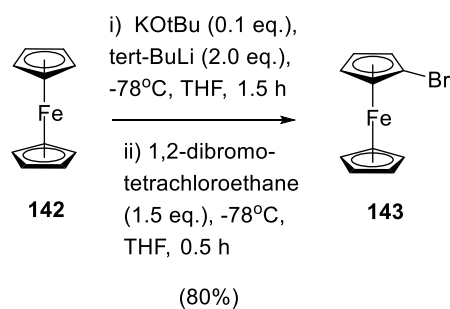
To a solution of tetracarbonyl 2-(4'-[(3''-triisopropylsilyl-prop-2-ynyl)oxy]methyl]phenyl) κ ,C²-pyridine- κ ,N) manganese(I) (1 eq., 1.10 mmol, 599 mg) in CH_2Cl_2 (2 mL) was added a solution

of TBAF·3H₂O (1.2 eq., 1.32 mmol, 417 mg) in acetonitrile (10 mL). The brown solution was stirred under air for 25 min, at which time the reaction was judged to be complete by TLC analysis. Water (10 mL) was added and the product was extracted with CH₂Cl₂ (3 × 15 mL). The organic layers were combined, dried with MgSO₄ and filtered. The solvent was removed *in vacuo* to yield the crude product, which was purified by flash column chromatography on silica gel, starting with petrol/EtOAc 10:1 *v/v*, moving to 20:3 *v/v*, to elute the product. The solvent was removed under reduced pressure to give the *title compound* as a light brown solid (0.253 g, 59% yield).

MP: 115°C (decomp., lit.: 107°C);¹³⁷ ¹H NMR (500 MHz, DMSO-*d*₆): δ (ppm) = 8.76 (d, *J* = 5.5 Hz, 1H, Ar-H), 8.24 (d, *J* = 8.0 Hz, 1H, Ar-H), 8.07-8.00 (m, 2H, Ar-H), 7.78 (s, 1H, Ar-H), 7.37 (m, 1H, Ar-H), 7.12 (dd, *J* = 1.0, 8.0 Hz, 1H, Ar-H), 4.57 (s, 2H, CH₂), 4.25 (t, *J* = 2.5 Hz, 2H, CH₂), 3.52 (d, *J* = 2.5 Hz, 1H, C≡C-H); ¹³C NMR (126 MHz, CDCl₃): δ 220.3, 214.4, 214.1 2 (Mn-C≡O); 175.3, 166.3, 154.1, 146.1, 141.3, 139.3, 138.2, 124.3, 124.3, 122.7, 119.7 (Ar); 80.1 (C≡C-H) 75.0 (C≡C-H); 72.3 (benzylic CH₂); 57.7 (propargylic CH₂); IR (CH₂Cl₂, cm⁻¹): 3664 (w), 3302 (w), 2964 (m), 2945 (m), 2929 (w), 2893 (m), 2866 (m), 2075 (s), 1991 (vs), 1976 (vs), 1932 (vs), 1605 (m), 1588 (m), 1566 (w), 1478 (m), 1468 (m); HRMS (ESI⁺): *m/z* = 411.9992 [MNa]⁺ (C₁₉H₁₂MnNNaO₅ requires 411.9994).

Lab book reference: BJA-1-007

Bromoferrocene (143)^{280,278}



To an oven-dried Schlenk tube containing a magnetic stirrer bar, ferrocene (1.0 eq., 5.4 mmol, 1.01 g) and KO^tBu (0.12 eq., 0.67 mmol, 76 mg) was added dry, degassed tetrahydrofuran (50 mL). The solution was cooled to -78 °C using a dry ice/acetone bath and ^tBuLi (2.0 eq., 10.8 mmol, 7.83 mL of 1.38 M solution in hexanes) was added dropwise over 20 min, producing a light brown solution. After stirring for 1 h 30 min, 1,2-dibromotetrachloroethane (1.5 eq., 8.1 mmol, 2.64 mg) was added. The resulting orange solution was stirred for a further 30 min, remaining at -78 °C. The cooling bath was removed and the solution was allowed to warm to room temperature. Water (30 mL) was added to quench the reaction. The product was then extracted using CH₂Cl₂ (3 × 50 mL) and washed with water (2 × 50 mL). The organic layers were combined,

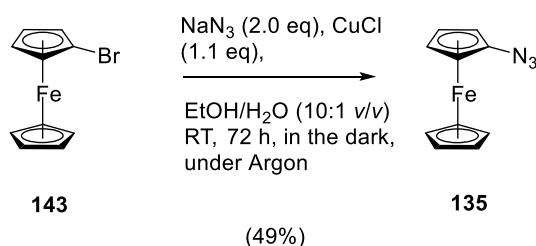
dried with MgSO₄ and filtered. The solvent was removed *in vacuo* to yield the crude product, contaminated with ferrocene (circa 10%, by NMR).

Due to the poor separation of ferrocene and bromoferrocene using chromatography, the procedure of Long and co-workers²⁸⁰ was used to purify this material. The crude mixture was dissolved in hexane (25 mL) and was repeatedly washed with an aqueous solution of 200 mM FeCl₃ (10 × 25 mL). The composition of the crude mixture was monitored by NMR spectroscopy, which showed that the purity of bromoferrocene improved after washing. The product was then washed with water until the aqueous layer was colourless and then dried with MgSO₄, then filtered through a pad of silica (~10 g), washed through with hexane. Note: the purification process is sensitive to both the concentration and volume of FeCl₃ solution used in each wash and this could be further optimised in future reactions by varying both parameters. The solvent was removed under reduced pressure to give the *title compound* as an orange solid (1.15 g, 80% yield).

MP: 28°C; ¹H NMR (400 MHz, CDCl₃): δ (ppm) = 4.41 (t, *J* = 2.0 Hz, 2H, Cp-H), 4.23 (s, 5H, Cp-H), 4.10 (t, *J* = 2.0 Hz, 2H, Cp-H); ¹³C NMR (101 MHz, CDCl₃) δ (ppm) = 77.8, 70.7, 70.3, 67.2 (Cp); IR (ATR, cm⁻¹): 3096 (m), 2954 (w), 2922 (w), 2853 (w), 1774 (w), 1725 (w), 1408 (m), 1381 (m), 1358 (m), 1344 (m), 1179 (w), 1151 (m), 1105 (s), 1054 (m), 1020 (m), 1001 (m), 871 (s), 819 (s), 809 (s), 775 (m), 759 (m), 725 (s), 639 (m), 618 (m), 476 (vs); HRMS (EI): *m/z* = 263.9238 [M]⁺ (C₁₀H₉FeBr requires 263.9237).

Lab book reference: BJA-1-008

Azidoferrocene (135)²⁷⁹



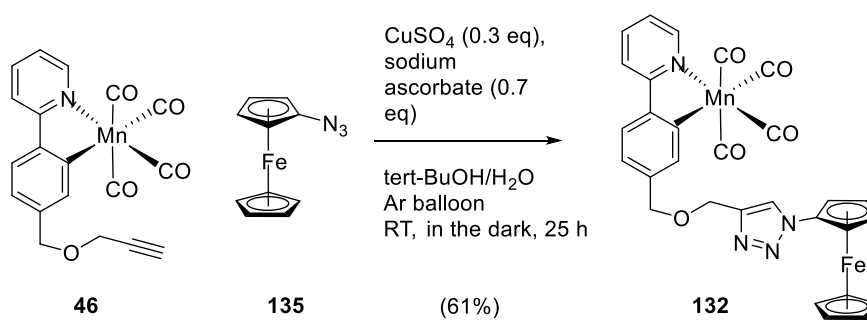
Bromoferrocene (1.0 eq., 1.0 mmol, 269 mg) and CuCl (1.1 eq., 1.1 mmol, 109 mg) were dissolved in degassed EtOH (4 mL). A solution of NaN₃ (2 eq., 2.0 mmol, 132 mg) in degassed water (400 μL) was added and the solution was stirred in the dark under an argon balloon for 72 h. The product was extracted using petrol (4 × 25 mL). The organic layers were washed with water (2 × 25 mL) and brine (25 mL) and dried over Na₂SO₄. After filtration, the solvent was removed under reduced pressure to give the *title compound* as a red solid (109 mg, 49% yield).

MP: 53°C; ¹H NMR (400 MHz, benzene-*d*₆): δ (ppm) = 4.11 (s, 5H, Cp-H), 4.10-4.07 (m, 2H, Cp-H), 3.77-3.72 (s, 2H, Cp-H); ¹³C NMR* (101 MHz, CDCl₃) δ (ppm) = 69.1, 65.2, 60.6 (Cp); IR (ATR, cm⁻¹): 3260 (w), 3110 (w), 3090 (w), 2960 (w), 2923 (w), 2852 (w), 2437 (w), 2323 (w), 2196 (w), 2107 (s), 1453 (s), 1407 (m), 1373 (m), 1283 (s), 1223 (w), 1163 (m), 1105 (m), 1057 (m), 1023 (s), 999 (s), 915 (m), 818 (s), 738 (m).

*The NMR signal for the carbon bonded to the azide group was not observed in the spectrum, the same situation was reported in the literature.²⁷⁹

Lab book reference: BJA-1-009

Tetracarbonyl(2-[4'-((1-(ferrocenyl)-1H-1,2,3-triazol-4-yl)methoxy)methyl)phenyl]-κ,C²]pyridine-κ,N) manganese(I) (132)



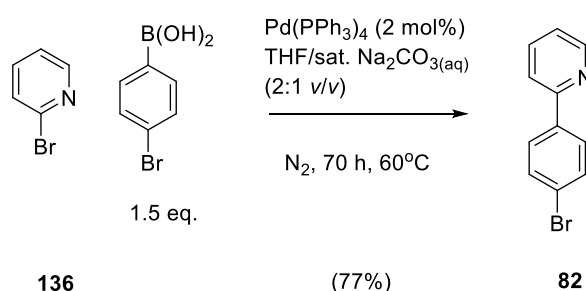
To a solution of tetracarbonyl 2-(4'-[(prop-2-ynoxy)methyl]phenyl) κ,C²-pyridine- κ,N) manganese (I) (1.0 eq., 0.2 mmol, 78 mg) in N₂-purged ^tBuOH (3 mL) was added azidoferrocene (1.0 eq., 0.2 mmol, 46 mg) and water (2.7 mL). Copper(II) sulfate (0.3 eq., 0.06 mmol, 200 μL of 300 mM aqueous solution) and sodium ascorbate (0.6 eq., 0.12 mmol, 120 μL of 500 mM aqueous solution) were added and the reaction mixture was stirred at room temperature in the dark under an argon balloon. After 24 h, the reaction mixture was diluted with water (20 mL). The product was extracted with EtOAc (4 × 20 mL). The combined organic layers were dried with MgSO₄ and filtered, before removal of the solvent yielded the crude product. The crude product was purified by flash column chromatography on silica, using petrol/EtOAc, starting with 3:2 v/v and moving to 1:1 v/v to elute the product. The solvent was removed to give the *title compound* (74 mg, 60% yield) as a yellow solid.

MP: 143°C (decomp.); *R*_f: 0.40 (petrol/EtOAc 3:2 v/v); ¹H NMR (500 MHz, CDCl₃): δ (ppm) = 8.72 (d, *J* = 5.5 Hz, 1H, Ar-H), 7.97 (d, *J* = 1.5 Hz, 1H, Ar-H), δ (ppm) 7.89-7.86 (m, 1H, Ar-H), 7.84 (s, 1H, Ar-H), 7.81-7.76 (m, 2H, Ar-H), 7.21 (dd, *J* = 8.0, 1.5 Hz, 1H, Ar-H), 7.12 (ddd, *J* = 7.5, 5.5, 1.5 Hz, 1H, Ar-H), 4.83 (t, *J* = 2.0 Hz, 2H, Cp-H), 4.82 (s, 2H, CH₂), 4.71 (s, 2H, CH₂), 4.26 (t, *J* = 2.0 Hz, 2H, Cp-H), 4.22 (s, 5H, Cp-H); ¹³C NMR (126 MHz, CDCl₃) δ (ppm)

= 220.3, 214.1, 214.0 (Mn-C≡O); 175.1, 166.1, 154.0, 145.9, 145.5, 140.7, 139.6, 138.0, 124.2, 123.9, 122.5, 122.3, 119.5 (Ar); 94.0 (Cp); 73.0 (CH₂); 70.3 (Cp); 66.8 (Cp); 64.2 (CH₂); 62.3 (Cp) ; HRMS (ESI⁺): m/z = 617.0292 [MH]⁺ (C₂₉H₂₂N₄O₅MnFe requires 617.0315); IR (CH₂Cl₂, cm⁻¹): 3048 (w), 2864 (w), 2076 (s), 1991 (vs), 1977 (vs), 1931 (s), 1606 (m), 1587 (m), 1567 (w), 1519 (w), 1472 (m), 1432 (w), 1312 (w), 1108 (m); Elemental analysis (CHN): C: 56.28%, H: 3.48%, N: 8.69% (calc. for C₂₉H₂₁N₄O₅MnFe C: 56.52%, H: 3.44%, N: 9.09%); UV-visible spectrum (CH₂Cl₂): λ_{max} (nm) = 270, ε (270 nm) = (2.84 ± 0.5) × 10⁴ dm³ mol⁻¹ cm⁻¹.

Lab book reference: BJA-1-011

2-(4'-Bromophenyl)pyridine (82)¹³⁷

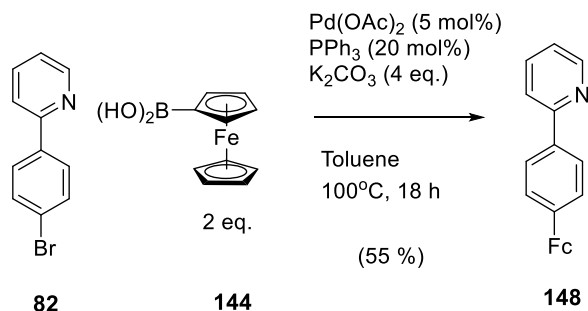


To an oven-dried Schlenk tube containing a stirrer bar were added 4-bromobenzene boronic acid (1.5 eq., 4.60 mmol, 923 mg) and Pd(PPh₃)₄ (2 mol%, 0.061 mmol, 70.2 mg). tetrahydrofuran (20 mL) and saturated aqueous sodium carbonate solution (9.5 mL), both N₂ saturated, were added, followed by 2-bromopyridine (1.0 eq., 3.15 mmol, 300 μL). The reaction was heated to 60°C for 70 h.

After the solution had cooled to room temperature, water (60 mL) was added and the product extracted with CH₂Cl₂ (3 × 60 mL). The yellow extract was dried with MgSO₄, filtered and the solvent removed under reduced pressure. The crude product, an orange oil, was purified by flash column chromatography with petrol/EtOAc, starting with 9:1 v/v and moving to 20:3 v/v. Removal of the solvent *in vacuo* afforded the product contaminated with trace unreacted 2-bromopyridine. This was removed by placing the compound under vacuum and heating in an oil bath to 45°C for several hours. The *title compound* was isolated as a white solid (551 mg, 77% yield).

MP: 64°C (lit.: 64°C)¹³⁷; ¹H NMR (400 MHz, CDCl₃): δ (ppm) = 8.69 (d, *J* = 4.5 Hz, 1H, Ar-H), 7.88 (d, *J* = 7.0 Hz, 2H, Ar-H), 7.76 (apr. td, *J* = 7.5, 1.5 Hz, 1H, Ar-H), 7.70 (d, *J* = 8.0 Hz, 2H, Ar-H), 7.60 (d, *J* = 8.5 Hz, 2H, Ar-H), 7.27-7.24 (m, 1H, under ref peak Ar-H); ¹³C NMR (101 MHz, CDCl₃) δ (ppm) 156.4, 150.0, 138.5, 137.0, 132.1, 128.6, 123.6, 122.6, 120.5 (Ar-H); HRMS (ESI⁺): m/z = 233.9916 [M-H]⁺ (C₁₁H₉NBr requires 233.9913).

Lab book reference: BJA-1-021

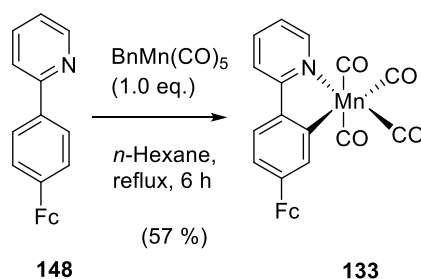
[4-(2'-Pyridinyl)phenyl]ferrocene (148)²⁸⁷

To an oven-dried Schlenk tube with stirrer bar were added 2-(4-bromophenyl)pyridine (1.0 eq., 0.20 mmol, 46.8 mg), ferroceneboronic acid (2.0 eq., 0.40 mmol, 92.9 mg), Pd(OAc)₂ (0.05 eq., 0.001 mmol, 2.2 mg), PPh₃ (0.21 eq., 0.43 mmol, 11.2 mg) and K₂CO₃ (4.0 eq., 0.80 mmol, 111 mg). The Schlenk tube was evacuated and backfilled with N₂ three times on a Schlenk line. Anhydrous, degassed toluene (10 mL) was added in one portion *via* syringe. The red reaction mixture was refluxed for 20 h, at which point TLC analysis showed complete consumption of the starting material and the appearance of a product spot. The reaction mixture was allowed to cool and the toluene was removed *in vacuo*. The mixture was re-suspended in chloroform (100 mL), washed with water (2 × 100 mL), dried with MgSO₄ and filtered. The solvent was removed *in vacuo* and the crude product was purified by flash column chromatography on silica gel using petrol/EtOAc, starting with 9:1 *v/v* and moving to 8:2 *v/v*. Removal of the solvent *in vacuo* and additional drying on a high vacuum line gave the *title compound* as an orange powder (37.5 mg, 55% yield).

MP: 122°C; ¹H NMR (400 MHz, CDCl₃): δ (ppm) = 8.69 (d, *J* = 4.5 Hz 1H, Ar-H), 7.93 (d, *J* = 8.0 Hz, 2H, Ar-H), 7.73 (d, *J* = 4.0 Hz, 2H, Ar-H), 7.58 (d, *J* = 8.0 Hz 2H, Ar-H), 7.21 (dd, *J* = 9.0, 4.0 Hz 1H, Ar-H), 4.71 (t, *J* = 2.0 Hz, 2H, Cp-H), 4.36 (t, *J* = 2.0 Hz, 2H, Cp-H), 4.05 (s, 5H, Cp-H); ¹³C NMR (101 MHz, CDCl₃) δ (ppm) = 157.4, 149.8, 140.5, 136.9, 136.8, 127.0, 126.4, 121.0, 120.3 (Ar); 84.6, 69.8, 69.3, 66.7 (Cp); HRMS (ESI⁺): *m/z* = 340.0770 [M-H]⁺ (C₂₁H₁₈FeN requires 340.0789); IR (CH₂Cl₂, cm⁻¹): 2967 (w), 2074 (s), 1990 (s), 1975 (s), 1931 (s), 1733 (w), 1606 (m), 1583 (m), 1563 (m), 1474 (m), 1425 (w).

Lab book reference: BJA-1-30

Tetracarbonyl (2-[4-Ferrocenyl]phenyl- κ ,C₂-pyridine- κ ,N) Manganese(I) (133)

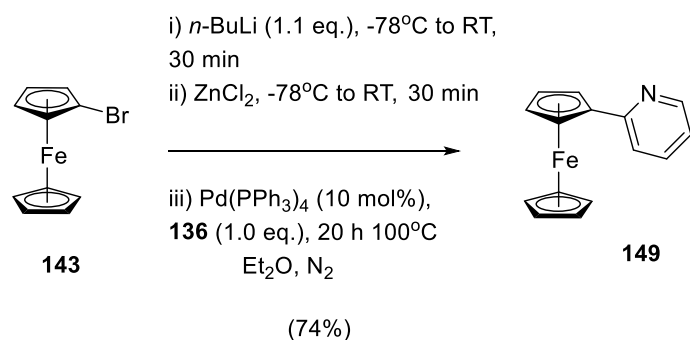


This reaction was performed using General Procedure 1 with $\text{BnMn}(\text{CO})_5$ (1 eq., 0.25 mmol, 72.5 mg), [4-(2'-pyridinyl)phenyl]ferrocene (1 eq., 0.25 mmol, 84.5 mg) and hexane (4 mL). Infrared spectroscopic analysis showed that the reaction was complete after 6 h. The *title compound* was purified by flash column chromatography, using petrol and then petrol/EtOAc 9:1 *v/v*. The solvent was removed *in vacuo* to afford a red microcrystalline solid (79 mg, 59% yield).

MP: 138°C (decomp.); ^1H NMR (700 MHz, CDCl_3): δ (ppm) = 8.70 (d, J = 5.0 Hz, 1H, Ar-H), 8.12 (s, 1H, Ar-H), 7.84 (d, J = 8.0 Hz, 1H, Ar-H), 7.77 (dd, J = 7.5, 7.5 Hz, 1H, Ar-H), 7.68 (d, J = 8.0 Hz, 1H, Ar-H), 7.28 (s, 1H, Ar-H), 7.08 (dd, J = 6.5 Hz, 6.0 Hz, 1H, Ar-H), 4.77 (t, J = 2.0 Hz, 2H, Cp-H), 4.37 (t, J = 2.0 Hz, 2H, Cp-H), 4.09 (s, 1H, Cp-H); ^{13}C NMR (176 MHz, CDCl_3) δ (ppm) = 220.4, 214.2, 214.1 (Mn-C \equiv O), 174.2, 166.2, 153.8, 144.0, 141.4, 139.0, 137.7, 123.9, 122.2, 121.8, 119.0 (Ar), 85.4, 69.8, 69.2, 67.1 (Cp); MS (LIFDI $^+$): m/z = 505.04 [M^+] ($\text{C}_{25}\text{H}_{16}\text{NO}_4\text{FeMn}$ requires 504.9809); IR (CH_2Cl_2 , cm^{-1}): 2967 (w), 2074 (s), 1990 (s), 1975 (s), 1931 (s), 1733 (w), 1606 (m), 1583 (m), 1563 (m), 1474 (m), 1425 (w); Elemental analysis (CHN): C: 59.69%, H: 3.27%, N: 2.73% ($\text{C}_{25}\text{H}_{16}\text{NO}_4\text{FeMn}$ requires C: 59.44%, H: 3.19%, N: 2.77%); UV-visible spectrum (CH_2Cl_2): λ_{max} (nm) = 314, 378, 460; ϵ (314 nm) = $(2.29 \pm .02) \times 10^4 \text{ dm}^3 \text{ mol}^{-1} \text{ cm}^{-1}$; ϵ (378 nm) = $(8.00 \pm .06) \times 10^3 \text{ dm}^3 \text{ mol}^{-1} \text{ cm}^{-1}$; ϵ (460 nm) = $(2.04 \pm 0.05) \times 10^3 \text{ dm}^3 \text{ mol}^{-1} \text{ cm}^{-1}$.

Lab book reference: BJA-1-032

2-(Ferrocenyl)pyridine (149)



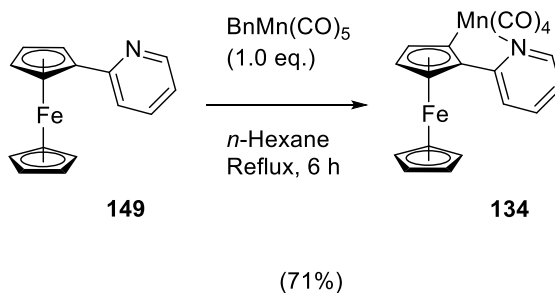
This reaction was performed by Sam Andrew under my supervision.²⁹⁰

Bromoferrocene (1.0 eq., 1.9 mmol, 513 mg) was stirred in dry EtOAc (10 mL) under nitrogen in an oven dried Schlenk tube at -78°C. After *n*-BuLi (1.1 eq., 2.0 mmol, 0.80 mL) was added dropwise, the solution was stirred for 15 minutes and then allowed to warm to room temperature and stirred for a further 10 minutes forming a bright orange precipitate. The reaction mixture was then cooled to -78°C and transferred under nitrogen to a Schlenk tube containing dry ZnCl₂ (2.0 eq., 3.8 mmol, 518 mg) at -78°C, allowed to warm to room temperature and stirred for 1 h. The reaction mixture was then transferred under nitrogen into a third Schlenk tube containing dry Pd(PPh₃)₄ (10 mol%, 0.19 mmol, 220 mg). 2-Bromopyridine (2.5 eq., 4.75 mmol, 0.45 mL) was added dropwise and the reaction mixture stirred for 19 hours. The reaction was quenched with saturated aqueous NH₄Cl solution (15 mL) and transferred into a separating funnel. The aqueous layer was extracted with chloroform (3 × 10 mL) and the organic phases combined and dried over MgSO₄, then filtered. The solvent was then removed *in vacuo* to afford an orange powder. The crude mixture was purified by silica gel flash column chromatography (petrol/EtOAc 9:1 *v/v*) to afford the *title compound* as an orange powder, 371 mg (74% yield).

Melting point: 90 – 92°C; *R*_f = 0.16 (petrol/Et₂O 9:1 *v/v*); ¹H NMR (400 MHz, CDCl₃): δ (ppm) = 8.51 (ddd, *J* = 5.0, 2.0, 1.0 Hz, 1H, Ar-H), 7.57 (ddd, *J* = 8.0, 7.5, 1.0 Hz, 1H, Ar-H), 7.41 (ddd, *J* = 8.0, 1.0, 1.0 Hz, 1H, Ar-H), 7.06 (ddd, *J* = 7.5, 5.0, 1.0 Hz, 1H, Ar-H), 4.92 (dd, *J* = 2.0, 2.0 Hz, 2H, Cp-H), 4.40 (dd, *J* = 2.0, 2.0 Hz, 2H, Cp-H), 4.05 (s, 5H, Cp-H); ¹³C NMR (101 MHz, CDCl₃): δ (ppm) = 159.3, 149.4, 136.0, 120.6, 120.2 (Ar); 83.7, 70.0, 69.7, 67.3 (Cp); HRMS (ESI⁺): *m/z* = 264.0473 [MH]⁺ (C₁₅H₁₄FeN requires 264.0470); IR (CH₂Cl₂, cm⁻¹): 1609 (m), 1588 (w), 1574 (w), 1469 (m), 1434 (m), 1277 (w).

Lab book reference: N/A, see reference.²⁹⁰

(±)-Tetracarbonyl (2-ferrocenyl-κ,C²-pyridine-κ,N) manganese(I) (134)

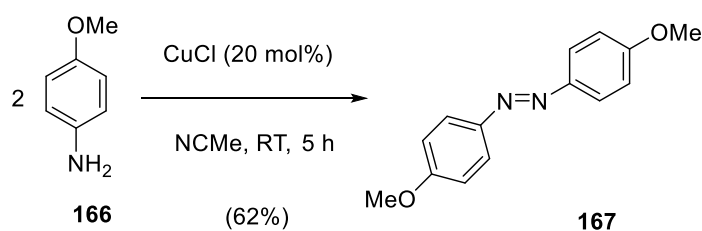


This reaction was performed using General Procedure 1 with BnMn(CO)_5 (1 eq., 4.56 mmol, 131 mg), 2-(ferrocenyl)pyridine (1 eq., 0.25 mmol, 84.5 mg) and *n*-hexane (10 mL). Infrared spectroscopic analysis showed that the reaction was complete after 20 h. The *title compound* was purified by flash column chromatography silica using petrol/ $\text{Et}_2\text{O}/\text{NEt}_3$ (94:5:1 v/v) to afford the *title compound* as a dark red solid (162 mg, 83% yield).

M.P.: 109–111°C; $R_f = 0.28$ (petrol/ Et_2O 9:1 v/v); $^1\text{H NMR}$ (700 MHz, CD_2Cl_2): δ (ppm) = 8.50 (d, $J = 5.0$ Hz, 1H, Ar-H), 7.65 (ddd, $J = 8.0, 7.5, 1.0$ Hz, 1H, Ar-H), 7.41 (d, $J = 8.0$ Hz, 1H, Ar-H), 7.02 (ddd, $J = 7.5, 5.0, 1.0$ Hz, 1H, Ar-H), 4.93 (d, $J = 2.0$ Hz, 1H, Cp-H), 4.66 (dd, $J = 2.0, 2.0$ Hz, 1H, Cp-H), 4.56 (d, $J = 2.0$ Hz, 1H, Cp-H), 4.07 (s, 5H, Cp-H). $^{13}\text{C NMR}$ (176 MHz, CD_2Cl_2): δ (ppm) = 221.1, 213.2, 212.3, 211.7 (Mn-C≡O); 169.0, 154.4, 137.5, 120.2, 119.5 (Ar); 103.1, 90.5, 77.4, 72.4, 69.6, 65.2 (Cp). MS (LIFDI⁺): $m/z = 426.9565$ [M^+] ($\text{C}_{19}\text{H}_{12}\text{NO}_4\text{MnFe}$ requires 426.9543). Elemental analysis (CHN): C 53.00%, H 2.91%, N 3.20% ($\text{C}_{19}\text{H}_{12}\text{NO}_4\text{MnFe}$ requires C 53.18%, H 2.82%, N 3.26%). IR (CH_2Cl_2 , cm^{-1}): 2077 (s), 1988 (vs), 1976 (vs), 1932 (vs), 1607 (m), 1498 (s); UV-visible spectrum (CH_2Cl_2): λ_{max} (nm) = 292, 486; ϵ (292 nm) = $(1.827 \pm .013) \times 10^4 \text{ dm}^3 \text{ mol}^{-1} \text{ cm}^{-1}$, ϵ (486 nm) = $(1.23 \pm 0.05) \times 10^3 \text{ dm}^3 \text{ mol}^{-1} \text{ cm}^{-1}$.

Lab book reference: BJA-2-095

4,4'-dimethoxyazobenzene (**167**)³¹⁰

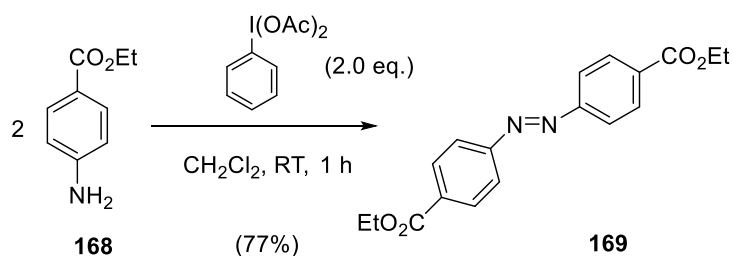


To a 100 mL round-bottomed flask with stirrer bar were added *p*-anisidine (1.0 eq., 5.0 mmol, 618 mg), cuprous chloride (0.2 eq., 1.0 mmol, 101 mg) and acetonitrile (25 mL). The reaction mixture was stirred under air at room temperature for 5 h, at which point thin layer chromatography showed complete consumption of *p*-anisidine. The reaction mixture was quenched using 2 M K₂CO₃ (25 mL) and the product extracted with Et₂O (3 × 25 mL). The combined organic layers were washed with brine (25 mL), dried with anhydrous MgSO₄, and filtered before the solvent was removed under reduced pressure. The crude product was purified by flash column chromatography on silica gel using EtOAc/petrol, starting with 1:9 *v/v* and moving to 1:2 *v/v*. Removal of the solvent afforded the *title compound* as a brown solid (378 mg, 62% yield).

MP: 156°C (lit.: 155-159°C);³⁶¹ *R*_f = 0.35 (EtOAc/petrol, 1:4, *v/v*); ¹H NMR (400 MHz, CDCl₃): δ (ppm) = 7.90-7.86 (m, 4H, Ar-H), 7.02-6.98 (m, 4H, Ar-H), 3.89 (s, 6 H, OCH₃); ¹³C NMR (101 MHz, CDCl₃): δ (ppm) = 161.7, 147.2, 124.4, 114.3 (Ar); 55.6 (OCH₃); HRMS (ESI⁺): *m/z* = 243.1134 [M-H]⁺ (C₁₄H₁₅N₂O₂ requires 243.1134); IR (CH₂Cl₂, cm⁻¹): 2842 (w), 1600 (s), 1583 (m), 1504 (s), 1463 (m), 1441 (m), 1181 (s), 1148 (s), 1104 (m), 1031 (s).

Lab book reference: BJA-2-090

4,4'-dicarboethoxyazobenzene (**169**)³¹¹



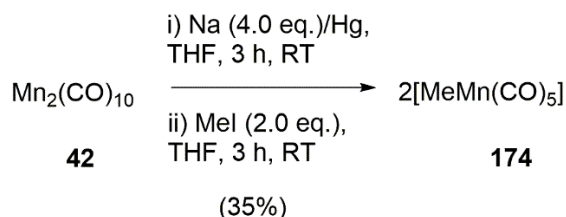
To a 250 mL round-bottomed flask with stirrer bar were added ethyl 4-aminobenzoate (1.0 eq., 7.5 mmol, 1.24 g), iodobenzene diacetate (1.0 eq., 7.5 mmol, 2.43 g) and CH₂Cl₂ (60 mL). The reaction mixture was stirred under air at room temperature for 1 h, at which point thin layer

chromatography showed complete consumption of ethyl 4-aminobenzoate. The solvent was removed under reduced pressure and the crude product was purified by flash column chromatography on silica gel using EtOAc/petrol, starting with 1:19 v/v and moving to 1:4 v/v. Removal of the solvent afforded the *title compound* as an orange solid (940 mg, 77% yield).

MP: 140°C (lit.: 135-136°C)³⁶¹; $R_f = 0.26$ (CH₂Cl₂); ¹H NMR (400 MHz, CDCl₃): δ (ppm) = 8.22-8.18 (m, 4H, Ar-H), 7.99-7.95 (m, 4H, Ar-H), 4.41 (q, 7.0 Hz, 4H, CO₂CH₂CH₃), 1.42 (t, 7.0 Hz, 6H, CO₂CH₂CH₃); ¹³C NMR (101 MHz, CDCl₃): δ (ppm) = 166.0 (CO₂Et); 155.0, 132.8, 130.7, 123.0 (Ar); 61.5 (CO₂CH₂CH₃); 14.4 (CO₂CH₂CH₃); HRMS (ESI⁺): $m/z = 349.1150$ [M-Na]⁺ (C₁₈H₁₈N₂NaO₄ requires 349.1164); IR: 2983 (w), 1714 (s), 1603 (w), 1466 (w), 1409 (w), 1366 (m), 1219 (w), 1174 (w), 1110 (m), 1015 (m); UV-visible spectrum (CH₂Cl₂): λ_{\max} (nm) = 330, ϵ (330 nm) = $(3.49 \pm 0.04) \times 10^4$ dm³ mol⁻¹ cm⁻¹.

Lab book reference: BJA-2-114

Methyl pentacarbonyl manganese(I) (174)



In the first step, a sodium amalgam was made. Mercury (6 mL) was added to an oven-dried Schlenk tube containing a magnetic stirrer. Sodium metal (4.0 eq., 21.4 mmol, 500 mg) was added to the stirring mercury under a positive pressure of nitrogen. The sodium must be added slowly in small pieces to prevent the amalgam from getting excessively hot.

In a separate oven-dried Schlenk tube, dimanganese decacarbonyl (1.0 eq., 5.36 mmol, 2.07 g) was dissolved in dry, degassed tetrahydrofuran (40 mL). This solution was then added to the amalgam by cannula transfer, and the reaction mixture was stirred for 3 h. In another Schlenk tube, methyl iodide (2.0 eq., 10.7 mmol, 675 μ L) was dried under vacuum with stirring for 1 minute at 0°C. The tetrahydrofuran solution was transferred into the methyl iodide at ambient temperature using a cannula filtration.

The mixture was stirred at ambient temperature for 3 h, then filtered through Celite™ and washed with diethyl ether (5 \times 20 mL). The filtrate was loaded onto silica and placed onto a 3 cm diameter pad of silica of approximately 3 cm depth. The pad was washed with petrol (3 \times 40 mL) and the

solvent was removed on a rotary evaporator. The *title compound* was obtained as colourless crystals (785 mg, 35% yield).

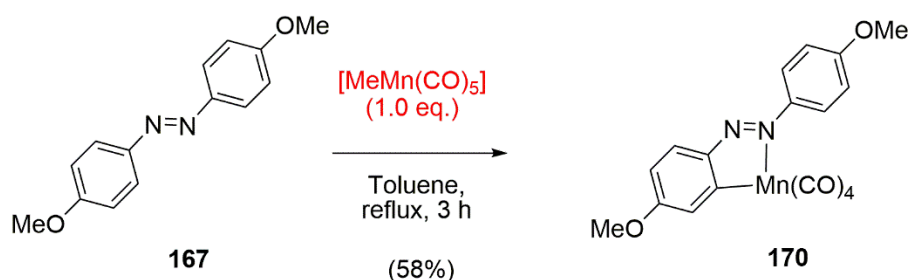
$R_f = 0.84$ (petrol); $^1\text{H NMR}$ (400 MHz, CDCl_3): δ (ppm) = -0.10 (s, 3H, Me); $^{13}\text{C NMR}$ (101 MHz, CDCl_3): δ (ppm) = 213.7, 210.5 (Mn-C \equiv O); -19.2 (Me); IR (CH_2Cl_2 , cm^{-1}): 2906 (w), 2111, (w), 2009 (vs), 1986 (m).

Lab book reference: BJA-1-079

Tetracarbonyl(4,4'-methoxyazobenzene)manganese (170)

Two methods were used to make complex **170**.

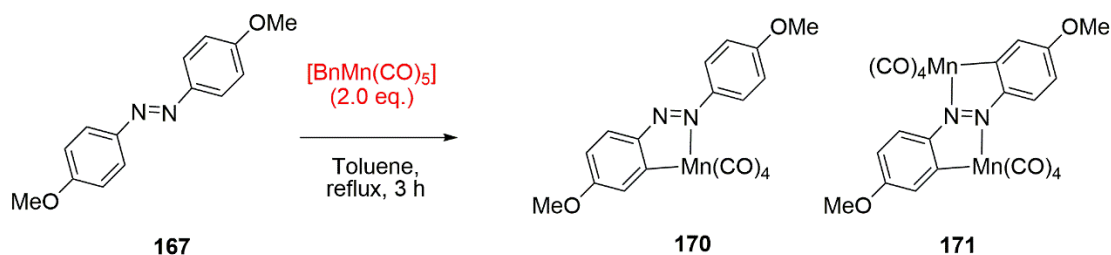
Method A:



The *title compound* was prepared using general procedure 3 with $[\text{MeMn}(\text{CO})_5]$ (1.0 eq., 0.20 mmol, 48.8 mg), 4,4'-dimethoxyazobenzene (1.0 eq., 0.20 mmol, 42.5 mg) and toluene (2 mL). A reaction time of 3 hours was used. Flash column chromatography was performed starting with CH_2Cl_2 and moving to $\text{CH}_2\text{Cl}_2/\text{MeOH}$ 99:1 v/v to afford an orange solid (47.6 mg, 58% yield).

Lab book reference: BJA-2-091

Method B:

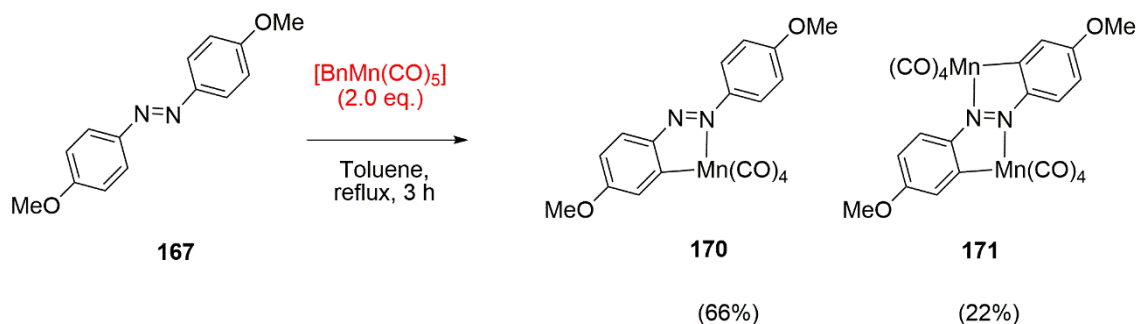


The *title compound* was prepared using general procedure 2 with 4,4'-dimethoxyazobenzene, (1.0 eq., 0.5 mmol, 121 mg), [BnMn(CO)₅] (2.0 eq., 1.0 mmol, 185 mg) and toluene (5 mL). Flash column chromatography was performed starting with *n*-hexane/CH₂Cl₂ 7:3 *v/v* and moving to *n*-hexane/CH₂Cl₂ 1:1 *v/v* to afford an orange solid (134 mg, 66% yield).

Lab book reference: BJA-2-092

M.P.: 74°C; *R*_f = 0.33 (*n*-hexane/CH₂Cl₂, 1:1, *v/v*); ¹H NMR (400 MHz, CDCl₃): δ (ppm) = 8.19 (d, *J* = 7.5 Hz, 1H, Ar-H), 7.54-7.48 (m, 3H, Ar-H), 6.98 (d, 9.0 Hz, 1H, Ar-H), 6.83 (m, 1H, Ar-H), 3.95 (s, 3H, OMe), 3.87 (s, 3H, OCH₃); ¹³C NMR (126 MHz, CDCl₃) δ (ppm) = 220.6, 213.3, 211.3 (Mn-C≡O); 184.3, 162.1, 161.9, 160.9, 151.5, 133.8, 124.9, 123.9, 114.2, 112.3 (Ar); 56.0, 55.9 (OCH₃); HRMS (ESI⁺): *m/z* = 409.0243 [M-H]⁺ (C₁₈H₁₄MnN₂O₆ requires 409.0232); IR (CH₂Cl₂, cm⁻¹): 2842 (w), 2081 (s), 1997 (vs), 1948 (vs), 1603 (w), 1580 (s), 1555 (m), 1503 (m), 1465 (w), 1434 (w), 1368 (w), 1322 (w), 1201 (w), 1175 (w), 1126 (w), 1112 (w), 1029 (m); UV-visible spectrum (CH₂Cl₂): λ_{max} (nm) = 378, 456, ε(378 nm) = (2.166 ± 0.008) × 10⁴ dm³ mol⁻¹ cm⁻¹, ε(578 nm) = (1.254 ± 0.005) × 10⁴ dm³ mol⁻¹ cm⁻¹.

Octacarbonyl(4,4'-dimethoxyazobenzene)dimanganese (171)



The *title compound* was prepared using general procedure 2 with 4,4'-dimethoxyazobenzene, (1.0 eq., 0.5 mmol, 121 mg), [BnMn(CO)₅] (2.0 eq., 1.0 mmol, 185 mg) and toluene (5 mL). The reaction time was 3 hours. Flash column chromatography was performed starting with *n*-hexane/CH₂Cl₂ 7:3 *v/v* and moving to *n*-hexane/CH₂Cl₂ 1:1 *v/v* to afford a purple solid (62.2 mg, 22% yield).

M.P.: 129°C (decomp.); *R*_f = 0.53 (*n*-hexane/CH₂Cl₂, 1:1, *v/v*); ¹H NMR (500 MHz, CDCl₃): δ (ppm) = 8.47 (d, *J* = 9.0 Hz, 2H, Ar-H), 7.61 (d, *J* = 2.5 Hz, 2H, Ar-H), 6.84 (dd, *J* = 9.0 Hz, 2.5 Hz, 2H, Ar-H), 3.98 (s, 6H, OCH₃); ¹³C NMR (126 MHz, CDCl₃) δ 220.7, 213.1, 210.3 (Mn-C≡O);

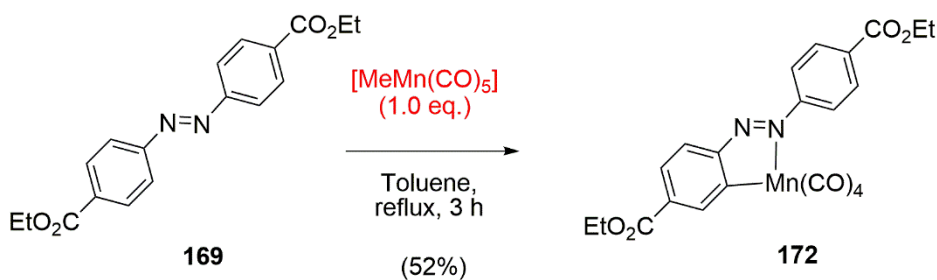
178.1, 161.1, 160.6, 129.9, 124.9, 111.9 (Ar); 56.0 (OCH₃); MS (LIFDI⁺): m/z = 573.87 [M⁺] (C₂₂H₁₂Mn₂N₂O₁₀ requires 573.93); IR (CH₂Cl₂, cm⁻¹): 2842 (w), 2077 (s), 2012 (vs), 1989 (vs), 1953 (vs), 1573 (s), 1554 (m), 1464 (w), 1434 (w), 1314 (w), 1176 (w), 1130 (w), 1121 (w), 1030 (m); Elemental analysis (CHN): C: 45.96%, H: 2.06%, N: 4.77% (C₂₂H₁₂Mn₂N₂O₁₀ requires C: 46.01%, H: 2.11%, N: 4.88%); UV-visible spectrum (CH₂Cl₂): λ_{max} (nm) = 456, 578, ε(456 nm) = (2.79 ± .02) × 10⁴ dm³ mol⁻¹ cm⁻¹, ε(578 nm) = (1.254 ± 0.005) × 10⁴ dm³ mol⁻¹ cm⁻¹.

Lab book reference: BJA-2-092

Tetracarbonyl(4,4'-dicarboethoxyazobenzene)manganese (172)

Two methods were used to make complex **172**.

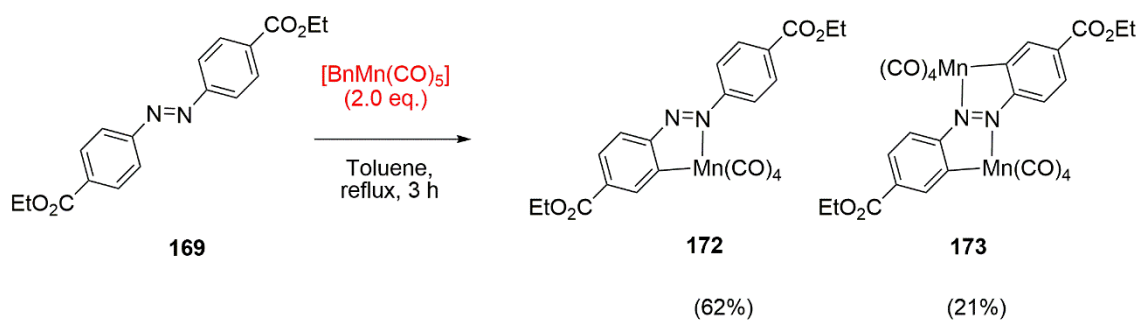
Method A:



The *title compound* was prepared using general procedure 3 with MeMn(CO)₅, (1.0 eq., 0.20 mmol, 64.5 mg), 4,4'-dicarboethoxyazobenzene (1.0 eq., 0.20 mmol, 42.6 mg) and toluene (2 mL). The reaction time was 3 hours. Flash column chromatography was performed starting with CH₂Cl₂ and moving to CH₂Cl₂/MeOH 98:2 v/v to afford a red solid (50.9 mg, 52% yield).

Lab book reference: BJA-2-084

Method B:

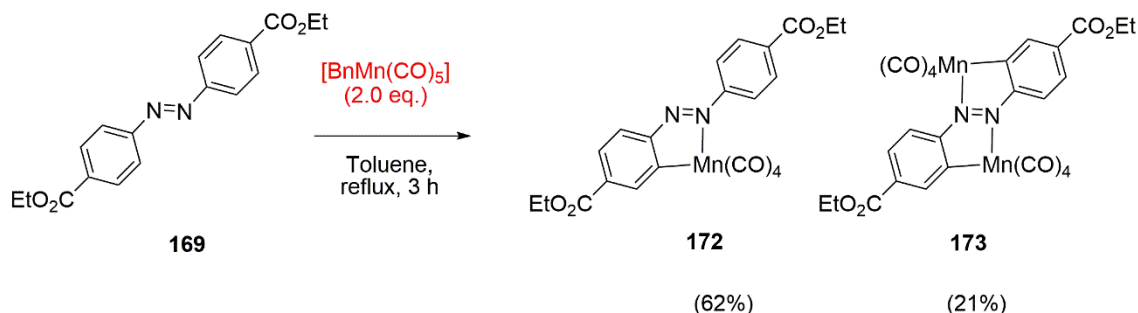


The *title compound* was prepared using general procedure 2 with 4,4'-dicarboethoxyazobenzene, (1.0 eq., 0.5 mmol, 161 mg), [BnMn(CO)₅] (2.0 eq., 1.0 mmol, 184 mg) and toluene (5 mL). The reaction time was 3 hours. Flash column chromatography was performed starting with CH₂Cl₂ and moving to CH₂Cl₂/MeOH 99:1 v/v to afford a red solid (152 mg, 62% yield).

Lab book reference: BJA-2-087

M.P.: 98°C (decomp.); *R*_f = 0.32 (CH₂Cl₂); ¹H NMR (400 MHz, CDCl₃): δ (ppm) = 8.77 (s, 1H, Ar-H), 8.41 (d, *J* = 8.0 Hz, 1H, Ar-H); 8.22 (d, *J* = 7.5 Hz, 1H, Ar-H), 8.02 (d, *J* = 7.5 Hz, 1H, Ar-H), 7.63 (d, *J* = 8.0 Hz, 1H, Ar-H), 4.47-4.38 (m, 4H, CO₂CH₂CH₃), 1.48-1.39 (m, 6H, CO₂CH₂CH₃); ¹³C NMR (126 MHz, CDCl₃) δ (ppm) = 219.8, 212.4, 209.7 (Mn-C≡O); 181.4 (Ar); 169.4 167.0, 165.7 (Ar/CO₂Et); 160.3 142.3, 132.7, 132.5, 132.4, 131.0, 127.2, 122.4 (Ar); 61.9, 61.9 (CO₂CH₂CH₃); 14.7, 14.7 (CO₂CH₂CH₃); HRMS (ESI⁺): *m/z* = 515.0286 [M-Na]⁺ (C₂₂H₁₇MnN₂NaO₈ requires 515.0263); IR (CH₂Cl₂, cm⁻¹): 2983 (w), 2084 (s), 2004 (vs), 1960 (vs), 1716 (s), 1604 (w), 1410 (w), 1389 (w), 1370 (w), 1234 (m), 1107 (s), 1035 (m), 1019 (m); Elemental analysis (CHN): C: 53.58%, H: 3.57%, N: 5.65% (C₂₂H₁₇MnN₂O₈ requires C: 53.67%, H: 3.48%, N: 5.69%); UV-visible spectrum (CH₂Cl₂): λ_{max} (nm) = 336, 434, ε(336 nm) = (1.58 ± .05) × 10⁴ dm³ mol⁻¹ cm⁻¹, ε(434 nm) = (3.0 ± 0.2) × 10³ dm³ mol⁻¹ cm⁻¹.

Octacarbonyl(4,4'-dicarboethoxyazobenzene)dimanganese (173)



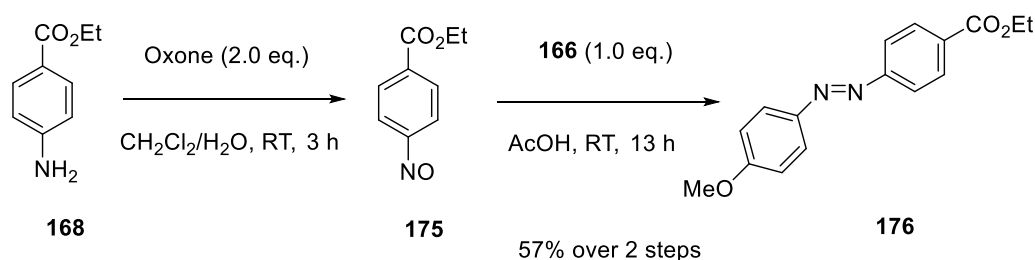
The *title compound* was prepared using general procedure 2 with 4,4'-dicarboethoxyazobenzene, (1.0 eq., 0.5 mmol, 161 mg), [BnMn(CO)₅] (2.0 eq., 1.0 mmol, 184 mg) and toluene (5 mL). The reaction time was 3 hours. Flash column chromatography was performed starting with CH₂Cl₂ and moving to CH₂Cl₂/MeOH 99:1 v/v to afford a black solid (68.1 mg, 21% yield).

M.P.: 108°C (decomp.); *R*_f = 0.45 (CH₂Cl₂); ¹H NMR (500 MHz, CDCl₃): δ (ppm) = 8.83 (d, *J* = 1.5 Hz, 2H, Ar-H); 8.67 (d, *J* = 8.5 Hz, 2H Ar-H); 8.02 (dd, *J* = 8.5, 1.5 Hz, 2H, Ar-H); 4.47 (q, *J* = 7.5 Hz, 4H, CH₂), 1.46 (t, *J* = 7.5 Hz, 6H, CH₃); ¹³C NMR (126 MHz, CDCl₃) δ (ppm) = 220.0,

212.3, 208.7 (Mn-C≡O); 178.3 (Ar); 169.0, 166.5 ((Ar/C₂O₂Et); 142.1, 131.7, 129.1, 127.2 (Ar); 62.0 (CO₂CH₂CH₃); 14.7 (CO₂CH₂CH₃); HRMS (ESI⁺): m/z = 680.9384 [M-Na]⁺ (C₂₆H₁₆Mn₂N₂NaO₁₂ requires 680.9362); IR (CH₂Cl₂, cm⁻¹): 2079 (s), 2019 (vs), 2000 (vs), 1963 (s), 1714 (s), 1218 (m), 1110 (s), 1031 (w); Elemental analysis (CHN): C: 47.87%, H: 2.44%, N: 4.20% (C₂₆H₁₆Mn₂N₂O₁₂ requires C: 47.43%, H: 2.45%, N: 4.25%); UV-visible spectrum (CH₂Cl₂): λ_{max} (nm) = 404, 522, 622, ε(404 nm) = (2.648 ± .010) × 10⁴ dm³ mol⁻¹ cm⁻¹, ε(522 nm) = (8.47 ± .06) × 10³ dm³ mol⁻¹ cm⁻¹, ε(622 nm) = (3.98 ± .03) × 10³ dm³ mol⁻¹ cm⁻¹.

Lab book reference: BJA-2-087

Ethyl 4-[2-(4-methoxyphenyl)diazenyl]-benzoate (**176**)³⁶²



To a round-bottomed flask with stirrer bar were added a solution of ethyl 4-aminobenzoate (1.0 eq., 5.0 mmol, 825 mg) in CH₂Cl₂ (15 mL). Water (30 mL) was added, followed by oxone (2.0 eq., 10.0 mmol, 3.08 g). The solution was stirred at room temperature for 3 hours, at which point thin layer chromatography showed consumption of ethyl 4-aminobenzoate.

The product was extracted into CH₂Cl₂ (4 × 15 mL) and the combined organic layers were washed with 1 M HCl (2 × 15 mL), water (15 mL) and brine (15 mL). The extracts were then dried over anhydrous MgSO₄ and filtered. The solvent was removed under reduced pressure to afford ethyl 4-nitrosobenzoate, intermediate **175**, in quantitative yield as a yellow solid. The product was immediately used in the synthesis of ethyl 4-[2-(4-methoxyphenyl)diazenyl]-benzoate without further purification.

To a round-bottomed flask with stirrer bar were added ethyl 4-nitrosobenzoate (1.0 eq., 3.44 mmol, 617 mg), *p*-anisidine (1.4 eq., 4.82 mmol, 594 mg) and acetic acid (14 mL). The reaction mixture was protected from light by aluminium foil and stirred at room temperature for 13 h.

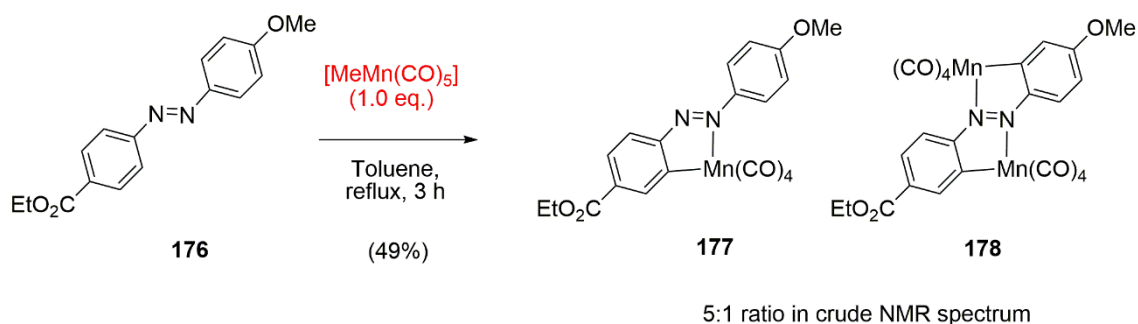
The reaction mixture was poured into water (40 mL) and the product extracted with EtOAc (4 × 50 mL). The organic layers were combined and washed with water (100 mL), saturated aqueous sodium bicarbonate (3 × 100 mL) and brine (100 mL). After drying with anhydrous MgSO₄ and filtration, the solvent was removed under reduced pressure. The crude product was purified using flash column chromatography on silica gel, starting with 1:1 v/v *n*-hexane/CH₂Cl₂ and moving to

CH₂Cl₂ to elute the product. Removal of the solvent gave the *title compound* as a bright orange powder (559 mg, 57% yield).

MP: 102°C (lit.: 103-104°C)³⁶³; $R_f = 0.15$ (*n*-hexane/ CH₂Cl₂, 1:1, *v/v*); ¹H NMR (400 MHz, CDCl₃): δ (ppm) = 8.19-8.16 (m, 2H, Ar-H), 7.97-7.94 (m, 2H, Ar-H), 7.92-7.89 (m, 2H, Ar-H), 7.05-7.01 (m, 2H, Ar-H), 4.41 (q, 7.0 Hz, 2H, CO₂CH₂CH₃), 3.91 (s, 3H, OCH₃), 1.43 (t, 7.0 Hz, 3H, CO₂CH₂CH₃); ¹³C NMR (101 MHz, CDCl₃) δ (ppm) = 166.3 (Ar); 163.0 (CO₂Et); 155.6, 147.3, 131.9, 130.9, 125.5, 122.7, 114.6 (Ar); 61.5 (CO₂CH₂CH₃); 56.0 (OCH₃); 14.7 (CO₂CH₂CH₃); HRMS (ESI⁺): $m/z = 307.1047$ [M-Na]⁺ (C₁₆H₁₆N₂NaO₃ requires 307.1059); IR (CH₂Cl₂, cm⁻¹): 2841 (w), 1712 (s), 1603 (s), 1585 (m), 1502 (s), 1465 (m), 1407 (m), 1368 (m), 1140 (s), 1109 (m), 1099 (m), 1030 (m), 1013 (m).

Lab book reference: BJA-2-086, BJA-2-088

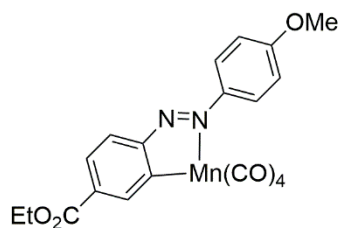
Tetracarbonyl(ethyl 4-[2-(4-methoxyphenyl)diazenyl]-benzoate)manganese isomer mixture (**177** and **178**)



The two compounds were prepared as a mixture using general procedure 3 with [MeMn(CO)₅] (1.0 eq., 0.50 mmol, 105 mg), ethyl 4-[2-(4-methoxyphenyl)diazenyl]-benzoate (1.0 eq., 0.50 mmol, 142 mg) and toluene (5 mL). The reaction time was 3 hours. The two isomeric complexes could not be separated using silica gel chromatography and were characterised as a ~5:1 mixture of complex **177** to complex **178**, which was a red solid (110 mg, 49 % yield).

Lab book reference: BJA-2-093

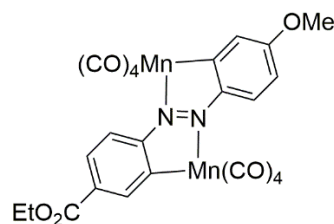
Tetracarbonyl 5-carboethoxy-2-([(4-methoxyphenyl)azo]phenyl κ ,C¹- κ ,N) manganese (I)
(177)



177

$R_f = 0.21$ (*n*-hexane/CH₂Cl₂, 1:1, *v/v*); ¹H NMR (400 MHz, CDCl₃): δ (ppm) = 8.72 (d, $J = 1.5$ Hz, 1H, Ar-H), 8.31 (d, $J = 8.0$ Hz, 1H, Ar-H), 7.98 (dd, $J = 8.0, 1.5$ Hz, 1H, Ar-H), 7.66 (d, $J = 9.0$ Hz, 2H, Ar-H), 7.01 (d, $J = 9.0$ Hz, 2H, Ar-H), 4.41 (q, 7.0 Hz, 2H, CO₂CH₂CH₃), 3.91 (s, 3H, OCH₃), 1.43 (t, 7.0 Hz, 3H, CO₂CH₂CH₃)

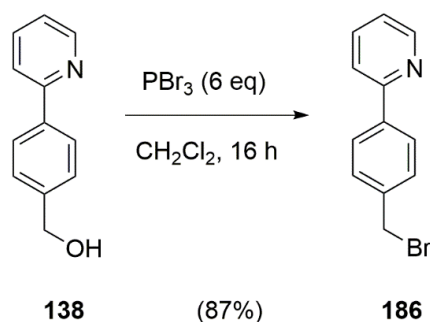
Tetracarbonyl 5-methoxy-2-([(4-carboethoxyphenyl)azo]phenyl κ ,C¹- κ ,N) manganese (I)
(178)



178

$R_f = 0.21$ (*n*-hexane/CH₂Cl₂, 1:1 *v/v*); ¹H NMR (400 MHz, CDCl₃): δ (ppm) = 8.26 (d, $J = 9.0$ Hz, 1H, Ar-H), 8.17 (d, $J = 8.5$ Hz, 2H, Ar-H), 7.62 (d, $J = 2.5$ Hz, 1H, Ar-H), 7.59 (d, $J = 8.5$ Hz, 2H, Ar-H), 6.86 (dd, $J = 9.0, 2.5$ Hz, 2H, Ar-H), 4.42 (q, 7.0 Hz, 2H, CO₂CH₂CH₃), 3.99 (s, 3H, OCH₃), 1.43 (t, 7.0 Hz, 3H, CO₂CH₂CH₃)

2-(4'-Bromomethyl-phenyl)pyridine (186)³⁶⁴

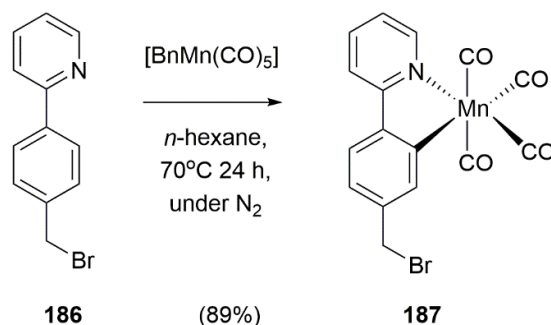


In a round-bottomed flask, a solution of 2-(4'-hydroxybenzyl)pyridine (1.0 eq., 2.60 mmol, 483 mg) in CH₂Cl₂ (30 mL) was cooled to 0°C in a water/ice bath and PBr₃ (6 eq., 16 mmol, 1.5 mL) was added dropwise with stirring. The flask was covered in foil, allowed to warm to room temperature and left for 16 h. The reaction mixture was cooled back to 0°C and saturated sodium carbonate solution was added slowly to quench the reaction, ensuring that the temperature was kept below 5°C. When the solution reached pH 7, as checked by pH paper, the product was extracted with CH₂Cl₂ (3 × 50 mL), the organic layers dried with MgSO₄ and filtered. The solvent was removed *in vacuo* to give the *title compound* as a white solid (559 mg, 87% yield).

MP: 65 °C (decomp., lit.: 45°C);³⁶⁴ ¹H NMR (400 MHz, CDCl₃): δ (ppm) = 8.70 (d, *J* = 5.0 Hz, 1H, Ar-H), 7.98 (d, *J* = 7.5 Hz, 2H, Ar-H), 7.79-7.71 (m, 2H, Ar-H), 7.50 (d, *J* = 8.0 Hz, 2H, Ar-H), 7.26-7.23 (m, 1H, Ar-H), 4.55 (s, 2H, CH₂); ¹³C NMR (126 MHz, CDCl₃) δ (ppm) = 156.8, 149.9, 139.6, 138.6, 137.0, 129.6, 127.5, 122.5, 120.7 (Ar); 33.1 (CH₂); HRMS (ESI⁺): *m/z* = 248.0061 [M-H]⁺ (C₁₂H₁₁NBr requires 248.0075).

Lab book reference: BJA-1-042

Tetracarbonyl 2-(4-[bromomethyl]phenyl) κ,C²-pyridine- κ,N) manganese (I) (187)



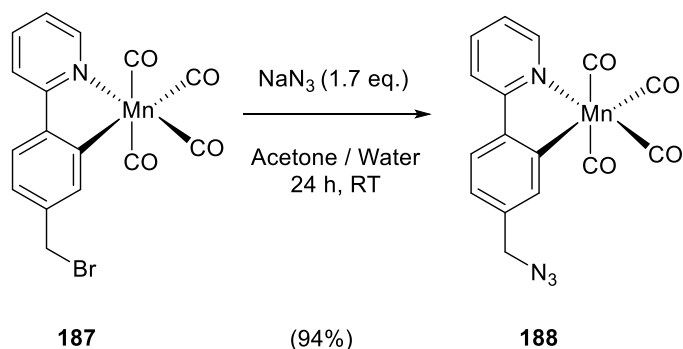
The reaction was performed using General Procedure 1 with BnMn(CO)₅ (1.0 eq., 0.86 mmol, 249 mg), 2-(4'-hydroxybenzyl)pyridine (1.0 eq., 0.86 mmol, 214 mg) and hexane (12 mL). Infrared spectroscopy showed that the reaction was complete after 24 h. The *title compound* was purified by flash column chromatography on silica gel, using petrol and then petrol/EtOAc 9:1 *v/v*. The solvent was removed *in vacuo* to afford a yellow solid (318 mg, 89% yield).

MP: 123°C (decomp.); ¹H NMR (500 MHz, CDCl₃): δ (ppm) = 8.73 (d, 5.5 Hz, 1H, Ar-H), 7.95 (d, 1.5 Hz, 1H, Ar-H), 7.87 (d, 8.0 Hz, 1H, Ar-H), 7.81 (apr. td, 7.5, 1.5 Hz, 1H, Ar-H), 7.75 (d, 8.0 Hz, 1H, Ar-H), 7.23 (dd, 8.0, 2.0 Hz, 1H, Ar-H), 7.14 (ddd, 6.5, 5.5, 1.5 Hz, 1H, Ar-H), 4.56 (s, 2H, CH₂); ¹³C NMR (101 MHz, CDCl₃) δ (ppm) = 220.0, 214.1, 213.8 (Mn-C≡O), 175.9, 165.8, 154.0, 146.4, 141.7, 139.4, 138.1, 125.3, 124.2, 122.8, 119.6 (Ar), 34.2 (CH₂); MS

(LIFDI⁺): $m/z = 412.94 [M^+]$ ($C_{16}H_9NO_4BrMn$ requires 412.9095); IR (CH_2Cl_2 , cm^{-1}): 2076 (s), 1992 (vs), 1979 (vs), 1935 (vs), 1605 (m), 1583 (m), 1567 (m), 1477 (s), 1432 (w), 1272 (w); Elemental analysis (CHN): C: 46.49%, H: 2.22%, N: 3.31% ($C_{16}H_9NO_4BrMn$ requires C: 46.41%, H: 2.19%, N: 3.38%).

Lab book reference: BJA-1-041

Tetracarbonyl 2-(4'-[azidomethyl]phenyl) κ,C^2 -pyridine- κ,N) manganese (I) (188)

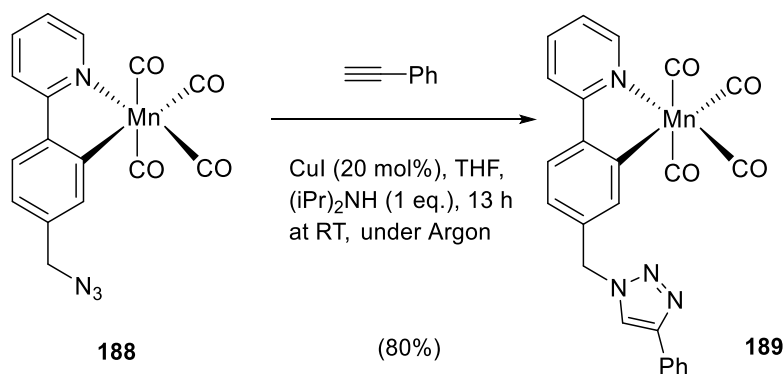


To a solution of tetracarbonyl 2-(4'-bromobenzyl) κ,C^2 -pyridine- κ,N) manganese(I) (1.0 eq., 0.2 mmol, 82.8 mg), in a mixture of water (0.2 mL) and acetone (0.9 mL) in a round-bottomed flask covered in aluminium foil was added sodium azide (1.7 eq., 0.34 mmol, 22 mg) in a single portion. The reaction mixture was stirred at room temperature for 24 h. The reaction was quenched by adding water (15 mL) and the product was extracted into EtOAc (3×10 mL). The combined organic layers were dried with $MgSO_4$, filtered and the solvent removed *in vacuo* to afford the *title compound* as a yellow solid (71 mg, 94% yield).

MP: 97°C (decomp.); 1H NMR (500 MHz, $CDCl_3$): δ (ppm) = 8.73 (d, $J = 5.5$ Hz, 1H, Ar-H), 7.91-7.87 (m, 2H, Ar-H), 7.84-7.77 (m, 2H, Ar-H), 7.16-7.12 (m, 2H, Ar-H), 4.41 (s, 2H, CH_2); ^{13}C NMR (126 MHz, $CDCl_3$) δ (ppm) = 220.0, 214.1, 213.8, (Mn-C \equiv O) 176.0, 165.9, 154.0, 146.2, 141.2, 138.0, 137.0, 124.2, 124.1, 122.7, 119.5, (Ar) 55.1 (CH_2); MS (LIFDI⁺): $m/z = 375.98 [M^+]$ ($C_{16}H_9N_4O_4Mn$ requires 376.0004); IR (CH_2Cl_2 , cm^{-1}): 2100 (s), 2076 (s), 1991 (vs), 1978 (vs), 1934 (vs), 1606 (m), 1586 (m), 1565 (m), 1479 (s), 1432 (w); Elemental analysis (CHN): C: 51.19%, H: 2.51%, N: 14.61% ($C_{16}H_9N_4O_4Mn$ requires C: 51.08%, H: 2.41%, N: 14.89%).

Lab book reference: BJA-1-043

Tetracarbonyl 2-(4'-[(1-(phenyl)-1H-1,2,3-triazol-4-yl)methyl]phenyl)- κ ,C²-pyridine- κ ,N) manganese (I) (189)

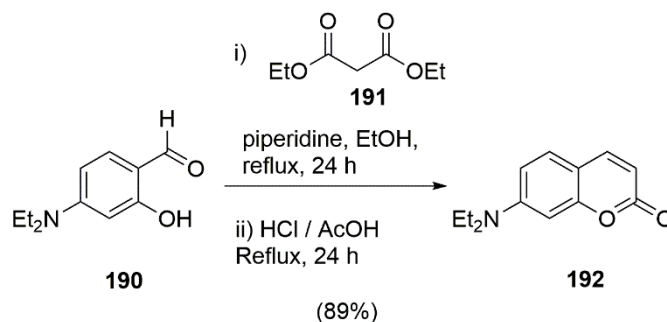


To a solution of tetracarbonyl 2-(4'-[azidomethyl]phenyl) κ ,C²-pyridine- κ ,N) manganese (I) (1.0 eq., 0.129 mmol, 48.6 mg), phenylacetylene (1.1 eq., 0.137 mmol, 15 μ L), and CuI (20 mol%, 0.027 mmol, 5.2 mg) in dry DMF (400 μ L) was added N,N-diisopropylamine (1.0 eq., 0.129 mmol, 18 μ L) dropwise. The reaction mixture was stirred under Ar in the dark at RT for 13 h, when the reaction was judged to be complete by TLC. The reaction mixture was diluted with CH₂Cl₂ (2 mL) and sat. aq. NH₄Cl (5 mL). The product was extracted with CH₂Cl₂ (5 \times 5 mL) and the organic layers were dried over MgSO₄, filtered and the solvent removed under reduced pressure. The product was purified by flash column chromatography on silica gel using petrol/EtOAc (7:3 v/v) and the solvent was removed to afford the *title compound* as a cream-coloured solid, 52.5 mg (80% yield).

M.P.: 162°C (decomp.); R_f = 0.20 (petrol/EtOAc 7:3 v/v); ¹H NMR (500 MHz, CDCl₃): δ (ppm) = 8.74 (d, J = 5.5 Hz, 1H, Ar-H), 7.87 (d, J = 8.0 Hz, 1H, Ar-H), 7.84-7.80 (m, 3H, Ar-H), 7.77 (s, 1H, triazole), 7.74 (d, J = 8.0 Hz, 1H, Ar-H), 7.40 (t, J = 7.5 Hz, 2H, Ar-H), 7.31 (t, J = 7.5 Hz, 2H, Ar-H), 7.16 (ddd, J = 7.0, 5.5, 1.5 Hz, 1H, Ar-H), 7.02 (dd, J = 8.0, 1.5 Hz, 1H, Ar-H), 5.63 (s, 2H, CH₂); ¹³C NMR (126 MHz, CDCl₃) δ (ppm) = 220.2, 214.2, 213.8 (Mn-C \equiv O); 176.9, 165.9, 154.3, 148.5, 146.9, 141.1, 138.4, 136.5, 131.0, 129.1, 128.4, 126.1, 124.7, 124.0, 123.2, 120.0, 119.9 (Ar); 54.8 (CH₂); HRMS (ESI⁺): m/z = 479.0552 [M-H]⁺ (C₂₄H₁₆N₄O₄Mn requires 479.0552); IR (CH₂Cl₂, cm⁻¹): 2077 (s), 1992 (vs), 1979 (vs), 1936 (vs), 1606 (m), 1586 (m), 1568 (w), 1477 (s), 1470 (m), 1075 (w), 1046 (w)

Lab book reference: BJA-1-062

7-(Diethylamino)coumarin (192)³³⁴

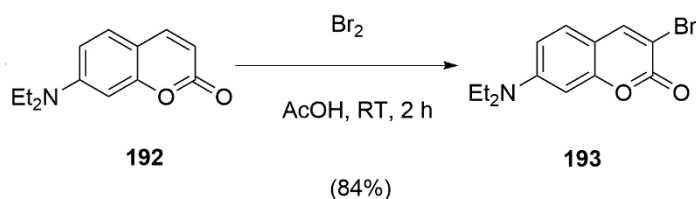


4-Diethylaminosalicylaldehyde (1.0 eq., 1.93 g, 10 mmol), diethylmalonate (2.0 eq., 3.2 g, 20 mmol) and piperidine (1 mL) were combined in absolute ethanol (30 mL) and stirred for 6 h under reflux conditions. Ethanol was evaporated under reduced pressure, then concentrated HCl (20 mL) and glacial acetic acid (20 mL) were added and the reaction mixture refluxed for another 6 h. The solution was cooled to room temperature and poured into ice water (100 mL). NaOH solution (40%) was added dropwise to adjust pH of the solution to 5.0, and a pale precipitate formed immediately. After stirring for 30 min, the mixture was filtered, washed with water and dried under vacuum to afford the product as a brown solid (1.94 g, 89% yield).

M.P.: 84-86°C (lit.: 87-89°C)³⁶⁵; ¹H NMR (400 MHz, CDCl₃): δ (ppm) = 7.53 (d, *J* = 9.5 Hz, 1H, Ar-H), 7.24 (d, *J* = 9.0 Hz, 1H, Ar-H), 6.56 (dd, *J* = 9.0, 2.5 Hz, 1H, Ar-H), 6.49 (d, *J* = 2.5 Hz, 1H, Ar-H), 6.03 (d, *J* = 9.5 Hz, 1H, Ar-H), 4.41 (s, 2H, CH₂), 3.41 (q, *J* = 7.0 Hz, 4H, NCH₂), 1.21 (t, *J* = 7.0 Hz, 6H, CH₃); ¹³C NMR (101 MHz, CDCl₃) δ (ppm) = 162.7; 157.1, 151.0, 144.1, 129.1, 109.5, 109.0, 108.6, 97.9 (Ar); 45.13 (CH₂), 12.77 (CH₃); HRMS (ESI⁺): *m/z* = 218.1180 [M-H]⁺ (C₁₃H₁₆NO₂ requires 218.1181); IR (CH₂Cl₂, cm⁻¹): 2979 (m), 1722 (s), 1711 (m), 1617 (s), 1605 (s), 1521 (m), 1417 (w), 1358 (w), 1197 (w), 1166 (w), 1130 (w).

Lab book reference: BJA-2-104

3-Bromo-7-(diethylamino)coumarin (193)³³⁴

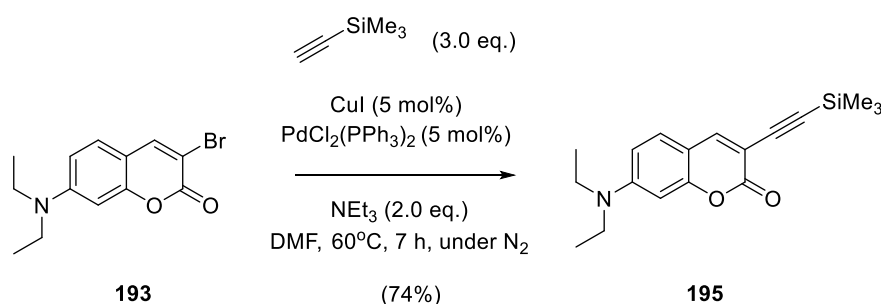


Br₂ (360 μL, 7.0 mmol) was added dropwise to a solution of 7-diethylaminocoumarin (1.52 g, 7.0 mmol) in acetic acid (40 mL), and the mixture was stirred at RT for 2 h. The resulting yellow solid was filtered, washed with acetic acid and dried under vacuum. The product was purified by silica gel flash column chromatography beginning with CH₂Cl₂/petrol (1:1 v/v) and moving to CH₂Cl₂ to elute the product, a yellow solid (1.5 g, 72% yield).

R_f: 0.42 (CH₂Cl₂); ¹H NMR (400 MHz, CDCl₃): δ (ppm) = 7.88 (s, 1H, Ar-H), 7.20 (d, *J* = 9.0 Hz, 1H, Ar-H), 6.57 (dd, *J* = 9.0, 2.5 Hz, 1H, Ar-H), 6.48 (d, *J* = 2.5 Hz 1H, Ar-H), 3.41 (q, *J* = 7.0 Hz, 4H, NCH₂), 1.21 (t, *J* = 7.0 Hz, 6H, CH₃); ¹³C NMR (101 MHz, CDCl₃) δ (ppm) = 158.7, 156.3, 151.2, 145.1, 128.5, 109.5, 109.3, 103.0, 97.4 (Ar); 45.2 (CH₂CH₃); 12.8 (CH₂CH₃); ; HRMS (ESI⁺): *m/z* = 296.0270 [M-H]⁺ (C₁₃H₁₅NO₂Br requires 296.0286); IR (CH₂Cl₂, cm⁻¹): 2982 (m), 2931 (w), 2902 (w), 2874 (m), 1727 (s), 1995 (w), 1619 (s), 1600 (m), 1520 (m), 1412 (w), 1360 (w), 1245 (m), 1189 (w), 1131 (m)

Lab book reference: BJA-2-105

3-(trimethylsilyl)ethynyl-7-(diethylamino)coumarin (195)³³⁴



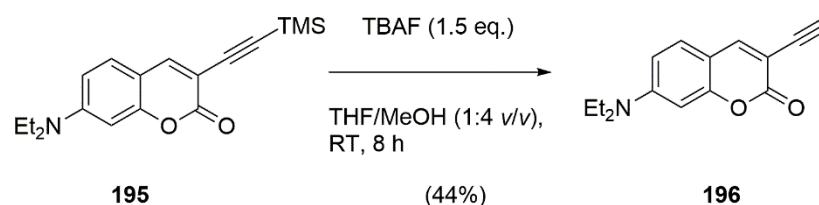
To a solution of 3-bromo-7-(diethylamino)coumarin (1.0 eq., 3.0 mmol, 888 mg) in anhydrous DMF (30 mL) was added [PdCl₂(PPh₃)₄] (5 mol%, 0.15 mmol, 105 mg), CuI (5 mol%, 0.15 mmol, 28.4 mg), triethylamine (2.0 eq., 5.9 mmol, 825 mmol), and trimethylsilylacetylene (3.0 eq., 9.0 mmol 1.25 mL). The reaction mixture was stirred at 60°C for 7 h under N₂. When the solution cooled to RT, it was diluted with water (30 mL) and extracted with CH₂Cl₂ (3 × 30 mL). The organic layers were combined, dried over MgSO₄, and the solvent was removed under reduced pressure. The crude product was purified by silica gel flash column chromatography using petrol/EtOAc (4:1 v/v) to afford the *title compound* as a yellow solid, 697 mg (74% yield).

R_f = 0.42 (CH₂Cl₂); ¹H NMR (400 MHz, CDCl₃): δ (ppm) = 7.75 (s, 1H, Ar-H), 7.21 (d, *J* = 9.0 Hz, 1H, Ar-H), 6.56 (dd, *J* = 9.0, 2.5 Hz, 1H, Ar-H), 6.47 (d, *J* = 2.5 Hz 1H, Ar-H), 3.41 (q, *J* =

7.0 Hz, 4H, NCH₂), 1.21 (t, *J* = 7.0 Hz, 6H, CH₃), 0.25 (s, 9H, SiMe₃); HRMS (ESI⁺): *m/z* = 314.1563 [M-H]⁺ (C₁₈H₂₄NO₂Si requires 314.1576).

Lab book reference: BJA-2-106

3-Ethynyl-7-(diethylamino)coumarin (196)³³⁴

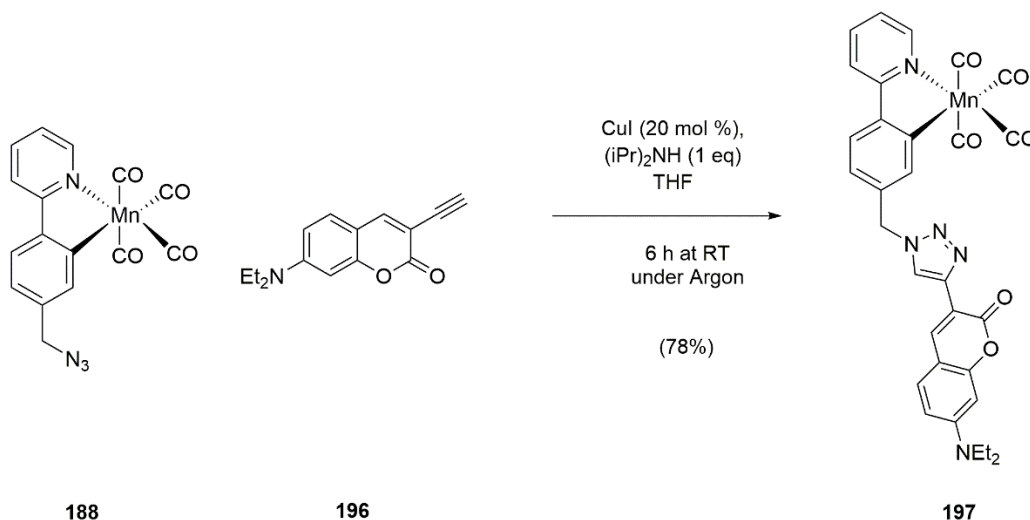


A 1.0 M solution of TBAF in tetrahydrofuran (1.5 eq., 2.8 mmol, 2.8 mL), was added to a solution of TMS-alkyne (1.0 eq., 1.9 mmol, 593 mg) in tetrahydrofuran and MeOH (final ratio 4:1 *v/v*). The solution was stirred at 30°C for 6 h, at which point the solvent was removed *in vacuo*. The product was isolated by silica gel flash chromatography using petrol/EtOAc (7:3 *v/v*) to afford the *title compound* as a yellow solid (201 mg, 44% yield).

*R*_f = 0.28 (petrol/EtOAc 7:3 *v/v*); ¹H NMR (400 MHz, CDCl₃): δ (ppm) = 7.78 (s, 1H, Ar-H), 7.23 (d, *J* = 9.0 Hz, 1H, Ar-H), 6.58 (dd, *J* = 9.0, 2.5 Hz, 1H, Ar-H), 6.47 (d, *J* = 2.5 Hz, 1H, Ar-H), 3.41 (q, *J* = 7.0 Hz, 4H, NCH₂), 3.26 (s, 1H, C≡C-H), 1.21 (t, *J* = 7.0 Hz, 6H, CH₃); ¹³C NMR (101 MHz, CDCl₃) δ (ppm) = 161.3, 156.6, 151.5, 147.1, 129.2, 109.4, 108.1, 103.4, 97.4 (Ar); 81.3, 78.7 (C≡C); 45.13 (CH₂), 12.77 (CH₃); HRMS (ESI⁺): *m/z* = 242.1170 [M-H]⁺ (C₁₅H₁₆NO₂ requires 242.1181); IR (CH₂Cl₂, cm⁻¹): 3301 (m), 2972 (m), 2108 (w), 1722 (m), 1623 (s), 1591 (s), 1524 (m), 1412 (w), 1354 (w), 1192 (w), 1137 (m).

Lab book reference: BJA-2-107

Tetracarbonyl 2-(4'-[(1-(3-[7-(diethylamino)-2-oxo-2H-1-benzopyran]-1H-1,2,3-triazol-4-yl)methyl]phenyl)- κ ,C²-pyridine- κ ,N) manganese (I) (197)



A round-bottomed flask containing 2-(4'-azidomethyl-phenyl)pyridine (1.0 eq., 0.357 mmol, 75.0 mg) was placed under an argon atmosphere and dissolved in dry tetrahydrofuran (3.5 mL). The solution was added to a round-bottomed flask under argon with stirrer bar containing 3-ethynyl-7-(diethylamino)coumarin (1.0 eq., 0.357 mmol, 86.1 mg) and CuI (0.2 eq., 0.073 mmol, 14.0 mg). DIPA (1.0 eq., 0.357 mmol, 50 μ L) was added dropwise. The reaction mixture was stirred at room temperature for 6 hours whereupon the reaction was adjudged to be complete by TLC. A colour change of the reaction mixture from yellow to orange was observed over this period.

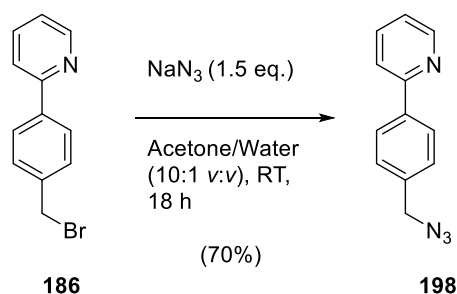
The reaction mixture was quenched with CH_2Cl_2 (20 mL) and saturated aqueous NH_4Cl (40 mL) was added. The product was extracted into CH_2Cl_2 (3 \times 20 mL) dried over MgSO_4 , filtered and the solvent removed on the rotary evaporator. The product was isolated by silica gel flash chromatography using EtOAc to afford the *title compound* as a yellow solid (124 mg, 77% yield).

MP: 162°C (decomp.); R_f : 0.05 (petrol/EtOAc 7:3 v/v); ^1H NMR (500 MHz, CDCl_3): δ (ppm) = 8.73 (d, J = 5.5 Hz, 1H, Ar-H), 8.63 (s, 1H, Ar-H), 7.94 (d, J = 1.5 Hz, 1H, Ar-H), 7.86 (d, J = 8.0 Hz, 1H, Ar-H), 7.81 (apr. td, J = 7.5, 1.5 Hz, 1H, Ar-H), 7.73 (d, J = 8.0 Hz, 1H, Ar-H), 7.40 (d, J = 9.0 Hz, 1H, Ar-H), 7.14 (ddd, J = 6.5, 5.5, 1.5 Hz, 1H, Ar-H), 7.01 (dd, J = 8.0, 2.0 Hz, 1H, Ar-H), 6.63 (dd, J = 9.0, 2.5 Hz, 1H, Ar-H), 6.52 (d, J = 2.5 Hz, 1H, Ar-H), 5.62 (s, 1H, Ar- $\underline{\text{C}}\text{H}_2$), 3.43 (q, J = 7.0 Hz, 4H, N- $\underline{\text{C}}\text{H}_2$ - CH_3), 1.22 (t, J = 7.0 Hz, 6H, CH_3); ^{13}C NMR (126 MHz, CDCl_3) δ (ppm) = 220.1, 214.2, 213.7 (Mn-C \equiv O); 176.7, 165.9, 161.0, 156.3, 154.2, 151.0, 146.8, 142.5, 141.0, 138.6, 138.3, 136.5, 129.8, 124.6, 123.9, 123.1, 123.0, 119.8, 111.3, 109.6, 109.0, 97.4 (Ar); 54.7 (benzylic CH_2); 45.2 (N- $\underline{\text{C}}\text{H}_2$ - CH_3); 12.8 (CH_3); HRMS (ESI⁺): m/z = 618.1168 [$\text{M}-\text{H}$]⁺ ($\text{C}_{31}\text{H}_{25}\text{N}_5\text{O}_6\text{Mn}$ requires 618.1185); IR (CH_2Cl_2 , cm^{-1}): 2983 (w), 2079 (s), 1992 (vs), 1980 (vs), 1932 (vs), 1712 (s), 1607 (vs), 1508 (m), 1475 (w), 1415 (w), 1361 (w), 1245 (m),

1189 (w), 1134 (m); Elemental analysis (CHN): C: 60.37%, H: 4.07%, N: 11.06% (C₃₁H₂₄N₅O₆Mn requires C: 60.30%, H: 3.92%, N: 11.34%); UV-visible spectrum (CH₂Cl₂): λ_{\max} (nm) = 264, 408, ϵ (264 nm) = $(4.13 \pm 0.09) \times 10^4 \text{ dm}^3 \text{ mol}^{-1} \text{ cm}^{-1}$, ϵ (408 nm) = $(3.65 \pm 0.04) \times 10^4 \text{ dm}^3 \text{ mol}^{-1} \text{ cm}^{-1}$.

Lab book reference: BJA-1-066

2-(4'-Azidomethyl-phenyl)pyridine (198)

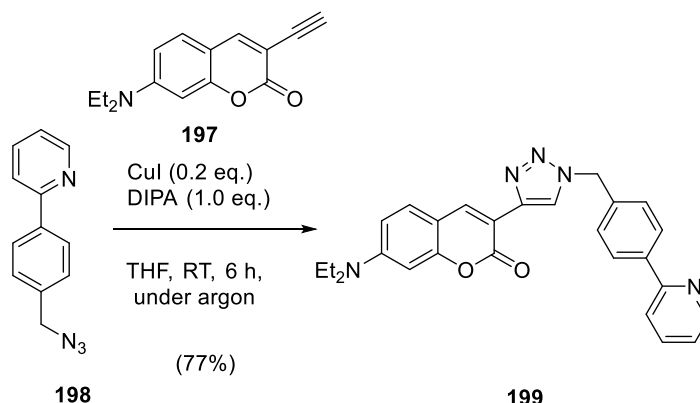


To a solution of 2-(4'-bromomethyl-phenyl)pyridine (1.0 eq., 0.81 mmol, 170 mg), in a mixture of water (0.6 mL) and acetone (2.4 mL) in a round-bottomed flask covered in aluminium foil was added sodium azide (1.3 eq., 1.0 mmol, 66.2 mg) in a single portion. The reaction mixture was stirred at room temperature for 16 h. The reaction was quenched by adding water (20 mL) and the product was extracted into EtOAc (3 \times 20 mL). The combined organic layers were dried with MgSO₄, filtered and the solvent removed *in vacuo* to afford the *title compound* as a yellow oil (102 mg, 70% yield).

R_f = 0.18 (petrol/EtOAc 1:1 v/v); ¹H NMR (400 MHz, CDCl₃): δ (ppm) = 8.70 (d, J = 4.5 Hz, 1H, Ar-H), 8.02 (d, J = 8.5 Hz, 2H, Ar-H), 7.80-7.72 (m, 2H, Ar-H), 7.44 (d, 8.5 Hz, 2H, Ar-H), 7.27-7.23 (m, 1H, Ar-H), 4.41 (s, 2H, CH₂); ¹³C NMR (101 MHz, CDCl₃) δ (ppm) = 157.1, 150.1, 139.8, 137.2, 136.4, 128.9, 127.7, 122.7, 120.9 (Ar); 54.8 (CH₂); HRMS (ESI⁺): m/z = 211.0984 [M-H]⁺ (C₁₂H₁₁N₄ requires 211.0984).

Lab book reference: BJA-2-100

2-(4'-[(1-(3-[7-(diethylamino)-2-oxo-2H-1-benzopyran]-1H-1,2,3-triazol-4-yl)methyl]phenyl)pyridine (199)



A round-bottomed flask containing 2-(4'-azidomethyl-phenyl)pyridine (1.0 eq., 0.357 mmol, 75.0 mg) was placed under an argon atmosphere and dissolved in dry tetrahydrofuran (3.5 mL). The solution was added to a round-bottomed flask under argon with stirrer bar containing 3-ethynyl-7-(diethylamino)coumarin (1.0 eq., 0.357 mmol, 86.1 mg) and CuI (0.2 eq., 0.073 mmol, 14.0 mg). DIPA (1.0 eq., 0.357 mmol, 50 μ L) was added dropwise. The reaction mixture was stirred at room temperature for 6 hours whereupon the reaction was adjudged to be complete by TLC. A colour change of the reaction mixture from yellow to orange was observed over this period.

The reaction mixture was quenched with CH_2Cl_2 (20 mL) and saturated aqueous NH_4Cl (40 mL) was added. The product was extracted into CH_2Cl_2 (3×20 mL) dried over MgSO_4 , filtered and the solvent removed on the rotary evaporator. The product was isolated by silica gel flash chromatography using EtOAc to afford the *title compound* as a yellow solid (124 mg, 77% yield).

M.P.: 196-201 $^\circ\text{C}$; R_f = 0.18 (petrol/EtOAc 1:1 v/v); ^1H NMR (400 MHz, CD_2Cl_2) δ (ppm) = 8.63 (apr. dt, J = 5.0, 1.5 Hz, 1H, Ar-H), 8.55 (s, 1H, Ar-H), 8.23 (s, 1H, Ar-H), 8.01 (dt, J = 8.5, 2.0 Hz, 2H, Ar-H), 7.76-7.70 (m, 2H, Ar-H), 7.42-7.37 (m, 3H, Ar-H), 7.24-7.19 (m, 1H), 6.63 (dd, J = 9.0, 2.5 Hz, 1H, Ar-H), 6.49 (d, J = 2.5 Hz, 1H, Ar-H), 5.59 (s, 2H, CH_{79r}), 3.40 (q, J = 7.0 Hz, 4H, NCH_2), 1.18 (t, J = 7.0 Hz, 6H, CH_3); ^{13}C NMR (126 MHz, CDCl_3) δ (ppm) = 161.0, 156.9, 156.3, 151.1, 150.1, 142.7, 140.1, 138.7, 137.2, 135.7, 129.8, 128.8, 127.9, 122.9, 122.7, 120.9, 111.1, 109.6, 109.0, 97.4 (Ar); 54.2 (benzylic CH_2); 45.2 ($\underline{\text{C}}\text{H}_2\text{CH}_3$); 12.8 ($\text{CH}_2\underline{\text{C}}\text{H}_3$); HRMS (ESI $^+$): m/z = 452.2095 [$\text{M}-\text{H}$] $^+$ ($\text{C}_{27}\text{H}_{26}\text{N}_5\text{O}_2$ requires 452.2087); IR (CH_2Cl_2 , cm^{-1}): 3008 (w), 2979 (m), 1715 (vs), 1607 (s), 1507 (w), 1471 (w), 1414 (w), 1355 (w), 1189 (w), 1134 (w).

Lab book reference: BJA-2-101

Appendix 1: Published Paper

This Appendix contains the paper published with the contribution of the author in connection with the work described in this Thesis:

B. J. Aucott, J. S. Ward, S. G. Andrew, J. Milani, A. C. Whitwood, J. M. Lynam, A. Parkin and I. J. S. Fairlamb, *Inorg. Chem.*, 2017, **56**, 5431–5440

Redox-Tagged Carbon Monoxide-Releasing Molecules (CORMs): Ferrocene-Containing $[\text{Mn}(\text{C}^{\wedge}\text{N})(\text{CO})_4]$ Complexes as a Promising New CORM Class

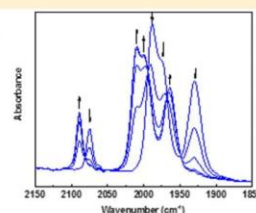
Benjamin J. Aucott,¹ Jonathan S. Ward, Samuel G. Andrew, Jessica Milani, Adrian C. Whitwood, Jason M. Lynam,^{1*} Alison Parkin,^{1*} and Ian J. S. Fairlamb^{1*}

Department of Chemistry, University of York, York, YO10 5DD, United Kingdom

Supporting Information

ABSTRACT: This study describes the synthesis and characterization of a new class of ferrocene-containing carbon monoxide-releasing molecules (CORMs, 1–3). The ferrocenyl group is both a recognized therapeutically viable coligand and a handle for informative infrared spectroelectrochemistry. Deoxymyoglobin CO-release assays and in situ infrared spectroscopy confirm compounds 2 and 3 as photoCORMs and 1 as a thermal CORM, attributed to the increased sensitivity of the Mn–ferrocenyl bond to protonation in 1. Electrochemical and infrared spectroelectrochemical experiments confirm a single reversible redox couple associated with the ferrocenyl moiety with the Mn tetracarbonyl center showing no redox activity up to +590 mV vs Fc/Fc⁺, though no concomitant CO release was observed in association with the redox activity. The effects of linker length on communication between the Fe and Mn centers suggest that the incorporation of redox-active ligands into CORMs focuses on the first coordination sphere of the CORM. Redox-tagged CORMs could prove to be a useful mechanistic probe; our findings could be developed to use redox changes to trigger CO release.

Ferrocenyl manganese(I) carbonyl CORMs



INTRODUCTION

Carbon monoxide (CO) is produced endogenously by mammals. The largest source of CO generation is the heme oxygenase (HO) family of enzymes, involved in the catabolism of heme.¹ Two heme oxygenase isoforms are known to catalyze this reaction: the inducible HO1 and the constitutive HO2.¹ A third, HO3, has been characterized to a lesser extent.² Studies of the ubiquitous HO1 show that this enzyme is upregulated during stress and plays a vital role in the biochemical response to many forms of stress.^{3,4}

The status of CO as a biochemical signaling molecule and the beneficial effects of exogenous CO are becoming established,^{5,6} including antimicrobial,^{7,8} antimalarial,⁹ and vasodilatory¹⁰ effects. Thus, the use of therapeutic CO represents an intriguing area of study in drug discovery. The administration of CO gas presents challenges in terms of localization and selectivity, in addition to engineering difficulties. An alternative approach is to employ carbon monoxide-releasing molecules (CORMs).¹¹ These compounds, predominantly metal carbonyl complexes, are designed to achieve controlled CO delivery, to specific tissue and cellular targets, for therapeutic prodrug applications.¹² The incorporation of redox-active ligands into CORMs could provide an alternative trigger for CO release. In addition to providing a conceivable way of modulating CO-release rates, redox-active

groups could also provide an additional mechanistic handle for the CO-release mechanism, which is often difficult to pin down.

Various methods have been used to promote CO release, including thermal, enzymatic, and photochemical triggers. Early work by Motterlini and co-workers involved simple structures such as the DMSO-soluble complexes $[\text{RuCl}_2(\text{CO})_3]_2$, $\text{Fe}(\text{CO})_5$, and $\text{Mn}_2(\text{CO})_{10}$, of which the latter two complexes require photolysis to deliver CO to myoglobin.¹³ Crucially, this work demonstrated that the vasodilatory and antihypertensive effects of HO1 could also be conferred by CO delivery from CORMs. The first water-soluble CORM, *fac*- $[\text{Ru}(\text{CO})_3\text{Cl}(\text{glycinate})]$ (CORM-3),¹⁴ has since become widely used to study the effects of CO release on biological systems.

In recent years, there has been considerable interest in photochemical CO release from so-called photoCORMs (Figure 1). A diverse array of metals and coligands has been employed, as comprehensively discussed in several recent reviews.^{15–18}

Many photoCORMs employ Mn(I) chemistry due to the thermal stability associated with this oxidation state, the relative ease of synthesis and handling, and the typically low toxicity of these compounds.^{19,20} This has allowed for further functionalization to improve selectivity and alter the CO release

Received: February 28, 2017

Published: April 19, 2017

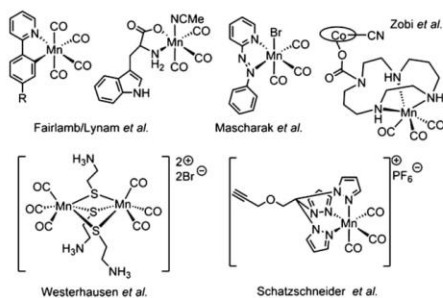


Figure 1. Selected Mn-containing photoCORMs.

properties. Schatzschneider and co-workers synthesized a versatile photoCORM based on a $[\text{Mn}(\text{CO})_3(\text{tpm})]^+$ scaffold [where tpm = tris(pyrazolyl)methane]. The tpm backbone allowed installation of an alkynyl group for further functionalization with peptides.²¹ Zobi and co-workers took a comparable approach in their synthesis of CORM conjugates with cobalamin.²² Mascharak and co-workers have combined theoretical and experimental approaches to better understand the photochemical properties of some Mn(I) tricarbonyl photoCORMs, leading to the development of one class of visible-light-triggered photoCORMs.²³ Soluble, water-stable, and nontoxic Mn(I) tricarbonyl complexes of amino acids^{19,24} and recently dinuclear complexes with cysteamine²⁰ have also been developed as photoCORMs with desirable properties. Fairlamb and co-workers additionally reported Mn(I) tetracarbonyl species bearing a readily functionalizable cyclo-manganated 2-phenylpyridine ligand, which can be functionalized to improve water solubility²⁵ and enable further conjugation via Suzuki couplings.²⁶

Complementary to the advances in photoCORMs is the drive to develop other mechanisms for triggering CO release. One such possibility is redox-triggered CO release. Many changes of state of both healthy and diseased cells are accompanied by a change in cellular redox balance.²⁷ It is therefore desirable to produce CORMs sensitive to a redox environment. Depending on the target, both oxidative and reductive mechanisms may be desirable. For example, reductive activation of other classes of anticancer compounds is already established,²⁸ while some ferricinium salts have been shown to have increased antitumor activity compared to ferrocene.²⁹

Taking forward structures related to those tested by Lynam and co-workers,³⁰ Pryce and co-workers demonstrated that a $\text{Cr}(\text{CO})_5(\text{aminocarbene})$ complex slowly releases 1 equiv of CO upon electrochemical oxidation.³¹ Further examples and mechanistic investigation are required to inform the design of future redox-triggered CORMs.

In designing a CORM, there is inherently a compromise between the inclusion of multiple equivalents of CO and the tendency of CO ligands to stabilize low oxidation states, shifting the redox potential. Controllable redox activity at the metal carbonyl center at a biologically relevant redox potential is challenging as a result of this.

In this work, three ferrocenyl-substituted CORMs, 1–3, based on the parent structure of the air- and water-stable photoCORM $\text{Mn}(\text{CO})_4(2\text{-phenylpyridine})$, are synthesized (Figure 2). The linker length connecting the Fe and Mn

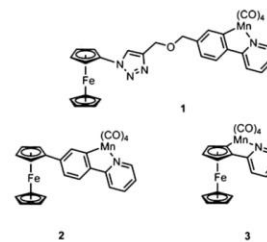


Figure 2. Ferrocenyl CORMs synthesized in this work. Note: complex 3 is racemic (planar chirality).

centers is varied and the electrochemical, photochemical, and CO-release properties are assessed. The reporter properties of both the metal carbonyl center and the ferrocenyl tag enable the effect of linker length on communication between the Fe and Mn centers to be studied. The ferrocenyl moiety can also be considered as a therapeutically active coligand complementary to CO; derivatives of ferrocene are validated as therapeutics, including anticancer³² and antimalarial³³ agents.

EXPERIMENTAL SECTION

Reagents and Solvents. Reactions in O_2 -free or anhydrous conditions were performed with dry, deoxygenated solvents under an inert atmosphere, using either standard Schlenk techniques (under N_2) or a balloon (of argon), as specified in the procedures. Commercial chemicals were purchased from either Acros Organics, Alfa Aesar, Fluorochem, or Sigma-Aldrich and were used without further purification unless otherwise stated. Dry Et_2O , THF, toluene, dichloromethane, and hexane were dispensed from a Pure Solv MD-7 solvent machine and stored in oven-dried ampules under N_2 . Dry THF and Et_2O were then deoxygenated by bubbling with N_2 and sonication. Water, EtOH, and tBuOH were deoxygenated by vigorous bubbling of N_2 through the solution for at least 1 h. "Petrol" refers to petroleum ether (by 40–60 °C).

Nuclear Magnetic Resonance Spectroscopy. Solution ^1H and ^{13}C NMR analysis was carried out at 298 K on JEOL ESC400/ESX400 and Bruker AV500/AV700 spectrometers. The spectra were processed by MNova software. All coupling constants are quoted to the nearest 0.5 Hz. All chemical shifts are reported in ppm and are referenced to the residual NMR solvent (^1H : CDCl_3 , 7.26 ppm; $\text{DMSO}-d_6$, 2.50 ppm; $\text{MeOH}-d_4$, 3.31 ppm; CD_2Cl_2 , 5.32 ppm. ^{13}C : CDCl_3 , 77.36 ppm; $\text{DMSO}-d_6$, 39.52 ppm; $\text{MeOH}-d_4$, 49.00 ppm; CD_2Cl_2 , 53.49 ppm). The ^{13}C NMR spectra of some tetracarbonyl manganese(I) complexes did not show the metal carbonyl resonances due to the long relaxation times of metal carbonyls. In such cases, infrared spectroscopic analysis confirmed the presence of these metal carbonyls.

Infrared Spectroscopy. Spectra were recorded on a Bruker Alpha IR spectrometer, usually at a resolution of 4 cm^{-1} . Details of the method (ATR, transmission cell, solvent etc.) are given next to the data. Peak intensities are grouped qualitatively as very strong (vs), strong (s), medium (m), and weak (w), according to common convention.

Mass Spectrometry. Mass spectrometry was carried out using a Bruker microTOF spectrometer in positive ion mode using electrospray ionization (ESI) or liquid injection field desorption ionization (LIFDI) as the ionization methods. High-resolution ESI data are within 5 ppm error of the theoretical value unless otherwise stated. All LIFDI data are within 120 ppm error.

Elemental Analysis. Elemental analyses were performed on an Exeter Analytical CE-440 elemental analyzer. The quoted percentage compositions of C, H, and N are the average of two experiments.

UV-Visible Spectroscopy. All UV-visible spectra were recorded with a JASCO V-560 spectrometer using standard methods. Extinction coefficients (ϵ) were calculated by fitting measured absorbance to the Beer-Lambert law using at least five different concentrations.

Melting Point Determination. Melting points were measured on a Stuart SMP30 apparatus (ramp rates of 2 or 3 °C min⁻¹) or using differential scanning calorimetry (DSC) on a PerkinElmer DSC7 machine calibrated with an indium standard. The DSC experiments were run at a ramp rate of 10 °C min⁻¹, and the melting point was taken as the onset of the observed endothermic peak.

Chromatography. Thin-layer chromatography (TLC) was carried out using aluminum-backed TLC plates (5554, Merck). Visualization was by quenching of fluorescence using a lamp with $\lambda_{\text{max}} = 254$ nm. Flash column chromatography was performed using silica gel 60 (Fluorochem, particle size 40–63 μm).

X-ray Crystallography. Single crystals were grown in ambient conditions using dichloromethane/pentane layering or slow evaporation. A suitable crystal was selected and mounted on an Oxford Diffraction SuperNova (Cu at zero, the orientation of the Cu source relative to the goniometer axes in the dual-source SuperNova X-ray diffractometer; the molybdenum source is offset relative to the goniometer axes), with an Eos diffractometer. The crystal was kept at 110 K during data collection. Using Olex2,³⁴ the structures were solved with the ShelXS³⁵ structure solution program using the Patterson method or Superflip using charge flipping. The structures were refined with the ShelXL³⁶ refinement package using least squares minimization.

Myoglobin CO-Release Assay. Experiments and data analysis were performed according to the procedures described previously.³⁷

Electrochemistry. Cyclic voltammograms were recorded in a three-electrode cell comprising a Pt disk working electrode, a Pt wire counter electrode, and an Ag wire pseudo-reference electrode. Each analyte was calibrated to the FeCp₂/FeCp₂⁺ redox couple by the addition of ferrocene or acetylferrocene [Fe(η -C₅H₄COMe)Cp]/[Fe(η -C₅H₄COMe)Cp]⁺ measured to be +276 mV vs FeCp₂/FeCp₂⁺ to enable potentials to be quoted against FeCp₂/FeCp₂⁺. All voltammograms were performed in the presence of NBu₄PF₆ at a concentration of 1 M, with a scan rate of 100 mV s⁻¹.

Synthetic Procedures and Characterization (General Procedure 1). This general procedure for cyclomanganation with BnMn(CO)₅ is referred to elsewhere as "general procedure 1".³⁸ A typical reaction was conducted on a 0.5 mmol scale. To an oven-dried Schlenk tube containing a stirrer bar, BnMn(CO)₅ (1 equiv), and "CH^{^N}" ligand (1 equiv) was added dry, deoxygenated hexane (16 mL/mmol of BnMn(CO)₅) via syringe. The solution was heated to reflux for between 6 and 24 h (covered in aluminum foil to exclude ambient light). Reaction progress was monitored by IR spectroscopic analysis by taking aliquots directly from the reaction mixture. On reaction completion, the mixture was allowed to cool to room temperature and then filtered through a pipet packed with cotton wool. Any solid product that precipitated out of solution was dissolved in a small amount of CH₂Cl₂. The solvent was removed in vacuo to afford the product. Where required, further purification was performed using flash column chromatography.

2-(4'-[(3'-Triisopropylsilyl-prop-2'-ynyl-oxy)methyl]phenyl)pyridine (4). To an oven-dried Schlenk tube containing a solution of 2-(4'-[(prop-2'-ynyl-oxy)methyl]phenyl)pyridine (1.0 equiv, 3.87 mmol, 0.865 g) in dry, deoxygenated THF (40 mL) at -78 °C was added a solution of LDA (1.0 equiv, 3.87 mmol, 9.6 mL) in THF via syringe over 5 min. The LDA was freshly prepared by lithiation of freshly distilled diisopropylamine with *n*-BuLi (titrated against *n*-benzylbenzamide before use).³⁹ After the addition of LDA was complete, the Schlenk tube was placed in an ice/water bath at 0 °C for 10 min before being cooled back to -78 °C for the addition of TIPS-Cl (1.0 equiv, 3.87 mmol, 0.84 mL). The reaction mixture was then allowed to warm (to rt) and left for 19 h, at which point TLC analysis indicated reaction completion. The reaction was quenched using saturated ammonium chloride (30 mL) and extracted with Et₂O (3 × 50 mL). The combined organic layers were washed with water (30 mL) and brine (30 mL), before being dried (MgSO₄) and filtered. The solvent was

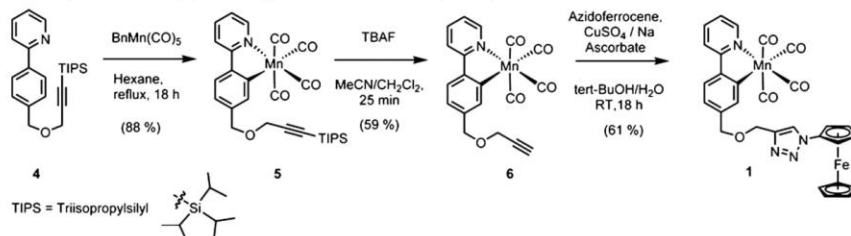
removed in vacuo to give the crude product, which was purified by flash column chromatography on silica, eluting with petrol and then petrol/Et₂O 4:1 v/v. The solvent was removed in vacuo to give the title compound as a yellow oil (1.25 g, 85% yield). ¹H NMR (400 MHz, CDCl₃): δ (ppm) = 8.69 (ddd, 5.0, 2.0, 1.0 Hz, 1H, Ar-H), 7.99 (d, 8.5 Hz, 2H, Ar-H), 7.77–7.71 (m, 2H, Ar-H), 7.47 (d, 8.0 Hz, 2H, Ar-H), 7.22 (ddd, 5.5, 5.0, 2.5 Hz, 1H, Ar-H), 4.70 (s, 2H, CH₂), 4.23 (s, 2H, CH₂), 1.09 (m, 21 H, CH and CH₃ from TIPS). ¹³C NMR (101 MHz, CDCl₃): δ (ppm) = 157.7, 150.2, 139.4, 138.8, 137.2, 129.0, 127.4, 122.5, 120.9 (Ar); 103.4 (C≡C-Si); 88.4 (C≡C-Si); 70.7 (benzylic CH₂); 57.8 (propargylic CH₂), 18.4 (TIPS CH₃); 11.0 (TIPS CH). HRMS (ESI⁺): m/z = 380.2391 [MH]⁺ (C₂₃H₃₁NO requires 380.2410). IR (CH₂Cl₂, cm⁻¹): 2170 (w), 1703 (w), 1603 (w), 1589 (w), 1580 (w), 1565 (w), 1468 (s), 1436 (m), 1384 (w), 1351 (m), 1210 (w), 1153 (w), 1079 (s), 1029 (w), 1017 (w), 998 (m), 991 (m).

Tetracarbonyl 2-(4'-[(3'-Triisopropylsilyl-prop-2'-ynyl-oxy)methyl]phenyl)- κ -C²-pyridine- κ ,N Manganese(I) (5). Using general procedure 1, BnMn(CO)₅ (1 equiv, 2.93 mmol, 840 mg) and 2-(4'-[(3'-triisopropylsilyl-prop-2'-ynyl-oxy)methyl]phenyl)pyridine (0.96 equiv, 2.82 mmol, 1.07 g) were reacted in hexane (40 mL). The title compound was isolated as a yellow solid (1.35 g, 88% yield) with no additional purification required. Mp: 82 °C (DSC). ¹H NMR (400 MHz, CDCl₃): δ (ppm) = 8.72 (d, 5.5 Hz, 1H, Ar-H), 7.92 (s, 1H, Ar-H), 7.87 (d, 8.0 Hz, 1H, Ar-H), 7.82–7.75 (m, 2H, Ar-H), 7.20 (dd, 8.0, 1.5 Hz, 1H, Ar-H), 7.11 (ddd, 7.5, 5.0, 1.5 Hz, 1H, Ar-H), 4.70 (s, 2H, CH₂), 4.30 (s, 2H, CH₂), 1.11 (m, 21H, CH and CH₃ from TIPS). ¹³C NMR (101 MHz, DMSO-*d*₆): δ (ppm) = 220.0, 214.5, 213.4 (Mn-C≡O); 172.5, 164.7, 154.4, 145.9, 140.9, 139.1, 139.0, 124.5, 124.0, 123.7, 120.0 (Ar); 104.3 (C≡C-Si); 86.8 (C≡C-Si); 70.5 (benzylic CH₂); 57.3 (propargylic CH₂); 18.4 (TIPS CH₃); 10.6 (TIPS CH). HRMS (ESI⁺): m/z = 568.1327 [MNa]⁺ (C₂₈H₃₃MnNaO₅Si requires 568.1328). Elemental analysis (CHN): C 61.48%, H 5.91%, N 2.51% (C₂₈H₃₃NO₅SiMn requires C 61.64%, H 5.91%, N 2.57%). IR (CH₂Cl₂, cm⁻¹): 3685 (w), 3157 (w), 2961 (m), 2946 (m), 2927 (m), 2893 (m), 2866 (m), 2076 (s), 1991 (vs), 1976 (vs), 1933 (vs), 1605 (m), 1587 (m), 1567 (m), 1479 (m), 1467 (m), 1351 (s).

Tetracarbonyl 2-(4'-[(Prop-2'-ynyl-oxy)methyl]phenyl)- κ -C²-pyridine- κ ,N Manganese(I) (6). To a solution of tetracarbonyl 2-(4'-[(3'-triisopropylsilyl-prop-2'-ynyl-oxy)methyl]phenyl)- κ -C²-pyridine- κ ,N manganese(I) (1 equiv, 1.10 mmol, 599 mg) in CH₂Cl₂ (2 mL) was added a solution of TBAF·3H₂O (1.2 equiv, 1.32 mmol, 417 mg) in CH₃CN (10 mL). The brown solution was stirred under air for 25 min, at which time the reaction was judged complete (TLC analysis). Water (10 mL) was added and the mixture extracted with CH₂Cl₂ (3 × 15 mL). The combined organic layers were dried (MgSO₄) and filtered. The solvent was removed in vacuo to yield the crude product, which was purified by flash column chromatography on silica gel, starting with petrol/EtOAc 10:1 v/v and increasing the gradient slightly to 10:1.5 v/v to afford the product. The solvent was removed in vacuo to give the title compound as a light brown solid (0.253 g, 59% yield). Mp: 107 °C (dec). ¹H NMR (400 MHz, DMSO-*d*₆): δ (ppm) = 8.76 (d, 5.5 Hz, 1H, Ar-H), 8.24 (d, 8.0 Hz, 1H, Ar-H), 8.07–8.00 (m, 2H, Ar-H), 7.78 (s, 1H, Ar-H), 7.37 (m, 1H, Ar-H), 7.12 (dd, 1.0, 8.0 Hz, 1H, Ar-H), 4.57 (s, 2H, CH₂), 4.25 (t, 2.5 Hz, 2H, CH₂), 3.52 (d, 2.5 Hz, 1H, C≡C-H). ¹³C NMR (101 MHz, CDCl₃): δ (ppm) = 175.4, 166.4, 154.2, 146.1, 141.4, 139.3, 138.2, 124.3, 124.3, 122.7, 119.7 (Ar); 80.1, 75.0, 72.3, 57.8 (propargylic CH₂). IR (CH₂Cl₂, cm⁻¹): 3664 (w), 3302 (w), 2964 (m), 2945 (m), 2929 (w), 2893 (m), 2866 (m), 2075 (s), 1991 (vs), 1976 (vs), 1932 (vs), 1605 (m), 1588 (m), 1566 (w), 1478 (m), 1468 (m). HRMS (ESI⁺): m/z = 411.9992 [MNa]⁺ (C₁₉H₁₃MnNaO₅ requires 411.9994). Elemental analysis (CHN): C 58.58%, H 3.23%, N 3.48% (C₁₉H₁₃NO₅Mn requires C 58.62%, H 3.11%, N 3.60%).

Tetracarbonyl 2-[4'-[(1-(Ferrocenyl)-1H-1,2,3-triazol-4-yl]methoxy)methyl]phenyl]- κ -C²-pyridine- κ ,N Manganese(I) (7). To a solution of tetracarbonyl 2-(4'-[(prop-2'-ynyl-oxy)methyl]phenyl)- κ -C²-pyridine- κ ,N manganese(I) (1.0 equiv, 0.2 mmol, 78 mg) in *N*₂-saturated ¹BuOH (3 mL) were added azidoferrrocene (1.0 equiv, 0.2

Scheme 1. Synthesis of Alkynyl Building Block 6 and Ferrocenyl Complex 1



mmol, 46 mg) and water (2.7 mL). Copper(II) sulfate (0.3 equiv, 0.06 mmol, 200 μ L of 300 mM aqueous solution) and sodium ascorbate (0.6 equiv, 0.12 mmol, 120 μ L of 500 mM aqueous solution) were added, and the reaction mixture was stirred at room temperature in the dark under an argon balloon. After 24 h, the reaction mixture was diluted with water (20 mL). The product was extracted with EtOAc (4 \times 20 mL). The combined organic layers were dried with MgSO₄ and filtered, before removal of the solvent yielded the crude product. The crude product was purified by flash column chromatography on silica, using petrol/EtOAc, starting with 3:2 v/v and moving to 1:1 v/v to elute the product. The solvent was removed to give the title compound (74 mg, 60% yield) as a yellow crystalline solid. Mp: 143 °C (dec). ¹H NMR (700 MHz, CDCl₃): δ (ppm) = 8.72 (d, 5.5 Hz, 1H, Ar-H), 7.97 (d, 1.5 Hz, 1H, Ar-H), 7.89–7.86 (m, 1H, Ar-H), 7.84 (s, 1H, Ar-H), 7.81–7.76 (m, 2H, Ar-H), 7.21 (dd, 8.0, 1.5 Hz, 1H, Ar-H), 7.12 (ddd, 7.0, 5.5, 1.5 Hz, 1H, Ar-H), 4.83 (t, 2.0 Hz, 2H, Cp-H), 4.82 (s, 2H, CH₂), 4.71 (s, 2H, CH₂), 4.26 (t, 2.0 Hz, 2H, Cp-H), 4.22 (s, 5H, Cp-H). ¹³C NMR (176 MHz, CDCl₃) δ (ppm) = 220.3, 214.1, 214.0 (M–C≡O); 175.1, 166.1, 154.0, 145.9, 145.5, 140.7, 139.6, 138.0, 124.2, 123.9, 122.5, 122.3, 119.5 (Ar); 94.0 (Cp); 73.0 (CH₂); 70.3 (Cp); 66.8 (Cp); 64.2 (CH₂); 62.3 (Cp). HRMS (ESI⁺): m/z = 617.0292 [MH]⁺ (C₂₉H₂₂N₄O₃MnFe requires 617.0315). IR (CH₂Cl₂, cm⁻¹): 3048 (w), 2864 (w), 2076 (s), 1991 (vs), 1977 (vs), 1931 (s), 1606 (m), 1587 (m), 1567 (w), 1519 (w), 1472 (m), 1432 (w), 1312 (w), 1108 (m). Elemental analysis (CHN): C 56.28%, H 3.48%, N 8.69% (C₂₉H₂₁N₄O₃MnFe requires C 56.52%, H 3.44%, N 9.09%). UV–visible: λ_{max} = 270 nm, ϵ (270 nm) = 28 500 dm³ mol⁻¹ cm⁻¹. R_f : 0.40 (petrol/EtOAc 3:2 v/v).

[4-(2'-Pyridinyl)phenyl]ferrocene (8). To an oven-dried Schlenk tube with stirrer bar were added 2-(4-bromophenyl)pyridine (1.0 equiv, 1.0 mmol, 234 mg), ferroceneboronic acid (2.0 equiv, 2.0 mmol, 461 mg), Pd(OAc)₂ (0.053 equiv, 0.053 mmol, 11.9 mg), PPh₃ (0.21 equiv, 0.21 mmol, 55.5 mg), and K₂CO₃ (4.0 equiv, 4.0 mmol, 555 mg). Anhydrous, deoxygenated toluene (10 mL) was added in one portion via syringe. The red reaction mixture was refluxed for 20 h, at which point TLC analysis showed complete consumption of the starting material and the appearance of a product spot. The reaction mixture was allowed to cool and the toluene was removed in vacuo. The mixture was resuspended in CHCl₃ (100 mL) and washed with water (2 \times 100 mL). The combined organic extract was dried (MgSO₄) and filtered. The solvent was removed in vacuo and the crude product was purified by flash column chromatography on silica gel using petrol/EtOAc, starting with 9:1 v/v and increasing the gradient to 8:2 v/v. Removal of the solvent in vacuo gave the title compound as an orange powder (173 mg, 55% yield). Mp: 122 °C. ¹H NMR (400 MHz, CDCl₃): δ (ppm) = 8.69 (d, 4.5 Hz, 1H, Ar-H), 7.93 (d, 8.0 Hz, 2H, Ar-H), 7.73 (d, 4.0 Hz, 2H, Ar-H), 7.58 (d, 8.0 Hz, 2H, Ar-H), 7.21 (dd, 9.0, 4.0 Hz, 1H, Ar-H), 4.71 (t, 2.0 Hz, 2H, Cp-H), 4.36 (t, 2.0 Hz, 2H, Cp-H), 4.05 (s, 5H, Cp-H). ¹³C NMR (101 MHz, CDCl₃) δ (ppm) = 157.4, 149.8, 140.5, 136.9, 136.8, 127.0, 126.4, 121.0, 120.3 (Ar); 84.6, 69.8, 69.3, 66.7 (Cp). HRMS (ESI⁺): m/z = 340.0770 [M – H]⁺ (C₂₁H₁₈FeN requires 340.0789).

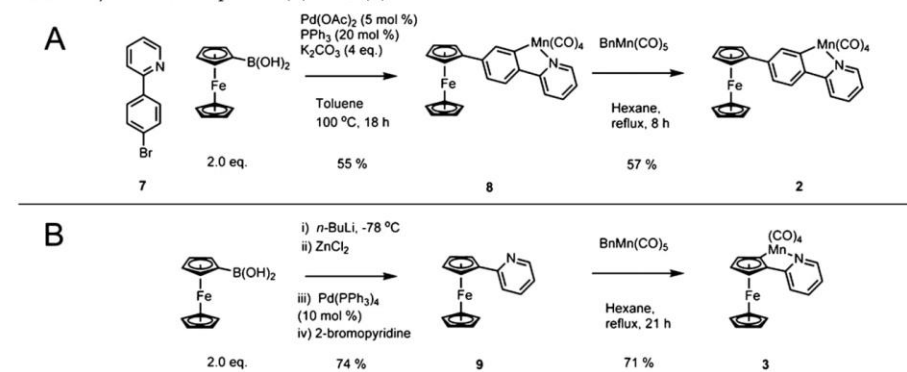
Tetracarbonyl (2-[4-Ferrocenyl]phenyl- κ -C²-pyridine- κ -N) Manganese(I) (2). This reaction was performed using general

procedure 1 with BnMn(CO)₅ (1.0 equiv, 0.25 mmol, 72.5 mg), [4-(2'-pyridinyl)phenyl]ferrocene (1.0 equiv, 0.25 mmol, 84.5 mg), and hexane (4 mL). Infrared spectroscopic analysis showed that the reaction was complete after 6 h. The title compound was purified by flash column chromatography on silica, using petrol and then petrol/EtOAc 9:1 v/v. The solvent was removed in vacuo to afford a red microcrystalline solid (79 mg, 59% yield). Mp: 138 °C (dec). ¹H NMR (700 MHz, CDCl₃): δ (ppm) = 8.70 (d, 5.0 Hz, 1H, Ar-H), 8.12 (s, 1H, Ar-H), 7.84 (d, 8.0 Hz, 1H, Ar-H), 7.77 (apr. t, 1H, Ar-H), 7.68 (d, 8.0 Hz, 1H, Ar-H), 7.28 (s, 1H, Ar-H), 7.08 (dd, 6.5, 6.0 Hz, 1H, Ar-H), 4.77 (t, 2.0 Hz, 2H, Cp-H), 4.37 (t, 2.0 Hz, 2H, Cp-H), 4.09 (s, 5H, Cp-H). ¹³C NMR (176 MHz, CDCl₃) δ (ppm) = 220.4, 214.2, 214.1 (Mn–C≡O); 174.2, 166.2, 153.8, 144.0, 141.4, 139.0, 137.7, 123.9, 122.2, 121.8, 119.0 (Ar); 85.4, 69.8, 69.2, 67.1 (Cp). MS (LIFDI⁺): m/z = 505.04 [M⁺] (C₂₉H₂₁N₄O₃MnFe requires 504.9809). Elemental analysis (CHN): C 59.69%, H 3.27%, N 2.73% (C₂₉H₂₁N₄O₃MnFe requires C 59.44%, H 3.19%, N 2.77%). IR (CH₂Cl₂, cm⁻¹): 2967 (w), 2074 (s), 1990 (s), 1975 (s), 1931 (s), 1733 (w), 1606 (m), 1583 (m), 1563 (m), 1474 (m), 1425 (w).

2-(Ferrocenyl)pyridine (9). Bromoferrocene (1.0 equiv, 1.9 mmol, 513 mg) was stirred in dry ethyl acetate (10 mL) at –78 °C. After the dropwise addition of *n*-BuLi (1.1 equiv, 2.0 mmol, 800 μ L) over 15 min, the solution was allowed to warm to room temperature and stirred for a further 10 min when a bright orange precipitate had formed. The reaction mixture was cooled back to –78 °C and transferred via cannula onto dry ZnCl₂ (2.0 equiv, 3.8 mmol, 518 mg) at –78 °C. After the reaction mixture had been stirred at room temperature for 1 h, it was transferred via cannula to a Schlenk tube containing Pd(PPh₃)₄ (10 mol %, 0.19 mmol, 220 mg), and 2-bromopyridine (2.5 equiv, 4.75 mmol, 450 μ L) was added dropwise. The reaction mixture was stirred at room temperature for 19 h and then quenched with sat. aq. NH₄Cl (15 mL). The aqueous layer was extracted with chloroform (3 \times 10 mL), and the combined organic layers were dried with MgSO₄ and filtered. Removal of the solvent in vacuo gave an orange powder. Further purification by silica gel flash column chromatography using petrol/EtOAc 9:1 v/v afforded an analytically pure sample of the title compound as an orange powder (371 mg, 74% yield). Mp: 90–92 °C. ¹H NMR (700 MHz, CD₂Cl₂): δ (ppm) = 8.51 (ddd, 5.0, 2.0, 1.0 Hz, 1H, Ar-H), 7.57 (ddd, 8.0, 7.5, 1.0 Hz, 1H, Ar-H), 7.41 (ddd, 8.0, 1.0, 1.0 Hz, 1H, Ar-H), 7.06 (ddd, 7.5, 5.0, 1.0 Hz, 1H, Ar-H), 4.92 (dd, 2.0, 2.0 Hz, 2H, Cp-H), 4.40 (dd, 2.0, 2.0 Hz, 2H, Cp-H), 4.05 (s, 5H, Cp-H). ¹³C NMR (176 MHz, CD₂Cl₂) δ (ppm) = 159.3, 149.4, 136.0, 120.6, 120.2 (Ar); 83.7, 70.0, 69.7, 67.3 (Cp). HRMS (ESI⁺): m/z = 264.0473 [M – H]⁺ (C₁₅H₁₄NFe requires 264.0470). IR (CH₂Cl₂, cm⁻¹): 1609 (m), 1588 (w), 1574 (w), 1469 (m), 1434 (m), 1277 (w). UV–visible: λ_{max} = 314 nm, ϵ (314 nm) = 22 900 dm³ mol⁻¹ cm⁻¹; 378 nm, ϵ (378 nm) = 8000 dm³ mol⁻¹ cm⁻¹; 460 nm, ϵ (460 nm) = 2040 dm³ mol⁻¹ cm⁻¹.

(\pm)-Tetracarbonyl (2-Ferrocenyl- κ -C²-pyridine- κ -N) Manganese(I) (3). This reaction was performed using general procedure 1 with BnMn(CO)₅ (1.0 equiv, 2.3 mmol, 65.2 mg), 2-(ferrocenyl)pyridine (1.0 equiv, 0.23 mmol, 60.0 mg), and hexane (6 mL). Infrared spectroscopic analysis showed that the reaction was complete after 6 h. The title compound was purified by flash column chromatography on

Scheme 2. Synthesis of Complexes 2 (A) and 3 (B)



silica using petrol/Et₂O/NEt₃ 94:5:1 v/v to afford a dark red solid (67.2 mg, 71% yield). Mp: 109–111 °C. ¹H NMR (700 MHz, CD₂Cl₂): δ (ppm) = 8.50 (d, 5.0 Hz, 1H, Ar–H), 7.65 (ddd, 8.0, 7.5, 1.0 Hz, 1H, Ar–H), 7.41 (d, 8.0 Hz, 1H, Ar–H), 7.02 (ddd, 7.5, 5.0, 1.0 Hz, 1H, Ar–H), 4.93 (d, 2.0 Hz, 1H, Cp–H), 4.66 (dd, 2.0, 2.0 Hz, 1H, Cp–H), 4.56 (d, 2.0 Hz, 1H, Cp–H), 4.07 (s, SH). ¹³C NMR (176 MHz, CD₂Cl₂): δ (ppm) = 221.1, 213.2, 212.3, 211.7 (Mn–C≡O); 169.0, 154.4, 137.5, 120.2, 119.5 (Ar); 103.1, 90.5, 77.4, 72.4, 69.6, 65.2 (Cp). MS (LIFDI⁺): *m/z* = 426.9565 [M⁺]. C₁₉H₁₂NO₂MnFe requires 426.9543. Elemental analysis (CHN): C 53.00%, H 2.91%, N 3.20% (C₁₉H₁₂NO₂MnFe requires C 53.18%, H 2.82%, N 3.26%). IR (CH₂Cl₂, cm⁻¹): 2077 (s), 1988 (vs), 1976 (vs), 1932 (vs), 1607 (m), 1498 (s). UV–visible: λ_{max} = 292 nm, ε(292 nm) = 18 300 dm³ mol⁻¹ cm⁻¹; 486 nm, ε(486 nm) = 1230 dm³ mol⁻¹ cm⁻¹. R_f: 0.28 (petrol/Et₂O 9:1 v/v).

RESULTS AND DISCUSSION

Compound **1**, which accommodates the ferrocenyl group in the most remote location relative to the Mn(I) center, was synthesized by employing the versatile alkynyl building block **6** (Scheme 1).

Complex **6** could not be synthesized directly by cyclomanganation of the corresponding terminal alkyne. On the basis of work by Nicholson and co-workers,⁴⁰ we hypothesized that addition of the alkyne into the Mn(I) center could compete with coordination of the pyridyl nitrogen directing group. The poor functional group tolerance of such a side reaction to bulky silyl substituents on the alkyne was exploited as a protecting group strategy, affording TIPS analogue **5** in 88% yield. Deprotection affords alkyne **6**, a readily functionalizable building block for the synthesis of remotely conjugated modular CORMs complementary to the current libraries. Alkyne **6** was shown to be a viable reagent in a copper-catalyzed azide–alkyne cycloaddition (CuAAC) reaction. Reaction with azidoferrrocene afforded the triazole product **1** in 61% yield after flash column chromatography. An alternative route may be envisaged whereby the click conjugation takes place before the cyclomanganation, although we anticipate that this would present a challenge for the inclusion of more-water-soluble derivatives, due to the nonpolar solvents typically employed in the cyclomanganation step. Compound **2** (Scheme 2), in which the ferrocenyl group is conjugated to the 2-phenylpyridyl ligand, was accessed via a Suzuki–Miyaura

coupling of aryl bromide **7** to afford ferrocenyl ligand **8** in an acceptable yield of 55%.

The yield represents a slight improvement on the previously reported Grignard-based synthesis of this molecule, where the reported yield was 38%.⁴¹ Late-stage Suzuki coupling of the cyclomanganated derivative of **7**, using ferroceneboronic acid with the conditions of Ward and co-workers,²⁵ was unsuccessful due to degradation of the starting complex at the high reaction temperatures required. With the desired ligand in hand, cyclomanganation with BnMn(CO)₅ proceeded in good yield to afford target **2**.

Finally, compound **3**, incorporating the redox-active moiety in the first coordination sphere of the metal, was synthesized via a Negishi coupling to afford ligand **9** in 74% yield before cyclomanganation with BnMn(CO)₅ to give **3**.

Single crystals of **1**, **2**, and **8** suitable for X-ray diffraction were obtained, either by layering pentane on a concentrated dichloromethane solution of the product (**1**) or by slow evaporation of a chloroform solution (**2** and **8**). Thermal ellipsoid plots are shown for target complexes **1** and **2** in Figure 3; a thermal ellipsoid plot for **8** is provided in the Supporting Information, along with summary data tables for all three structures.

Comparison of **1** and **2** with other Mn(I) phenylpyridine complexes shows the same slight distortion from the idealized octahedral structure at manganese, due to the rigidity of the 2-phenylpyridine system.³⁸ The structures also suggest that the cyclomanganation of **8** forces the pyridyl and phenyl rings to become planar in complex **2**, having been twisted slightly in **8**, the torsion angle increasing from –8.9(6)° in **8** to –20.3(2)° in **2**.

Complexation of the ligands to manganese was also evidenced by NMR and infrared spectroscopies. The ¹H NMR spectra of **3** and **9** in CD₂Cl₂ (Figure 4) showed a significant change in the region of the ferrocenyl protons on the substituted Cp ring. The two triplets at δ = 4.92 and 4.40 ppm were replaced by three resonances each corresponding to a single proton, reflecting the deprotonation and desymmetrization of this ring upon cyclomanganation. Smaller changes in chemical shifts were also observed for the protons on the unsubstituted Cp ring and the pyridyl ring.

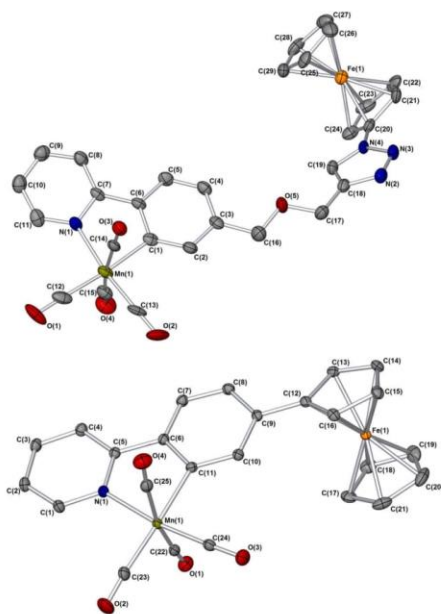


Figure 3. X-ray crystal structures of compounds **1** (top) and **2** (bottom), with hydrogen atoms omitted. Atoms are displayed as thermal ellipsoids at 50% probability.

The infrared spectra of the three complexes all show the expected four carbonyl stretching bands for a C_3 or pseudo- C_{3v} symmetry (vide infra, Table 2). The carbonyl stretches for the three complexes reflect the similarity of the first coordination sphere of the manganese in each of the compounds.

Electrochemical characterization of the three Mn complexes, along with starting materials **8** and **9**, was carried out to understand their redox properties. Cyclic voltammetry was performed on solutions of each complex in dichloromethane. An example voltammogram of **1** is shown in Figure 5.

For each compound, repeated scans showed a single reversible one-electron redox reaction that was attributed to the ferrocenyl portions of the molecules. In each voltammo-

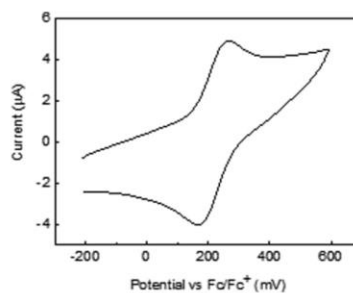


Figure 5. Cyclic voltammogram of a 1 mM dichloromethane solution of **1**. The electrolyte was tetra-*n*-butylammonium hexafluorophosphate, present at a concentration of 1 M, and the scan rate was 100 mV s^{-1} .

gram, the separation between the anodic and cathodic peaks was comparable to that of the ferrocene/ferrocenium calibration run, although solution resistance led to these values being higher than the ideal 59 mV, up to 170 mV.⁴²

The midpoint potentials ($E_{1/2}$) are compiled in Table 1. Triazole **1** displays a relatively high redox potential of +220 mV

Table 1. Midpoint Potentials and Peak Current Ratios of Ferrocenyl Mn Complexes **1–3** and Two Uncomplexed Derivatives (**8** and **9**) in Dichloromethane^a

compd	$E_{1/2}$ (mV)	i_a/i_c
1	+220	1.05
2	+31	0.94
3	-138	1.04
8	+48	1.03
9	+76	0.97

^aPeak currents were calculated by linearly extrapolating the baseline current. The electrolyte was 1 M tetra-*n*-butylammonium hexafluorophosphate. Potentials are referenced against the Fc/Fc^+ redox couple.

vs Fc/Fc^+ , though this is consistent with other ferrocenyl triazoles and is a result of the electron-withdrawing nature of the triazole, which destabilizes the cation relative to the neutral molecule.⁴³ The midpoint potentials for **2** and **8** show a very slight decrease in $E_{1/2}$ of 17 mV upon cyclomanganation. This suggests that the effect of cyclomanganation on the redox properties of ferrocene in this position is small. A similar trend

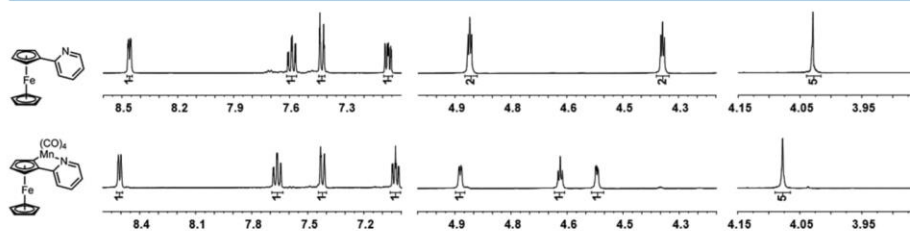


Figure 4. A stack of 700 MHz ^1H NMR spectra showing cyclomanganated complex **3** versus ligand **9**. Spectra were recorded at 298 K in CD_2Cl_2 (the proton integrals are displayed as integers).

is seen upon the reaction of **9** to form **3**, but the incorporation of the ferrocenyl group into the first coordination sphere of the Mn makes this effect much more pronounced with a lowering of $E_{1/2}$ from +76 to -138 mV, both vs Fc/Fc⁺. The change in $E_{1/2}$ implies that the effect of cyclomanganation is to stabilize the cation more than the neutral molecule, so **2** and **3** are more easily oxidized than their counterparts **8** and **9**. It can therefore be concluded that the electron density on the ferrocenyl moiety increases as a result of cyclomanganation.

Repeated scans of each complex were performed, but no new peaks were observed, and the peaks due to the complexes remained, suggesting that **1**–**3** are all stable to repeated oxidation and reduction.

The response of the infrared stretches of the carbonyl stretches to oxidation of the ferrocenyl moiety was assessed by infrared spectroelectrochemistry. The results, shown in Figure 6, demonstrate the importance of the linker length in

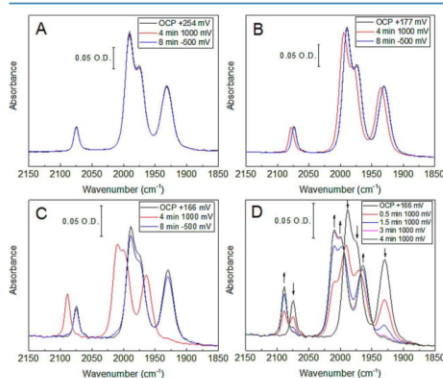


Figure 6. Infrared spectroelectrochemistry of complexes **1**–**3** (panels A–C, respectively). Experiments were performed in dichloromethane at 298 K, at a concentration of 5.0 mM in the presence of 1.0 M tetra-*n*-butylammonium hexafluorophosphate as the electrolyte. Spectra were recorded 240 s after the potential was applied to allow complete electrolysis of the solution to occur. All spectra are subject to a single-point baseline correction at 2050 cm⁻¹. (D) Selected spectra from the oxidation step of panel C showing the isosbestic points.

determining the extent of communication between the iron and manganese centers. The carbonyl bands in complex **1** (Figure 6A), showed no change upon oxidation, confirming that the oxidation is that of the iron center. Complex **2**, with the less remote reporter group (Figure 6B) shows a small increase of around 5 cm⁻¹ in each carbonyl band when oxidized. Complex **3** (Figure 6C) shows much larger shifts of the bands, ranging from 12 to 32 cm⁻¹. Overlaying a series of spectra during the oxidation of **3** (Figure 6D) shows that the oxidized and reduced species share isosbestic points at 2081, 1994, 1968, and 1949 cm⁻¹, suggesting that no other metal carbonyl-containing species are present during this conversion. This remains the case for the reduction back to the neutral species, the spectra for which have been omitted for clarity.

The observed increase in stretching frequency is consistent with the removal of electron density from the manganese, resulting in weaker π -back-bonding to the carbonyl groups.

This is consistent with a through-bond communication between the two metal centers and suggests that redox-active ligands should be incorporated into the first coordination sphere of the manganese carbonyl. Consistent with the reversibility of the single redox process in the voltammetric results, the spectra show that the oxidized ferricenium cation of each complex can be reduced back to the neutral form. There is no electrochemically triggered CO release upon oxidation of the iron center. Despite the lack of redox-triggered CO release, these results demonstrate the communication between the iron redox state and the bonding properties of the metal carbonyls. The infrared stretches of the reduced and oxidized forms of the three complexes are tabulated below (Table 2).

Table 2. Infrared Stretching Frequencies^a for the Neutral and Oxidized Forms of Complexes **1**–**3**

compd	$\nu(\text{CO})$ (cm ⁻¹)
1	2076 (s), 1991 (vs), 1977 (vs), 1931 (s)
1 ⁺	2076 (s), 1991 (vs), 1977 (vs), 1931 (s)
2	2074 (s), 1990 (vs), 1975 (vs), 1931 (s)
2 ⁺	2078 (s), 1995 (vs), 1980 (vs), 1936 (s)
3	2077 (s), 1988 (vs), 1976 (vs), 1932 (s)
3 ⁺	2089 (s), 2010 (vs), 2000 (vs), 1964 (s)

^aRecorded in a dichloromethane solution.

As related Mn(I) tetracarbonyl complexes bearing 2-phenylpyridine-derived ligands have previously been shown to release CO photochemically,²⁵ the light-triggered CO release properties of ferrocenyl complexes **1**–**3** were assessed.

The results in Figure 7 show that **1** is stable in DMSO solution in ambient light for >1 h, but degradation occurs with a half-life of 21 min upon irradiation, as shown by the bleaching of the peaks at 2076, 1990, and 1975 cm⁻¹. The peak at 1931 cm⁻¹ changes only slightly during the irradiation, suggesting that another peak grows in near this wavenumber from the photoproduct. New peaks rapidly grow in at 2012 and 1904 cm⁻¹, indicating that a metal-carbonyl-containing photoproduct accumulates. The three bands are consistent with the formation of a pseudo-C_{3v} symmetric tricarbonyl species in which a DMSO solvent molecule has substituted one of the *trans*-carbonyl ligands. The sulfur-oxygen stretching mode for a bound DMSO was not observed at the concentrations studied. This intermediate then degrades over a longer time scale, as another peak grows in at 1862 cm⁻¹. A very similar result was obtained for the degradation of complex **2**, suggesting that the triazole moiety of **1** does not coordinate to the Mn as part of the degradation process.

Direct observation of CO release from **2** was carried out in water using the well-established UV-visible myoglobin CO release assay (Figure 8). Complex **2** is stable in water in the absence of light, with CO release photochemically triggered by 400 nm LED irradiation. An assay using 40 μM **2** and ca. 45 μM deoxymyoglobin approached saturation of the myoglobin after 240 min. The slow time scale of CO release may be due to the poor water solubility of **2**. This must be accounted for when comparing the CO release kinetics of this complex with analogous CORMs. The relatively poor water solubility of the ferrocenyl group could be overcome by further functionalization of the 2-phenylpyridine coligand or oxidation to the ferricenium salt with a water-soluble anion. However, the concentrations of CORM used in the myoglobin assay (tens of micromolar) are still very high for practical therapeutic use and

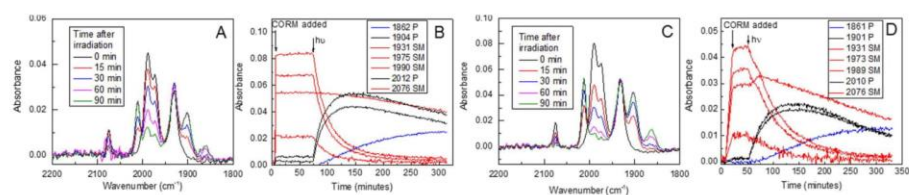


Figure 7. In situ infrared spectroscopic monitoring of compounds **1** and **2** in DMSO. The start of continuous irradiation with a 365 nm LED drawing a power of 5.0 W is indicated on the graphs. (A) Selected spectra of a 12 mM solution of compound **2** after irradiation began. (B) Peak height, fitted to a two-point baseline, of selected peaks over time of compound **2**. (C) Selected spectra of a 20 mM solution of compound **1** after irradiation began. (D) Peak height, fitted to a two-point baseline, of selected peaks over time of compound **1**.

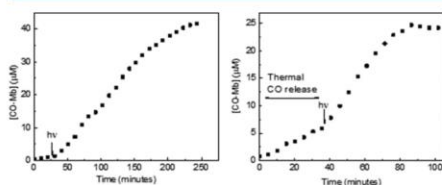


Figure 8. Myoglobin CO release assays. Irradiation from a 400 nm LED drawing 5.0 W power began where indicated. Irradiation was performed in cycles of 2 min on, 3 min off. Left: A 40 μM assay of **2**. Right: A 10 μM assay of **3**.

such a high concentration of CORM in solution is unlikely to be required.

Complex **3**, in which the ferrocenyl group is closest to the manganese, was also assessed using the myoglobin assay (Figure 8). In this case, slow conversion of myoglobin to carboxymyoglobin was observed in the dark. Irradiation of a solution of **3** with a 400 nm LED accelerated CO release, but the complex also displays significant thermal release.

It was hypothesized that the thermal CO release behavior of **3** was due to the susceptibility of the Mn–Cp bond to protonation in protic solvents. To test this, a solution of **1** was prepared in dichloromethane, and aliquots of the non-coordinating proton source $[\text{HNMe}_2\text{Ph}]\text{BF}_4$ were added via syringe. The resulting decomposition of **3** was monitored using in situ infrared spectroscopy (Figure 9). The electrochemical and infrared spectroelectrochemical results have demonstrated that **3** does not degrade upon oxidation on the same time scale as it does during addition of $[\text{HNMe}_2\text{Ph}]\text{BF}_4$, suggesting that

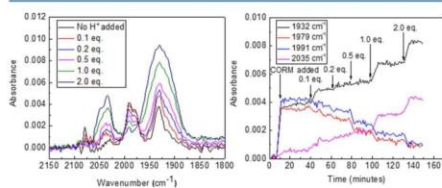


Figure 9. Effect of successive additions of the proton source $[\text{HNMe}_2\text{Ph}]\text{BF}_4$ to a 20 mM solution of **3** in dichloromethane solution. Left: Changes in the infrared bands with the total $[\text{HNMe}_2\text{Ph}]\text{BF}_4$ stoichiometry. Right: Evolution of selected bands over time.

protonation, rather than oxidation, by H^+ is responsible for the decomposition observed. The results are consistent with NMR spectroscopic studies that clearly show formation of protonated ligand **9**. This result demonstrates that **3** is sensitive to protons and its CO release rate could therefore be modulated on the basis of pH.

CONCLUSIONS

Redox-tagged ferrocenyl-CORMs have been synthesized and fully characterized. The ferrocenyl moiety is a validated isostere of the phenyl group in drug discovery and for the first time this has been incorporated into the structure of a CORM class. Compounds **1** and **2** display photochemical degradation at the same wavelengths as analogous Mn(I) tetracarbonyl complexes,²⁶ while compound **3** additionally releases CO in water in the dark, a process which appears to be triggered by protonation.

The versatility of alkynyl building block **6** has been showcased in a CuAAC functionalization reaction, enabling a series of compounds to be made analogously to other modular CORM classes.

Each redox-tagged CORM exhibited a single-electron reversible redox couple due to oxidation of the ferrocenyl moiety, while the Mn(I) tetracarbonyl moiety was redox silent within the electrochemical window assessed (up to a potential of +590 mV vs Fc/Fc⁺). However, previous studies on Mn(I) tricarbonyl systems have shown that an irreversible oxidation of the Mn(I) center does occur at very strongly oxidizing potentials.^{44,45}

Infrared spectroelectrochemistry revealed the effect of ferrocene oxidation upon the Mn center as being dependent on the linker length between the two metal centers. Comparison of CORMs **1**–**3** showed that a substantial shift in the metal carbonyl stretching frequencies took place only when the ferrocenyl moiety was in the first coordination sphere of the Mn(I) center. Although the perturbation to the structure of the complexes on oxidation was not sufficient to promote CO release, these observations provide motivation for further incorporation of redox-active groups into the first coordination sphere of CORMs with the ultimate goals of triggering and monitoring CO release electrochemically in a tunable and predictable manner.

ASSOCIATED CONTENT

Supporting Information

The Supporting Information is available free of charge on the ACS Publications website at DOI: 10.1021/acs.inorgchem.7b00509.

General synthetic procedures of known compounds, representative NMR spectra, UV–visible spectra, electrochemical results, and a summary tables of X-ray data (PDF)

Crystallography data for **1**, **2**, and **8** in CIF format (CIF)

AUTHOR INFORMATION

Corresponding Authors

*J.M.L. e-mail: jason.lynam@york.ac.uk.

*A.P. e-mail: alison.parkin@york.ac.uk.

*I.J.S.F. e-mail: ian.fairlamb@york.ac.uk.

ORCID

Benjamin J. Aucott: 0000-0002-1213-1839

Alison Parkin: 0000-0003-4715-7200

Ian J. S. Fairlamb: 0000-0002-7555-2761

Present Address

J.S.W.: Department of Chemistry, Durham University, Lower Mountjoy, South Road, Durham, DH1 3LE, United Kingdom.

Notes

The authors declare no competing financial interest.

ACKNOWLEDGMENTS

We are grateful to the BBSRC (BB/F017316/1) and EPSRC (EP/M506680/1) for supporting Ph.D. studentship funding for J.S.W. and B.J.A. We thank the funding contribution from the Wild fund to the Ph.D. studies of J.M. The project was underpinned by investments made in equipment as part of the EPSRC “ENERGY” grant (EP/K031589/1) and supported by a TARGeTED Project (University of York Antimicrobials) grant on CO-RMs. Christopher Morrell is thanked for initial experiments toward the synthesis and characterization of complex **3**. Chemistry Department workshops (C. Mortimer, Dr. C. Rhodes, and A. Storey) are acknowledged for the design and manufacture of equipment for the photochemical and electrochemical studies.

ABBREVIATIONS USED

CORM, carbon monoxide-releasing molecule; DSC, differential scanning calorimetry; HO, heme oxygenase; Mb, myoglobin; Mb-CO, carbonmonoxymyoglobin; OCP, open-circuit potential

REFERENCES

- (1) Kikuchi, G.; Yoshida, T.; Noguchi, M. Heme Oxygenase and Heme Degradation. *Biochem. Biophys. Res. Commun.* **2005**, *338*, 558–567.
- (2) McCoubrey, W. K.; Huang, T. J.; Maines, M. D. Isolation and Characterization of a cDNA From the Rat Brain that Encodes Hemoprotein Heme Oxygenase-3. *Eur. J. Biochem.* **1997**, *247*, 725–732.
- (3) Morse, D.; Lin, L.; Choi, A. M. K.; Ryter, S. W. Heme Oxygenase-1, a Critical Arbitrator of Cell Death Pathways in Lung Injury and Disease. *Free Radical Biol. Med.* **2009**, *47*, 1–12.
- (4) Piantadosi, C. A.; Withers, C. M.; Bartz, R. R.; MacGarvey, N. C.; Fu, P.; Sweeney, T. E.; Welty-Wolf, K. E.; Suliman, H. B. Heme Oxygenase-1 Couples Activation of Mitochondrial Biogenesis to Anti-inflammatory Cytokine Expression. *J. Biol. Chem.* **2011**, *286*, 16374–16385.
- (5) Gibbons, S. J.; Verhulst, P. J.; Bharucha, A.; Farrugia, G. Carbon monoxide in Gastrointestinal Physiology and its Potential in Therapeutics. *Aliment. Pharmacol. Ther.* **2013**, *38*, 689–702.
- (6) Motterlini, R.; Otterbein, L. E. The Therapeutic Potential of Carbon Monoxide. *Nat. Rev. Drug Discovery* **2010**, *9*, 728–743.

(7) Wilson, J. L.; Jesse, H. E.; Hughes, B.; Lund, V.; Naylor, K.; Davidge, K. S.; Cook, G. M.; Mann, B. E.; Poole, R. K. Ru(CO)₃Cl(Glycinate) (CORM-3): A Carbon Monoxide-releasing Molecule with Broad-spectrum Antimicrobial and Photosensitive Activities Against Respiration and Cation Transport in *Escherichia coli*. *Antioxid. Redox Signaling* **2013**, *19*, 497–509.

(8) Smith, H.; Mann, B. E.; Motterlini, R.; Poole, R. K. The Carbon Monoxide-releasing Molecule, CORM-3 (Ru(CO)₃ Cl(Glycinate)), Targets Respiration and Oxidases in *Campylobacter jejuni*, Generating Hydrogen Peroxide. *IUBMB Life* **2011**, *63*, 363–371.

(9) Pena, A. C.; Penacho, N.; Mancio-Silva, L.; Neres, R.; Seixas, J. D.; Fernandes, A. C.; Romão, C. C.; Mota, M. M.; Bernardes, G. J. L.; Pamplona, A. A Novel Carbon Monoxide-releasing Molecule Fully Protects Mice From Severe Malaria. *Antimicrob. Agents Chemother.* **2012**, *56*, 1281–1290.

(10) Foresti, R.; Hammad, J.; Clark, J. E.; Johnson, T. R.; Mann, B. E.; Friebe, A.; Green, C. J.; Motterlini, R. Vasoactive Properties of CORM-3, a Novel Water-soluble Carbon Monoxide-releasing Molecule. *Br. J. Pharmacol.* **2004**, *142*, 453–460.

(11) Garcia-Gallego, S.; Bernardes, G. J. L. Carbon-Monoxide-Releasing Molecules for the Delivery of Therapeutic CO in Vivo. *Angew. Chem., Int. Ed.* **2014**, *53*, 9712–9721.

(12) Heinemann, S. H.; Hoshi, T.; Westerhausen, M.; Schiller, A. Carbon Monoxide—Physiology, Detection and Controlled Release. *Chem. Commun.* **2014**, *50*, 3644–3660.

(13) Motterlini, R.; Clark, J. E.; Foresti, R.; Sarathchandra, P.; Mann, B. E.; Green, C. J. Carbon Monoxide-Releasing Molecules: Characterization of Biochemical and Vascular Activities. *Circ. Res.* **2002**, *90*, 17e–e24.

(14) Clark, J. E.; Naughton, P.; Shurey, S.; Green, C. J.; Johnson, T. R.; Mann, B. E.; Foresti, R.; Motterlini, R. Cardioprotective Actions by a Water-soluble Carbon Monoxide-releasing Molecule. *Circ. Res.* **2003**, *93*, e2–e8.

(15) Ford, P. C. From Curiosity to Applications. A Personal Perspective on Inorganic Photochemistry. *Chem. Sci.* **2016**, *7*, 2964–2986.

(16) Marhenke, J.; Trevino, K.; Works, C. The Chemistry, Biology and Design of Photochemical CO Releasing Molecules and the Efforts to Detect CO for Biological Applications. *Coord. Chem. Rev.* **2016**, *306*, 533–543.

(17) Wright, M. A.; Wright, J. A. PhotoCORMs: CO Release Moves into the Visible. *Dalton Trans.* **2016**, *45*, 6801–6811.

(18) Gonzales, M. A.; Mascharak, P. K. Photoactive Metal Carbonyl Complexes as Potential Agents for Targeted CO Delivery. *J. Inorg. Biochem.* **2014**, *133*, 127–135.

(19) Ward, J. S.; Lynam, J. M.; Moir, J.; Fairlamb, I. J. S. Visible-Light-Induced CO Release from a Therapeutically Viable Tryptophan-Derived Manganese (I) Carbonyl (TryptoCORM) Exhibiting Potent Inhibition Against *E. coli*. *Chem. - Eur. J.* **2014**, *20*, 15061–15068.

(20) Mede, R.; Klein, M.; Claus, R. A.; Kriek, S.; Quickert, S.; Görts, H.; Neugebauer, U.; Schmitt, M.; Gessner, G.; Heinemann, S. H.; Popp, J.; Bauer, M.; Westerhausen, M. CORM-EDE1: A Highly Water-Soluble and Nontoxic Manganese-Based photoCORM with a Biogenic Ligand Sphere. *Inorg. Chem.* **2016**, *55*, 104–113.

(21) Pfeiffer, H.; Rojas, A.; Niesel, J.; Schatzschneider, U. Sonogashira and “Click” Reactions for the N-terminal and Side-chain Functionalization of Peptides with [Mn(CO)₃(tpm)]⁺-based CO Releasing Molecules (tpm = tris(pyrazolyl)methane). *Dalton Trans.* **2009**, *22*, 4292–4298.

(22) Zobi, F.; Quaroni, L.; Santoro, G.; Zlateva, T.; Blacque, O.; Sarafimov, B.; Schaub, M. C.; Bogdanova, A. Y. Live-Fibroblast IR Imaging of a Cytoprotective PhotoCORM Activated with Visible Light. *J. Med. Chem.* **2013**, *56*, 6719–6731.

(23) Chakraborty, I.; Carrington, S. J.; Mascharak, P. K. Design Strategies to Improve the Sensitivity of Photoactive Metal Carbonyl Complexes (photoCORMs) to Visible Light and their Potential as CO-donors to Biological Targets. *Acc. Chem. Res.* **2014**, *47*, 2603–2611.

- (24) Mohr, F.; Niesel, J.; Schatzschneider, U.; Lehmann, C. W. Synthesis, Structures, and CO Releasing Properties of two Tricarbonyl Manganese(I) Complexes. *Z. Anorg. Allg. Chem.* **2012**, *638*, 543–546.
- (25) Ward, J. S.; Lynam, J. M.; Moir, J. W. B.; Sanin, D. E.; Mountford, A. P.; Fairlamb, I. J. S. A Therapeutically Viable Photoactivated Manganese-based CO-releasing Molecule (photo-CO-RM). *Dalton Trans.* **2012**, *41*, 10514–10517.
- (26) Ward, J. S.; Bray, J. T. W.; Aucott, B. J.; Wagner, C.; Pridmore, N. E.; Whitwood, A. C.; Moir, J. W. B.; Lynam, J. M.; Fairlamb, I. J. S. Photoactivated Functionizable Tetracarbonyl Phenylpyridine Manganese(I) Complexes as CO-releasing Molecules: A Direct Suzuki-Miyaura Cross-coupling on a Thermally-stable CO-RM. *Eur. J. Inorg. Chem.* **2016**, *2016*, 5044–5051.
- (27) Schafer, F.; Buettner, G. Redox Environment of the Cell as Viewed Through the Redox State of the Glutathione Disulfide/Glutathione Couple. *Free Radical Biol. Med.* **2001**, *30*, 1191–1212.
- (28) Graf, N.; Lippard, S. J. Redox Activation of Metal-based Prodrugs as a Strategy for Drug Delivery. *Adv. Drug Delivery Rev.* **2012**, *64*, 993–1004.
- (29) Köpf-Maier, P.; Köpf, H.; Neuse, E. W. Ferricenium Complexes: A New Type of Water-soluble Antitumor Agent. *J. Cancer Res. Clin. Oncol.* **1984**, *108*, 336–340.
- (30) Zhang, W.-Q.; Whitwood, A. C.; Fairlamb, I. J. S.; Lynam, J. M. Group 6 Carbon Monoxide-releasing Metal Complexes with Biologically-compatible Leaving Groups. *Inorg. Chem.* **2010**, *49*, 8941–8952.
- (31) McMahon, S.; Rochford, J.; Halpin, Y.; Manton, J. C.; Harvey, E. C.; Greetham, G. M.; Clark, I. P.; Rooney, A. D.; Long, C.; Pryce, M. T. Controlled CO Release Using Photochemical, Thermal and Electrochemical Approaches from the Amino Carbene Complex $[(CO)_5CrC(NC_6H_5)CH_3]$. *Phys. Chem. Chem. Phys.* **2014**, *16*, 21230–21233.
- (32) Ornelas, C. Application of Ferrocene and its Derivatives in Cancer Research. *New J. Chem.* **2011**, *35*, 1973–1985.
- (33) Wani, W. A.; Jameel, E.; Baig, U.; Mumtazuddin, S.; Hun, L. T. I. Ferroquine and its Derivatives: New Generation of Antimalarial Agents. *Eur. J. Med. Chem.* **2015**, *101*, 534–551.
- (34) Dolomanov, O. V.; Bourhis, L. J.; Gildea, R. J.; Howard, J. A. K.; Puschmann, H. OLEX2: A Complete Structure Solution, Refinement and Analysis Program. *J. Appl. Crystallogr.* **2009**, *42*, 339–341.
- (35) Sheldrick, G. M. A Short History of SHELX. *Acta Crystallogr., Sect. A: Found. Crystallogr.* **2008**, *64*, 112–122.
- (36) Sheldrick, G. M. Crystal Structure Refinement with SHELXL. *Acta Crystallogr., Sect. C: Struct. Chem.* **2015**, *71*, 3–8.
- (37) Atkin, A. J.; Lynam, J. M.; Moulton, B. E.; Sawle, P.; Motterlini, R.; Boyle, N. M.; Pryce, M. T.; Fairlamb, I. J. S. Modification of the Deoxy-myoglobin/Carbonmonoxy-myoglobin UV-vis Assay for Reliable Determination of CO-release Rates from Organometallic Carbonyl Complexes. *Dalton Trans.* **2011**, *40*, 5755–5761.
- (38) Djukic, J.-P.; Dötz, K. H.; Pfeffer, M.; De Cian, A.; Fischer, J. Reactivity of Cyclomanganated 2-Phenylpyridine Derivatives toward Organolithium Reagents. Synthesis of Novel Chelated Tricarbonyl(η -3-benzyl)manganese(I) Complexes. *Organometallics* **1997**, *16*, 5171–5182.
- (39) Burchat, A. F.; Chong, J. M.; Nielsen, N. Titration of Alkylolithiums with a Simple Reagent to a Blue Endpoint. *J. Organomet. Chem.* **1997**, *542*, 281–283.
- (40) Robinson, N. P.; Depree, G. J.; de Wit, R. W.; Main, L.; Nicholson, B. K. Indenols, Indenones and (Arylcyclohexadienyl)Mn(CO)₃ π -complexes from the Thermally Promoted Reactions of Alkynes with Ortho-Mn(CO)₄ Aryl Ketone, Amide, Ester and Aldehyde Derivatives. *J. Organomet. Chem.* **2005**, *690*, 3827–3837.
- (41) Rajput, J.; Moss, J. R.; Hutton, A. T.; Hendricks, D. T.; Arendse, C. E.; Imrie, C. Synthesis, Characterization and Cytotoxicity of some Palladium(II), Platinum(II), Rhodium(I) and Iridium(I) Complexes of Ferrocenylpyridine and Related Ligands. Crystal and Molecular Structure of trans-dichlorobis(3-ferrocenylpyridine)palladium(II). *J. Organomet. Chem.* **2004**, *689*, 1553–1568.
- (42) Nicholson, R. S.; Shain, I. Stationary Electrode Polarography. *Anal. Chem.* **1964**, *36*, 706–723.
- (43) Plazuk, D.; Rychlik, B.; Blauz, A.; Domagala, S. Synthesis, Electrochemistry and Anticancer Activity of Novel Ferrocenyl Phenols Prepared via Azide-alkyne 1,3-cycloaddition Reaction. *J. Organomet. Chem.* **2012**, *715*, 102–112.
- (44) Hershberger, J. W.; Kochi, J. K. Ligand Effects on the Redox Potentials of Metal Carbonyls. *Polyhedron* **1983**, *2*, 929–934.
- (45) Mede, R.; Gläser, S.; Suchland, B.; Schowka, B.; Mandel, M.; Görls, H.; Kriek, S.; Schiller, A.; Westerhausen, M. Manganese(I)-Based CORMs with 5-Substituted 3-(2-Pyridyl)Pyrazole Ligands. *Inorg. Chem.* **2017**, *5*, 8–21.

Appendix 2: X-Ray Diffraction Data

Compound 132

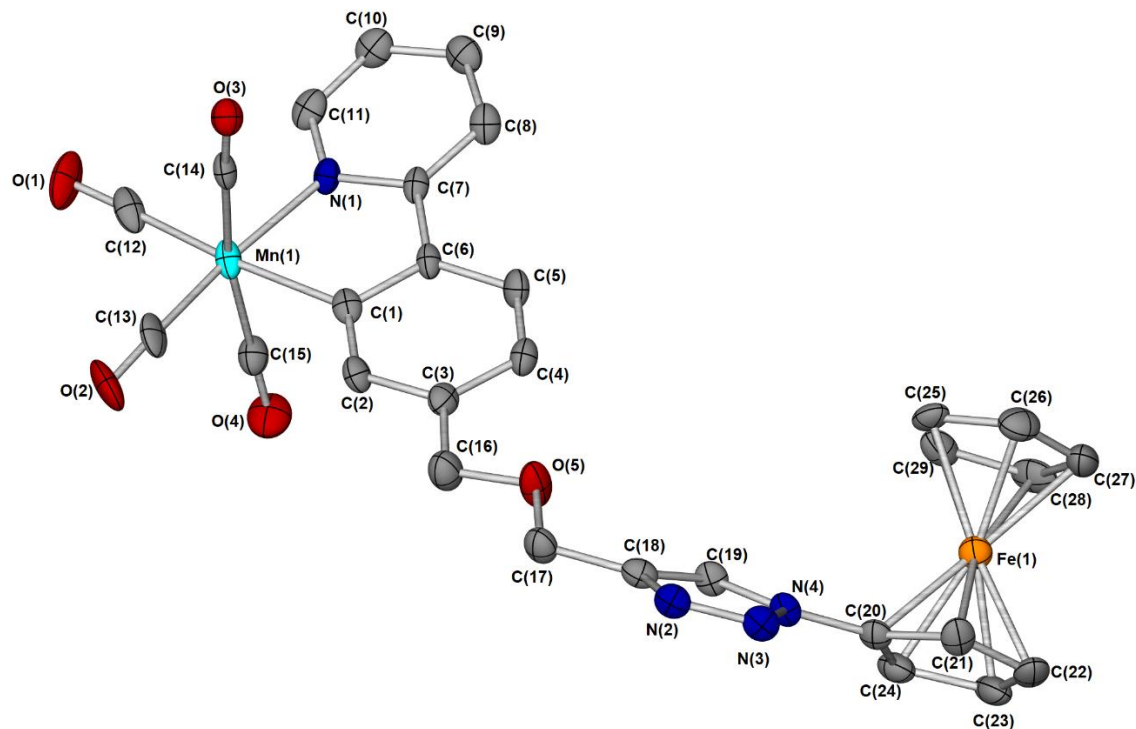


Figure 147: An X-ray crystal structure of compound 132 with hydrogen atoms omitted for clarity. Atoms are displayed as thermal ellipsoids at 50% probability. Selected bond lengths (Å): C(1)-Mn(1) = 2.056(5), C(12)-Mn(1) = 1.836(6), C(13)-Mn(1) = 1.805(6), C(14)-Mn(1) = 1.853(5), C(15)-Mn(1) = 1.867(5), N(1)-Mn(1) = 2.059(4). Selected bond angles (°): C(1)-Mn(1)-N(1) = 80.04(18), C(12)-Mn(1)-C(1) = 174.9(2), C(14)-Mn(1)-(C15) = 168.8(2), C(13)-Mn(1)-N(1) = 172.65(19), C(13)-Mn(1)-C(12) = 92.3(2), C(15)-Mn(1)-(C1) = 84.1(2)

Table 24: Crystal data and structure refinement for compound 132.

Identification code	ijsf1519
Empirical formula	C ₂₉ H ₂₁ FeMnN ₄ O ₅
Formula weight	616.29
Temperature/K	110.05(10)
Crystal system	monoclinic
Space group	P2 ₁ /c
a/Å	23.7914(8)
b/Å	10.0173(3)
c/Å	10.9284(3)
α/°	90.00
β/°	91.969(3)
γ/°	90.00
Volume/Å ³	2602.98(14)
Z	4
ρ _{calc} /g/cm ³	1.573
μ/mm ⁻¹	1.091
F(000)	1256.0
Crystal size/mm ³	0.216 × 0.1439 × 0.0548
Radiation	MoKα (λ = 0.71073)
2θ range for data collection/°	3.42 to 51.82
Index ranges	-28 ≤ h ≤ 26, -6 ≤ k ≤ 12, -12 ≤ l ≤ 13
Reflections collected	9705
Independent reflections	4891 [R _{int} = 0.0344, R _{sigma} = 0.0554]
Data/restraints/parameters	4891/0/361
Goodness-of-fit on F ²	1.068
Final R indexes [I >= 2σ (I)]	R ₁ = 0.0592, wR ₂ = 0.1345
Final R indexes [all data]	R ₁ = 0.0907, wR ₂ = 0.1516
Largest diff. peak/hole / e Å ⁻³	0.62/-0.50

Data collected and structure solved by Dr Jessica Milani.

Compound 133

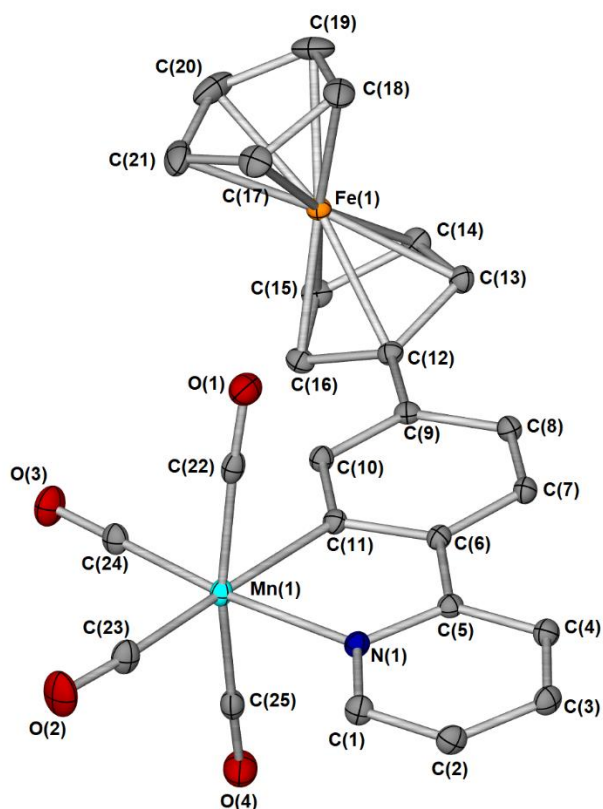


Figure 148: An X-ray crystal structure of compound 133 with hydrogen atoms omitted for clarity. Atoms are displayed as thermal ellipsoids at 50% probability. Selected bond lengths (Å): C(11)-Mn(1) = 2.0538(13), C(22)-Mn(1) = 1.8622(15), C(23)-Mn(1) = 1.8344(14), C(24)-Mn(1) = 1.8048(14), C(25)-Mn(1) = 1.8541(15), N(1)-Mn(1) = 2.0694(12). Selected bond angles (°): C(11)-Mn(1)-N(1) = 79.83(5), C(24)-Mn(1)-N(1) = 172.14(5), C(23)-Mn(1)-C(11) = 176.65(6), C(25)-Mn(1)-C(22) = 167.63(6), C(23)-Mn(1)-N(1) = 97.07(6), C(24)-Mn(1)-C(23) = 90.79(6). Selected torsion angles (°): N(1)-C(5)-C(6)-C(11) = 0.49(17), C(10)-C(9)-C(12)-C(13) = 20.3(2).

Table 25: Crystal data and structure refinement for compound 133.

Identification code	jml1523
Empirical formula	C ₂₅ H ₁₆ FeMnNO ₄
Formula weight	505.18
Temperature/K	111(1)
Crystal system	monoclinic
Space group	P2 ₁ /c
a/Å :	7.18991(17)
b/Å	20.2412(6)
c/Å	14.1249(3)
α/°	90.00
β/°	93.049(2)
γ/°	90.00
Volume/Å ³	2052.71(9)
Z	4
ρ _{calc} /g/cm ³	1.635
μ/mm ⁻¹	1.356
F(000)	1024.0
Crystal size/mm ³	0.229 × 0.1218 × 0.088
Radiation	MoKα (λ = 0.71070)
2θ range for data collection/°	6.7 to 64.1
Index ranges	-10 ≤ h ≤ 10, -29 ≤ k ≤ 30, -20 ≤ l ≤ 20
Reflections collected	25249
Independent reflections	6625 [R _{int} = 0.0334, R _{sigma} = 0.0291]
Data/restraints/parameters	6625/0/289
Goodness-of-fit on F ²	1.063
Final R indexes [I >= 2σ (I)]	R ₁ = 0.0287, wR ₂ = 0.0660
Final R indexes [all data]	R ₁ = 0.0353, wR ₂ = 0.0694
Largest diff. peak/hole / e Å ⁻³	0.44/-0.47

Data collected and structure solved by Dr Adrian Whitwood.

Compound 148

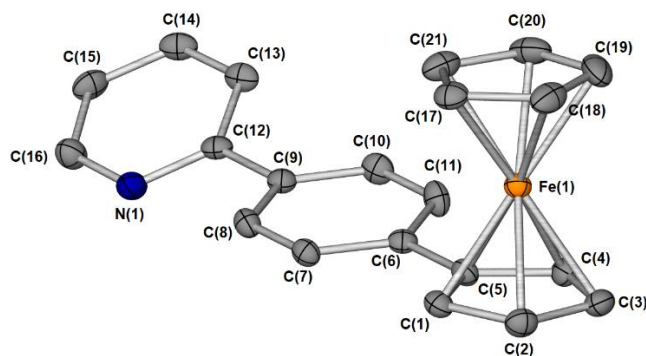


Figure 149: X-ray crystal structure of protonated ligand 148 with hydrogen atoms omitted for clarity. Atoms are displayed as thermal ellipsoids at 50% probability. Selected bond lengths (Å): C(9)-C(12) = 1.485(5), C(5)-C(6) = 1.472(5), C(16)-N(1) = 1.366(5), C(7)-C(8) = 1.383(5), C(3)-C(4) = 1.421(5), C(1)-Fe(1) = 2.037(4) Selected bond angles (°): C(6)-C(5)-C(1) = 124.0(3), N(1)-C(12)-C(9) = 116.8(3) Selected torsion angles (°): C(8)-C(9)-C(12)-N(1) = 21.6(5), C(1)-C(5)-C(6)-C(7) = 8.9(6).

Table 26: Crystal data and structure refinement for compound 148.

Identification code	ijsf1601_twin1_hklf4
Empirical formula	C ₂₁ H ₁₇ FeN
Formula weight	339.21
Temperature/K	110.05(10)
Crystal system	monoclinic
Space group	P2 ₁ /c
a/Å	16.0034(9)
b/Å	9.3009(4)
c/Å	10.3112(5)
α/°	90
β/°	98.974(5)
γ/°	90
Volume/Å ³	1516.00(13)
Z	4
ρ _{calc} /cm ³	1.486
μ/mm ⁻¹	7.935
F(000)	704.0
Crystal size/mm ³	0.164 × 0.118 × 0.031
Radiation	CuKα (λ = 1.54184)
2θ range for data collection/°	11.038 to 143.156
Index ranges	-19 ≤ h ≤ 19, -11 ≤ k ≤ 11, -12 ≤ l ≤ 8
Reflections collected	4139
Independent reflections	4139 [R _{int} = ?, R _{sigma} = 0.0315]
Data/restraints/parameters	4139/0/209
Goodness-of-fit on F ²	1.044
Final R indexes [I >= 2σ (I)]	R ₁ = 0.0460, wR ₂ = 0.1174
Final R indexes [all data]	R ₁ = 0.0560, wR ₂ = 0.1231
Largest diff. peak/hole / e Å ⁻³	0.63/-0.59

Compound 170

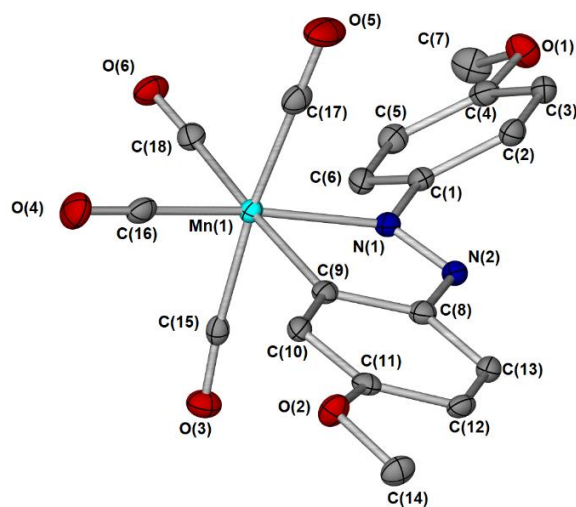


Figure 150: An X-ray crystal structure of compound 170 with hydrogen atoms omitted for clarity. Atoms are displayed as thermal ellipsoids at 50% probability. Selected bond lengths (Å): N(1)-N(2) = 1.278(2), C(9)-Mn(1) = 2.0346(19), C(15)-Mn(1) = 1.869(2), C(16)-Mn(1) = 1.815(2), C(17)-Mn(1) = 1.858(2), C(18)-Mn(1) = 1.846(2), N(1)-Mn(1) = 2.0505(16). Selected bond angles (°): C(9)-Mn(1)-N(1) = 77.92(7), C(16)-Mn(1)-N(1) = 168.53(8), C(18)-Mn(1)-C(9) = 176.45(8), C(17)-Mn(1)-C(15) = 173.45(8), C(18)-Mn(1)-N(1) = 98.56(7), C(16)-Mn(1)-C(18) = 92.82(8).

Table 27: Crystal data and structure refinement for compound 170.

Identification code	ijsf1616
Empirical formula	C ₁₈ H ₁₃ MnN ₂ O ₆
Formula weight	408.24
Temperature/K	110.05(10)
Crystal system	monoclinic
Space group	P2 ₁ /n
a/Å	10.1379(2)
b/Å	13.6627(2)
c/Å	13.2843(2)
α/°	90
β/°	106.937(2)
γ/°	90
Volume/Å ³	1760.21(5)
Z	4
ρ _{calc} /cm ³	1.541
μ/mm ⁻¹	6.453
F(000)	832.0
Crystal size/mm ³	0.389 × 0.281 × 0.156
Radiation	CuKα (λ = 1.54184)
2θ range for data collection/°	9.504 to 134.156
Index ranges	-8 ≤ h ≤ 12, -16 ≤ k ≤ 16, -15 ≤ l ≤ 15
Reflections collected	6206
Independent reflections	3146 [R _{int} = 0.0281, R _{sigma} = 0.0363]
Data/restraints/parameters	3146/0/246
Goodness-of-fit on F ²	1.048
Final R indexes [I >= 2σ (I)]	R ₁ = 0.0326, wR ₂ = 0.0844
Final R indexes [all data]	R ₁ = 0.0352, wR ₂ = 0.0874
Largest diff. peak/hole / e Å ⁻³	0.27/-0.36

Data collected and structure solved by Rachel R. Parker.

Compound 173

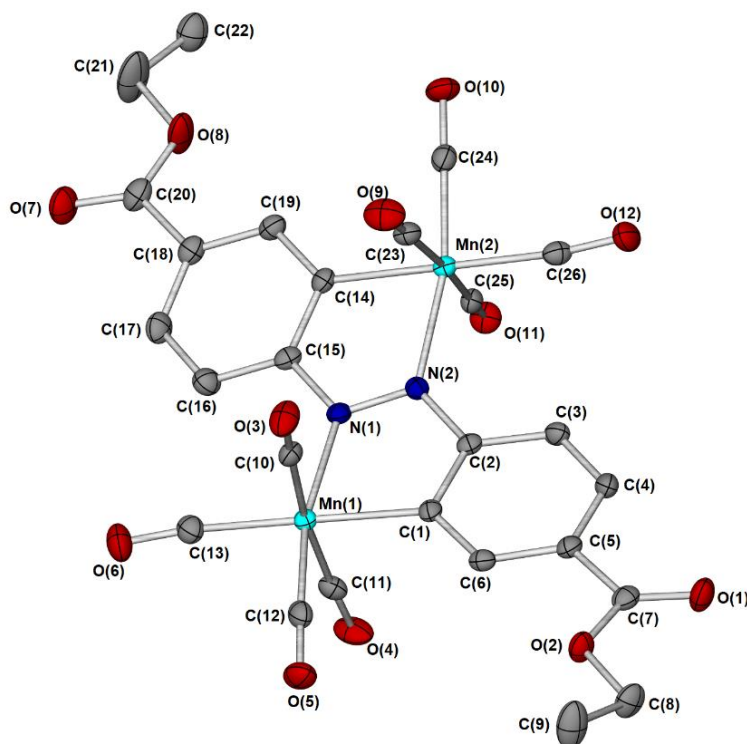


Figure 151: An X-ray crystal structure of compound 173 with hydrogen atoms omitted for clarity. Atoms are displayed as thermal ellipsoids at 50% probability. Selected bond lengths (Å): N(1)-N(2) = 1.299(3), C(1)-Mn(1) = 2.018(2), C(10)-Mn(1) = 1.877(3), C(11)-Mn(1) = 1.861(3), C(12)-Mn(1) = 1.801(3), C(13)-Mn(1) = 1.849(3), N(1)-Mn(1) = 2.083(2). Selected bond angles (°): C(1)-Mn(1)-N(1) = 77.74(9), C(12)-Mn(1)-N(1) = 167.63(10), C(13)-Mn(1)-C(1) = 177.44(11), C(10)-Mn(1)-C(11) = 173.17(11), C(13)-Mn(1)-N(1) = 104.11(10), C(13)-Mn(1)-C(12) = 88.19(12).

Table 28: Crystal data and structure refinement for compound 173.

Identification code	ijsf1615
Empirical formula	C ₂₆ H ₁₆ Mn ₂ N ₂ O ₁₂
Formula weight	658.29
Temperature/K	110.05(10)
Crystal system	triclinic
Space group	P-1
a/Å	9.9783(5)
b/Å	11.3469(6)
c/Å	12.2798(4)
α/°	78.620(4)
β/°	84.152(4)
γ/°	89.076(4)
Volume/Å ³	1355.92(11)
Z	2
ρ _{calc} /cm ³	1.612
μ/mm ⁻¹	8.193
F(000)	664.0
Crystal size/mm ³	0.151 × 0.117 × 0.082
Radiation	CuKα (λ = 1.54184)
2θ range for data collection/°	7.38 to 134.16
Index ranges	-11 ≤ h ≤ 11, -13 ≤ k ≤ 13, -14 ≤ l ≤ 9
Reflections collected	8747
Independent reflections	4834 [R _{int} = 0.0341, R _{sigma} = 0.0476]
Data/restraints/parameters	4834/0/381
Goodness-of-fit on F ²	1.046
Final R indexes [I >= 2σ (I)]	R ₁ = 0.0368, wR ₂ = 0.0921
Final R indexes [all data]	R ₁ = 0.0431, wR ₂ = 0.0978
Largest diff. peak/hole / e Å ⁻³	0.57/-0.41

Data collected and structure solved by Rachel R. Parker

Compound 188

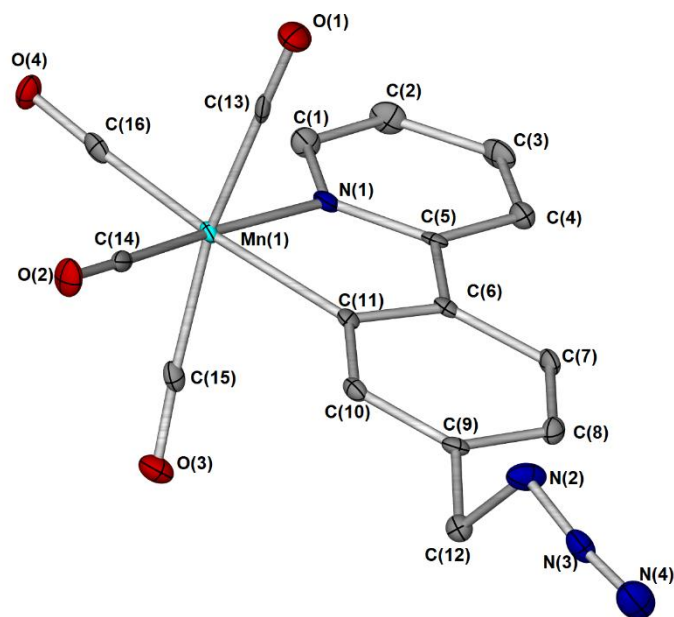


Figure 152: An X-ray crystal structure of compound 188 with hydrogen atoms omitted for clarity. Atoms are displayed as thermal ellipsoids at 50 % probability. Selected bond lengths (Å): C(11)-Mn(1) = 2.054(3), C(13)-Mn(1) = 1.841(3), C(14)-Mn(1) = 1.796(3), C(15)-Mn(1) = 1.857(3), C(16)-Mn(1) = 1.842(3), N(1)-Mn(1) = 2.073(2). Selected bond angles (°): C(11)-Mn(1)-N(1) = 79.53(11), C(16)-Mn(1)-C(11) = 172.33(12), C(13)-Mn(1)-C(15) = 166.55(12), C(14)-Mn(1)-N(1) = 172.93(12), C(14)-Mn(1)-C(16) = 93.50(13), C(15)-Mn(1)-C(11) = 81.79(12).

Table 29: Crystal data and structure refinement for compound 188.

Identification code	ijsf1613
Empirical formula	C ₁₆ H ₉ MnN ₄ O ₄
Formula weight	376.21
Temperature/K	110.05(10)
Crystal system	orthorhombic
Space group	P2 ₁ 2 ₁ 2 ₁
a/Å	8.87104(16)
b/Å	10.98540(18)
c/Å	15.5918(3)
α/°	90
β/°	90
γ/°	90
Volume/Å ³	1519.45(5)
Z	4
ρ _{calc} /cm ³	1.645
μ/mm ⁻¹	7.359
F(000)	760.0
Crystal size/mm ³	0.352 × 0.233 × 0.209
Radiation	CuKα (λ = 1.54184)
2θ range for data collection/°	9.85 to 134.13
Index ranges	-7 ≤ h ≤ 10, -13 ≤ k ≤ 9, -14 ≤ l ≤ 18
Reflections collected	3399
Independent reflections	2261 [R _{int} = 0.0176, R _{sigma} = 0.0290]
Data/restraints/parameters	2261/0/226
Goodness-of-fit on F ²	1.101
Final R indexes [I >= 2σ (I)]	R ₁ = 0.0264, wR ₂ = 0.0671
Final R indexes [all data]	R ₁ = 0.0271, wR ₂ = 0.0676
Largest diff. peak/hole / e Å ⁻³	0.34/-0.42
Flack parameter	-0.010(5)

Data collected and structure solved by Rachel R. Parker.

Compound 189

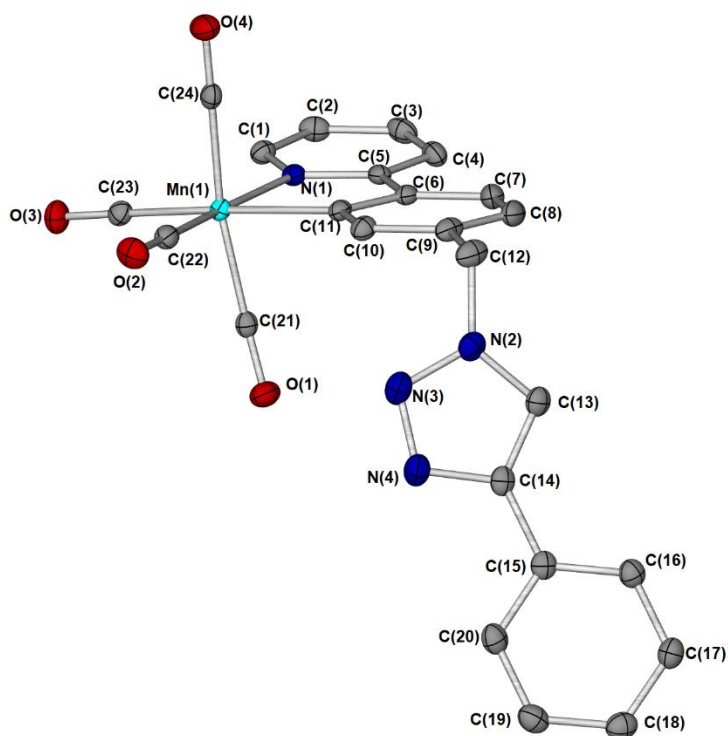


Figure 153: An X-ray crystal structure of compound 189 with hydrogen atoms omitted for clarity. Atoms are displayed as thermal ellipsoids at 50 % probability. Selected bond lengths (Å): C(11)-Mn(1) = 2.0574(14), C(21)-Mn(1) = 1.8595(14), C(22)-Mn(1) = 1.8025(15), C(23)-Mn(1) = 1.8303(15), C(24)-Mn(1) = 1.8476(14), N(1)-Mn(1) = 2.0661(11). Selected bond angles (°): C(11)-Mn(1)-N(1) = 79.64(5), C(23)-Mn(1)-C(11) = 173.00(6), C(24)-Mn(1)-C(21) = 168.48(6), C(22)-Mn(1)-N(1) = 173.35(6), C(22)-Mn(1)-C(23) = 92.02(6), C(21)-Mn(1)-C(11) = 80.95(5).

Table 30: Crystal data and structure refinement for compound 189.

Identification code	ijsf1603
Empirical formula	C ₂₄ H ₁₅ MnN ₄ O ₄
Formula weight	478.34
Temperature/K	110.05(10)
Crystal system	monoclinic
Space group	P2 ₁ /c
a/Å	22.2501(4)
b/Å	10.85157(17)
c/Å	8.51201(14)
α/°	90
β/°	92.1533(15)
γ/°	90
Volume/Å ³	2053.76(6)
Z	4
ρ _{calc} /g/cm ³	1.547
μ/mm ⁻¹	0.684
F(000)	976.0
Crystal size/mm ³	0.266 × 0.168 × 0.054
Radiation	MoKα (λ = 0.71073)
2θ range for data collection/°	7.012 to 64.41
Index ranges	-31 ≤ h ≤ 33, -16 ≤ k ≤ 15, -12 ≤ l ≤ 12
Reflections collected	25949
Independent reflections	6729 [R _{int} = 0.0306, R _{sigma} = 0.0293]
Data/restraints/parameters	6729/0/298
Goodness-of-fit on F ²	1.075
Final R indexes [I >= 2σ (I)]	R ₁ = 0.0360, wR ₂ = 0.0843
Final R indexes [all data]	R ₁ = 0.0459, wR ₂ = 0.0898
Largest diff. peak/hole / e Å ⁻³	0.42/-0.39

Data collected and structure solved by Dr Adrian Whitwood.

Compound 197

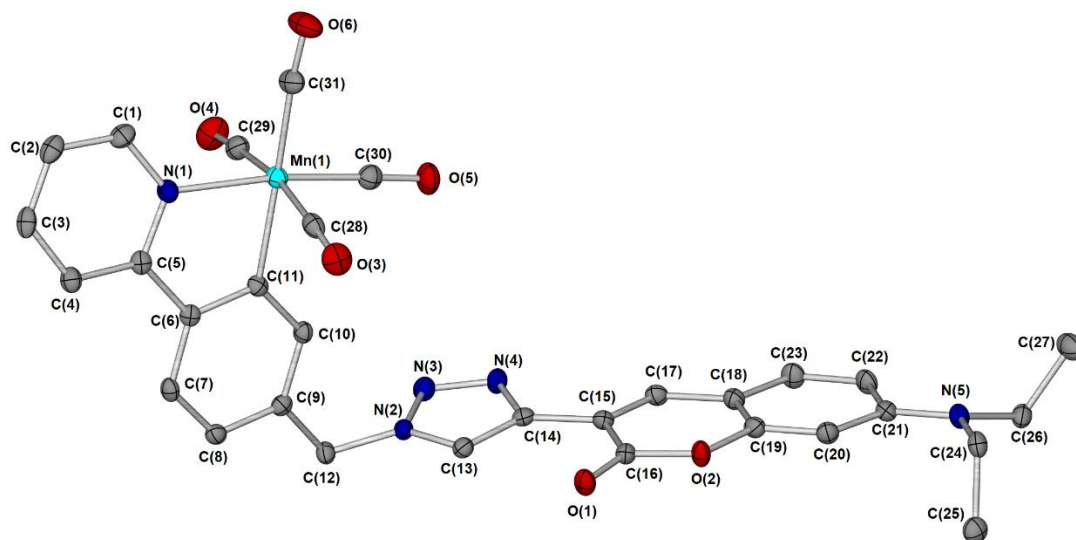


Figure 154: An X-ray crystal structure of compound 197 with hydrogen atoms omitted for clarity. Atoms are displayed as thermal ellipsoids at 50 % probability. Selected bond lengths (Å): C(11)-Mn(1) = 2.048(2), C(28)-Mn(1) = 1.853(3), C(29)-Mn(1) = 1.864(3), C(30)-Mn(1) = 1.8310(3), C(31)-Mn(1) = 1.8451(3), N(1)-Mn(1) = 2.065(2). Selected bond angles (°): C(11)-Mn(1)-N(1) = 79.45(9), C(31)-Mn(1)-C(11) = 174.82(10), C(28)-Mn(1)-(C29) = 168.69(12), C(30)-Mn(1)-N(1) = 171.61(10), C(30)-Mn(1)-C(31) = 90.66(12), C(28)-Mn(1)-(C11) = 81.32(10).

Table 31: Crystal data and structure refinement for compound 197.

Identification code	ijsf1617
Empirical formula	C ₃₁ H ₂₄ MnN ₅ O ₆
Formula weight	617.49
Temperature/K	110.05(10)
Crystal system	triclinic
Space group	P-1
a/Å	8.6041(5)
b/Å	10.1823(3)
c/Å	15.9801(8)
α/°	85.026(3)
β/°	80.913(4)
γ/°	87.771(4)
Volume/Å ³	1376.78(11)
Z	2
ρ _{calc} /cm ³	1.490
μ/mm ⁻¹	4.371
F(000)	636.0
Crystal size/mm ³	0.198 × 0.128 × 0.096
Radiation	CuKα (λ = 1.54184)
2θ range for data collection/°	8.72 to 134.154
Index ranges	-10 ≤ h ≤ 10, -12 ≤ k ≤ 6, -19 ≤ l ≤ 19
Reflections collected	8858
Independent reflections	4912 [R _{int} = 0.0332, R _{sigma} = 0.0468]
Data/restraints/parameters	4912/0/390
Goodness-of-fit on F ²	1.071
Final R indexes [I >= 2σ (I)]	R ₁ = 0.0432, wR ₂ = 0.1180
Final R indexes [all data]	R ₁ = 0.0472, wR ₂ = 0.1222
Largest diff. peak/hole / e Å ⁻³	0.30/-0.44

Data collected and structure solved by Rachel R. Parker.

Appendix 3: UV-Visible Spectroscopic Data

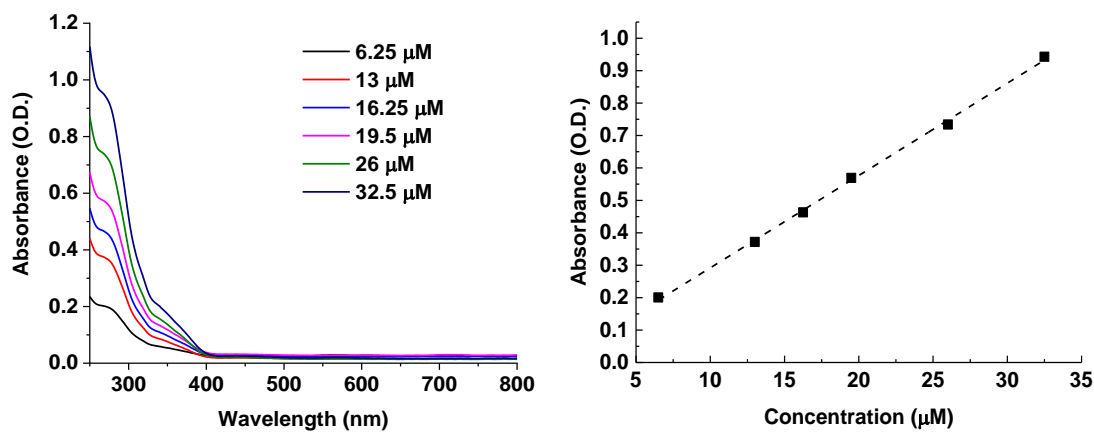


Figure 155 Left: Spectra of 132 in CH_2Cl_2 at the concentrations shown. Right: Beer-Lambert plot for 132 in CH_2Cl_2 at 270 nm. The dashed line is a linear fit giving $\epsilon(270 \text{ nm}) = (2.84 \pm 0.5) \times 10^4 \text{ dm}^3 \text{ mol}^{-1} \text{ cm}^{-1}$.

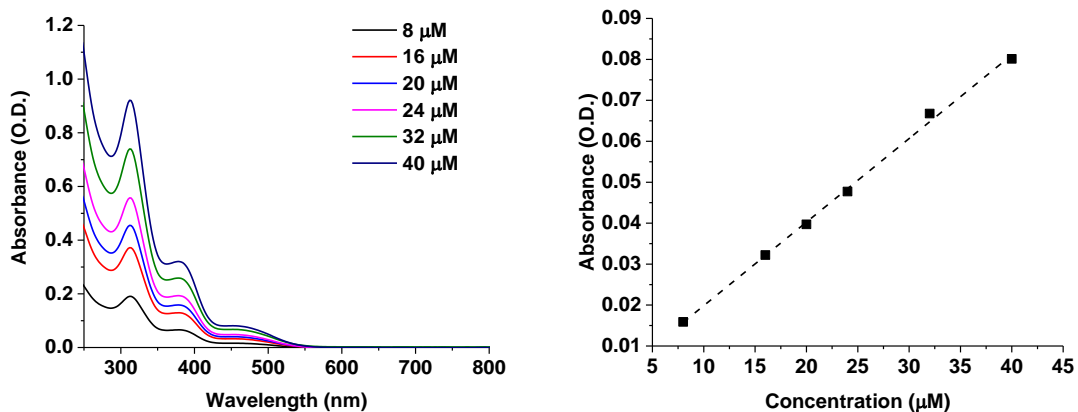


Figure 156 Left: Spectra of 133 in CH₂Cl₂ at the concentrations shown. Right: Beer-Lambert plot for 133 in CH₂Cl₂ at 460 nm. The dashed line is a linear fit giving $\epsilon(460 \text{ nm}) = (2.04 \pm 0.05) \times 10^3 \text{ dm}^3 \text{ mol}^{-1} \text{ cm}^{-1}$.

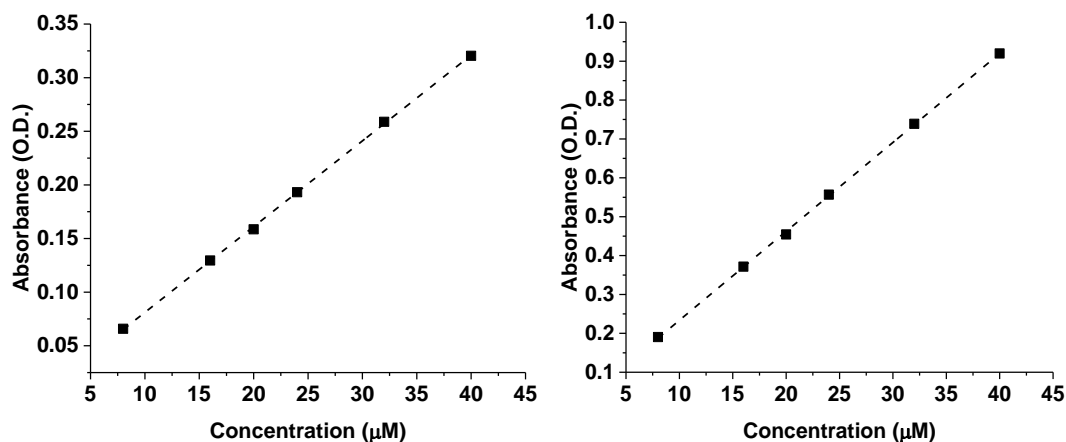


Figure 157 Left: Beer-Lambert plot for 133 in CH₂Cl₂ at 378 nm. The dashed line is a linear fit giving $\epsilon(378 \text{ nm}) = (8.00 \pm .06) \times 10^3 \text{ dm}^3 \text{ mol}^{-1} \text{ cm}^{-1}$. Right: Beer-Lambert plot for 133 in CH₂Cl₂ at 314 nm. The dashed line is a linear fit giving $\epsilon(314 \text{ nm}) = (2.29 \pm .02) \times 10^4 \text{ dm}^3 \text{ mol}^{-1} \text{ cm}^{-1}$.

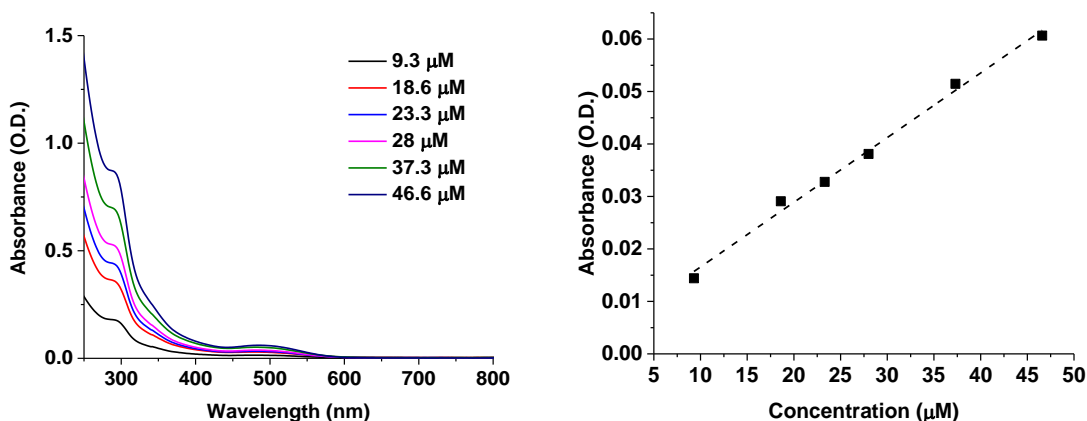


Figure 158 Left: Spectra of 134 in CH₂Cl₂ at the concentrations shown. Right: Beer-Lambert plot for 134 in CH₂Cl₂ at 486 nm. The dashed line is a linear fit giving $\epsilon(486 \text{ nm}) = (1.23 \pm 0.05) \times 10^3 \text{ dm}^3 \text{ mol}^{-1} \text{ cm}^{-1}$.

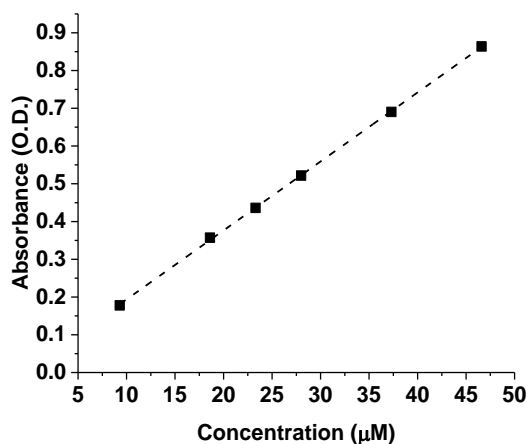


Figure 159: Beer-Lambert plot for 134 in CH₂Cl₂ at 292 nm. The dashed line is a linear fit giving $\epsilon(292 \text{ nm}) = (1.827 \pm .013) \times 10^4 \text{ dm}^3 \text{ mol}^{-1} \text{ cm}^{-1}$.

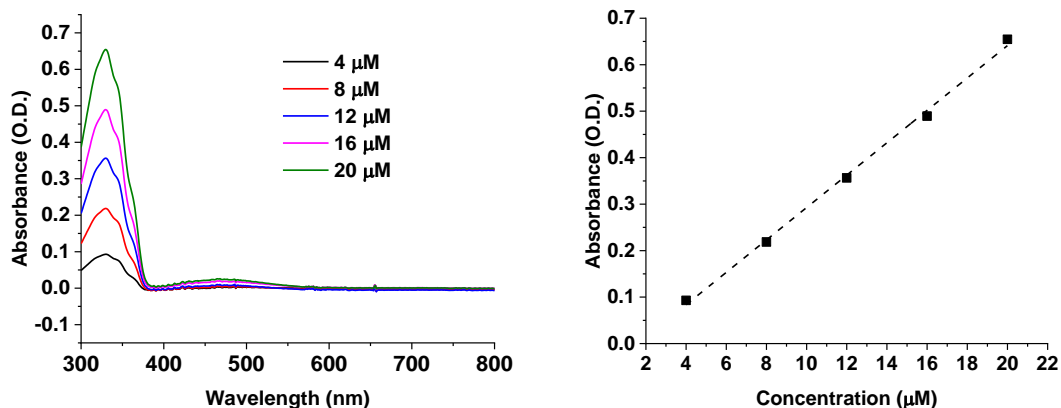


Figure 160 Left: Spectra of 169 in CH₂Cl₂ at the concentrations shown. Right: Beer-Lambert plot for 169 in CH₂Cl₂ at 330 nm. The dashed line is a linear fit giving $\epsilon(330 \text{ nm}) = (3.49 \pm 0.04) \times 10^4 \text{ dm}^3 \text{ mol}^{-1} \text{ cm}^{-1}$.

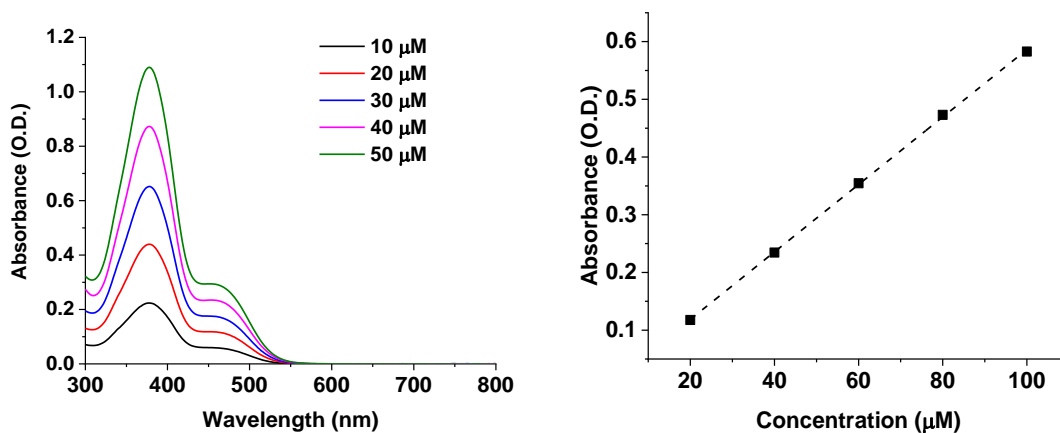


Figure 161 Left: Spectra of 170 in CH₂Cl₂ at the concentrations shown. Right: Beer-Lambert plot for 170 in CH₂Cl₂ at 456 nm. The dashed line is a linear fit giving $\epsilon(456 \text{ nm}) = (5.84 \pm .05) \times 10^3 \text{ dm}^3 \text{ mol}^{-1} \text{ cm}^{-1}$.

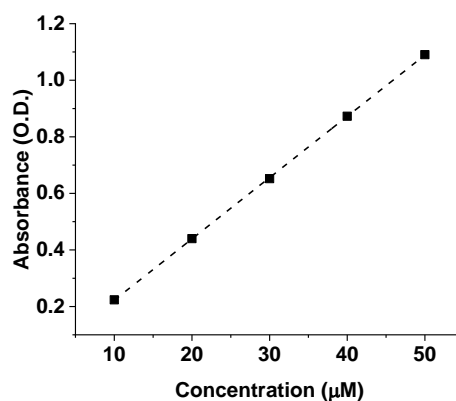


Figure 162: Beer-Lambert plot for 170 in CH₂Cl₂ at 378 nm. The dashed line is a linear fit giving $\epsilon(378 \text{ nm}) = (2.166 \pm .008) \times 10^4 \text{ dm}^3 \text{ mol}^{-1} \text{ cm}^{-1}$.

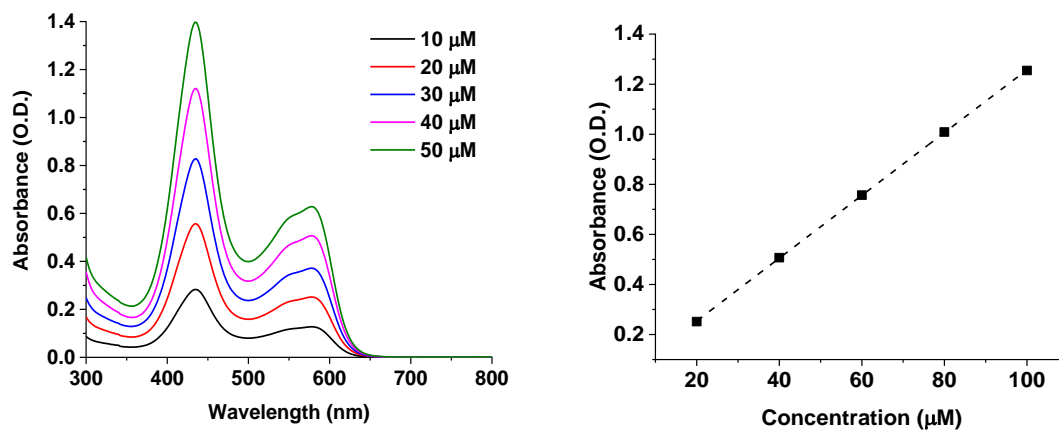


Figure 163 Left: Spectra of 171 in CH_2Cl_2 at the concentrations shown. Right: Beer-Lambert plot for 171 in CH_2Cl_2 at 578 nm. The dashed line is a linear fit giving $\epsilon(578 \text{ nm}) = (1.254 \pm 0.005) \times 10^4 \text{ dm}^3 \text{ mol}^{-1} \text{ cm}^{-1}$.

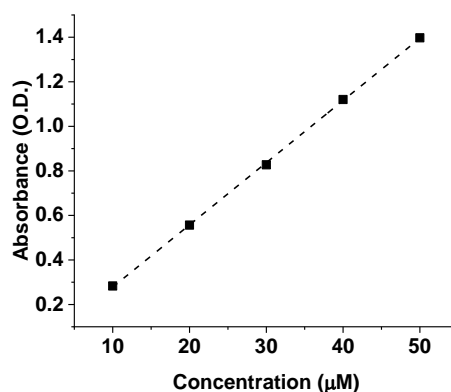


Figure 164: Beer-Lambert plot for 171 in CH_2Cl_2 at 456 nm. The dashed line is a linear fit giving $\epsilon(456 \text{ nm}) = (2.79 \pm .02) \times 10^4 \text{ dm}^3 \text{ mol}^{-1} \text{ cm}^{-1}$.

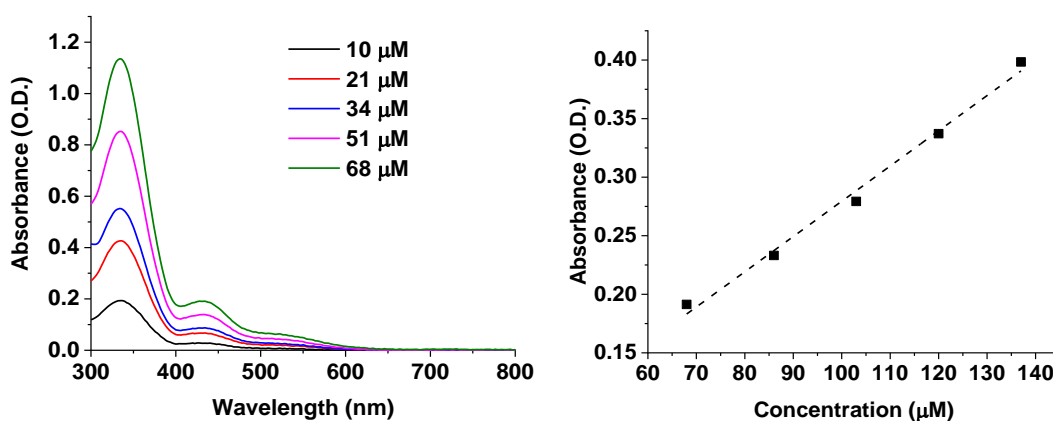


Figure 165 Left: Spectra of 172 in CH_2Cl_2 at the concentrations shown. Right: Beer-Lambert plot for 172 in CH_2Cl_2 at 434 nm. The dashed line is a linear fit giving $\epsilon(434 \text{ nm}) = (3.0 \pm 0.2) \times 10^3 \text{ dm}^3 \text{ mol}^{-1} \text{ cm}^{-1}$. Spectra recorded by Alice de Palo under my supervision.

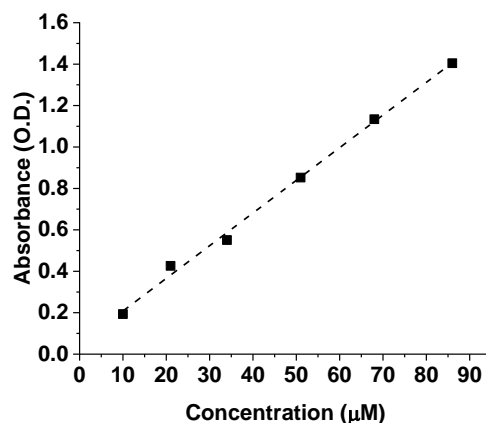


Figure 166: Beer-Lambert plot for 172 in CH_2Cl_2 at 336 nm. The dashed line is a linear fit giving $\epsilon(336 \text{ nm}) = (1.58 \pm .05) \times 10^4 \text{ dm}^3 \text{ mol}^{-1} \text{ cm}^{-1}$. Spectra recorded by Alice de Palo under my supervision.

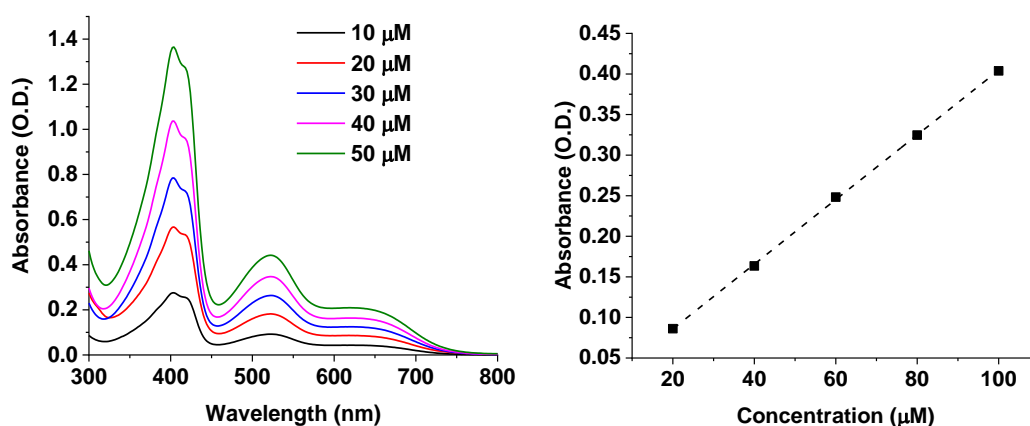


Figure 167 Left: Spectra of 173 in CH_2Cl_2 at the concentrations shown. Right: Beer-Lambert plot for 173 in CH_2Cl_2 at 622 nm. The dashed line is a linear fit giving $\epsilon(622 \text{ nm}) = (3.98 \pm .03) \times 10^3 \text{ dm}^3 \text{ mol}^{-1} \text{ cm}^{-1}$.

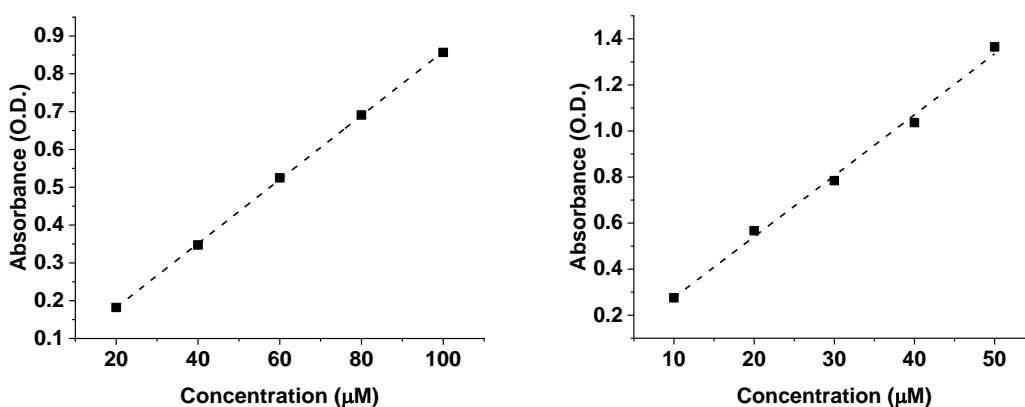


Figure 168 Left: Beer-Lambert plot for 173 in CH_2Cl_2 at 522 nm. The dashed line is a linear fit giving $\epsilon(522 \text{ nm}) = (8.47 \pm .06) \times 10^3 \text{ dm}^3 \text{ mol}^{-1} \text{ cm}^{-1}$. Right: Beer-Lambert plot for 173 in CH_2Cl_2 at 404 nm. The dashed line is a linear fit giving $\epsilon(404 \text{ nm}) = (2.648 \pm .010) \times 10^4 \text{ dm}^3 \text{ mol}^{-1} \text{ cm}^{-1}$.

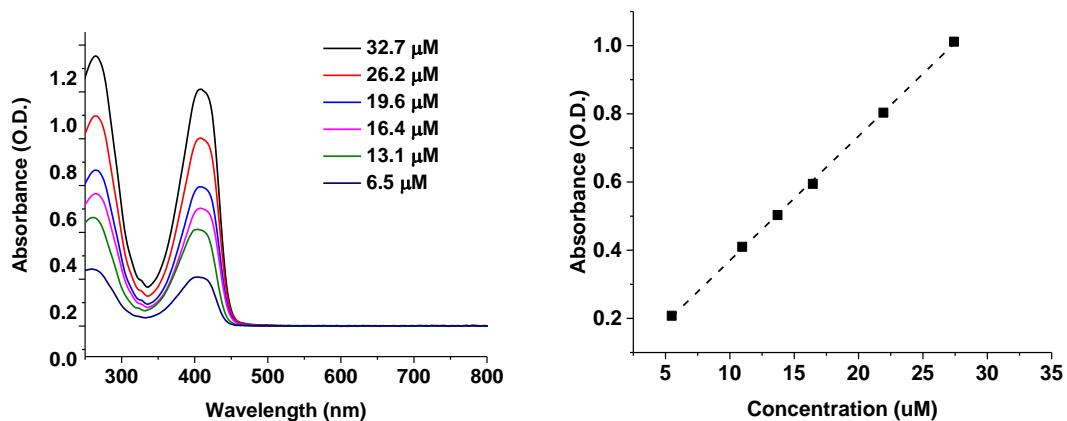


Figure 169 Left: Spectra of 197 in CH₂Cl₂ at the concentrations shown. Right: Beer-Lambert plot for 197 in CH₂Cl₂ at 408 nm. The dashed line is a linear fit giving $\epsilon(408 \text{ nm}) = (3.65 \pm 0.04) \times 10^4 \text{ dm}^3 \text{ mol}^{-1} \text{ cm}^{-1}$.

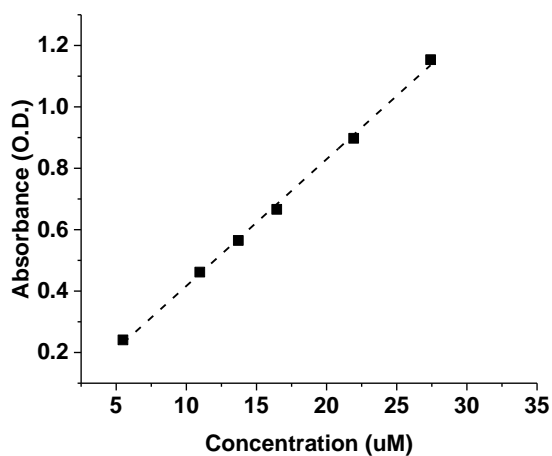


Figure 170: Beer-Lambert plot for 197 in CH₂Cl₂ at 264 nm. The dashed line is a linear fit giving $\epsilon(264 \text{ nm}) = (4.13 \pm 0.09) \times 10^4 \text{ dm}^3 \text{ mol}^{-1} \text{ cm}^{-1}$.

Appendix 4: TRIR Spectroscopic Data

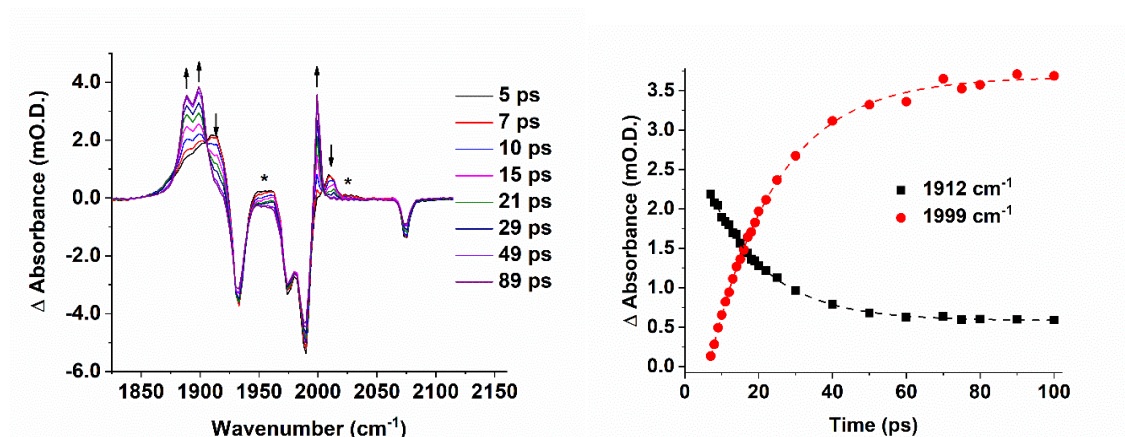


Figure 171 Left: TRIR spectra of $[\text{Mn}(\text{ppy})(\text{CO})_4]$ (88) photolyzed in THF under an atmosphere of CO to form solvent complexes $113_{\text{THF}(\sigma)}$ and $113_{\text{THF}(\text{O})}$. The triplet excited state bands are marked with asterisks. Right: Evolution of the $113_{\text{THF}(\sigma)}$ 1912 cm^{-1} band and the $113_{\text{THF}(\text{O})}$ 1999 cm^{-1} band from 5 to 99 ps. The dashed lines are single exponential fits.

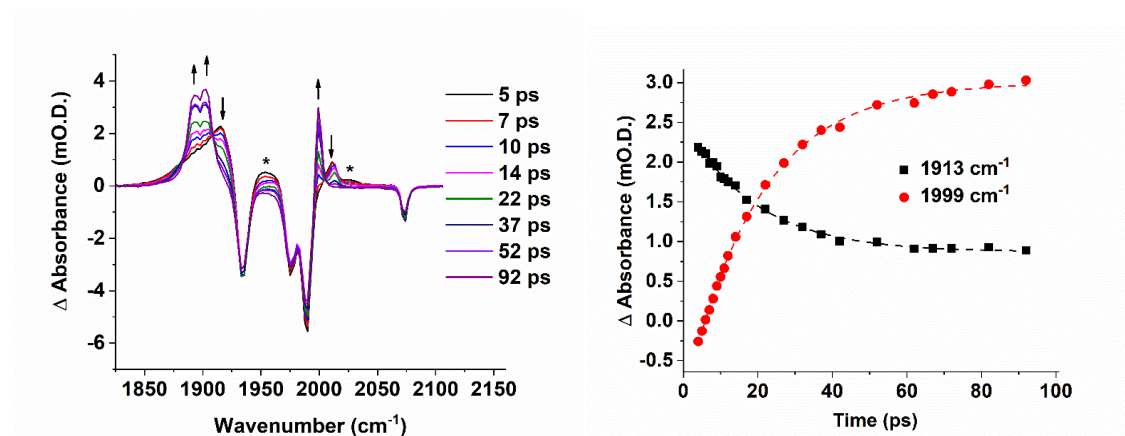


Figure 172 Left: TRIR spectra of 94 photolyzed in THF to form the corresponding C-H σ - and O-bound complexes. The triplet excited state bands are marked with asterisks. Right: Evolution of the σ - 1913 cm^{-1} band and the O-bound 1999 cm^{-1} band from 5 to 92 ps. The dashed lines are single exponential fits.

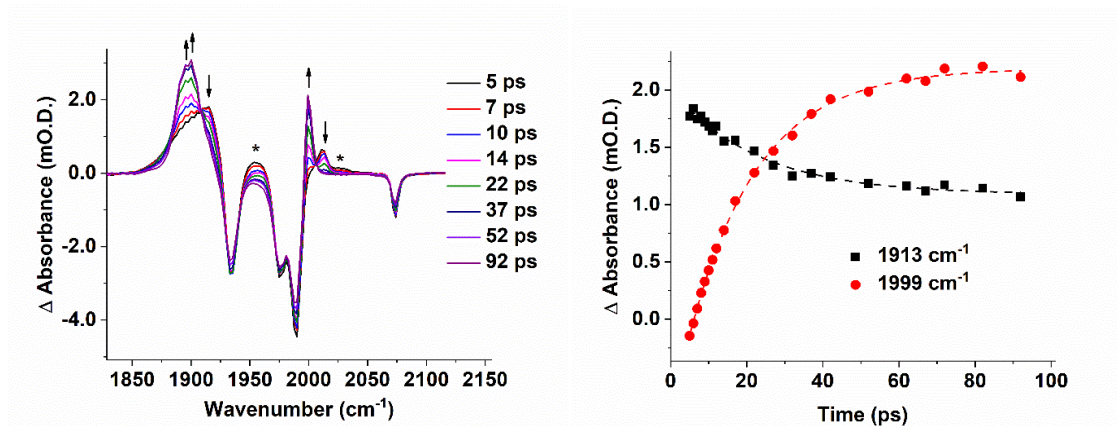


Figure 173 Left: TRIR spectra of 95 photolyzed in THF to form the corresponding C-H σ - and O-bound complexes. The triplet excited state bands are marked with asterisks. Right: Evolution of the σ - 1913 cm^{-1} band and the O-bound 1999 cm^{-1} band from 5 to 92 ps. The dashed lines are single exponential fits.

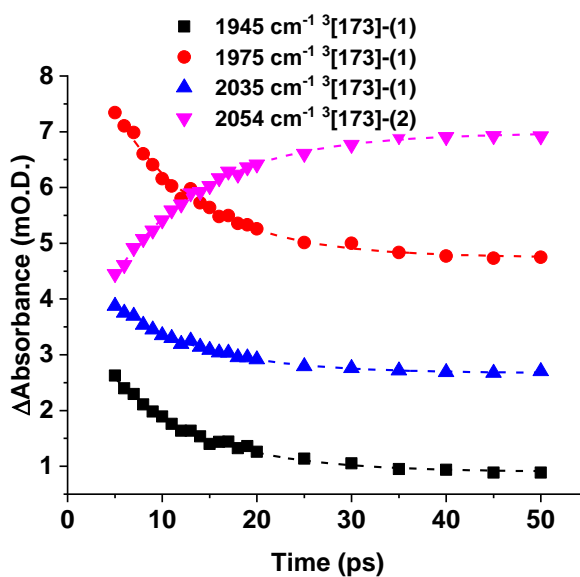


Figure 174: Kinetic profiles of selected TRIR bands for 173 on the picosecond timescale. The dashed lines are single exponential fits.

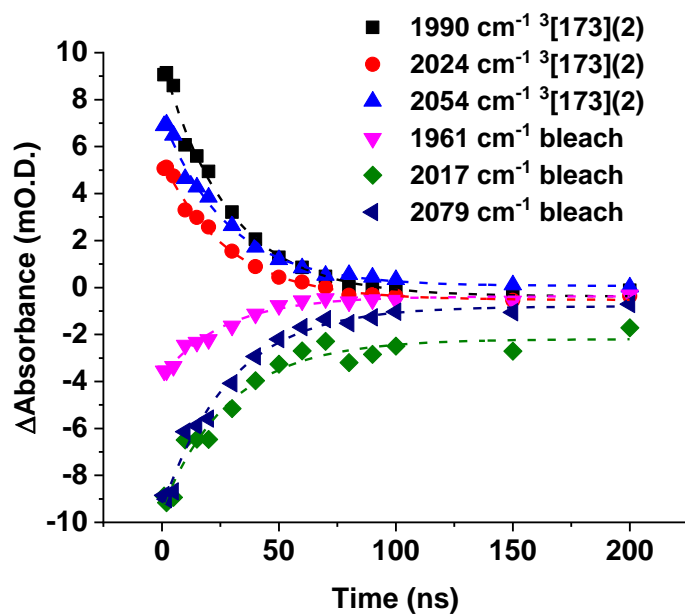


Figure 175: Kinetic profiles of selected TRIR bands for 173 on the nanosecond timescale. The dashed lines are single exponential fits.

Appendix 5: Growth Curves

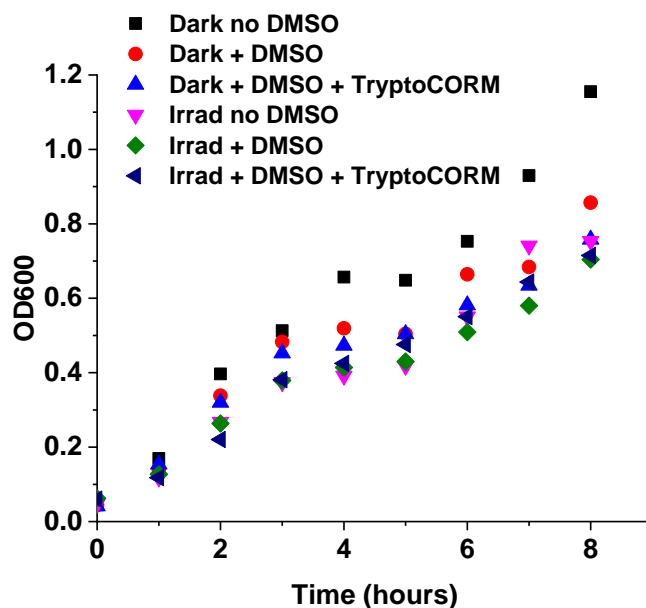


Figure 176: Growth curves with *E. coli* BL21 in 50% LB media under the conditions shown. All cultures containing DMSO were 1% DMSO by volume. The TryptoCORM concentration used was 100 μ M. Irradiation with a 2.4 W power 400 nm LED took place between 0 and 2 hours and comprised cycles of 3 minutes off, 2 minutes on.

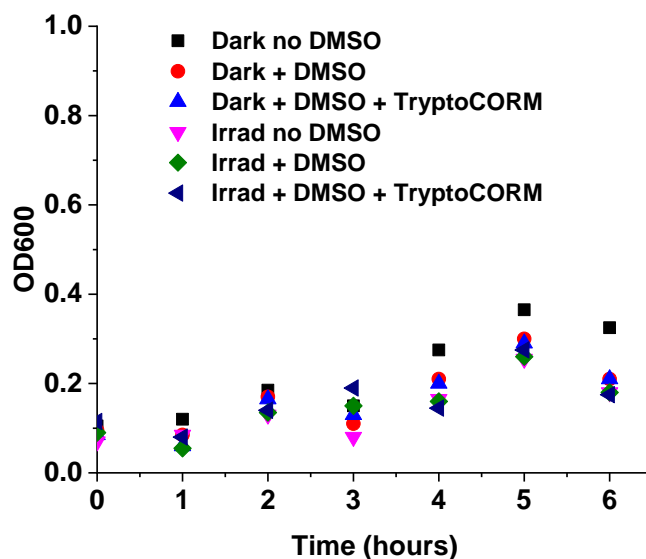


Figure 177: Growth curves with *E. coli* BL21 in 10% LB media under the conditions shown. All cultures containing DMSO were 1% DMSO by volume. The TryptoCORM concentration used was 100 μ M. Irradiation with a 2.4 W power 400 nm LED took place between 0 and 2 hours and comprised cycles of 3 minutes off, 2 minutes on.

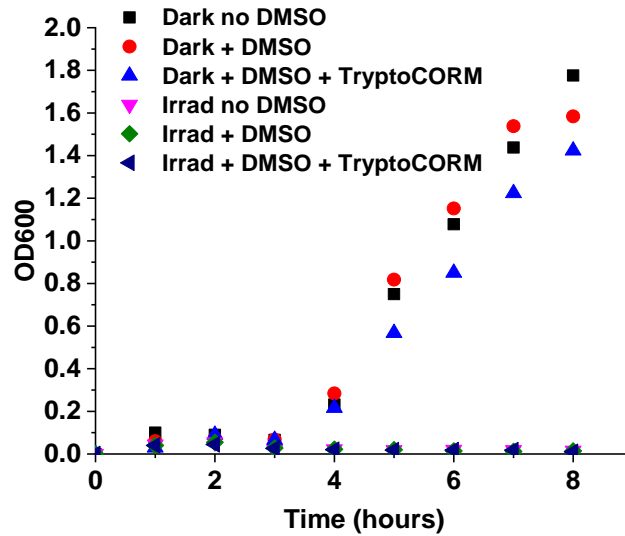


Figure 178: Growth curves with *E. coli* BL21 under the conditions shown. All cultures containing DMSO were 1% DMSO by volume. The TryptoCORM concentration used was 100 μ M. Irradiation with a 2.4 W power 400 nm LED took place between 0 and 2 hours and comprised cycles of 3 minutes off, 2 minutes on. This is a repeat of the experiment in Figure 138.

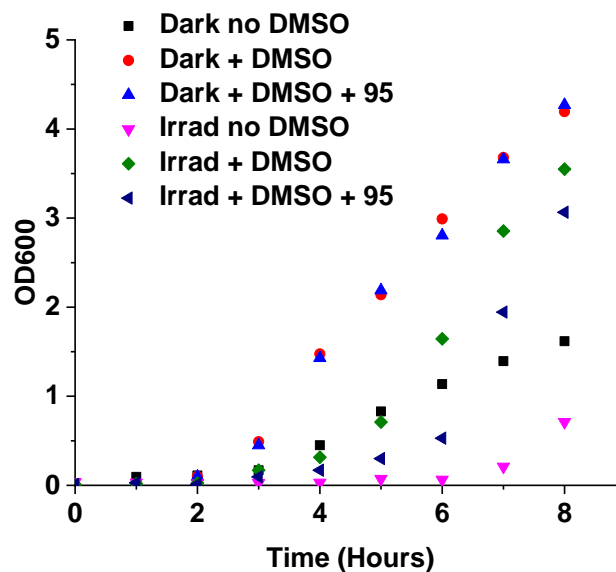


Figure 179: Growth curves with *E. coli* BL21 under the conditions shown. All cultures containing DMSO were 1% DMSO by volume. The concentration of 95 used was 100 μ M. Irradiation with a 2.4 W power 400 nm LED took place between 0 and 2 hours and comprised cycles of 3 minutes off, 2 minutes on. This is a repeat of the experiment in Figure 140 with bacteria from a different plate.

Appendix 6: NMR Spectra

Filename: r4107yuk
Reference: BnMn(CO)₅

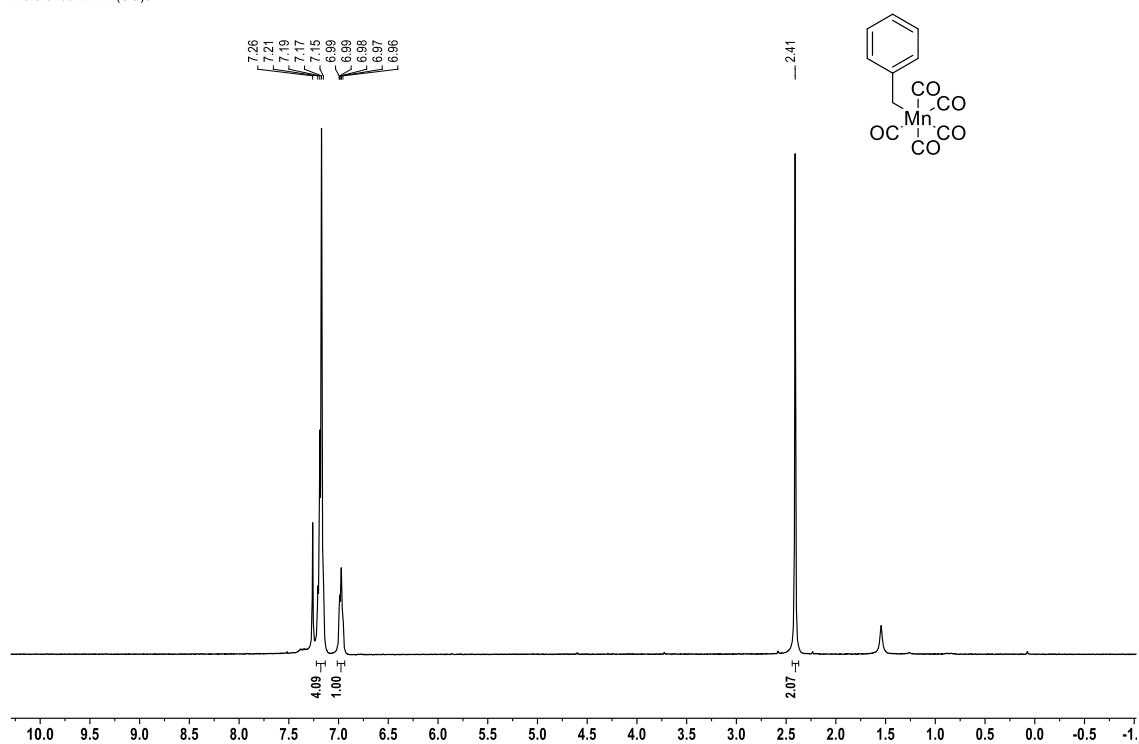


Figure 180: A 400 MHz ¹H NMR spectrum of 87 in CDCl₃.

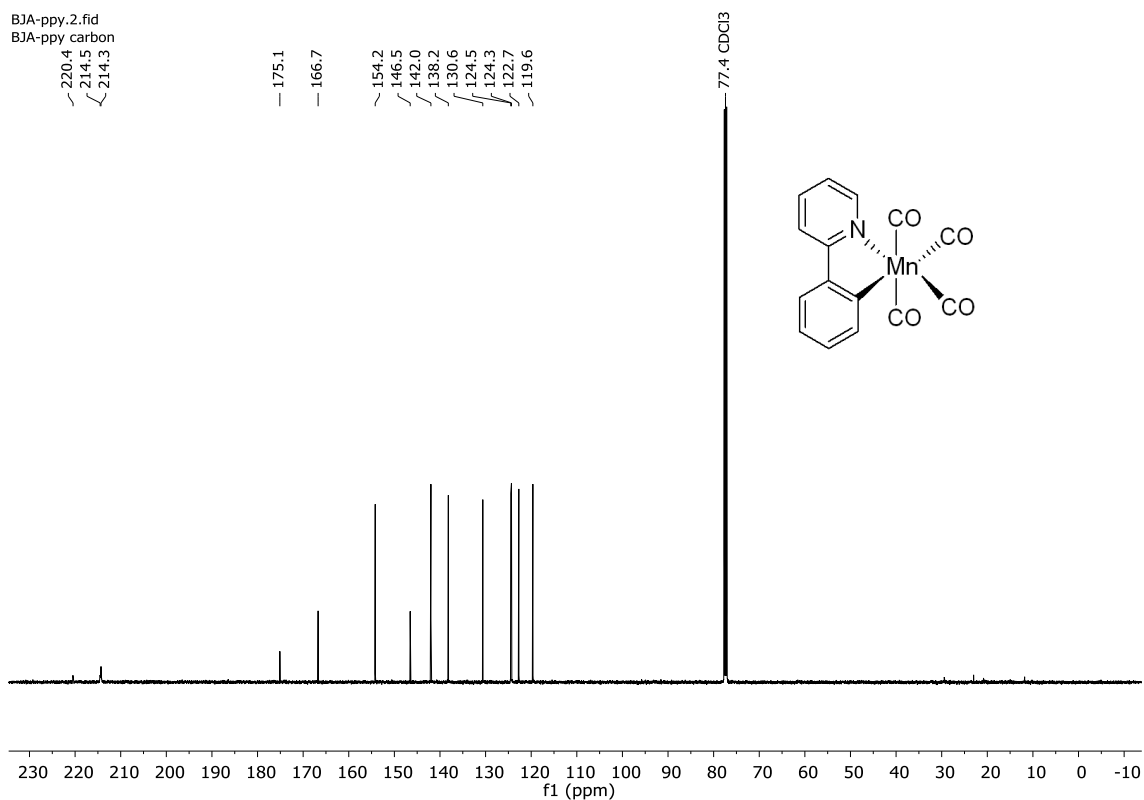


Figure 183 A 126 MHz ¹³C NMR spectrum of 88 in CDCl₃.

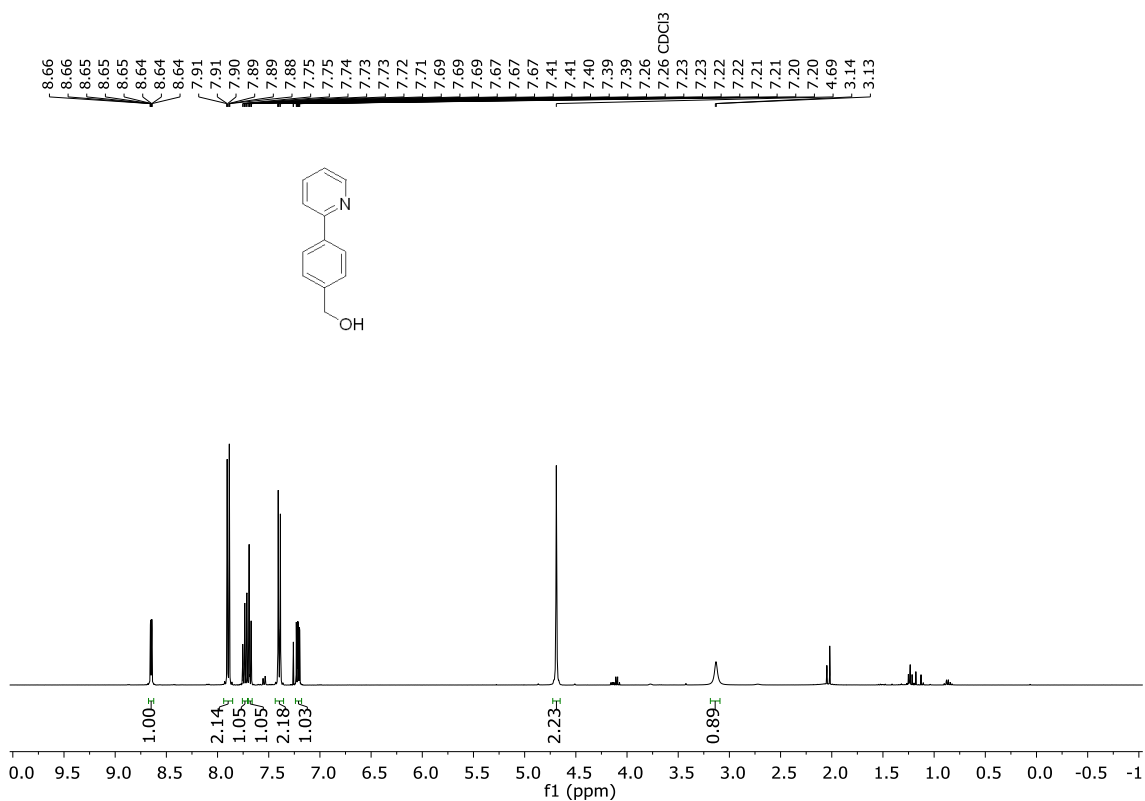


Figure 184: A 400 MHz ¹H NMR spectrum of 138 in CDCl₃.

Filename: c96711mm_CARBON-2_jdf
Reference: c96711mm

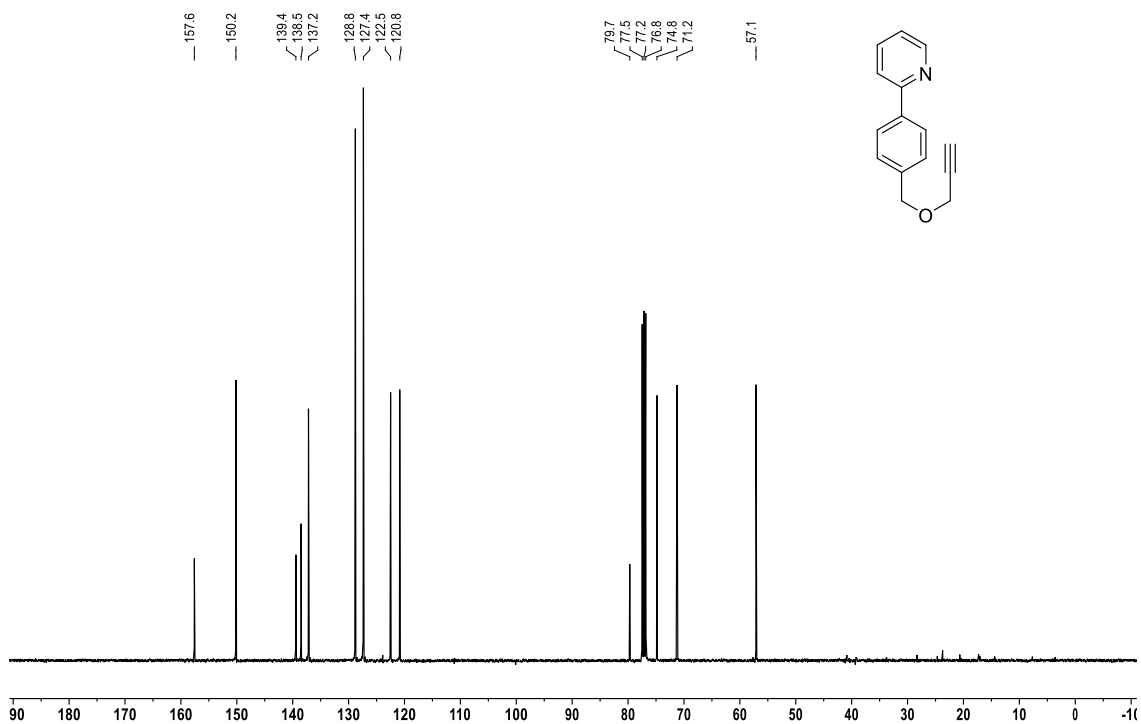


Figure 187: A 101 MHz ^{13}C NMR spectrum of 139 in CDCl_3 .

Filename: d02411mm_PROTON-2_jdf
Reference: d02411mm

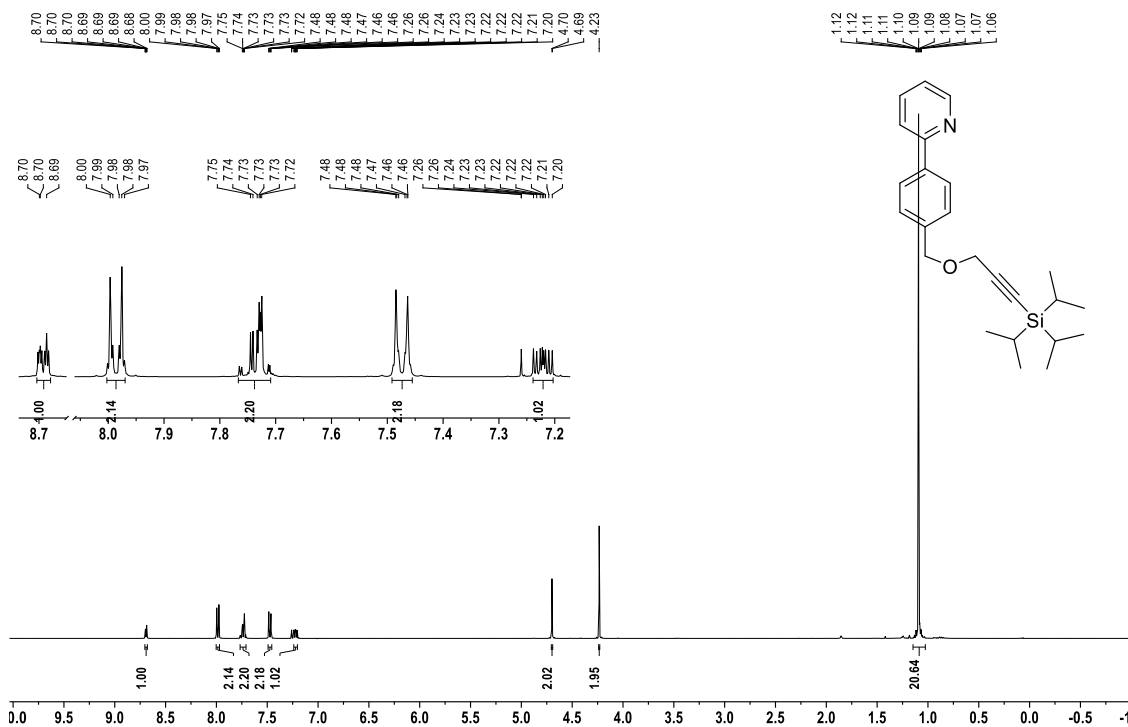


Figure 188: A 400 MHz ^1H NMR spectrum of 140 in CDCl_3 .

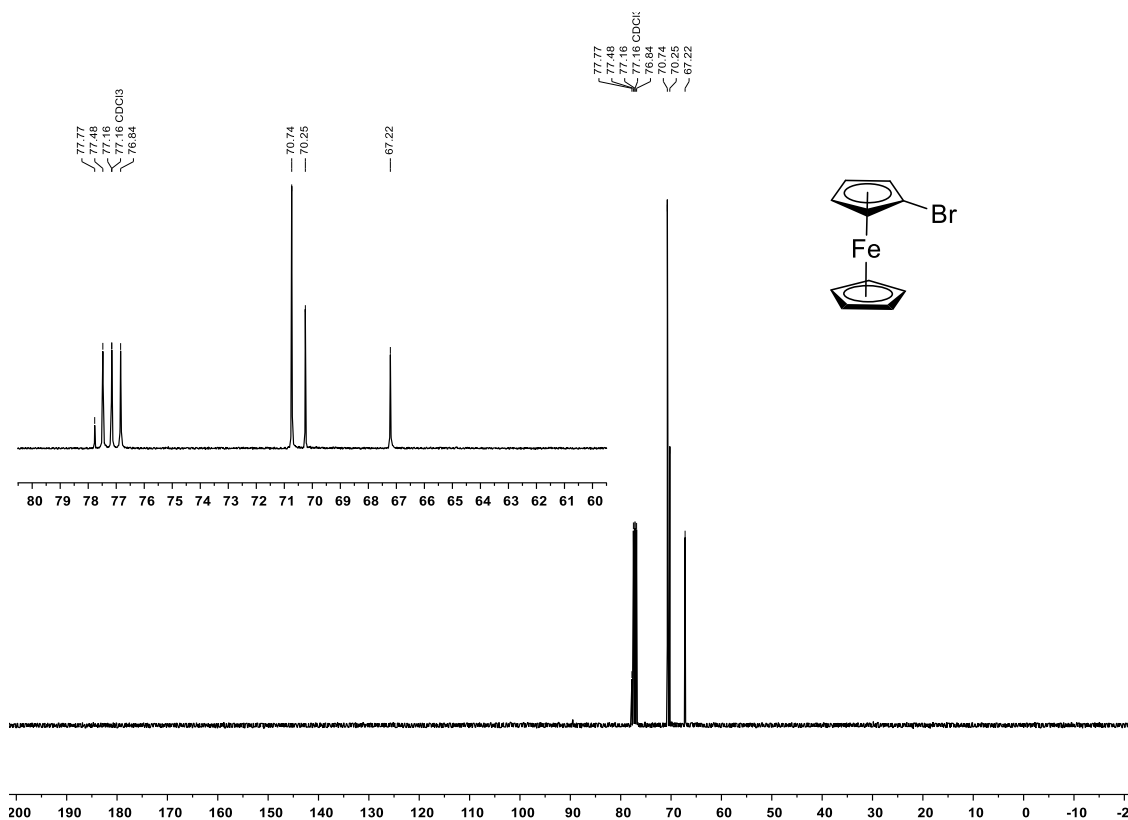


Figure 195: A 101 MHz ^{13}C NMR spectrum of 143 in CDCl_3 .

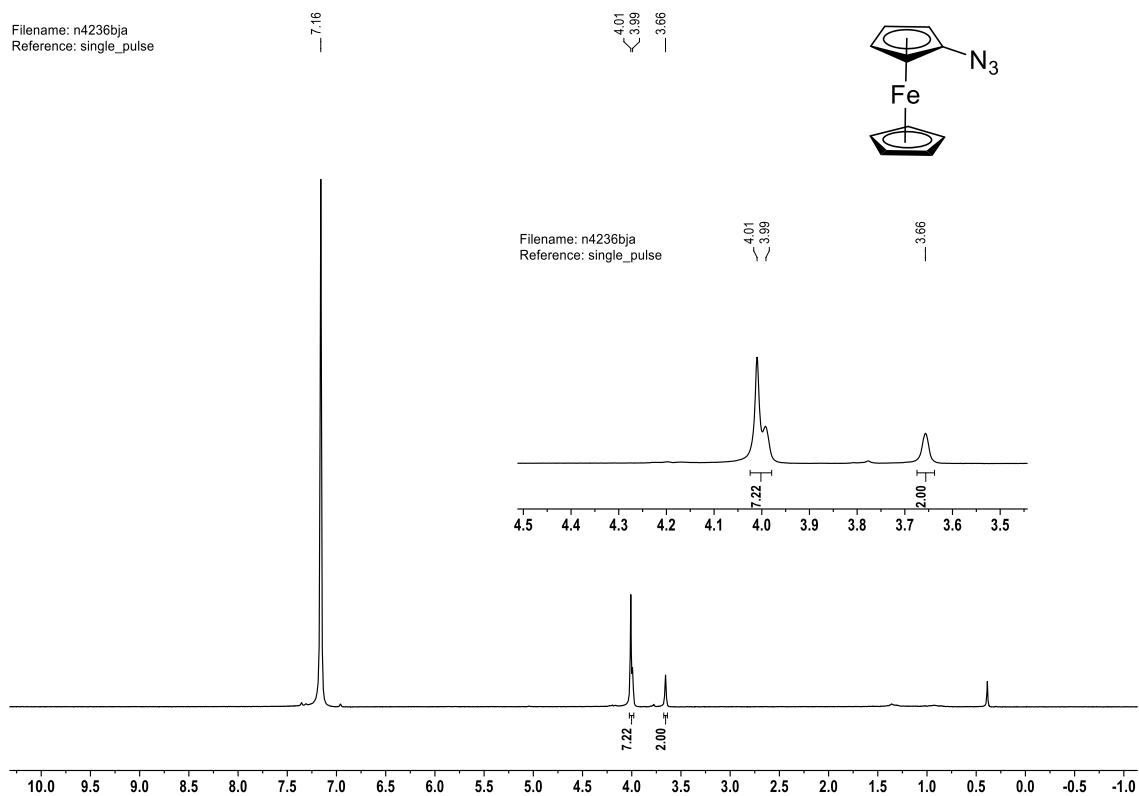


Figure 196: A 400 MHz ^1H NMR spectrum of 135 in CDCl_3 .

Filename: d8335bja
Reference: ben aucott bja-1-014-f

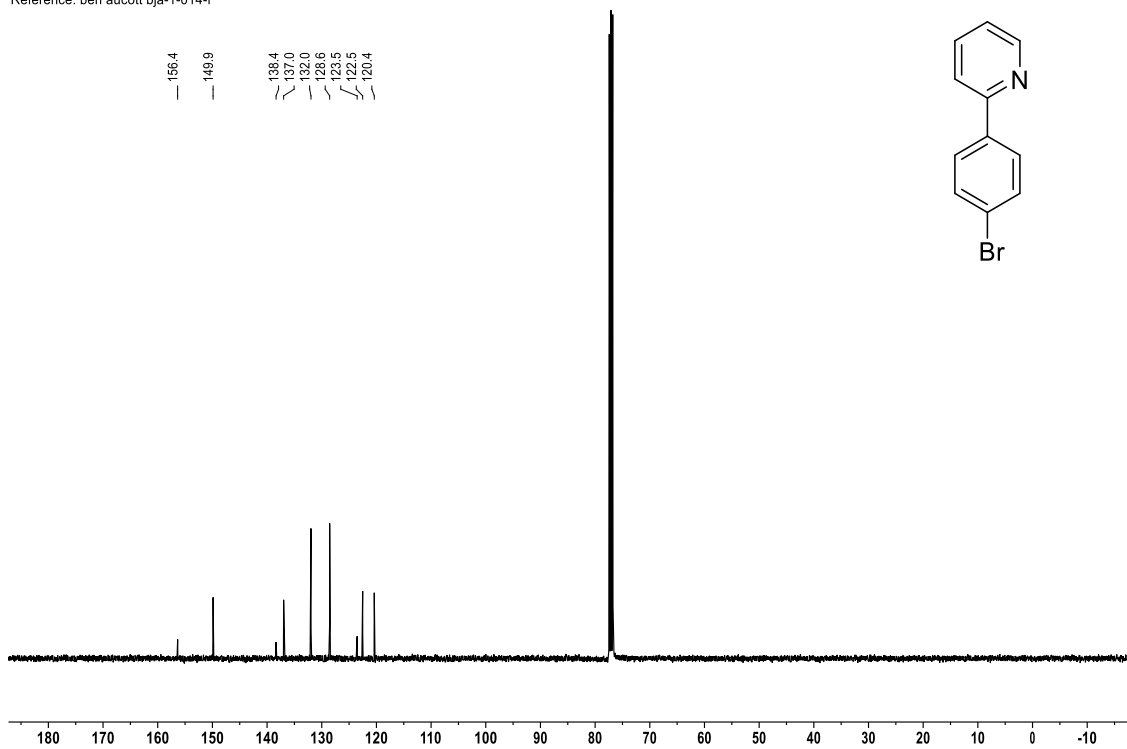


Figure 201: A 101 MHz ^{13}C NMR spectrum of 82 in CDCl_3 .

a3141bja
ben aucott bja-1-055

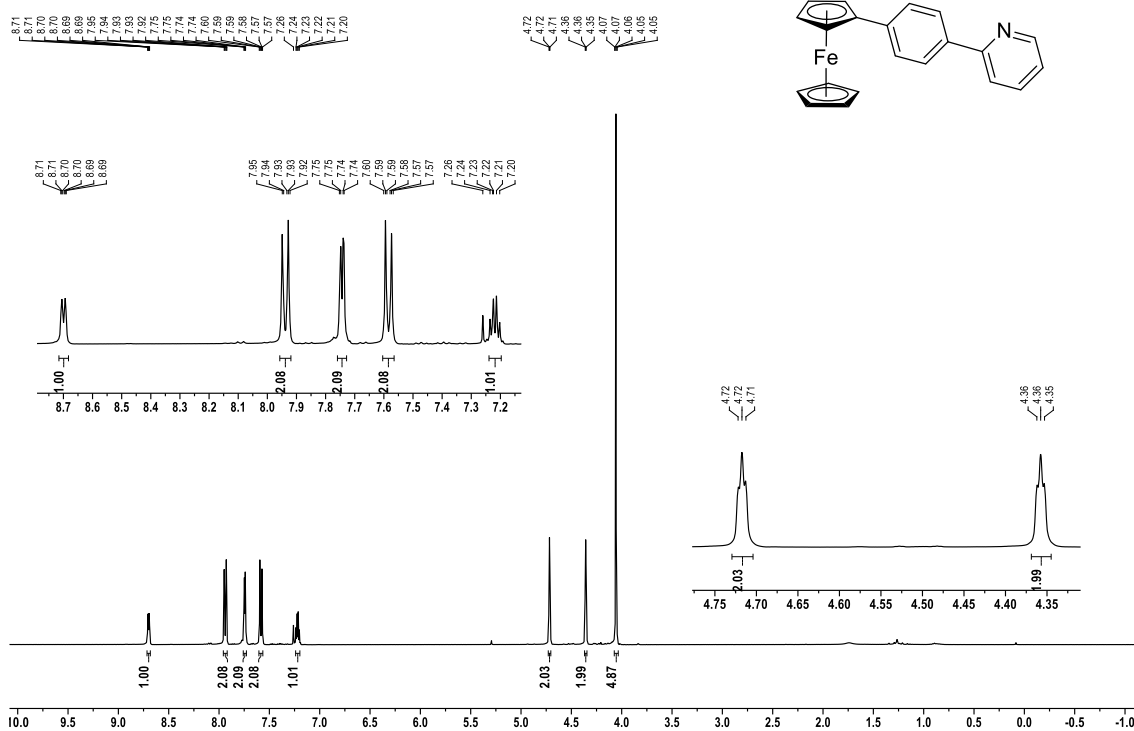


Figure 202: A 400 MHz ^1H NMR spectrum of 148 in CDCl_3 .

p5342bja
ben aucott bja-1-055

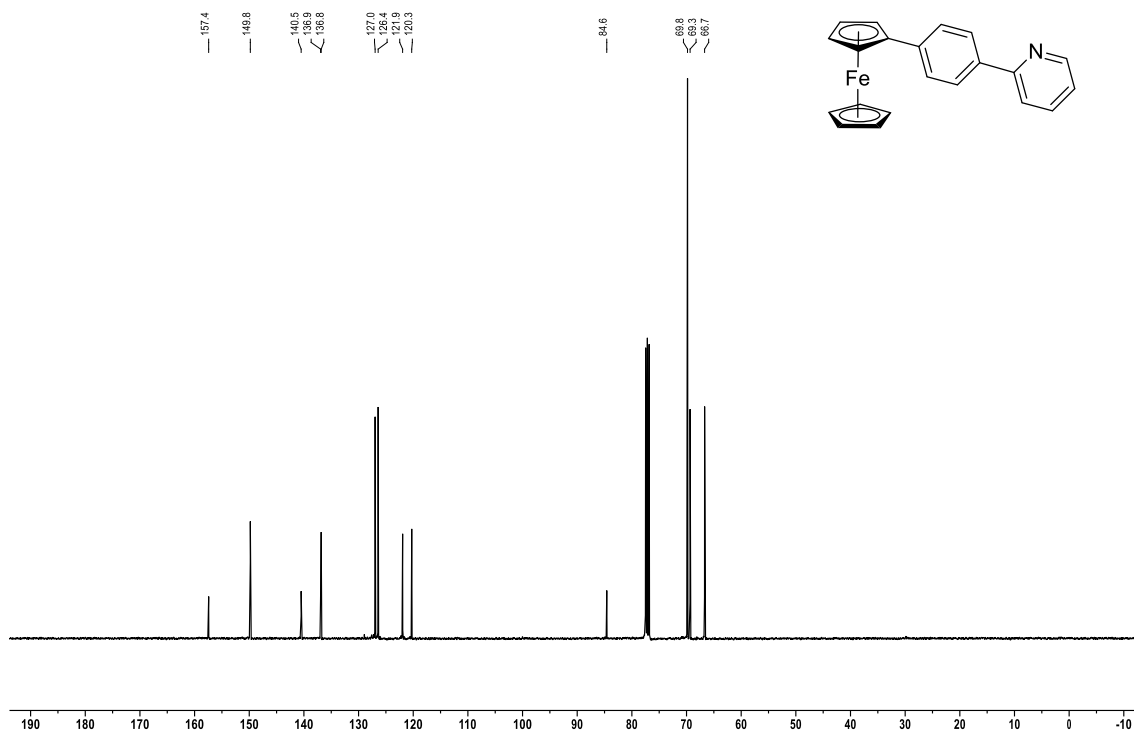


Figure 203: A 101 MHz ^{13}C NMR spectrum of 148 in CDCl_3 .

Filename: BJA_1_56.1.fid
Reference: BJA-1-056

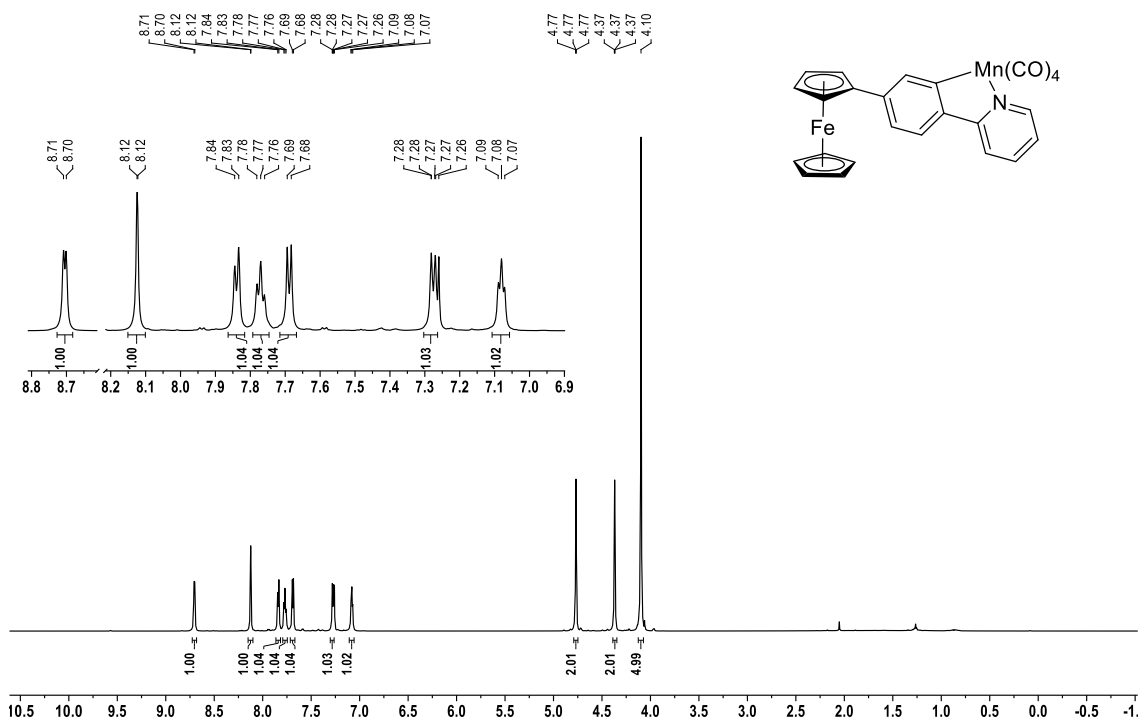


Figure 204: A 700 MHz ^1H NMR spectrum of 133 in CDCl_3 .

Filename: BJA_1_56.8.fid
Reference: BJA-1-056

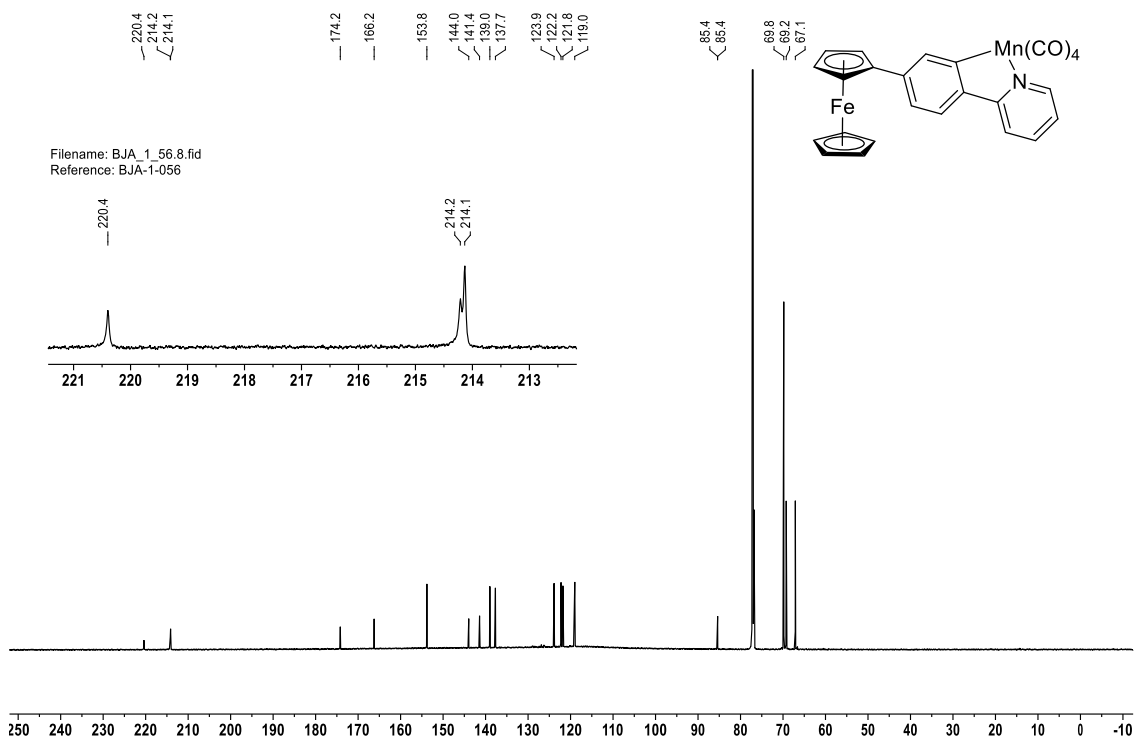


Figure 205: A 176 MHz ^{13}C NMR spectrum of 133 in CDCl_3 .

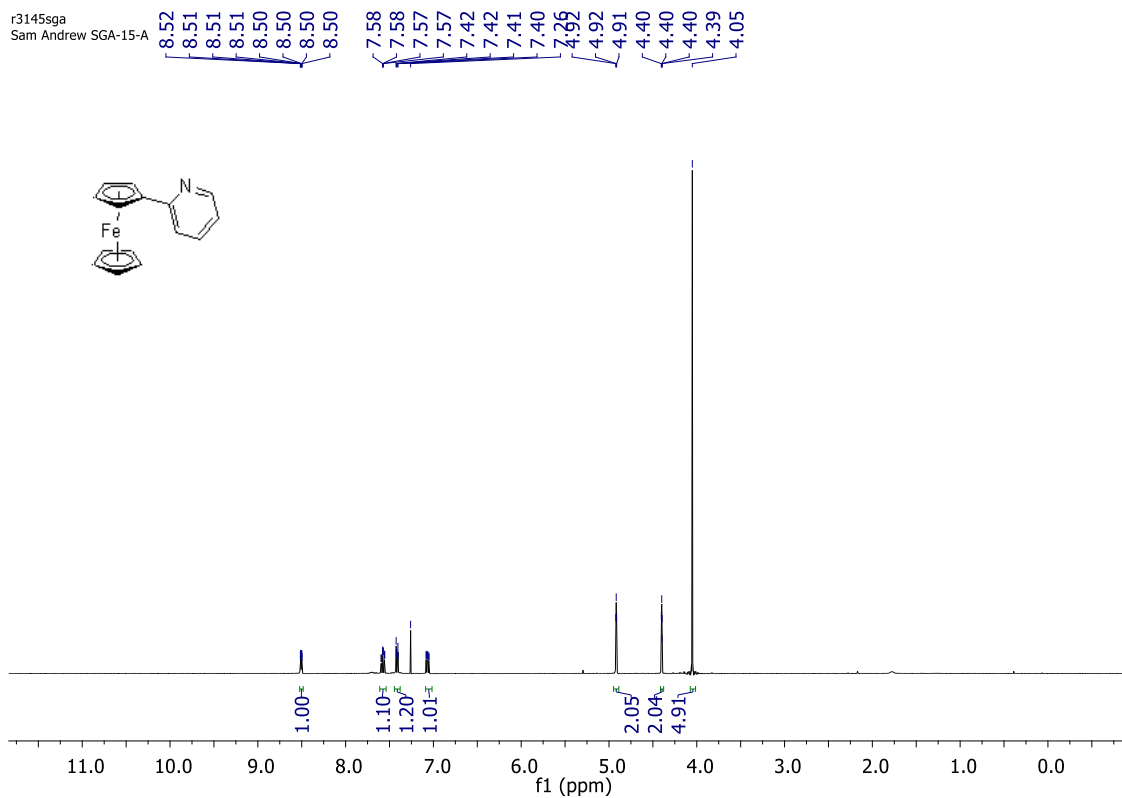


Figure 206: A 700 MHz ^1H NMR spectrum of 149 in CD_2Cl_2 .

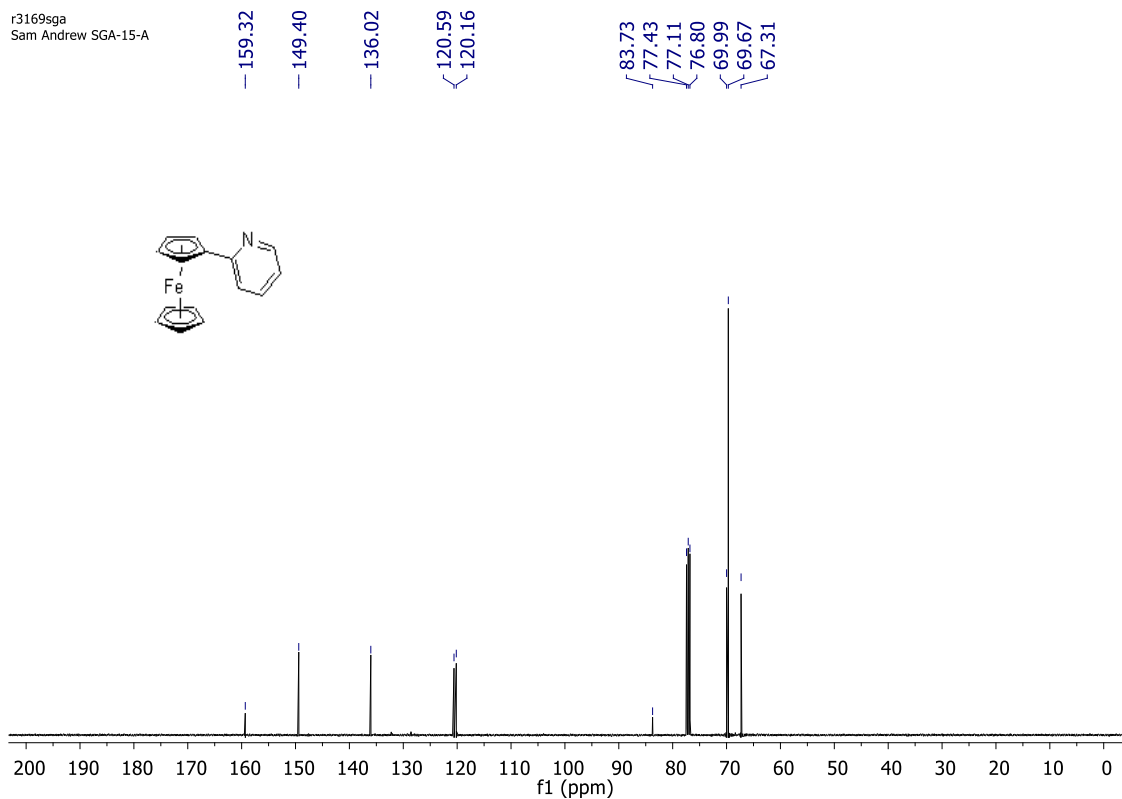


Figure 207: A 176 MHz ^{13}C NMR spectrum of 149 in CD_2Cl_2 .

SAndrew_SGA_16.1.fid
S. Andrew
SGA-16

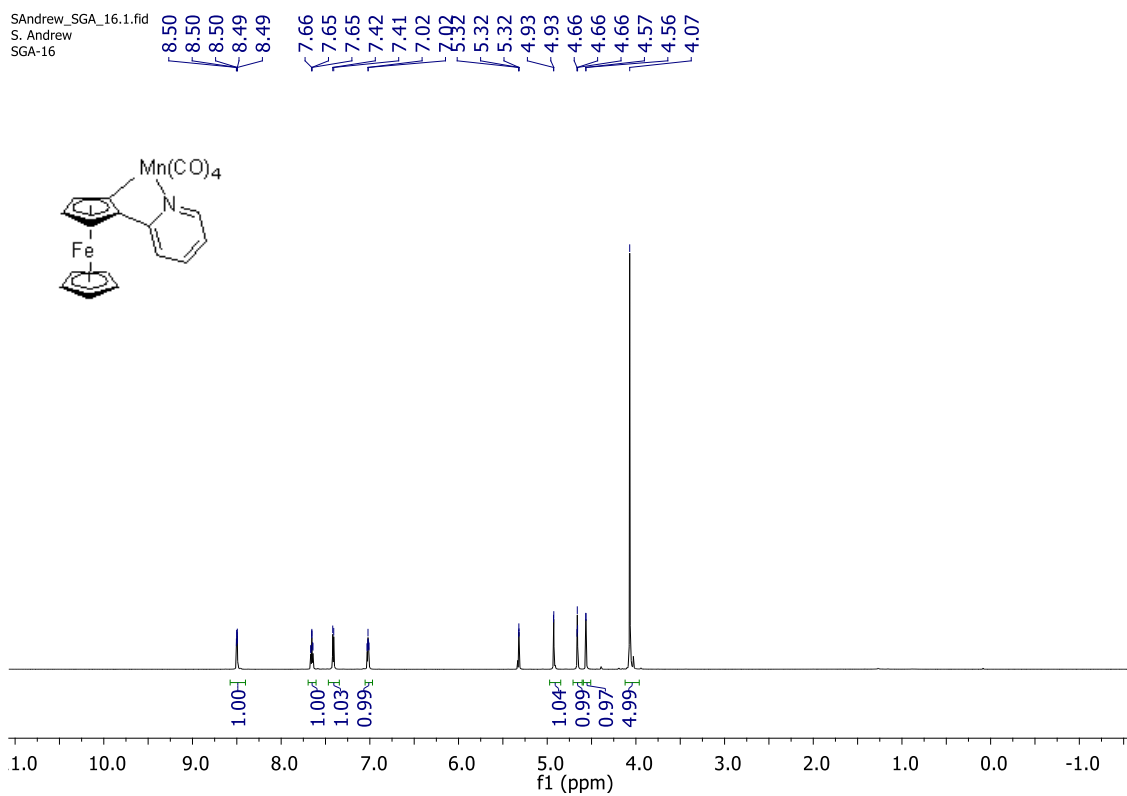
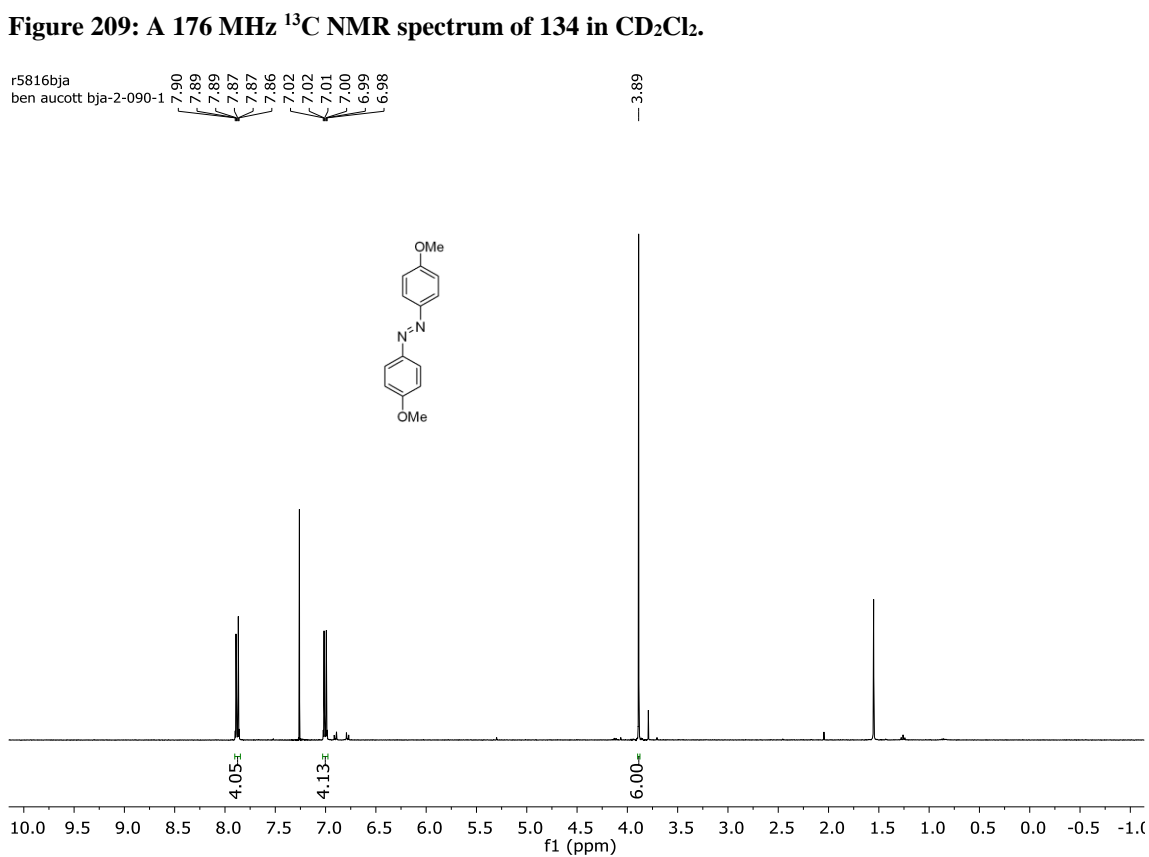
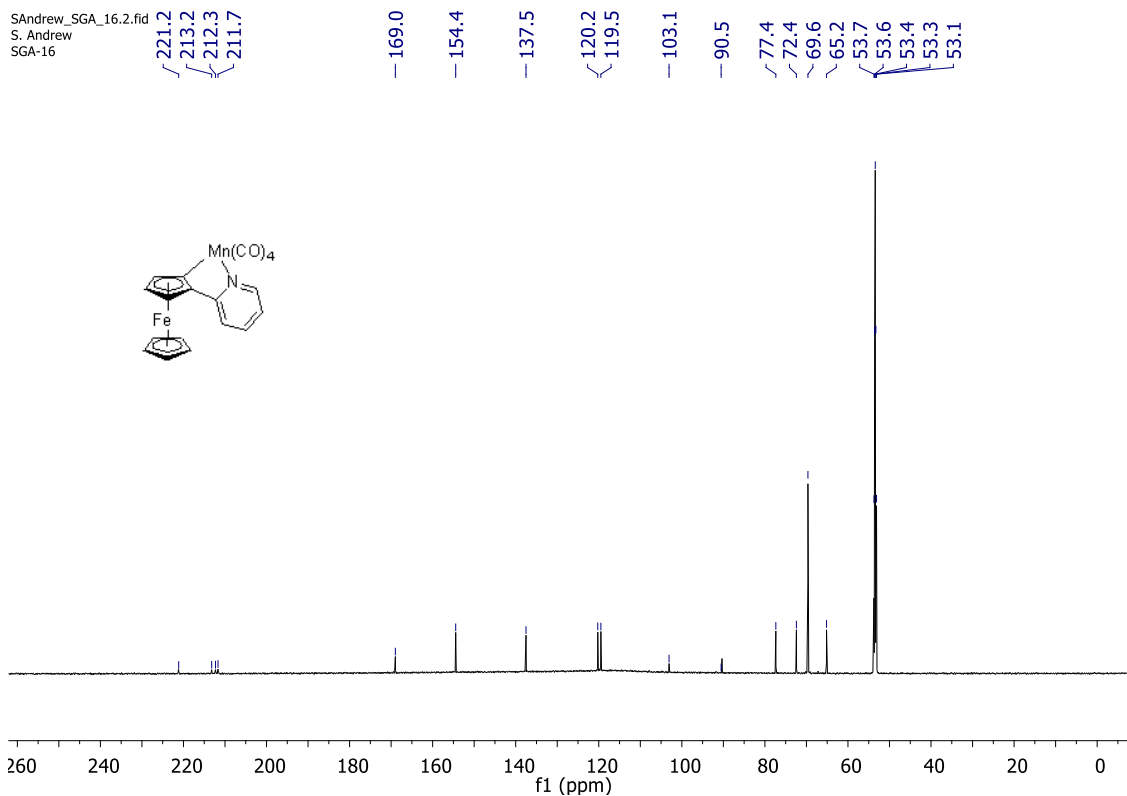


Figure 208: A 700 MHz ^1H NMR spectrum of 134 in CD_2Cl_2 .



n2267bja
Ben Aucott BJA-2-90

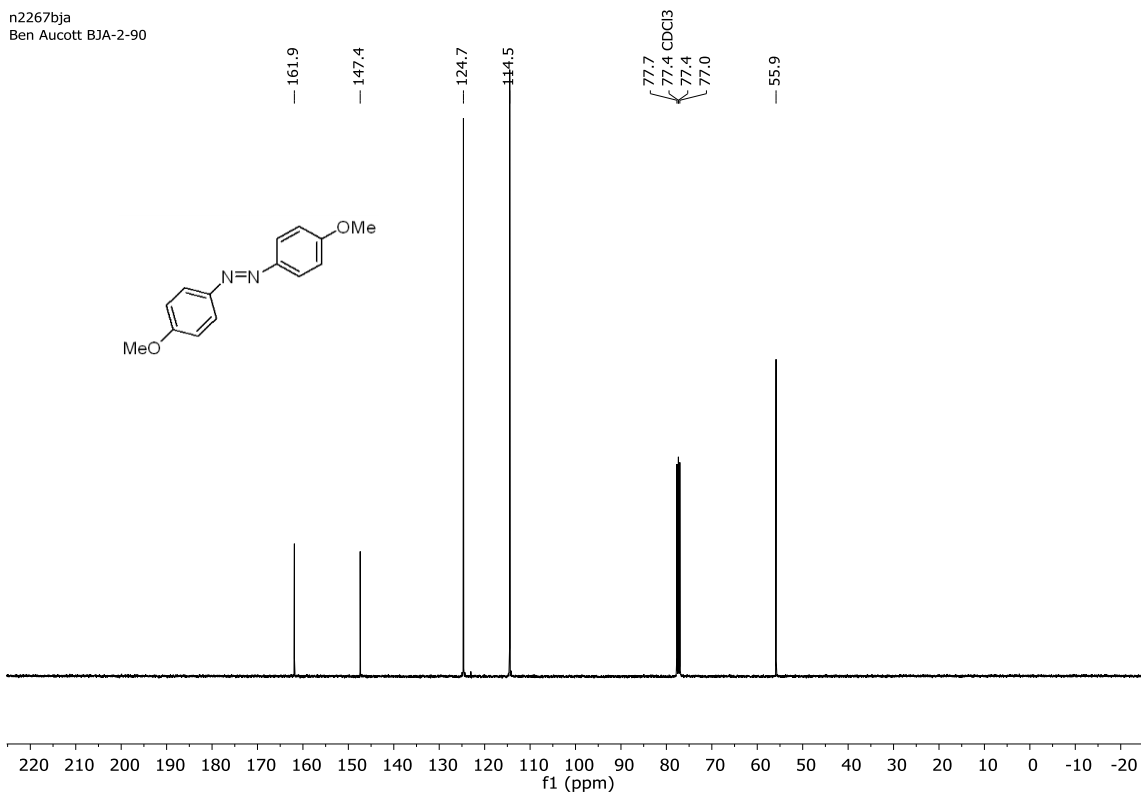


Figure 211: A 126 MHz ^{13}C NMR spectrum of 167 in CDCl_3 .

k7115bja
ben aucott bja-2-114-p

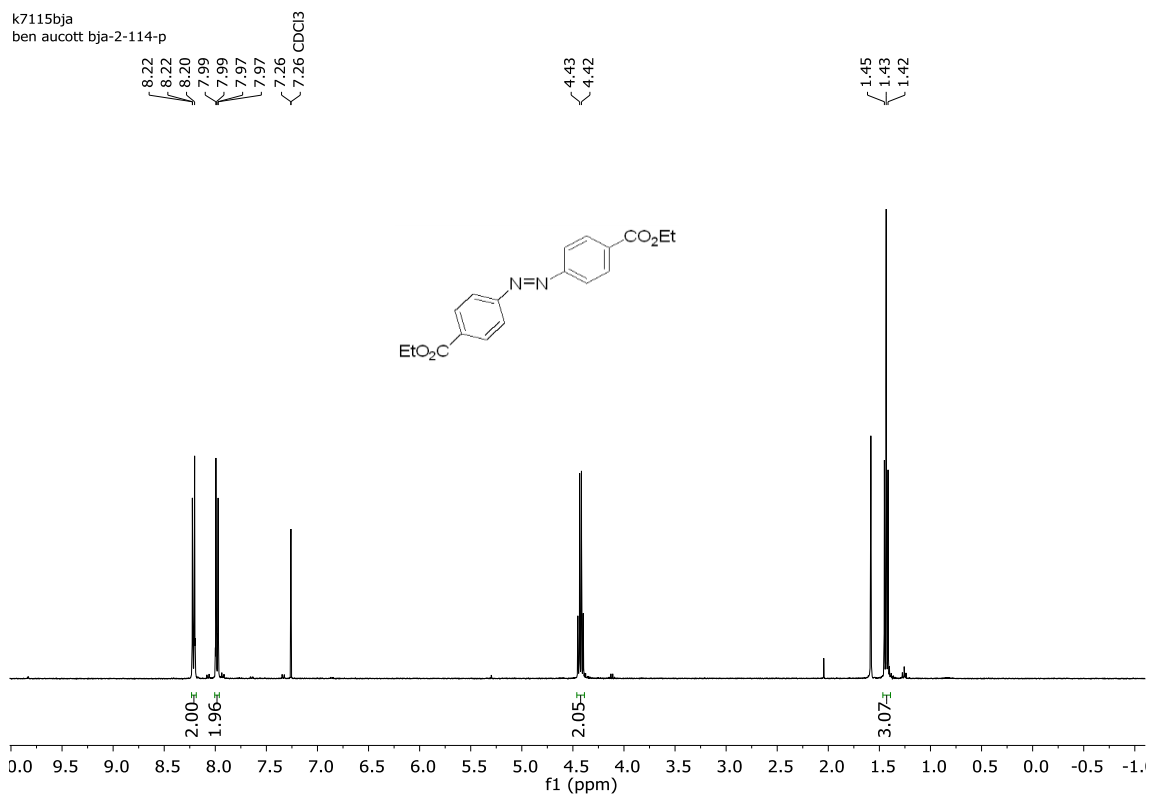


Figure 212: A 400 MHz ^1H NMR spectrum of 169 in CDCl_3 .

n2269bjja
Ben Aucott BJA-2-114

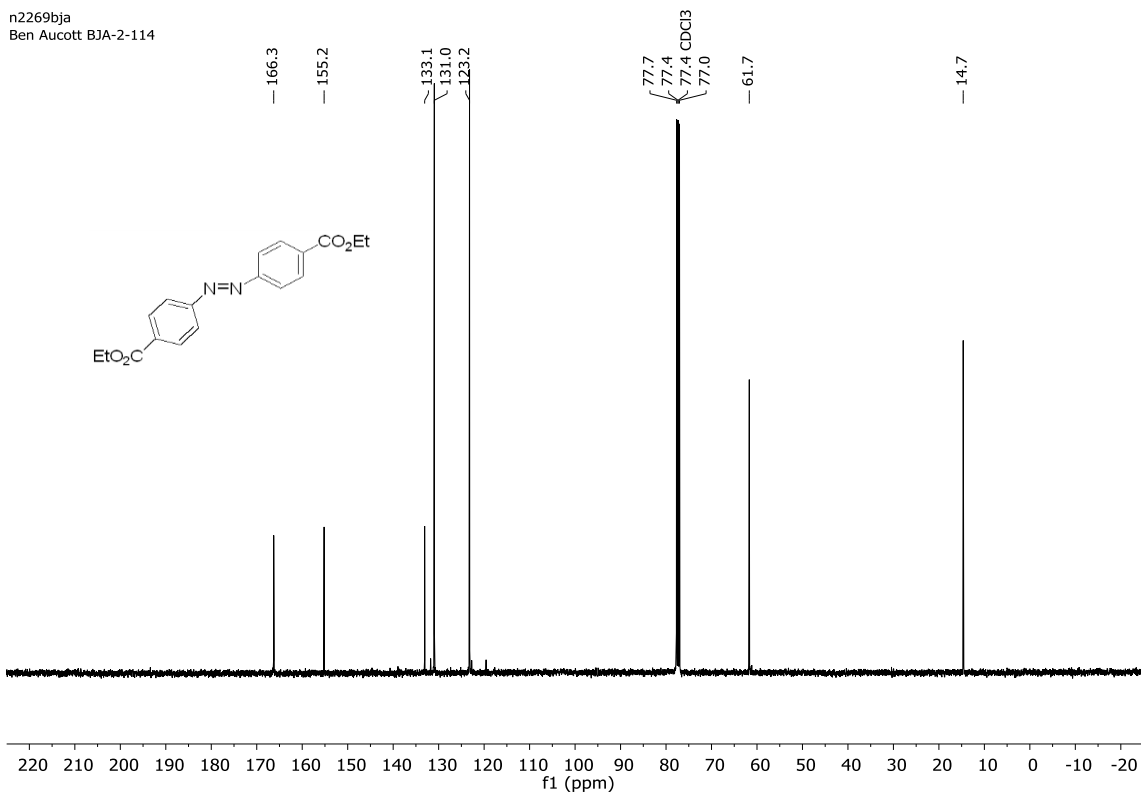


Figure 213: A 126 MHz ^{13}C NMR spectrum of 169 in CDCl_3 .

BJA-memnc5.1.fid
BJA-memnc5

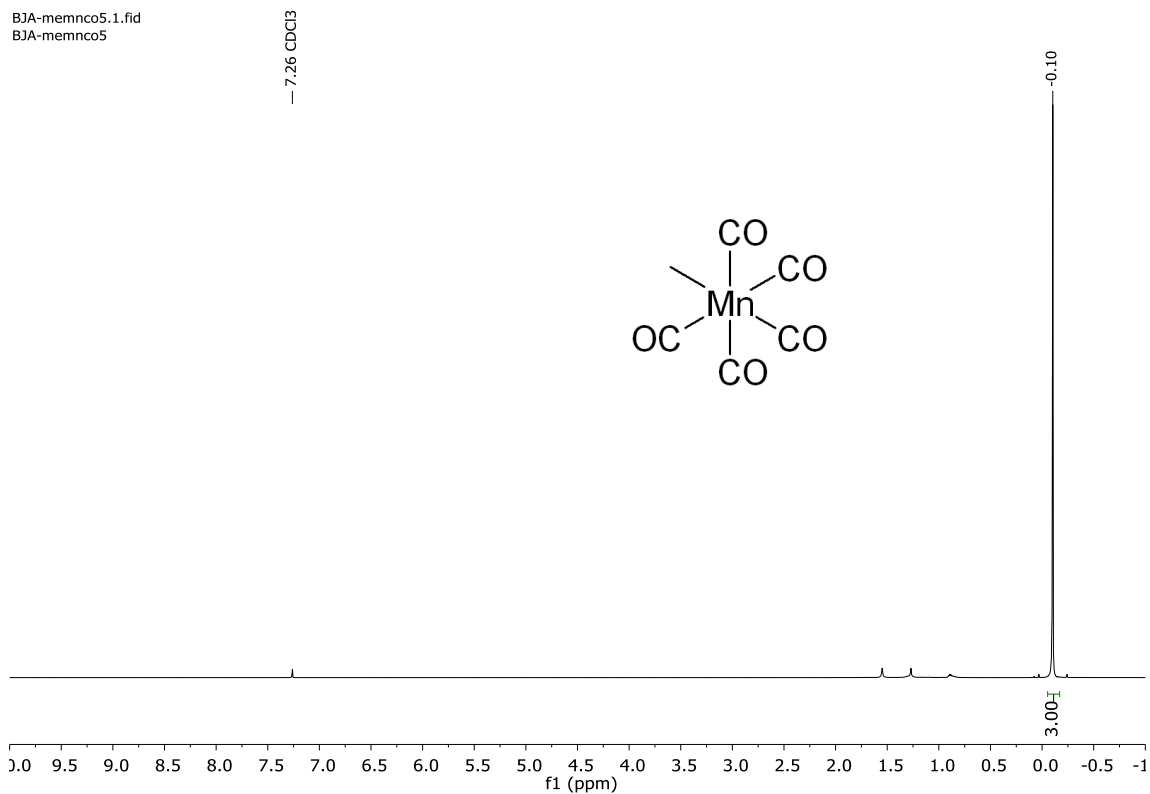


Figure 214: A 500 MHz ^1H NMR spectrum of 174 in CDCl_3 .

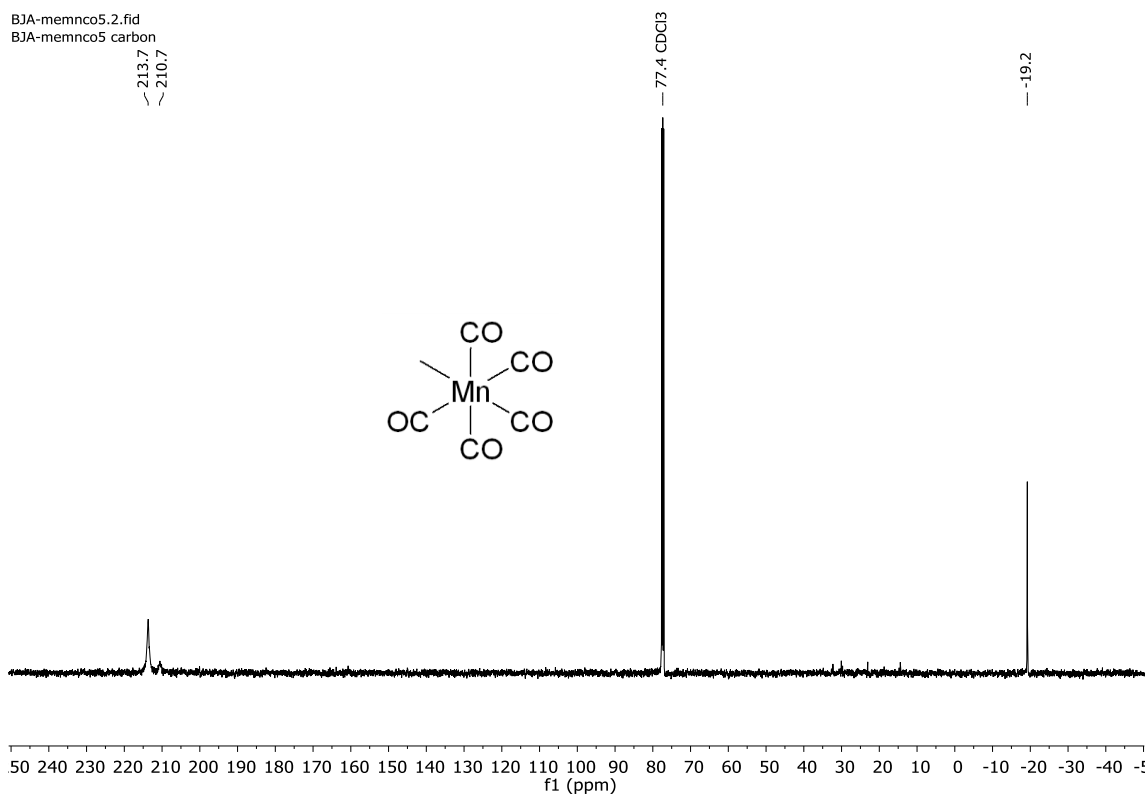


Figure 215: A 126 MHz ¹³C NMR spectrum of 174 in CDCl₃.

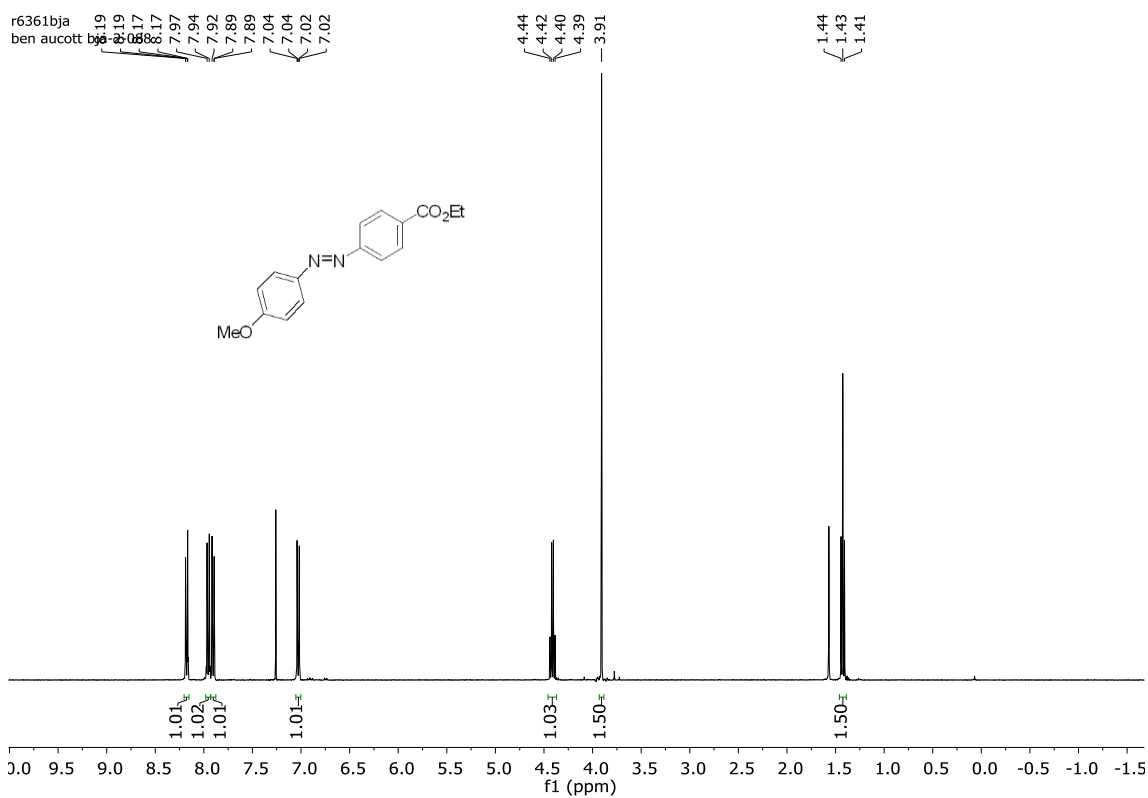


Figure 216: A 400 MHz ¹H NMR spectrum of 176 in CDCl₃.

r6417bja
ben aucott bja-2-088

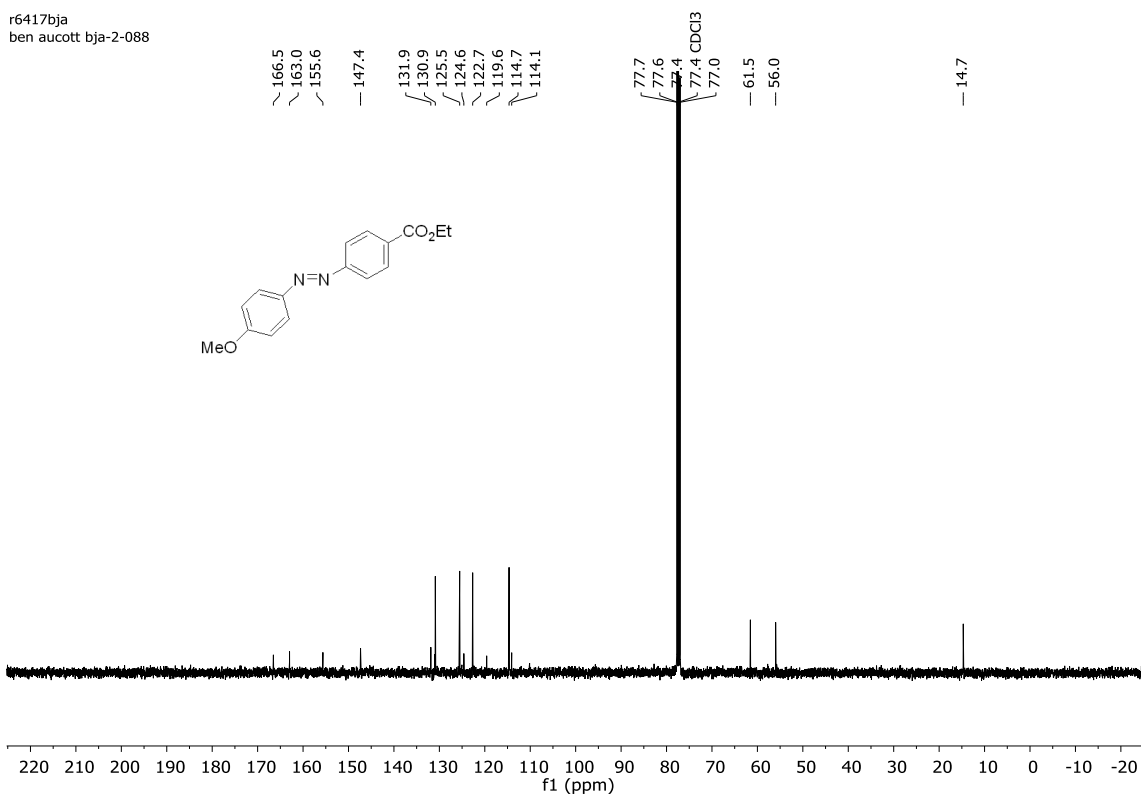


Figure 217: A 126 MHz ^{13}C NMR spectrum of 176 in CDCl_3 .

BJA-2-92-mono.1.fid

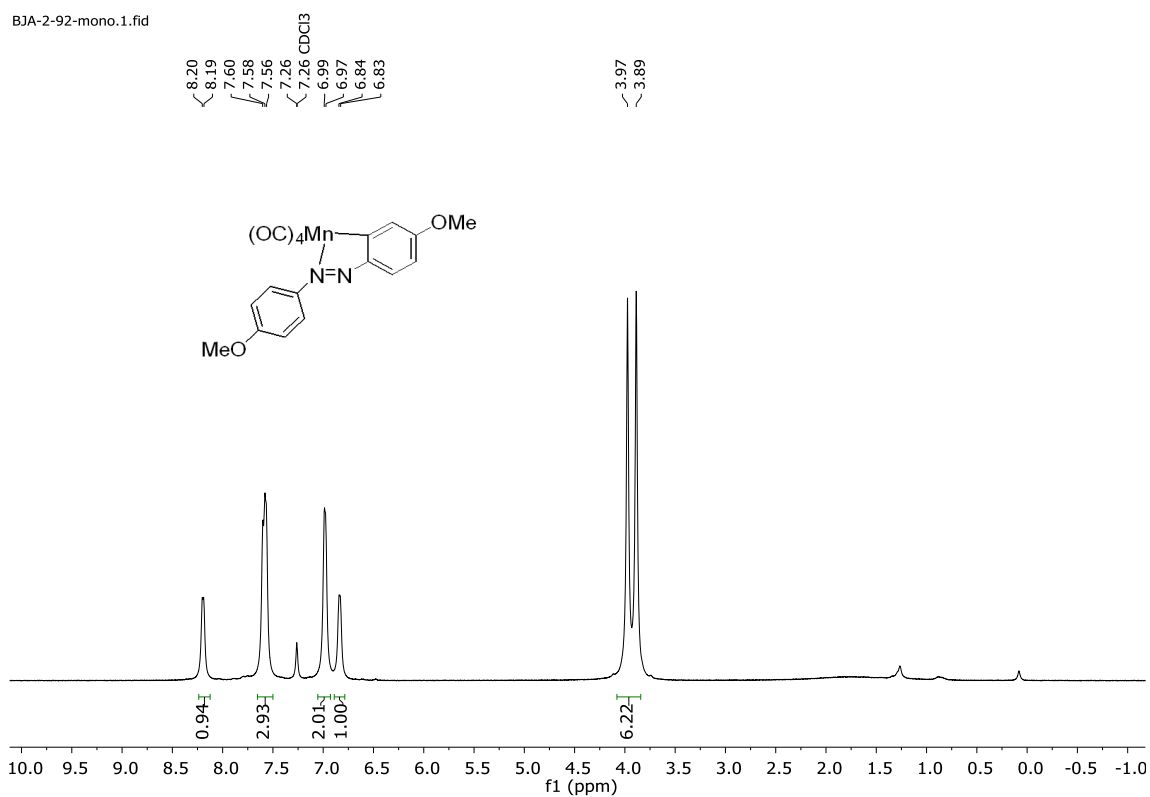


Figure 218: A 400 MHz ^1H NMR spectrum of 170 in CDCl_3 .

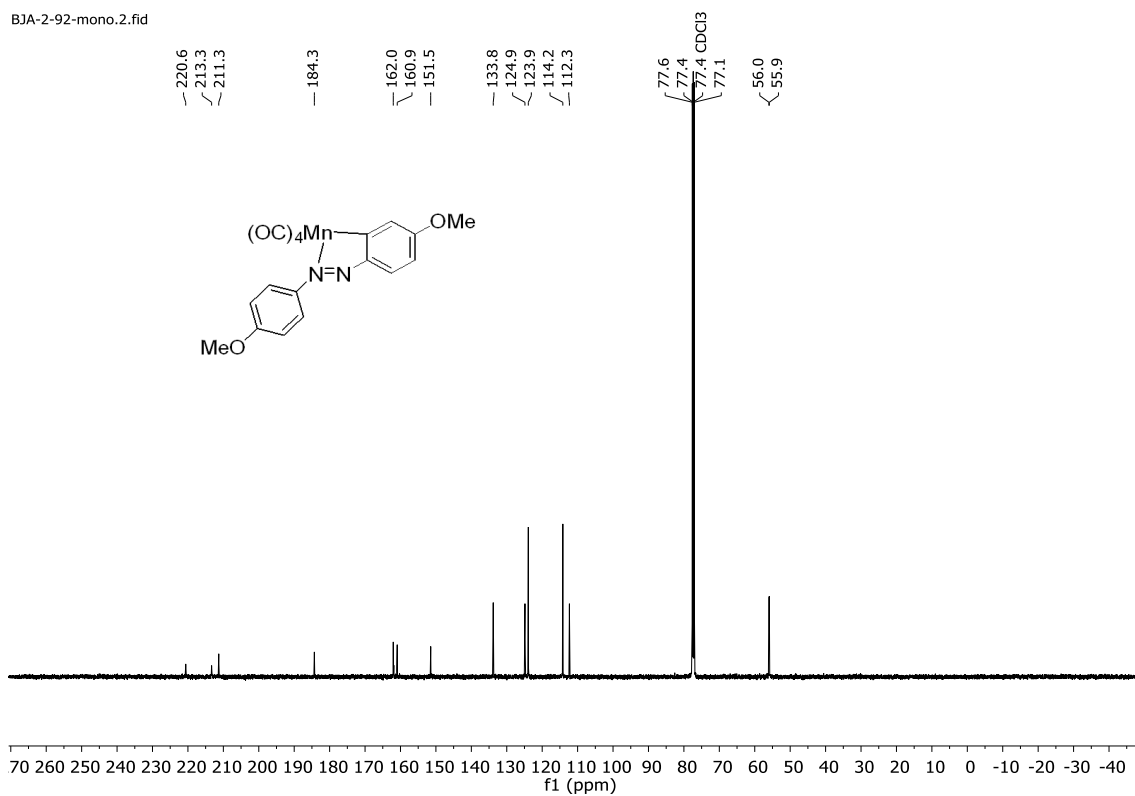


Figure 219: A 126 MHz ^{13}C NMR spectrum of 170 in CDCl_3 .

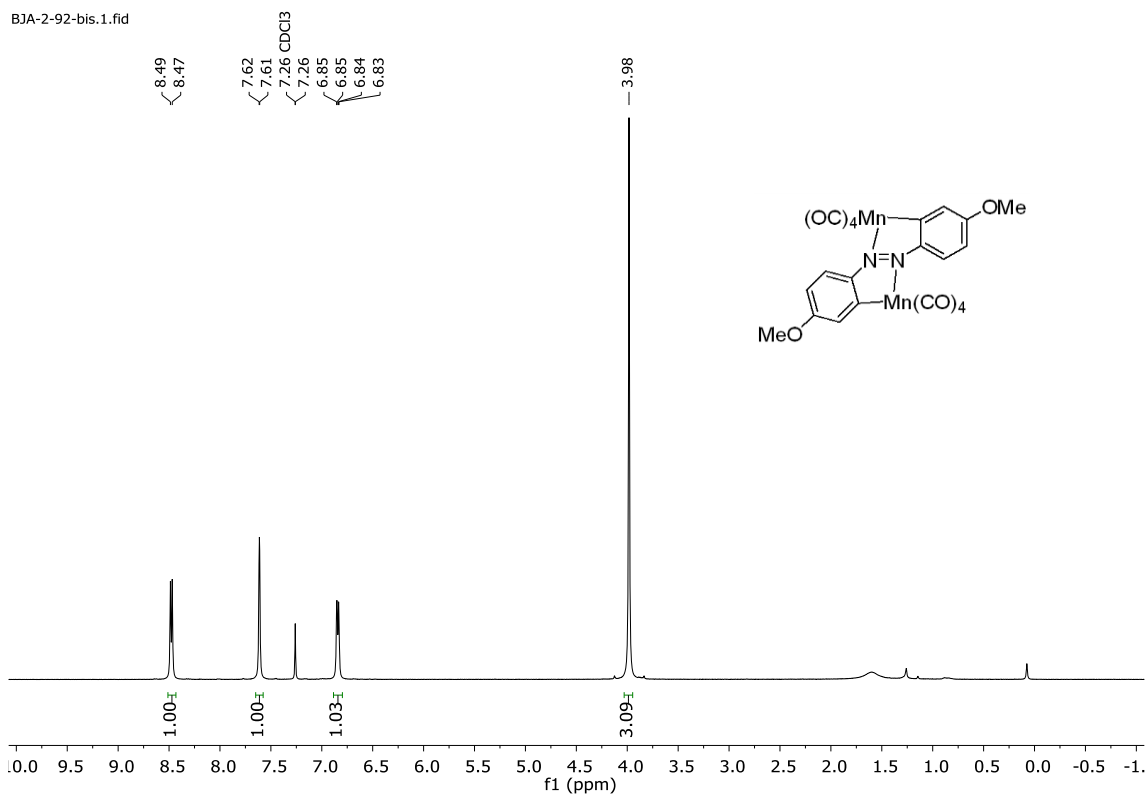


Figure 220: A 500 MHz ^1H NMR spectrum of 171 in CDCl_3 .

BJA-2-92-bis.2.fid

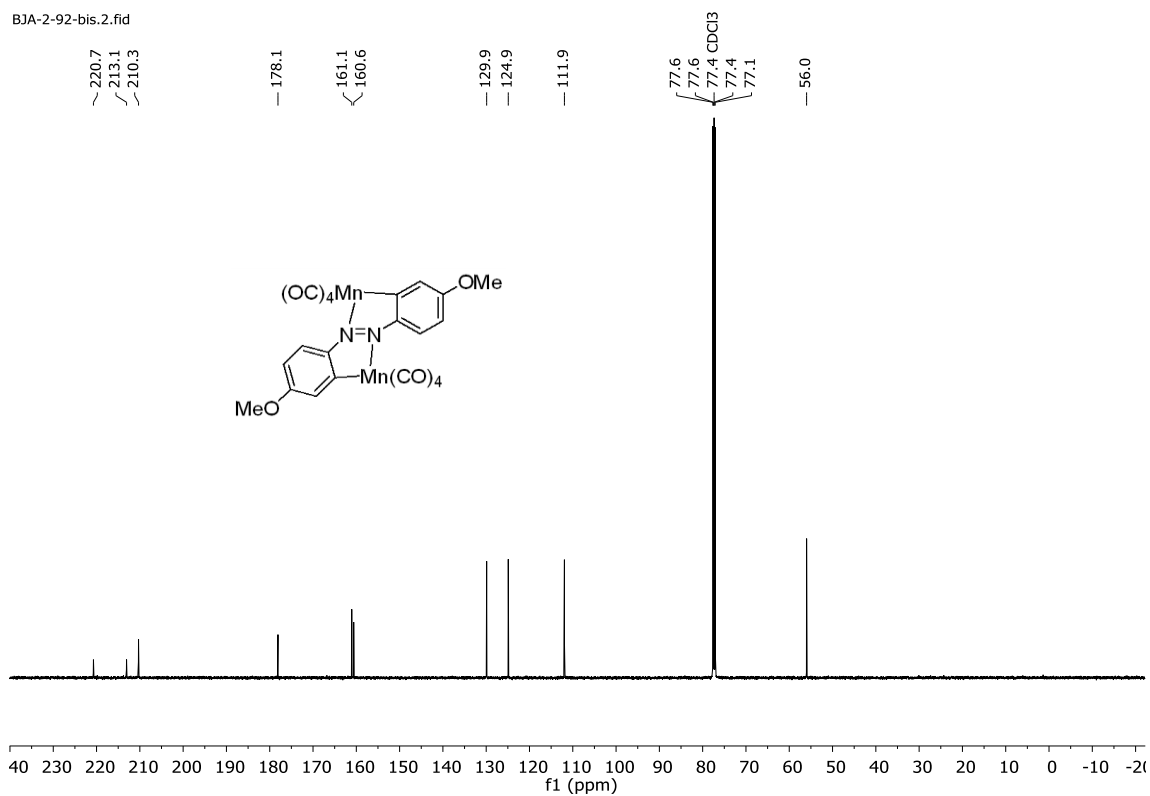


Figure 221: A 126 MHz ^{13}C NMR spectrum of 171 in CDCl_3 .

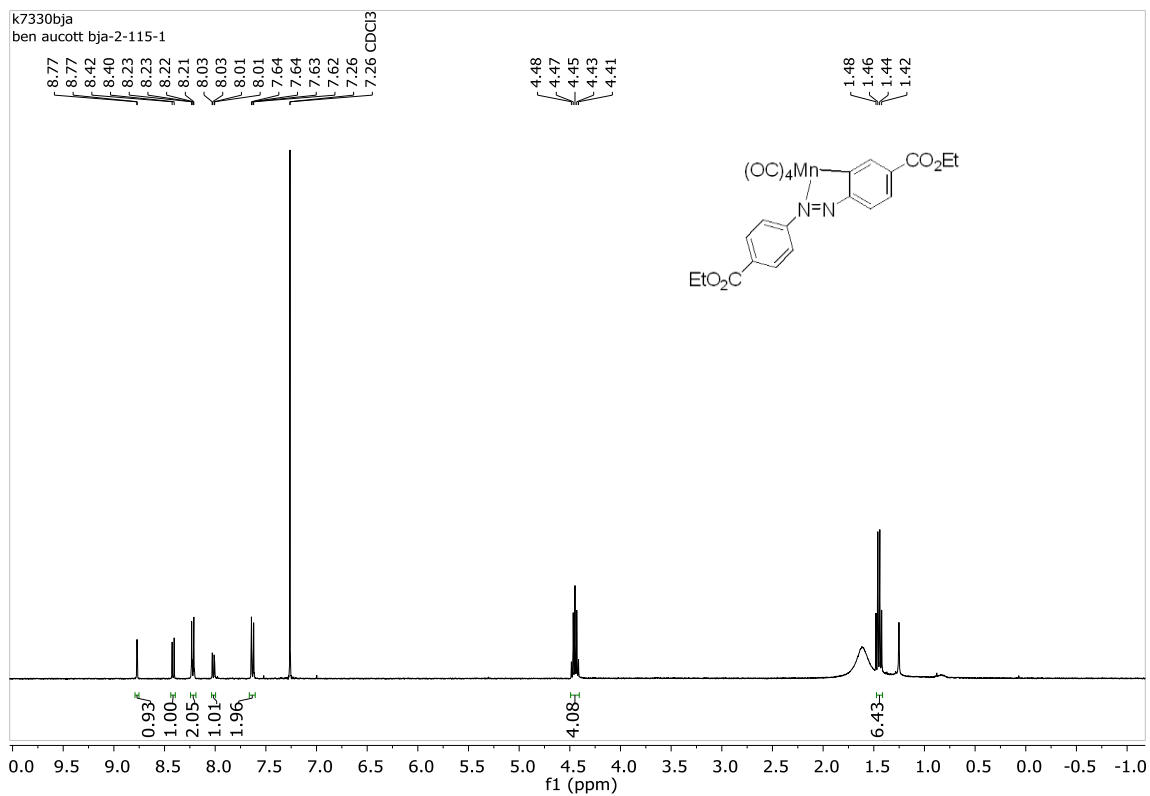


Figure 222: A 500 MHz ^1H NMR spectrum of 172 in CDCl_3 .

BJA-2-084.2.fid

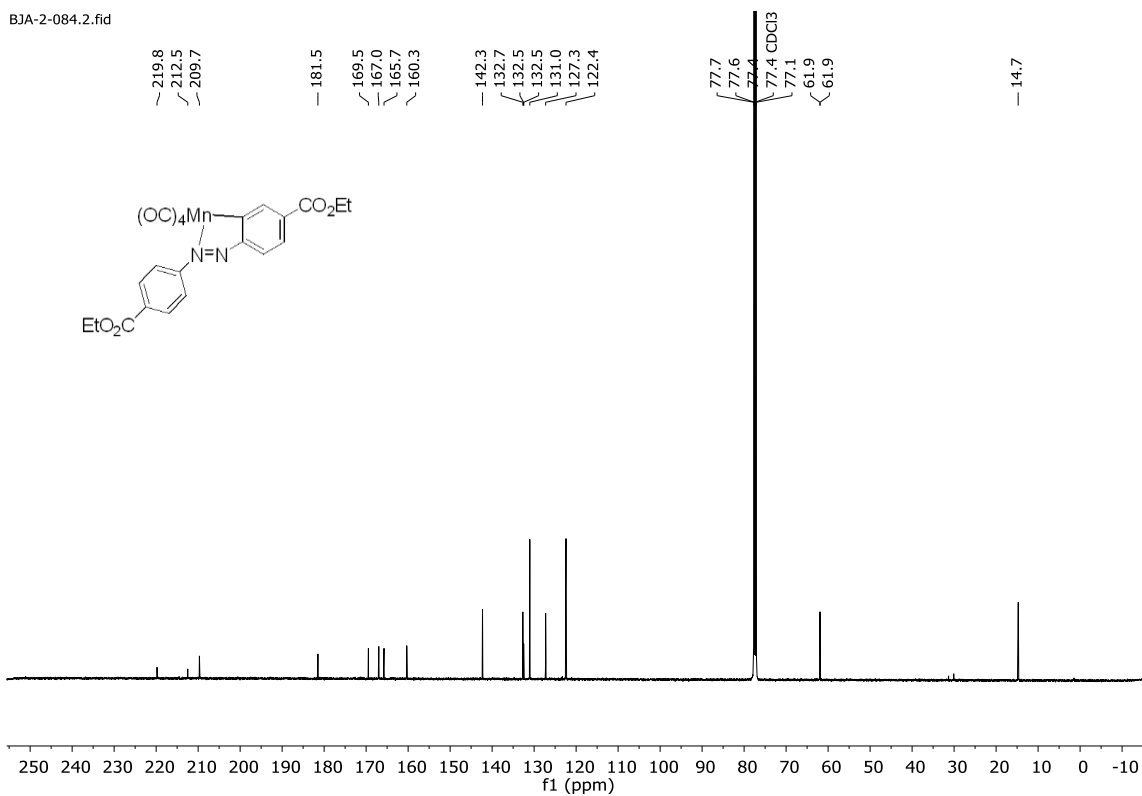


Figure 223: A 126 MHz ^{13}C NMR spectrum of 172 in CDCl_3 .

BJA-2-87-bis.1.fid

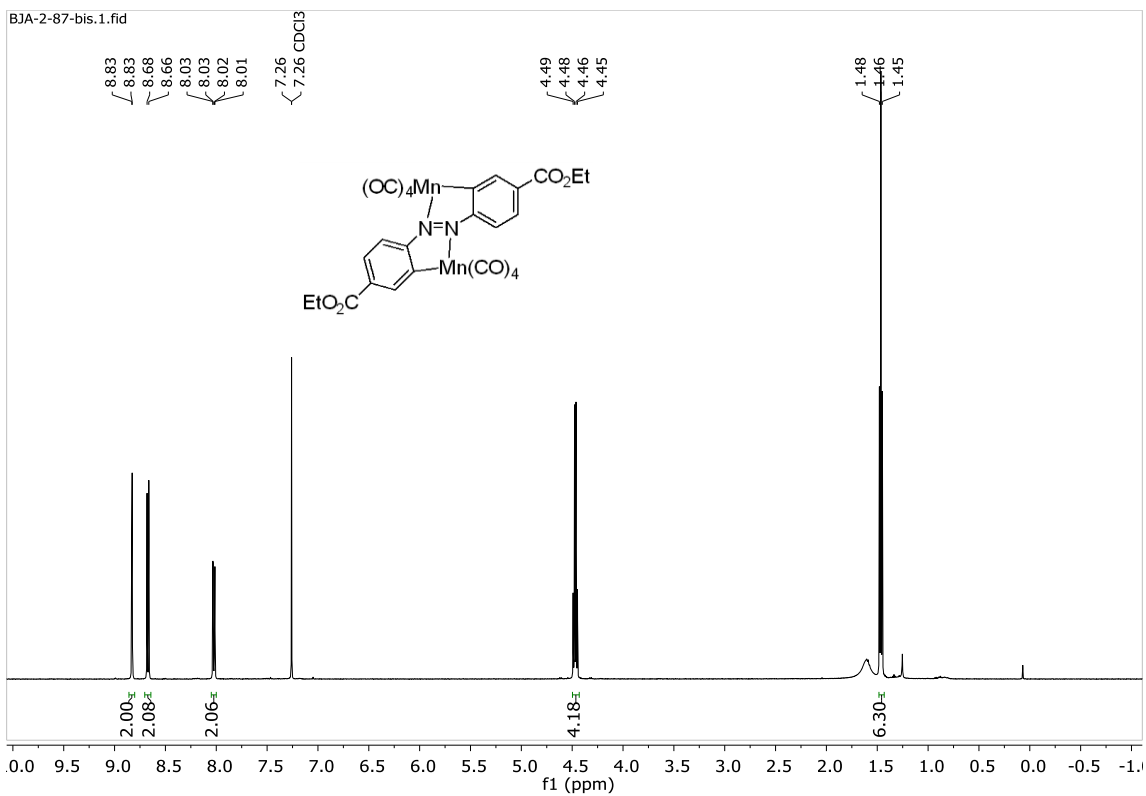


Figure 224: A 500 MHz ^1H NMR spectrum of 173 in CDCl_3 .

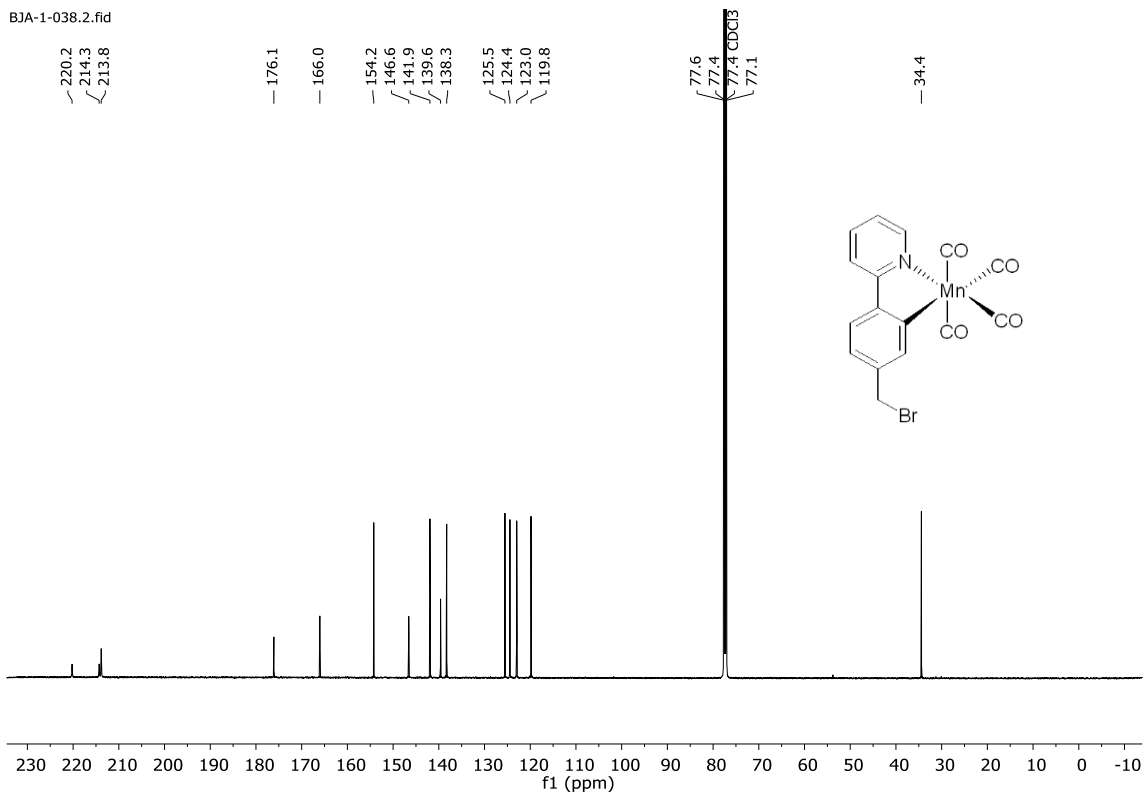


Figure 227: A 126 MHz ^{13}C NMR spectrum of 187 in CDCl_3 .

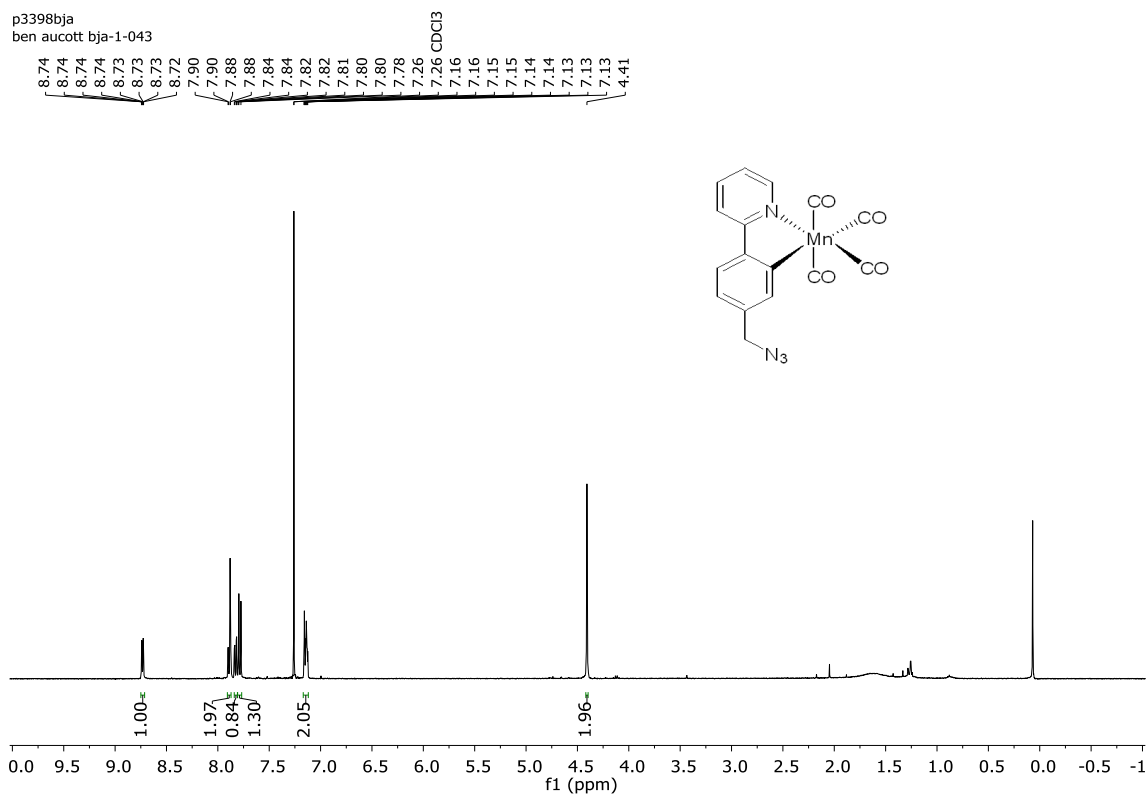


Figure 228: A 400 MHz ^1H NMR spectrum of 188 in CDCl_3 .

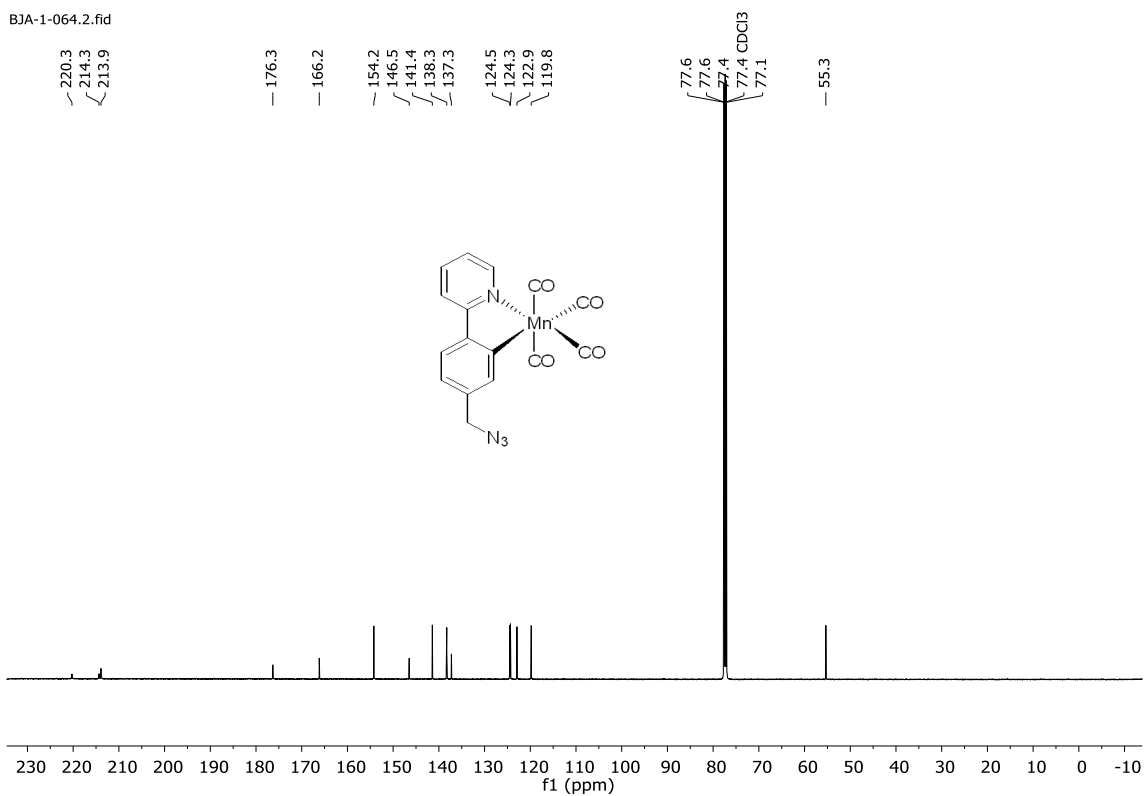


Figure 229: A 126 MHz ^{13}C NMR spectrum of 188 in CDCl_3 .

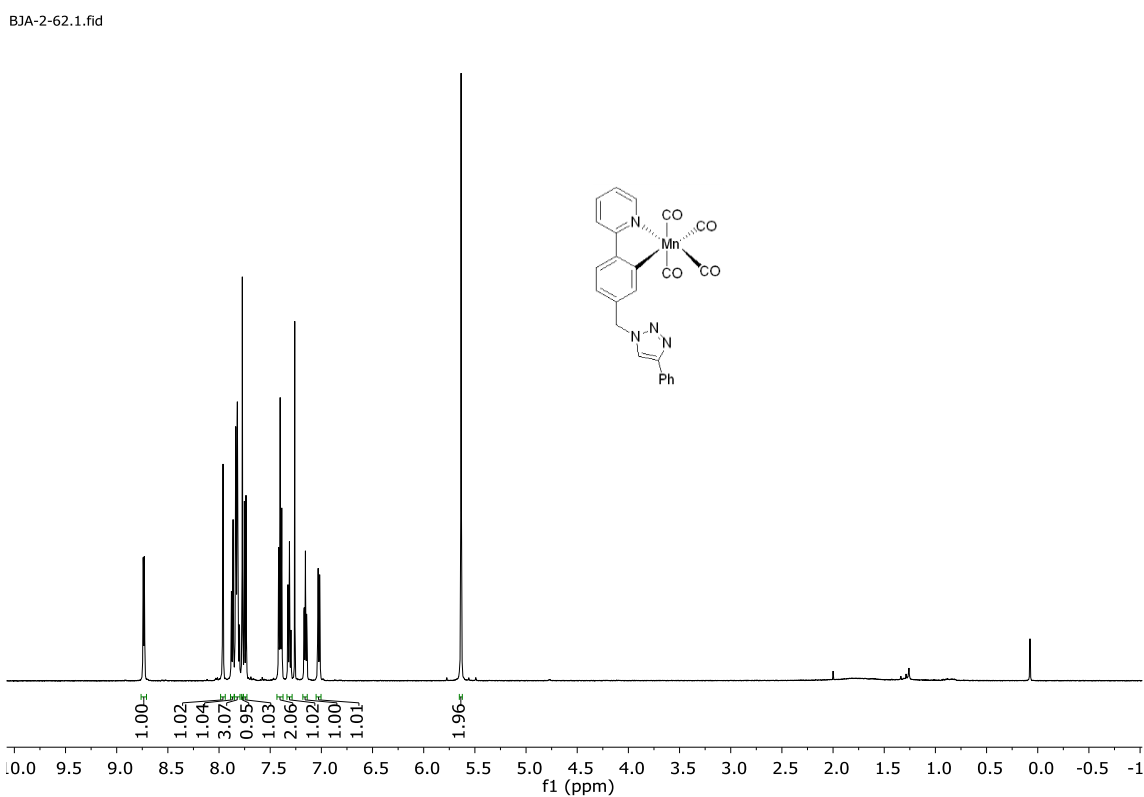


Figure 230: A 500 MHz ^1H NMR spectrum of 189 in CDCl_3 .

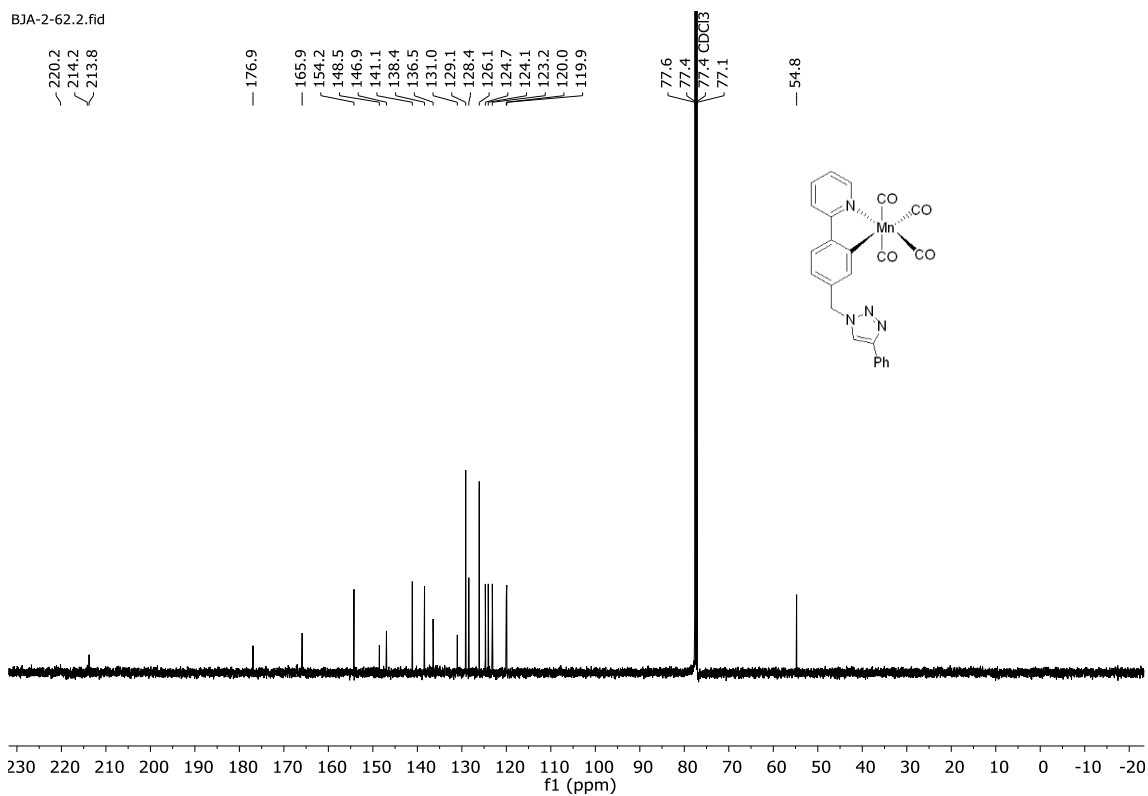


Figure 231: A 126 MHz ^{13}C NMR spectrum of 189 in CDCl_3 .

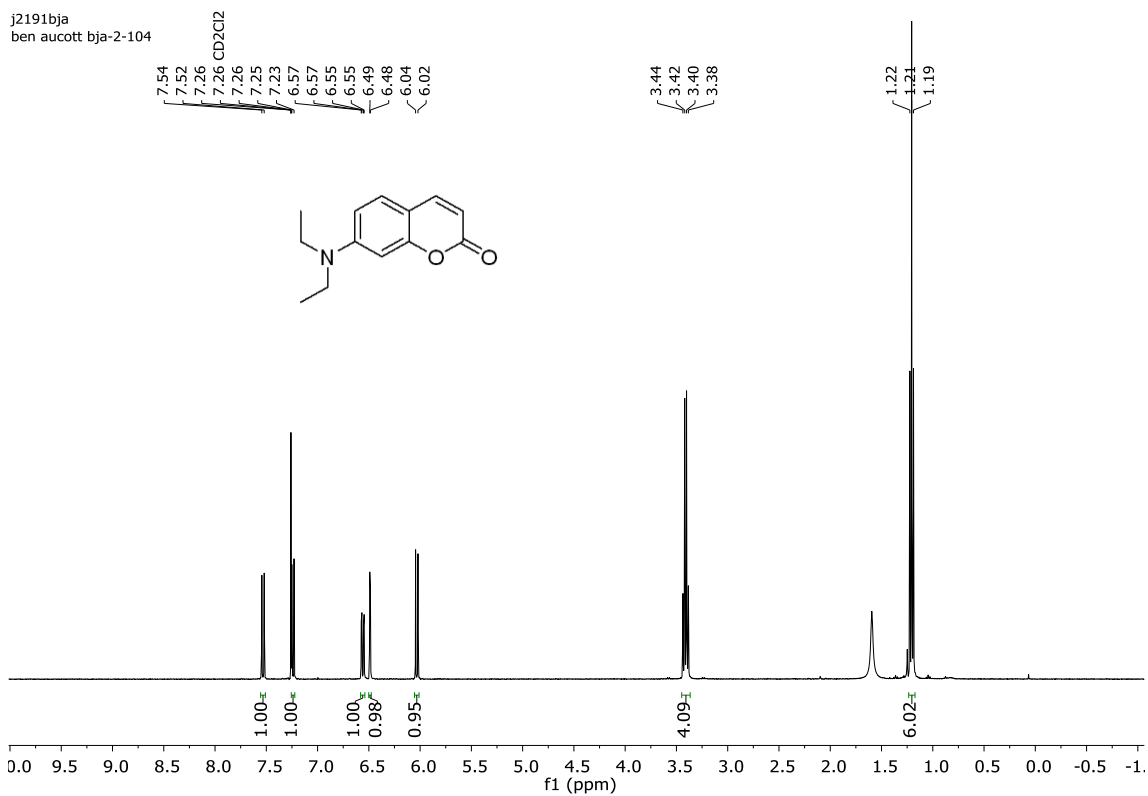


Figure 232: A 400 MHz ^1H NMR spectrum of 192 in CDCl_3 .

j2191bja
ben aucott bja-2-104

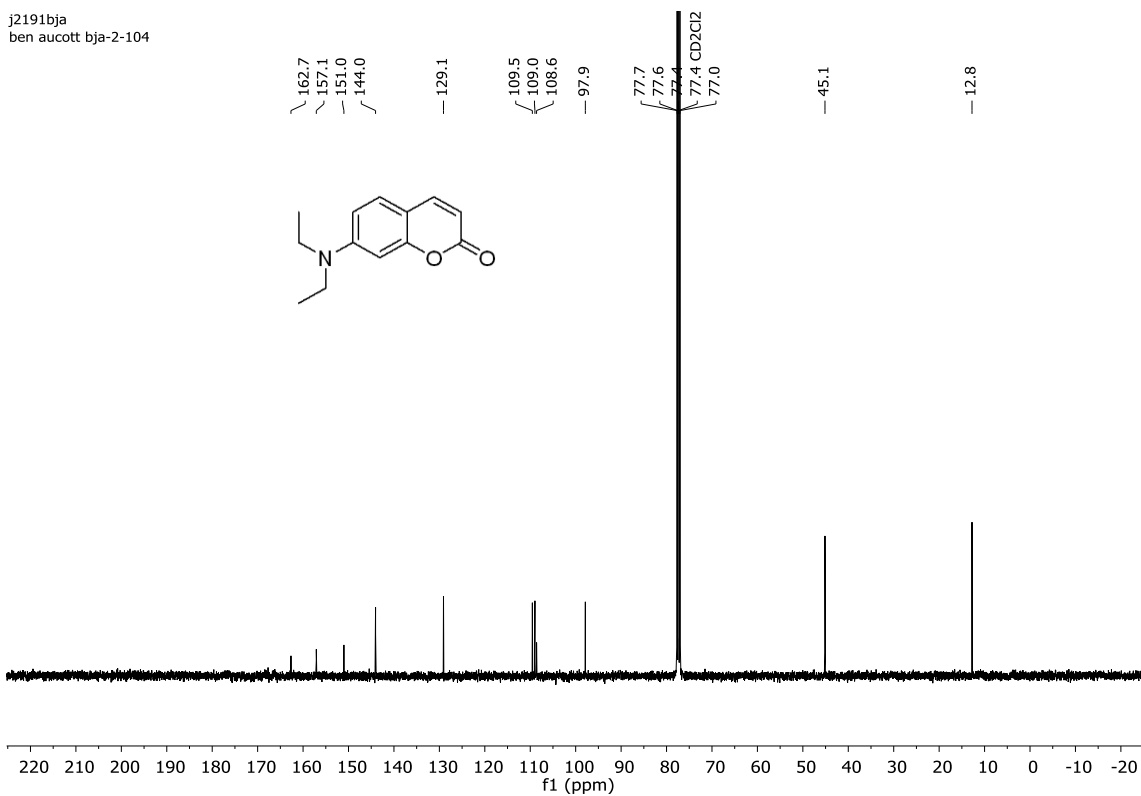


Figure 233: A 101 MHz ^{13}C NMR spectrum of 192 in CDCl_3 .

j2325bja
ben aucott bja-2-105F

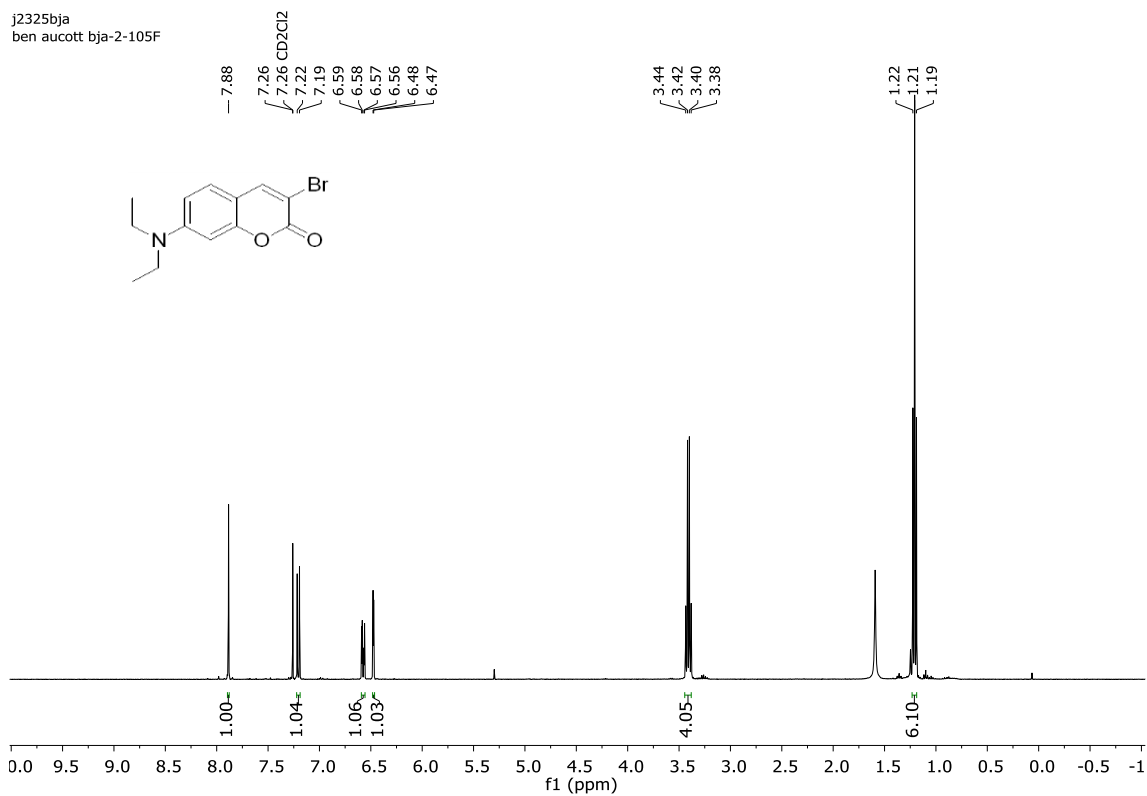


Figure 234: A 400 MHz ^1H NMR spectrum of 193 in CDCl_3 .

n2268bja
Ben Aucott BJA-2-105

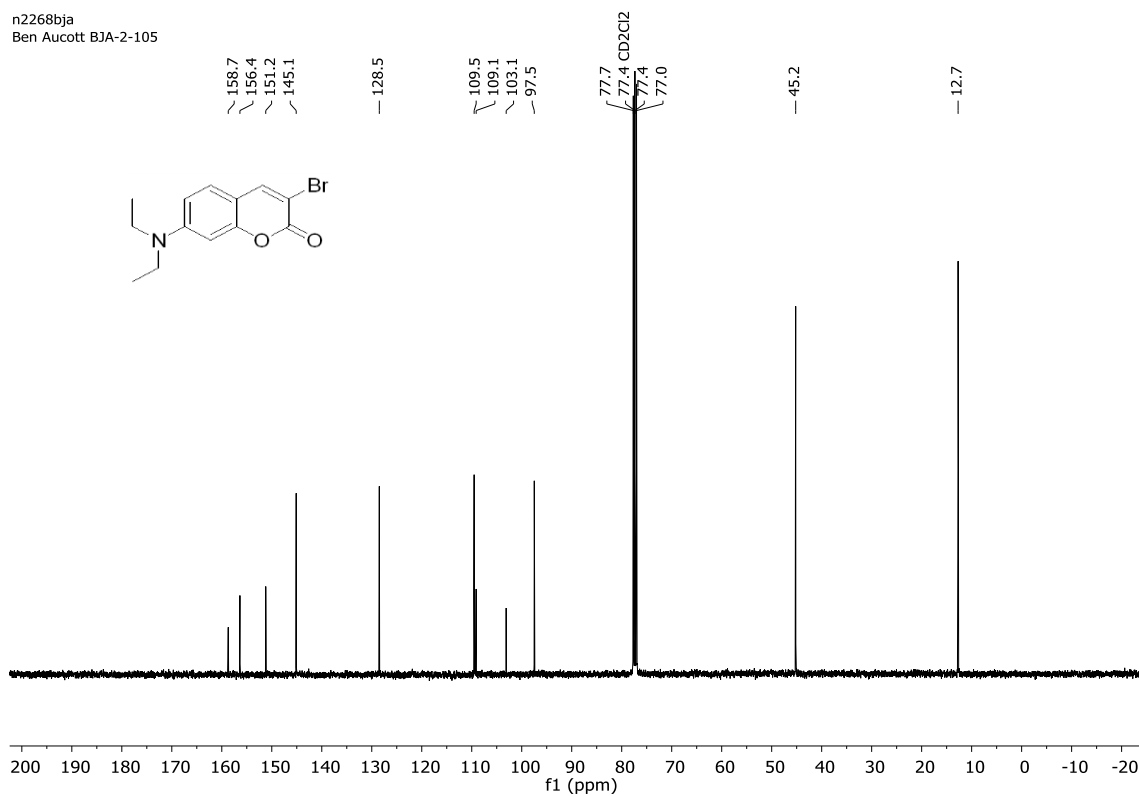


Figure 235: A 101 MHz ^{13}C NMR spectrum of 193 in CDCl_3 .

j3297bja
ben aucott bja-2-106



Figure 236: A 400 MHz ^1H NMR spectrum of 195 in CDCl_3 .

j3366bja
ben aucott bja-2-107

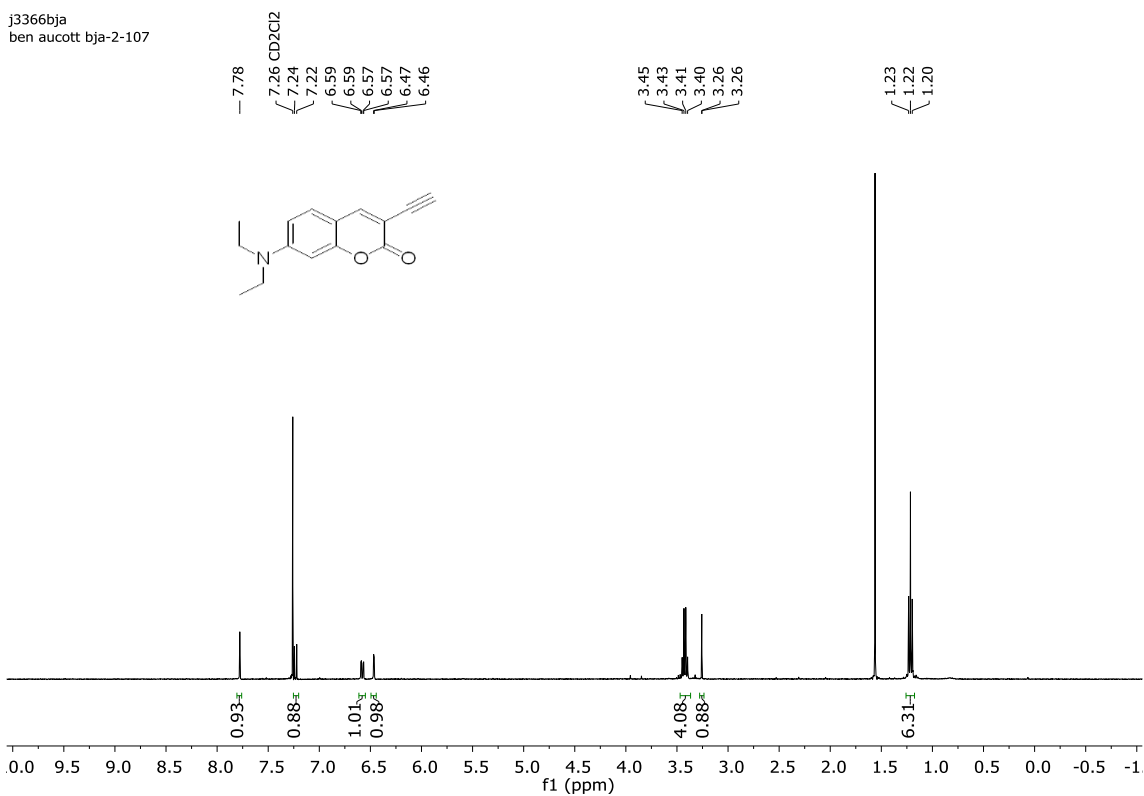


Figure 237: A 400 MHz ^1H NMR spectrum of 196 in CDCl_3 .

j3406bja
ben aucott bja-2-107

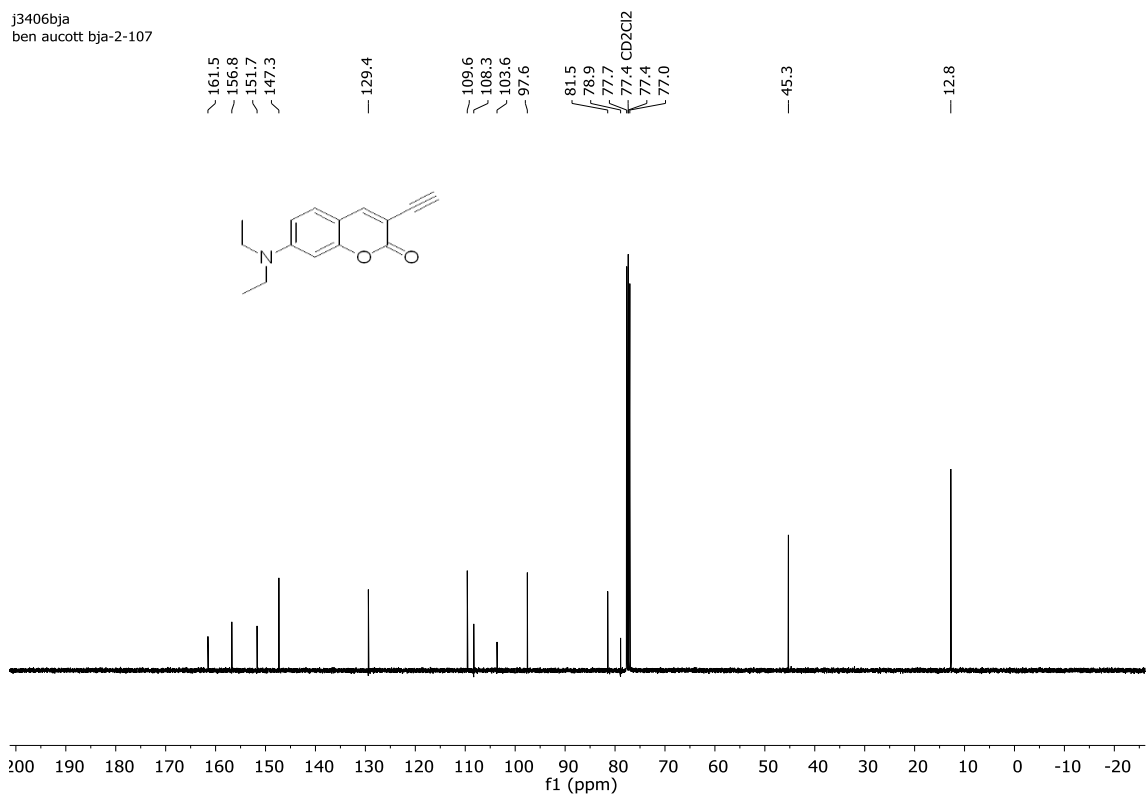


Figure 238: A 101 MHz ^{13}C NMR spectrum of 196 in CDCl_3 .

BJA-2-66.1.fid

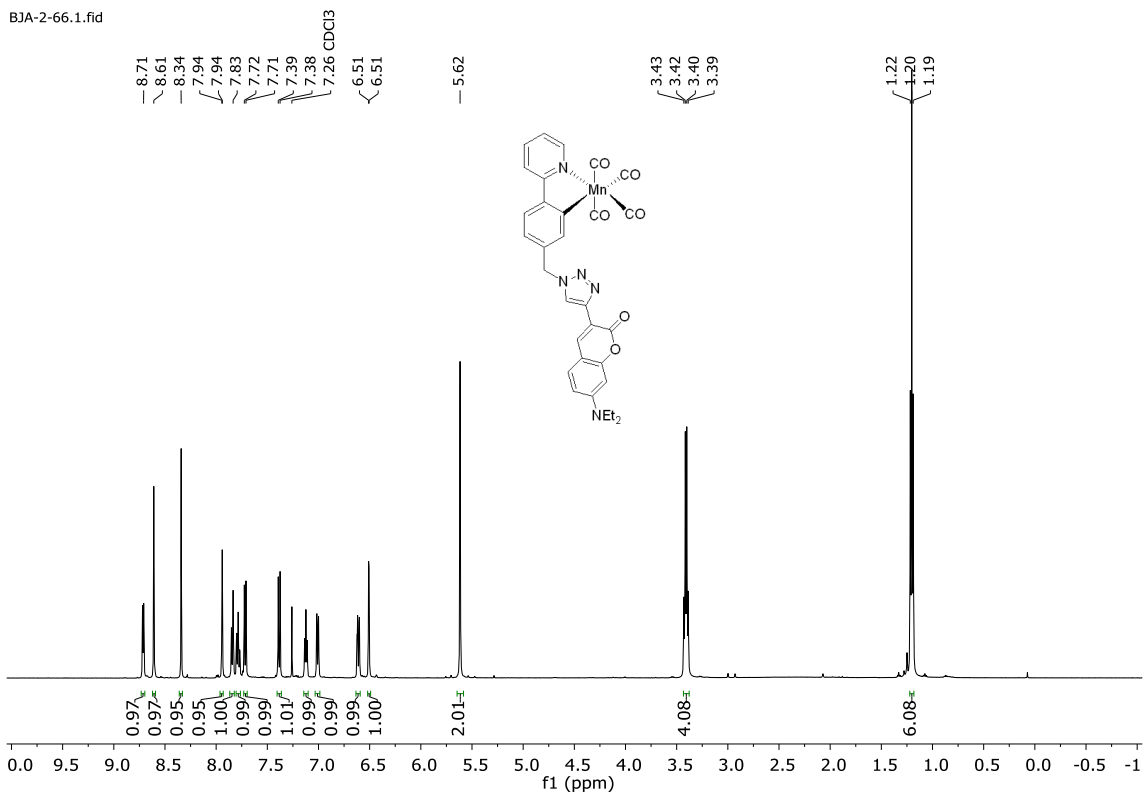


Figure 239: A 500 MHz ¹H NMR spectrum of 197 in CDCl₃.

BJA-2-66.2.fid

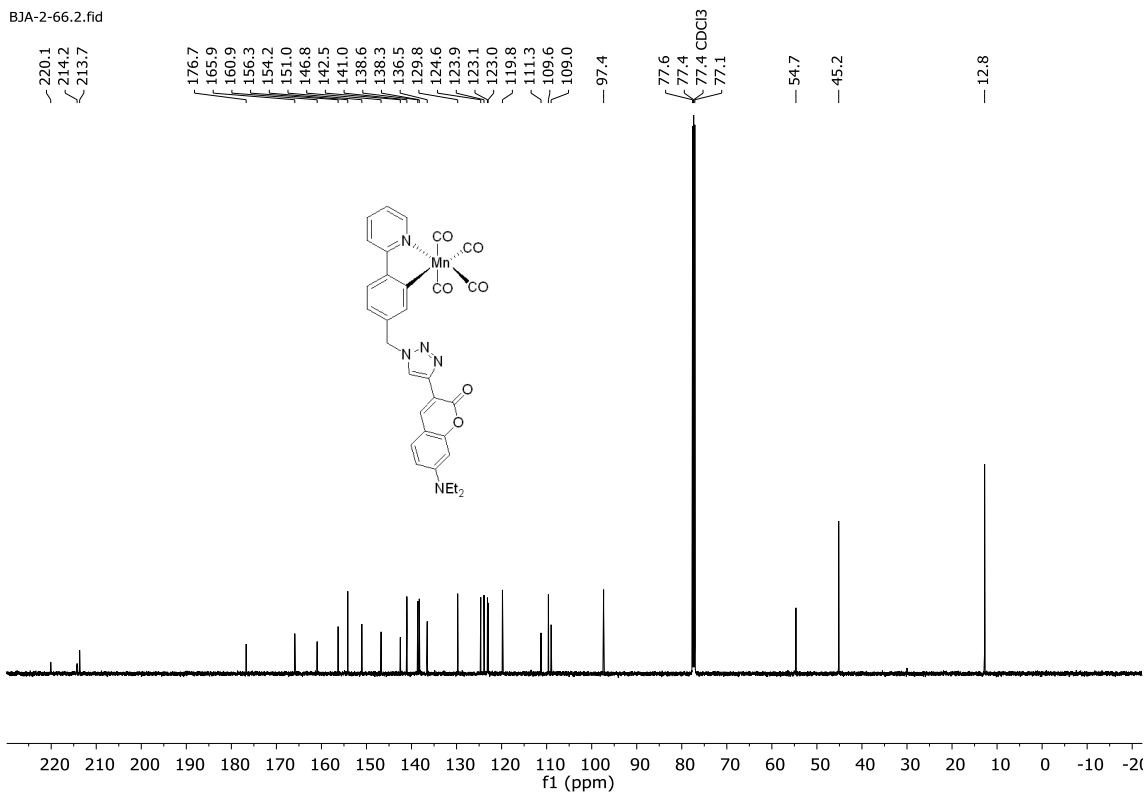


Figure 240: A 126 MHz ¹³C NMR spectrum of 197 in CDCl₃.

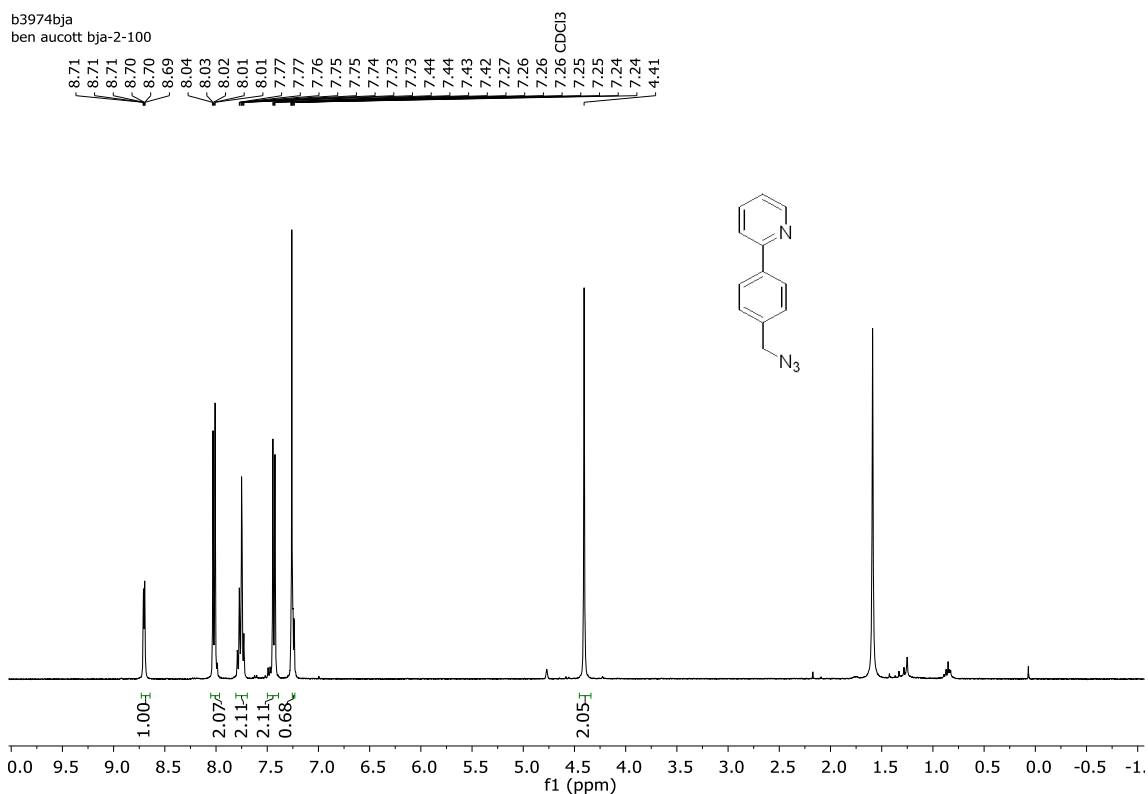


Figure 241: A 400 MHz ^1H NMR spectrum of 198 in CDCl_3 .

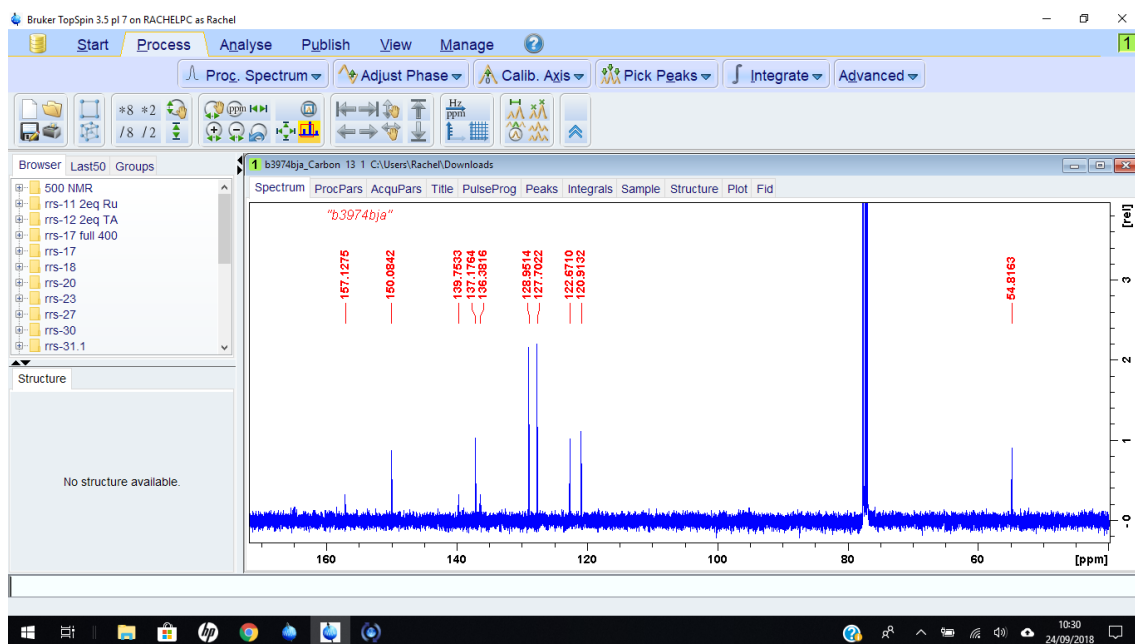


Figure 242: A 101 MHz ^{13}C NMR spectrum of 198 in CDCl_3 .

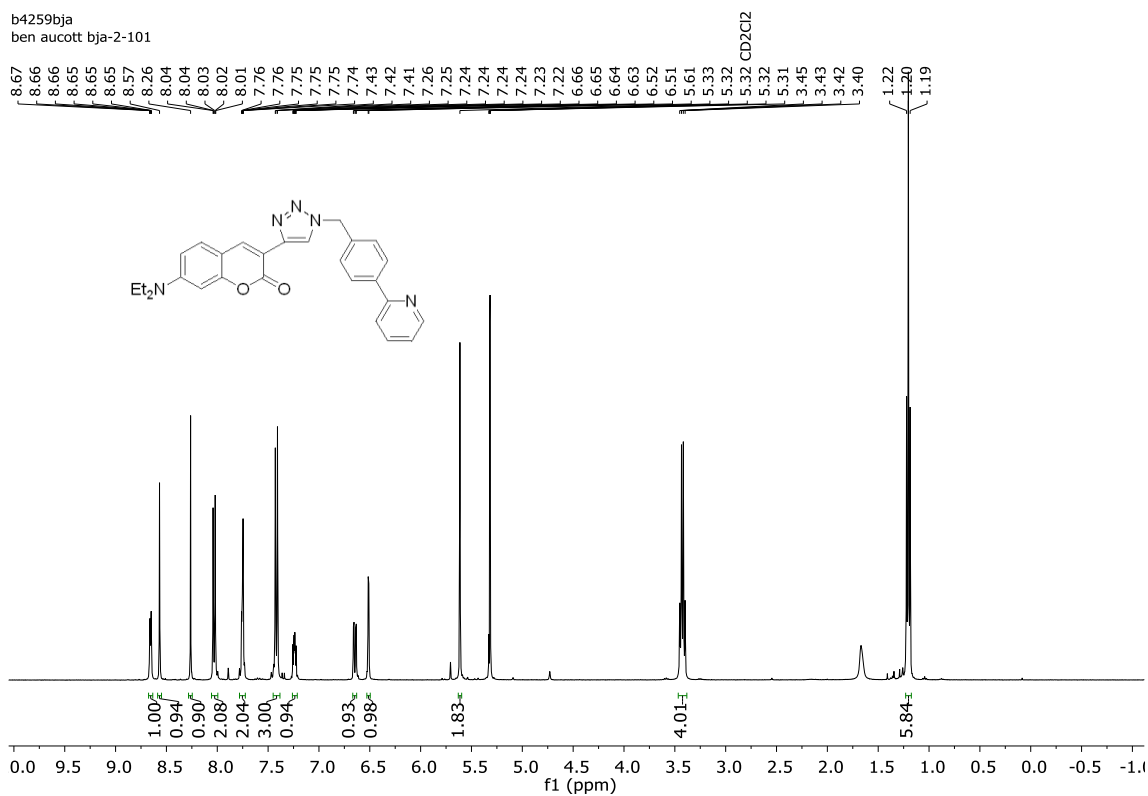


Figure 243: A 400 MHz ^1H NMR spectrum of 199 in CD_2Cl_2 .

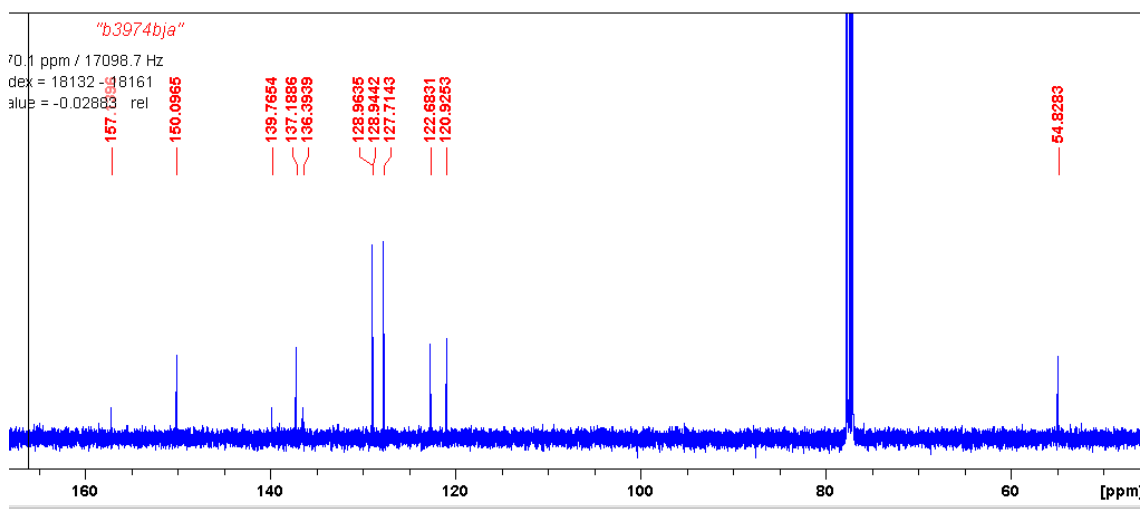


Figure 244: A 101 MHz ^{13}C NMR spectrum of 199 in CDCl_3 .

Appendix 7: Mass Spectrum of [132]⁺

York - Chemistry - Mass Spectrometry Service Report

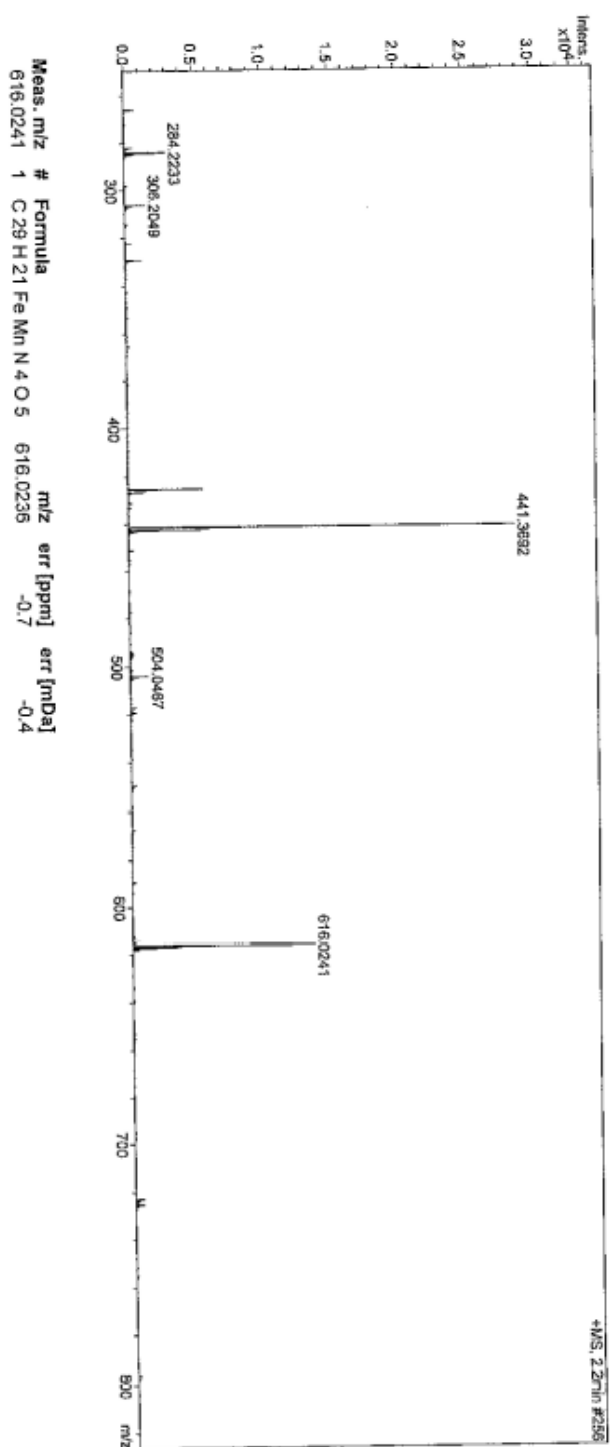
bja-1-049

Analysis Information

Analysis Filename if54360ba_P1-C-6_01_60662.D
Method 600p_meso11260_2c1s.m
Submission Name if54360ba
Instrument micrOTOF
ESI Positive

Acquisition Date

25/08/2015 14:38:21



Abbreviations

1-MeIm	1-Methylimidazole
ax	Axial
azpy	2-Phenylazopyridine
Bn	Benzyl
bpy	2,2-bipyridine
Bu	Butyl
<i>ca.</i>	<i>Circa</i>
cGMP	Cyclic Guanosine Monophosphate
CLF	Central Laser Facility
CO-Hb	Carboxyhaemoglobin
CORM	Carbon Monoxide Releasing Molecule
CORMA	Carbon Monoxide Releasing Material
COSMO	Conductor-like screening model
Cp	Cyclopentadienyl
d	Doublet
DDQ	2,3-Dichloro-5,6-dicyano-1,4-benzoquinone
DFT	Density Functional Theory
DMApy	4-Dimethylaminopyridine
DMF	Dimethyl formamide
DMSO	Dimethyl Sulfoxide
DNA	Deoxyribonucleic acid
en	1,2-diaminoethane
EPR	Electron Paramagnetic Resonance
eq	Equatorial
ESI	Electrospray Ionisation
Et	Ethyl
ET-CORM	Enzyme-Triggered CO Releasing Molecule

fac	Facial
Fc	Ferrocenyl
GSH	Glutathione
GSSG	Glutathione Disulfide
GTP	Guanosine Triphosphate
Hb	Haemoglobin
HO	Haem Oxygenase
HO-1	Haem Oxygenase 1
HO-2	Haem Oxygenase 2
HO-3	Haem Oxygenase 3
HOMO	Highest Occupied Molecular Orbital
ICP-MS	Inductively Coupled Plasma Mass Spectrometry
iNOS	Inducible Nitric Oxide Synthase
IR	Infrared
L	Ligand
LB	Lysogeny Broth
LDA	Lithium diisopropylamide
LDH	Lactate dehydrogenase
LED	Light-Emitting Diode
LIFDI	Liquid Injection Field Desorption Ionisation
LUMO	Lowest Unoccupied Molecular Orbital
M	Metal
m (IR)	Medium
m (NMR)	Multiplet
MAPK	Mitrogen-activated Protein Kinase
Mb	Myoglobin
Mb-CO	Carboxymyoglobin
Me	Methyl

mer	Meridional
MLCT	Metal-to-ligand Charge Transfer
MO	Molecular Orbital
MP	Melting Point
<i>n</i>	Normal
NADP	Nicotinamide Adenine Sinucleotide Phosphate
NHE	Normal Hydrogen Electrode
NIR	Near Infrared
NMR	Nuclear Magnetic Resonance
NORM	Nitrous Oxide Releasing Molecule
NORMA	Nitrous Oxide Releasing Material
NOS	Nitric Oxide Synthase
OD600	Optical Density 600 nm
OCP	Open Circuit Potential
PBS	Phosphate Buffered Saline
photoCORM	Photochemical Carbon Monoxide Releasing Molecule
PI	Propidium Iodide
PMMA	Poly(methyl methacrylate)
ppm	Parts Per Million
ppy	2-Phenylpyridyl
py	Pyridine
<i>R_f</i>	Retention Factor
ROS	Reactive Oxygen Species
RT	Room Temperature
S	Solvent
s (IR)	Strong
s (NMR)	Singlet
sGC	Soluble Guanylyl Cyclase

SOD	Superoxide Dismutase
t	Triplet
<i>t</i>	Tertiary
TA	Transient Absorbance
TBAF	Tetrabutylammonium fluoride
THF	Tetrahydrofuran
TIPS	Triisopropyl Silyl
TLC	Thin Layer Chromatography
tpm	Tris(2-pyrazolyl)methane
TRIR	Time-Resolved Infrared
TRMPS	Time-Resolved Multiple Probe Spectroscopy
UV	Ultraviolet
v:v	Volume Ratio
w	Weak
X-Phos	2-(Dicyclohexylphosphino)-2',4',6'-triisopropylbiphenyl

References

- 1 J. Haldane, *J. Physiol.*, 1895, **18**, 430–462.
- 2 C. G. Douglas, J. S. Haldane and J. B. S. Haldane, *J. Physiol.*, 1912, **44**, 275–304.
- 3 C. G. Douglas, *Obit. Not. Fellows R. Soc.*, 1936, **2**, 114–139.
- 4 B. Y. Chin and L. E. Otterbein, *Curr. Opin. Pharmacol.*, 2009, **9**, 490–500.
- 5 N. B. Hampson and N. M. Hauff, *Am. J. Emerg. Med.*, 2008, **26**, 665–669.
- 6 R. Okeda, N. Funata, S. Song, F. Higashino, T. Takano and K. Yokoyama, 1982, **56**, 265–272.
- 7 L. R. Goldbaum, T. Orellano and E. Dergal, *Ann. Clin. Lab. Sci.*, 1976, **6**, 372–376.
- 8 B. Y. E. M. Killick and J. V Marchant, *J. Physiol.*, 1959, 274–298.
- 9 S. R. Thom, *Toxicol. Rev.*, 2005, **24**, 157–158.
- 10 N. A. Buckley, G. K. Isbister, B. Stokes and D. N. Juurlink, *Toxicol. Rev.*, 2005, **24**, 75–92.
- 11 N. B. Hampson, C. A. Piantadosi, S. R. Thom and L. K. Weaver, *Am. J. Respir. Crit. Care Med.*, 2012, **186**, 1095–1101.
- 12 N. A. Buckley and D. N. Juurlink, *Am. J. Respir. Crit. Care Med.*, 2013, **187**, 1390.
- 13 K. N. Iheagwara, S. R. Thom, C. S. Deutschman and R. J. Levy, *Biochim. Biophys. Acta Mol. Basis Dis.*, 2007, **1772**, 1112–1116.
- 14 B. S. Zuckerbraun, B. Y. Chin, M. Bilban, J. de Costa d’Avila, J. Rao, T. R. Billiar and L. E. Otterbein, *FASEB J.*, 2007, **21**, 1099–1106.
- 15 J. D. Roderique, C. S. Josef, M. J. Feldman and B. D. Spiess, *Toxicology*, 2015, **334**, 45–58.
- 16 R. Tofighi, N. Tillmark, E. Daré, A. M. Åberg, J. E. Larsson and S. Ceccatelli, *Brain Res.*, 2006, **1098**, 1–8.
- 17 C. S. F. Queiroga, A. S. Almeida and H. L. A. Vieira, *Biochem. Res. Int.*, 2012, **749845**, 1–9.
- 18 J. Zhang and C. A. Piantadosi, *J. Clin. Invest.*, 1992, **90**, 1193–1199.
- 19 S. D. Brown and C. A. Piantadosi, *J. Appl. Physiol.*, 1990, **68**, 604–10.
- 20 R. Motterlini and R. Foresti, *Am. J. Physiol. Cell Physiol.*, 2017, **312**, 302–313.
- 21 T. Sjöstrand, *Nature*, 1949, **164**, 404–405.

- 22 T. Sjöstrand, *Nature*, 1951, **168**, 1039–1040.
- 23 T. R. Johnson, B. E. Mann, J. E. Clark, R. Foresti, C. J. Green and R. Motterlini, *Angew. Chemie Int. Ed.*, 2003, **42**, 3722–3729.
- 24 P. R. Ortiz de Montellano, *Acc. Chem. Res.*, 1998, **31**, 543–549.
- 25 D. Morse, L. Lin, A. M. K. Choi and S. W. Ryter, *Free Radic. Biol. Med.*, 2009, **47**, 1–12.
- 26 G. Kikuchi, T. Yoshida and M. Noguchi, *Biochem. Biophys. Res. Commun.*, 2005, **338**, 558–567.
- 27 S. W. Ryter, J. Alam and A. M. K. Choi, *Physiol. Rev.*, 2006, **86**, 583–650.
- 28 R. Motterlini, R. Foresti, R. Bassi, V. Calabrese, J. E. Clark and C. J. Green, *J. Biol. Chem.*, 2000, **275**, 13613–13620.
- 29 P. J. Lee, B.-H. Jiang, B. Y. Chin, N. V. Iyer, J. Alam, G. L. Semenza and A. M. K. Choi, *J. Biol. Chem.*, 1997, **272**, 5375–5381.
- 30 M. S. Carraway, A. J. Ghio, J. D. Carter and C. A. Piantadosi, *Am. J. Physiol. Lung Cell. Mol. Physiol.*, 2000, **278**, L806-12.
- 31 C. T. Wagner, W. Durante, N. Christodoulides, J. D. Hellums and A. I. Schafer, *J. Clin. Invest.*, 1997, **100**, 589–596.
- 32 S. Shibahara, R. M. Müller and H. Taguchi, *J. Biol. Chem.*, 1987, **262**, 12889–12892.
- 33 S. M. Keyse and R. M. Tyrrell, *Proc. Natl. Acad. Sci. U. S. A.*, 1989, **86**, 99–103.
- 34 D. Lautier, P. Luscher and R. M. Tyrrell, *Carcinogenesis*, 1992, **13**, 227–232.
- 35 J. O. Ossola and M. L. Tomaro, *Int. J. Biochem. Cell Biol.*, 1998, **30**, 285–92.
- 36 M. D. Maines, *Annu. Rev. Pharmacol. Toxicol.*, 1997, **37**, 517–54.
- 37 W. K. Mccoubrey, T. J. Huang and M. D. Maines, *Eur. J. Biochem.*, 1997, **247**, 725–732.
- 38 L. Lad, D. J. Schuller, H. Shimizu, J. Friedman, H. Li, P. R. Ortiz de Montellano and T. L. Poulos, *J. Biol. Chem.*, 2003, **278**, 7834–7843.
- 39 L. Schrödinger, The PyMOL Molecular Graphics System, Version 2.2.0, Schrödinger, LLC, 2018.
- 40 M. J. Alcaraz, P. Fernández and M. I. Guillén, *Curr. Pharm. Des.*, 2003, **9**, 2541–51.
- 41 K. D. Poss and S. Tonegawa, *Proc. Natl. Acad. Sci.*, 1997, **94**, 10925–10930.
- 42 F. Seta, L. Bellner, R. Rezzani, R. F. Regan, M. W. Dunn, N. G. Abraham, K. Gronert and M. Laniado-Schwartzman, *Am. J. Pathol.*, 2006, **169**, 1612–1623.
- 43 R. Motterlini and L. E. Otterbein, *Nat. Rev. Drug Discov.*, 2010, **9**, 728–743.

- 44 S. W. Ryter, *Front. Pharmacol.*, 2012, **3**, 1–8.
- 45 V. G. Kharitonov, V. S. Sharma, R. B. Pilz, D. Magde and D. Koesling, *Proc. Natl. Acad. Sci.*, 1995, **92**, 2568–2571.
- 46 I. F. Ghalayini, *Int. J. Impot. Res.*, 2004, **16**, 459–469.
- 47 S. W. Ryter and L. E. Otterbein, *BioEssays*, 2004, **26**, 270–280.
- 48 B. Brüne and V. Ullrich, *Mol. Pharmacol.*, 1987, **32**, 497–504.
- 49 C. Thorup, C. L. Jones, S. S. Gross, L. C. Moore and M. S. Goligorsky, *Am. J. Physiol.*, 1999, **277**, F882–F889.
- 50 L. O. Cardell, I. F. Ueki, P. Stjärne, C. Agusti, K. Takeyama, A. Lindén and J. A. Nadel, *Br. J. Pharmacol.*, 1998, **124**, 1065–1068.
- 51 T. Morita, M. A. Perrella, M. E. Lee and S. Kourembanas, *Proc. Natl. Acad. Sci.*, 1995, **92**, 1475–1479.
- 52 B. E. McLaughlin, M. L. Chretien, C. Choi, J. F. Brien, K. Nakatsu and G. S. Marks, *Can. J. Physiol. Pharmacol.*, 2000, **78**, 343–9.
- 53 R. Makino, Y. Obata, M. Tsubaki, T. Iizuka, Y. Hamajima, Y. Kato-Yamada, K. Mashima and Y. Shiro, *Biochemistry*, 2018, **57**, 1620–1631.
- 54 J. W. Denninger and M. A. Marletta, *Biochim. Biophys. Acta Bioenerg.*, 1999, **1411**, 334–350.
- 55 A. Friebe, G. Schultz and D. Koesling, *EMBO J.*, 1996, **15**, 6863–6868.
- 56 N. Schallner and L. E. Otterbein, *Front. Physiol.*, 2015, **6**, 1–4.
- 57 C. A. Piantadosi, *Free Radic. Biol. Med.*, 2008, **45**, 562–569.
- 58 H. J. Zhang, W. Zhao, S. Venkataraman, M. E. C. Robbins, G. R. Buettner, K. C. Kregel and L. W. Oberley, *J. Biol. Chem.*, 2002, **277**, 20919–20926.
- 59 S. Moncada, R. M. Palmer and E. A. Higgs, *Pharmacol. Rev.*, 1991, **43**, 109 LP-142.
- 60 C. Farah, L. Y. M. Michel and J.-L. Balligand, *Nat. Rev. Cardiol.*, 2018, **15**, 292–316.
- 61 J. W. W. Coleman, *Int. Immunopharmacol.*, 2001, **1**, 1397–1406.
- 62 L. Xue, G. Farrugia, S. M. Miller, C. D. Ferris, S. H. Snyder and J. H. Szurszewski, *Proc. Natl. Acad. Sci.*, 2000, **97**, 1851–1855.
- 63 R. Motterlini, C. J. Green and R. Foresti, *Antioxid. Redox Signal.*, 2002, **4**, 615–624.
- 64 K. A. White and M. A. Marietta, *Biochemistry*, 1992, **31**, 6627–6631.
- 65 J. L. Scragg, M. L. Dallas, J. A. Wilkinson, G. Varadi and C. Peers, *J. Biol. Chem.*, 2008,

283, 24412–24419.

- 66 S. H. Heinemann, T. Hoshi, M. Westerhausen and A. Schiller, *Chem. Commun.*, 2014, **50**, 3644–3660.
- 67 L. E. Otterbein, F. H. Bach, J. Alam, M. Soares, H. Tao Lu, M. Wysk, R. J. Davis, R. A. Flavell and A. M. K. Choi, *Nat. Med.*, 2000, **6**, 422–428.
- 68 M. J. Mitchell and M. R. King, *J. Breath Res.*, 2014, **7**, 1–23.
- 69 K. Ling, F. Men, W.-C. C. Wang, Y.-Q. Q. Zhou, H.-W. W. Zhang and D.-W. W. Ye, *J. Med. Chem.*, 2018, **61**, 2611–2635.
- 70 C. Szabo, *Nat. Rev. Drug Discov.*, 2016, **15**, 185–203.
- 71 B. Wegiel, D. Gallo, E. Csizmadia, C. Harris, J. Belcher, G. M. Vercellotti, N. Penacho, P. Seth, V. Sukhatme, A. Ahmed, P. P. Pandolfi, L. Helczynski, A. Bjartell, J. L. Persson and L. E. Otterbein, *Cancer Res.*, 2013, **73**, 7009–7021.
- 72 I. Chakraborty, J. Jimenez and P. K. Mascharak, *Chem. Commun.*, 2017, **53**, 5519–5522.
- 73 I. Chakraborty, S. J. Carrington, G. Roseman and P. K. Mascharak, *Inorg. Chem.*, 2017, **56**, 1534–1545.
- 74 L. S. Nobre, J. D. Seixas, C. C. Romao and L. M. Saraiva, *Antimicrob. Agents Chemother.*, 2007, **51**, 4303–4307.
- 75 L. K. Wareham, R. K. Poole and M. Tinajero-Trejo, *J. Biol. Chem.*, 2015, **290**, 18999–19007.
- 76 A. Kumar, J. C. Toledo, R. P. Patel, J. R. Lancaster and A. J. C. Steyn, *Proc. Natl. Acad. Sci.*, 2007, **104**, 11568–11573.
- 77 Proterris Website, http://proterris.com/?page_id=11900, (accessed 10 September 2018).
- 78 C. C. Romão, W. A. Blättler, J. D. Seixas and G. J. L. Bernardes, *Chem. Soc. Rev.*, 2012, **41**, 3571.
- 79 N. Abeyrathna, K. Washington, C. Bashur and Y. Liao, *Org. Biomol. Chem.*, 2017, **15**, 8692–8699.
- 80 R. Motterlini, B. E. Mann, T. R. Johnson, J. E. Clark, R. Foresti and C. J. Green, *Curr. Pharm. Des.*, 2003, **9**, 2525–39.
- 81 C. Elschenbroich and A. Salzer, in *Organometallics A Concise Introduction*, Wiley VCH, First Edit., 1989, pp. 226–227.
- 82 J. S. Muentzer, *J. Mol. Spectrosc.*, 1975, **55**, 490–491.
- 83 G. Frenking, C. Loschen, A. Krapp, S. Fau and S. Strauss, *J. Comput. Chem.*, 2007, **28**,

117–126.

- 84 G. Bistoni, S. Rampino, N. Scafuri, G. Ciancaleoni, D. Zuccaccia, L. Belpassi and F. Tarantelli, *Chem. Sci.*, 2016, **7**, 1174–1184.
- 85 S. García-Gallego and G. J. L. Bernardes, *Angew. Chemie Int. Ed.*, 2014, **53**, 9712–9721.
- 86 R. Motterlini, J. E. Clark, R. Foresti, P. Sarathchandra, B. E. Mann and C. J. Green, *Circ. Res.*, 2002, **90**, 17–24.
- 87 R. Foresti, J. Hammad, J. E. Clark, T. R. Johnson, B. E. Mann, A. Friebe, C. J. Green and R. Motterlini, *Br. J. Pharmacol.*, 2004, **142**, 453–460.
- 88 I. J. S. Fairlamb, A. K. Duhme-Klair, J. M. Lynam, B. E. Moulton, C. T. O'Brien, P. Sawle, J. Hammad and R. Motterlini, *Bioorganic Med. Chem. Lett.*, 2006, **16**, 995–998.
- 89 I. J. S. Fairlamb, J. M. Lynam, B. E. Moulton, I. E. Taylor, A. K. Duhme-Klair, P. Sawle and R. Motterlini, *Dalton Trans.*, 2007, **9226**, 3603–3605.
- 90 A. J. Atkin, S. Williams, P. Sawle, R. Motterlini, J. M. Lynam and I. J. S. Fairlamb, *Dalton Trans.*, 2009, **19**, 3653–3656.
- 91 T. Santos-Silva, A. Mukhopadhyay, J. D. Seixas, G. J. L. Bernardes, C. C. Romão and M. J. Romão, *J. Am. Chem. Soc.*, 2011, **133**, 1192–1195.
- 92 D. E. Bikiel, E. G. Solveyra, F. Di Salvo, H. M. S. Milagre, M. N. Eberlin, R. S. Corrêa, J. Ellena, D. A. Estrin and F. Doctorovich, *Inorg. Chem.*, 2011, **50**, 2334–2345.
- 93 F. Zobi, O. Blacque, R. A. Jacobs, M. C. Schaub and A. Y. Bogdanova, *Dalton Trans.*, 2012, **41**, 370–378.
- 94 A. C. Pena, N. Penacho, L. Mancio-Silva, R. Neres, J. D. Seixas, A. C. Fernandes, C. C. Romão, M. M. Mota, G. J. L. Bernardes and A. Pamplona, *Antimicrob. Agents Chemother.*, 2012, **56**, 1281–1290.
- 95 P. C. Kunz, H. Meyer, J. Barthel, S. Sollazzo, A. M. Schmidt and C. Janiak, *Chem. Commun.*, 2013, **49**, 4896.
- 96 M. Chaves-Ferreira, I. S. Albuquerque, D. Matak-Vinkovic, A. C. Coelho, S. M. Carvalho, L. M. Saraiva, C. C. Romão and G. J. L. Bernardes, *Angew. Chemie Int. Ed.*, , DOI:10.1002/anie.201409344.
- 97 J. E. Clark, P. Naughton, S. Shurey, C. J. Green, T. R. Johnson, B. E. Mann, R. Foresti and R. Motterlini, *Circ. Res.*, 2003, **93**, 2–8.
- 98 M. D. Pizarro, J. V. Rodriguez, M. E. Mamprin, B. J. Fuller, B. E. Mann, R. Motterlini and E. E. Guibert, *Cryobiology*, 2009, **58**, 248–255.

- 99 A. Sandouka, B. J. Fuller, B. E. Mann, C. J. Green, R. Foresti and R. Motterlini, *Kidney Int.*, 2006, **69**, 239–247.
- 100 H. Fujimoto, M. Ohno, S. Ayabe, H. Kobayashi, N. Ishizaka, H. Kimura, K. I. Yoshida and R. Nagai, *Arterioscler. Thromb. Vasc. Biol.*, 2004, **24**, 1848–1853.
- 101 S. Lancel, S. M. Hassoun, R. Favory, B. Decoster, R. Motterlini and R. Neviere, *J. Pharmacol. Exp. Ther.*, 2009, **329**, 641–648.
- 102 M. Desmard, K. S. Davidge, O. Bouvet, D. Morin, D. Roux, R. Foresti, J. D. Ricard, E. Denamur, R. K. Poole, P. Montravers, R. Motterlini and J. Boczkowski, *FASEB J.*, 2009, **23**, 1023–1031.
- 103 M. L. Ferrándiz, N. Maicas, I. Garcia-Arlandis, M. C. Terencio, R. Motterlini, I. Devesa, L. A. B. Joosten, W. B. Van Den Berg and M. J. Alcaraz, *Ann. Rheum. Dis.*, 2008, **67**, 1211–1217.
- 104 Sigma Aldrich Website,
<https://www.sigmaaldrich.com/catalog/product/sigma/sml0496?lang=en®ion=GB>,
 (accessed 10 September 2018).
- 105 B. E. Mann, *Organometallics*, 2012, **31**, 5728–5735.
- 106 T. R. Johnson, B. E. Mann, I. P. Teasdale, H. Adams, R. Foresti, C. J. Green and R. Motterlini, *Dalton Trans.*, 2007, **15**, 1500–1508.
- 107 T. Santos-Silva, A. Mukhopadhyay, J. D. Seixas, G. J. L. Bernardes, C. C. Romão and M. J. Romão, *Curr. Med. Chem.*, 2011, **18**, 3361–3366.
- 108 L. Helm and A. E. Merbach, *Coord. Chem. Rev.*, 1999, **187**, 151–181.
- 109 F. Ulbrich, K. B. Kaufmann, A. Meske, W. A. Lagr, M. Augustynik, H. Buerkle, C. C. Ramao, J. Biermann and U. Goebel, *PLoS One*, 2016, **11**, 1–18.
- 110 J. M. Calderón-Montaña, E. Burgos-Morón, M. L. Orta, N. Pastor, C. A. Austin, S. Mateos and M. López-Lázaro, *Toxicol. Lett.*, 2013, **222**, 64–71.
- 111 R.-K. Kim, M.-J. Kim, C.-H. Yoon, E.-J. Lim, K.-C. Yoo, G.-H. Lee, Y.-H. Kim, H. Kim, Y. B. Jin, Y.-J. Lee, C.-G. Cho, Y. S. Oh, M. C. Gye, Y. Suh and S.-J. Lee, *Mol. Pharmacol.*, 2012, **82**, 400–407.
- 112 C. D. Sergeant, I. Ott, A. Sniady, S. Meneni, R. Gust, A. L. Rheingold and R. Dembinski, *Org. Biomol. Chem.*, 2008, **6**, 73–80.
- 113 K. Schmidt, M. Jung, R. Keilitz, B. Schnurr and R. Gust, *Inorganica Chim. Acta*, 2000, **306**, 6–16.
- 114 M. A. Gonzalez, N. L. Fry, R. Burt, R. Davda, A. Hobbs and P. K. Mascharak, *Inorg.*

- Chem.*, 2011, **50**, 3127–3134.
- 115 L. Hewison, S. H. Crook, B. E. Mann, A. J. H. M. Meijer, H. Adams, P. Sawle and R. A. Motterlini, *Organometallics*, 2012, **31**, 5823–5834.
- 116 S. Romanski, B. Kraus, U. Schatzschneider, J.-M. Neudörfl, S. Amslinger and H.-G. Schmalz, *Angew. Chem. Int. Ed. Engl.*, 2011, **50**, 2392–6.
- 117 N. S. Sitnikov, Y. Li, D. Zhang, B. Yard and H.-G. Schmalz, *Angew. Chemie Int. Ed.*, 2015, **54**, 12314–12318.
- 118 Y. Hua and S. Nair, *Biochim. Biophys. Acta*, 2015, **1852**, 195–208.
- 119 C. López-Otín and J. S. Bond, *J. Biol. Chem.*, 2008, **283**, 30433–30437.
- 120 Y. Zheng, B. Yu, Z. Li, Z. Yuan, C. L. Organ, R. K. Trivedi, S. Wang, D. J. Lefer and B. Wang, *Angew. Chemie Int. Ed.*, 2017, **56**, 11749–11753.
- 121 T. Slanina and P. Šebej, *Photochem. Photobiol. Sci.*, 2018, **14**, 213–228.
- 122 E. Kottelat and Z. Fabio, *Inorganics*, 2017, **5**, 24.
- 123 M. A. Wright and J. A. Wright, *Dalton Trans.*, 2016, **45**, 6801–6811.
- 124 R. N. Perutz, O. Torres and A. Vlcek, in *Comprehensive Inorganic Chemistry II (Second Edition)*, Oxford: Elsevier, 2013, vol. 8, pp. 229–253.
- 125 A. Vogel and V. Venugopalan, *Chem. Rev.*, 2003, **103**, 577–644.
- 126 S. Waldchen, J. Lehmann, T. Klein, S. Van De Linde and M. Sauer, *Sci. Rep.*, 2015, **5**, 15348.
- 127 I. Chakraborty, S. J. Carrington and P. K. Mascharak, *Acc. Chem. Res.*, 2014, **47**, 2603–2611.
- 128 V. Yempally, S. J. Kyran, R. K. Raju, W. Y. Fan, E. N. Brothers, D. J. Darensbourg and A. A. Bengali, *Inorg. Chem.*, 2014, **53**, 4081–4088.
- 129 F. Mohr, J. Niesel, U. Schatzschneider and C. W. Lehmann, *Zeitschrift für Anorg. und Allg. Chemie*, 2012, **638**, 543–546.
- 130 J. S. Ward, J. M. Lynam, J. Moir and I. J. S. Fairlamb, *Chem. Eur. J.*, 2014, **20**, 15061–15068.
- 131 J. S. Ward, R. Morgan, J. M. Lynam, I. J. S. Fairlamb and J. W. B. Moir, *Med. Chem. Commun.*, 2017, **8**, 346–352.
- 132 R. Kretschmer, G. Gessner, H. Görls, S. H. Heinemann and M. Westerhausen, *J. Inorg. Biochem.*, 2011, **105**, 6–9.

- 133 R. Mede, M. Klein, R. A. Claus, S. Kriek, S. Quickert, H. Görls, U. Neugebauer, M. Schmitt, G. Gessner, S. H. Heinemann, J. Popp, M. Bauer and M. Westerhausen, *Inorg. Chem.*, 2016, **55**, 104–113.
- 134 S. H. C. Askes, G. U. Reddy, R. Wyrwa, S. Bonnet and A. Schiller, *J. Am. Chem. Soc.*, 2017, **139**, 15292–15295.
- 135 H. Pfeiffer, A. Rojas, J. Niesel and U. Schatzschneider, *Dalton Trans.*, 2009, **22**, 4292.
- 136 H. C. Kolb, M. G. Finn and K. B. Sharpless, *Angew. Chemie Int. Ed.*, 2001, **40**, 2004–2021.
- 137 J. S. Ward, PhD Thesis, University of York, UK, 2014.
- 138 M. Wilchek and E. A. Bayer, *Anal. Biochem.*, 1988, **171**, 1–32.
- 139 F. Zobi, L. Quaroni, G. Santoro, T. Zlateva, O. Blacque, B. Sarafimov, M. C. Schaub and A. Y. Bogdanova, *J. Med. Chem.*, 2013, **56**, 6719–6731.
- 140 C. C. C. R. de Carvalho and P. Fernandes, *Front. Microbiol.*, 2014, **5**, 3845–3855.
- 141 K. Fujita, Y. Tanaka, T. Sho, S. Ozeki, S. Abe, T. Hikage, T. Kuchimaru, S. Kizaka-Kondoh and T. Ueno, *J. Am. Chem. Soc.*, 2014, **136**, 16902–16908.
- 142 K. Fujita, Y. Tanaka, S. Abe and T. Ueno, *Angew. Chemie Int. Ed.*, 2016, **55**, 1056–1060.
- 143 H. Inaba, K. Fujita and T. Ueno, *Biomater. Sci.*, 2015, **3**, 1423–1438.
- 144 U. Hasegawa, A. J. van der Vlies, E. Simeoni, C. Wandrey and J. A. Hubbell, *J. Am. Chem. Soc.*, 2010, **132**, 18273–18280.
- 145 A. E. Pierri, P.-J. Huang, J. V Garcia, J. G. Stanfill, M. Chui, G. Wu, N. Zheng and P. C. Ford, *Chem. Commun.*, 2015, **51**, 2072–2075.
- 146 R. Motterlini, P. Sawle, J. Hammad, S. Bains, R. Alberto, R. Foresti and C. J. Green, *FASEB J.*, 2005, **19**, 284–286.
- 147 D. Wang, E. Viennois, K. Ji, K. Damera, A. Draganov, Y. Zheng, C. Dai, D. Merlin and B. Wang, *Chem. Commun.*, 2014, **50**, 15890–15893.
- 148 X. Ji, C. Zhou, K. Ji, R. E. Aghoghovbia, Z. Pan, V. Chittavong, B. Ke and B. Wang, *Angew. Chemie Int. Ed.*, 2016, **55**, 15846–15851.
- 149 J. T. B. Kueh, N. J. Stanley, R. J. Hewitt, L. M. Woods, L. Larsen, J. C. Harrison, D. Rennison, M. A. Brimble, I. A. Sammut and D. S. Larsen, *Chem. Sci.*, 2017, **8**, 5454–5459.
- 150 P. Peng, C. Wang, Z. Shi, V. K. Johns, L. Ma, J. Oyer, A. Copik, R. Igarashi and Y. Liao, *Org. Biomol. Chem.*, 2013, **11**, 6671.

- 151 L. A. P. Antony, T. Slanina, P. Šebej, T. Šolomek and P. Klán, *Org. Lett.*, 2013, **15**, 4552–4555.
- 152 W. Zhang, A. Tao, T. Lan, G. Cepinskas, R. Kao, C. M. Martin and T. Rui, *Basic Res. Cardiol.*, 2017, **112**, 1–12.
- 153 Y. Wei, P. Chen, M. de Bruyn, W. Zhang, E. Bremer and W. Helfrich, *BMC Gastroenterol.*, 2010, **10**, 42.
- 154 U. Schatzschneider, *Br. J. Pharmacol.*, 2015, **172**, 1638–1650.
- 155 H. M. Southam, T. W. Smith, R. L. Lyon, C. Liao, C. R. Trevitt, L. A. Middlemiss, F. L. Cox, J. A. Chapman, S. F. El-Khamisy, M. Hippler, M. P. Williamson, P. J. F. Henderson and R. K. Poole, *Redox Biol.*, 2018, **18**, 114–123.
- 156 S. McLean, R. Begg, H. E. Jesse, B. E. Mann, G. Sanguinetti and R. K. Poole, *Antioxid. Redox Signal.*, 2013, **19**, 1999–2012.
- 157 A. F. N. Tavares, M. Teixeira, C. C. Romão, J. D. Seixas, L. S. Nobre and L. M. Saraiva, *J. Biol. Chem.*, 2011, **286**, 26708–26717.
- 158 J. L. Wilson, H. E. Jesse, B. Hughes, V. Lund, K. Naylor, K. S. Davidge, G. M. Cook, B. E. Mann and R. K. Poole, *Antioxid. Redox Signal.*, 2013, **19**, 497–509.
- 159 J. S. Ward, J. M. Lynam, J. W. B. B. Moir, D. E. Sanin, A. P. Mountford and I. J. S. S. Fairlamb, *Dalton Trans.*, 2012, **41**, 10514–10517.
- 160 A. J. Atkin, J. M. Lynam, B. E. Moulton, P. Sawle, R. Motterlini, N. M. Boyle, M. T. Pryce and I. J. S. Fairlamb, *Dalton Trans.*, 2011, **40**, 5755.
- 161 Y. Lee and J. Kim, *Anal. Chem.*, 2007, **79**, 7669–7675.
- 162 W. Q. Zhang, A. C. Whitwood, I. J. S. Fairlamb and J. M. Lynam, *Inorg. Chem.*, 2010, **49**, 8941–8952.
- 163 Z. Tao, J. Goodisman and A. K. Souid, *J. Phys. Chem. A*, 2008, **112**, 1511–1518.
- 164 J. Esteban, J. V Ros-Lis, R. Martinez-Manez, M. D. Marcos, M. M, J. Soto and S. F, *Angew. Chem., Int. Ed.*, 2010, **49**, 4934–4937.
- 165 B. W. Michel, A. R. Lippert and C. J. Chang, *J. Am. Chem. Soc.*, 2012, **134**, 15668–15671.
- 166 J. Wang, J. Karpus, B. S. Zhao, Z. Luo, P. R. Chen and C. He, *Angew. Chemie Int. Ed.*, 2012, **51**, 9652–9656.
- 167 R. D. Rimmer, A. E. Pierri and P. C. Ford, *Coord. Chem. Rev.*, 2012, **256**, 1509–1519.
- 168 A. P. Scott and L. Radom, *J. Phys. Chem.*, 1996, **100**, 16502–16513.
- 169 J. Jimenez, I. Chakraborty, A. Dominguez, J. Martinez-Gonzalez, W. M. C. Sameera and

- P. K. Mascharak, *Inorg. Chem.*, 2018, **57**, 1766–1773.
- 170 S. Kyu Kim, S. Pedersen and A. H. Zewail, *Chem. Phys. Lett.*, 1995, **233**, 500–508.
- 171 J. Z. Zhang and C. B. Harris, *J. Chem. Phys.*, 1991, **95**, 4024–4032.
- 172 C. Pollak, A. Rosa and E. J. Baerends, *J. Am. Chem. Soc.*, 1997, **119**, 7324–7329.
- 173 J. A. Calladine, K. Q. Vuong, X. Z. Sun and M. W. George, *Pure Appl. Chem.*, 2009, **81**, 1667–1675.
- 174 C. Ruckebusch, M. Sliwa, P. Pernot, A. de Juan and R. Tauler, *J. Photochem. Photobiol. C Photochem. Rev.*, 2012, **13**, 1–27.
- 175 M. Fei, M. Jarenmark, P. Persson, E. Nordlander and A. Yartsev, *RSC Adv.*, 2016, **6**, 20507–20515.
- 176 A. Vlček Jr., I. R. Farrell, D. J. Liard, P. Matousek, M. Towrie, A. W. Parker, D. C. Grills and M. W. George, *Dalton Trans.*, 2002, **5**, 701–712.
- 177 H.-M. Berends and P. Kurz, *Inorganica Chim. Acta*, 2012, **380**, 141–147.
- 178 R. Dale Rimmer, H. Richter and P. C. Ford, *Inorg. Chem.*, 2010, **49**, 1180–1185.
- 179 S. Hostachy, C. Policar and N. Delsuc, *Coord. Chem. Rev.*, 2017, **351**, 172–188.
- 180 L. C. C. Lee, K. K. Leung and K. K. W. Lo, *Dalton Trans.*, 2017, **46**, 16357–16380.
- 181 A. E. Pierri, A. Pallaoro, G. Wu and P. C. Ford, *J. Am. Chem. Soc.*, 2012, **134**, 18197–18200.
- 182 S. J. Carrington, I. Chakraborty, J. M. L. Bernard and P. K. Mascharak, *Inorg. Chem.*, 2016, **55**, 7852–7858.
- 183 M. Bruce, B. Goodall and I. Matsuda, *Aust. J. Chem.*, 1975, **28**, 1259–1264.
- 184 J. S. Ward, J. T. W. Bray, B. J. Aucott, C. Wagner, N. E. Pridmore, A. C. Whitwood, J. W. B. Moir, J. M. Lynam and I. J. S. Fairlamb, *Eur. J. Inorg. Chem.*, 2016, **2016**, 5044–5051.
- 185 N. C. Bruno, M. T. Tudge and S. L. Buchwald, *Chem. Sci.*, 2013, **4**, 916–920.
- 186 J. M. Butler, M. W. George, J. R. Schoonover, D. M. Dattelbaum and T. J. Meyer, *Coord. Chem. Rev.*, 2007, **251**, 492–514.
- 187 C. Daniel, *Coord. Chem. Rev.*, 2015, **282–283**, 19–32.
- 188 T. J. Meyer and J. V. Caspar, *Chem. Rev.*, 1985, **85**, 187–218.
- 189 A. Waldman, S. Ruhman, S. Shaik and G. N. Sastry, *Chem. Phys. Lett.*, 1994, **230**, 110–116.

- 190 A. Fox, A. Poe and R. Ruminski, *J. Am. Chem. Soc.*, 1982, **104**, 7327–7329.
- 191 P. Rudolf, F. Kanal, J. Knorr, C. Nagel, J. Niesel, T. Brixner, U. Schatzschneider and P. Nuernberger, *J. Phys. Chem. Lett.*, 2013, **4**, 596–602.
- 192 T. P. Dougherty and E. J. Heilweil, *Chem. Phys. Lett.*, 1994, **227**, 19–25.
- 193 T. Lian, S. E. Bromberg, M. C. Asplund, H. Yang and C. B. Harris, *J. Phys. Chem.*, 1996, **100**, 11994–12001.
- 194 S. McMahon, J. Rochford, Y. Halpin, J. C. Manton, E. C. Harvey, G. M. Greetham, I. P. Clark, A. D. Rooney, C. Long and M. T. Pryce, *Phys. Chem. Chem. Phys.*, 2014, **16**, 21230–21233.
- 195 S. McMahon, S. Amirjalayer, W. J. Buma, Y. Halpin, C. Long, A. D. Rooney, S. Woutersen and M. T. Pryce, *Dalton Trans.*, 2015, **44**, 15424–15434.
- 196 J. P. Lomont, S. C. Nguyen and C. B. Harris, *Organometallics*, 2014, **33**, 6179–6185.
- 197 A. Vlček, *Coord. Chem. Rev.*, 2002, **230**, 225–242.
- 198 D. Guillaumont, C. Daniel and A. Vlcek, *Inorg. Chem.*, 1997, **36**, 1684–1688.
- 199 R. W. Balk, T. Snoeck, D. J. Stufkens and A. Oskam, *Inorg. Chem.*, 1980, **19**, 3015–3021.
- 200 I. R. Farrell, P. Matousek, M. Towrie, A. W. Parker, D. C. Grills, M. W. George and A. Vlček, *Inorg. Chem.*, 2002, **41**, 4318–4323.
- 201 I. G. Virrels, M. W. George, J. J. Turner, J. Peters and A. Vlček, *Organometallics*, 1996, **15**, 4089–4092.
- 202 J. Víchová, F. Hartl and A. Vlček, *J. Am. Chem. Soc.*, 1992, **114**, 10903–10910.
- 203 D. Guillaumont, A. Vlček, and C. Daniel, *J. Phys. Chem. A*, 2001, **105**, 1107–1114.
- 204 S. Záliš, I. R. Farrell, A. Vlček and A. Vlček, *J. Am. Chem. Soc.*, 2003, **125**, 4580–4592.
- 205 E. Baerends, *Coord. Chem. Rev.*, 1998, **177**, 97–125.
- 206 S. Villaume, A. Strich, C. Daniel, S. A. Perera and R. J. Bartlett, *Phys. Chem. Chem. Phys.*, 2007, **9**, 6115.
- 207 S. A. Trushin, K. Kosma, W. Fuß and W. E. Schmid, *Chem. Phys.*, 2008, **347**, 309–323.
- 208 K. Pierloot, E. Tsokos and L. G. Vanquickenborne, *J. Phys. Chem.*, 1996, **100**, 16545–16550.
- 209 A. Vlcek Jr., *Coord. Chem. Rev.*, 1998, **177**, 219–256.
- 210 G. M. Greetham, D. Sole, I. P. Clark, A. W. Parker, M. R. Pollard and M. Towrie, in *Review of Scientific Instruments*, 2012, vol. 83.

- 211 F. A. Cotton and C. S. Kraihanzel, *J. Am. Chem. Soc.*, 1962, **84**, 4432–4438.
- 212 A. Vlcek, F.-W. Gravelis and T. L. Snoeck Dark J Stufkens, *Inorganica Chim. Acta*, 1998, **278**, 83–90.
- 213 M. George and J. J. Turner, *Coord. Chem. Rev.*, 1998, **177**, 201–217.
- 214 J. M. Andersen and J. R. Moss, *Organometallics*, 1994, **13**, 5013–5020.
- 215 F. J. G. Alonso, A. Llamazares, V. Riera, M. Vivanco, M. R. Díaz and S. G. Granda, *J. Chem. Soc., Chem. Commun.*, 1991, **4**, 1058–1060.
- 216 W. T. Boese and P. C. Ford, *J. Am. Chem. Soc.*, 1995, **117**, 8381–8391.
- 217 A. S. Weller, F. M. Chadwick and A. I. McKay, *Adv. Organomet. Chem.*, 2016, **66**, 223–276.
- 218 A. J. Cowan and M. W. George, *Coord. Chem. Rev.*, 2008, **252**, 2504–2511.
- 219 G. I. Childs, D. C. Grills, X. Z. Sun and M. W. George, *Pure. Appl. Chem.*, 2001, **73**, 443–447.
- 220 S. P. Church, F. W. Gravelis, H. Hermann and K. Schaffner, *Inorg. Chem.*, 1985, **24**, 418–422.
- 221 J. M. Kelly, D. V Bent, H. Hermann, D. Schulte-Frohlinde and E. Koerner Von Gustorf, *J. Organomet. Chem.*, 1974, **69**, 259–269.
- 222 L. Biber, D. Reuvenov, T. Revzin, T. Sinai, A. Zahavi and R. H. Schultz, *Dalton Trans.*, 2007, **5**, 41–51.
- 223 R. Krishnan and R. H. Schultz, *Organometallics*, 2001, **20**, 3314–3322.
- 224 U. Prinz, U. Koelle, S. Ulrich, A. E. Merbach, O. Maas and K. Hegetschweiler, *Inorg. Chem.*, 2004, **43**, 2387–2391.
- 225 M. D. Clerk and M. J. Zaworotko, *J. Chem. Soc. Chem. Commun.*, 1991, **774**, 1607–1608.
- 226 P. W. Atkins and J. de Paula, in *Physical Chemistry*, Oxford University Press, Ninth Edit., 2010, pp. 831–875.
- 227 J. E. Shanoski, E. A. Glascoe and C. B. Harris, *J. Phys. Chem. B*, 2006, **110**, 996–1005.
- 228 M. Gómez-Gallego and M. A. Sierra, *Chem. Rev.*, 2011, **111**, 4857–4963.
- 229 R. Battino, S. Bo, H. L. Clever, J. C. Gjaldbaek, D. A. Wiesenburg, E. Wilhelm, Y. P. Yampolskii and C. Young, *Solubility Data Series: Volume 43 Carbon Monoxide*, Pergamon Press, Oxford, 1990.
- 230 X.-Z. Sun, D. C. Grills, S. M. Nikiforov, M. Poliakoff and M. W. George, *J. Am. Chem.*

- Soc.*, 1997, **119**, 7521–7525.
- 231 B. E. Moulton, PhD Thesis, University of York, UK, 2008.
- 232 M. Katari, E. Nicol, V. Steinmetz, G. van der Rest, D. Carmichael and G. Frison, *Chem. Eur. J.*, 2017, **23**, 8414–8423.
- 233 M. K. Kesharwani, B. Brauer and J. M. L. Martin, *J. Phys. Chem. A*, 2015, **119**, 1701–1714.
- 234 D. J. Lawes, S. Geftakis and G. E. Ball, *J. Am. Chem. Soc.*, 2005, **127**, 4134–4135.
- 235 O. Torres, J. A. Calladine, S. B. Duckett, M. W. George and R. N. Perutz, *Chem. Sci.*, 2015, **6**, 418–424.
- 236 J. A. Calladine, S. B. Duckett, M. W. George, S. L. Matthews, R. N. Perutz, O. Torres and K. Q. Vuong, *J. Am. Chem. Soc.*, 2011, **133**, 2303–2310.
- 237 S. Geftakis and G. E. Ball, *J. Am. Chem. Soc.*, 1998, **120**, 9953–9954.
- 238 M. D. Walter, P. S. White, C. K. Schauer and M. Brookhart, *J. Am. Chem. Soc.*, 2013, **135**, 15933–15947.
- 239 B. Zhou, P. Ma, H. Chen and C. Wang, *Chem. Commun.*, 2014, **50**, 14558–14561.
- 240 W. Liu, J. Bang, Y. Zhang and L. Ackermann, *Angew. Chemie Int. Ed.*, 2015, **54**, 14137–14140.
- 241 B. Zhou, H. Chen and C. Wang, *J. Am. Chem. Soc.*, 2013, **135**, 1264–1267.
- 242 N. P. Yahaya, K. M. Appleby, M. Teh, C. Wagner, E. Troschke, J. T. W. Bray, S. B. Duckett, L. A. Hammarback, J. S. Ward, J. Milani, N. E. Pridmore, A. C. Whitwood, J. M. Lynam and I. J. S. Fairlamb, *Angew. Chemie Int. Ed.*, 2016, **55**, 12455–12459.
- 243 J. R. Carney, B. R. Dillon and S. P. Thomas, *Eur. J. Org. Chem.*, 2016, **2016**, 3912–3929.
- 244 L. A. Hammarback, I. P. Clark, I. V. Sazanovich, M. Towrie, A. Robinson, F. Clarke, I. J. S. Fairlamb and J. M. Lynam, *Nat. Catal.*, 2018, **1**, 830–840.
- 245 P. J. Dyson and P. G. Jessop, *Catal. Sci. Technol.*, 2016, **6**, 3302–3316.
- 246 H. M. Chase, T. J. McDonough, K. R. Overly and C. M. Laperle, *J. Phys. Org. Chem.*, 2013, **26**, 322–326.
- 247 U. Schatzschneider, *Inorganica Chim. Acta*, 2011, **374**, 19–23.
- 248 F. Schafer and G. Buettner, *Free Radic. Biol. Med.*, 2001, **30**, 1191–1212.
- 249 A. A. Dombkowski, K. Z. Sultana and D. B. Craig, *FEBS Lett.*, 2014, **588**, 206–212.
- 250 C. V. Smith, D. P. Jones, T. M. Guenther, L. H. Lash and B. H. Lauterburg, *Toxicol.*

- Appl. Pharmacol.*, 1996, **140**, 1–12.
- 251 E. H. Sarsour, M. G. Kumar, L. Chaudhuri, A. L. Kalen and P. C. Goswami, *Antioxid. Redox Signal.*, 2009, **11**, 2985–3011.
- 252 C. Hwang, A. Sinskey and H. Lodish, *Science*, 1992, **257**, 1496–1502.
- 253 T. Finkel, *J. Cell Biol.*, 2011, **194**, 7–15.
- 254 C. C. Winterbourn, A. J. Kettle and M. B. Hampton, *Annu. Rev. Biochem.*, 2016, **85**, 765–792.
- 255 T. Soboleva, H. J. Esquer, A. D. Benninghoff and L. M. Berreau, *J. Am. Chem. Soc.*, 2017, **139**, 9435–9438.
- 256 B. Liu, J. Wang, G. Zhang, R. Bai and Y. Pang, *ACS Appl. Mater. Interfaces*, 2014, **6**, 4402–4407.
- 257 G. Upendar Reddy, J. Axthelm, P. Hoffmann, N. Taye, S. Gläser, H. Görls, S. L. Hopkins, W. Plass, U. Neugebauer, S. Bonnet and A. Schiller, *J. Am. Chem. Soc.*, 2017, **139**, 4991–4994.
- 258 J. W. Hersherberger and J. K. Kochi, *Polyhedron*, 1983, **2**, 929–934.
- 259 R. A. Yeary, *Toxicol. Appl. Pharmacol.*, 1969, **15**, 666–676.
- 260 M. Patra and G. Gasser, *Nat. Rev. Chem.*, 2017, **1**, 66.
- 261 C. Ornelas, *New J. Chem.*, 2011, **35**, 1973.
- 262 D. Dive and C. Biot, *ChemMedChem*, 2008, **3**, 383–391.
- 263 T. Lozano-Cruz, P. Ortega, B. Batanero, J. L. Copa-Patiño, J. Soliveri, F. J. de la Mata and R. Gómez, *Dalton Trans.*, 2015, **44**, 19294–19304.
- 264 M. Wenzel, M. Patra, C. H. R. Senges, I. Ott, J. J. Stepanek, A. Pinto, P. Prochnow, C. Vuong, S. Langklotz, N. Metzler-Nolte and J. E. Bandow, *ACS Chem. Biol.*, 2013, **8**, 1442–1450.
- 265 Z. H. Chohan, *Appl. Organomet. Chem.*, 2006, **20**, 112–116.
- 266 M. A. Divakar, V. Sudhamani, S. Shanmugam, T. Muneeswaran, S. Tamilzhalagan, M. Ramakritinan and K. Ganesan, *RSC Adv.*, 2015, **5**, 8362–8370.
- 267 W. A. Wani, E. Jameel, U. Baig, S. Mumtazuddin and L. T. Hun, *Eur. J. Med. Chem.*, 2015, **101**, 534–551.
- 268 T. N. Wells and R. H. van Huijsduijnen, *Lancet Infect. Dis.*, 2015, **15**, 1365–1366.
- 269 J. Held, C. Supan, C. L. O. Salazar, H. Tinto, L. N. Bonkian, A. Nahum, B. Moulero, A.

- Sié, B. Coulibaly, S. B. Sirima, M. Siribie, N. Otsyula, L. Otieno, A. M. Abdallah, R. Kimutai, M. Bouyou-Akotet, M. Kombila, K. Koiwai, C. Cantalloube, C. Din-Bell, E. Djeriou, J. Waitumbi, B. Mordmüller, D. Ter-Minassian, B. Lell and P. G. Kremsner, *Lancet Infect. Dis.*, 2015, **15**, 1409–1419.
- 270 N. Chavain, H. Vezin, D. Dive, N. Touati, J.-F. Paul, E. Buisine and C. Biot, *Mol. Pharm.*, 2008, **5**, 710–716.
- 271 E. Hillard, A. Vessières, L. Thouin, G. Jaouen and C. Amatore, *Angew. Chemie Int. Ed.*, 2005, **45**, 285–290.
- 272 A. Kondratskyi, K. Kondratska, F. Vanden Abeele, D. Gordienko, C. Dubois, R.-A. Toillon, C. Slomianny, S. Lemièrre, P. Delcourt, E. Dewailly, R. Skryma, C. Biot and N. Prevarskaya, *Sci. Rep.*, 2017, **7**, 15896.
- 273 G. Jaouen, A. Vessières and S. Top, *Chem. Soc. Rev.*, 2015, **44**, 8802–8817.
- 274 A. Vessières, C. Corbet, J. M. Heldt, N. Lories, N. Jouy, I. Laios, G. Leclercq, G. Jaouen and R.-A. Toillon, *J. Inorg. Biochem.*, 2010, **104**, 503–511.
- 275 C. Bruyère, V. Mathieu, A. Vessières, P. Pigeon, S. Top, G. Jaouen and R. Kiss, *J. Inorg. Biochem.*, 2014, **141**, 144–151.
- 276 H. D. Kaesz, R. Bau, D. Hendrickson and J. Michael Smith, *J. Am. Chem. Soc.*, 1967, **89**, 2844–2851.
- 277 N. P. Robinson, G. J. Depree, R. W. de Wit, L. Main and B. K. Nicholson, *J. Organomet. Chem.*, 2005, **690**, 3827–3837.
- 278 K. Sünkel and S. Bernhartzeder, *J. Organomet. Chem.*, 2011, **696**, 1536–1540.
- 279 D. Plażuk, B. Rychlik, A. Błauż and S. Domagała, *J. Organomet. Chem.*, 2012, **715**, 102–112.
- 280 M. S. Inkpen, S. Du, M. Driver, T. Albrecht and N. J. Long, *Dalton Trans.*, 2013, **42**, 2813–2816.
- 281 S. M. Ghodse and V. N. Telvekar, *Tetrahedron Lett.*, 2017, **58**, 524–526.
- 282 D. Johnson, MChem Thesis, University of York, UK, 2018.
- 283 B. Floris and G. Illuminati, *J. Organomet. Chem.*, 1978, **150**, 101–113.
- 284 M. Cariello, S. Ahn, K.-W. Park, S.-K. Chang, J. Hong and G. Cooke, *RSC Adv.*, 2016, **6**, 9132–9138.
- 285 J. Fernández-Ariza, R. M. Krick Calderón, J. Perles, M. S. Rodríguez-Morgade, D. M. Guldi and T. Torres, *Chem. Commun.*, 2017, **53**, 8525–8528.

- 286 X. Wang, S. Min, S. K. Das, W. Fan, K.-W. Huang and Z. Lai, *J. Catal.*, 2017, **355**, 101–109.
- 287 J. Rajput, J. R. Moss, A. T. Hutton, D. T. Hendricks, C. E. Arendse and C. Imrie, *J. Organomet. Chem.*, 2004, **689**, 1553–1568.
- 288 C. Imrie, C. Loubser, P. Engelbrecht and C. W. McClelland, *J. Chem. Soc. Perkin Trans.*, 1999, **17**, 2513–2523.
- 289 P. Tagliatesta, A. Lembo and A. Leoni, *New J. Chem.*, 2013, **37**, 3416–3419.
- 290 S. G. Andrew, MChem Thesis, University of York, UK.
- 291 A. M. Bond, K. B. Oldham and G. A. Snook, *Anal. Chem.*, 2000, **72**, 3492–3496.
- 292 N. G. Tsierkezos, *J. Solution Chem.*, 2007, **36**, 289–302.
- 293 A. J. Bard and L. R. Faulkner, in *Electrochemical Methods: Fundamentals and Applications*, Wiley, 1980, pp. 226–260.
- 294 N. G. Connelly and W. E. Geiger, *Chem. Rev.*, 1996, **96**, 877–910.
- 295 R. Mede, S. Gläser, B. Suchland, B. Schowtka, M. Mandel, H. Görls, S. Kriek, A. Schiller and M. Westerhausen, *Inorganics*, 2017, **5**, 8.
- 296 P. Kopf-Maier, H. Kopf and E. W. Neuse, *J. Cancer Res. Clin. Oncol.*, 1984, **108**, 336–340.
- 297 B. J. Aucott, J. S. Ward, S. G. Andrew, J. Milani, A. C. Whitwood, J. M. Lynam, A. Parkin and I. J. S. Fairlamb, *Inorg. Chem.*, 2017, **56**, 5431–5440.
- 298 M. A. Gonzalez, M. A. Yim, S. Cheng, A. Moyes, A. J. Hobbs and P. K. Mascharak, *Inorg. Chem.*, 2012, **51**, 601–608.
- 299 M. A. Gonzalez, S. J. Carrington, N. L. Fry, J. L. Martinez and P. K. Mascharak, *Inorg. Chem.*, 2012, **51**, 11930–11940.
- 300 S. J. Carrington, I. Chakraborty and P. K. Mascharak, *Chem. Commun.*, 2013, **49**, 11254.
- 301 E. Kottelat, A. Ruggi and F. Zobi, *Dalton Trans.*, 2016, **45**, 6920–6927.
- 302 R. F. Heck, *J. Am. Chem. Soc.*, 1968, **90**, 313–317.
- 303 M. I. Bruce, B. L. Goodall and F. G. A. Stone, *J. Chem. Soc. Dalton Trans.*, 1978, **7**, 687–694.
- 304 Y. Okada and Z. Morita, *Dye. Pigment.*, 1992, **18**, 259–270.
- 305 M. M. Tauber, G. M. Guebitz and A. Rehorek, *Appl. Environmental Microbiol.*, 2005, **71**, 2600–2607.

- 306 E. Merino, *Chem. Soc. Rev.*, 2011, **40**, 3835–3853.
- 307 World Health Organization, *WHO Model List of Essential Medicines - 20th List*, 2017.
- 308 O. H. Nielsen and L. K. Munck, *Nat. Clin. Pract. Gastroenterol. Hepatol.*, 2007, **4**, 160–170.
- 309 Y. Niu, J. Huang, C. Zhao, P. Gao and Y. Yu, *Acta Crystallogr. Sect. E Struct. Reports Online*, 2011, **67**, 2671.
- 310 W. Lu and C. Xi, *Tetrahedron Lett.*, 2008, **49**, 4011–4015.
- 311 H. Ma, W. Li, J. Wang, G. Xiao, Y. Gong, C. Qi, Y. Feng, X. Li, Z. Bao, W. Cao, Q. Sun, C. Veaceslav, F. Wang and Z. Lei, *Tetrahedron*, 2012, **68**, 8358–8366.
- 312 M. I. Bruce, M. Z. Iqbal and F. G. A. Stone, *J. Chem. Soc.*, 1970, 3204–3209.
- 313 R. Bennett, M. Bruce, B. Goodall and F. Stone, *Aust. J. Chem.*, 1974, **27**, 2131–2133.
- 314 M. Bruce, M. Liddell, M. Snow and E. Tiekink, *Aust. J. Chem.*, 1988, **41**, 1407–1415.
- 315 A. Hafner, L. S. Hegedus, G. deWeck, B. Hawkins and K. H. Dötz, *J. Am. Chem. Soc.*, 1988, **110**, 8413–8421.
- 316 F. Bureš, *RSC Adv.*, 2014, **4**, 58826–58851.
- 317 T. Fujii, Y. Hara, T. Osawa, H. Kashida, X. Liang, Y. Yoshida and H. Asanuma, *Chem. Eur. J.*, 2012, **18**, 10865–10872.
- 318 D. H. McDaniel and H. C. Brown, *J. Org. Chem.*, 1958, **23**, 420–427.
- 319 I. R. Farrell, P. Matousek and A. Vlček, *J. Am. Chem. Soc.*, 1999, **121**, 5296–5301.
- 320 A. Vlček, *Coord. Chem. Rev.*, 2000, **200**, 933–977.
- 321 J. L. Sadler and A. J. Bard, *J. Am. Chem. Soc.*, 1968, **90**, 1979–1989.
- 322 B. K. G. Boto and F. G. Thomas, *Aust. J. Chem.*, 1973, **26**, 1251–8.
- 323 K. G. Boto and F. G. Thomas, *Aust. J. Chem.*, 1971, **24**, 975–80.
- 324 D. M. Peloquin, D. R. Dewitt, S. S. Patel, J. W. Merkert, B. T. Donovan-Merkert and T. A. Schmedake, *Dalton Trans.*, 2015, **44**, 18723–18726.
- 325 Q. Lin, Q. Li, C. Batchelor-McAuley and R. G. Compton, *J. Phys. Chem. C*, 2015, **119**, 1489–1495.
- 326 H. M. D. Bandara and S. C. Burdette, *Chem. Soc. Rev.*, 2012, **41**, 1809–1825.
- 327 J. J. Walsh, C. L. Smith, G. Neri, G. F. S. Whitehead, C. M. Robertson and A. J. Cowan, *Faraday Discuss.*, 2015, **183**, 147–160.

- 328 C. Riplinger, M. D. Sampson, A. M. Ritzmann, C. P. Kubiak and E. A. Carter, *J. Am. Chem. Soc.*, 2014, **136**, 16285–16298.
- 329 M. Bourrez, F. Molton, S. Chardon-Noblat and A. Deronzier, *Angew. Chemie Int. Ed.*, 2011, **50**, 9903–9906.
- 330 J. M. Smieja, M. D. Sampson, K. A. Grice, E. E. Benson, J. D. Froehlich and C. P. Kubiak, *Inorg. Chem.*, 2013, **52**, 2484–2491.
- 331 G. Uden and J. Bongaerts, *Biochim. Biophys. Acta Bioenerg.*, 1997, **1320**, 217–234.
- 332 N. Huther, P. T. McGrail and A. F. Parsons, *Eur. J. Org. Chem.*, 2004, 1740–1749.
- 333 E. J. Yoo, M. Ahlquist, I. Bae, K. B. Sharpless, V. V. Fokin and S. Chang, *J. Org. Chem.*, 2008, **73**, 5520–5528.
- 334 L. Liu, D. Huang, S. M. Draper, X. Yi, W. Wu and J. Zhao, *Dalton Trans.*, 2013, **42**, 10694–10706.
- 335 S. Ast, H. Muller, R. Flehr, T. Klamroth, B. Walz and H. Holdt, *Chem. Commun.*, 2011, **47**, 4685–4687.
- 336 T. Schwarze, J. Riemer, S. Eidner and H. Holdt, *Chem. Eur. J.*, 2015, **21**, 11306–11310.
- 337 S. Ast, T. Schwarze, H. Muller, A. Sukhanov, S. Michaelis, J. Wegener, O. S. Wolfbeis, T. Korzdorfer, A. Durkop and H. Holdt, *Chem. Eur. J.*, 2013, **19**, 14911–14917.
- 338 A. Wu, J. L. Kolanowski, B. B. Boumelhem, K. Yang, R. Lee, A. Kaur, S. T. Fraser, E. J. New and L. M. Rendina, *Chem. Asian J.*, 2017, **12**, 1704–1708.
- 339 E. H. El-mossalamy, A. Y. Obaid and S. A. El-daly, *Opt. Laser Technol.*, 2011, **43**, 1078–1083.
- 340 D. Lee, G. Kim and H. Kim, *Tetrahedron Lett.*, 2009, **50**, 4766–4768.
- 341 M. Timm, L. Saaby, L. Moesby and E. W. Hansen, *Cytotechnology*, 2013, **65**, 887–894.
- 342 W. W. Souba and A. J. Pacitti, *J. Parenter. Enter. Nutr.*, 1992, **16**, 569–578.
- 343 M. A. Peppercorn and P. Goldman, *J. Pharmacol. Exp. Ther.*, 1972, **181**, 555–562.
- 344 H. Chen, *Microbiology*, 2005, **151**, 1433–1441.
- 345 Z. Mandić, B. Nigović and B. Šimunić, *Electrochim. Acta*, 2004, **49**, 607–615.
- 346 H. Nohl, W. Jordan and R. J. Youngman, *Adv. Free Radic. Biol. Med.*, 1986, **2**, 211–279.
- 347 D. J. Darensbourg, K. K. Klausmeyer and J. H. Reibenspies, *Inorg. Chem.*, 1996, **35**, 1529–1534.
- 348 R. M. Ramadan, *J. Coord. Chem. J Coord. Chem*, 1997, **42342**, 181–187.

- 349 D. Weir and J. K. S. Wan, *J. Organomet. Chem.*, 1981, **220**, 323–331.
- 350 K. Fernandez, MChem Thesis, University of York, UK, 2017.
- 351 A. J. Reay, L. A. Hammarback, J. T. W. Bray, T. Sheridan, D. Turnbull, A. C. Whitwood and I. J. S. Fairlamb, *ACS Catal.*, 2017, **7**, 5174–5179.
- 352 G. M. Greetham, P. Burgos, Q. Cao, I. P. Clark, P. S. Codd, R. C. Farrow, M. W. George, M. Kogimtzis, P. Matousek, A. W. Parker, M. R. Pollard, D. A. Robinson, Z.-J. Xin and M. Towrie, *Appl. Spectrosc.*, 2010, **64**, 1311–1319.
- 353 R. Compton and G. Sanders, in *Electrode Potentials*, Oxford Science Publications, 1998.
- 354 O. V. Dolomanov, L. J. Bourhis, R. J. Gildea, J. A. K. Howard and H. Puschmann, *J. Appl. Crystallogr.*, 2009, **42**, 339–341.
- 355 L. Palatinus, S. J. Prathapa and S. van Smaalen, *J. Appl. Crystallogr.*, 2012, **45**, 575–580.
- 356 L. Palatinus and G. Chapuis, *J. Appl. Crystallogr.*, 2007, **40**, 786–790.
- 357 L. Palatinus and A. van der Lee, *J. Appl. Crystallogr.*, 2008, **41**, 975–984.
- 358 G. M. Sheldrick, *Acta Crystallogr. Sect. A Found. Crystallogr.*, 2008, **64**, 112–122.
- 359 G. R. Fulmer, A. J. M. Miller, N. H. Sherden, H. E. Gottlieb, A. Nudelman, B. M. Stoltz, J. E. Bercaw and K. I. Goldberg, *Organometallics*, 2010, **29**, 2176–2179.
- 360 K. Nakamoto, *Infrared and Raman Spectra of Inorganic and Coordination Compounds Part B*, 2009.
- 361 I. Capanec, M. Litvić, J. Udiković, I. Pogorelić and M. Lovrić, *Tetrahedron*, 2007, **63**, 5614–5621.
- 362 L. S. Runtsch, D. M. Barber, P. Mayer, M. Groll, D. Trauner and J. Broichhagen, *Beilstein J. Org. Chem.*, 2015, **11**, 1129–1135.
- 363 T. H. L. Nguyen, N. Gigant, S. Delarue-Cochin and D. Joseph, *J. Org. Chem.*, 2016, **81**, 1850–1857.
- 364 X. Zeng, A. S. Batsanov and M. R. Bryce, *J. Org. Chem.*, 2006, **71**, 9589–9594.
- 365 F. Jafarpour, N. Jalalimanesh, M. B. A. Olia and A. O. Kashani, *Tetrahedron*, 2010, **66**, 9508–9511.